

7F

AGARD-R-741

AGARD-R-741

0.2

JUN 5 1971

AGARD

ADVISORY GROUP FOR AEROSPACE RESEARCH & DEVELOPMENT

7 RUE ANCELLE 92200 NEUILLY SUR SEINE FRANCE

AGARD REPORT No.741

Computation of Three-Dimensional Boundary Layers Including Separation

PROPERTY OF U.S. AIR FORCE
AEDC TECHNICAL LIBRARY

NORTH ATLANTIC TREATY ORGANIZATION



DISTRIBUTION AND AVAILABILITY

ON BACK COVER

TECHNICAL REPORTS
FILE COPY

PROPERTY OF U.S. AIR FORCE
AEDC TECHNICAL LIBRARY

PROPERTY OF U.S. AIR FORCE
AEDC TECHNICAL LIBRARY
ARNOLD AFB, TN 37389

NORTH ATLANTIC TREATY ORGANIZATION
ADVISORY GROUP FOR AEROSPACE RESEARCH AND DEVELOPMENT
(ORGANISATION DU TRAITE DE L'ATLANTIQUE NORD)

AGARD Report No.741
**COMPUTATION OF THREE-DIMENSIONAL BOUNDARY LAYERS
INCLUDING SEPARATION**

The material assembled in this book was prepared under the combined sponsorship of the Fluid Dynamics Panel, the von Kármán Institute and the Consultant and Exchange Program of AGARD and was presented as an AGARD Special Course at the von Kármán Institute, Rhode-St-Genèse, Belgium on 14—18 April 1986.

THE MISSION OF AGARD

The mission of AGARD is to bring together the leading personalities of the NATO nations in the fields of science and technology relating to aerospace for the following purposes:

- Exchanging of scientific and technical information;
- Continuously stimulating advances in the aerospace sciences relevant to strengthening the common defence posture;
- Improving the co-operation among member nations in aerospace research and development;
- Providing scientific and technical advice and assistance to the Military Committee in the field of aerospace research and development (with particular regard to its military application);
- Rendering scientific and technical assistance, as requested, to other NATO bodies and to member nations in connection with research and development problems in the aerospace field;
- Providing assistance to member nations for the purpose of increasing their scientific and technical potential;
- Recommending effective ways for the member nations to use their research and development capabilities for the common benefit of the NATO community.

The highest authority within AGARD is the National Delegates Board consisting of officially appointed senior representatives from each member nation. The mission of AGARD is carried out through the Panels which are composed of experts appointed by the National Delegates, the Consultant and Exchange Programme and the Aerospace Applications Studies Programme. The results of AGARD work are reported to the member nations and the NATO Authorities through the AGARD series of publications of which this is one.

Participation in AGARD activities is by invitation only and is normally limited to citizens of the NATO nations.

The content of this publication has been reproduced
directly from material supplied by AGARD or the authors.

Published February 1987

Copyright © AGARD 1987
All Rights Reserved

ISBN 92-835-0407-0



*Printed by Specialised Printing Services Limited
40 Chigwell Lane, Loughton, Essex IG10 3TZ*

PREFACE

The aim of this special course was to present the current state of knowledge on three-dimensional boundary layer computations. The emphasis was placed on turbulent boundary layers which develop on wings or fuselages including separation.

Introductory lectures presented basic information about the fundamental equations, boundary and initial conditions, coordinate systems, integral and differential methods, turbulence models, and interactive procedures.

The discussion of experimental aspects of three-dimensional boundary layers was directed towards the use of fundamental experiments to improve models for turbulence and for transition.

A review of various calculation methods was given: it included the presentation of available techniques for calculating transition and the discussion of turbulence models. In addition, a few lectures were devoted to the evaluation of results of boundary layer calculations with regard to design aerodynamics, in particular when boundary layer separation is involved.

An important part of the course was reserved for viscous-inviscid interactive schemes. The numerical procedures were described in detail and applications were presented.

Finally, the calculation of corner and tip region flows was discussed.

SPECIAL COURSE STAFF

Special Course Director: Mr J.Cousteix
Complexe Aérospatial de Lespinet
2 Avenue Edouard Belin
B.P. 4025
31055 Toulouse Cedex
France

LECTURERS

Dr D.Arnal
ONERA/CERT
Dept d'Aérodynamique
B.P. 4025
2 Avenue Edouard Belin
31055 Toulouse Cedex
France

Mr J.C.Le Balleur
ONERA
B.P. 72
92322 Châtillon
France

Prof. Dr E.H.Hirschel
MBB-LKE 122
Postfach 80 11 60
D-8000 München 80
Federal Republic of Germany

Dr B.van den Berg
NLR
Anthony Fokkerweg 2
1059 Amsterdam
Netherlands

Dr P.Bradshaw
Imperial College
Dept. of Aeronautics
Prince Consort Road
London SW7 2BY
United Kingdom

Dr T.Cebeci
Douglas Aircraft Company
3855 Lakewood Boulevard
Long Beach
CA 90846
USA

Dr T.R.Govindan
Scientific Associate Incorporation
P.O. Box 498
Glastonbury
Connecticut 06033
USA

LOCAL COORDINATOR

Professor M.Carbonaro
Von Kármán Institute for Fluid Dynamics
Chaussée de Waterloo 72
B-1640 Rhode-Saint-Genèse
Belgium

AGARD REPRESENTATIVE

Mr R.H.Rollins II
Fluid Dynamics Panel Executive
AGARD
7 rue Ancelle
92200 Neuilly-sur-Seine
France

CONTENTS

	Page
PREFACE	iii
SPECIAL COURSE STAFF	iv
	Reference
THREE-DIMENSIONAL BOUNDARY LAYERS. INTRODUCTION TO CALCULATION METHODS by J.Cousteix	1
PHYSICS AND MODELLING OF THREE-DIMENSIONAL BOUNDARY LAYERS by P.Bradshaw	2
THREE-DIMENSIONAL SHEAR LAYER EXPERIMENTS AND THEIR USE AS TEST CASES FOR CALCULATION METHODS by B.van den Berg	3
THREE-DIMENSIONAL BOUNDARY LAYERS: LAMINAR-TURBULENT TRANSITION by D.Arnal	4
EVALUATION OF RESULTS OF BOUNDARY-LAYER CALCULATIONS WITH REGARD TO DESIGN AERODYNAMICS by E.H.Hirschel	5
AN APPROACH TO PRACTICAL AERODYNAMIC CALCULATIONS by T.Cebeci	6
PROGRESS IN VISCOUS-INVISCID SOLVERS (VIS) by J.C.Le Balleur	7
COMPUTATION OF TIP AND CORNER REGION FLOWS by Tr. Govindam and H.McDonald	8

THREE-DIMENSIONAL BOUNDARY LAYERS. INTRODUCTION TO CALCULATION METHODS

Jean COUSTEIX

Office National d'Etudes et de Recherches Aérospatiales
Centre d'Etudes et de Recherches de TOULOUSE
Département d'aérothermodynamique
2 avenue Edouard Belin - 31055 TOULOUSE Cedex (FRANCE)

SUMMARY

This paper gives an outline of problems encountered when faced with the calculation of three-dimensional boundary layers. The various topics which are discussed are : geometry of axis-systems, boundary layer equations, global equations, nature of the system of equations, integral methods, singularities in boundary layer calculations, numerical techniques, turbulence modelling.

The classification of flows into mono-, two- and three-dimensional flows is clear as far as laminar flows are considered. In a turbulent flow, the definitions need to be completed because turbulence is always three-dimensional. As it is usual to do in most analyses, any characteristic of a turbulent flow is decomposed into a mean quantity and a fluctuating quantity. So, the classification into mono-, two- and three-dimensional flows refers to the nature of the mean flow.

For convenience, three-dimensional flows may be classified into three categories according to the number of main directions of diffusion :

1) Thin shear layers in which the (mean) momentum is diffused in a preferred direction.

2) Slender shear flows in which a main flow can be defined along which the diffusion is negligible.

3) Full three-dimensional flow.

Let us notice that the word "diffusion" is used to denote a process due to viscosity or to turbulence.

For categories 1) and 2), a main flow direction can be defined and the flow lying in a plane normal to the main direction is called secondary flow.

The archetype of the first category is the boundary layer flow developing on a wing at low incidence. The diffusion takes place along the normals to the wall. This kind of flow is associated with simplifications of the basic equations. In a first approximation, let us say that the equations are the extension of the classical two-dimensional boundary layer equations : the normal pressure gradient is zero and the components of the pressure gradient parallel to the surface are known.

The second category of three-dimensional flows is represented by the flow in the neighborhood of the corners of a square duct or by the flow near the junction of a wing and of a fuselage. Another example is the development of a longitudinal vortex imbedded in a boundary layer. These flows are associated with another kind of simplification of the basic equations. Roughly speaking, the diffusion in the main flow direction is neglected and the streamwise component of pressure gradient is known.

The third category of flows is governed by the full NAVIER-STOKES equations. No particular approximations can be applied.

The first two categories of three-dimensional flows are characterized by the formation of secondary flows which are associated with the formation of longitudinal vorticity. The sources of this vorticity are determined by a few basic mechanisms.

The first source of secondary flows can be explained from purely inviscid considerations. In a three-dimensional inviscid (or viscous) flow, a longitudinal vorticity can be induced by the skewing of an existing lateral vorticity component or by the interaction between the velocity field and the vorticity field. The corresponding secondary flows are called secondary flows of the first kind, following the PRANDTL nomenclature. A second possible mechanism is purely turbulent ; a mean longitudinal vorticity can be induced by correlations between the fluctuating velocity and vorticity fields because of the non linearity of the basic equations. These secondary flows are called secondary flows of the second kind. Finally, the third mechanism is associated with wall boundary conditions and can occur in a laminar or in a turbulent flow ; in both cases, the no-slip condition at the wall applies so that a lateral motion of the wall leads to a cross flow : this is what happens in a flow over a spinning body (see for example the experiments of FULACHIER et al, 1982).

In fact, it is often very difficult to separate the various origins of three-dimensionality in a given flow. For example, on a swept wing, we will see that the three-dimensionality in the outer part of the boundary layer can be explained by the first mechanism but, near the wall, it is clear that the no-slip condition enforces the secondary flow to be zero. Therefore, near the wall, the third mechanism is involved.

A fourth source of secondary flow, as mentioned by BRAOSHAW, 1986, is the formation of streamwise vorticity due to an instability process. In fact, several types of instability can develop. This is for example the formation of TAYLOR-GORTLER vortices in laminar or turbulent flows on a longitudinally curved wall. Another form of instability leading to streamwise vorticity occurs in a laminar three-dimensional boundary layer which develops on a swept wing for example. This instability comes from the development of crossflow in the laminar boundary layer and participates in the process of laminar-turbulent transition. Finally, let us mention the very interesting recent results obtained in the study of a three-dimensional boundary layer generated by a discontinuity in the wall velocity (FULACHIER et al, 1982) : a turbulent boundary layer develops on an axial circular cylinder whose forward part is stationary and rearward part rotates around the axis. Downstream of the discontinuity, visualizations in a water tunnel have shown very regular longitudinal structures which become more random as the boundary layer develops and restructures (COLLINI-FULACHIER, 1986).

1 - PRELIMINARY REMARKS

As it is usual in most analyses of turbulent flows, any characteristic of the flow is decomposed into a mean quantity and a fluctuating (or turbulent) quantity. For the sake of generality, it is convenient to define a mean value as an ensemble average : this is a statistical average determined from a sampling of instantaneous values taken over a large number of independent realizations of the same flow. In this way, the case of unsteady turbulent flows is not excluded from the study : the flow is unsteady if the ensemble averages are time-dependent.

If the flow is incompressible ($\rho = \text{cst}$), the mean velocity and the mean pressure are defined as :

$$u_i = U_i + u_i' \quad ; \quad U_i = \lim_{N \rightarrow \infty} \frac{\sum U_i^{(n)}}{N}$$

$$p = P + p' \quad ; \quad P = \lim_{N \rightarrow \infty} \frac{\sum p^{(n)}}{N}$$

where u_i and p are the instantaneous values, U_i and P are the mean values, u_i' and p' are the fluctuations. $U_i^{(n)}$ and $p^{(n)}$ are samples determined from independent realizations of the same flow.

In the case of a compressible flow, a mass-weighted average is often used as recommended by FAVRE (see for example FAVRE et al, 1976).

1.1. Mean flow

The general effect of turbulence on the mean flow is to smooth out the variation of mean momentum or of temperature because turbulence acts as a good mixer. In a boundary layer, it follows that the mean velocity profile is fuller than in the case of a laminar flow because the velocity is close to the external velocity. Indeed, it is known that the velocity defect $U_e - U$ between the external velocity and the boundary layer velocity decreases as the REYNOLDS number increases. Obviously, the no-slip condition at the wall remains valid and it results that the slope of the mean velocity profile at the wall is larger than in laminar flow. Therefore, the skin friction coefficient is larger in turbulent flow. In the same way, the heat exchange coefficient at the wall is larger in turbulent flow.

Another consequence is that the mean kinetic energy is larger and a turbulent boundary layer is able to sustain a much larger adverse pressure gradient without separation than a laminar boundary layer.

The basic equations describing a turbulent flow are the NAVIER-STOKES equations.

Indeed, it is generally accepted that the NAVIER-STOKES equations are valid for describing the instantaneous flow because the smaller turbulent length scales and time scales are very different from the molecular scales. This means that the entire turbulent motion can be considered as the flow of a continuum. Then, in the case of an incompressible flow, the mean flow equations are derived by taking the average of the continuity equation and of the NAVIER-STOKES equations. In a cartesian axis system, the mean flow equations are (for an incompressible flow) :

$$(1.3) \quad \frac{\partial U_i}{\partial x_i} = 0$$

$$(1.4) \quad \rho \frac{\partial u_i}{\partial t} = \rho \frac{\partial u_i}{\partial t} + \rho u_j \frac{\partial u_i}{\partial x_j} = - \frac{\partial p}{\partial x_i} + \frac{\partial}{\partial x_j} (2\mu s_{ij} - \rho \langle u'_i u'_j \rangle)$$

s_{ij} is the rate of strain tensor :

$$(1.5) \quad s_{ij} = \frac{1}{2} \left[\frac{\partial u_i}{\partial x_j} + \frac{\partial u_j}{\partial x_i} \right]$$

and $2\mu s_{ij}$ is the viscous stress tensor.

The quantity $-\rho \langle u'_i u'_j \rangle$ involves the average of the product of velocity fluctuations ; it is called the REYNOLDS stress tensor. Because of it, the mean flow equations do not form a closed set of equations as the number of unknowns is larger than the number of equations. The equations and hypotheses which are developed to close this system are called the closure assumptions.

The origin of the REYNOLDS stresses lies in the non linearity of the convection term. In incompressible flow, the NAVIER-STOKES equations for the instantaneous flow can be written in a vectorial form as :

$$(1.6) \quad \int_D \rho \frac{\partial \vec{v}}{\partial t} d\tau + \int_S \rho \vec{v} (\vec{v} \cdot \vec{n}) d\sigma = \int_S \vec{t} d\sigma$$

where the components of the vector \vec{t} are :

$$t_i = (-p \delta_{il} + 2\mu s_{il}) n_l$$

$$s_{il} = \frac{1}{2} \left[\frac{\partial u_i}{\partial x_l} + \frac{\partial u_l}{\partial x_i} \right]$$

where n_l are the components of the outer normal to the surface S bounding the volume D .

Taking the average of (1.6), we get :

$$(1.7) \quad \int_D \rho \frac{\partial \vec{v}}{\partial t} d\tau + \int_S \rho \vec{v} (\vec{v} \cdot \vec{n}) d\sigma + \int_S \rho \langle \vec{v}' \cdot \vec{v}' \rangle (\vec{v}' \cdot \vec{n}) d\sigma = \int_S \vec{t} d\sigma$$

The i -component of the turbulent term can be written :

$$\int_S \rho \langle u'_i u'_l \rangle n_l d\sigma$$

which shows that the REYNOLDS stresses are due to a flux of momentum. From the momentum theorem, this term can be put in the right member of (1.7) as this is done in eq. (1.4) and interpreted as an apparent turbulent stress having the same modulus but the opposite direction as the flux of momentum.

Another interpretation of this term is given by TENNEKES-LUMLEY, 1972, who write the equation (1.4) as :

$$(1.8) \quad \rho \frac{\partial \vec{v}}{\partial t} + 2\rho \vec{\omega} \times \vec{v} + \rho \text{grad} \frac{v^2}{2} = -\text{grad} P - 2\rho \langle \vec{\omega}' \times \vec{v}' \rangle - \rho \text{grad} \frac{\langle v'^2 \rangle}{2} + \mu \Delta \vec{v}$$

with $\vec{\omega} = 1/2 \text{curl} \vec{v}$
 $\vec{\omega}' = 1/2 \text{curl} \vec{v}'$

Generally, the turbulent kinetic energy :

$$k = \frac{\langle v'^2 \rangle}{2} = \frac{\langle u'_i u'_i \rangle}{2}$$

is small compared with the kinetic energy of the mean motion so that the contribution of turbulence in eq. (1.8) occurs mainly as an apparent volume force $-2\rho \langle \vec{\omega}' \times \vec{v}' \rangle$ due to the interaction between the fluctuation of the velocity field and of the vorticity field. Indeed this is a very important property of a turbulent flow to have very strong vorticity fluctuations.

The turbulent shear stresses are also present in the equation for the mean flow vorticity. For an incompressible flow, this equation is :

$$(1.9) \quad \frac{\partial \Omega_i}{\partial t} + u_l \frac{\partial \Omega_i}{\partial x_l} = \Omega_l s_{il} + \nu \frac{\partial^2 \Omega_i}{\partial x_l \partial x_l} - \frac{\partial}{\partial x_l} \left[\frac{\epsilon_{ijk}}{2} \frac{\partial}{\partial x_j} \langle u'_k u'_l \rangle \right]$$

where ϵ_{ijk} is the permutation tensor ($\epsilon_{ijk} = 1$ if i, j, k are in cyclic order ; $\epsilon_{ijk} = -1$ if i, j, k are not in cyclic order ; $\epsilon_{ijk} = 0$ if two or three indices are equal).

As in the case of an inviscid flow, the interaction between the velocity field and

the vorticity field (term Ω_{111}) can be a source of vorticity. Let us remind that this is possible only in a three-dimensional flow: in a two-dimensional inviscid flow, the vorticity is constant. Vorticity can be generated (or destroyed) by a vortex stretching (or squeezing) mechanism: in the Ω_x -equation, for example, the corresponding term is $\Omega_x \partial U / \partial x$. If $\partial U / \partial x > 0$, there is a production of Ω_x . Let us remind that, in inviscid flow, a vortex surface or a vortex tube are also a stream surface or a stream tube; a fluid particle belonging to the vortex surface or the vortex tube is displaced along the same vortex surface or vortex tube. Then, if $\partial U / \partial x > 0$, a vortex tube aligned with the x-axis is stretched. If $\partial U / \partial x < 0$, there is a destruction of Ω_x : a vortex tube aligned with the x-axis is compressed. Another mechanism of vorticity generation is the vortex tilting: in the Ω_x -equation, the corresponding terms are

$\Omega_y \frac{1}{2} \left[\frac{\partial U}{\partial y} + \frac{\partial V}{\partial x} \right] + \Omega_z \frac{1}{2} \left[\frac{\partial U}{\partial z} + \frac{\partial W}{\partial x} \right]$. This term is responsible for longitudinal vorticity production in the outer part of a three-dimensional boundary layer. Let us consider a boundary layer which is initially two-dimensional and let us assume that the streamlines are forced to incurve in a plane parallel to the surface (under the action of a pressure gradient). The flow cannot remain two-dimensional (fig. 1.1). In the initial boundary layer, the velocity gradient $\partial U / \partial y$ leads to a z-vorticity component. If there was no vorticity production, this vorticity vector would be simply conserved ($\partial \Omega / \partial t = 0$) but the rotation of streamlines implies the existence of a $\partial W / \partial x$ term which interacts with $\partial U / \partial y$ to create a x-vorticity component. For a small turning α of the streamlines with respect to the x-axis, the vorticity vector turns by an angle $-\alpha$ with respect to the x-axis. Then the rotation of the vorticity vector with respect to the streamlines is -2α : this result is known as the SQUIRE-WINTER formula. In a boundary layer, the crossflow is zero at the outer edge and the sign of the induced longitudinal vorticity implies the creation of a secondary flow directed towards the inner side of the curvature of the external streamlines (fig. 1.1).

Obviously, the no-slip condition at the wall enforces the secondary flow to be zero at the wall and the velocity gradient component $\partial W / \partial y$ changes sign near the wall.

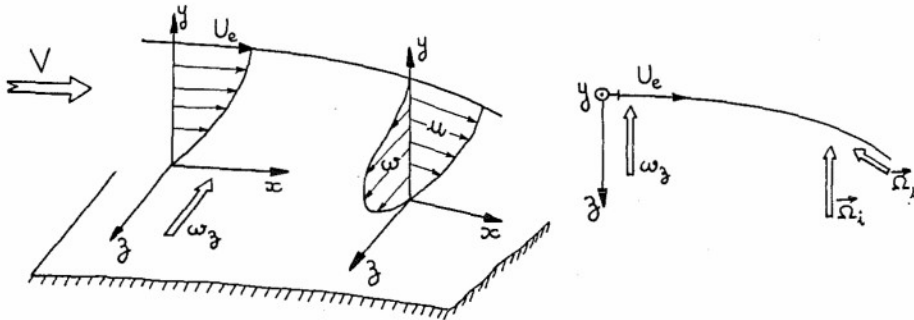


Fig. 1.1 - Generation of crossflow in a boundary layer

Another explanation of the formation of a crossflow in a boundary layer is as follows. The curvature of the external streamlines is due to a crosswise pressure force directed towards the inner side of the curvature. In a boundary layer, the normal pressure derivative $\partial P / \partial y$ is zero and therefore, the crosswise pressure force is constant within the boundary layer. Due to the smaller velocity in the boundary layer, the inertia is smaller and the fluid particles tend to move towards the inner side of the curvature of the external streamlines. When the external streamlines have an inflexion point, the crossflow reverses but the change of sign does not occur at the same time in the whole boundary layer. The crossflow changes sign near the wall at first, because the inertia is smaller in this region. Then, S-shaped crossflow velocity profiles can be observed.

The vorticity equation (1.9) also shows that the turbulence stresses can be a source of vorticity. More precisely, the gradient of the REYNOLDS stress tensor can be responsible for vorticity flux. If equation (1.9) is integrated over a volume Ω and if the gradient of the REYNOLDS stress tensor is zero on the surface bounding Ω , it appears that the turbulence term contributes to transport vorticity from one point to another point inside Ω without global production or destruction. There can be concentration of positive vorticity in certain zones and, by compensation, concentration of negative vorticity in other zones.

In the Ω_x -equation for example, the turbulence term is:

$$\frac{1}{2} \left[- \frac{\partial^2}{\partial y \partial x} \langle w' u' \rangle + \frac{\partial^2}{\partial z \partial x} \langle v' u' \rangle - \frac{\partial^2}{\partial y \partial z} \langle w'^2 \rangle + \frac{\partial^2}{\partial y \partial z} \langle v'^2 \rangle - \frac{\partial^2}{\partial y^2} \langle w' v' \rangle + \frac{\partial^2}{\partial z^2} \langle v' w' \rangle \right]$$

This expression shows that there is no effect of turbulence on the mean vorticity if turbulence is isotropic.

1.2. General background of classical turbulence modelling

In eq. (1.4), the apparent turbulent stress is combined with the viscous stress and contributes to the diffusion of mean momentum. This analogy is often advocated to introduce the concept of eddy viscosity to express the REYNOLDS stresses as a function of the mean velocity gradient in the same way as the viscous stresses; the reasoning is based on a hypothetical resemblance between the molecular motion and the turbulent motion and it leads to the mixing length scheme. In fact, it is better to introduce these concepts as resulting from a dimensional necessity (TENNEKES-LUMLEY, 1972). Let us consider a shear flow in which the velocity gradient has a predominant component, let us say $\partial U/\partial y$. On the other hand, it is assumed that the energy-containing eddies can be characterized by a velocity scale u and a length scale l . The mixing length hypothesis consists of assuming that the mean flow imposes its time scale to the turbulent flow and we get :

$$\frac{u}{l} = \frac{\partial U}{\partial y}$$

The mixing length model is deduced by assuming a good correlation between the fluctuations u' and v' .

Let us notice that the analogy between the viscous stresses and the apparent turbulent stresses is unfortunate because the viscosity is a property of the fluid whereas the turbulence is a property of the flow in the sense that the viscosity exists even if the fluid is at rest whereas turbulence disappears if the fluid is at rest. However, this does not mean that the turbulence is independent of the fluid properties. In particular, another important characteristic of turbulence is the dissipation process which is directly connected to the viscosity. From the comparison between the kinetic energy equation and the enthalpy equation, it is shown that the work performed by the viscous stresses transforms the kinetic energy into heat. In compressible flows, these equations written for the instantaneous flow read :

$$(1.10a) \quad \rho \frac{\partial}{\partial t} \frac{u_i u_i}{2} + \rho u_j \frac{\partial}{\partial x_j} \frac{u_i u_i}{2} = \rho \frac{\partial u_i}{\partial x_i} + \frac{\partial}{\partial x_j} (t_{ij} u_i) - \mu \Phi_D$$

$$(1.10b) \quad \rho \frac{\partial h}{\partial t} + \rho u_j \frac{\partial h}{\partial x_j} = \frac{\partial}{\partial x_i} \left[\frac{\lambda}{c_p} \frac{\partial h}{\partial x_i} \right] + \frac{\partial p}{\partial t} + u_j \frac{\partial p}{\partial x_j} + \mu \Phi_D$$

where $t_{ij} = -p\delta_{ij} + 2\mu s_{ij} - 2/3 \mu (\partial u_i/\partial x_i) \delta_{ij}$

and Φ_D is the dissipation function :

$$\Phi_D = \left[2s_{ij} - \frac{2}{3} \frac{\partial u_i}{\partial x_i} \delta_{ij} \right] s_{ij}$$

From equations (1.10a) and (1.10b), it is clear that the work $\mu \Phi_D$ of the viscous stresses represents an exchange between kinetic energy and heat. In addition, Φ_D is always positive because :

$$(1.11) \quad \Phi_D = \left[\frac{\partial u}{\partial y} + \frac{\partial v}{\partial x} \right]^2 + \left[\frac{\partial v}{\partial z} + \frac{\partial w}{\partial y} \right]^2 + \left[\frac{\partial w}{\partial x} + \frac{\partial u}{\partial z} \right]^2 + \frac{2}{3} \left[\left[\frac{\partial u}{\partial x} - \frac{\partial v}{\partial y} \right]^2 \right. \\ \left. + \left[\frac{\partial v}{\partial y} - \frac{\partial w}{\partial z} \right]^2 + \left[\frac{\partial w}{\partial z} - \frac{\partial u}{\partial x} \right]^2 \right]$$

In the case of an incompressible flow, we have :

$$\Phi_D = 2 s_{ij} s_{ij}$$

The average value of the total kinetic energy is :

$$K + k = \frac{\langle u_i u_i \rangle}{2} = \frac{U_i U_i}{2} + \frac{\langle u_i' u_i' \rangle}{2}$$

The dissipation rate of the kinetic energy K of the mean flow (for a unit mass) is :

$$(1.12) \quad D = 2\nu S_{ij} S_{ij}$$

and the dissipation rate of the turbulent kinetic energy k (for a unit mass) is :

$$(1.13) \quad \epsilon = 2\nu \langle s_{ij}' s_{ij}' \rangle$$

This dissipation ϵ comes from the work performed by the fluctuations of viscous stresses. When the REYNOLDS number is large, as required to have a fully developed turbulence, ϵ is much larger than D .

The dissipation ϵ plays a central role in the classical description of turbulence which can be summarized as follows. Let us consider a shear flow with a dominant velocity gradient component $\partial U/\partial y$. The source of turbulence is the shear $\partial U/\partial y$ which imposes its time scale to the energy-containing eddies.

By considering the equations for the kinetic energy of the turbulent motion and of the mean motion, it is shown that an exchange of energy takes place between the turbulent and the mean flow at a rate $-\langle u'v' \rangle \partial U / \partial y$; generally, this term contributes to a production of turbulent kinetic energy and therefore to a destruction of mean kinetic energy. If the REYNOLDS number ul/v , characterizing the energy-containing eddies, is large enough, an inviscid process takes place in which the turbulent eddies form smaller and smaller eddies in connection with a vortex stretching mechanism. This process continues until the REYNOLDS number characterizing the smaller eddies is of order unity: the viscosity becomes effective and the energy is transformed into heat by the viscous dissipation. The scales of these dissipative eddies are obtained from a dimensional consideration of (1.13). If τ is the characteristic time scale of the fluctuation s_{ij} responsible for the dissipation, we have:

$$(1.14) \quad \epsilon \sim \frac{v^3}{\tau}$$

On the other hand, if η and u are characteristic length and velocity of the dissipation eddies, the hypothesis that their characteristic REYNOLDS number is of order unity gives:

$$(1.15) \quad \frac{u\eta}{v} = 1$$

Finally the relationship between scales:

$$(1.16) \quad u = \frac{\eta}{\tau}$$

leads to the KOLMOGOROV scales which characterize the dissipative eddies:

$$(1.17) \quad \eta = \left[\frac{v^3}{\epsilon} \right]^{1/4} \quad u = (\epsilon v)^{1/4} \quad \tau = \left[\frac{v}{\epsilon} \right]^{1/2}$$

These scales are related to those characterizing the energy-containing eddies. To show this, let us consider the fully developed flow in a pipe (FAVRE et al, 1972). The equations of the flow show that the dissipation rate of $(K + k)$ averaged over the pipe section is:

$$(1.18) \quad D = \lambda \frac{\bar{U}^3}{4R}$$

where λ is the pressure drop coefficient, \bar{U} the velocity averaged over the pipe section and R is the pipe radius. As said before, if the REYNOLDS number is large enough, the dissipation rate D is nearly equal to the average of ϵ over the pipe section.

In the case of a smooth wall, λ varies as $(\bar{U}R/v)^{-1/4}$ and in the case of a fully rough wall, λ is independent of the REYNOLDS number. Let us notice that in the case of the smooth wall, the viscous stresses are larger than the REYNOLDS stresses in a thin layer near the wall; therefore, the flow is not fully turbulent over the entire cross section of the pipe. On the contrary, in the case of the fully rough wall, the flow can be considered as fully turbulent everywhere. Then, it appears that in a fully turbulent flow, the non dimensional dissipation rate is independent of the REYNOLDS number and, in particular, of the viscosity v . The problem is that, from its definition (1.13), ϵ is apparently proportional to v .

The solution to solve this paradox is to assume that the dissipative rate is determined from the characteristic scales u and l of the energy-containing eddies. From a dimensional analysis, it results the following crucial relationship:

$$(1.19) \quad \epsilon = \frac{u^3}{l}$$

In fact, the consideration of the spectral energy equation leads to assume that the dissipation rate ϵ is nearly equal to the rate of energy transfer from the large to the small eddies. As this process does not involve the viscosity, the relationship (1.19) seems natural.

The comparison between (1.14) and (1.19) shows that the dissipative eddies have to adjust their time scale τ in order that ϵ is independent of v . Precisely, τ is proportional to $v^{1/2}$.

Using (1.19), the ratios of scales characterizing the energy-containing eddies (u , l , θ) and the dissipative eddies (η , τ) are:

$$(1.20) \quad \frac{u}{\eta} = R_1^{-1/4} \quad \frac{l}{\eta} = R_1^{-3/4} \quad \frac{\tau}{\theta} = R_1^{-1/2}$$

with

$$R_1 = \frac{u l}{v}$$

These expressions show that the gap between the two families of eddies increases as the REYNOLDS number R_L increases ; the structure of the dissipative eddies becomes independent of the structure of the large eddies at high REYNOLDS number. In addition, these formulae describe the adaptation of the flow structure to the REYNOLDS number so that the viscosity can be effective. Indeed this is a very general property of the viscosity which is such that the flow structure adjusts in such a way that the viscosity is always effective in a part of the flow (TENNEKES-LUMLEY). Let us consider a flow with a velocity U around an obstacle with a characteristic length L . When the REYNOLDS number UL/ν is of order unity (STOKES flow), the viscosity is effective in a domain the size of which is L . When the REYNOLDS number increases, a laminar boundary layer of thickness δ forms along the walls of the obstacle and the viscosity is effective in this boundary layer which is characterized by the REYNOLDS number $U\delta/\nu$ ($R_\delta \ll R_L$) ; this is a first adaptation of the flow. If the REYNOLDS number R_δ increases, it is more and more difficult for the viscosity to be effective in the laminar boundary layer since the REYNOLDS number is the ratio of the orders of magnitude between the inertia effects and viscosity effects. A turbulent boundary layer forms and the viscosity becomes effective in the small dissipative eddies characterized by a REYNOLDS number $u\eta/\nu$ of order unity. When the REYNOLDS number UL/ν increases, we see that there is a continuous adjustment of the small eddies.

2 - GEOMETRY OF BOUNDARY LAYER AXIS SYSTEM

The boundary layer equations are written in a curvilinear axis system formed from two families of lines drawn on the surface along which the boundary layer develops. Before writing the equations, it could be useful to remind a few geometrical definitions and properties.

2.1. Geometrical definitions

Let us consider a curve (Γ) drawn on the surface (S) . $\vec{E}_1, \vec{E}_2, \vec{E}_3$ are unit vectors and define the FRENET reference system. \vec{E}_1 is tangent to (Γ) ; \vec{E}_2 is along the normal to (Γ) ; \vec{E}_3 is orthogonal to \vec{E}_1 and \vec{E}_2 . If s is the length along (Γ) , we have :

$$(2.1a) \quad \frac{d\vec{E}_1}{ds} = \frac{\vec{E}_2}{R}$$

$$(2.1b) \quad \frac{d\vec{E}_2}{ds} = -\frac{\vec{E}_1}{R} + \frac{\vec{E}_3}{T}$$

$$(2.1c) \quad \frac{d\vec{E}_3}{ds} = -\frac{\vec{E}_2}{T}$$

where $1/R$ is the curvature of (Γ) and $1/T$ is the torsion of (Γ) .

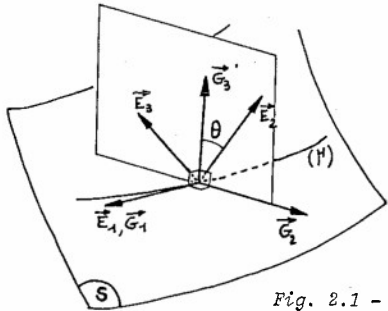


Fig. 2.1 - Reference system

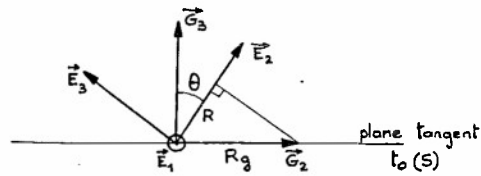


Fig. 2.2 - Definitions

The base vectors $(\vec{E}_1, \vec{E}_2, \vec{E}_3)$ are associated with the curve (Γ) . We now define a second system $(\vec{G}_1, \vec{G}_2, \vec{G}_3)$ associated with the curve (Γ) and the surface (S) . \vec{G}_1 is a unit vector tangent to (Γ) ; \vec{G}_2 is normal to \vec{G}_1 in the plane tangent to (S) ; \vec{G}_3 is normal to (S) . We have the following relationships :

$$(2.2a) \quad \frac{d\vec{G}_1}{ds} = \frac{\vec{G}_2}{R_g} + \frac{\vec{G}_3}{R_n}$$

$$(2.2b) \quad \frac{d\vec{G}_2}{ds} = -\frac{\vec{G}_1}{R_g} + \frac{\vec{G}_3}{T_g}$$

$$(2.2c) \quad \frac{d\vec{G}_3}{ds} = -\frac{\vec{G}_1}{R_n} - \frac{\vec{G}_2}{T_g}$$

where $1/R_g = \sin\theta/R$ is the geodesic curvature ; $1/R_n = \cos\theta/R$ is the normal curvature ; $1/T_g = 1/T + d\theta/ds$ is the geodesic torsion (fig. 2.2).

2.2. Surface oriented locally monoclinic coordinates

The boundary layer equations are conveniently written in an axis system formed by two families of curves drawn on the surface. These curves are not necessarily orthogonal. The system is completed with a third axis which is normal to the surface.

The theory of such axis systems has been presented by HIRSCHEL-KORDULLA, 1981.

In figure 2.3, a surface oriented locally monoclinic coordinate system is depicted.

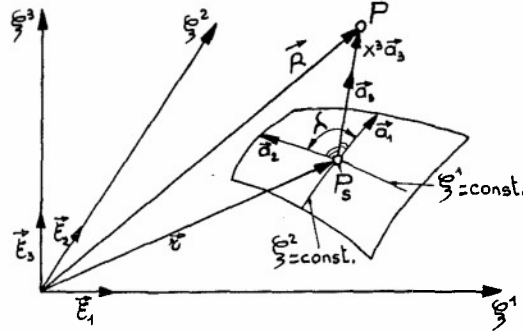


Fig. 2.3 - Definition of surface-oriented locally monoclinic coordinates

The vectors \vec{a}_i are covariant base vectors : \vec{a}_1 and \vec{a}_2 are tangent to the surface and are not necessarily unit vectors ; \vec{a}_3 is a unit vector normal to the surface. x^1, x^2, x^3 are the associated contravariant coordinates. A cartesian system is defined with \vec{e}_i as unit vectors and ξ^i are the associated coordinates.

Let us notice that the base vectors \vec{a}_1 and \vec{a}_2 are known at point P_S belonging to the surface (S) and not elsewhere. We have :

$$(2.3) \quad \vec{r} = x^\alpha \vec{a}_\alpha = \xi_S^i \vec{e}_i \quad \alpha = 1, 2 \quad i = 1, 2, 3$$

where the subscript S denotes the point P_S (fig. 2.3).

The base vectors \vec{a}_1 and \vec{a}_2 are such as :

$$(2.4) \quad \vec{a}_\alpha = \frac{\partial \vec{r}}{\partial x^\alpha} = \frac{\partial \xi_S^1}{\partial x^\alpha} \vec{e}_1 + \frac{\partial \xi_S^2}{\partial x^\alpha} \vec{e}_2 + \frac{\partial \xi_S^3}{\partial x^\alpha} \vec{e}_3$$

The position of a point P off the surface S is given by :

$$(2.5) \quad \vec{R} = \xi^i \vec{e}_i = \vec{r}(x^1, x^2) + x^3 \vec{a}_3(x^1, x^2)$$

The vector \vec{a}_3 is such as :

$$(2.6) \quad \vec{a}_3 = \frac{\partial \vec{R}}{\partial x^3} = \frac{\partial \xi^i}{\partial x^3} \vec{e}_i$$

Local base vectors \vec{g}_j can be associated with the coordinates x^j :

$$(2.7) \quad \vec{R} = \xi^i \vec{e}_i = x^j \vec{g}_j$$

The base vectors \vec{g}_j are such as :

$$(2.8) \quad \vec{g}_j = \frac{\partial \vec{R}}{\partial x^j} = \frac{\partial \xi^i}{\partial x^j} \vec{e}_i$$

From equations (2.5) and (2.4), we have :

$$(2.9a) \quad \frac{\partial \vec{R}}{\partial x^\alpha} = \frac{\partial \vec{r}}{\partial x^\alpha} + x^3 \frac{\partial \vec{a}_3}{\partial x^\alpha} = \vec{a}_\alpha + x^3 \frac{\partial \vec{a}_3}{\partial x^\alpha} \quad \alpha = 1, 2$$

$$(2.9b) \quad \frac{\partial \vec{R}}{\partial x^3} = \vec{a}_3$$

Then, from (2.8) and (2.9), we get :

$$(2.10a) \quad \vec{g}_\alpha = \vec{a}_\alpha + x^3 \frac{\partial \vec{a}_3}{\partial x^\alpha} \quad \alpha = 1 \text{ or } 2$$

$$(2.10b) \quad \vec{g}_3 = \vec{a}_3$$

Noting that \vec{a}_3 is normal to \vec{a}_1 and \vec{a}_2 and that $\vec{a}_3 \frac{\partial \vec{a}_3}{\partial x^\alpha} = \frac{1}{2} \frac{\partial}{\partial x^\alpha} (\vec{a}_3 \vec{a}_3) = 0$, the relationships (2.10) show that the metric tensor $g_{ij} = \vec{g}_i \vec{g}_j$ takes the form :

$$(2.11) \quad g_{ij} = \begin{bmatrix} g_{11} & g_{12} & 0 \\ g_{21} & g_{22} & 0 \\ 0 & 0 & 1 \end{bmatrix}$$

On the surface S, this metric tensor reduces to :

$$(2.12) \quad [g_{ij}]_{x_3=0} = \begin{bmatrix} a_{11} & a_{12} & 0 \\ a_{21} & a_{22} & 0 \\ 0 & 0 & 1 \end{bmatrix}$$

with :

$$(2.13) \quad a_{\alpha\beta} = \vec{a}_\alpha \vec{a}_\beta \quad (\alpha = 1 \text{ or } 2) ; \beta = 1 \text{ or } 2$$

From (2.4), these coefficients are given by :

$$(2.14) \quad a_{\alpha\beta} = \frac{\partial \xi_S^1}{\partial x^\alpha} \frac{\partial \xi_S^1}{\partial x^\beta} + \frac{\partial \xi_S^2}{\partial x^\alpha} \frac{\partial \xi_S^2}{\partial x^\beta} + \frac{\partial \xi_S^3}{\partial x^\alpha} \frac{\partial \xi_S^3}{\partial x^\beta}$$

Let us consider an element of curve given by :

$$(2.15) \quad d\vec{M} = dx^j \vec{g}_j$$

The length ds of this element is given by :

$$(2.16) \quad (ds)^2 = g_{11}(dx^1)^2 + 2g_{12} dx^1 dx^2 + g_{22}(dx^2)^2 + (dx^3)^2$$

If the curve is drawn on the surface, its length is :

$$(2.17) \quad (ds)^2 = a_{11}(dx^1)^2 + 2a_{12} dx^1 dx^2 + a_{22}(dx^2)^2$$

2.3. Application to boundary layer equations

Generally, the tensorial notation is not used in literature on boundary layer theory.

The axis system is defined by X = cst- and Z = cst-lines drawn on the surface along which the boundary layer develops (fig. 2.4). The y-axis is normal to the wall.

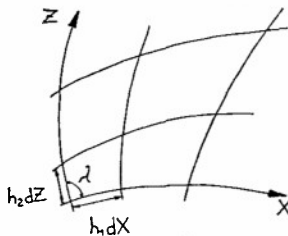


Fig. 2.4 - Non orthogonal axis system

The metric elements h_1 and h_2 are related to the coefficients $a_{\alpha\beta}$ defined previously (eq. 2.13) :

$$(2.18) \quad h_1 = \sqrt{a_{11}} \quad h_2 = \sqrt{a_{22}}$$

The metric element h_3 along y is unity :

$$(2.19) \quad h_3 = 1$$

The coefficient g is defined as :

$$(2.20) \quad g = h_1 h_2 \cos \lambda \quad (g = a_{12})$$

According to the boundary layer assumptions, the thickness δ of the boundary layer is small compared with the radii of curvature of the surface. It results that the variations of the metric tensor g_{ij} within the boundary layer can be neglected ; this means we can take $g_{\alpha\beta} = a_{\alpha\beta}$. In other words, h_1 and h_2 are functions of X and Z only :

$$(2.21a) \quad h_1 = h_1(X, Z) \quad h_2 = h_2(X, Z)$$

In the same way, we have :

$$(2.21b) \quad \lambda = \lambda(X, Z)$$

The metric coefficients are given by (2.14) :

$$(2.22a) \quad h_1^2 = \left[\frac{\partial \xi_S^1}{\partial X} \right]^2 + \left[\frac{\partial \xi_S^2}{\partial X} \right]^2 + \left[\frac{\partial \xi_S^3}{\partial X} \right]^2$$

$$(2.22b) \quad h_2^2 = \left[\frac{\partial \xi_S^1}{\partial Z} \right]^2 + \left[\frac{\partial \xi_S^2}{\partial Z} \right]^2 + \left[\frac{\partial \xi_S^3}{\partial Z} \right]^2$$

$$(2.22c) \quad g = \frac{\partial \xi_S^1}{\partial X} \frac{\partial \xi_S^1}{\partial Z} + \frac{\partial \xi_S^2}{\partial X} \frac{\partial \xi_S^2}{\partial Z} + \frac{\partial \xi_S^3}{\partial X} \frac{\partial \xi_S^3}{\partial Z}$$

where ξ_S^i are the cartesian coordinates of a point P_S on (S) .

The length of any element of curve is :

$$(2.23) \quad ds^2 = h_1^2 dX^2 + 2gdXdZ + h_2^2 dZ^2 + dy^2$$

In the boundary layer equations, the geodesic curvatures K_1 and K_2 of the X - and Z -axes are present. The geometrical meaning of the geodesic curvature has been presented in § 2.1.. From (2.2), (2.4) and (2.13), the values of K_1 and K_2 can be calculated as a function of $a_{\alpha\beta}$ or as a function of h_1 , h_2 and λ :

$$(2.24a) \quad K_1 = \frac{1}{h_1 h_2 \sin \lambda} \left[\frac{\partial}{\partial X} (h_2 \cos \lambda) - \frac{\partial h_1}{\partial Z} \right]$$

$$(2.24b) \quad K_2 = \frac{1}{h_1 h_2 \sin \lambda} \left[\frac{\partial}{\partial Z} (h_1 \cos \lambda) - \frac{\partial h_2}{\partial X} \right]$$

3 - BOUNDARY LAYER EQUATIONS

3.1. Equations in a curvilinear axis system

The boundary layer equations are written in a non orthogonal curvilinear axis system defined in fig. 3.1. The X - and Z -axes form two families of curves drawn on the surface and the y -axis is normal to the wall. λ is the angle between the X - and Z -axes. The metric elements along X and Z are h_1 and h_2 .

The physical velocity components along X -, Z -, y are respectively U , W , V .

The total enthalpy h_i is related to the static enthalpy by :

$$(3.1) \quad h_i = h + \frac{U^2 + W^2 + 2UW \cos \lambda}{2}$$

Let us notice that the contribution of the velocity component v is neglected in the boundary layer approximation.

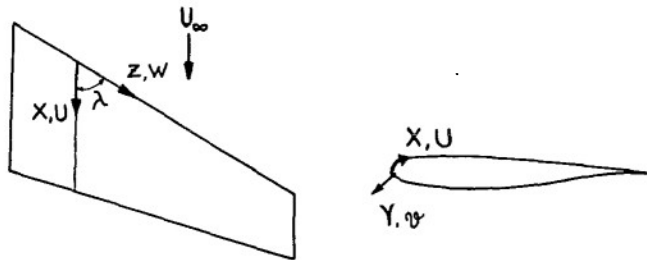


Fig. 3.1 - Boundary layer axis system

In compressible flow, the mass-weighted averages are equivalent to the classical average if the MACH number is not too large. In addition, we neglect the correlations between the fluctuations of density and velocity. The boundary layer equations are :

$$(3.2a) \quad \frac{\partial \rho}{\partial t} + \frac{1}{q} \frac{\partial}{\partial X} \left[\rho U \frac{q}{h_1} \right] + \frac{1}{q} \frac{\partial}{\partial Z} \left[\rho W \frac{q}{h_2} \right] + \frac{\partial}{\partial y} \rho v = 0$$

$$(3.2b) \quad \rho \frac{\partial U}{\partial t} + \rho \frac{U}{h_1} \frac{\partial U}{\partial X} + \rho \frac{W}{h_2} \frac{\partial U}{\partial Z} + \rho v \frac{\partial U}{\partial y} - \frac{\cos \lambda}{\sin \lambda} K_1 \rho U^2 + \frac{K_2}{\sin \lambda} \rho W^2 + K_{12} \rho UW \\ = a_1 \frac{\partial P}{\partial X} + a_2 \frac{\partial P}{\partial Z} + \frac{\partial}{\partial y} \left[\mu \frac{\partial U}{\partial y} - \rho \langle u'v' \rangle \right]$$

$$(3.2c) \quad \rho \frac{\partial W}{\partial t} + \rho \frac{U}{h_1} \frac{\partial W}{\partial X} + \rho \frac{W}{h_2} \frac{\partial W}{\partial Z} + \rho v \frac{\partial W}{\partial y} + \frac{K_1}{\sin \lambda} \rho U^2 - K_2 \frac{\cos \lambda}{\sin \lambda} \rho W^2 + K_{21} \rho UW \\ = b_1 \frac{\partial P}{\partial X} + b_2 \frac{\partial P}{\partial Z} + \frac{\partial}{\partial y} \left[\mu \frac{\partial W}{\partial y} - \rho \langle w'v' \rangle \right]$$

$$(3.2d) \quad \rho \frac{\partial h_i}{\partial t} + \rho \frac{U}{h_1} \frac{\partial h_i}{\partial X} + \rho \frac{W}{h_2} \frac{\partial h_i}{\partial Z} + \rho v \frac{\partial h_i}{\partial y} = \frac{\partial P}{\partial t} + \frac{\partial}{\partial y} \left[\mu \frac{\partial h_i}{\partial y} \right] \\ + \frac{\partial}{\partial y} \left[\left(\frac{1}{P} - 1 \right) \mu \frac{\partial h_i}{\partial y} \right] + \frac{\partial}{\partial y} (\rho C_p \langle v'T' \rangle) \\ + \frac{\partial}{\partial y} [- \rho \langle u'v' \rangle U - \rho \langle w'v' \rangle W - \rho \langle u'v' \rangle W \cos \lambda - \rho \langle w'v' \rangle U \cos \lambda]$$

K_1 and K_2 are the geodesic curvatures of the X- and Z-axes (eq. 2.24). P is the PRANDTL number.

The other coefficients are :

$$q = h_1 h_2 \sin \lambda$$

$$K_{12} = \frac{1}{\sin \lambda} \left[- (K_1 + \frac{1}{h_1} \frac{\partial \lambda}{\partial X}) + \cos \lambda (K_2 + \frac{1}{h_2} \frac{\partial \lambda}{\partial Z}) \right]$$

$$K_{21} = \frac{1}{\sin \lambda} \left[- (K_2 + \frac{1}{h_2} \frac{\partial \lambda}{\partial Z}) + \cos \lambda (K_1 + \frac{1}{h_1} \frac{\partial \lambda}{\partial X}) \right]$$

$$a_1 = - \frac{1}{h_1 \sin^2 \lambda} ; a_2 = \frac{\cos \lambda}{h_2 \sin^2 \lambda} ; b_1 = \frac{\cos \lambda}{h_1 \sin^2 \lambda} ; b_2 = - \frac{1}{h_2 \sin^2 \lambda}$$

The wall boundary conditions are the no-slip condition : $U = W = V = 0$ (in the case of an impermeable wall) ; the wall temperature distribution or the heat flux distribution is prescribed.

At the boundary layer edge, we have :

$$U = U_e \quad W = W_e \quad h_i = h_{ie}$$

The external boundary conditions are such as :

$$(3.3a) \quad \rho_e \frac{\partial U_e}{\partial t} + \rho_e \frac{U_e}{h_1} \frac{\partial U_e}{\partial X} + \rho_e \frac{W_e}{h_2} \frac{\partial U_e}{\partial Z} - \frac{\cos \lambda}{\sin \lambda} K_1 \rho_e U_e^2 + \frac{K_2}{\sin \lambda} \rho_e W_e^2 + K_{12} \rho_e U_e W_e \\ = a_1 \frac{\partial P}{\partial X} + a_2 \frac{\partial P}{\partial Z}$$

$$(3.3b) \quad \rho_e \frac{\partial W_e}{\partial t} + \rho_e \frac{U_e}{h_1} \frac{\partial W_e}{\partial X} + \rho_e \frac{W_e}{h_2} \frac{\partial W_e}{\partial Z} + \frac{K_1}{\sin \lambda} \rho_e U_e^2 - K_2 \frac{\cos \lambda}{\sin \lambda} \rho_e W_e^2 + K_{21} \rho_e U_e W_e \\ = b_1 \frac{\partial P}{\partial X} + b_2 \frac{\partial P}{\partial Z}$$

$$(3.3c) \quad \rho_e \frac{\partial h_{ie}}{\partial t} + \rho_e \frac{U_e}{h_1} \frac{\partial h_{ie}}{\partial X} + \rho_e \frac{W_e}{h_2} \frac{\partial h_{ie}}{\partial Z} = \frac{\partial P}{\partial t}$$

Let us remind that the normal pressure gradient $\partial P / \partial y$ is zero within the boundary layer.

In steady flow, the outer condition simplifies as $h_{ie} = \text{cst}$.

The calculation methods are based on the solution of equations (3.2). However, this

set of equations is not closed : the turbulent stresses - $\rho \langle u'v' \rangle$, - $\rho \langle w'v' \rangle$ and the turbulent heat flux - $\rho C_p \langle v'T' \rangle$ need to be represented by some turbulence model.

3.2. Integral equations

Very often, practical calculations are performed by using global equations which are an integrated form of equation (3.2) : the integration is performed between the wall and the boundary layer edge. Such a set of equations is the basis of integral methods. In fact, an infinity of global equations can be imagined : the most evident equations are the integrated equations (3.2) but sometimes other equations are used, for example, the global kinetic energy equation ; the momentum equations can also be multiplied by y before integration and we obtain moment of momentum global equations.

The most often used integral equations are the integrated forms of the continuity and momentum equations. In the case of an unsteady compressible flow, these equations are :

$$(3.3a) \quad \frac{U_e}{u_e} \frac{1}{h_1} \frac{\partial \delta}{\partial X} + \frac{W_e}{u_e} \frac{1}{h_2} \frac{\partial \delta}{\partial Z} + \frac{1}{u_e} \frac{\partial \delta}{\partial t} - \frac{V_e}{u_e} = \frac{1}{\rho_e u_e} \frac{\partial}{\partial t} [\rho_e (\delta - \delta_p)] \\ + \frac{1}{\rho_e u_e q} \frac{\partial}{\partial X} \left[\frac{\rho_e u_e q}{h_1} \left[\delta \frac{U_e}{u_e} - \Delta_1 \right] \right] + \frac{1}{\rho_e u_e q} \frac{\partial}{\partial Z} \left[\frac{\rho_e u_e q}{h_2} \left[\delta \frac{W_e}{u_e} - \Delta_2 \right] \right]$$

$$(3.3b) \quad \frac{Cf_X}{2} = \frac{1}{\rho_e u_e^2} \frac{\partial}{\partial t} (\rho_e u_e \Delta_1) - \frac{U_e}{\rho_e u_e^2} \frac{\partial}{\partial t} (\rho_e \delta_p) \\ + \frac{1}{\rho_e u_e^2 q} \left[\frac{\partial}{\partial X} \left[\frac{\rho_e u_e^2 q}{h_1} \theta_{11} \right] + \frac{\partial}{\partial Z} \left[\frac{\rho_e u_e^2 q}{h_2} \theta_{12} \right] \right] + \frac{\Delta_1}{u_e h_1} \frac{\partial U_e}{\partial X} + \frac{\Delta_2}{u_e h_2} \frac{\partial U_e}{\partial Z} \\ - K_1 \frac{\cos \lambda}{\sin \lambda} \left[\frac{U_e}{u_e} \Delta_1 + \theta_{11} \right] + \frac{K_2}{\sin \lambda} \left[\frac{W_e}{u_e} \Delta_2 + \theta_{22} \right] + K_{12} \left[\frac{U_e}{u_e} \Delta_2 + \theta_{12} \right]$$

$$(3.3c) \quad \frac{Cf_Z}{2} = \frac{1}{\rho_e u_e^2} \frac{\partial}{\partial t} (\rho_e u_e \Delta_2) - \frac{W_e}{\rho_e u_e^2} \frac{\partial}{\partial t} (\rho_e \delta_p) \\ + \frac{1}{\rho_e u_e^2 q} \left[\frac{\partial}{\partial X} \left[\frac{\rho_e u_e^2 q}{h_1} \theta_{21} \right] + \frac{\partial}{\partial Z} \left[\frac{\rho_e u_e^2 q}{h_2} \theta_{22} \right] \right] + \frac{\Delta_1}{u_e h_1} \frac{\partial W_e}{\partial X} + \frac{\Delta_2}{u_e h_2} \frac{\partial W_e}{\partial Z} \\ - K_2 \frac{\cos \lambda}{\sin \lambda} \left[\frac{W_e}{u_e} \Delta_2 + \theta_{22} \right] + \frac{K_1}{\sin \lambda} \left[\frac{U_e}{u_e} \Delta_1 + \theta_{11} \right] + K_{21} \left[\frac{W_e}{u_e} \Delta_1 + \theta_{21} \right]$$

The global kinetic energy equation is used sometimes. Its expression is given by SWAFFORD, 1983, for example.

The global energy equation is used when the wall heat flux is involved but its use is limited to steady flows. In this case, this equation is :

$$(3.3d) \quad \frac{\phi_w}{\rho_e u_e h_{ie}} = \frac{1}{\rho_e u_e h_{ie} q} \left[\frac{\partial}{\partial X} \left[\frac{\rho_e u_e h_{ie} q}{h_1} \theta_{1t} \right] + \frac{\partial}{\partial Z} \left[\frac{\rho_e u_e h_{ie} q}{h_2} \theta_{2t} \right] \right]$$

The definition of the various global quantities is :

δ : boundary layer thickness

$$\frac{Cf_X}{2} = \frac{\tau_{WX}}{\rho_e u_e^2} ; \quad \frac{Cf_Z}{2} = \frac{\tau_{WZ}}{\rho_e u_e^2}$$

$$\Delta_1 = \int_0^\delta \frac{\rho_e U_e - \rho U}{\rho_e U_e} dy ; \quad \Delta_2 = \int_0^\delta \frac{\rho_e W_e - \rho W}{\rho_e U_e} dy ; \quad \delta_p = \int_0^\delta \frac{\rho_e - \rho}{\rho_e} dy$$

$$\theta_{1t} = \int_0^\delta \frac{\rho U (h_i - h_{ie})}{\rho_e u_e h_{ie}} dy ; \quad \theta_{2t} = \int_0^\delta \frac{\rho W (h_i - h_{ie})}{\rho_e u_e h_{ie}} dy$$

$$\theta_{11} = \int_0^\delta \frac{\rho U (U_e - U)}{\rho_e U_e^2} dy \quad ; \quad \theta_{22} = \int_0^\delta \frac{\rho W (W_e - W)}{\rho_e U_e^2} dy$$

$$\theta_{12} = \int_0^\delta \frac{\rho W (U_e - U)}{\rho_e U_e^2} dy \quad ; \quad \theta_{21} = \int_0^\delta \frac{\rho U (W_e - W)}{\rho_e U_e^2} dy$$

In the above equations, τ_{wx} and τ_{wz} are the wall shear stress components along X and Z. \dot{q}_w is the wall heat flux. u_e is the external resultant velocity which is related to the X- and Z-components by :

$$u_e^2 = U_e^2 + W_e^2 + 2U_e W_e \cos \lambda$$

3.3. Streamline coordinate system

The boundary layer equations are often written in a streamline coordinate system. The x-axis is formed by the streamlines and the z-axis by the orthogonal lines. Then, equations (3.2) are slightly simplified since :

$$\lambda = \pi/2 \quad ; \quad W_e = 0 \quad ; \quad U_e = u_e$$

In the streamline coordinate system, the velocity components are u and w and the boundary layer characteristics are noted with small letters (δ , θ , ...) :

$$\frac{Cf_x}{2} = \frac{\tau_{wx}}{\rho_e u_e^2} \quad ; \quad \frac{Cf_z}{2} = \frac{\tau_{wz}}{\rho_e u_e^2}$$

$$\delta_1 = \int_0^\delta \left[1 - \frac{\rho u}{\rho_e u_e} \right] dy \quad ; \quad \delta_2 = \int_0^\delta - \frac{\rho w}{\rho_e u_e} dy$$

$$\theta_{1t} = \int_0^\delta \frac{\rho u}{\rho_e u_e} \left[\frac{h_i}{h_{ie}} - 1 \right] dy \quad ; \quad \theta_{2t} = \int_0^\delta \frac{\rho w}{\rho_e u_e} \left[\frac{h_i}{h_{ie}} - 1 \right] dy$$

$$\theta_{11} = \int_0^\delta \frac{\rho u}{\rho_e u_e} \left[1 - \frac{u}{u_e} \right] dy \quad ; \quad \theta_{22} = \int_0^\delta - \frac{\rho w^2}{\rho_e u_e^2} dy$$

$$\theta_{12} = \int_0^\delta \frac{\rho w}{\rho_e u_e} \left[1 - \frac{u}{u_e} \right] dy \quad ; \quad \theta_{21} = \int_0^\delta - \frac{\rho u w}{\rho_e u_e^2} dy$$

The shape parameter of the streamwise velocity profile is :

$$H = \frac{\delta_1}{\theta_{11}}$$

The ratio of the wall shear stress components defines the angle β_0 (or β_w) between the limiting wall streamline and the external streamline (fig. 3.2) :

$$\tan \beta_0 = \frac{\tau_{wz}}{\tau_{wx}} = \left[\frac{\frac{\partial w}{\partial y}}{\frac{\partial u}{\partial y}} \right]_{y=0} = \lim_{y \rightarrow 0} \frac{w}{u}$$

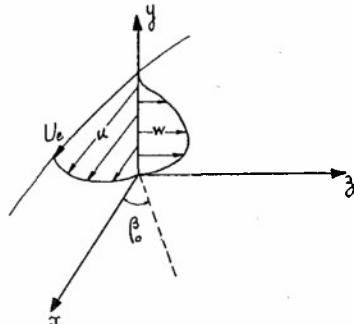


Fig. 3.2 - Velocity profiles in the streamline coordinate system

3.4. Displacement thickness - Equivalent wall transpiration velocity

The effect of the boundary layer on the external flow is determined with the help of a matching condition between the boundary layer and the external flow. The boundary layer is often represented by its displacement thickness or by the equivalent wall transpiration velocity.

These concepts are introduced by defining a fictitious flow which is the extension of the external flow within the boundary layer. Let v^* be the velocity normal to the wall of this fictitious flow at any point y within the boundary layer. If the wall curvature radii are large compared with the boundary layer thickness, the density and the streamwise velocity of the extended flow are constant and equal to the edge boundary layer values ρ_e and u_e .

The normal velocity v^* is defined by a TAYLOR series expansion around $y = \delta$:

$$(3.4) \quad v^*(y) = v^*(\delta) + (y - \delta) \left[\frac{\partial v^*}{\partial y} \right]_{y=\delta}$$

The term $\left[\frac{\partial v^*}{\partial y} \right]_{y=\delta}$ is expressed from the continuity equation written for the fictitious flow and we get :

$$\frac{v^*(y)}{u_e} = \frac{v^*(\delta)}{u_e} - (y - \delta) \left[\frac{1}{\rho_e u_e} \frac{\partial \rho_e}{\partial t} + \frac{1}{\rho_e u_e q} \frac{\partial}{\partial x} \left[\frac{\rho_e u_e q}{h_1} \right] + \frac{1}{\rho_e u_e q} \frac{\partial}{\partial z} \left[\frac{\rho_e w_e q}{h_2} \right] \right]$$

The matching between the boundary layer flow and the external flow is given by the condition :

$$v^*(\delta) = v_e$$

where v_e is the normal velocity at the boundary layer edge calculated by the boundary layer global continuity equation (3.3a). Then, the velocity v^* of the fictitious flow is :

$$\begin{aligned} \frac{v^*(y)}{u_e} = & \frac{1}{\rho_e u_e} \frac{\partial}{\partial t} (\rho_e \delta_e) + \frac{1}{\rho_e u_e q} \frac{\partial}{\partial x} \left[\frac{\rho_e u_e q}{h_1} \Delta_1 \right] + \frac{1}{\rho_e u_e q} \frac{\partial}{\partial z} \left[\frac{\rho_e u_e q}{h_2} \Delta_2 \right] \\ & - y \left[\frac{1}{\rho_e u_e} \frac{\partial \rho_e}{\partial t} + \frac{1}{\rho_e u_e q} \frac{\partial}{\partial x} \left[\frac{\rho_e u_e q}{h_1} \right] + \frac{1}{\rho_e u_e q} \frac{\partial}{\partial z} \left[\frac{\rho_e w_e q}{h_2} \right] \right] \end{aligned}$$

The ratio $v^*(y)/u_e$ is the boundary condition which has to be prescribed to the external inviscid flow at the distance y from the wall in order to represent the boundary layer effects. In principle, the distance y from the wall could be any value between $y = 0$ and $y = \delta$. In practice, the boundary condition of the external flow is applied either along the displacement surface or at the wall.

In unsteady flow, we can define the displacement surface in such a way that at every time, the inviscid flow is tangent to it. Following this definition, the displacement thickness δ^* and the velocity $v^*(\delta^*)$ are given by :

$$\begin{aligned} \frac{1}{q} \frac{\partial}{\partial x} \left[\frac{\rho_e u_e q}{h_1} \left[\delta^* \frac{u_e}{u_e} - \Delta_1 \right] \right] + \frac{1}{q} \frac{\partial}{\partial z} \left[\frac{\rho_e u_e q}{h_2} \left[\delta^* \frac{w_e}{u_e} - \Delta_2 \right] \right] + \delta^* \frac{\partial \rho_e}{\partial t} - \frac{\partial}{\partial t} (\rho_e \delta_e) = 0 \\ \frac{v^*(\delta^*)}{u_e} = \frac{u_e}{u_e} \frac{1}{h_1} \frac{\partial \delta^*}{\partial x} + \frac{w_e}{u_e} \frac{1}{h_2} \frac{\partial \delta^*}{\partial z} \end{aligned}$$

In the case of a streamline coordinate system, this condition reads :

$$\frac{v^*(\delta^*)}{u_e} = \frac{\partial \delta^*}{h_1 \partial x}$$

Let us notice that we could define a thickness Δ^* giving expressions which are more symmetrical with respect to time and space :

$$\begin{aligned} \frac{1}{q} \frac{\partial}{\partial x} \left[\frac{\rho_e u_e q}{h_1} \left[\Delta^* \frac{u_e}{u_e} - \Delta_1 \right] \right] + \frac{1}{q} \frac{\partial}{\partial z} \left[\frac{\rho_e u_e q}{h_2} \left[\Delta^* \frac{w_e}{u_e} - \Delta_2 \right] \right] + \frac{1}{\rho_e u_e} \frac{\partial}{\partial t} [\rho_e (\Delta^* - \delta_e)] = 0 \\ \frac{v^*(\Delta^*)}{u_e} = \frac{1}{u_e} \frac{\partial \Delta^*}{\partial t} + \frac{u_e}{u_e} \frac{1}{h_1} \frac{\partial \Delta^*}{\partial x} + \frac{w_e}{u_e} \frac{1}{h_2} \frac{\partial \Delta^*}{\partial z} \end{aligned}$$

The effect of the boundary layer can also be interpreted as a wall transpiration velocity : in this case, the velocity v^* is calculated at the wall ($y = 0$) and we have :

$$\frac{v^*(0)}{u_e} = \frac{1}{\rho_e u_e} \left[\frac{\partial}{\partial t} (\rho_e \delta_e) + \frac{1}{q} \frac{\partial}{\partial x} \left[\frac{\rho_e u_e q}{h_1} \Delta_1 \right] + \frac{1}{q} \frac{\partial}{\partial z} \left[\frac{\rho_e u_e q}{h_2} \Delta_2 \right] \right]$$

4 - NATURE OF THE SYSTEM OF BOUNDARY LAYER EQUATIONS

The system of boundary layer equations will be analyzed in laminar flow only, because the study of the turbulent case depends on the chosen model.

Before presenting the analysis of the three-dimensional equations, we will consider a simple problem which depicts most of the properties of the boundary layer equations.

4.1. Analysis of a simple problem

Let us consider the partial differential equation :

$$(4.1) \quad \frac{\partial f}{\partial t} + V \frac{\partial f}{\partial x} = a^2 \frac{\partial^2 f}{\partial y^2}$$

where a and V are constants.

We assume that this equation represents a certain phenomenon in an infinite medium and we look for the response to a perturbation which represents a DIRAC distribution at $x = 0$, $t = 0$, $y = 0$.

The new system of variables (X, Y, T) is introduced :

$$X = x - Vt \quad Y = y \quad T = t$$

In this new system, eq. (4.1) becomes :

$$\frac{\partial f}{\partial T} = a^2 \frac{\partial^2 f}{\partial Y^2}$$

and the solution to our above problem is :

$$f = \frac{1}{2a\sqrt{\pi T}} e^{-\frac{Y^2}{4a^2 T}}$$

Returning to the original variable, the solution is :

$$(4.2) \quad f = \frac{1}{2a\sqrt{\pi t}} e^{-\frac{y^2}{4a^2 t}} \text{ for } x = Vt ; -\infty < y < +\infty$$

$$f = 0 \quad \text{for } x \neq Vt ; -\infty < y < +\infty$$

The solution (4.2) shows that a perturbation introduced at a point (x, y, t) propagates immediately along the entire y -axis whereas the (x, t) plane is affected along the line $x = Vt$; the perturbation contaminates a semi-infinite plane (P) defined by the y -axis and the line $x = Vt$ ($t > 0$) (fig. 4.1).

The propagation in the (x, t) plane is due to the convective nature of equation (4.1) (left hand side of 4.1); the propagation velocity is V since the perturbed domain is characterized by $x = Vt$.

The propagation along the y -axis is due to the diffusive nature of equation (4.1) (right hand side of 4.1); the propagation velocity along y is infinite because at a small time t , the entire y -axis is affected by the perturbation. However, it should be noticed that the perturbation is damped as t increases.

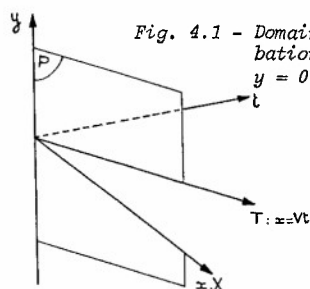


Fig. 4.1 - Domain influenced by a perturbation introduced at point $x = 0$, $y = 0$, $t = 0$

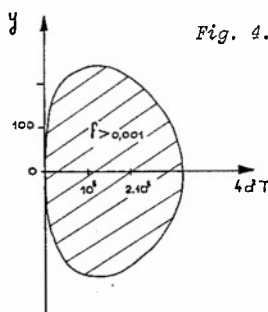


Fig. 4.2 - Practical domain of influence of a point

The above analysis has defined the mathematical domain of influence of a point. However the intensity of the perturbation is not the same everywhere. In certain regions of the perturbed space, the value of f is very very small and, in practice, we can say that the regions are not perturbed. Then we can try to define the domain where the perturbation is significant. Obviously the definition of "significant" will be arbitrary. For example, we can decide that the perturbation is significant if $f > 0.001$. This leads to a "practical domain" of influence which is finite as shown in figure 4.2.

The solution (4.2) also shows that the perturbation is amplified when time decreases ($t < 0$). This means that the solution of (4.1) should be sought for increasing values of t only.

4.2. Analysis of boundary layer equations

Let us consider a quasi linear system of partial differential equations :

$$(4.3) \quad A_i \frac{\partial F}{\partial x_i} = B \quad i = 1, m$$

The number of coordinates is m ; F is a n -dimensional column vector ; A_i are $n \times n$ matrices and B is a n -dimensional column vector containing coefficients which depend only on x_i and F .

The nature of the system (4.3) is studied by means of the characteristic determinant :

$$|A_i \lambda_i| = 0$$

where λ_i are the components of the vector normal to the characteristic surfaces.

We consider the laminar incompressible three-dimensional equations written in a cartesian axis-system (in fact, the results of the analysis are the same if the equations are written in a general curvilinear axis-system).

The system is reduced to a quasi linear system by writing :

$$(4.4a) \quad \frac{\partial U}{\partial y} = 0$$

$$(4.4b) \quad \frac{\partial W}{\partial y} = \bar{W}$$

$$(4.4c) \quad \frac{\partial U}{\partial x} + \frac{\partial V}{\partial y} + \frac{\partial W}{\partial z} = 0$$

$$(4.4d) \quad U \frac{\partial U}{\partial x} + V \frac{\partial U}{\partial y} + W \frac{\partial U}{\partial z} - \nu \frac{\partial U}{\partial y} = - \frac{1}{\rho} \frac{\partial p}{\partial x}$$

$$(4.4e) \quad U \frac{\partial W}{\partial x} + V \frac{\partial W}{\partial y} + W \frac{\partial W}{\partial z} - \nu \frac{\partial W}{\partial y} = - \frac{1}{\rho} \frac{\partial p}{\partial z}$$

where $p(x, z)$ is a given function.

The characteristic determinant is :

$$(4.5) \quad \nu^2 \lambda_y^5 = 0$$

According to the classical classification, the system is parabolic as all the characteristic roots are real and identical. The characteristic planes are normal to the surface. This property is associated with the diffusive nature of momentum equations (second y -derivative in equations (4.4a) and (4.4e)) and with the term $\partial V / \partial y$ in the continuity equation.

The presence of the viscous terms hides the role of the convective terms in momentum equations. To appreciate their influence, we study the subcharacteristics of the system formed with the next lower order derivatives (WANG, 1971, KRAUSE, 1973). The system is written as :

$$(4.6a) \quad \frac{\partial U}{\partial x} + \frac{\partial V}{\partial y} + \frac{\partial W}{\partial z} = 0$$

$$(4.6b) \quad U \frac{\partial U}{\partial x} + V \frac{\partial U}{\partial y} + W \frac{\partial U}{\partial z} = - \frac{1}{\rho} \frac{\partial p}{\partial x} + \nu \frac{\partial^2 U}{\partial y^2}$$

$$(4.6c) \quad U \frac{\partial W}{\partial x} + V \frac{\partial W}{\partial y} + W \frac{\partial W}{\partial z} = - \frac{1}{\rho} \frac{\partial p}{\partial z} + \nu \frac{\partial^2 W}{\partial y^2}$$

The characteristic determinant is :

$$(4.7) \quad \lambda_y (U \lambda_x + V \lambda_y + W \lambda_z)^2 = 0$$

This shows that the surfaces normal to the wall and the stream surfaces are subcharacteristic surfaces. The root $\lambda_y = 0$ is related to the continuity equation whereas the roots $U \lambda_x + V \lambda_y + W \lambda_z = 0$ are related to the convective terms of momentum equations.

These subcharacteristics associated with the diffusive nature along normals to the wall determine zones of influence and dependence. A perturbation at a point P is carried along the y-axis by the diffusion process and along the boundary layer streamlines by convection in the downstream direction. Let us notice that, because of the diffusion process, a perturbation which travels along a streamline affects the whole surface normal to the wall containing this streamline. Therefore the domain of influence of a point P is a volume delimited by surfaces normal to the wall containing the outermost streamlines which cross the normal to the wall passing through P. In the same way, a domain of dependence of P can be defined (fig. 4.3). In fact, as for eq. (4.1), the practical domains of influence do not extend to infinity.

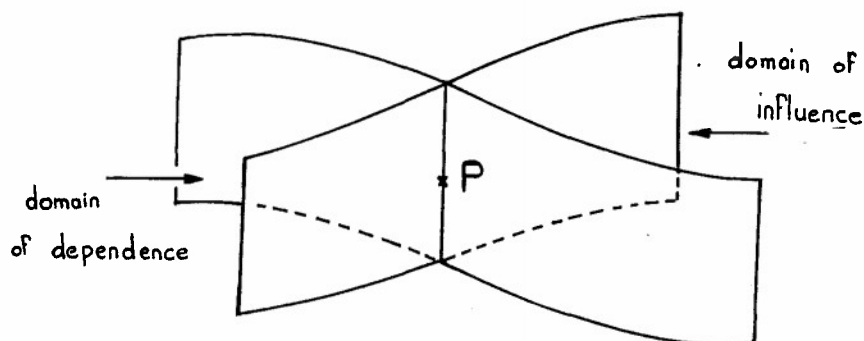


Fig. 4.3 - Domains of influence and of dependence

4.3. Initial and boundary conditions

The definition of the domains of influence and of dependence dictates the initial and boundary conditions. As a general rule, if we wish to calculate the boundary layer in a domain D bounded by a surface normal to the wall, initial or boundary conditions must be prescribed along the sides through which the fluid enters the domain D.

In principle, the velocity normal to the wall cannot be prescribed but must be calculated from the initial conditions. Only the U- and W-profiles need to be specified because the continuity equation provides a compatibility condition for the normal velocity component (KRAUSE, 1973). In practice, the initial conditions are provided by particular solutions, for example self-similar solutions.

The boundary layer calculation on a fuselage-like body can be initiated at, or near, the stagnation point where self-similar solutions exist (see for example CRABTREE et al, 1963). In the immediate vicinity of the stagnation point and by using a suitable axis system (locally cartesian), the outer flow is given by :

$$(4.8) \quad U_e = AX \quad W_e = 8Z$$

where the coefficients A and B depend on the local geometry. The self-similar solution is such as :

$$(4.9) \quad \frac{U}{U_e} = f'(\eta) \quad \frac{W}{W_e} = g'(\eta) \quad \eta = y \sqrt{\frac{U_e}{\nu x}}$$

and the velocity profiles are solutions of the following system :

$$(4.10a) \quad f''' + ff'' - f'^2 + 1 + \frac{B}{A} gf'' = 0$$

$$(4.10b) \quad g''' + fg'' - \frac{B}{A} (g'^2 - gg'' - 1) = 0$$

where the primes denote η -derivatives.

If B/A is small, the solution for f is the classical solution for a two-dimensional stagnation point.

Another useful self-similar solution is the solution along the attachment line of an infinite swept wing. Let Z be the coordinate parallel to the leading edge and X the coordinate normal to it. The outer velocity is given by :

$$(4.11) \quad U_e = kX \quad W_e = W_\infty = \text{cst}$$

The self-similar solution is such as :

$$(4.12) \quad \frac{U}{U_e} = f'(\eta) \quad \frac{W}{W_e} = g'(\eta) \quad \eta = y \sqrt{\frac{U_e}{vX}}$$

and the velocity profiles are solutions of the following equations :

$$(4.13a) \quad f''' + ff'' - f'^2 + 1 = 0$$

$$(4.13b) \quad g''' + fg'' = 0$$

The numerical integration gives :

$$(4.14) \quad \begin{aligned} \Delta_1 &= 0.648 \sqrt{\frac{v}{k}} & \theta_{11} &= 0.292 \sqrt{\frac{v}{k}} \\ \Delta_2 &= 1.026 \sqrt{\frac{v}{k}} & \theta_{22} &= 0.404 \sqrt{\frac{v}{k}} & \tau_{WZ} &= 0.57 W_e \sqrt{k\mu} \end{aligned}$$

In the X -direction, the solution is the solution for a two-dimensional stagnation point. In fact, this results from a general property of the laminar boundary layer flow on an infinite swept wing : the flow along the X -direction is independent of the flow along the Z -direction and is solution of two-dimensional equations. This follows from the infinite swept wing equations :

$$(4.15a) \quad \frac{\partial U}{\partial X} + \frac{\partial V}{\partial y} = 0$$

$$(4.15b) \quad U \frac{\partial U}{\partial X} + V \frac{\partial U}{\partial y} = -\frac{1}{\rho} \frac{\partial P}{\partial X} + \nu \frac{\partial^2 U}{\partial y^2}$$

$$(4.15c) \quad U \frac{\partial W}{\partial X} + V \frac{\partial W}{\partial y} = \nu \frac{\partial^2 W}{\partial y^2}$$

with the boundary conditions :

$$\begin{aligned} U = W = V &= 0 & y &= 0 \\ U &= U_e(X) & W_e &= W_\infty = \text{cst} & y &\rightarrow \infty \end{aligned}$$

Let us notice finally that if the swept wing is not "infinite", the solution (4.13) is often used to start the boundary layer calculations by assuming that the flow is locally identifiable with the flow on the leading edge of an equivalent infinite swept wing.

5 - INTEGRAL METHODS

As demonstrated by the 1968 and 1980-1981 STANFORD Conferences, integral methods remain a valuable engineering tool to calculate the effects of boundary layers.

In this section, the principle of integral methods will be first presented in two-dimensional flows. Afterwards, various types of methods will be discussed in three-dimensional flows and finally the method we have developed will be presented.

5.1. Integral methods in two-dimensional laminar flows

Nearly all integral methods use the global momentum equation known as the Von KARMAN equation. In incompressible flow, this equation is :

$$(5.1) \quad \frac{d\theta}{dx} = \frac{Cf}{2} - \theta \frac{(H+2)}{U_e} \frac{du_e}{dx}$$

To solve this equation, closure relationships are needed.

In the Von KARMAN-POHLHAUSEN method, these relationships are obtained by describing the velocity profiles by means of a polynomial representation, for example :

$$(5.2) \quad \frac{u}{U_e} = 2\eta - 2\eta^3 + \eta^4 + \frac{\Lambda}{6} \eta(1-\eta)^3 \quad ; \quad \eta = \frac{y}{\delta} \quad \Lambda = \frac{\delta^2}{\nu} \frac{du_e}{dx}$$

The formula (5.2) represents a family of velocity profiles which depends on the POHLHAUSEN pressure gradient parameter Λ . In fact, the boundary layer thickness δ does not appear in equation (5.1) and it is more appropriate to replace the parameter Λ by Λ_2 defined as :

$$(5.3) \quad \Lambda_2 = \frac{\theta^2}{\nu} \frac{du_e}{dx}$$

Indeed, it is easy to express Λ_2 as a function of Λ because θ/δ can be calculated as a function of Λ by using (5.2) :

$$(5.4) \quad \Lambda_2 = \Lambda \left[\frac{37}{315} - \frac{\Lambda}{945} - \frac{\Lambda^2}{9 \cdot 072} \right]^2$$

The closure relationships needed to solve the Von KARMAN equation are deduced from (5.2). The skin friction coefficient and the shape parameter are expressed as :

$$(5.5) \quad \frac{C_f}{2} R_\theta = \left[\frac{37}{315} - \frac{\Lambda}{945} - \frac{\Lambda^2}{9 \cdot 072} \right] \left[2 + \frac{\Lambda}{6} \right]$$

$$(5.6) \quad H = \frac{\frac{3}{10} - \frac{\Lambda}{120}}{\frac{37}{315} - \frac{\Lambda}{945} - \frac{12}{9 \cdot 072}}$$

Another way for constructing the closure relationships is to use the properties of the self-similar FALKNER-SKAN solutions. Indeed, from these solutions, it is straightforward to get the relationships $H(\Lambda_2)$ and $(C_f/2)R_\theta(\Lambda_2)$.

One drawback of these methods is that the properties of the family of velocity profiles are parametrized by Λ_2 . This implies, for example, that if the velocity distribution has a maximum, the boundary layer characteristics are given by the flat plate solution. This is not true because the boundary layer does not respond immediately to the pressure gradient. To overcome this difficulty, the Von KARMAN equation is complemented with a second integral equation. Generally, this equation is chosen as the global kinetic energy equation. Another possible choice is the global continuity equation (entrainment equation). It has often been argued that this latter choice is not convenient as the boundary layer thickness δ is not well defined. In fact, it has been shown (COUSTEIX, 1984) that it is possible to define δ in such a way that the solution of the global momentum and continuity equations is compatible with the FALKNER-SKAN solutions and the global kinetic energy equation. Then, the constructed method is based on the following set of equations :

$$(5.7a) \quad \frac{d\theta}{dx} = \frac{C_f}{2} - \theta \frac{(H+2)}{u_e} \frac{du_e}{dx}$$

$$(5.7b) \quad \frac{d}{dx} (\delta - \delta_1) = C_E - \frac{\delta - \delta_1}{u_e} \frac{du_e}{dx}$$

In the global continuity equation, the quantity $C_E = (d\delta/dx) - (v_e/u_e)$ is called the entrainment coefficient because it represents the rate at which the external flow enters the boundary layer through its external edge.

The closure relationships are deduced from the FALKNER-SKAN solution as the following functions :

$$(5.8a) \quad H = H(H^*) \quad H^* = \frac{\delta - \delta_1}{\theta}$$

$$(5.8b) \quad \frac{C_f}{2} R_\theta = \frac{C_f}{2} R_\theta(H)$$

$$(5.8c) \quad \frac{C_E R_\theta}{H^*} = \frac{C_E R_\theta}{H^*}(H)$$

The analytical expression of these functions are given below :

$$\frac{H^*}{H^*} + a \frac{H_0^*}{H^*} = b \left[\frac{1}{H} + \frac{H}{(4.02923)^2} \right] + c$$

$$\begin{array}{llll} a = 1.2706 & b = -1.5022 & c = 3.1924 & H < 4.02923 \\ a = 0.33044 & b = 0.31993 & c = 1.03094 & H > 4.02923 \\ H_0^* = 12.37 & & & \end{array}$$

$$\delta = 2.99259 \left[\left[\frac{1}{H} - \frac{1}{8.05846} \right]^{1.7} - \left[\frac{1}{8.05846} \right]^{1.7} \right] ; H < 4.02923$$

$$D = B - (H - 1) \left[-0.06815 + 4.336355 \left[\frac{1}{H} - \frac{1}{4.02923} \right]^{2.095065} \right] ; H < 4.02923$$

$$D = 0.20644 - 90.30936 \left[\left[\frac{1}{4.02923} \right]^{1.3} - \frac{1}{H^{1.3}} \right]^{3.35661} ; H > 4.02923$$

$$B = D + (H - 1) \left[-0.06815 + 46.34236 \left[\frac{1}{(4.02923)^2} - \frac{1}{H^2} \right]^{2.338238} \right] ; H > 4.02923$$

$$\frac{C_E R_\theta}{H^*} = -\frac{2}{H-1} B + \frac{H+1}{H-1} D$$

$$\frac{C_f}{2} R_\theta = B$$

5.2. Integral methods in two-dimensional turbulent flow

As in laminar flow, the integral methods in turbulent flow are based on the Von KARMAN equation and most of them use a second global equation which can be the entrainment equation or the global kinetic energy equation or a moment of momentum integral equation.

Various techniques have been employed to determine the closure relationships. A few of these techniques are described below.

5.2.1. Velocity profiles

The velocity profiles are sometimes represented by the classical power law :

$$(5.9) \quad \frac{u}{u_e} = \left[\frac{y}{\delta} \right]^{\frac{H-1}{2}}$$

More elaborate models have been proposed on the basis of a physical understanding of the boundary layer. These models are derived from the decomposition of the boundary layer into an inner region and an outer region, between which a logarithmic overlap exists ; this property is certainly the key to the success of such representations.

Let us recall that in the inner region, it is assumed that the velocity scales on the friction velocity :

$$(5.10) \quad u_\tau = u_e (C_f/2)^{1/2}$$

and the velocity profile follows a universal law :

$$(5.11) \quad u^+ = f(y^+) \quad u^+ = \frac{u}{u_\tau} \quad y^+ = \frac{y u_\tau}{\nu}$$

In the outer region, the velocity defect $u_e - u$ scales on the friction velocity and we have :

$$(5.12) \quad \frac{u_e - u}{u_\tau} = F'(\eta) \quad \eta = \frac{y}{\delta}$$

Compatibility of the behaviour of the velocity profile in the two regions leads to a logarithmic form in the overlap region ($y^+ \rightarrow \infty$ and $\eta \rightarrow 0$) which, in terms of inner variable, is :

$$(5.13) \quad u^+ = \frac{1}{\chi} \ln y^+ + C_1$$

where χ and C_1 are universal constants ($\chi = 0.41$, $C_1 = 5$). In terms of outer variables, the logarithmic form in the overlap region is :

$$(5.14) \quad \frac{u_e - u}{u_\tau} = -\frac{1}{\chi} \ln \eta + C_2$$

where C_2 is a constant depending on the pressure gradient.

The compatibility between (5.13) and (5.14) leads to the skin friction law :

$$(5.15) \quad \frac{u_e}{u_\tau} = \left[\frac{2}{Cf} \right]^{1/2} = \frac{1}{\chi} \ln \frac{u_\tau \delta}{v} + C_1 + C_2$$

In terms of physical distances, the inner region is very thin (if the REYNOLDS number is high enough). Therefore, a representation of the velocity defect law is sufficient to calculate the integral thicknesses. One of the well-known representations has been proposed by COLES, 1956. This is based on eq. (5.12) and (5.14) :

$$(5.16) \quad F'(\eta) = -\frac{1}{\chi} \ln \eta + \frac{B}{\chi} (2 - w(\eta))$$

The wake function w is approximated by :

$$(5.17) \quad w = 1 - \cos(\pi \eta)$$

where B is the parameter of the velocity profiles family.

Other analytical forms have been proposed to represent the velocity profiles. A rather sophisticated formulation has been given by WHITFIELD, 1980, which is valid over the whole thickness of the boundary layer.

Another method to generate a velocity profiles family consists of establishing self-similar solutions. Such solutions have been studied by MELLOR-GIBSON, 1963, and, later, MICHEL et al, 1968, used them in a systematic way to develop an integral method. The principle of these solutions is to assume that, for a certain class of boundary layers, the velocity defect profiles are a function of η alone and not of η and x . These boundary layers are called equilibrium boundary layers. This hypothesis transforms the partial differential equations into ordinary differential equations. For increasing REYNOLDS number, the skin friction tends to zero and this leads to simplification of the resulting equation. In the outer region, the momentum equation becomes :

$$(5.18) \quad \frac{\tau}{\tau_w} = \frac{-\rho \langle u'v' \rangle}{\tau_w} = 1 - \frac{F}{F(1)} + P\eta F'$$

with :

$$F' = \frac{u_e - u}{u_\tau} ; F(\eta) = \int_0^\eta F'(\eta) d\eta ; F_1 = F(1) = \frac{\delta_1}{\delta \sqrt{Cf/2}} ; P = \frac{1}{F_1} + 2\beta ; \beta = -\frac{\delta}{u_\tau} \frac{du_e}{dx}$$

Let us notice that the existence of (approximate) equilibrium boundary layers has been proved experimentally : these flows are such as β is constant (CLAUSER, 1954 ; Rotta, 1950).

The equation (5.18) has been solved by using a mixing length scheme to express the REYNOLDS stress $-\rho \langle u'v' \rangle$. This produces a one-parameter family of velocity profiles which can be used in an integral method. The parameter which characterizes a particular profile of the family is any quantity associated with the profile. MICHEL et al, 1968, use the CLAUSER parameter G :

$$(5.19) \quad G = \frac{\int_0^1 F'^2 d\eta}{\int_0^1 F' d\eta} = \frac{H - 1}{H(Cf/2)^{1/2}}$$

5.2.2. Skin friction law

The skin friction law is obtained either empirically or from the velocity profiles representation.

The most famous empirical skin friction law is due to LUOWIEG-TILLMAN, 1949 :

$$(5.20) \quad Cf = 0.246 R_0^{-0.268} 10^{-0.678H}$$

This law is valid over a wide range of attached boundary layers.

Another method is based on equation (5.15). For example, the use of the COLES velocity profiles gives the logarithmic law :

$$(5.21) \quad \left[\frac{2}{Cf} \right]^{1/2} = \frac{1}{\chi} \ln \frac{u_\tau \delta}{v} + C_1 + \frac{2B}{\chi}$$

5.2.3. Entrainment function

If the entrainment equation is used, a closure relationship is needed to express the entrainment coefficient. This function is very important because it describes the rate at which the outer fluid is entrained into the boundary layer. This process controls the growth of the boundary layer to a large extent and is intimately associated with the structure of turbulence in the boundary layer.

In many methods, the entrainment coefficient C_E is estimated with reference to equilibrium boundary layers. For such boundary layers, the x -dependence is eliminated, so the integral equations give algebraic relationships between C_E and the boundary layer characteristics. From the self-similar solutions, it has been shown that the entrainment coefficient is :

$$(5.22) \quad C_E = P\gamma = \frac{\delta}{\delta_1} \frac{C_f}{2} \left[1 - 2 \frac{\delta_1}{\tau_w} \rho_e U_e \frac{du_e}{dx} \right]$$

From this expression, experimental results such as those given by EAST-SAWYER, 1979, can be used to get the entrainment coefficient. Another way to get it is to use the results of the self-similar solutions.

In certain circumstances, history effects can be very important, for example in flows which have first increasing and then decreasing positive pressure gradient. It has been argued that the flow near the wall adjusts very rapidly to change in some parameter, for example the pressure gradient (TANI in KLINE et al, 1968). On the other hand, the outer layer dominated by large eddies and the inertia of which is large, does not respond instantaneously to external variations when the boundary layers are in non equilibrium. This physical idea led some investigators to the use of a lag-equation for calculating the entrainment coefficient. GREEN et al, 1972, have used as guidelines the turbulent kinetic energy equation as modelled by BRADSHAW et al (in KLINE et al, ed., 1968) from which they inferred a lag entrainment equation. Essentially, the effects of history are included through the difference between the actual pressure gradient and a fictitious equilibrium pressure gradient, which would give the same boundary layer characteristics.

Let us notice that if the global kinetic energy equation is used instead of the global continuity equation, a dissipation function D has to be modelled :

$$D = \int_0^\delta [-\langle u'v' \rangle + \nu \frac{\partial u}{\partial y}] \frac{\partial u}{\partial y} dy$$

A similar discussion as above can be done because in the same way as the entrainment coefficient, the dissipation function is strongly associated with a turbulence model.

5.3. Integral methods in three-dimensional turbulent flows

As in the two-dimensional case, the integral methods are based on the global momentum equation but, in the three-dimensional case, there are two momentum equations which have been given in § 3.2.. Most of the methods use a third equation which can be the global continuity equation (MYRING, 1970, SMITH, 1972, COUSTEIX, 1974, STOCK, 1979, CROSS, 1979, OKUNO, 1976) or the global kinetic energy equation (SWAFFORD, 1983). OKUNO uses a fourth equation which is the moment integral equation of the crosswise momentum.

The closure relationships are often obtained from the use of streamwise and crosswise velocity profiles. It is generally assumed that the streamwise velocity profiles behave in the same way as the velocity profiles in a two-dimensional boundary layer. MYRING, SMITH, OKUNO use the power law profiles ; COUSTEIX uses the self-similar solution developed by MICHEL et al, 1968 ; STOCK uses the COLES velocity profiles.

The streamwise skin friction coefficient and the entrainment coefficient are also generally calculated from two-dimensional relationships.

The modelling of crosswise velocity profiles is often very empirical.

The MAGER representation is often used (MYRING, SMITH, STOCK) ; this is written :

$$(5.23) \quad \frac{w}{u} = \tan \beta_0 (1 - \eta)^2$$

Even when the crossflow profile is simple, such a formulation often gives rather crude relationships for the dependence between the crossflow characteristics.

A triangular representation of the polar plot $w(u)$ has been proposed by GRUSCHWITZ, 1935, and re-used by JOHNSTON, 1960. The location of the apex of the triangle at a fixed y^+ value ($y^+ = 13$) allows a relationship to be set up from which the limiting angle β_0 is calculated. In many cases, this formulation yields satisfactory relationships for the thicknesses. However, the law for the limiting angle β_0 seems to be less well founded.

More generally, polynomial representations have been proposed (EICHELBRENNER, 1965, SHANE BROOK-HATCH, 1970, OKUNO, 1976) ; for example :

$$(5.24) \quad \frac{w}{u_0} = \tan \beta_D P_1(\eta) + C P_2(\eta)$$

In the method proposed by EICHELBRENNER, an equation is provided to calculate the second parameter. This equation can be considered as an extension of the SQUIRE-WINTER relation discussed in § 1.1.. In the method developed by OKUNO, a moment of momentum integral equation is used to calculate the second parameter.

In the method developed by COUSTEIX, the crossflow velocity profiles have been generated from an extension to three-dimensional boundary layer of the self-similar solutions. The resulting closure relationships are given in appendix.

Finally, let us mention the method proposed by COLES which gives a vectorial representation of the velocity profile within the boundary layer. This is an extension of the law of the wall-law of the wake used in two-dimensional flow. The boundary layer velocity vector is given by :

$$(5.25) \quad \vec{Q} = \vec{Q}_\tau \left[\frac{1}{X} \ln \frac{y |\vec{Q}_\tau|}{v} + C + \frac{\pi}{X} w \left[\frac{y}{\delta} \right] \right]$$

where \vec{Q}_τ is parallel to the skin friction vector $\vec{\tau}_p$ and its modulus is $\sqrt{\tau_p/\rho}$. π is a tensor such that $\pi \vec{Q}_\tau$ is parallel to the external velocity.

In this formulation, the velocity vector turns from the direction of the limiting wall streamline to the direction of the external velocity. A similar model has been used by CROSS, 1979 and LE BALLEUR, 1983.

From the brief presentation of the various hypotheses used to establish the closure relationships, two main difficulties can be discussed.

The first difficulty is the modelling of the entrainment coefficient. As already said for the two-dimensional case, this coefficient is intimately associated with the boundary layer turbulence structure. Now, the experiments of ELSENAAR-BOELSMA, 1974, and BRADSHAW-PONTIKOS, 1985, have shown that the turbulence structure is modified by the three-dimensionality of the flow. In particular, the main axes of the stress tensor are no longer aligned with the main axes of the velocity gradient tensor ; the transport velocity for the turbulent kinetic energy decreases ; the magnitude of the shear stress decreases compared with an equivalent two-dimensional boundary layer. These effects result from the effect of crossflow on large eddies and it is probable that the entrainment rate decreases when the three-dimensionality develops. This is not taken into account when it is assumed that the entrainment coefficient follows the same rules as in two-dimensional flow.

The second difficulty to establish the closure relationships is that there is no counterpart of the two-dimensional law of the wall which is important for the success of the representation of velocity profiles. Several attempts have been made to extend this law of the wall. Generally, the behaviour of the velocity profile is obtained by solving the basic equations with a similarity hypothesis and by using a turbulence model, for example a mixing length model (Van den BERG, 1975). In two-dimensional flow, the reasoning is not at all the same : the logarithmic law of the wall comes from the analysis of the double-layer structure of the boundary layer and turbulence models are devised to reproduce the properties of the velocity profile. Recently, GOLDBERG-RESHOTKO, 1984, have performed an asymptotic analysis of the three-dimensional boundary layer. They found that the direction of the velocity is constant in the inner layer ; at very large REYNOLDS number, this result is certainly true but, in practice, it is insufficient because the experimental results show that the velocity direction can vary rapidly near the wall. In the JOHNSTON's model, the apex of the polar plot is around $y^+ = 13$; this means that it cannot be assumed that the velocity direction in the logarithmic region is equal to the wall limiting angle β_D .

5.4. Calculation of the transition region

A review of problems arising from the laminar-turbulent region is provided by the AGARD Special Course on Stability and Transition in Laminar Flow (AGARD Report N° 709) and the paper by ARNAL, 1986.

The practical calculation of a laminar-turbulent transition region involves two problems. The first one is the determination of the onset of transition and the second one is the calculation of the transition region itself.

The calculation of the transition region can be performed by weighting the properties of a fictitious laminar boundary layer and a fictitious turbulent boundary layer; this is the so-called "intermittency" method. The weighting function γ is defined from the evolution of the momentum thickness:

$$\gamma = 1 - \exp \left[-2.5 \left[\frac{\theta_{11}}{\theta_{11T}} - 1 \right] \right]$$

where θ_{11T} is the value of the momentum thickness at the onset of transition.

Although this treatment is crude, the influence on the downstream boundary layer is not very large. It is more important to predict accurately the location of transition onset.

In two-dimensional flow, transition can be caused by several mechanisms. In the case of the so-called natural transition, the first stage of the process is described by the occurrence and the amplification of instabilities which are called TOLLMIEN-SCHLICHTING waves. The linear stability theory enables us to calculate the characteristics of these waves as eigensolutions of the linearized NAVIER-STOKES equations. From this theory, there exists a REYNOLDS number below which all the disturbances are damped. We will call this REYNOLDS number R_{ins} .

One of the most successful criterion for the onset of transition is based on the calculation of the amplification of the TOLLMIEN-SCHLICHTING waves when the REYNOLDS number is larger than R_{ins} . The e^n -method (SMITH-GAMBERONI, 1956, Van INGEN, 1956, 1977) says that the onset of transition occurs when the amplification is equal to e^n where n is a coefficient which depends on the turbulence level of the external flow. ARNAL et al, 1984, have applied this technique to the FALKNER-SKAN laminar self-similarity solutions and they deduced a practical criterion for the onset of transition which extends the GRANVILLE criterion (1953) by taking into account the effects of external turbulence. This criterion also includes the effects of pressure gradients. It is given by (fig. 5.1):

$$(5.26) \quad R_{\theta T} - R_{\theta ins} = -206 \exp(25.7 \bar{\Lambda}_2) (\ln 16.8 Tu - 2.77 \bar{\Lambda}_2)$$

where Tu is the turbulence intensity in the external flow:

$$(5.27) \quad Tu = (\langle u'^2 \rangle + \langle v'^2 \rangle + \langle w'^2 \rangle) / 3u_e^2)^{1/2}$$

$\bar{\Lambda}_2$ is a mean value of the POHLHAUSEN parameter:

$$(5.28) \quad \bar{\Lambda}_2 = \frac{1}{x - x_{ins}} \int_{x_{ins}}^x \frac{\theta^2}{\nu} \frac{du_e}{dx} dx$$

The location x_T of the transition onset is determined when the value of the REYNOLDS number R_θ calculated in laminar flow is equal to the value of $R_{\theta T}$ given by the formula (5.26). This formula also involves the calculation of x_{ins} and $R_{\theta ins}$. The values of x_{ins} and $R_{\theta ins}$ are determined when the REYNOLDS number R_θ calculated in laminar flow is equal to the value of a critical REYNOLDS number $R_{\theta cr}$ (at the point $x = x_{ins}$, we have $R_\theta = R_{\theta cr} = R_{\theta ins}$). This REYNOLDS number $R_{\theta cr}$ is obtained from the analysis of the stability properties of the self-similar solutions. It is assumed that $R_{\theta cr}$ is a function of the shape parameter H :

$$(5.29a) \quad R_{\theta cr} = \left[\frac{e^{5.27+17.2 \left[\frac{1}{H} - 0.39 \right]^{0.5}}}{H} \right] \quad H < 2.5$$

$$R_{\theta cr} = \left[\frac{e^{3.5 + \frac{2.897}{H} + \frac{22.230}{H^{10}}}}{H} \right] \quad H > 2.5$$

where H is the value of the shape parameter of the boundary layer calculated in laminar flow.

Other mechanisms than the TOLLMIEN-SCHLICHTING waves can lead to transition and a number of parameters can delay or promote the location of "natural" transition given by (5.29). In these cases, specific criteria are needed.

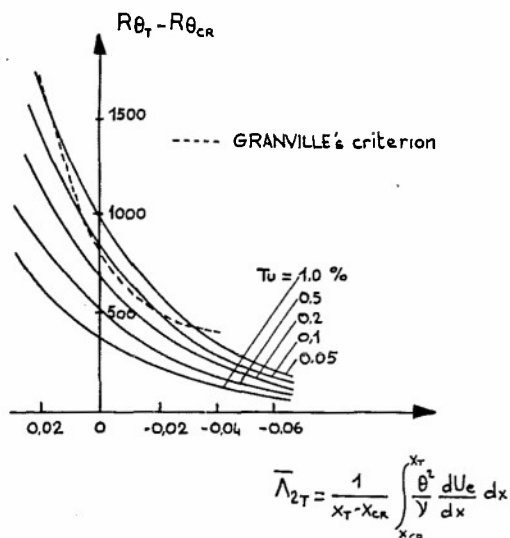


Fig. 5.1 - Transition criterion in two-dimensional flow (ARNAL et al, 1984)

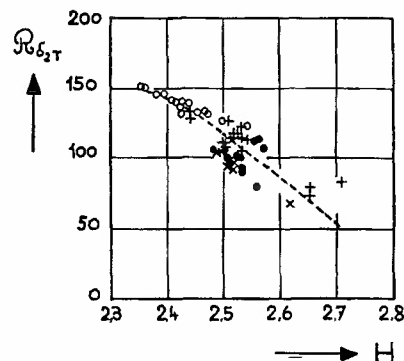


Fig. 5.2 - Transition criterion for the crossflow (from ARNAL et al, 1984)

○ POLL × SCHMITT-MANIE + BOLTZ et al
● ARNAL et al

$$--- R\delta_{2T} = \frac{300}{\pi} \operatorname{Arctg}\left(\frac{0.106}{(H - 2.3)^2}^{0.52}\right) \\ 2.3 < H < 2.7$$

In a three-dimensional flow, the "natural" transition can occur from the same type of instability as in two-dimensional flow. For practical calculation, it is assumed that the properties of stability of the streamwise velocity profiles are the same as those of a two-dimensional velocity profiles. The transition can also occur from an instability of the crossflow and this crossflow instability can develop in regions where the streamwise velocity profile is stable. On a swept wing, it results that this crossflow instability can cause a transition very close to the leading edge even if the streamwise velocity profile is stable in this region.

From experimental data, ARNAL et al, 1984, have extended the BEASLEY, 1973, criterion for predicting the onset of crossflow transition (fig. 5.2) :

$$(5.30) \quad (R\delta_2)_T = \frac{300}{\pi} \operatorname{atan} \left[\frac{0.106}{(H - 2.3)^{2.052}} \right] ; 2.3 < H < 2.7$$

where δ_2 is given by :

$$\delta_2 = \int_0^\delta - \frac{w}{u_e} dy$$

For practical calculation, it is assumed that the streamwise and crosswise transition processes are uncoupled. This means that transition occurs when one of the two criteria (5.29) or (5.30) is first satisfied. The criterion (5.29) is applied to the streamwise boundary layer and the criterion (5.30) is applied to the crossflow.

A third kind of transition can occur due to the so-called leading edge contamination. In this process, the boundary layer developing along the leading edge (attachment line) can be perturbed by the boundary layer coming from the fuselage. From various experiments (see, for example, POLL, 1984), it results that the boundary layer along the leading edge is laminar if the REYNOLDS number $W_e \theta / \nu$ is less than 100 (W_e is the external velocity component along the leading edge and θ is the momentum thickness of the corresponding boundary layer). If the REYNOLDS number $W_e \theta / \nu$ is larger than 100 (or 150), it is probable that the leading edge is turbulent. However, due to the negative pressure gradient downstream of the leading edge, the boundary layer can relaminarize. A criterion used by LAUNDER-JONES, 1968, in two-dimensional flow and by BEASLEY, 1973, in three-dimensional flow is :

$$(5.31) \quad \frac{\nu}{u_e^2} \frac{\partial u_e}{\partial s} = 5 \cdot 10^{-6}$$

where s is the distance along an external streamline.

5.5. Description of an integral method

The integral method we have developed (COUSTEIX-QUEMARD, 1972, COUSTEIX, 1974) for calculating three-dimensional boundary layers is based on the solution of global equations of continuity and of momentum (eq. 3.3). The equations are written in a non orthogonal curvilinear axis system.

The method has been developed in laminar and turbulent flow. The transition location can be prescribed a priori or calculated as described in § 5.4..

The closure relationships, in the laminar and turbulent cases, have been obtained from self-similar solutions. They are valid in compressible flow ($M_e < 4$) on an adiabatic wall. These relationships are given in appendix. For convenience, they are given in a streamline coordinate system but they can be transformed into relationships for the boundary layer characteristics expressed in any curvilinear non orthogonal axis system. These relationships have also been extended to calculate a three-dimensional wake.

The procedure is first illustrated in the case of an incompressible two-dimensional dissymmetrical wake. We define an upper half-wake and a lower half-wake separated by the line y_0 which is the minimum velocity line. Along this line y_0 , it is assumed that the shear stress is zero. Then the global equations for each part of the wake are :

- upper half wake (subscript u)

$$(5.32a) \quad \frac{d\theta_u}{dx} = \frac{v_0}{u_e} \frac{u_e - u_m}{u_e} - \theta_u \frac{H_u + 2}{u_e} \frac{du_e}{dx}$$

$$(5.32b) \quad \frac{d(\delta - \delta_1)_u}{dx} = C_{Eu} + \frac{v_0}{u_e} - \frac{(\delta - \delta_1)_u}{u_e} \frac{du_e}{dx}$$

- lower half wake (subscript l)

$$(5.33a) \quad \frac{d\theta_l}{dx} = - \frac{v_0}{u_e} \frac{u_e - u_m}{u_e} - \theta_l \frac{H_l + 2}{u_e} \frac{du_e}{dx}$$

$$(5.33b) \quad \frac{d(\delta - \delta_1)_l}{dx} = C_{El} - \frac{v_0}{u_e} - \frac{(\delta - \delta_1)_l}{u_e} \frac{du_e}{dx}$$

where v_0 is the vertical velocity along the y_0 -line and u_m is the minimum velocity.

For each part of the wake, the velocity profile is modelled by :

$$(5.34) \quad \frac{u_e - u}{u_e - u_m} = [\eta^{3/2} - 1]^2 \quad ; \quad \eta = \frac{y - y_0}{\delta}$$

We deduce the following relationships :

$$(5.35a) \quad \frac{u_e - u_m}{u_e} = \frac{H - 1}{0.7013 H}$$

$$(5.35b) \quad \frac{\delta_1}{\delta} = 0.45 \frac{u_e - u_m}{u_e}$$

For each part of the wake, the entrainment coefficient is given by :

$$(5.36) \quad C_E = 0.14 \frac{u_e - u_m}{u_e}$$

For a given value of v_0 , the systems (5.32, 5.35, 5.36) and (5.33, 5.35, 5.36) for the upper half-wake and the lower half-wake can be solved separately. In general, these solutions will lead to different values of u_m for the upper half-wake and the lower half-wake. The value of v_0 is calculated step by step to have the same value of u_m ; this calculation is performed by a shooting method.

In the case of a three-dimensional wake, the principle is the same except that the crosswise global momentum equations are used to calculate the crossflow.

It is assumed that the streamwise velocity profile behaves like in a two-dimensional flow and relationships (5.34), (5.35), (5.36) are used to model the streamwise velocity profile.

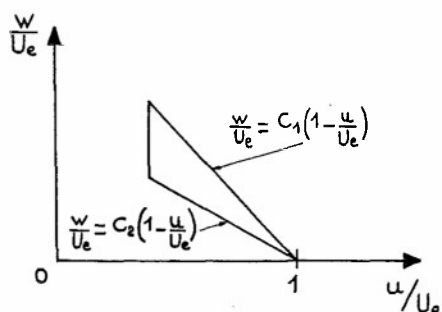


Fig. 5.3 - Modelling of the crossflow in a three-dimensional wake

The crosswise velocity profile is obtained by assuming a triangular polar plot (fig. 5.3). From this modelling, we deduce the following relationships for each part of the wake :

$$\delta_2 = -CH\theta_{11} ; \theta_{21} = -C\theta_{11} ; \theta_{12} = C(H-1)\theta_{11} ; \theta_{22} = -C^2(H-1)\theta_{11}$$

The values of C_1 and C_2 result from the solution of crosswise momentum equations written for each half-wake.

In compressible flow, the total enthalpy h_t in the wake can be assumed constant if the wake develops behind a wing with an adiabatic wall. If it is also assumed that the velocity profiles can be modelled by the same representation as in incompressible flow, it is easy to extend the method to this case.

5.6. Examples of application

A first example of application of the integral method in turbulent flow is given in fig. 5.4. This is the study of the flow around the M6 wing (SCHMITT-COUSTEIX, 1975). Calculated wall streamlines are compared with experimental wall flow visualization. The free stream velocity is 90 ms^{-1} ; the angle of attack is 15° . The initial condition for the boundary layer calculations have been prescribed from cross-checking with boundary layer measurements at a few stations on the wing.

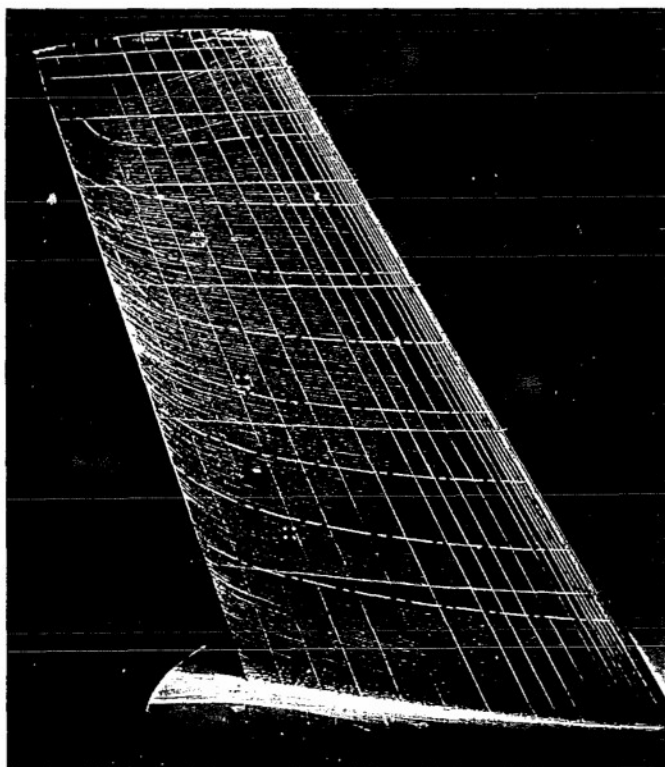


Fig. 5.4 - Boundary layer calculations on the M6 wing
— . — calculated wall streamlines

Another example is the study of the turbulent boundary layer in supersonic flow in a curved channel (COUSTEIX-MICHEL, 1975). The MACH number is about $M_\infty = 1.6$. The initial conditions have been prescribed from boundary layer measurements at the initial station. In addition, boundary conditions have been prescribed along the upper wall bounding the nozzle. The crossflow is assumed to be zero along this boundary. Samples of results are given in fig. 5.5.

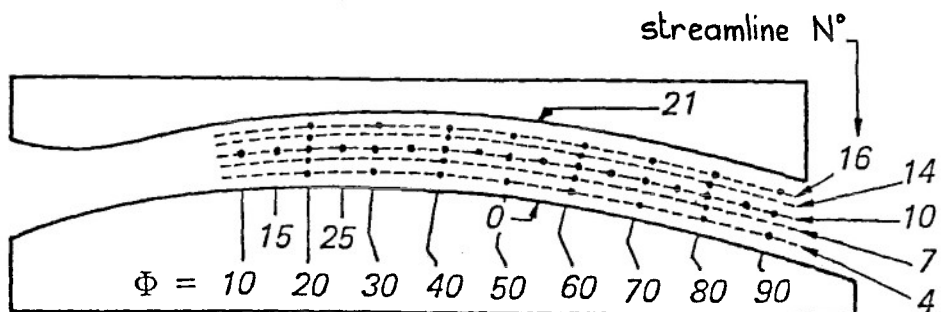


Fig. 5.5a - Boundary layer calculation in a curved supersonic nozzle

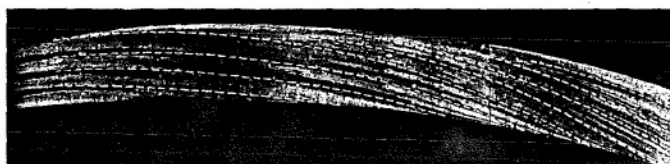


Fig. 5.5b - Experimental and calculated wall streamlines (integral method) - ---- Calculations

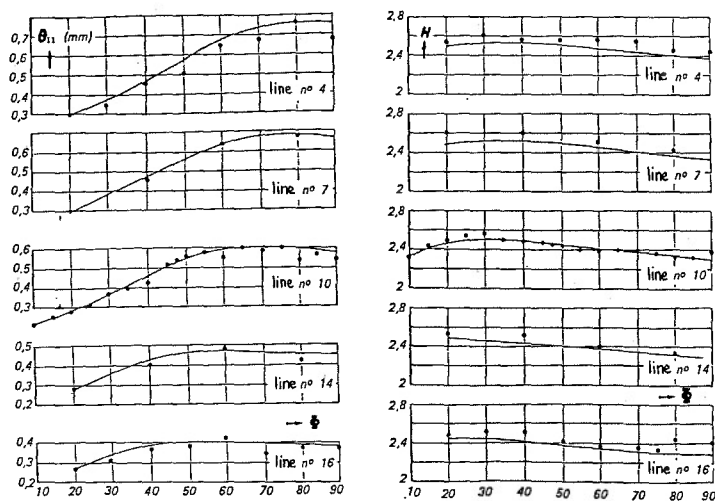
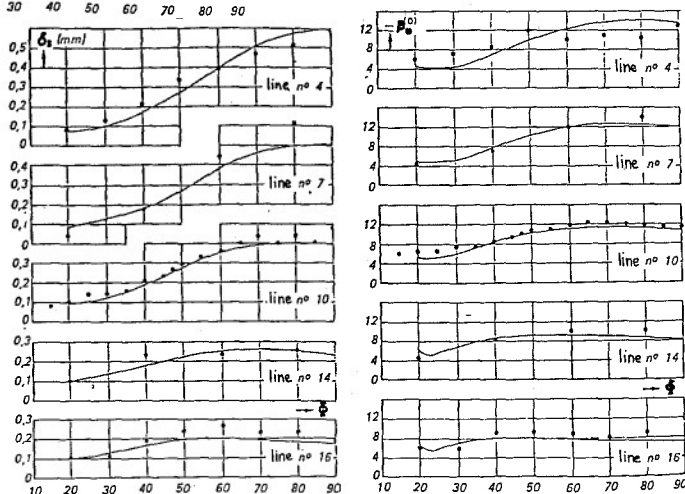


Fig. 5.5c - Boundary layer characteristics calculated with an integral method

Fig. 5.5d - Boundary layer characteristics calculated with an integral method



The integral method has also been applied to the boundary layer developing on a swept wing (PAILHAS, 1979). The experimental set up and the external velocity distribution are shown in fig. 5.6a. The section of the model is an ONERA D airfoil ; the sweep angle is 22.5° ; the normal incidence is 8° ; the free stream velocity is 35 ms^{-1} . Initial conditions for the boundary layer calculations have been prescribed from experimental results. The evolution of the calculated results is presented in fig. 5.6b.

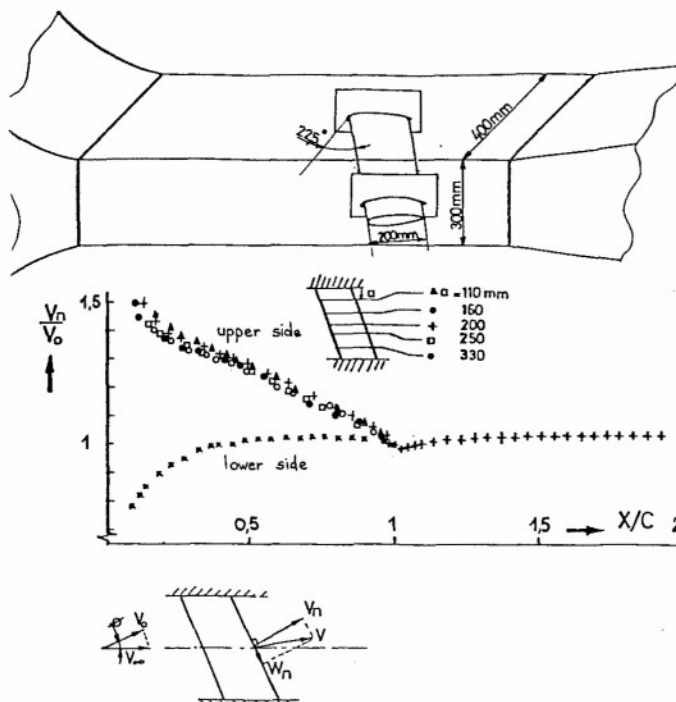


Fig. 5.6a - Study of a boundary layer developing on a swept wing

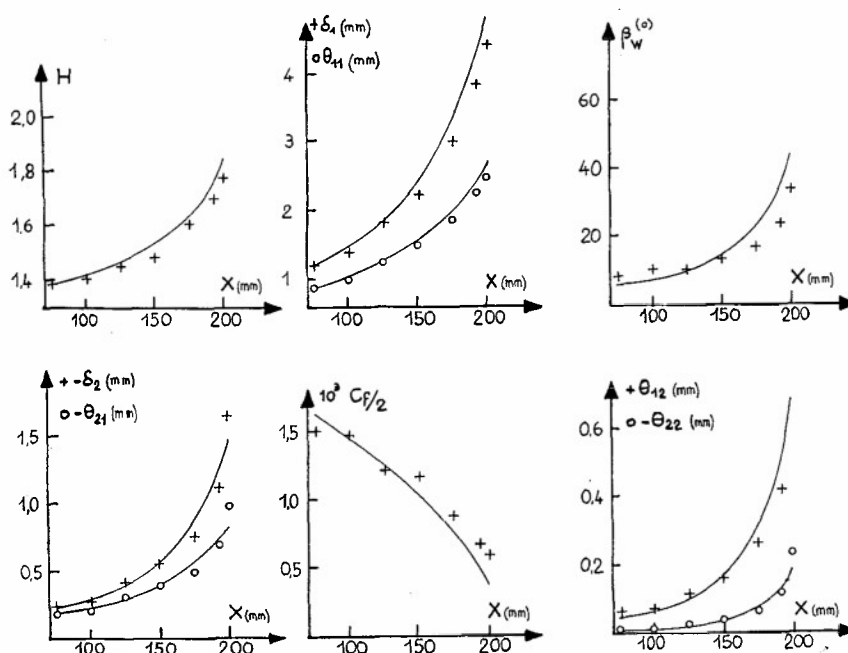


Fig. 5.6b - Calculation of the boundary layer developing on a swept wing (integral method)

Another application of the integral method has been provided by the experiment performed by MEIER et al, 1984, on an ellipsoid. In these experiments, the external flow conditions (magnitude and direction of external velocity) have not been measured. These data have been calculated from the measured wall pressure distribution as described in GLEYZES-COUSTEIX, 1984. Several cases have been calculated. The first one is at low REYNOLDS number, in laminar flow, for an angle of attack of 10° . The calculated wall streamlines are compared to the experimental wall streamlines obtained from measurements with directional skin friction gauges (fig. 5.7). The calculations stop when a singularity is detected; this problem will be discussed further in paragraph 6. The locus of the termination points suggests the formation of a separation line whose location compares rather well with experiments.

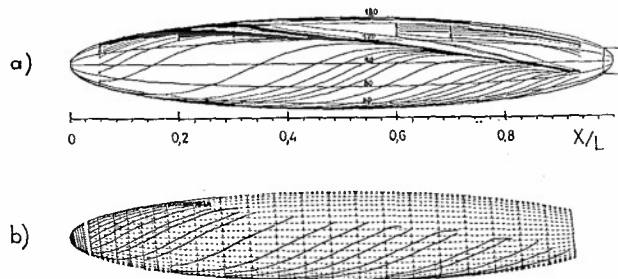


Fig. 5.7 - Boundary layer on an ellipsoid - Wall streamlines - Laminar flow - $\alpha = 10^\circ$ - $Re = 1.6 \cdot 10^6$
a) Experimental results (MEIER et al, 1984) - b) Calculated results (integral method)

The boundary layer on the ellipsoid has also been calculated at a higher REYNOLDS number for the same angle of attack 10° . In this case, the boundary layer is laminar, transitional and turbulent. In the calculations, the onset of transition has been prescribed from the experimental data. The calculated wall streamlines compare well with the experimental results (fig. 5.8); in particular, they suggest the occurrence of a separated zone in the rear region as in the experiment. A more detailed comparison is given in fig. 5.8 where the thicknesses δ_1 and δ_2 and the shape parameter H are plotted as a function of the azimuth for two sections. (These boundary layer characteristics have been calculated by GLEYZES et al from the velocity profile data supplied by MEIER et al, 1984). The general behaviour of δ_1 and δ_2 is well reproduced but the maximum of δ_2 is overestimated.

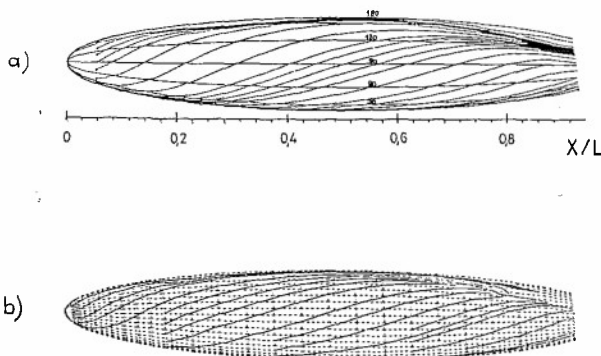


Fig. 5.8a - Boundary layer on an ellipsoid - Wall streamlines - $\alpha = 10^\circ$ - $Re = 7.2 \cdot 10^6$
a) Experiments (MEIER et al, 1984)
b) Calculations (integral method)

Fig. 5.8b - Boundary layer in an ellipsoid - $\alpha = 10^\circ$ - $Re = 7.2 \cdot 10^6$

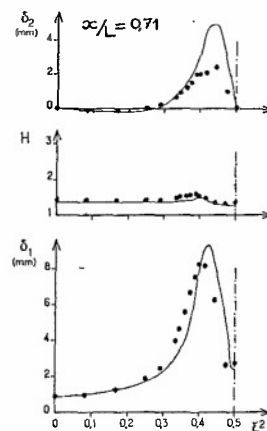
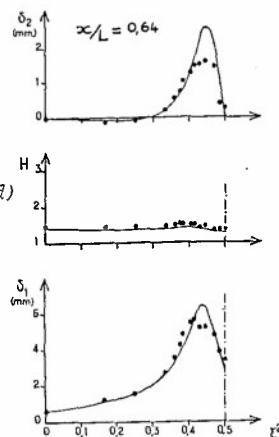
• Experiment (MEIER et al, 1984)

— Calculations (integral method)

ξ^2 = circumferential coordinate

($\xi^2 = 0$ windward line of symmetry)

δ_1 - $\xi^2 = 0.5$ leeward line of symmetry)



The last example is an application of the integral method to the experiment performed by BRADSHAW and PONTIKOS, 1985 (GLEYZES-COUSTEIX, 1986, unpublished). This experiment is a study of a three-dimensional boundary layer developing on an "infinite swept wing". The conditions are similar to those of the Van den BERG et al experiment, except that the initial boundary layer is thinner so that separation is not reached. The main set of data has been taken at four stations on a line parallel to the tunnel axis.

The comparisons between the calculated results and the experimental results (fig. 5.9) show a good overall agreement on the streamwise and on the crosswise characteristics. However it should be noticed that the calculations are sensitive to initial data as described below. In principle, the experiment has been devised in such a way that the boundary layer characteristics are invariant along the spanwise direction. In fact, there are slight variations of the boundary layer characteristics along the initial data line parallel to the span (PONTIKOS, 1982). At first sight, these variations are within the accuracy of measurements but if calculations are performed by using two different sets of initial data taken at two stations along the initial data line, it is seen that the results are significantly different (fig. 5.9). Indeed the initial differences between the data are not damped but they are amplified. This means that to avoid misinterpretations, a very high accuracy of measurements is needed especially in the initial data.

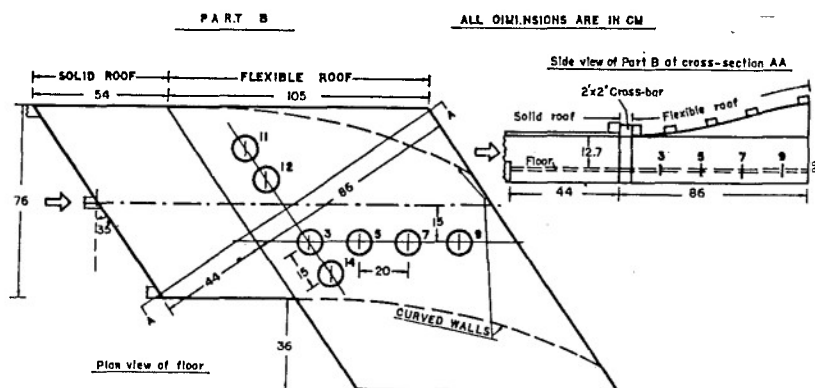


Fig. 5.9a - Experimental set-up used by BRADSHAW-PONTIKOS, 1985

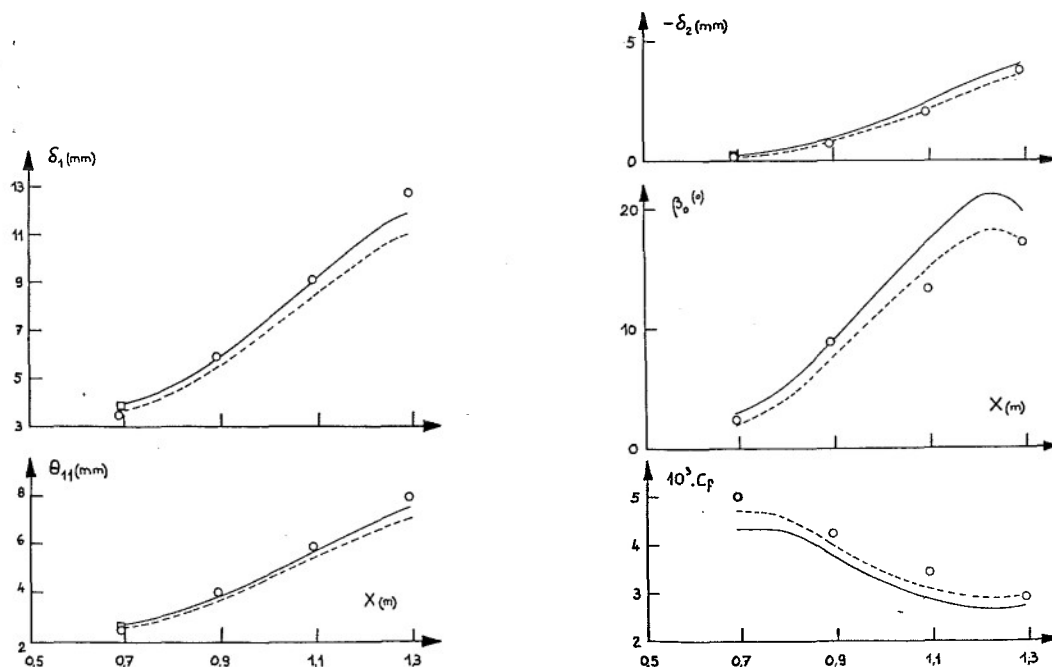


Fig. 5.9b - Comparisons experiment - calculations - o Data taken at stations 3-5-7-9 (BRADSHAW-PONTIKOS)

□ Data taken at station 12 -

Integral method — Calculations with initial conditions at station 12

----- Calculations with initial conditions at station 3 (GLEYZES-COUSTEIX)

6 - SINGULARITIES IN BOUNDARY LAYER CALCULATIONS

The boundary layer equations (either local or global) are completed by closure relationships and are associated with appropriate initial and boundary conditions. Then, it is assumed that the problem is mathematically well posed and numerical means are employed to solve it. However, it is not known a priori that a solution exists in any preassigned domain.

From the local equations, the analysis of this problem is generally performed in laminar flow although it has not been shown that the turbulence model has no influence.

6.1. Steady two-dimensional boundary layer

The GOLDSTEIN, 1948, analysis of local equations in laminar flows has shown that a possible stop of computations is due to a singularity in the equations which is characterized by an unbounded vertical velocity and a zero skin friction. This has been confirmed by a number of numerical results. The wall shear stress vanishes as the square root of the distance from where it is zero and no solution exists downstream.

Obviously the singularity is not physical, but it is often argued that the behaviour of the solution near the singularity is an exaggeration of the actual flow.

The properties of integral methods (in laminar or turbulent flow) have strong similarities with local methods. Let us consider the system of the global continuity and momentum equations :

$$(6.1) \quad \frac{d(\delta - \delta_1)}{dx} + \frac{\delta - \delta_1}{u_e} \frac{du_e}{dx} = C_E$$

$$(6.2) \quad \frac{d\theta}{dx} + \theta \frac{H + 2}{u_e} \frac{du_e}{dx} = \frac{C_f}{2}$$

The closure relationship for $H^* = (\delta - \delta_1)/\theta$ has the form :

$$(6.3) \quad H^* = H^*(H)$$

This is exactly the form of the relationship used in laminar flow. In turbulent flow, this form is an approximation of the actual relationship because H^* depends also slightly on the REYNOLDS number, but this dependence is weak.

If equation (6.3) is used in equations (6.1) and (6.2), we obtain the following system :

$$(6.4') \quad \frac{d\theta}{dx} = \frac{C_f}{2} - \frac{\theta(H + 2)}{u_e} \frac{du_e}{dx}$$

$$(6.5) \quad (H^* - HH^{*'}) \frac{d\theta}{dx} + H^* \frac{d\delta_1}{dx} = C_E - H^* \frac{\theta}{u_e} \frac{du_e}{dx}$$

where $H^{*'} = \frac{dH^*}{dH}$.

From equations (6.4) and (6.5), the derivatives $d\theta/dx$ and $d\delta_1/dx$ can be calculated if $H^{*'} \neq 0$. In fact, the case $H^{*'} = 0$ can occur because the function $H^*(H)$ has a minimum at a point $H^* = H_C^*$, $H = H_C$. This minimum is obtained for $H_C = 4.03$ in laminar flow and around $H_C = 2.6$ in turbulent flow. These values are associated with the zero skin friction point.

As with the local equations, it is not possible to continue the calculation beyond the point $H = H_C$ because equations (6.4) and (6.5) can be combined to give :

$$(6.6) \quad \theta \frac{dH^*}{dx} = C_E - H^* \frac{C_f}{2} + H^*(H + 1) \frac{\theta}{u_e} \frac{du_e}{dx}$$

In a calculation, when a point $x = x_c$ is reached where $H = H_C$, the right member of (6.6) is generally non zero and negative so that H^* becomes smaller than H_C^* and equation (6.3) gives no solution for H .

Another problem related to the occurrence of a singularity is that the results obtained at locations close to a possible singularity are very sensitive to various factors, such as (for example) the numerical scheme, the evaluation of the pressure gradient, the closure relationships. Small modifications in these factors can lead to large differences in the results. Therefore, it is difficult to separate the influence of each factor, particularly the influence of the closure relationships (when working with the local equations, these relationships are the turbulence model). This can lead to unfortunate misinterpretations.

6.2. Inverse method in two-dimensional flow

Instead of solving equations (6.1), (6.2), (6.3) with a prescribed velocity distribution $u_e(x)$, it is possible to consider that u_e is an unknown and that $\delta_1(x)$ is prescribed. This is the so-called inverse mode (CATHERALL-MANGLER, 1963). In fact, an infinite variety of inverse modes can be imagined; instead of prescribing $\delta_1(x)$, it is possible to prescribe the function $H(x)$ or any other function of boundary layer characteristics.

If $\delta_1(x)$ is prescribed, equations (6.1) and (6.2) can be rewritten as a system for θ and u_e :

$$(6.7) \quad \frac{d\theta}{dx} + \theta \frac{H+2}{u_e} \frac{du_e}{dx} = \frac{Cf}{2}$$

$$(6.8) \quad (H^* - HH^*) \frac{d\theta}{dx} + H^* \frac{\theta}{u_e} \frac{du_e}{dx} = C_E - H^* \frac{d\delta_1}{dx}$$

In general, the calculation of $d\theta/dx$ and $d\delta_1/dx$ is possible even when $H > H_c$.

The inverse methods can be used in design techniques where a certain optimisation condition is prescribed.

The inverse methods have also been widely used in viscous-inviscid interaction techniques. In this case, the problem is not to solve the boundary layer equations alone but the coupled system of boundary layer equations and inviscid equations. A very clear presentation of the problem is given for example by VELDMAN, 1980.

6.3. Three-dimensional boundary layer

The nature of the system of global equations used in an integral method has been studied by MYRING, 1970 and COUSTEIX-HOUDEVILLE, 1981. The integral method is based on three global equations (continuity and momentum equations) which are complemented with closure relationships.

The equations form a system of three first order partial differential equations. It has been shown that the system has three characteristic directions which are always real and distinct. The system is hyperbolic. This property is related to the fact that the boundary layer streamlines are subcharacteristics of the system of local equations and, due to the integration with respect to y , the number of characteristics reduces. This number is equal to the number of global equations.

The calculation of characteristic roots of the set of global equations has been performed (COUSTEIX-HOUDEVILLE, 1981) with approximate closure relationships. The angle of the characteristic directions is defined with respect to the external streamline; its value is $\tan^{-1}\gamma$. The three characteristic roots are:

$$(6.9) \quad \gamma_1 = \frac{C(H-1)}{1-\beta H}$$

$$(6.10) \quad \gamma_2 = C(H-1)$$

$$(6.11) \quad \gamma_3 = \frac{C(H-1)}{(2\alpha + \beta)H + 1}$$

$$\alpha = 0.631 \quad \beta = -\alpha + \sqrt{\alpha^2 + \alpha} = 0.382$$

The coefficient C in eqs. (6.9), (6.10), (6.11) is a parameter defining the crossflow velocity profiles: for the calculation of γ , the crosswise integral thicknesses are calculated with an approximate crossflow velocity profile: $w/u_e = C(1-u/u_e)$.

From the closure relationships used in the integral method, it has been shown that the γ_1 -characteristic line is very close to the limiting wall streamline. The other two characteristic lines lie between the limiting wall streamline and the external streamline (fig. 6.1).

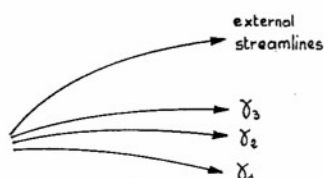


Fig. 6.1 - Characteristic lines of the set of global equations

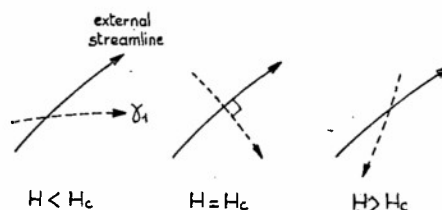


Fig. 6.2 - Variation of the direction of the γ_1 characteristic line with the value of the shape parameter

The hyperbolicity of the set of global equations leads to the concept of dependence and influence domains which are very similar to the domains defined from the analysis of the nature of local equations. From the global equations, the domain of dependence of a point P is bounded by the γ_1 - and γ_3 -characteristic lines passing through P. Roughly, this domain can be approximated by the domain bounded by the limiting wall streamline and the external streamline.

The values of the characteristic roots depend on the value of the shape parameter H and therefore the opening of the domain of dependence depends on H. In the range $1 < H < \infty$, the angle between the γ_2 - (and γ_3 -) characteristic line and the external streamline is between $-\pi/2$ and $\pi/2$:

$$\begin{aligned} -\pi/2 &< \tan^{-1} \gamma_2 < \pi/2 & 1 < H < \infty \\ -\pi/2 &< \tan^{-1} \gamma_3 < \pi/2 \end{aligned}$$

but the angle between the γ_1 -characteristic line and the external streamline can be larger (fig. 6.2) :

$$-\pi < \tan^{-1} \gamma_1 < \pi$$

Obviously, this opening of dependence domain must be taken into account in the numerical methods because the equations cannot be integrated against the direction of the characteristic lines.

The γ_1 -characteristic line and the external streamline are at right angle when $H = H_c = 2.6$. This value of H corresponds to a zero-streamwise skin friction. However, this point is not singular except if the flow has a locally two-dimensional behaviour in the same way as discussed in § 6.1..

Generally, in the three-dimensional case, the singularities are not local. They must be sought rather in configurations leading to a focusing (convergence) of the characteristic lines belonging to the same family. More precisely, the γ_1 -characteristic lines (which are close to the wall streamline) are likely to converge and to form a shock (in the sense of the theory of characteristics). In fact, it has been shown analytically that the formation of a shock is possible. This shock is a line of discontinuity for certain boundary layer thicknesses. Obviously such a discontinuity is physically meaningless but it can be argued that it is an exaggeration of the actual behaviour of the flow and that it results from the use of the direct mode. It is probable that the formation of such a discontinuity line is a signal that reveals the need of calculating the flow with a viscous-inviscid coupling technique.

An example of computed results is presented in fig. 6.3. The support of the calculations is an experimental study by LINDHOUT et al. This experiment has been used as a test case for a workshop on three-dimensional boundary layers held in AMSTERDAM, September 1979. The objective was to calculate the boundary layer developing on a wing root. The data consist of the magnitude and direction of the velocity in inviscid flow. Boundary layer characteristics were given as initial data along a starting line close to the leading edge. The calculations were performed by using full closure relationships that are more accurate than those used to analyze the properties of equations.

The computed results given in fig. 6.3 show the external streamlines and the wall limiting streamlines. They also show the contours of the leading and trailing edges. The calculated wall streamlines form a line of convergence and the overall topology of these wall streamlines suggest the occurrence of a separated zone. The experimental results, based on wall flow visualizations, confirm the existence of a three-dimensional separation in the same region. In the experiment, this separation leads to a strong vortex flow.

In the domain ($X/b > 0.3$, $Z/b < 0.2$), we note the fan-shaped pattern of the computed wall streamlines and we note also the existence of a dividing line which is also revealed by the experiment.

It is doubtful that a boundary layer calculation method can reproduce the flow in separated vortex flow. In addition, it is clear that the flow should be calculated by accounting for the strong viscous-inviscid interaction which has not been done in the present calculation. However it is interesting to note that a rather simple method is able to give very useful information.

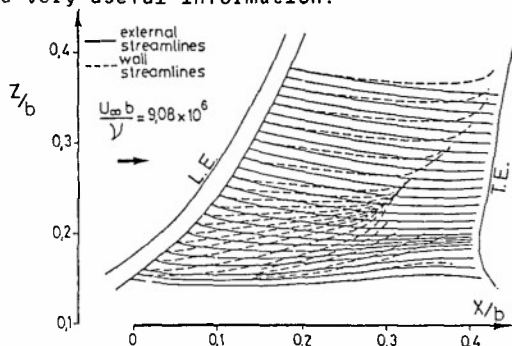


Fig. 6.3 - Calculation of the three-dimensional boundary layer on a wing root section (calculated by COUSTEIX & AUPOIX in LINDHOUT et al., 1981)

— external streamlines
 ---- wall streamlines
 L.E. : leading edge ; T.E. : trailing edge

The following example also involves a separation phenomenon. This is the boundary layer flow on an "infinite" swept wing investigated experimentally by Van den BERG et al and ELSENAAR-BOELSMA. The boundary layer flow was generated on a 35° swept flat plate ; a pressure-inducing body placed above the plate was designed to produce a pressure gradient which causes the separation of the boundary layer on the plate. In this case, the separation is characterized by the wall streamlines which become parallel to the plate leading edge.

The calculations presented in fig. 6.4 have been performed with an integral method. In fact, the results of two calculations are presented. Firstly an inverse method has been applied.

In these calculations, the input is the experimental distributions of δ_1 and δ_2 whereas the distributions of the modulus and of the direction of the external velocity are results of the calculation. The characteristics of the boundary layer other than δ_1 and δ_2 are also results of the calculation.

As shown in figure 6.4, good agreement with experiment is obtained for H , β_0 , the modulus u_e of the external velocity and its direction α defined with respect to a normal to the leading edge. In particular, the experimental location of separation is well reproduced (the separation is characterized by $\alpha + \beta_0 = 90^\circ$: the wall streamlines are parallel to the leading edge).

The second calculations have been performed in the direct mode : the external velocity distribution (the modulus u_e and its direction α) is the input whereas the distributions of δ_1 and δ_2 and of the other characteristics of boundary layer are results of the calculations. In these calculations, the distributions of u_e and α are not taken from the experiments but from the outputs of the inverse calculations presented above. Surprisingly, the calculated distributions of H and β_0 are very different in the direct and inverse methods. In particular, the direct calculations do not indicate a separation. This discrepancy is obviously a result of numerical difficulties in the direct mode caused by the proximity of a singularity. Let us notice that direct calculations performed with the experimental distributions of u_e and α lead to results which are similar to those obtained with the distributions of u_e and α taken from the inverse calculations.

These results clearly demonstrate the kinds of misinterpretations that can result in the neighborhood of an expected singularity if the calculations are performed in the direct mode. They also imply that it is incorrect to calibrate a calculation model from direct mode calculations of a boundary layer close to separation because it is impossible to attribute such and such a cause to such and such an effect. It is believed that the same problems occur with a method solving the local boundary layer equations. In this case, it is incorrect to try to calibrate the turbulence model from direct mode calculations near separation. Moreover, as stressed by CEBECI, 1984, a kind of flow as the Van den BERG et al experiment, which involves separation, is mainly pressure driven and the turbulence model is unimportant. Other parameters such as the normal pressure gradient should be considered very carefully.

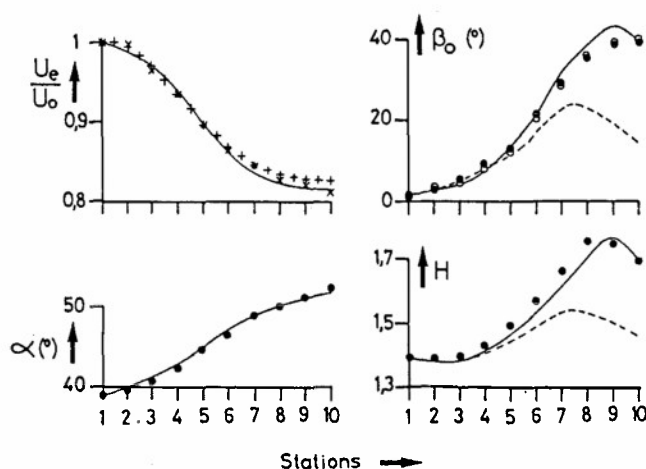


Fig. 6.4 - Calculation of Van den BERG et al's (1975) experiments with an integral method (COUSTEIX, 1982) ;
 — inverse mode (δ_1 and δ_2 prescribed from experiment) ; ---- direct mode (external velocity distribution prescribed from the results of the inverse mode calculations) ; + experimental external velocity from wall pressures ; x experimental external velocity from boundary layer edge measurements ; • experimental values

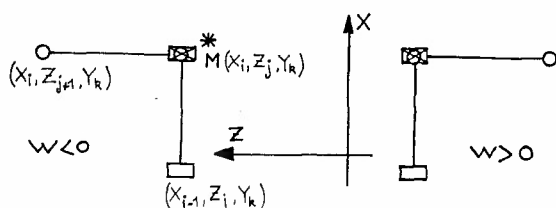
Except for a few particular solutions, the boundary layer equations cannot be solved analytically. Then, numerical methods are employed. The general principle of these methods is nearly the same for laminar or turbulent boundary layers. In the literature, several papers are devoted to the description of the numerical methods (see for example the review papers by KRAUSE, 1972, SMITH, 1982). Here we will describe only the general features of two simple and representative schemes.

7.1. Numerical methods

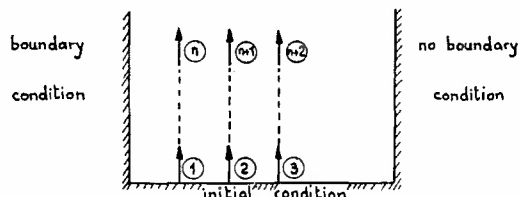
Fig. 7.1 - Example of an "explicit" scheme

A second example of a finite-difference molecule is given in fig. 7.2a. The equations are written at point M and the convention for writing the various derivatives is the same as in fig. 7.1. The solution is now sought at point M. The difference with respect to the scheme of fig. 7.1 is that the solution at point M cannot be determined explicitly as function of the known points. In effect, the solution at point M depends on the solution at all the points belonging to the y_k -column; in this sense, the scheme is implicit and the solution is sought simultaneously along a complete y_k -column. (The use of three points to express the y-second derivatives leads to solve a three-diagonal matrix). The CFL condition restricts the application of this scheme to the case $W < 0$, but there is no restriction on the X-step (if $W < 0$). If $W > 0$, the symmetrical molecule shown in fig. 7.2a, is used.

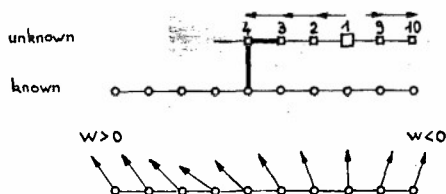
This scheme seems very interesting as there is no restriction on the X-step but the problem is that, in general, the W -component is not positive (or negative) everywhere. When W changes sign in the calculation domain, it is necessary to switch operators. This method has been used by LINDHOUT et al, 1981, who have constructed an algorithm defining the scanning sequence shown in fig. 7.2c. According to the sign of W , a left or a right implicit operator (fig. 7.2a) is used and the switch is performed by using an explicit operator. In the sequence shown in fig. 7.2c, the first operation is to determine the point 1 by using the explicit operator; afterwards, the points 2, 3, 4, ... are calculated by using the implicit operator ($W > 0$) and finally, the points 9, 10, ... are calculated by using the implicit operator ($W < 0$). The advantage of this sequence is that the restriction on the X-step is minimized because the explicit operator is used when W changes sign, that is, when W is small.



a) Finite difference molecule



b) Scanning sequence ($W < 0$)



c) Sequence used by LINDHOUT et al ($W < 0$ and $W > 0$)

Fig. 7.2 - Example of an "implicit" scheme

Other efficient numerical schemes have been developed to calculate three-dimensional boundary layers. Let us mention the zig-zag scheme by KRAUSE et al, 1969, and the box scheme, the zig-zag box scheme and characteristic box scheme developed by CEBECI et al, 1979.

Although several numerical schemes are satisfactory, this problem should not be considered as solved. As stressed by CEBECI, 1984, improvements on the accuracy and economy of calculation methods become increasingly important as the methods are increasingly used for design purposes. Indeed, such applications involve a very large number of runs and the calculation time is of prime concern. This is one of the reasons why integral methods are still used. From results obtained at the AMSTERDAM Workshop on three-dimensional boundary layers (LINDHOUT et al, 1981), it is found that integral methods are an order of magnitude faster than local methods, even with a simple turbulence model. In addition, they are often able to give enough accurate answers to practical problems. However, it is clear that integral methods can only calculate flows for which they have been tailored. The hope which is placed in the solution of local differential equations is their potential of applicability to a wider range of flows. In laminar flow, there is no doubt that the solution of local equations is more accurate but, in turbulent flow, the accuracy is strongly dependent upon the turbulence model. This problem is discussed in the next paragraph.

7.2. Turbulence modelling

The simplest three-dimensional turbulence models are direct extensions of two-dimensional models. For example, the mixing length model used by COUSTEIX et al, 1971, reads :

$$(7.3) \quad \tau_{tx} = \mu \frac{\partial U}{\partial y} - \rho \langle u'v' \rangle = \rho(v + v_t) \frac{\partial U}{\partial y}; \quad \tau_{tz} = \mu \frac{\partial W}{\partial y} - \rho \langle w'v' \rangle = \rho(v + v_t) \frac{\partial W}{\partial y}$$

with

$$(7.4) \quad v_t = F^2 l^2 \left[\left[\frac{\partial U}{\partial y} \right]^2 + \left[\frac{\partial W}{\partial y} \right]^2 + 2 \frac{\partial U}{\partial y} \frac{\partial W}{\partial y} \cos \lambda \right]^{1/2}$$

The mixing length is expressed by the same formula as in two-dimensional flow :

$$(7.5a) \quad \frac{l}{\delta} = 0.085 \tanh \left[\frac{\chi}{0.085} \frac{y}{\delta} \right] \quad \chi = 0.41$$

and the viscous damping function is given by :

$$(7.5b) \quad F = 1 - \exp \left[- \frac{1}{26\chi\mu} \left((\tau_{tx}^2 + \tau_{tz}^2 + 2\tau_{tx}\tau_{tz} \cos \lambda)^{1/2} \rho \right)^{1/2} \right]$$

In compressible flow, this scheme is completed by the heat flux modelling with the hypothesis of a constant "turbulent PRANDTL number" :

$$(7.6) \quad \phi = - \rho \left[\frac{v}{P} + \frac{v_t}{P_t} \right] \frac{\partial h}{\partial y}$$

$$P = 0.725 \quad P_t = 0.89$$

In the same way, the extension of the classical k-ε model in fully turbulent flow gives :

$$(7.7) \quad - \langle u'v' \rangle = C_\mu \frac{k^2}{\epsilon} \frac{\partial U}{\partial y}; \quad - \langle w'v' \rangle = C_\mu \frac{k^2}{\epsilon} \frac{\partial W}{\partial y}$$

where k and ε are calculated from :

$$(7.8a) \quad \frac{\partial k}{\partial t} = P - \epsilon + \frac{\partial}{\partial y} \left[\frac{C_\mu}{\sigma_k} \frac{k^2}{\epsilon} \frac{\partial k}{\partial y} \right]$$

$$(7.8b) \quad \frac{\partial \epsilon}{\partial t} = C_{\epsilon 1} P \frac{\epsilon}{k} - C_{\epsilon 2} \frac{\epsilon^2}{k} + \frac{\partial}{\partial y} \left[\frac{C_\mu}{\sigma_\epsilon} \frac{k^2}{\epsilon} \frac{\partial \epsilon}{\partial y} \right]$$

with

$$(7.9) \quad P = - \langle u'v' \rangle \frac{\partial U}{\partial y} - \langle w'v' \rangle \frac{\partial W}{\partial y} - \left[\langle u'v' \rangle \frac{\partial W}{\partial y} + \langle w'v' \rangle \frac{\partial U}{\partial y} \right] \cos \lambda$$

and

$$(7.10) \quad C_\mu = 0.09 \quad C_{\epsilon 1} = 1.44 \quad C_{\epsilon 2} = 1.92 \quad \sigma_k = 1 \quad \sigma_\epsilon = 1.3$$

Among the various problems encountered in the turbulence modelling of three-dimensional boundary layer, the near wall treatment is one which is difficult to solve. In two-dimensional flow, all the models are based, explicitly or implicitly, on the existence of the law of the wall. This leads to express the turbulent shear stress in the near wall turbulent region (the logarithmic region) as :

$$(7.11) \quad - \langle u'v' \rangle = \chi^2 y^2 \left[\frac{\partial U}{\partial y} \right]^2$$

This formulation is accepted, at least, with moderate pressure gradient.

In three-dimensional, the opposite reasoning is done because the starting point is the assumption that the three-dimensional counterpart of (7.11) is valid. This is clearly what is done with the mixing length model (7.4). This is also the case of the (k-ε) model ; indeed, in the near wall turbulent region, the classical approximations reduce this model to :

$$(7.12a) \quad P = \epsilon$$

$$(7.12b) \quad C_{\epsilon 1} P \frac{\epsilon}{k} - C_{\epsilon 2} \frac{\epsilon^2}{k} + \frac{\partial}{\partial y} \left[\frac{C_\mu}{\sigma_\epsilon} \frac{k^2}{\epsilon} \frac{\partial \epsilon}{\partial y} \right] = 0$$

From these equations, we deduce :

$$(7.13a) \quad \varepsilon = c \frac{k^{3/2}}{y} \quad ; \quad c^2 = \frac{C\mu}{\sigma_\varepsilon (C_{\varepsilon 2} - C_{\varepsilon 1})}$$

$$(7.13b) \quad -\langle u'v' \rangle = \frac{C\mu}{c} k^{1/2} y \frac{\partial u}{\partial y} \quad ; \quad -\langle w'v' \rangle = \frac{C\mu}{c} k^{1/2} y \frac{\partial w}{\partial y}$$

$$(7.13c) \quad \frac{\tau}{\rho k} = C\mu^{1/2}$$

$$(7.13d) \quad \tau = \rho \left[\frac{C\mu^{3/4}}{c} \right]^2 y^2 \left[\left[\frac{\partial u}{\partial y} \right]^2 + \left[\frac{\partial w}{\partial y} \right]^2 + 2 \frac{\partial u}{\partial y} \frac{\partial w}{\partial y} \cos \lambda \right]$$

with

$$\tau = \rho \left[\langle u'v' \rangle^2 + \langle w'v' \rangle^2 + 2 \langle u'v' \rangle \langle w'v' \rangle \cos \lambda \right]^{1/2}$$

Then, by using the momentum equations, it is possible to deduce a "three-dimensional law of the wall" which results from the hypothesis of a mixing length formula.

As already said in § 5.3., an asymptotic analysis of the three-dimensional turbulent boundary layer has been performed by GOLDBERG-RESHOTKO, 1984. They found that the direction of the velocity is constant in the inner layer. At very large REYNOLDS numbers, this result is certainly true but the experimental results show that the velocity direction can vary very rapidly near the wall.

In spite of these restrictions, most of the available methods use the hypotheses which have been described above. These methods produce satisfactory results, at least for the mean flow.

This does not mean, however, that the turbulence modelling problem in three-dimensional turbulent boundary layer is solved because experimental data show that several hypotheses presented above are wrong. The experimental data of Van den BERG et al, 1975, and of BRADSHAW-PONTIKOS, 1985, show that the three-dimensionality of the flow affects the turbulence structure. These experiments deal with a boundary layer developing on an "infinite" swept wing and the experimental set up is such that the initial boundary layer is nearly two-dimensional ; downstream, the flow becomes three-dimensional due to the combination of the effect of an adverse pressure gradient and of the sweep angle. As the three-dimensionality develops, the experimental results show that the outer level of the mixing length reduces and the ratio τ/k decreases (fig. 7.3). Therefore, there is a significant decrease in the magnitude of shear stress compared with an equivalent two-dimensional boundary layer. In addition, the direction of the shear stress vector $\vec{\tau}$ ($-\langle u'v' \rangle$, $-\langle w'v' \rangle$) lags considerably behind the vector of components $(\partial u/\partial y, \partial w/\partial y)$: this means that the eddy viscosity is not isotropic.

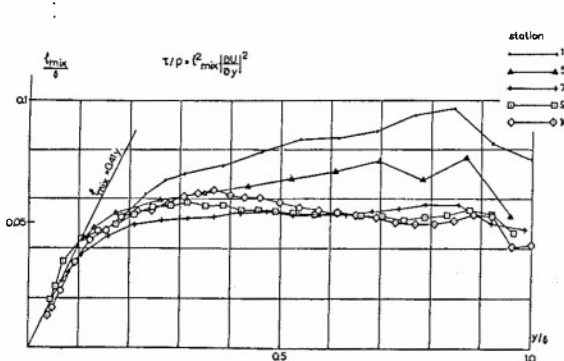


Fig. 7.3a - Boundary layer on an infinite swept wing (from ELSENAAR-BOELSMA) - Evolution of the mixing length

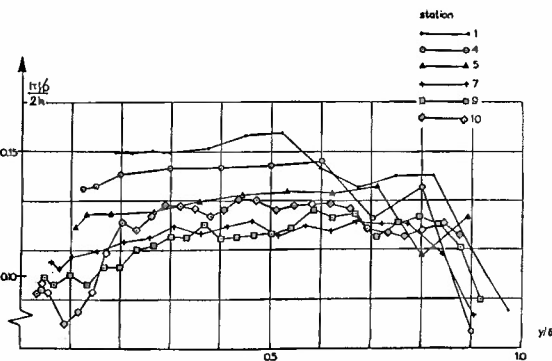


Fig. 7.3b - Evolution of the ratio of shear stress and turbulent energy

Therefore, the classical turbulence models do not represent the physics of the phenomena. This is not at variance with the fact that the associated calculation methods are able to reproduce the mean flow with a certain success. In fact, if we consider the Van den BERG et al experiment, the flow is pressure driven and the turbulence model is not too much important. Nevertheless, many endeavours have been devoted to elaborate models that remove the hypothesis of isotropic eddy viscosity but serious numerical difficulties in the calculations of Van den BERG et al experiment (in the direct model) due to the problem of singularity have prevented a correct discussion of the turbulence modelling : this has been shown by COUSTEIX, 1982 and has been discussed in § 6.3..

Again, it is important to stress that it is dangerous to calibrate a turbulence model by trying to calculate a separated boundary layer in the direct mode. We have shown (§ 6.3) that the application of a simple integral method (in the inverse mode) to the Van den BERG et al experiment leads to quite reasonable results. Later, ABID-SCHMITT, 1984, examined a few turbulence models by solving the local differential equations in the inverse mode. Comparisons with Van den BERG et al results show that the mean flow is little affected by the turbulence model. The standard $k-\epsilon$ model gives a rather good agreement with experiments ; the mean flow prediction is only slightly improved by using an algebraic stress model developed by ROOI and LAUNDER (see for example the 1980-1981 STANFORD Conference, KLINE et al). It is probable that this is due to the fact that the flow is pressure driven. To illustrate this point, fig. 7.4 shows the evolution of the slope of the polar plot in the outer part of the boundary layer. On one hand, this slope can be obtained from experiment ; if we assume that the polar plot is linear in the whole boundary layer :

$$\frac{W}{u_e} = c \left[1 - \frac{u}{u_e} \right]$$

we deduce :

$$(7.14a) \quad c = - \frac{\delta_2}{\delta_1}$$

On the other hand, we can calculate this slope from inviscid considerations (SQUIRE-WINTER formula). A simplified form gives :

$$(7.14b) \quad c = 2(\alpha - \alpha_0)$$

where $(\alpha - \alpha_0)$ represents the turning angle of the external streamlines and α_0 the starting point. By adjusting the value of α_0 , a good correlation is obtained between (7.14a) and (7.14b) (fig. 7.3). The same has been observed by BRADSHAW-PONTIKOS, 1985, and these authors argued that such a good agreement is partly a coincidence because the entrainment into the boundary layer is neglected but they think that it is certainly an indication that the flow is pressure driven. Obviously, this is not true near the wall and, in this region, the turbulence model is important.

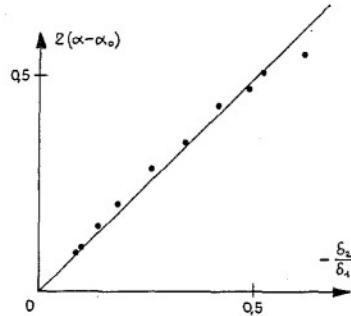


Fig. 7.4 - Calculation of the slope of the polar plot in the outer part of the boundary layer - Experiments : Van den BERG et al

Among the various attempts at improving the classical models, let us mention the approach proposed by ROTTI, 1979, who tried to reproduce the anisotropy of the eddy viscosity as evidenced by the Van den BERG et al experiments. In a cartesian axis-system, this model is :

$$(7.15a) \quad - \langle u'v' \rangle = \nu_t \left[a_{xx} \frac{\partial u}{\partial y} + a_{xz} \frac{\partial w}{\partial y} \right]$$

$$(7.15b) \quad - \langle w'v' \rangle = \nu_t \left[a_{zx} \frac{\partial u}{\partial y} + a_{zz} \frac{\partial w}{\partial y} \right]$$

$$a_{xx} = \frac{u^2 + Tw^2}{u^2 + w^2}$$

$$a_{xz} = a_{zx} = (1 - T) \frac{uw}{u^2 + w^2}$$

$$a_{zz} = \frac{Tu^2 + w^2}{u^2 + w^2}$$

In the above equations, T is a constant which represents the ratio of transverse and longitudinal eddy viscosities expressed in an axis system based on the local boundary layer velocity. This model is able to reproduce the non isotropy of the eddy viscosity if $T \neq 1$. A first drawback is that T is not a universal constant. A second drawback is that T depends on the axis system because the model is not invariant by a galilean transformation.

Fig. 7.5 shows an example of applications of a few models to the BRADSHAW-TERRELL, 1969, experiments. These authors studied the relaxation of a three-dimensional boundary layer towards a two-dimensional boundary layer. The mixing length model and the $k-\epsilon$ model (with $T = 1$) give the correct decay of the wall limiting streamlines angle β_0 whereas the integral method underpredicts the rate of decay of β_0 at the beginning of the relaxation. This illustrates the greater flexibility of the solution of local equations. In addition, this comparison shows that the classical models work well in this situation. Indeed, results not given here, show that if T is given a value different from $T = 1$, the rate of decay of β_0 is not well predicted ; if $T < 1$, the rate of decay of β_0 is too low.

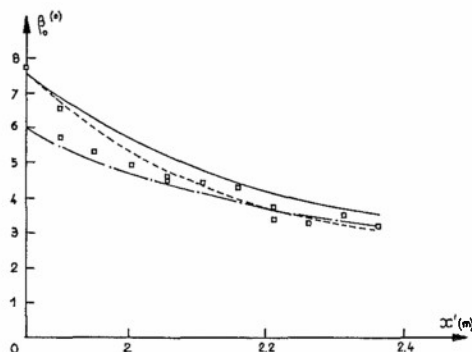


Fig. 7.5 - Calculation of BRADSHAW-TERRELL experiments (45° infinite swept wing) : relaxation of an initially three-dimensional boundary layer towards a two-dimensional boundary layer - x' : distance from leading edge along tunnel centerline - β_0 : crossflow angle at surface - — mixing length - ---- $k-\epsilon$ - .-.- integral method

Another illustration is provided by the calculation of the wake developing behind a swept wing (COUSTEIX-AUPOIX-PAILHAS, 1980). The calculations have been performed by using a four-equation model : the eddy viscosity model is replaced by transport equations to calculate the shear stress - $\langle u'v' \rangle$ and - $\langle w'v' \rangle$. In this model, the effect of the parameter T is included in the production terms. As shown in figure 7.6, the best results are obtained with $T = 1$. A lower value of T produces a too low rate of decay of the crossflow. This confirms the results obtained with the application to BRADSHAW-TERRELL experiments. However, it should not be concluded that the isotropic eddy viscosity model always gives the best results since experimental results show that the departure from isotropic eddy viscosity is important as the three-dimensionality develops along the flow.

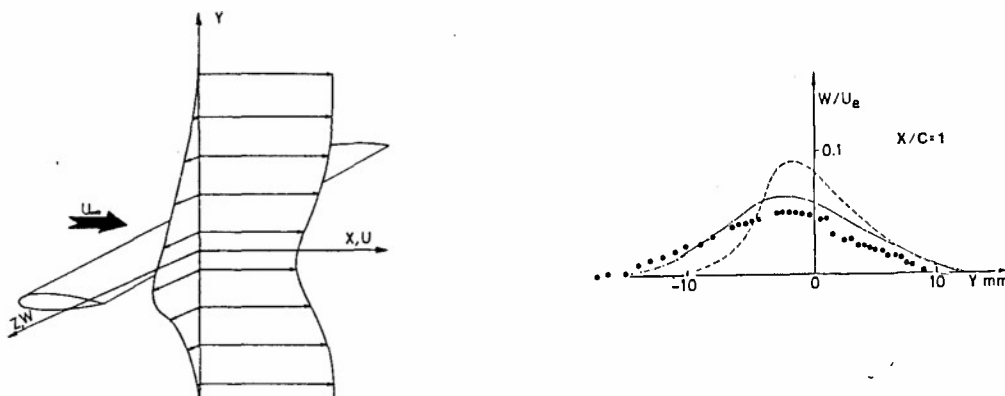


Fig. 7.6 - Crossflow velocity profile in a wake behind a swept wing - Exp. : \bullet ; Calc. : $k-\epsilon-\overline{u'v'}-\overline{w'v'}$ model — $T = 1$; ---- $T = 0.5$

Another possible solution to the modelling problem is to use a full transport equation model for the REYNOLDS stresses. In a cartesian axis system, these equations are :

$$\frac{D}{Dt} \langle u_i' u_j' \rangle = P_{ij} + \phi_{ij} - D_{ij} + T_{ij}$$

where P_{ij} is the so-called production term :

$$P_{ij} = - \langle u_i' u_k' \rangle \frac{\partial u_j}{\partial x_k} - \langle u_j' u_k' \rangle \frac{\partial u_i}{\partial x_k}$$

where ϕ_{ij} , D_{ij} , T_{ij} are respectively the velocity pressure correlations, the destruction term and the transport term.

According to the modelling proposed by LAUNDER et al (see for example the 1980-1981 STANFORD Conference, KLINE et al), these terms are given by :

$$T_{ij} = C_s \frac{\partial}{\partial x_k} \left[\langle u_k' u_l' \rangle \frac{k}{\epsilon} \frac{\partial}{\partial x_l} \langle u_i' u_j' \rangle \right]$$

$$D_{ij} = \frac{2}{3} \epsilon \delta_{ij}$$

$$\phi_{ij} = \phi_{ij,1} + \phi_{ij,2} + \phi_{ij,w}$$

and

$$\phi_{ij,1} = - C_1 \frac{\epsilon}{k} \left[\langle u_i' u_j' \rangle - \frac{2}{3} \delta_{ij} k \right]$$

$$\phi_{ij,2} = - C_2 \left[P_{ij} - \frac{1}{3} \delta_{ij} P_{kk} \right]$$

$$\begin{aligned} \phi_{ij,w} = & \left[C_1' \frac{\epsilon}{k} \left[\langle u_k' u_m' \rangle n_k n_m \delta_{ij} - \frac{3}{2} \langle u_k' u_i' \rangle n_k n_j - \frac{3}{2} \langle u_k' u_j' \rangle n_k n_i \right] \right. \\ & \left. + C_2' \left[\phi_{km,2} n_k n_m \delta_{ij} - \frac{3}{2} \phi_{ik,2} n_k n_j - \frac{3}{2} \phi_{jk,2} n_k n_i \right] \right] f \end{aligned}$$

$$f = \frac{k^{3/2}}{2.5 \epsilon x_n}$$

where n_i are the components of a unit vector normal to the surface and x_n is the normal distance from the wall.

If the boundary layer approximation are applied, the transport equations are simplified because the velocity gradient components other than $\partial U/\partial y$ and $\partial W/\partial y$ are neglected. Calculations with a model of this type (with $\phi_{ij,w} = 0$) have been performed by COUSTEIX-AUPOIX-PAILHAS, 1980. The results have shown that this model is not sufficient to explain a departure from the isotropic eddy viscosity.

The modelling of transport equations is often simplified to give the so-called algebraic stress model which also leads to an isotropic eddy viscosity. This model is obtained with the following approximations :

$$\frac{D}{Dt} \langle u_i' u_j' \rangle - T_{ij} = \frac{\langle u_i' u_j' \rangle}{k} \left[\frac{Dk}{Dt} - T_{kk} \right] = \frac{\langle u_i' u_j' \rangle}{k} (P - \epsilon) = P_{ij} + \phi_{ij} - \frac{2}{3} \delta_{ij} \epsilon$$

where $P = P_{kk}/2$ is the production rate of k .

From these equations, we get :

$$\langle u_i' u_j' \rangle = \frac{2}{3} \delta_{ij} k + \frac{(1 - C_2) \left[\frac{P_{ij}}{\epsilon} - \frac{2}{3} \delta_{ij} \frac{P}{\epsilon} \right] + \frac{\phi_{ij,w}}{\epsilon}}{C_1 + \frac{P}{\epsilon} - 1}$$

If the velocity gradient components other than $\partial U/\partial y$ and $\partial W/\partial y$ are neglected, we get :

$$\langle u' v' \rangle = \frac{C_2 \left[1 - \frac{3}{2} C_2' f \right] - 1}{C_1 + \frac{P}{\epsilon} - 1 + \frac{3}{2} C_1' f} \frac{k}{\epsilon} \langle v'^2 \rangle \frac{\partial U}{\partial y}$$

$$\langle w' v' \rangle = \frac{C_2 \left[1 - \frac{3}{2} C_2' f \right] - 1}{C_1 + \frac{P}{\epsilon} - 1 + \frac{3}{2} C_1' f} \frac{k}{\epsilon} \langle v'^2 \rangle \frac{\partial W}{\partial y}$$

Then, these expressions give an isotropic eddy viscosity. Calculations performed by ABID-SCHMITT, 1984, have shown that this model works well when applied to the Van den BERG et al experiments. The good agreement results probably from a reduction in the net production of REYNOLDS stresses - $\langle u'v' \rangle$ and - $\langle w'v' \rangle$, but it is not clear if this result comes from an effect of the three-dimensionality or if a similar effect would be obtained also in two-dimensional flow.

Possibly, it is not correct to neglect the velocity gradient components other than $\partial U/\partial y$ and $\partial W/\partial y$. Indeed it is known that small extra rate of strain can strongly affect the development of REYNOLDS stresses. Now, the three-dimensionality is characterized by a curvature of the streamlines and this effect is not taken into account if only $\partial U/\partial y$ and $\partial W/\partial y$ are retained. This means that practically all the velocity gradient components should be retained ; it has not yet been shown that this could improve the model.

8 - CONCLUSION

It is clear that our capacity to predict the three-dimensional turbulent boundary layers developing on wings or on fuselages is not very large. This is partly a result of a poor knowledge of the turbulence mechanisms in general. In addition, it should be recognized that the advanced studies on turbulence deal with rather simple configurations where the effects of three-dimensionality are avoided. On the other hand, the mathematical tools to model the effects of turbulence are rudimentary.

For attached three-dimensional boundary layers, the situation is not too bad however. Several calculation methods have been developed and widely applied. The earliest techniques solve the global equations and these integral methods have been shown to be a very valuable tool for practical purposes. Solutions of local equations have been developed more recently. Even with simple eddy viscosity models, they add a degree of flexibility and are able to reproduce the mean velocity profiles with reasonable accuracy. The REYNOLDS stress transport equations are potentially superior, but this advantage has not been clearly proven yet. The current tendency is to prefer the use of the so-called algebraic stress model instead of the full REYNOLDS stress equations.

This optimistic aspect should not hide that many problems remain unsolved. One of them is the near wall treatment and the associated difficulty of the extension of the law of the wall in three-dimensional boundary layer.

The major problem is the three-dimensional separation. Very often, a three-dimensional separation is associated with an increasing three-dimensionality of the flow and we have seen that this affects the structure of turbulence. Fortunately, the mean flow is generally pressure driven and a very accurate turbulence model is probably not needed, but this point is not completely clear because other factors such as variations of pressure normally to the wall are important. A recent positive result is that singularities occurring in boundary layer calculations are now slightly better understood, but the link with separation is hypothetical. At the best, the singularity is a sign for the need of a strong coupling between the boundary layer and the inviscid flow.

In the case of attached boundary layers, techniques of interaction between the viscous and inviscid flows are well appropriate to calculate the whole flow field. In the case of separated boundary layers, the advantage of these interactive techniques tends to disappear. If the separated zone is developed, the classical boundary layer approximations are no longer valid. In particular, the component of the pressure gradient normal to the wall is not negligible. In addition, a separation in a three-dimensional flow often leads to a formation of vortices in which it is very difficult to recognize a familiar boundary layer.

In two-dimensional flow, other techniques than viscous-inviscid interactions have proved fruitful. These methods consist of solving the so-called parabolized NAVIER-STOKES equations or thin layer equations (RUBIN-REDDY, 1983). These techniques can be considered as an extension of classical boundary layer solutions that include the direct and inverse methods ; in addition, the effects of the normal pressure gradient are taken into account. The extension to three-dimensional flow deserves to be considered.

A last problem which should be mentioned is the laminar-turbulent transition. It is often argued that this transition is unimportant at high REYNOLDS numbers, but this is not always true. For example, the design of "laminar wings" or the presence of favourable pressure gradients can require an accurate determination of the transition region. The three-dimensionality adds a further difficulty due to the crossflow instability. Experiments on swept wings have shown that this instability can lead to transition in a favourable pressure gradient. Thus, the advantages of the properties of a laminar airfoil at zero sweep angle can be lost when the sweep angle increases. Then, methods for calculating transition in three-dimensional flow are being developed as they should be a tool of aerodynamic design (ARNAL, 1986).

APPENDIX

CLOSURE RELATIONSHIPS USED IN THE INTEGRAL METHOD

A.1. Closure relationships in laminar flow

In compressible flow, intermediate transformed variables have been introduced ; between these variables, we have the same closure relationships as between variables in incompressible flow. The transformed variables are noted with an overbar ($\bar{}$). The closure relationships given below are valid for $\bar{H} \leq 4.029$; they are given in a stream-line coordinate system :

$$\frac{\bar{H}^*}{12.37} + 1.2706 \frac{12.37}{\bar{H}^*} = -1.5022 \left[\frac{1}{\bar{H}} + \frac{\bar{H}}{(4.02923)^2} \right] + 3.1924$$

$$B = 2.99259 \left[\left[\frac{1}{\bar{H}} - \frac{1}{8.05846} \right]^{1.7} - \left[\frac{1}{8.05846} \right]^{1.7} \right]$$

$$0 = \theta - (\bar{H} - 1) \left[-0.06815 + 4.336355 \left[\frac{1}{\bar{H}} - \frac{1}{4.02923} \right]^{2.095065} \right]$$

$$\frac{\bar{C}_E \bar{R}_{\theta 11}}{\bar{H}^*} = -\frac{2}{\bar{H} - 1} B + \frac{\bar{H} + 1}{\bar{H} - 1} D$$

$$\frac{\bar{C}_f}{2} \bar{R}_{\theta 11} = \theta$$

$$\bar{T} = \left| \frac{\theta_{21}/\theta_{11}}{k \theta_{11} \bar{R}_{\theta 11} h_{ie}/h_e} \right| ; k = \text{geodesic curvature of external streamlines}$$

$$\frac{\bar{\delta}_2}{\bar{\theta}_{21} \bar{H}} = \frac{\alpha_1 \bar{T} + \alpha_2}{\bar{T} + 1.2} ; \alpha_1 = 0.58 - 0.0515 (\bar{H} - 2.2) ; \alpha_2 = 1.72 + 0.0516 (\bar{H} - 4)(\bar{H} + 3.38)$$

$$\frac{\bar{\theta}_{12}}{\bar{\theta}_{21}} = 1 - \frac{\bar{\delta}_2}{\bar{\theta}_{21}}$$

$$\frac{\bar{\theta}_{22} \bar{\theta}_{11}}{\bar{\theta}_{21}^2 (\bar{H} - 1)} = -1.65 - 1.27 \left[\frac{\bar{\theta}_{12}}{\bar{\theta}_{21} (\bar{H} - 1)} + 1.2 \right] \left[\frac{\bar{\theta}_{12}}{\bar{\theta}_{21} (\bar{H} - 1)} - 0.95 \right]$$

$$\frac{\tan \bar{\beta}_0 \bar{R}_{\theta 11} \bar{C}_f / 2}{-\bar{\theta}_{21} / \bar{\theta}_{11}} = \frac{1 + 7\bar{T} + 0.5\bar{T}^2}{\alpha_3 \bar{T} + \alpha_4 \bar{T}^2} ; \alpha_3 = 2.2 - 0.33 (\bar{H} - 4)(\bar{H} + 0.7) ; \alpha_4 = \frac{2.75\bar{H} - 2.66}{\bar{H} - 1.45}$$

$$H = \frac{h_{ie}}{h_e} \bar{H} + \frac{h_{ie}}{h_e} - 1$$

$$H^* = \bar{H}^* ; \frac{\bar{C}_f}{2} \bar{R}_{\theta 11} = \frac{\bar{C}_f}{2} \bar{R}_{\theta 11} ; \frac{\bar{C}_E}{\bar{C}_f} = \frac{\bar{C}_E}{\bar{C}_f}$$

$$\frac{\bar{\delta}_2}{\bar{\theta}_{12}} = \frac{\bar{\delta}_2}{\bar{\theta}_{12}} \quad \frac{\bar{\theta}_{22} \bar{\theta}_{11}}{\bar{\theta}_{21}^2} = \frac{\bar{\theta}_{22} \bar{\theta}_{11}}{\bar{\theta}_{21}^2} \quad \frac{\bar{\delta}_2}{\bar{\theta}_{21}} = \frac{\bar{\delta}_2}{\bar{\theta}_{21}} \quad \frac{\tan \bar{\beta}_0}{\bar{\theta}_{21} / \bar{\theta}_{11}} = \frac{\tan \bar{\beta}_0}{\bar{\theta}_{21} / \bar{\theta}_{11}}$$

A.2. Closure relationships in turbulent flow

The closure relationships are expressed in a streamline coordinate system. "Incompressible" thicknesses are defined as :

$$\begin{aligned}\delta_{1i} &= \int_0^\delta \left[1 - \frac{u}{u_e} \right] dy & \theta_{11i} &= \int_0^\delta \frac{u}{u_e} \left[1 - \frac{u}{u_e} \right] dy & H &= \frac{\delta_{1i}}{\theta_{11i}} \\ \delta_{2i} &= \int_0^\delta -\frac{w}{u_e} dy; \theta_{21i} = \int_0^\delta -\frac{w}{u_e} \frac{u}{u_e} dy; \theta_{12i} = \int_0^\delta \frac{w}{u_e} \left[1 - \frac{u}{u_e} \right] dy; \theta_{22i} = \int_0^\delta -\frac{w^2}{u_e^2} dy\end{aligned}$$

The relationships for the "incompressible" or transformed variables are :

$$\frac{\delta_{1i}}{\delta} = \bar{\gamma} F_1; H_i = \frac{1}{1 - G\bar{\gamma}}; \bar{\gamma} = \left[\frac{Cf_X}{2} \right]^{1/2}; \frac{1}{\bar{\gamma}} = \frac{1}{0.41} \ln H_i \bar{R}_\theta + D^*; C_E = P\bar{\gamma}$$

$$F_1 = (0.613G - [3.6 + 76.86 (1/G - 0.154)^2]/G) (1 + 10/G^2)$$

$$D^* = 1.74074G + 29.693/G - 12$$

$$P = 0.074G - 1.0957/G$$

$$\theta_{21i} = \delta_{2i} + \theta_{12i}; \frac{\delta_{2i}}{\theta_{12i}} = -\phi_1 \frac{H_i}{H_i - 1}; \frac{\theta_{22i} \delta_{1i}}{\delta_{2i}^2} = -\phi_2 \frac{H_i - 1}{H_i}; \tan \bar{\beta}_0 = \frac{-\delta_{2i}/\delta_{1i}}{\frac{\epsilon_1}{F_1} \frac{GH_i}{H_i - 1} - \epsilon_2}$$

$$T_i = \left| \frac{\delta_{2i}/\delta}{k \delta} \right|; \epsilon = 2F_1/T_i; k = \text{geodesic curvature of external streamlines}$$

$$\phi_1 = 1 + \left[\frac{3.5}{G^{3/2}} \left[1 + \frac{1}{0.6 + \bar{R}_{\theta 11}/30000} \right] \right]; \phi_2 = \frac{1}{1 + 1.65(\phi_1 - 1)}$$

$$\epsilon_1 = \frac{1}{[\alpha_3 (\alpha_1 (\alpha_2 - 1) + 1)]}; \epsilon_2 = \frac{\epsilon}{\epsilon + 1/F_1}$$

$$\alpha_1 = \frac{20.6 F_1^{1/2}}{G^2}; \alpha_2 = \frac{\epsilon + 0.317}{2.21 + 0.423\epsilon} + 0.856 \cdot 10^{-0.1175\epsilon^{0.86}}; \alpha_3 = \frac{2.18 G^2 - 6.3 G}{2F_1^2}$$

The relationships for the compressible variables are :

$$\bar{\gamma} = \gamma (1 + 0.106 M_e^2)^{1/2}; \gamma = (Cf_X/2)^{1/2}$$

$$\bar{R}_{\theta 11} = R_{\theta 11} \frac{\mu_e}{\mu^*}; \frac{T^*}{T_e} = 1 + 0.126 M_e^2; \frac{\mu^*}{\mu_e} = \sqrt{\frac{T^*}{T_e} \frac{1 + S/T_e}{1 + S/T^*}}; S = 110.4 K$$

$$H = H_i + (0.4 + 0.141 (H_i - 1)) M_e^2$$

$$H^* = H_i^* (1 + 0.01125 M_e^2) + 0.207 M_e^{3/2}$$

$$\frac{\theta_{21}}{\theta_{21i}} = \frac{\theta_{11}}{\theta_{11i}}$$

$$\frac{\delta_2}{\theta_{21}} = 1 + \left[\frac{\delta_{2i}}{\theta_{21i}} - 1 \right] (1 - 0.045 M_e); \frac{\delta_2^2}{\theta_{22} \theta_{11}} = -4.05 + \left[\frac{\delta_{2i}^2}{\theta_{22i} \theta_{11i}} + 4.05 \right] [1 + 0.02 M_e^2]$$

$$\theta_{21} = \delta_2 + \theta_{12}$$

$$\tan \beta_0 = \tan \bar{\beta}_0 (1 + 0.0325 M_e^2)$$

REFERENCES

- ABID R., SCHMITT R. "Etude critique de modèles de turbulence appliqués à une couche limite tridimensionnelle décollée" - La Recherche Aérospatiale N° 1984-6
- ARNAL D. "Description and prediction of transition in two-dimensional, incompressible flow" - AGARD Report N° 709 Special Course on Stability and Transition of Laminar Flow (1984)
- ARNAL D. "Three-dimensional boundary layers : laminar-turbulent transition" - Lecture Series on Computation of Three-dimensional Boundary Layers Including Separation - V.K.I. (1986)
- ARNAL D., HABIBALLAH M., CDUSTOLS E. "Théorie de l'instabilité laminaire et critères de transition en écoulements bi- et tridimensionnel" - La Recherche Aérospatiale N° 1984-2
- BEASLEY J.A. "Calculation of the laminar boundary layer and the prediction of transition on a sheared wing" - ARC R & M 3787 (1973)
- BRADSHAW P. "Turbulent secondary flows" - Annual Review of Fluid Mechanics (to appear) (1986)
- BRADSHAW P., PONTIKOS N.S. "Measurements in the turbulent boundary layer on an "infinite" swept wing" - J. Fluid Mech. Vol. 159, pp. 105-130 (1985)
- BRADSHAW P., TERRELL M.G. "The response of a turbulent boundary layer on an infinite swept wing to the sudden removal of pressure gradient" - NPL Aero Rep. 1305 (1969)
- CATHERALL D., MANGLER W. "An indirect method for the solution of the NAVIER-STOKES equations for laminar incompressible flow at large REYNOLDS number" - RAE Report Aero 2683 (1963)
- CEBECI T. "Problems and opportunities with three-dimensional boundary layers" - AGARD Report N° 719 Three-dimensional Boundary Layers (1984)
- CEBECI T., KHATTAB A.A., STEWARTSON K. "Prediction of three-dimensional laminar and turbulent boundary layers on bodies of revolution at high angles of attack" - PGOC 2nd Inter. Symp. on Turbulent Shear Flows, LONDDN (1979)
- CLAUSER F. "Turbulent boundary layers in adverse pressure gradients" - J. of the Aeron. Sc., Vol. 21 (1954)
- COLES D. "The law of the wake in the turbulent boundary layer" - J. Fluid Mech., Vol. 1, pp. 191-226 (1956)
- CDLLINI P., FULACHIER L. "Structure striée d'une couche limite turbulente sur paroi mobile transversalement" - Projet de note à l'Académie des Sciences, PARIS (1986)
- CDUSTEIX J. "Theoretical analysis and prediction method for a three-dimensional turbulent boundary layer" - ONERA N.T. 157 - Engl. Transl. ESA TT-23B (1974)
- COUSTEIX J. "Aérodynamique en fluide visqueux - Couches limites laminares" - Ecole Nationale Supérieure de l'Aéronautique et de l'Espace, TOULOUSE (1984)
- COUSTEIX J. "Three-dimensional and unsteady boundary layer computations" - Annual Review of Fluid Mechanics, Vol. 18, pp. 173-196 (1986)
- CDUSTEIX J., AUPOIX B., PAILHAS G. "Synthèse de résultats théoriques et expérimentaux sur les couches limites et sillages turbulents tridimensionnels" - ONERA N.T. 1980-4
- COUSTEIX J., HDUDEVILLE R. "Singularities in three-dimensional turbulent boundary layers. Calculations and separation phenomena" - AIAA Journal Vol. 19, N° 8, pp. 976-985 (1981)
- COUSTEIX J., QUEMARD C. "Velocity profiles and wall shear stress of three-dimensional turbulent boundary layers" - ONERA TP 1134 (1972)
- CDUSTEIX J., QUEMARD C., MICHEL R. "Application d'un schéma amélioré de longueur de mélange à l'étude des couches limites turbulentes tridimensionnelles" - AGARD CP N° 93 on Turbulent Shear Flows (1971)
- COUSTEIX J., MICHEL R. "Analyse expérimentale et théorique des couches limites turbulentes tridimensionnelles dans un canal supersonique courbe" - La Recherche Aérospatiale N° 1975-1
- CRABTREE L.F., KUCHEMANN D., SDWERBY L. "Three-dimensional boundary layers" in "Laminar Boundary Layers", ROSENHEAD L. ed. (1963)
- CROSS A.G.T. "Calculation of compressible three-dimensional turbulent boundary layers with particular reference to wings and bodies" - British Aerospace Brough YAD 3379 (1979)

- EAST L.F. "Computation of three-dimensional turbulent boundary layers" - EUROMECH 60, TRONDHEIM - FFA TN AE-1211 (1975).
- EAST L.F., SAWYER W.G. "An investigation of the structure of equilibrium turbulent boundary layers" - AGARD CP N° 271 (1979)
- EICHELBRENNER E.A. "La couche limite tridimensionnelle en régime turbulent d'un fluide compressible : cas de la paroi athermane" - AGARDograph 97 (1965)
- ELSENAAR A., BOELSMA S.H. "Measurements of the REYNOLDS stress tensor in a three-dimensional turbulent boundary layer under infinite swept wing conditions" - NLR TR 74095 U (1974)
- FAVRE A., KOVASZNY L.S.G., DUMAS R., GAVIGLIO J., COANTIC M. "La turbulence en mécanique des fluides" - GAUTHIER-VILLARS Ed. (1976)
- FULACHIER L., ARZUMANIAN E., DUMAS R. "Effect on a developed turbulent boundary layer of a sudden local wall motion" - IUTAM Symp. on Three-dimensional Turbulent Boundary Layers. Springer Verlag, H.H. FERNHOLZ-E. KRAUSE Ed. (1982)
- GLEYZES C., COUSTEIX J. "Calcul des lignes de courant à partir des pressions pariétales sur un corps fuselé" - La Recherche Aéronautique N° 1984-3
- GLEYZES C., COUSTEIX J., AUPOIX B. "Couches limites tridimensionnelles sur des corps de type fuselage" - R.T. OA N° 4/5025 AYD (DERAT N° 4/5025 DY) (1985)
- GOLDBERG U.C., RESHOTKO E. "Scaling and modelling of three-dimensional, end wall, turbulent boundary layers" - NASA CR 3792 (1984)
- GRANVILLE P.S. "The calculation of the viscous drag of bodies of revolution" - David TAYLOR Model Basin Report B49 (1953)
- GREEN J.E., WEEKS D.J., BROOMAN J.W.F. "Prediction of turbulent boundary layers and wakes in incompressible flow by a lag entrainment method" - RAE TR 72231 (1972)
- GRUSCHWITZ E. "Turbulente Reibungsschichten mit Sekundärströmungen" - Ing. Arch. Bd 6, pp.355 (1935)
- HIRSCHEL E.H., KORDULLA W. "Shear flow in surface oriented coordinates" - Notes Numer. Fluid Mech., Vol. 4 - BRAUMSCHWEIG/WIESBADEN Vieweg (1981)
- HUMPHREYS D.A. "Comparison of boundary layer calculations for a wing" - The May 1978 STOCKHOLM Workshop Test Case - FFA TN AE-1522 (1979)
- JOHNSTON J.P. "On the three-dimensional turbulent boundary layer generated by secondary flow" - Journal of Basic Engineering - Series D, Trans. ASME, Vol. B2, pp. 233-248 (1960)
- KLINE S.J., CANTWELL B.J., LILLEY G.M. 1980-B1 AFOSR-HTTM STANFORD Conference on Complex Turbulent Flows
- KLINE S.J., MORKOVIN M.V., SOVRAN G., COCKRELL D.J. "Computation of turbulent boundary layers" - 1968 AFOSR-IFP STANFORD Conference (1968)
- KRAUSE E. "Numerical treatment of boundary layer problems" - AGARD Lecture Series N° 64 in Advances in Numerical Fluid Dynamics (1973)
- KRAUSE E., HIRSCH E.H., BOTHMANN T.H. "Die numerische Integration der Bewegungsgleichungen dreidimensionaler laminarer kompressibler Grenzschichten" - Fachtagung Aerodynamik, BERLIN (1968) - DGLR-Fachbuchreihe Band 3, BRAUMSCHWEIG (1969)
- LAUNDER B.E., JONES W.P. "On the prediction of laminarisation" - ARC CP 1036 (1968)
- LAUNDER B.E., REECE G.J., RODI W. "Progress in the development of a REYNOLDS stress turbulence closure" - J. Fluid Mech. N° 68, pp. 537-566 (1975)
- LE BALLEUR J.C. "Numerical viscous-inviscid interaction in steady and unsteady flows" - Second Symposium on Numerical and Physical Aspects of Aerodynamic Flows - T. CEBECI, ed. (1983)
- LINDHOUT J.P.F., MOEK G., DE BOER E., VAN DEN BERG B. "A method for the calculation of three-dimensional boundary layers on practical wing configurations" - Trans. ASME Journal of Fluids Engineering, Vol. 103, pp. 104-111 (1981)
- LINDHOUT J.P.F., VAN DEN BERG B., ELSENAAR A. "Comparison of boundary layer calculations for the root section of a wing" - The September 1979 AMSTERDAM Workshop Test Case - NLR MP BD D2B U (1981)
- LUDWIG H., TILLMAN W. "Untersuchungen über die Wandschubspannung in turbulenten Reibungsschichten" - Ing. Arch. XVII Band (1949)
- MAGER A. "Generalization of boundary layer momentum integral equation to three-dimensional flows including those of rotating system" - NACA Report 1067 (1952)

MEIER H.U., KREPLIN H.P., LANDHAUSSER A., BAUMGARTEN D. "Mean velocity distributions in three-dimensional boundary layers, developing on a 1:6 prolate spheroid with natural transition" - Internal Report DFVLR N° 18 228-84 A 10 (1984)

MEIER H.U., KREPLIN H.P., VOLLMERS H. "Development of boundary layer and separation patterns on a body of revolution at incidence" - 2nd Symposium on Numerical and Physical Aspects of Aerodynamic Flows, LONG BEACH (17-20 January, 1983)

MELLOR G.L., GIBSON D.M. "Equilibrium turbulent boundary layers" - FLO N° 13, PRINCETON University (1963)

MICHEL R., QUEMARD C., DURANT R. "Hypothesis on the mixing length and application to the calculation of the turbulent boundary layers" - AFOSR-IFP STANFORD Conference on Computations of Turbulent Boundary Layers - S.J. KLINE, M.V. MORKOVIN, G. SOVRAN, D.J. COCKRELL Ed. (1968)

MYRING D.F. "An integral prediction method for three-dimensional turbulent boundary layers" - RAE TR 70147 (1970)

OKUNO T. "Distribution of wall shear stress and crossflow in three-dimensional turbulent boundary layer on ship hull" - Journ. Soc. Nav. Arch., JAPAN, Vol. 139 (1976)

PAILHAS G. "Couche limite et sillage turbulents tridimensionnels - Champ moyen - Tensions de REYNOLDS" - Mémoire CNAM (1979)

POLL D.I.A. "Transition description and prediction in three-dimensional flows" - AGARD R-709 (1984)

PONTIKOS N.S. "The structure of three-dimensional turbulent boundary layers" - Ph. D. Thesis, Imperial College, LONDON (1982)

QUEMARD C., COUSTEIX J. "Calculation methods of three-dimensional boundary layers with and without rotation of the walls" - ONERA TP 1135 (1972)

ROTTA J.C. "Über die Theorie der turbulenten Grenzschichten" - Mitteilungen aus dem M.P.I. für Strömungsforschung N° 1, GÖTTINGEN (1950)

ROTTA J.C. "A family of turbulence models for three-dimensional boundary layers" - Turbulent Shear Flow I, BERLIN, Springer Verlag, pp. 267-278 (1979)

RUBIN S.G., REDDY D.R. "Global solution procedures for incompressible laminar flow with strong pressure interaction and separation" - Numerical and Physical Aspects of Aerodynamic Flows, T. CEBECI Ed., pp. 79-97, Springer Verlag (1983)

SCHMITT V., COUSTEIX J. "Boundary layers on a swept wing up to high angles of attack" - EUROMECH 60-TRONDHEIM (1975)

SHANEBROOK J.R., HATCH D.E. "Discussion" - Journal of Basic Engineering, Vol. 92, N° 1, pp. 9D-91 (1970)

SMITH A.M.O., GAMBERONI N. "Transition, pressure gradient and stability theory" - DOUGLAS Aircraft Co. Rpt. ES 26388, EL SEGUNDO, CALIFORNIA (1956)

SMITH P.D. "An integral prediction method for three-dimensional compressible turbulent boundary layers" - ARC R & M 3739 (1972)

SMITH P.D. "The numerical computation of three-dimensional boundary layers" - IUTAM Symposium on Three-dimensional Turbulent Boundary Layers - H.H. FERNHOLZ, E. KRAUSE Ed., Springer Verlag (1982)

SQUIRE H.B., WINTER K.G. "The secondary flow in a cascade of airfoils in a non uniform stream" - J. Aero. Sci. 18 (1951)

STOCK H.W. "Calculation of three-dimensional boundary layers on wings and bodies of revolution" - Proceedings DEA Meeting "Viscous and interacting flow field effects" - MEERSBURG (1979)

SWAFFORD T.S. "Three-dimensional, time-dependent, compressible, turbulent integral boundary layer equations in general curvilinear coordinates and their numerical solution" - Ph. D. Thesis, MISSISSIPPI State, MISSISSIPPI (1983)

TENNEKES H., LUMLEY J.L. "A first course in turbulence" - MIT Press (1973)

VAN DEN BERG B. "A three-dimensional law of the wall for turbulent shear flows" - J. Fluid Mech, Vol. 70, p. 149 (1975)

VAN DEN BERG B., ELSENAAR A., LINDHOUT J.P.F., WESSELING P. "Measurements in an incompressible three-dimensional turbulent boundary layer under infinite swept wing conditions and comparison with theory" - J. Fluid Mech., Vol. 70, pp. 127-149 (1975)

VAN INGEN J.L. "A suggested semi-empirical method for the calculation of the boundary layer transition region" - Univ. of Tech., Dpt. of Aero. Eng., Rept. UTH 74, DELFT (1956)

VAN INGEN J.L. "Transition, pressure gradient, suction, separation and stability theory" AGARD CP 224 (1977)

VELDMAN A.E.P. "The calculation of incompressible boundary layers with strong viscous-inviscid interaction" - AGARD CP N° 291, pp. 12.1-12.12 (1980)

WANG K.C. "On the determination of the zones of influence and dependence for three-dimensional boundary layer equations" - J. Fluid Mech., Vol. 48, Part 2, pp. 397-404 (1971)

WHITFIELD D.L., SWAFFORD T.W., JACOCKS J.L. "Calculation of turbulent boundary layers with separation, reattachment and viscous-inviscid interaction" - AIAA Paper N° 80-1439 (1980)

WIGTON L., YOSHIHARA H. "Viscous-inviscid interactions with a three-dimensional inverse boundary layer code" - Proc. Symp. Num. Phys. Aspects of Aerod. Flows, LONG BEACH, CALIFORNIA, ed. T. CEBECI, Paper 8.4 (1983)

PHYSICS AND MODELLING OF THREE-DIMENSIONAL BOUNDARY LAYERS

by

P. Bradshaw
Department of Aeronautics, Imperial College
Prince Consort Road
London SW7 2BY
United Kingdom

SUMMARY

This section of the course is an introduction to the physics of three-dimensional (3D) turbulent flows and a discussion of "modelling" - the use of experimental data in developing calculation methods. Only conventional Reynolds-averaged calculation methods will be discussed: for simplicity, only "differential" methods, in which variables are predicted at each point in the boundary layer, will be treated, but similar principles should apply to "integral" methods.

1.0 INTRODUCTION

The term "Three-dimensional boundary layers" is taken to include flows such as wakes or jets - which obey a 3D version of the boundary layer approximation even though they are not layers on boundaries - and "slender" flows, such as those in wing/body junctions (Figs. 1 and 2), which grow slowly in the streamwise direction even though they do not obey the 3D boundary layer approximation completely. In 3D flow with the X axis in the general direction of motion, e.g. along the centre line of an aircraft or a duct, the W-component motion, and the associated V-component motion, are called "secondary" flow, as distinct from the "primary" flow in the X direction. Our theme, therefore, is the generation of "secondary" motion in boundary layers and other 3D turbulent flows. We exclude highly three dimensional flows with massive separations, such as those behind bluff bodies.

Even within this restricted class, corresponding roughly to the different sub-regions of flow over an aircraft, a bewilderingly large variety of flow geometries can appear. Since, as usual, the number of flow phenomena is much smaller than the number of hardware configurations, we restrict ourselves to a general discussion of physical principles and do not consider particular aerospace geometries.

As always in turbulence studies intended for engineering application, the main question is "what do the Reynolds stresses do, and why?" Strictly, the effect of turbulent velocity fluctuations in a fluid flow is to provide an extra rate of momentum transfer, in addition to the convection of momentum by the mean flow and the diffusion of momentum by collisions between molecules. However, just as momentum transfer by molecular collisions is commonly regarded as equivalent to internal viscous stresses, turbulent momentum transfer is equated to extra (Reynolds) stresses. Since the Navier-Stokes equations represent Newton's second law of motion "rate of change of momentum equals applied force" for a viscous fluid, the mathematical process of transferring the velocity-fluctuation terms from the left hand side of the equation to the right hand side is exactly equivalent to interpreting the extra rates of momentum transfer as an extra stress (force per unit area).

The Reynolds stresses are extra unknowns in the time-averaged equations of motion for the rate of change of velocity, and although we can use the original time-dependent equations of motion to deduce equations for the rates of change of the Reynolds stresses, the latter equations contain extra unknowns, and an infinite series of higher-order time-averaged equations would be required to contain all the information provided by the original time-dependent Navier-Stokes equations. Therefore, experimental data or other sources of inspiration must be used to truncate the series. The current approach is to model the terms on the right hand side of the Reynolds-stress "transport" equations as functions of (i) the Reynolds stresses themselves, (ii) the mean velocity gradients, and (iii) one or more length scales of the turbulent eddies, which obey independently-determined equations.

Turbulence is essentially three-dimensional, in the sense that the fluctuating parts of all three velocity components are of the same order, and it might be thought that the essential processes of turbulence development would be unaffected by mild three-dimensionality of the mean flow. This is, indeed, the principle on which most turbulence models initially developed for two-dimensional mean flows have been extended to 3D flows. However, over the last ten years it has become clear that apparently-plausible extensions of 2D models do not give very good agreement with 3D experiments, such as those of van den Berg and collaborators at NLR (Ref. 1) on a slightly-idealized swept wing boundary layer. Predictions of secondary flow in non-circular ducts (Fig. 3) or outside long non-circular bodies (such as the ship hull in Fig. 4) are also in a less than satisfactory state; in these cases, the flow in the cross-sectional plane is actually generated by the Reynolds stresses. In particular, it can be shown that an isotropic "eddy viscosity", such as is used in

the simpler calculation methods, is essentially unable to predict stress-induced secondary flow.

The only alternative to modelling of the Reynolds stresses for substitution into time-averaged equations is solution of the time-dependent Navier-Stokes equations for the mean and fluctuating motion. Even if the smallest-scale turbulent eddies are modelled, the computing times required are so large that this is at present an approach for basic research work rather than day-to-day industrial use. However, time-dependent turbulent simulations of 3D flows are about to start, and should materially improve our understanding in the near future.

2.0 PHYSICS OF 3D FLOWS

2.1 Classification

Many years ago, Prandtl (Ref. 2) identified two main kinds of "secondary flow" - that is, velocity components in a shear layer at right angles to the main flow direction. By far the most important of these, called the "first kind of secondary flow", occurs because a given spanwise pressure gradient, applied to a boundary layer or other shear layer, will deflect the slow-moving fluid in the shear layer more strongly than it deflects the free-stream fluid. Therefore, a "crossflow" velocity component arises, as shown in Fig. 5. As we shall see below, the mechanism by which this crossflow is generated is essentially inviscid - assuming that viscous or turbulent stresses have generated a shear layer in the first place - and in fact this kind of crossflow tends to be reduced by viscous or turbulent stresses in the crossflow plane (the Y-Z plane in Fig. 5). An obvious example of this reduction is that the crossflow velocity falls smoothly to zero at the surface: the so-called "no-slip" condition requires $w=0$ as well as $U=0$ at the surface, and a secondary internal boundary layer is set up, as shown in Fig. 6(b), in which the spanwise component shear stress acts to smooth out the velocity profile. Note the use of streamline coordinates to show up departures of flow direction from that in the external flow. Clearly, if the crossflow velocity w is greater than zero, as in most of the examples in this section of the course, then $\partial w / \partial y < 0$ outside the internal layer. This description is valid for laminar and for turbulent flow: note that in either case the internal boundary layer, in which the shear stress and total pressure are perturbed, may be very much thinner than the boundary layer as a whole. It is convenient to consider what happens when an initially two-dimensional laminar or turbulent boundary layer suddenly runs into a region of spanwise pressure gradient - a simple example is the flow in a square duct, with a thin boundary layer on the floor, as it encounters a smoothly-radiused bend as shown in plan view in Fig. 5. If the flow is laminar, the streamwise flow and the crossflow (outside the internal layer) can in certain circumstances be regarded as independent, but in turbulent flow the generation of mean crossflow leads to changes in all the Reynolds stresses, even in the outer part of the boundary layer. The main theme of this series of lectures is the prediction of turbulent (Reynolds) stresses in such three-dimensional flows.

Prandtl's "secondary flow of the second kind" occurs only in the turbulent case, where Reynolds stresses can create a crossflow. The simplest example is a straight rectangular duct (Fig. 3), with, say, fairly thin boundary layers on the walls, in which the Reynolds-stress gradients that appear near the corner actually drive the secondary flow. Since one normally expects viscous or turbulent stresses to smooth out, rather than to cause, changes in velocity, secondary flow of the second kind is an unexpected and fascinating phenomenon. The large amount of attention that has been paid to it is more nearly proportional to its fascination than to its practical importance, which is really rather small. In most practical cases, square ducts or other "corner" flows contain bends or other changes in direction which generate secondary flows of the first kind, generally overwhelming secondary flows of the second kind. Of course, secondary flows of the second kind provide a very severe test case for a turbulence model for three-dimensional flow. However, in the present state of turbulence studies a turbulence model (i.e. a calculation method) is unlikely to be applicable to all kinds of flows: therefore models ought to be adjusted for optimum performance in the more common secondary flows of the first kind, and if necessary optimised separately for secondary flows of the second kind.

The secondary flow which is set up by centrifugal instability or buoyant instability - such as longitudinal Taylor-Görtler vortices in a boundary layer over a concave surface (Ref. 3), the vortex rolls that lead to cloud streets in an unstably-buoyant atmosphere (Ref. 4), or the wind-rows that form on the ocean surface (Ref. 5) - might be called "secondary flow of the third kind" but we will not discuss it further in the present lecture series.

As well as distinguishing two main mechanisms for the generation of "secondary flow", we have to consider two main configurations. We recall that the "boundary layer approximation" (which is also applicable to jets and wakes) rests upon rates of change in the streamwise direction being small - compared to rates of change in the direction normal to the surface in a boundary layer or normal to the plane of the shear layer in a nominally two-dimensional jet or wake. In 3D flow, we need to distinguish cases in which the rates of change in the spanwise direction are small and cases in which they are not. If we consider the boundary layer on a swept-back wing, far from root or tip (Fig. 1), we see that if the sweep angle is of the order

of 45°, spanwise rates of change are of the same order as streamwise rates of change, and are therefore small compared to rates of change normal to the surface of the wing. Therefore, the arguments which are used to derive the boundary layer equations in two dimensional flow, where we have to consider only the U-component of momentum, can be extended to three-dimensional flow and applied to the W-component momentum equation as well. The two key results are that, as in two dimensions, the pressure within the shear layer differs negligibly from the pressure just outside the shear layer and can, accordingly, be regarded as "known" from a solution for the external flow, and that spanwise diffusion of momentum by viscous or turbulence stresses can be neglected, just as streamwise diffusion is neglected in the 2D - and 3D - cases.

Let us use the notation that τ_{ij} represents the total (viscous plus turbulent) stress acting in the X_i direction on a plane normal to the X_j direction - so that τ_{xy} represents the usual 2D shear stress acting in the x direction on a plane normal to the y direction. Then the effect of applying the 3D version of the boundary-layer approximation is to reduce the X-component and Z-component time-averaged Navier-Stokes equations (sometimes called the Reynolds equations) from

$$\frac{DU}{Dt} \equiv U \frac{\partial U}{\partial X} + V \frac{\partial U}{\partial Y} + W \frac{\partial U}{\partial Z} = -\frac{1}{\rho} \frac{\partial p}{\partial X} + \frac{1}{\rho} \left(\frac{\partial \tau_{xx}}{\partial X} + \frac{\partial \tau_{xy}}{\partial Y} + \frac{\partial \tau_{xz}}{\partial Z} \right) \quad (1)$$

$$\frac{DW}{Dt} \equiv U \frac{\partial W}{\partial X} + V \frac{\partial W}{\partial Y} + W \frac{\partial W}{\partial Z} = -\frac{1}{\rho} \frac{\partial p}{\partial Z} + \frac{1}{\rho} \left(\frac{\partial \tau_{zx}}{\partial X} + \frac{\partial \tau_{zy}}{\partial Y} + \frac{\partial \tau_{zz}}{\partial Z} \right) \quad (2)$$

to

$$\frac{DU}{Dt} = -\frac{1}{\rho} \frac{\partial p}{\partial X} + \frac{1}{\rho} \frac{\partial \tau_{xy}}{\partial Y} \quad (3)$$

$$\frac{DW}{Dt} = -\frac{1}{\rho} \frac{\partial p}{\partial Z} + \frac{1}{\rho} \frac{\partial \tau_{zy}}{\partial Y} \quad (4)$$

where we use the transport operator D/Dt for compactness. We see that only Y derivatives of stresses remain, these being large compared to the X and Z derivatives of any stress. In the general case we have

$$\tau_{xy} = \mu \frac{\partial U}{\partial Y} - \rho \overline{u'v'} \quad (5)$$

$$\tau_{zy} = \mu \frac{\partial W}{\partial Y} - \rho \overline{w'v'} \quad (6)$$

Note that although our main concern is with turbulent flow, the viscous-stress terms may be easier to follow. Thin, slowly-growing three-dimensional shear flows that obey the boundary layer approximation are sometimes called "boundary sheets": here we prefer "3D thin shear layers", because Eqs.(3 and 4) apply to wakes (though not to trailing vortices) as well as boundary layers.

The boundary-layer assumption implies that the V-component velocity (normal to the surface) is small compared to U and W. Near the root or tip of a swept wing, for example, spanwise rates of change are large and, more or less as a direct consequence, V becomes of the same order as W, perhaps with both small compared with U. At this point, we need to generalize the concept of "crossflow" into the concept of "longitudinal vorticity". Formally the vorticity vector is the curl of the velocity vector, so that in conventional X, Y, Z axes we have

$$\omega_x = \frac{\partial W}{\partial Y} - \frac{\partial V}{\partial Z} \quad (7a)$$

$$\omega_y = \frac{\partial U}{\partial Z} - \frac{\partial W}{\partial X} \quad (7b)$$

$$\omega_z = \frac{\partial V}{\partial X} - \frac{\partial U}{\partial Y} \quad (7c)$$

In what we have called "3D thin shear layers", $\partial V/\partial Z$ has been small compared to $\partial W/\partial Y$, but these two constituents of the longitudinal vorticity are of the same order in flows near the root and tip of a swept wing, in the trailing vortices behind the aircraft, or near the corners of a rectangular duct: we call these "slender shear flows". By taking the Y derivative of the Z-component Navier-Stokes equation we can derive an equation for $\partial W/\partial Y$, and a similar equation can be derived for $\partial V/\partial Z$. A term $\partial^2 p/\partial Y \partial Z$ appears in each equation. Combining the two, we derive an equation for the X-component vorticity itself,

$$\frac{D\omega_x}{Dt} = \omega_x \frac{\partial U}{\partial X} + \omega_y \frac{\partial U}{\partial Y} + \omega_z \frac{\partial U}{\partial Z} - \left(\frac{\partial^2}{\partial Y^2} - \frac{\partial^2}{\partial Z^2} \right) \overline{w'w'} + \frac{\partial^2}{\partial Y \partial Z} (\overline{v'^2 - w'^2}) + v \nabla^2 \omega_x \quad (8)$$

The $\partial^2 p / \partial Y \partial Z$ terms cancel exactly: note that pressure gradients in the (Y-Z) plane are not negligible in the momentum equations in "slender" flows. The vorticity transport equation (8) implies that, in the absence of viscous or turbulent stresses, vortex lines remain locked to the same elements of fluid, but their vorticity will be modified by the "skewing" terms (second and third on the right) and the first, "stretching", term. A stimulating review of vorticity dynamics has been given recently by Morton (Ref. 6).

The final, general, form of the vorticity equation necessarily contains the mechanisms of generation of secondary flow of the first (skew-induced) kind and the second (stress-induced) kind: in our chosen axes, the main generation term for secondary flow of the first kind is the third term on the right of equation (X), since we suppose that the initial vorticity is mainly in the Z direction so that ω_x and ω_y are small. Stress-induced secondary flow is generated by the second derivatives of Reynolds stresses, which are generally all of the same order. The only simplification that we can usually make in "slender" flows like those near the root or tip of a swept wing is that X derivatives are small compared to Y or Z derivatives, but the latter two are of the same order.

Some skew-induced secondary flows are so strongly deflected that a discrete vortex is formed within the shear layer, with $\partial w / \partial Y$ and $\partial v / \partial Z$ of the same order. The best known examples are flows round obstacles in boundary layers, such as wing-body junction flows (Fig. 2) which are becoming increasingly important as aircraft shapes become more slender. Fig. 2 shows the distortion of elementary vortex lines and their accumulation into a "horseshoe" vortex wrapped round the leading edge. Mehta (Ref. 7) has shown that the ratio of leading-edge radius of curvature to body boundary-layer thickness has a large effect on the flow pattern: in the case of a sharp leading edge the horseshoe vortex is relatively weak. We expect that viscous or turbulent stresses will generally act to reduce the crossflow velocities. As has been shown in the recent experiments of Kornilov and Kharitonov (Ref. 8), and of Nakayama and Rahai (Ref. 9), stress-induced secondary flow will eventually take over, far enough downstream of the leading edge, leading to a pair of longitudinal vortices in each corner as shown (for a duct flow) in Fig. 3. However, the distance required for stress-induced secondary flow to take over is many times the chord of a typical wing, and the usual situation at a wing trailing edge is that a pair of vortices (one per corner) is dumped into the body boundary layer and continues to transport wing boundary-layer fluid towards the body.

Probably the most spectacular occasion on which thin shear layers roll up into quasi-longitudinal vortices is on the lee side of a body - for example a delta wing - at incidence. The topology of the surface streamlines in a separating flow is itself an interesting study: an extensive review is given by Tobak & Peake (Ref. 10), and discussions of topology by Hunt et al. (Ref. 11) and Hornung & Perry (Ref. 12). The general introduction to vorticity and 3D separation by Lighthill in Ref. 13 is also still useful. Qualitatively at least, the flow in the crossflow plane over a slender body of revolution corresponds to impulsively-started two-dimensional flow over a spanwise circular cylinder, with separation occurring just downstream of the "equator": at fairly small body incidences, a symmetrical vortex pair is formed, although, at sufficiently large incidence, vortices are shed alternately from each side of the body so that the flow in the crossflow plane looks rather like the traditional Karman vortex street. In any case, crossflow vorticity generated in a thin shear layer rolls up into a nearly-concentrated vortex, imbedded in the boundary layer if the incidence is small and effectively distinct from it if the incidence is large.

Three main imbedded-vortex configurations need to be considered (Fig. 8). The first is an isolated vortex imbedded in a turbulent boundary layer; the second is a vortex pair with the "common" flow between the vortices directed downwards towards the surface, as in the flow on the lee side of a body of revolution (Fig. 7) or downstream of a wing/body junction; and the third is the case where the common flow between the vortices is upwards, so that their common induced velocity convects them slowly away from the surface, entraining boundary-layer fluid as they go. This last case appears in the flow out of an S-bend engine intake or a wind-tunnel contraction (Ref. 14), and in both cases causes a large and unwelcome eruption of shear-layer fluid into the main flow. Flow over surface-mounted bluff bodies results in imbedding of nearly-longitudinal vortices in free shear layers and boundary layers (e.g. Ref. 15). A comparatively simple flow is that over a surface-mounted body with a streamlined nose and a blunt base, such as the "half-bullet" shape tested in Ref. 16. This is a 3D equivalent of the popular 2D backward-facing step (see Ref. 17 for a review of the latter).

A characteristic feature of strong longitudinal vortices is that the turbulence near the axis is damped out by the effect of "centrifugal forces", according to the Rayleigh criterion for flows with angular momentum increasing outwards. Centrifugal stabilization has spectacular effects in the trailing vortices far behind aircraft, and the lack of radial mixing can result in quite large longitudinal velocities being induced by pressure gradient. The phenomenon is well understood qualitatively, but presents a considerable quantitative challenge to turbulence modelling.

2.2 Transition mechanisms in three dimensional flow

This is an introduction to a subject to be discussed in later lectures. In two dimensional laminar boundary layers, the usual mechanism of transition in flows with small external turbulence level is the growth of Tollmien-Schlichting waves, which are, essentially, alternating regions of high and low spanwise vorticity. As is well known, Tollmien-Schlichting waves grow more rapidly if the velocity profile has a point of inflexion (i.e. a point where $\partial^2 u / \partial y^2 = 0$). In 3D flows, there is, necessarily, a point of inflexion in the crossflow velocity profile (Fig. 6) and the "inflexion-point instability" leads to the generation of longitudinal vortices with their axes near the point of inflexion. Fig. 9 shows the Z-component velocity profiles obtained for several different orientations of the axes, showing that inflexions occur over a range of axes. Correspondingly, vortices with a range of directions in plan view can be generated, but in practice the most noticeable are those which have zero net crossflow velocity at the inflexion point (the large cross in Fig. 9) so that the vortex pattern appears fixed in space. In practice the pattern will be locked in position by spanwise irregularities in the oncoming flow. Longitudinal vortex "streaks" are evident in many flow-visualization pictures of flow over swept wings (as sketched in Fig. 10, after Fig. 9.20 of Ref. 13) or over rotating discs. Recent computational work by Hall (Ref. 18) has shown that the longitudinal-vortex mode of "crossflow instability" easily overwhelms Taylor-Gortler instability on concave surfaces, just as either easily overwhelms the very slowly growing viscous-generated Tollmien-Schlichting mode. As usual with transition prediction, there is a large gap between nominally-accurate calculations for the rate of growth of small disturbances, and empirical results for the onset of turbulent flow. Cebeci and collaborators have compared experiments and detailed stability calculations for three dimensional flows, and shown that the onset of transition occurs after an amplification of as much as e^{40} compared to the traditional amplification factor of 2D Tollmien-Schlichting waves.

On strongly swept-back wings, the mechanism of transition is commonly "transverse contamination", in which flow along the leading edge of the swept wing transports and propagates turbulence from the body boundary layer out along the wing, rendering any discussion of transition mechanisms downstream of the leading edge irrelevant. Fortunately, there is a fairly simple empirical criterion for "spanwise contamination": it does not occur if the momentum-thickness Reynolds number of the leading edge boundary layer is less than about 100.

Since instability occurs sooner when either the axial or crossflow velocity component has a point of inflexion, there is, or ought to be, considerable interest in lateral contamination of a laminar boundary layer from turbulence generated in streamwise corners, longitudinal vortices, or other flows which contain points of inflexion over only a limited spanwise distance. The state of the art appears to be the empirical observation that spanwise contamination occurs at about the same rate as transverse contamination from turbulent spots - that is, at a half-angle of about 11° .

2.3 Generation of crossflow by pressure gradient

The Squire-Winter-Hawthorne (SWH) inviscid secondary flow formula is a special case of the vorticity equation (8) in which all viscous and Reynolds stresses are negligible and the initial vorticity vector is in the spanwise direction so $\omega_x = \omega_y = 0$. Eq.(8) therefore reduces to

$$U \frac{\partial \omega_x}{\partial x} = \omega_z \frac{\partial U}{\partial z} = \omega_z \frac{\partial W}{\partial x} \quad (8a)$$

which indicates that the initial, spanwise, vorticity vector skews (to the left, say) at the same rate at which the velocity vector skews to the right. That is, the angle of the vorticity vector to the velocity vector changes by twice as much as the flow direction, if the flow deflection is small. Now in x, y, z axes aligned with the external streamline, the cross-stream component of vorticity is approximately $-\partial u / \partial y$ and the streamwise component $\partial w / \partial y$. Therefore the slope of the outer portion of the velocity profile in the polar plot of Fig. 12, $dw/du = (\partial w / \partial y) / (\partial u / \partial y)$ is, to a first approximation, simply (minus) twice the angle through which the velocity vector has turned.

A semi-graphical proof of the SWH relation is to note from Fig. 11(a) that the decrease of pressure towards the centre of curvature (shown in Fig. 5) implies an increase in velocity according to Bernoulli's equation: in fact $U r = \text{constant}$. Thus a fluid element at E, initially lying along AB, will be convected, in a time δt say, to the point E', and will then lie along CD. The difference in lengths of the arcs AC and BD is δt times the difference in velocity across the width of the duct, which is to a first approximation proportional to (minus) the difference in radius. It follows that the angle between AB and CD is equal to the "turning angle" $\angle AOE'$. In Fig. 11(b) the fluid element is replaced by the vorticity vector, which, we recall, is permanently locked to a fluid element in the absence of viscous or turbulent diffusion. The vorticity vector is skewed, without radial stretching, to lie along CD: the vector CP then has a component PQ in the original direction of flow, but a component PR, twice as large, in the local flow direction which is normal to the radial line CR.

There are two reasons for departures of real velocity profiles from this simple

linear formula - (i) that the formula applies only to small turning angles, and (ii) that the effects of Reynolds-stress gradients opposing the secondary flow have been neglected. Nevertheless, the SWH formula provides a surprisingly good description of the outer layer of 3D turbulent boundary layers, especially those generated when a well-developed 2D boundary layer encounters a spanwise pressure gradient. From the viewpoint of predicting 3D flows this is a good thing, but it implies that, at least in some cases, a comparison of predictions with mean-flow measurements alone may not be a significant test of the Reynolds-stress model in the outer layer. That is, turbulence measurements are needed. This kind of flow, with an essentially-inviscid outer layer, is typical of flows around obstacles such as wing-body junctions: of course, the SWH formula in its simple form is not valid when the axial vorticity becomes large, even if the process of generation is essentially inviscid, but the equations of motion of inviscid rotational flow can still be integrated numerically in some form (e.g. Ref. 19).

We can now compare the response of a two-dimensional boundary layer to pressure gradient with that of a three-dimensional boundary layer - for simplicity, one in which the SWH formula for longitudinal vorticity is qualitatively accurate. In 2D flow, we can write the boundary layer equation as

$$(\partial P / \partial s)_\phi = -(\partial \bar{u} \bar{v} / \partial y)_s \quad (9)$$

where P is the total pressure, equal to $p + (1/2)\rho u^2$ in constant density flow, and s is measured along a streamline, $\phi = \text{constant}$. This shows that the total pressure on a given streamline remains constant unless affected by stress gradients. If we suddenly apply a pressure gradient which is large compared to the pre-existing stress gradients, the flow near the solid surface is constrained by (i) the no-slip condition at the surface, $u=0$, (ii) the momentum equation written at the surface,

$$0 = \nu \partial^2 u / \partial y^2 - (1/\rho) \partial p / \partial x \quad (10)$$

which requires that, at the surface, any pressure gradient shall be opposed by an equal stress gradient. At the surface, of course, the total pressure equals the static pressure. The development of total pressure and shear stress along a given streamline (i.e. a given value of stream function ϕ) in a 2D flow in adverse pressure gradient is shown in Fig. 13. Clearly, the effect of the no-slip condition at the surface gradually propagates outwards, producing a region in which the total pressure increases according to Eq. 9, the total pressure in the outer layer being constant, which is the "inviscid flow" approximation. In 3D flow, the response of total pressure to streamwise pressure gradient is qualitatively the same (Fig. 14): note that if for example we consider a high-aspect-ratio swept wing, the isobars coincide with the generators, so streamwise and spanwise pressure gradients are connected. The quasi-inviscid result for the outer layer is of course the skew-induced crossflow described, for small turning angles, by the SWH secondary flow formula. As already seen in Fig. 6, the no-slip condition on w in a 3D boundary layer leads to the generation of an internal layer in which w reduces to zero at the surface. In a calculation method, the exact relation between "streamwise" and "spanwise" internal layers depends on the turbulence model, but they are expected to be of about the same thickness. In the flow over the rotating rear part of an axisymmetric body (Fig. 18: see Ref. 20 for a recent experiment on a partly-rotating body) a w -component internal layer forms, but there is no direct effect on the axial motion. The 3D equation corresponding to the total-pressure equation, Eq.(9), is

$$\underline{U} (\partial P / \partial s) = -\underline{u} \partial \bar{u} \bar{v} / \partial y - \underline{w} \partial \bar{v} \bar{w} / \partial y \quad (11)$$

where \underline{U} is the resultant velocity, and is not so useful.

The effects of pressure gradient on the turbulent stresses in 3D flow is essentially different from the 2D case. In laminar flow, the imposition of a crossflow component of mean shear $\partial w / \partial y$ immediately produces a shear stress $\mu \partial w / \partial y$, but in turbulent flow there is no such close connection between the crossflow velocity field and the crossflow Reynolds stresses. In 3D thin shear layers we can define a streamwise component of eddy viscosity as the ratio of the shear stress in the $(x-y)$ plane, $-\bar{u} \bar{v}$, to the corresponding mean velocity gradient $\partial \bar{u} / \partial y$ - just as in 2D flow - and also define a crossflow eddy viscosity as $-\bar{v} \bar{w} / (\partial \bar{w} / \partial y)$. Unfortunately, these two eddy viscosities are not guaranteed to be the same - that is, the eddy viscosity is not necessarily "isotropic". Experimental results like those sketched in Fig. 14(a) show that although $\partial \bar{u} / \partial y$ does not alter to a first approximation, the value of $-\bar{u} \bar{v}$ on a given streamline decreases significantly in the presence of crossflow, while $-\bar{v} \bar{w}$ increases more slowly than $\partial \bar{w} / \partial y$. The result is that the streamwise eddy viscosity decreases, but the crossflow eddy viscosity, $-\bar{v} \bar{w} / (\partial \bar{w} / \partial y)$, is even smaller. The slow response of Reynolds stresses to changes in mean flow is qualitatively obvious from the Reynolds-stress transport equations, to be discussed below, which state that the rate of change of stress, rather than the stress itself, depends on the mean velocity gradients. However, the reduction of $\bar{u} \bar{v}$ in response to crossflow - that is, a distortion in a plane normal to that of $-\bar{u} \bar{v}$ - is less easy to explain, even qualitatively.

2.4 Generation of cross flow by stress gradients

Pioneering experiments performed in the 1930's, principally by Nikuradse at Göttingen, showed that, in long straight non-circular ducts or open channels, V and W-component velocities could be generated, obviously by Reynolds-stress gradients. The rather unsatisfactory "explanation" is that three-dimensionality can set up Reynolds stresses tending to produce longitudinal mean vorticity according to equation (8). The Reynolds-stress terms in the longitudinal-vorticity transport equation are all spatial gradients, so that their integral over a complete cross-sectional plane of the turbulent flow is zero; and it follows that their contribution to circulation, defined as the integral of vorticity over a complete cross-sectional plane, is also zero. That is, these are "diffusion" rather than "generation" terms. Indeed, we usually find that stress-induced vortices occur as equal and opposite vortices in, say, the corners of a duct (Fig. 3). Obviously, the integral of the Reynolds stresses over an area which comprises one of the vortices in the pair will be non-zero.

Probably the simplest stress-induced secondary flow to understand is that in a duct with a partly-rough wall (Fig. 16): the direction of secondary flow is away from the regions of high turbulence intensity. The complicated second derivatives of Reynolds stresses in Eq. (8) suggest that we cannot expect a simple interpretation in general, and Morton (Ref. 4) has pointed out that arguments based on angular momentum are insecure because the axis of reference cannot be chosen rigorously. Another fairly simple example is the jet from a non-circular nozzle, say a rectangular nozzle of large aspect ratio. As might be expected, the stress-induced secondary flows which arise tend to make the cross section circular, but the secondary flows do not fall to zero as rapidly as the eccentricity of the cross section. The result is that the cross section "overshoots" the circular shape, so that the jet from a nozzle which is wider than it is high goes through an approximately circular shape and then forms a jet which is higher than it is wide before finally relaxing back to a circular asymptotic shape. This is a nice example of the lack of close connection between turbulence stresses and mean-velocity behaviour. An example of an exceptionally large effect of stress-induced flows is the wall jet from a circular nozzle (Fig. 17) which spreads very rapidly in the spanwise direction - several times faster than it spreads normal to the surface. This flow is discussed by Launder & Rodi (Ref. 21) but the mechanism is still controversial.

The secondary-flow velocities in stress-induced secondary flow are of the order of the root-mean-square velocities of the turbulence, whereas the SWH formula implies that the cross-plane velocities in skew-induced secondary flows are of the order of the streamwise velocity times the flow deflection angle (radians). In strongly deflected flows, for example that in the wing-body junction of Fig. 2, the deflection angle is of the order of one radian. This is the essential reason why skew-induced secondary flows so easily overwhelm stress-induced secondary flows in practice, however fascinating the latter may be in principle.

3.0 MODELLING AND THE USE OF EXPERIMENTAL DATA

3.1 The Reynolds-stress transport equations

Without prejudice to the approximations that may be made for engineering purposes, we begin with the exact transport equations for Reynolds stress. These equations can be derived, without approximation, from the Navier-Stokes equations. They contain further unknowns (time averages of complicated turbulence quantities) on the right-hand side. We use tensor notation for compactness, $u_i u_j$ being a stress acting in the x_i direction on a plane normal to the x_j direction. Each subscript can take any desired value: if a subscript is repeated in a given term, that term is summed over all three values of the subscript. Our main interest here is in the general layout of the terms and the reader can ignore the subscripts.

$$\begin{aligned} \frac{Du_i u_j}{Dt} = & - \left(\overline{u_i u_l} \frac{\partial u_j}{\partial x_l} + \overline{u_j u_l} \frac{\partial u_i}{\partial x_l} \right) + p' \left(\frac{\partial u_i}{\partial x_j} + \frac{\partial u_j}{\partial x_i} \right) \\ & - \frac{\partial}{\partial x_i} \left(\overline{p' u_j} \right) - \frac{\partial}{\partial x_j} \left(\overline{p' u_i} \right) - \frac{\partial}{\partial x_l} \left(\overline{u_i u_j u_l} \right) \\ & + \nu \left(\frac{\partial^2 \overline{u_i u_j}}{\partial x_l^2} + \frac{\partial^2 \overline{u_j u_i}}{\partial x_l^2} \right) \end{aligned} \quad (12)$$

The left-hand side is the rate of change of any component of Reynolds stress along a mean streamline: the right-hand side comprises (i) generation of Reynolds stress by interaction of the existing turbulence with the mean velocity gradients, (ii) spatial diffusion or "turbulent transport" of Reynolds stresses by the turbulence, (iii) the redistribution of Reynolds stresses between different

components by the action of pressure fluctuations, and (iv) destruction or diffusion by viscous-stress fluctuations. Viscous diffusion of Reynolds stress is small, except in the viscous sublayer very close to a solid surface, and viscous destruction is important only for the normal stresses, where it dissipates turbulent kinetic energy into heat. In most turbulent flows, the terms representing generation by interaction between the turbulence and the mean shear are approximately balanced by the "redistribution" or "destruction" terms, and our chief problem is the modelling of the latter. Details will be discussed below: briefly, pressure fluctuations within the flow act to "scramble" the turbulence and make it more nearly isotropic - that is, to reduce all the shear stresses and to equalize the normal stresses - while viscous dissipation reduces the normal stresses but has little effect on the shear stresses. (It must be remembered that the resolution of the stress tensor into shear stresses and normal stresses depends on the axes chosen, and there is always one set of axes, the so-called "principal" axes, in which all shear stress component are zero, leaving only the "principal" normal stresses: however principal axes are not much used in turbulence studies.)

3.2 Boundary-layer approximation and "Region of Influence"

The boundary-layer approximation can be applied, where it is physically justifiable, to the Reynolds-stress transport equations as well as to the momentum-transport ("mean motion") equations. Since the "diffusion" or "turbulent transport" terms in the Reynolds-stress transport equations are spatial gradients of turbulence quantities, application of the boundary-layer approximation implies neglect of the spanwise and streamwise components of this diffusion, leaving only diffusion in the y direction. In plan view, this means that turbulent stress, like momentum, is merely convected along the mean streamlines at an angle $\tan^{-1} w/u$ to the axes, and diffusion away from the streamline in plan view is negligible.

This convection of information (that is, momentum and Reynolds stress) along mean streamlines in plan view implies a considerable simplification in the equations of motion and their solution. The Navier-Stokes equations are elliptic, and in principle the influence of disturbances at a given point can be propagated either by convection by the mean velocity, or by viscous or turbulent diffusion, or by pressure perturbations. In the 3D boundary layer equations, however, we have eliminated propagation by pressure disturbances, by requiring the pressure to be equal to that at the edge of the shear layer (determined by an inviscid flow solution, say). We have also agreed to neglect viscous or turbulent diffusion, and the result is that information is propagated in the crossflow plane only via pure convection. Thus the limits of spanwise propagation of a perturbation originating at a point P (Fig. 15) are the most-leftward and most-rightward streamlines originating at the X, Z value of P - diffusive propagation of information in the Y direction being assumed "immediate". As will be seen in later lectures, the confinement of the "region of influence" of P to a wedge with its apex at P has important and useful implications in numerical methods, because the finite-difference "molecule" used to compute conditions at a given point must adequately represent the arrival of information at that point. (Experts may note that, in particular, "integral" methods for 3D boundary layers yield purely hyperbolic equations in the $(Y-Z)$ plane.)

In stress-induced secondary flows, turbulent diffusion of momentum or Reynolds stress in the $(Y-Z)$ crossflow plane is a vital part of the process, and the equations which include this diffusion can loosely be called "elliptic" in the $(Y-Z)$ plane. A perturbation at a point P can in principle reach any part of the flow downstream of P , not just the inside of a wedge. (Again for experts, the slender-flow equations in X, Y and Z , with only X -wise diffusion neglected, are actually parabolic, like the closely-analogous equation for unsteady two-dimensional heat transfer in - say - t, Y and Z , but each step of a marching solution leads to an elliptic problem in the $(Y-Z)$ plane.)

3.3 Turbulence modelling - details

As indicated above, the Reynolds-stress transport equations are exact consequences of the Navier-Stokes equations, and therefore any empirical turbulence model must, at least, be compatible with these equations. The most advanced turbulence models involve term-by-term approximation of the equations, representing each term as a dimensionally-correct combination of Reynolds stresses and their gradients, and, where appropriate, mean-velocity gradients also. For example, the pressure-strain "redistribution" term, which, like all the other terms, has the dimensions $(\text{velocity})^3 / (\text{length})$, could be represented as $(\text{Reynolds stress})^{3/2} / (\text{length scale})$. Alternatively, of course, the same term could be represented as the product of a Reynolds stress and a mean-velocity gradient, which again has the required dimensions: and we shall see in Sec. 3.5 that the equation governing the generation of pressure fluctuations within the flow warns us that the best model of the "redistribution" terms will involve both representations.

There is an ambiguity in the modelling of the turbulent transport terms also: these terms, once more, have the dimensions $(\text{velocity})^3 / (\text{length})$, but the length dimension is supplied by the spatial gradient, and the most obvious model is therefore one which represents the triple product inside the gradient as some suitable combination of Reynolds stresses to the power $3/2$. However, most calculation methods model the turbulent transport terms by using the "gradient

diffusion" concept, which rests on the same insecure foundations as eddy viscosity (Sec. 3.4) but seems adequate for correlating data. It assumes that the triple products are proportional to the Reynolds-stress gradients, with a diffusivity whose dimensions are the same as viscosity and which is therefore taken proportional to (Reynolds stress)^{1/2} x (length scale).

The combinations of existing variables must be chosen for the best physical plausibility, but, whichever dimensionally-correct representation is chosen, it merely defines a dimensionless constant, "(term in equation) / (dimensionally correct combination of variables)". If the combination of variables exactly represented the physical process, the constants so defined would be genuine universal constants, like the coefficients of the Navier-Stokes equations which are ρ , ν or unity. Unfortunately, such simplified equations for turbulence are inevitably less accurate than the Navier-Stokes equations, and the "constants" not only depend on the type of flow considered but may also depend on the position in that flow. Since even the exact Reynolds-stress transport equations are not complete descriptions of turbulence, because information has been lost by time averaging, the model constants would have to be found by experiment even if they were truly universal. Unfortunately, very few 3D experiments contain sufficient information to evaluate all the terms in the Reynolds-stress transport equations (pressure fluctuations within the flow cannot be measured with any assurance of accuracy, so that pressure-strain "redistribution" terms must always be determined as the net sum of the other, measured, terms).

3.4 Simpler modelling concepts - eddy viscosity

The simplest way to model the Reynolds shear stress in a 2D thin shear layer is to assume that the eddy viscosity, defined as the ratio of the $u'v'$ shear stress to the mean shear $\partial u/\partial y$, can be related to mean flow parameters: for example, in the popular Cebeci-Smith model, the eddy viscosity in the outer layer of a boundary layer is represented by $0.0168u_e\delta$. The difficulty with this kind of correlation is that the eddy viscosity is defined as the ratio of a turbulence quantity (the Reynolds stress) to a mean-flow quantity (the mean velocity gradient), whereas the correlation implies that the eddy viscosity depends only on the mean-flow scales and not on the turbulence scales. The same anomaly appears, in reverse, if the eddy viscosity is itself obtained from transport equations, as in the popular k , epsilon model: this wrongly implies that the eddy viscosity is a property of the turbulence alone.

The "mixing length" concept is close to that of eddy viscosity, both in principle and in practical results. It relates the shear stress to the square of a velocity gradient: this leads to a fully non-linear differential equation for the mean velocity, which is a nuisance numerically. Therefore eddy viscosity is currently the more popular for discussion or use, but we shall use mixing length in a discussion of the inner layer of a turbulent wall flow, $y/\delta < 0.2$ say, in Section 3.7.

In the inner layer, the turbulence is near "equilibrium", with the generation term (i) in Eq. (12) nearly balanced by the redistribution or viscous-destruction terms. In this case, the length and velocity scales of the mean flow are nearly proportional to the length and velocity scales of the turbulent motion, and the anomaly in the eddy viscosity concept is unimportant. Even in the outer layer, the turbulence may not be too far from equilibrium if the flow is changing slowly. However, skew-induced 3D flows are often quite strongly out of equilibrium, because the mean shear in the crossflow plane is generated by an essentially inviscid mechanism rather than by the cumulative effect of stress gradients: therefore, local-equilibrium concepts like eddy viscosity are likely to be unreliable. "Reliability" in this context means universality or simple behaviour of empirical constants: we can always define an eddy viscosity as the ratio of a Reynolds stress to the corresponding rate of strain so that

$$\nu_{ij} = -\overline{u'_i u'_j} / (\partial u_i / \partial x_j + \partial u_j / \partial x_i) \quad (13)$$

- but note that for complete generality we ought to allow $\overline{u'_i u'_j}$ to depend on rate-of-strain components in planes other than $(x_i - x_j)$, implying that eddy viscosity is really a fourth-order tensor!

In 3D boundary layers our main interest is in $\overline{u'v'}$ and $\overline{v'w'}$, so a basic question is whether the eddy viscosity deduced from experimental data is the same for both these shear stresses. As discussed in Dr van den Berg's lectures, several experiments in 3D boundary layers show that the eddy viscosity is anisotropic. Specifically, the eddy viscosity for the $\overline{v'w'}$ shear stress is significantly different from the eddy viscosity for $\overline{u'v'}$. That is, the direction of the "shear stress vector", whose components are $(-\overline{u'v'}, -\overline{v'w'})$, is different from that of the "velocity gradient vector" whose components are $(\partial u/\partial y, \partial w/\partial y)$. If an initially 2D boundary layer is skewed in the $(x-z)$ plane, a crossflow velocity gradient $\partial w/\partial y$ develops immediately, roughly as predicted by the Squire-Winter-Hawthorne formula described above, but the crossflow shear stress $-\overline{v'w'}$ responds more slowly - as turbulence usually does - so the shear-stress vector skews more slowly. However we shall see below that the behaviour of eddy viscosity in 3D flow cannot be explained entirely by

this semi-obvious lag effect.

In quantitative discussions about "streamwise flow" and "crossflow", we immediately encounter the basic difficulty that the definitions of the X and Z directions are arbitrary: about the only meaningful definition of X is as the direction of an initial quasi-two-dimensional motion before the imposition of a spanwise (z-wise) pressure gradient. The usual "invariance" principle, that a physical phenomenon is independent of the axes used to describe it, also makes it difficult to defend the concept of special "streamwise" and "cross-stream" (x and z) axes. A special case of the principle is that the description of a phenomenon ought not to be altered by uniform translation of the axes (Galilean invariance), and it follows that the direction of the mean-velocity vector, whether in the free stream or elsewhere, cannot be rigorously used as a preferred direction in the flow - that is, we should not make our turbulence model depend on it. Thus, even if one accepts that eddy viscosity is an adequate concept in 2D flow, the choice of axes to define the components of eddy viscosity in 3D flow is difficult. The same applies to other modelling parameters, as we shall see below.

The Navier-Stokes equations and the Reynolds-stress transport equations, as quoted above, are of course exact, and are therefore valid for any choice of X, Z axes. The same applies to any thin-shear-layer form of the equations if gradients in the X and Z directions are small: clearly the y direction (in which gradients are large) cannot be chosen arbitrarily. The "slender shear flow" equations, for flow in wing/body junctions and ducts, require X to be chosen as the direction of small gradient, but are invariant with respect to rotation in the Y-Z plane. Therefore the difficulties of definition encountered with eddy viscosity will not necessarily appear in the case of other models.

This writer's opinion is that, in 3D even more than in 2D, calculation methods for the more demanding flows ought to be based directly on the Reynolds-stress transport equations - simplified as far as possible, of course. As we have just seen, the "lag effect" on shear-stress direction, which is the result of mean-flow transport of Reynolds stress (i.e. the rate of change of Reynolds stress along a mean streamline) is often too big to neglect in 3D flows. If transport of Reynolds stresses by the mean flow and transport by the turbulence itself are both negligible, each shear-stress transport equation reduces to "generation" equals "destruction": that is, interaction between the existing turbulence and the mean shear is balanced by pressure-strain redistribution, otherwise called the "return-to-isotropy" or "scrambling" term. This "local equilibrium" is a fair first approximation for flows which are changing slowly in the streamwise direction (small mean-flow transport), because turbulent transport is generally fairly small except near the outer edge of a shear layer. Even this simplified case brings us back to the modelling of the pressure-strain redistribution term, term (iii) in Eq. (12), as being the most critical part of the development of a calculation method.

3.5 The pressure-strain "redistribution" term

If we take the divergence of the Navier Stokes equations, i.e. differentiate the x_i -component equation with respect to x_i and sum over all values of i , we obtain a Poisson equation for the pressure fluctuation. This equates the Laplacian of the pressure fluctuation p' to a "source" term, which depends not only on the turbulence intensity at the point considered but also on the mean-velocity gradients. This curious situation, that a fluctuating quantity depends on mean-flow gradients, is just a consequence of the way in which we take averages, but the result is that the formal solution of the Poisson equation for p' implies that the pressure-strain redistribution term also consists of two parts.

Both parts of the redistribution term with the Poisson solution substituted for p' are, strictly, integrals over the whole of the flow field. One part is determined entirely by the fluctuating quantities, while the other depends on the mean velocity gradients: the latter is called the "rapid" part - in this context, because it responds immediately to any change in mean velocity gradient. This fact was pointed out by P.Y. Chou (Zhou) in 1945, by Rotta in 1951 and by Lilley and other workers on aerodynamic noise in the early 1960s, but was slow to gain acceptance in turbulence modelling. Even with all possible approximations, this implies that the pressure-strain redistribution term at a given point in a 3D thin shear layer depends not only upon the turbulence quantities but also on the two components of the mean velocity gradient (mean shear), $\partial u/\partial y$ and $\partial w/\partial y$.

If we regard the two shear-stress components $-\overline{u'v'}$ and $-\overline{v'w'}$ as the components of a two dimensional vector, the pressure-strain terms in the corresponding Reynolds-stress transport equations are also the components of a two-dimensional vector, and in general the direction of the pressure-strain "vector" will not be the same as that of the shear stress - that is, the pressure-strain "redistribution" term does not merely reduce the magnitude of the shear stress vector but may also alter its direction. The simplest two-term model has one term whose vector direction is that of the mean-shear velocity gradient $(\partial u/\partial y, \partial w/\partial y)$ and another whose direction is that of the shear stress vector $(-\overline{u'v'}, -\overline{v'w'})$. However this model will never lead to the creation of a difference between the direction of the mean-velocity gradient vector and that of the shear stress vector if the two initially coincide, and experimental results imply that the difference between the directions cannot be

completely explained as the "lag effect" due to the mean-flow transport terms, described above. To meet this objection, Rotta (Ref. 22) has suggested a more general model of the pressure-strain term, including a "anisotropy" factor. Rotta's model as originally proposed uses the mean-velocity direction as an axis, contrary to the invariance concept presented above; and in practice - e.g. Abid, Ref. 23 - the Rotta model seems to yield only a small difference between the directions of velocity gradient and shear stress in the initial stages of the calculation, followed by an excessively rapid divergence between the two directions as the crossflow increases.

In slender shear layers, the predominant mean-velocity gradients are $\partial U/\partial Y$ and $\partial U/\partial Z$, and both will appear in the modelled pressure-strain terms. However the problem is obscured by the apparent need for modelling parameters in slender wall flows to depend on the distance from each surface ("wall effect"): empirical adjustments for wall effect may hide deficiencies in the basic pressure-strain model.

3.6 Length scales

The part of the pressure-strain term that depends solely on turbulence quantities must be expressed as the cube of a velocity scale - say (turbulent energy)^{3/2} - divided by a length scale. In 2D transport models, the length scale is almost always derived from a model of the dissipation transport equation (the "epsilon equation"), and at present the same equation is normally used in 3D without extra terms or changes in the coefficients. The approximation to the dissipation that is normally modelled is a scalar (isotropic) quantity distributed equally among the three Reynolds normal stresses. However the epsilon equation is used to give a length scale of the large, energy-containing eddies, and is, at best, a plausible modelled equation for the rate of transfer of energy from the large eddies to the small ones. This rate is nominally equal to the dissipation rate but is not isotropically distributed. We may therefore expect trouble in 3D. Even if one ignores the vector character of "epsilon", the coefficients in the epsilon equation are likely to depend on the three-dimensionality of the flow. The main use of the length scale is in modelling the pressure-strain term, where general uncertainties at present mask 3D effects on the epsilon equation.

3.7 The inner layer

In the inner layer of a turbulent boundary layer, the resultant of the mean-shear velocity gradient "vector" ($\partial u/\partial y$, $\partial w/\partial y$) is large compared to any other velocity gradient such as $\partial w/\partial x$, and the turbulent eddies are small enough for their lifetimes to be short compared to a typical mean-flow development time. We therefore expect to recover local-equilibrium results, like the two-dimensional "mixing length" formula which equates the resultant shear stress to the square of the resultant velocity gradient multiplied by the square of the mixing length, the latter being directly proportional to the distance from the surface, i.e.

$$\sqrt{[(-\overline{u'v'})^2 + (-\overline{v'w'})^2]} = l^2((\partial u/\partial y)^2 + (\partial w/\partial y)^2) \quad (14)$$

where $l = Ky = 0.41y$. However, this "local equilibrium" result that the shear stress and the mean velocity gradient are in the same direction does not necessarily apply to the viscous sublayer, for which a simple but illuminating analysis is given by van den Berg (Ref. 24). Pierce et al. (Ref. 25) provide a general review of models for the 3D inner layer, but those which have a simple physical interpretation are either special cases or equivalents of van den Berg's. Fortunately the main effect of non-equilibrium in the sublayer is that the velocity difference between the solid surface and the edge of the sublayer acquires an extra component transverse to the direction of the surface shear stress. Van den Berg's semi-empirical estimate of this extra slip velocity could be, but has not been, improved by experiment.

Many 3D turbulent flows in real life - or in laboratory experiment - can be predicted quite well by the Squire-Winter-Hawthorne inviscid secondary flow formula, providing that the Reynolds stresses in the internal layer near the surface (Fig. 6) are modelled adequately. That is, the inner-layer model is if anything more crucial than the outer-layer model, at least for skew-induced secondary flows.

3.8 Use of data

We now consider how experimental data can help the modelling process. As in 2D flows, we immediately hit the difficulty that the all-important pressure-strain term cannot be measured directly. Although evaluating the pressure-strain term as the difference of other measured terms may give adequately accurate values for the term as a whole, it cannot show the relative sizes of the two parts, the "rapid" part, depending on the mean strain rate, and the purely-turbulent part. In fact, even full time-dependent turbulent simulations, yielding u' , v' , w' and p' as functions of time, will not usually do this directly, but the two parts can be recovered separately by evaluating one afterwards from the calculated fluctuations. Time-dependent simulations of 3D flows, whether full turbulent simulations (FTS) or large-eddy simulations (LES) with a model for the fine structure, are only just starting to be feasible for 3D flows such as those on "infinite" swept wings, but will be a useful supplement, and perhaps eventually a replacement, for experimental data.

The situation in practice is that turbulence models for 2D flows are being adjusted empirically for 3D flows. Abid and others have used Rotta's model of the pressure-strain term to define and optimise a constant T , related to the eddy viscosity ratio but implying a directional preference of the pressure-strain term. Rotta's model does not represent the even more spectacular effect of crossflow in decreasing the shear-stress magnitude, which implies an increase in magnitude of the pressure-strain term (leading to a faster return to isotropy). However no significant improvement of Rotta's model seems to have been offered.

There are now several experiments which contain reliable measurements of all the Reynolds stresses (including the hard-to-measure $v'w'$) but there are few data on the triple products, even in 3D boundary layers. In strongly-skewed boundary layers they appear to decrease in magnitude as the crossflow increases, just as the resultant shear stress and turbulence intensity do. This would be qualitatively represented by an extension of any existing 2D model for $u'v'$ to give $v'w'$ also. Unless it contained an extra constant analogous to Rotta's T , such a model would imply that these two triple products behaved similarly although the quantities they transport, $u'v'$ and $v'w'$, do not. However, elucidation of any odd vector behaviour of triple products is a much lower priority than improved modelling of the pressure-strain term.

4.0 CONCLUSIONS

Even after 20 years of computer modelling of turbulence, the position is that even models based as faithfully - and expensively - as possible on the Reynolds stress transport equations cannot satisfactorily predict the Reynolds stresses in flow over swept wings. As pointed out above, a good model for the inner layer suffices to give adequate predictions of surface shear stress in boundary layers on wings not too close to the stall, but outer-layer models are still questionable. The user of calculation methods must therefore keep close watch on the predicted results, and, in particular, should check the method in a flow as similar as possible to the one for which predictions are required.

REFERENCES

- 1 Van den BERG, B.
ELSENAAR, A.
LINDHOUT, J.P.F.
WESSELING, P. Measurements in an incompressible three-dimensional turbulent boundary layer under infinite swept wing conditions and comparison with theory. J. Fluid Mech. vol. 70, p.127, 1975.
- 2 PRANDTL, L. Essentials of Fluid Mechanics. Blackie, London, 1953.
- 3 HOFFMANN, P.H.
MUCK, K.C.
BRADSHAW, P. The effect of concave surface curvature on turbulent boundary layers. J. Fluid Mech. vol. 161, p.371, 1985.
- 4 MASON, P.J. A numerical study of cloud streets in the planetary boundary layer. Boundary-Layer Met. vol. 32, p.281, 1985.
- 5 THORPE, S.A. Small scale processes in the upper ocean boundary layer. Nature vol.318, p.519, 1985.
- 6 MORTON, B.R. The generation and decay of vorticity. Geophys. and Astrophys. Fluid Mech. vol.28, p.277, 1984.
- 7 MEHTA, R.D. Effect of wing nose shape on the flow in a wing/body junction. Aero J. vol.88, p.456, 1984.
- 8 KORNILOV, V.I.
KHARITONOV, A.M. Investigation of the structure of turbulent flows in streamwise asymmetric corners. Expts in Fluids. vol.2, p.205, 1984.
- 9 NAKAYAMA, A.
RAHAI, H.R. Measurements of turbulent flow behind a flat plate mounted normal to the wall. AIAA J. vol. 22, p.1817, 1984.

- 10 TOBAK, M.
PEAKE, D.J. Topology of three dimensional separated flows. Ann
Rev. Fluid Mech. vol.14, p.61, 1982.

- 11 HUNT, J.C.R.
ABELL, C.J.
PETERKA, J.A.
WOO, H. Kinematical studies of the flows around free or surface-
mounted obstacles; applying topology to flow
visualization. J. Fluid Mech. vol. 86, p.179, 1978.

- 12 HORNUNG, H.
PERRY, A.E. Some aspects of three-dimensional separation. Part I:
stream surface bifurcations. Part II: vortex skeletons.
Z. Flugwiss. vol.8, p.77 and p.155, 1984.

- 13 ROSENHEAD, L. (Ed.) Laminar Boundary Layers. Clarendon Press, Oxford, 1963.

- 14 MOKHTARI, S
BRADSHAW, P. Longitudinal vortices in wind tunnel wall boundary layers.
Aero. J. vol.87, p.233, 1983.

- 15 CASTRO, I.P.
ROBINS, A.G. The flow around a surface-mounted cube in uniform and
turbulent streams. J. Fluid Mech. vol.79, p.307, 1977.

- 16 HANDFORD, P.M. Measurements and calculations in three-dimensional
separated flows. PhD thesis, Imperial College, 1986.

- 17 EATON, J.K.
JOHNSTON, J.P. A review of research on subsonic flow reattachment.
AIAA J. vol.19, p.1093, 1981.

- 18 HALL, P. The Görtler vortex instability mechanism in three-
dimensional boundary layers. NASA CR-172370, ICASE
Rept. 84-17, 1984.

- 19 RUBEL, A. Inviscid axisymmetric jet impingement with
recirculating stagnation regions. AIAA J. vol.21,
p.351, 1983.

- 20 HEBBAR, S.V.
DRIVER, D. A three-dimensional turbulent boundary layer undergoing
transverse strains and streamwise pressure gradient.
NASA TM 86758, 1985.

- 21 LAUNDER, B.E.
RODI, W. The turbulent wall jet - measurements and model.
Ann. Rev. Fluid Mech. vol.15, p.429, 1983.

- 22 ROTTA, J.C. A family of turbulence models for three-dimensional thin
shear layers. Proceedings, First Symposium on Turbulent
Shear Flows (F.Durst et al., eds.) Springer, New York,
p.267, 1979.

- 23 ABID, R.
SCHMITT, R. Critical examination of turbulence models for a separated
three dimensional turbulent boundary layer. Rech. Aerosp.
no. 1984-6, p.385, 1984.

- 24 Van den BERG, B. A three dimensional law of the wall for turbulent shear
flows. J. Fluid Mech. vol.70, p.149, 1975.

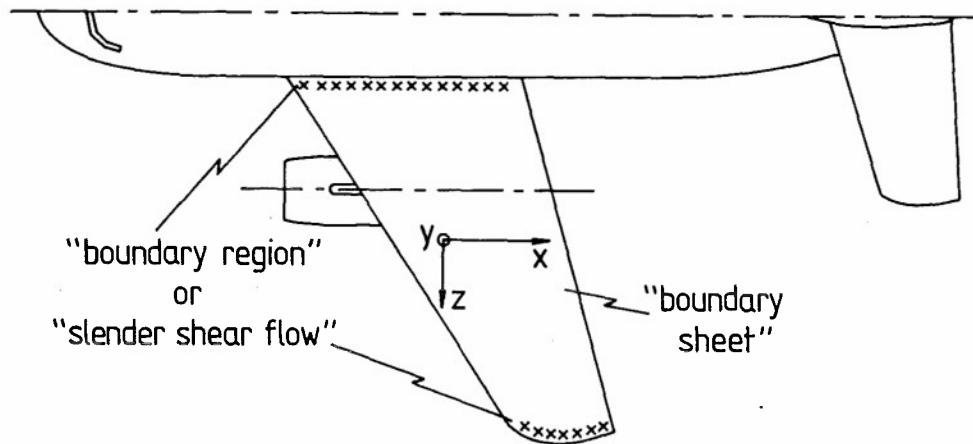


Fig. 1 Types of 3D flow

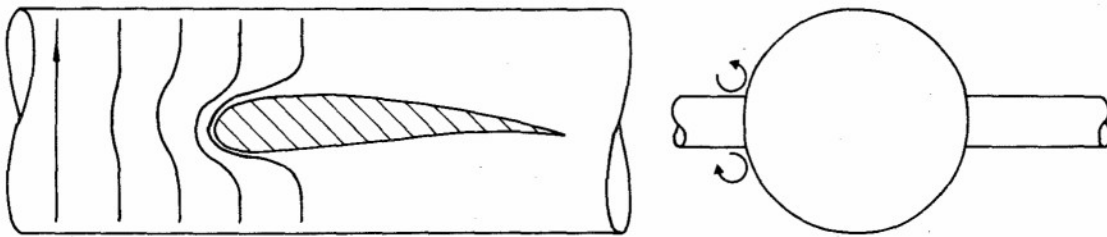


Fig. 2 Generation of streamwise vorticity by distortion of cross-stream vortex lines (secondary flow of the first kind).

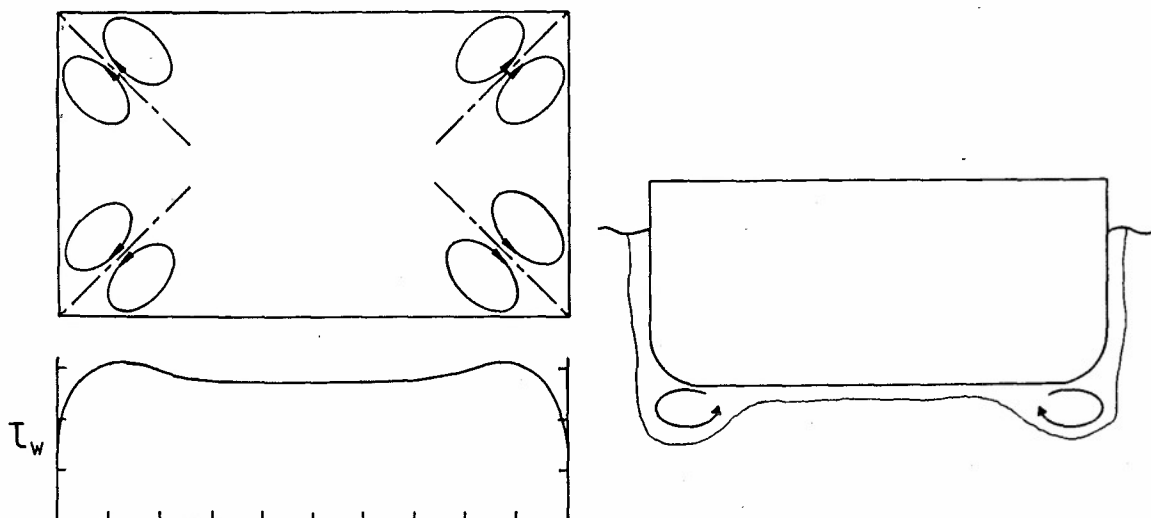


Fig. 3 Generation of streamwise vorticity by Reynolds stresses (secondary flow of the second kind).

Fig. 4 Ship "bilge vortices" - initially skew-induced secondary flow followed by sharp-corner effects.

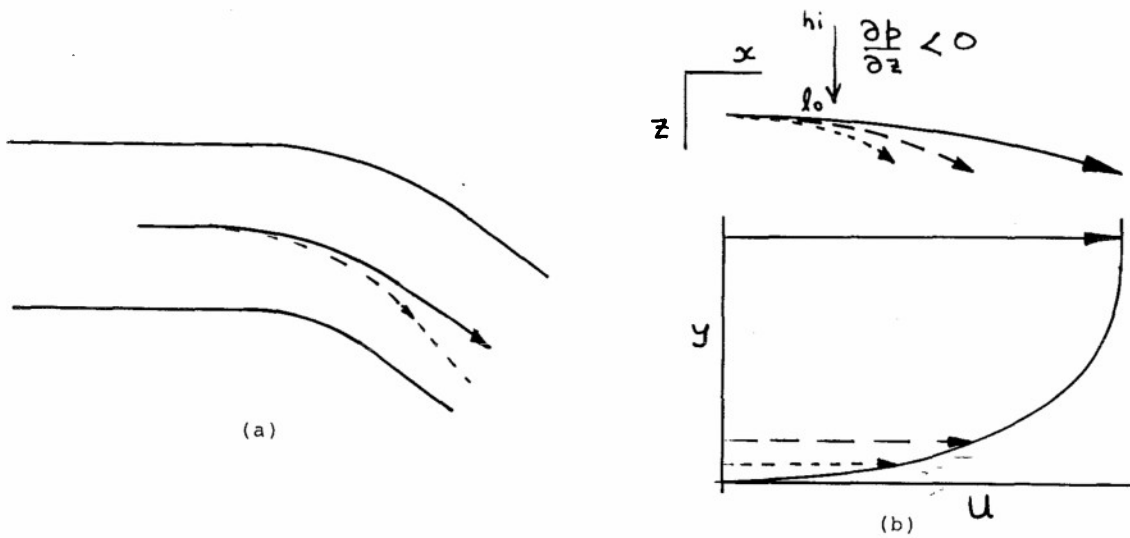


Fig. 5 Development of crossflow by stronger deflection of slow-moving boundary layer fluid in cross-stream pressure gradient.

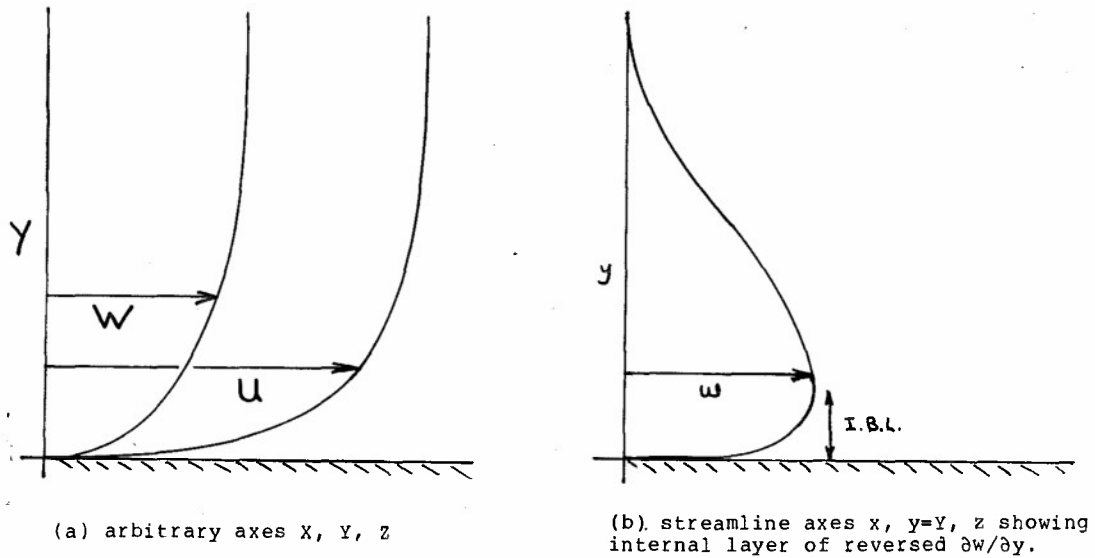


Fig. 6 Crossflow velocity profile

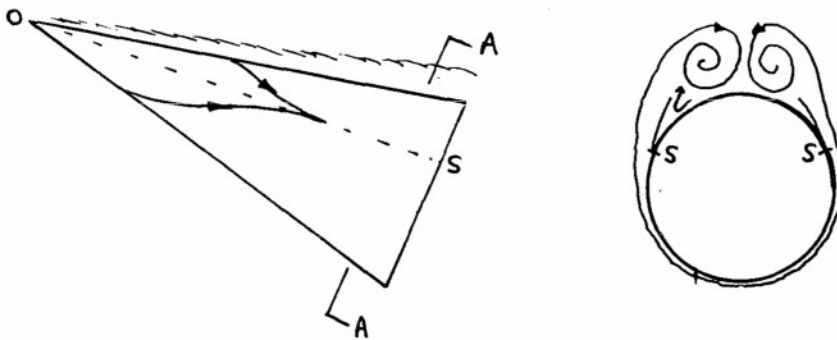
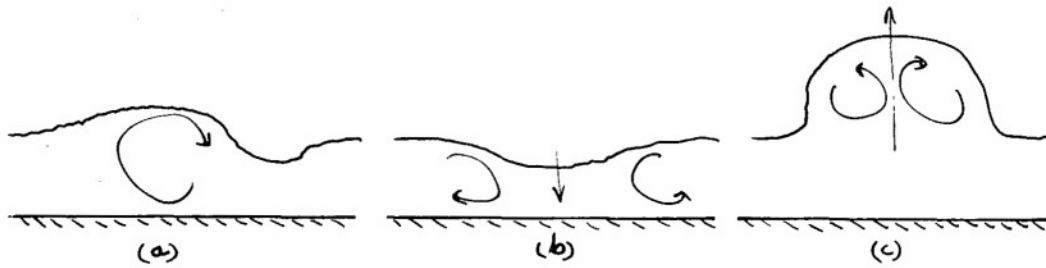


Fig. 7 Vortices on lee side of cone at incidence. Secondary flow in Section A-A approximates to impulsively-started 2D flow over circular cylinder. Note convergence of surface streamlines at separation line



(a) isolated vortex (b) vortex pair with "common" flow downwards (c) "common flow" upwards

Fig. 8 Cross section (yz plane) of vortices imbedded in boundary layers

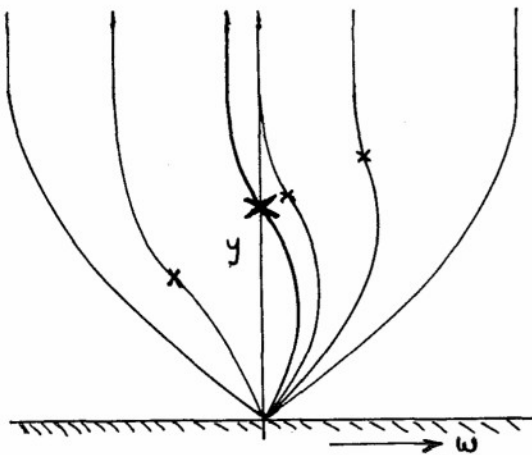


Fig. 9 W-component velocity profiles in a given laminar boundary layer for different directions of X,Z axes.

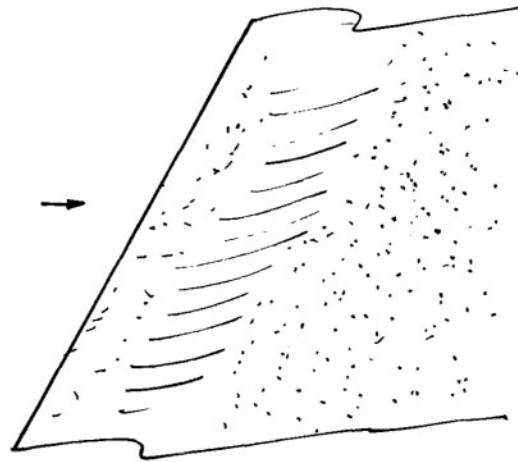
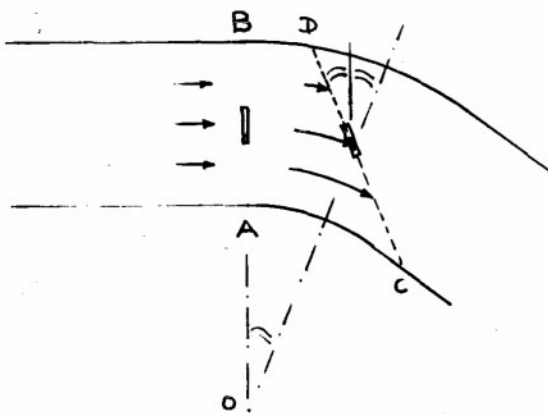
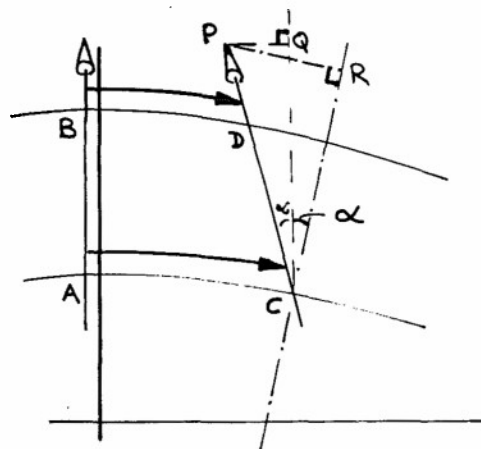


Fig.10 Transition on swept wing, showing successive laminar flow, vortex streaks and turbulent flow.



(a) anticlockwise deflection of fluid elements due to clockwise deflection of velocity vector



(b) enlargement; equal and opposite deflections of vorticity vector and velocity vector.

Fig.11 Illustration of Squire Winter Hawthorne secondary flow formula.

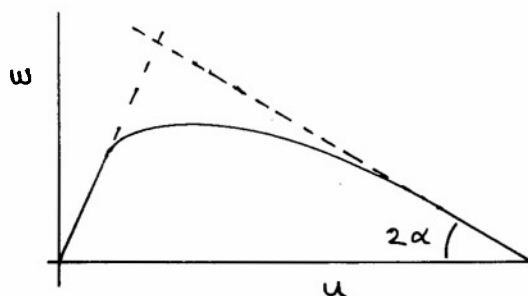


Fig. 12 Gruschwitz/Johnston "polar plot" of w against u in streamline coordinates ($w_e = 0$).
 $\frac{dw}{du} = (\partial w / \partial y) / (\partial u / \partial y) \approx -2\alpha$ where α is turning angle

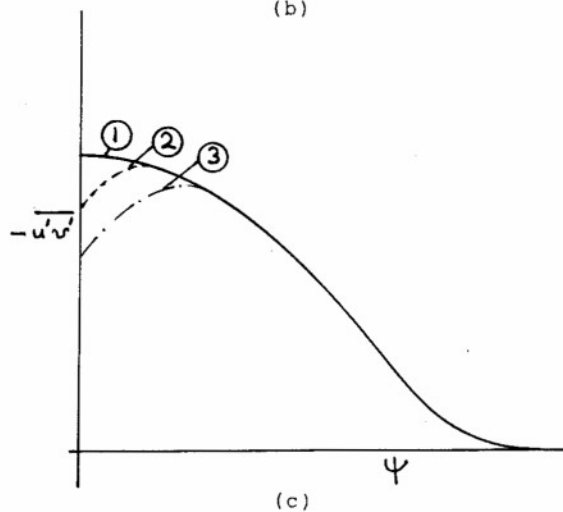
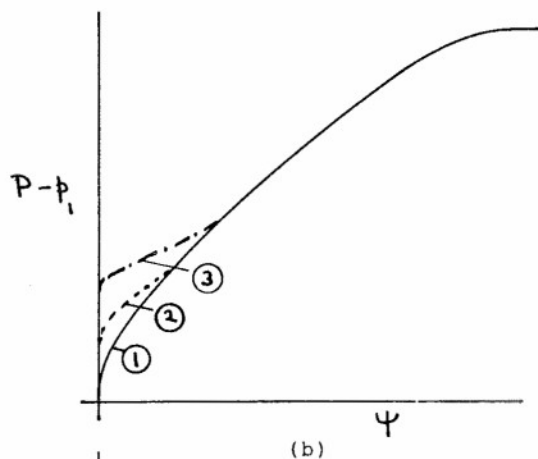
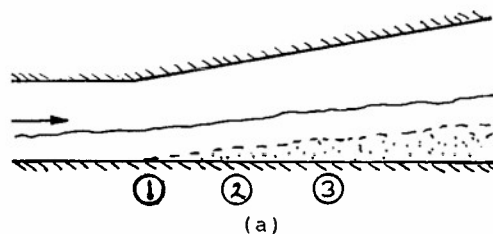


Fig. 13 Response of 2D boundary layer to adverse pressure gradient
 total pressure and shear stress remain constant on a given streamline ($\Psi = \text{constant}$) except in internal layer near surface.

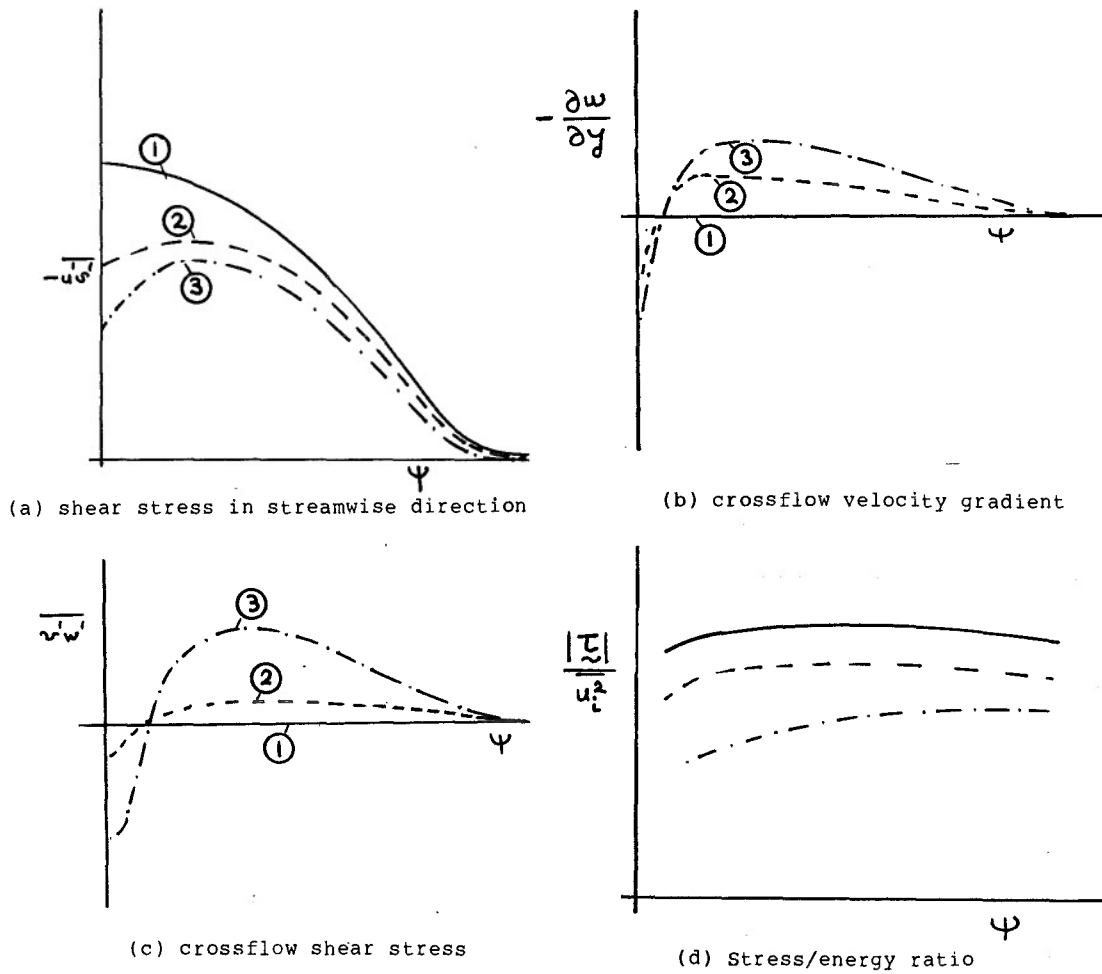


Fig.14 Response of 3D boundary layer to adverse pressure gradient (leading to crossflow)

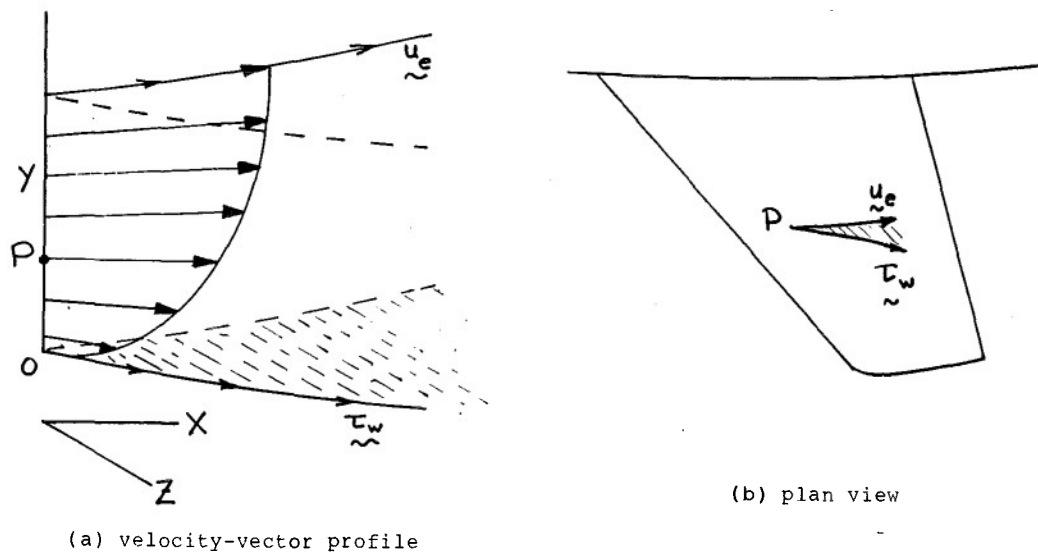


Fig.15 Region of influence of a point P in a 3D boundary layer



Fig.16 Stress-induced secondary flow in duct with partly-rough wall - secondary flow tends to be down gradient of turbulent intensity.

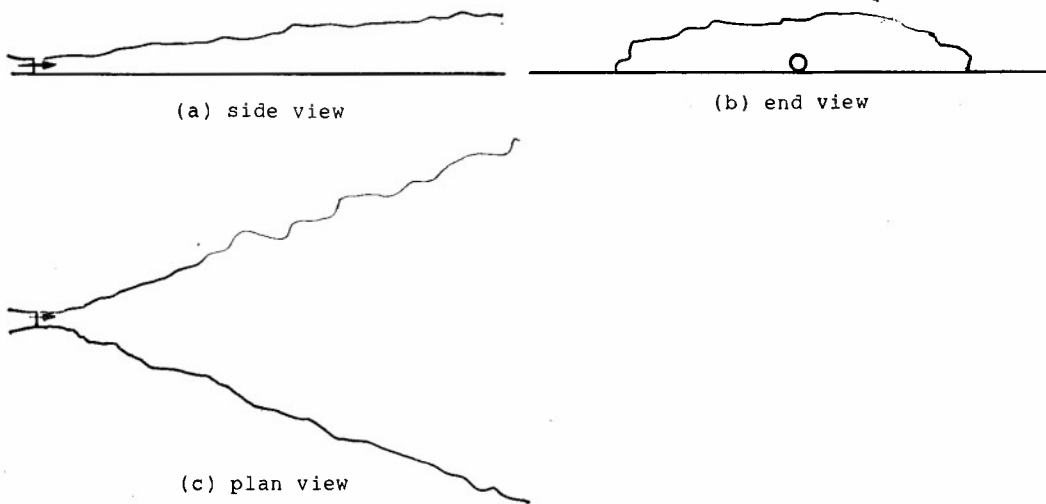


Fig.17 3D wall jet from circular nozzle

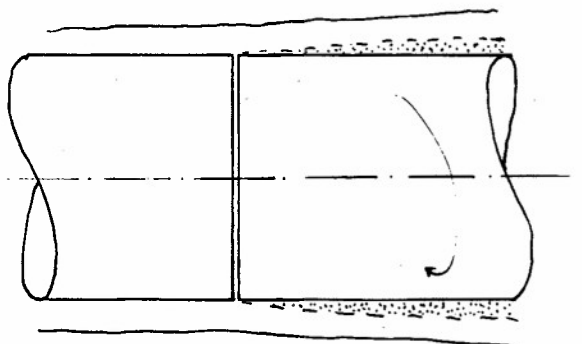


Fig.18 Axisymmetric body with rotating rear part (showing internal layer)

THREE-DIMENSIONAL SHEAR LAYER EXPERIMENTS AND THEIR USE AS TEST CASES FOR CALCULATION METHODS

by

B. van den Berg
National Aerospace Laboratory NLR
Anthony Fokkerweg 2, 1059 CM Amsterdam
The Netherlands

SUMMARY

Three-dimensional shear layer experiments are discussed with a view to those developing calculation methods. The emphasis is on the selection of useful experiments for comparisons with calculations and the proper way to perform the comparisons. A review of more recent three-dimensional shear layer experiments is included.

LIST OF SYMBOLS

C_p	pressure coefficient, $C_p = (p - p_\infty)/q_\infty$
M	Mach number
p	static pressure
q	dynamic pressure
Re_θ	Reynolds number based on momentum thickness
U, V, W	mean velocity components
u', v', w'	fluctuating velocity components
x, y, z	coordinates
α	external flow angle, relative to x-axis
β	flow angle in shear layer, relative to external flow direction
δ_1	displacement thickness
τ	shear stress

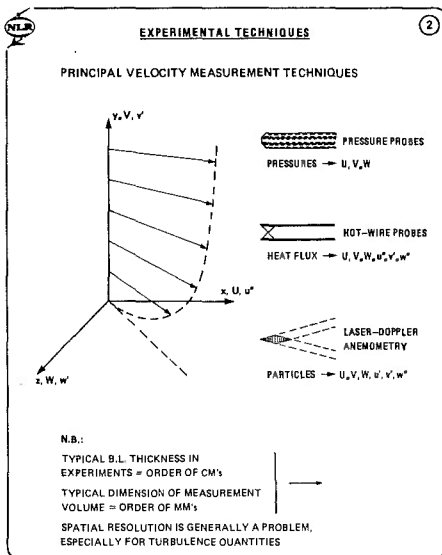
subscripts

e	at shear layer edge
w	at wall
∞	in free-stream

NLR	1
CONTENTS	
EXPERIMENTAL TECHNIQUES	
REQUIREMENTS FOR USEFUL DATA	
REVIEW OF EXPERIMENTS	
USE OF EXPERIMENTAL DATA	
PRESENT STATUS AND PROSPECTS	

INTRODUCTION

The intended reading public of this paper on experiments in three-dimensional shear layers are those active in developing calculation methods for this type of flow rather than experimentalists. Therefore experimental techniques will be discussed here only very globally, mainly mentioning some of the most important problems associated with measurements in turbulent flows and the measurement accuracy. More attention will be paid to the way to select experiments, which are best suited for checking calculation methods. The choice may depend on the intended application area of the calculation method considered. Then a review will be given of the available three-dimensional thin shear layer experiments, with the emphasis on the more recent experiments and the experiments used earlier for extensive theory experiment comparisons in Workshops. Subsequently the use of experimental data for comparisons with calculations will be discussed comprehensively. To draw valid conclusions from a comparison, a more extensive study must be made of the consequences of experimental errors for the calculation results and the role of the assumptions made in the calculation methods. Finally the present status in three-dimensional shear layer research will be summarized and the need for further research will be mentioned.

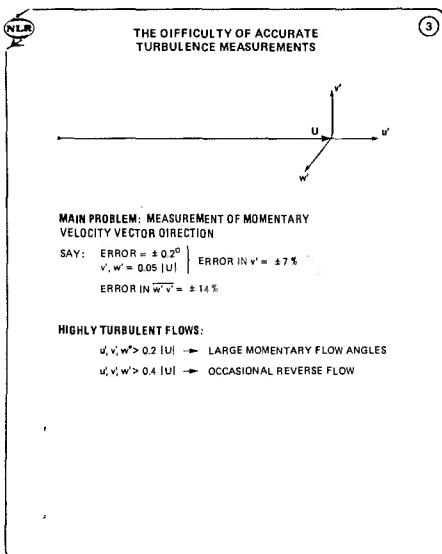


EXPERIMENTAL TECHNIQUES

Before discussing velocity measurement techniques, it is useful to explain the nomenclature: Mean velocity components are U, V, W with fluctuating parts u', v', w' , while $V \ll U, W$ in the thin shear layer along the x - z plane.

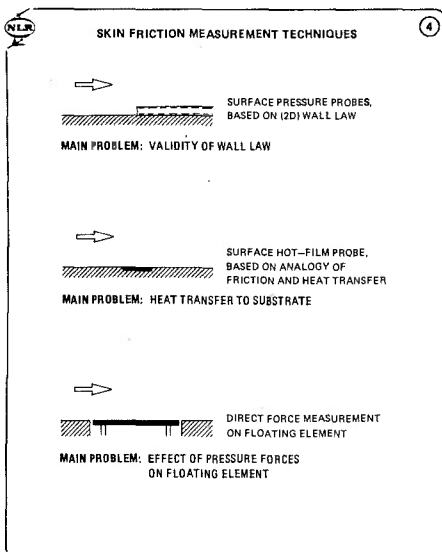
The three principle techniques to measure flow velocities are: i) Pressure probes. Measured pressure differences are used to deduce the local flow velocity. Merely mean velocities are obtained and that only approximately in strongly fluctuating flows. The technique is, however, fast and easy. ii) Hot wire probes. The velocity is related to the heat transfer from the thin hot wires. Mean and fluctuating velocities are obtained. Accuracy is limited by calibration drift. Hot wires are the most usual technique for measuring fluctuating turbulence quantities. iii) Laser Doppler Anemometry. The velocity of small particles, which are seeded in the fluid, is measured using laser light beams. This is a rather new technique with great potentials. A special advantage is the absence of aerodynamic probe interference.

All these experimental techniques have in common a fairly large measuring volume, generally with dimensions of the order of 1 mm. This is important as most laboratory boundary layers are fairly thin, of the order of cm's, so that spatial resolution is often a problem, especially for turbulence measurements because of the small eddies in the flow.



The usefulness of an experiment as a basis for improving calculation methods generally increases with the amount of detail experimental information available. Particularly the presence of turbulence data is desirable. Unfortunately accurate turbulence measurements are not easy to perform. To clarify the problem the measurement accuracy of the momentary local flow velocity in a turbulent flow will be considered. Tentatively the measurement error in the flow angle will be assumed to be $\pm 0.2^\circ$, which actually is a fairly high standard of accuracy. For a turbulent velocity fluctuation level of 5 % of the mean velocity, the corresponding relative error in v' and w' (the fluctuating velocity components normal to the mean velocity vector) then becomes $\pm 7\%$. It will be clear that in the circumstances accurate measurements are difficult to perform.

In adverse pressure gradient flows close to separation much higher turbulence levels occur. Consequently smaller relative errors in the fluctuating velocities are likely for the same absolute error in the flow angle. However, for velocity fluctuation levels higher than 20 %, the momentary flow angle may exceed at times the acceptable range of a probe with e.g. crossed hot wires. When the fluctuation level exceeds 40 % occasional reverse flow may occur, requiring velocity measurement techniques, which distinguish reverse flow, such as Laser Doppler Anemometry.



Since in turbulent boundary layers large velocity variations occur in a thin layer near the wall, it is useful to know the magnitude and direction of the skin friction, i.e. the limiting conditions at the surface. Again there are three principle measuring techniques: i) Surface pressure probes. The skin friction measurement is based here on the assumption that in the near-wall region a universal velocity distribution exists, dependent only on the local skin friction and the fluid properties. This so-called law of the wall, however, has a restricted range of validity and assumes no velocity vector rotation in the near-wall region, so that the skin friction direction found, e.g. by rotating the pressure probe, is no more than at best a mean flow direction over the probe height. ii) Surface hot film probes, using hot films glued on the surface. Analogy of skin friction and heat transfer is assumed and the skin friction direction may be obtained by using two surface hot films at right angles. A problem to be considered is the heat transfer to the substrate and its effect on the calibration. iii) Force measurements on a floating surface element. This is the only direct and in principle indisputable measurement technique. In practice, however, accurate force measurements may be difficult to perform as the skin friction force to be measured is small and unwanted pressure forces on the floating element easily impair the measurements.

EXPERIMENTAL ERROR ESTIMATES	
(NUMBERS GIVEN ARE NO MORE THAN GLOBAL INDICATIONS)	
	TYPICAL ERROR
SURFACE PRESSURE	$\pm 0.2\%$ of q_{max}
MEAN VELOCITY	$\pm 0.5\%$ of U_θ
FLOW ANGLE	$\pm 0.5^\circ$
SKIN FRICTION	$\pm 5\%$ of τ_w
REYNOLDS STRESS	$\pm 10\%$ of $u'v'$, ETC.
ERROR VERSUS MISTAKE: INDEPENDENT CHECKS RECOMMENDABLE, PREFERABLY USING ESSENTIALLY DIFFERENT MEASURING TECHNIQUES	

No generally valid error estimates for the various measuring quantities can be given, of course. Yet it seems useful to state here the global error level, which should be normally achieved in the author's opinion. As indicated in the adjacent table, surface pressure measurement errors may be expected to be small, which is fortunate as the pressure gradient is the quantity of interest. Reasonably accuracy is generally achieved for the mean velocity magnitude and direction. The attainable measurement accuracy for the skin friction is much more a problem. This is worse still for the turbulence measurements, as discussed earlier, leading to a large typical measurement error estimate for the Reynolds stress components.

Besides normal measurement errors the possibility can never be excluded that the data are just wrong, due to malfunctioning of the measurement instrument or mistakes in the data processing software. A parallel with numerical calculation methods can be drawn. Though the numerical truncation error (cf. measurement error) should be considered, the main problem is generally to get the computer program free of faults (cf. measurement mistakes). In view of the above, independent check measurements should be regarded as an essential part of an experiment to prove its reliability.

REQUIREMENTS FOR USEFUL DATA	
i) EXPERIMENTAL DATA RELIABLE? ii) FLOW WELL DEFINED FOR CALCULATIONS? iii) FLOW INTERESTING AS TEST CASE?	
i) EXPERIMENTAL DATA RELIABLE?	
<ul style="list-style-type: none"> • COMPARATIVE MEASUREMENTS MADE? (E.G. DATA WITH DIFFERENT MEASUREMENT TECHNIQUES) • DATA INTERNALLY CONSISTENT? (E.G. CORRESPONDENCE OF SKIN FRICTION AND REYNOLDS SHEAR STRESS NEAR WALL) • GLOBAL LAWS SATISFIED? (E.G. MASS AND MOMENTUM INTEGRAL BALANCE) 	

REQUIREMENTS FOR USEFUL DATA

After the short discussion on experimental techniques, attention will be focussed now on the selection of experiments, which can be used profitably for comparisons with calculations. To decide whether an experiment is suitable as a test case for calculation methods, three questions have to be addressed. These concern the reliability, the completeness and the interest of the experimental data. First the data reliability will be considered.

As noted earlier, an important means to check the reliability of the data is by making comparative measurements, preferably using different experimental techniques. The ultimate check is to perform duplicate measurements in two different test set-ups, which are geometrically and otherwise similar. Besides direct check measurements of the same flow quantities, the internal consistency of the data set may provide an indication of data reliability. A simple example is the measured Reynolds stresses, $u'v'$ and $w'v'$, in the near wall region (but outside the viscous sublayer), which should extrapolate to the independently measured skin friction components. A third check is to investigate the accuracy with which global flow laws are satisfied by the data. The best known example is the momentum integral balance. Application of the momentum integral balance means checking the correspondence between the skin friction and mean flow data.

ii) FLOW WELL DEFINED FOR CALCULATIONS?	
<ul style="list-style-type: none"> • FLOW SIMILARITY PARAMETERS (E.G. REYNOLDS NUMBER) PROVIDED? • INITIAL CONDITIONS PROVIDED IN SUFFICIENT DETAIL? • SURFACE PRESSURES OR OTHER BOUNDARY CONDITIONS PROVIDED SUFFICIENTLY CLOSELY SPACED? 	

The second question to be addressed is whether the experiment provides sufficient data to make calculations possible. In the first place the flow similarity parameters, such as the Reynolds number, must be provided (and be constant for a data set). Assuming boundary layer calculations with a marching procedure, boundary layer data should be provided along an initial line. The initial conditions should preferably include measured turbulence quantities, as these may affect the downstream boundary layer development over a substantial distance. Downstream of the initial line with given data, a region of influence and a region of determinacy can be distinguished. The latter region is the computable region for the given initial conditions. This region is indicated in the sketch. In simple three-dimensional boundary layer flows the borders of the computable region coincide with an external streamline and a wall streamline. In this region the surface pressure distribution must be provided sufficiently accurate and sufficiently closely spaced. The pressure data must be differentiable, also at the boundaries of the computational region. If other boundary conditions are required, the other conditions should be provided sufficiently accurate and closely spaced by the measurements.

NLR
8

III) FLOW INTERESTING AS TEST CASE?

OBJECTIVE OF THEORY EXPERIMENT COMPARISON:
TO CHECK EMPIRICAL ASSUMPTIONS
(E.G. TURBULENCE MODEL)

FIRST REQUIREMENT:

- SUFFICIENT COMPARISON DATA
(PREFERABLY TURBULENCE DATA)
AVAILABLE IN COMPUTABLE REGION

EMPIRICAL ASSUMPTIONS ARE SELOOM UNIVERSALLY TRUE →

SECOND REQUIREMENT:

- FLOW PARAMETERS IN THE EXPERIMENT IN THE RANGE
OF THOSE OF THE PRACTICAL FLOWS TO BE
CALCULATED WITH THE METHOD AT HAND

NLR
9

SOME IMPORTANT FLOW PARAMETERS

- INITIAL TURBULENCE PROPERTIES
(MAY BE AFFECTED BY TRANSITION
TRIPPING DEVICE IN EXPERIMENT)
- REYNOLDS NUMBER, R_0
(USUALLY LOW IN EXPERIMENTS;
ACCEPTABLE FOR $R_0 > 5000$)
- MACH NUMBER, M
(USUALLY LOW IN EXPERIMENTS;
ACCEPTABLE FOR $M \approx 1$)
- PRESSURE GRADIENT,
PARAMETER E.G. $\lambda = (\delta_1/q_0)(\partial p/\partial x)$
(USUALLY LARGE IN EXPERIMENTS
→ PRESSURE FORCES DOMINATE)
- FLOW DEVELOPMENT RATE,
PARAMETER E.G. $\delta_1(\partial \lambda/\partial x)$
(USUALLY LARGE IN EXPERIMENTS
→ TURBULENCE HISTORY DOMINATES)

NLR
10

REVIEW OF EXPERIMENTS

EARLIER REVIEWS:

JOHNSTON 1976: EXTENSIVE REVIEW
HUMPHREYS ET AL 1980: STANFORD CONF.
PATEL 1982: SHIP-LIKE GEOMETRIES

WORKSHOPS:

TRONDHEIM 1975: 6 TEST CASES
STOCKHOLM 1978: 1 TEST CASE
AMSTERDAM 1979: 1 TEST CASE
GÖTEBORO 1980: 2 TEST CASES
BERLIN 1982: 5 TEST CASES

PRESENT REVIEW:

MORE RECENT EXPERIMENTS
EXPERIMENTS USED IN WORKSHOPS

3D THIN SHEAR LAYERS
(NO SHIP STERN FLOWS)

The final question, but not the least important one, is whether the experimental flow is interesting as a test case for calculations. The objective of the theory experiment comparison must then be clearly posed first. The most common objective is to check the empirical assumptions in the calculation method, e.g. contained in the turbulence model applied. To perform comparisons, in the first place sufficient comparison data must be available in the computable region. As detail comparisons are usually more instructive, the availability of measured turbulence data is an advantage, especially if the calculation method uses a turbulence model.

A fact, which is generally underexposed, is the limited validity range of most empirical assumptions. This holds also for the empirical assumptions made in current calculation methods for turbulent shear layers, even if sophisticated turbulence models are used. Because of their limited validity, checking the accuracy of empirical assumptions is only sensible in the type of shear flows for which the calculation method is intended. Various flow parameters may be expected to affect the turbulence properties and so the empiricism. All these parameters should be considered when selecting experiments for checking empirical assumptions. Some of the important flow parameters will be reviewed hereafter.

- To be useful as a test case, the initial turbulence properties of the shear layer in the experiment should be similar to those in practical flows. In experiments turbulence properties may be affected e.g. by crude transition tripping.

- The test Reynolds number should be in the range of the practical application area of the calculation method. Usually the Reynolds number is low in experiments, but this is probably acceptable if $R_0 > 5000$.

- The test Mach number should be in the correct range. Usually the Mach number is low in experiments, as turbulence measurements are difficult to perform in high-speed flows. Fortunately compressibility effects on turbulence are probably fairly small, unless $M \gg 1$.

- The pressure gradients in the experiment should be of the order of magnitude encountered in practical flows. However, because of the spatial resolution problem, thick boundary layers are preferred for the measurements, while test section dimensions are limited. Consequently the pressure gradient parameter $\lambda = (\delta_1/q_0)(\partial p/\partial x)$ is often large in experiments, so that pressure forces dominate.

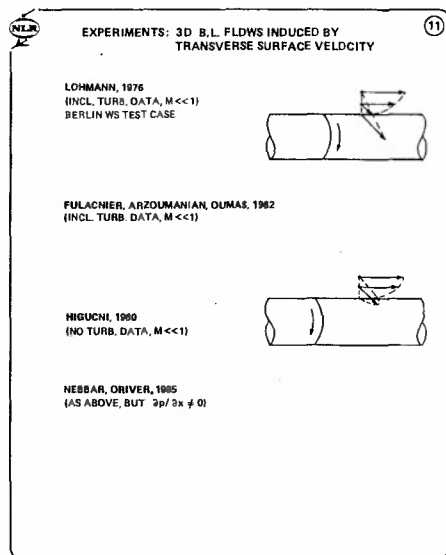
- The flow development rate should be comparable with that in practical flows. Because of the limited test section length and the thick boundary layer, the flow development rate, $\delta_1(\partial \lambda/\partial x)$, is usually large in experiments, so that turbulence history effects dominate.

REVIEW OF EXPERIMENTS

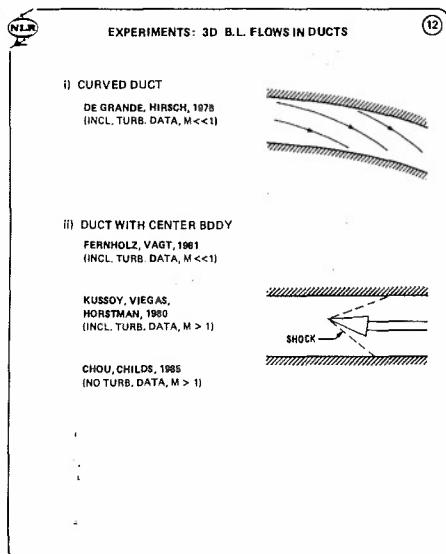
An extensive and thorough review was given ten years ago by Johnston (1976). For the 1980-81 Stanford conference, experiments were evaluated on their possible use as test cases by Humphreys and Van den Berg (1980). Viscous shear layers around ship-like bodies were reviewed recently by Patel (1982).

Some experiments have been employed already extensively for theory experiment comparisons in Workshops. Several such Workshops have taken place in the last ten years, starting in 1976 with the so-called "Trondheim Trials" (East 1976). The Workshops in Stockholm (1978) and in Amsterdam (1979) considered simple swept wing flows (Humphreys 1979; Lindhout, Van den Berg, Elsenaar 1980), while ship boundary layers were the subject of the 1980 Göteborg Workshop (Larsson 1981). In 1982 a Workshop with several test cases took place in Berlin (Van den Berg, Humphreys, Krause, Lindhout 1986).

The experiments used as test cases for Workshops are important as the usefulness of the data should be expected to have been established and also because other calculation results are available. The present review will include these experiments, so far they provide detail boundary layer data, but further will be restricted to the more recent thin shear layer experiments. Note that inclusion of an experiment in this review does not necessarily mean that it satisfies the requirements discussed in the preceding section.

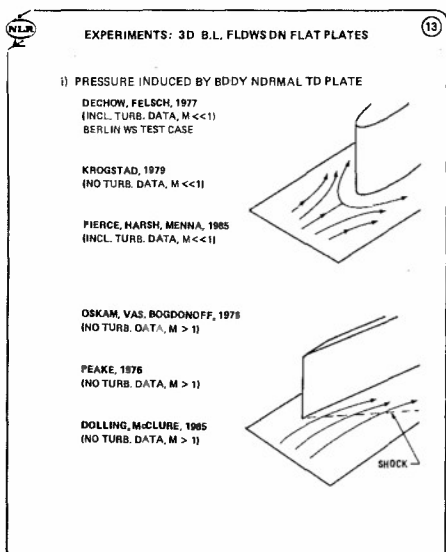


A fundamental type of experiment is the three-dimensional flow obtained when a zero-pressure-gradient boundary layer encounters a local transverse motion of the bounding surface. The interesting feature of the flow is that the three-dimensionality is related here solely with the transverse shear forces. In practical test set-ups such a boundary layer flow may be generated on a cylinder with a stationary and rotating section. When the front section is stationary, the initially two-dimensional boundary layer becomes three-dimensional after the transition to the rotating part. This flow was measured amongst others by Lohmann (1976) and more recently by Fulachier, Arzoumanian and Dumas (1982). The data of Lohmann were used as a test case for the Berlin Workshop. When the front section is rotating, the three-dimensional boundary layer generated relaxes to a two-dimensional flow on the downstream stationary section. This flow was measured by Higuchi (1980) and later by Hebbar and Driver (1985), using the same test set-up, but with a streamwise pressure gradient imposed. The boundary layer thickness in these experiments was in all cases not small relative to the cylinder radius, so that transverse curvature and rotation will have affected the turbulence properties.



The flow along a duct wall provides a conveniently measured boundary layer, which will be three-dimensional when the duct is curved. A simple case is the boundary layer along one of the two flat walls of a duct with the other walls curved, as applied for instance by De Grande and Hirsch (1978). The turbulence properties in the duct corners deviate from those in normal thin shear layers. Because of possible turbulence history effects, the region of influence of the corner flows should preferably not be part of the measurement region. This may restrict the usable boundary layer development length in the duct.

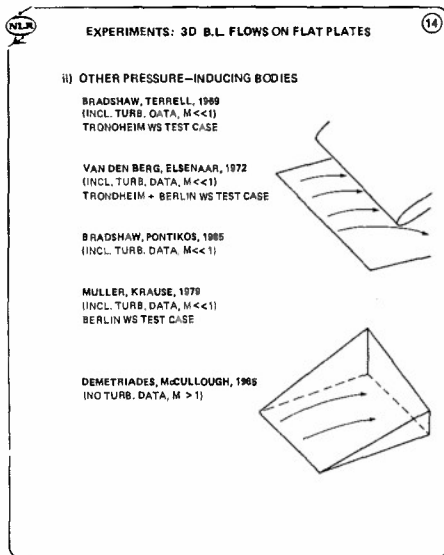
Also straight ducts with a center body have been applied. The investigation of Fernholz and Vagt (1981) concerns the three-dimensional boundary layer along a circular cylinder in a duct with a skew-mounted back plate. Kusssoy, Viegas and Horstman (1980) and Chou and Childs (1985) have investigated the boundary layer along a circular duct with an asymmetric center body. In these two experiments the flow was supersonic and the center body induced a three-dimensional shock wave boundary layer interaction on the duct wall. The experiment of Kusssoy et al was selected as a test case for the 1980-81 Stanford Conference. In these flows the ratio of the boundary layer thickness to the wall radius was not small and consequently curvature effects are not negligible.



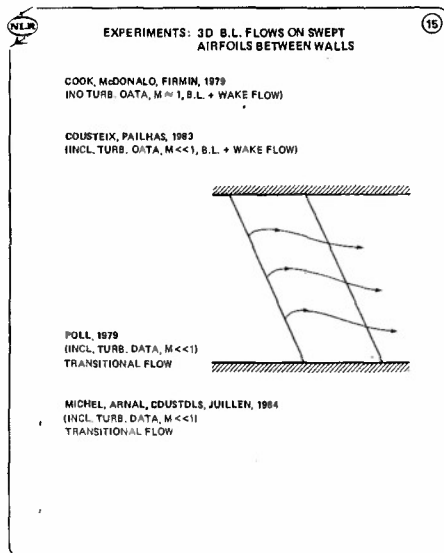
A frequently used test configuration consists of a flat plate with a two-dimensional body mounted normal to it, which induces a three-dimensional boundary layer on the plate. Close to the body a three-dimensional separation region occurs. The measurement data obtained in such a test set-up by Dechow and Felsch (1977) were used in the Berlin Workshop. Further the measurements by Krogstad (1979) and Pierce, Harsh and Menna (1985) will be mentioned here. The latter data set is unique in that it includes skin friction results in a three-dimensional boundary layer from force measurements on a floating element (McAllister, Pierce, Tennant 1982).

In supersonic flows a sharp-edged plate at angle of attack normal to the flat test surface may be employed to induce a three-dimensional shock wave boundary layer interaction on the flat plate. Several variances of this set-up have been tested. Here mention will be made of the measurements by Oskam, Vas, Bogdonoff (1976), by Peake (1976), both 1980-81 Stanford Conference test cases, and those by Dolling and McClure (1985).

A common problem with test set-ups of this type is the relative short distance in which boundary layer three-dimensionality develops. Consequently turbulence history effects tend to dominate. Actually a data analysis shows that the turbulent shear stresses in some cases may be regarded as very nearly frozen (Van den Berg 1982).

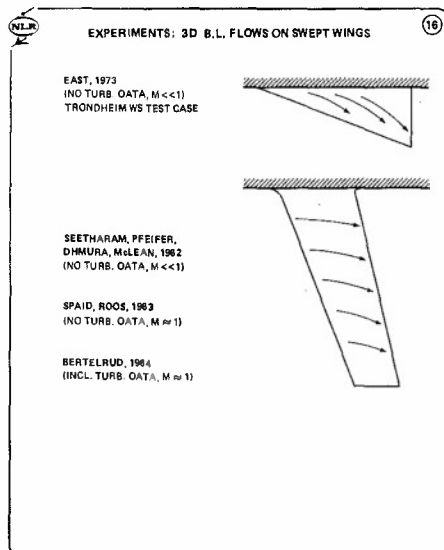


A three-dimensional boundary layer flow on a flat plate can be induced by any combination of nearby bodies. The early experiment of Bradshaw and Terrell (1969), used as a Trondheim Workshop test case, concerns the quasi-two-dimensional turbulent boundary layer on a flat plate behind a swept body fixed on the plate. The experiment of Van den Berg and Elsenaar (1972), used in the Trondheim and Berlin Workshops, also concerns a quasi-two-dimensional flow as it occurs on infinite swept wings. The pressure distribution on the surface is induced by a swept, wing-like body suspended above the test plate. The initially two-dimensional boundary layer on the test plate gradually develops into a three-dimensional separation. In the test set-up of Bradshaw and Pontikos (1985) the same boundary layer flow has been reproduced with good approximation except that the flow does not quite separate. The results confirm on the whole the earlier data and add significantly to the detail information about this flow. The experiment by Müller and Krause (1979) provides data in a fully three-dimensional boundary layer on a flat plate with deflecting walls and a suspended body. This experiment was used as test case for the Berlin Workshop. Finally the supersonic three-dimensional turbulent boundary layer experiment by Demetriades and McCullough (1985) should be mentioned.



A number of measurements have been carried out in the shear layers of a swept cylindrical airfoil spanning a tunnel test section. Note that a quasi-two-dimensional infinite swept wing flow is generally not well simulated with such a test set-up due to the flow constraint caused by the end walls. Cook, McDonald and Firmin (1979) obtained boundary layer and near-wake data for an airfoil between tunnel walls at two sweep angles and at high subsonic speeds. Low speed data in the shear layers at and behind the trailing edge of a swept airfoil between walls have been reported by Cousteix and Pailhas (1980, 1983).

Two experiments on transitional boundary layer flow will be mentioned here. The three-dimensionality of the flow introduces two additional mechanisms for transition from laminar to turbulent flow. The first one is transition by "attachment line contamination". A transitional boundary layer of this type has been investigated for instance extensively by Poll (1979). The second transition mechanism typical for three-dimensional boundary layers is transition by "cross flow instability". Such a transitional flow on a swept airfoil between walls was measured amongst others by Michel, Arnal, Coustol and Juillen (1984).



Three-dimensional turbulent boundary layer measurements on swept wings of finite span should be expected to provide particular useful information. Measurements on a half-model of a slender delta wing with a leading edge vortex above the surface were performed by East (1973). The flow studied approximates closely to conic conditions. The data have been employed for the Trondheim Workshop. Boundary layer measurements on a model of the horizontal and vertical swept tailplanes of a typical transport aircraft were carried out by Seetharam, Pfeiffer, Ohmura and McLean (1982.) The tests were performed in a large wind tunnel allowing the use of a large scale model with fairly thick boundary layers.

Measurements on a swept-wing half-model at transonic and high subsonic speed were carried out by Spaid and Roos (1983) (see also Spaid 1984). The data at the higher Mach numbers suffer from some flow unsteadiness due to shock movements. Flight measurements on the wing boundary layers of a Saab Lansen aircraft have been performed by Bertelrud (1984) at various high subsonic and transonic speeds. A large amount of data has been gathered in many flights.

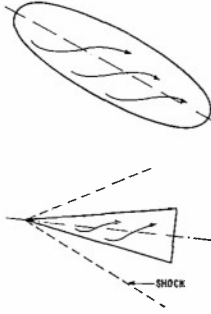
EXPERIMENTS: 3D B.L. FLOW ON BODIES OF REVOLUTION (17)

RAMAPRIAN, PATEL, CHOI, 1981
(NO TURB. DATA, $M < 1$)

MEIER, KREPLIN, VOLLMEYER, 1983
(INCL. TURB. DATA, $M < 1$)
TRANSITIONAL AND TURBULENT FLOW

SMITT, CHANETZ, 1985
(INCL. TURB. DATA, $M < 1$)

AUSHERMAN, YANTA, 1983
(NO TURB. DATA, $M > 1$)



The diagram illustrates flow over two bodies of revolution. The top part shows a prolate spheroid with streamlines indicating flow separation. The bottom part shows a cone with a shock wave (labeled 'SHOCK') and streamlines indicating flow separation.

The three-dimensional boundary layer flow around slender bodies of revolution at angle of attack leads further downstream generally to two open separation regions at the lee-side of the body. This flow has been studied also by several investigators. Ramaprian, Patel and Choi (1981) investigated the turbulent boundary layer on a hemisphere-spheroid combination at a moderate angle of attack. A prolate spheroid at various angles of attack and various Reynolds numbers was measured by Meier, Kreplin and Vollmers (1983). Measurements were carried out without a transition trip, so that a large transitional region was present especially at the lower Reynolds numbers, and for some conditions also with a transition trip leading to a turbulent boundary layer in the measurement region. The three-dimensional laminar and turbulent boundary layer on an ellipsoid-cylinder model at high angle of attack was investigated by Schmitt and Chanetz (1985). The measurements were focussed here particularly on the development of the open separation into a vortex. The supersonic turbulent boundary layer on a conical body at angle of attack was measured by Ausherman and Yanta (1983).

USE OF EXPERIMENTAL DATA (18)

TO PRODUCE CORRECT RESULTS
CALCULATION METHODS MUST:

i) SOLVE THE EQUATIONS CORRECTLY

- a) SOLUTION STABLE AND CONVERGENT?
- b) NUMERICAL ERROR ACCEPTABLE?

ERROR VS MISTAKE: INDEPENDENT CHECKS
RECOMMENDABLE (WORKSHOPS)

ii) SOLVE THE CORRECT EQUATIONS

- a) NEGLECTED TERMS INDEED NEGLIGIBLE?
- b) EMPIRICAL ASSUMPTIONS CORRECT?

CHECK OF EMPIRICAL ASSUMPTIONS IS
USUALLY THE MAIN OBJECTIVE OF
THEORY EXPERIMENT COMPARISONS

USE OF EXPERIMENTAL DATA

In an early phase of research experiments, have chiefly an exploratory character, the main aim being to make evident the prevailing physical mechanisms. In later phases experiments often serve more directly as test cases for calculation methods to assess their accuracy and to improve the calculation methods where necessary by tracing the origin of apparent discrepancies by detail comparisons with the experimental data. In boundary layer research the emphasis is presently on the use of experiments as such test cases.

Calculation methods should, of course, in the first place solve the mathematical equations correctly. The numerical solution should be stable and convergent and the truncation error small, but also the computer program should be free of faults, which is difficult to ascertain in practice. It is therefore sensible to take advantage of Workshops in which other (possibly very similar) calculation methods have been applied, which results can be used in a way as a check.

Besides solving the equations correctly, the correct equations should be solved. No non-negligible terms should have been omitted in the equations and the terms containing empirical approximations should be sufficiently accurate. The investigation of the accuracy of the empirical assumptions is actually the principal objective of most theory experiment comparisons.

EMPIRICAL ASSUMPTIONS (19)

INTEGRAL METHODS: VELOCITY PROFILE
FAMILY, SKIN FRICTION LAW, ETC.

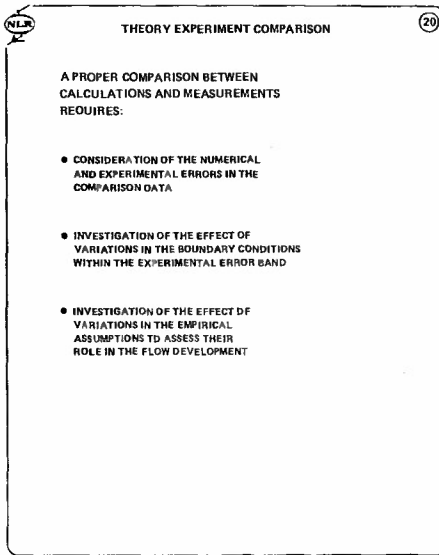
FIELD METHODS: TURBULENCE MODEL

- NO REAL PROSPECT FOR UNIVERSAL PROFILE
FAMILY, SKIN FRICTION LAW, ETC.
- NO SOON PROSPECT FOR UNIVERSAL TURBULENCE MODEL

CONSEQUENCE:
CHECK OF EMPIRICAL ASSUMPTIONS IS
ONLY USEFUL IN EXPECTED VALIDITY RANGE

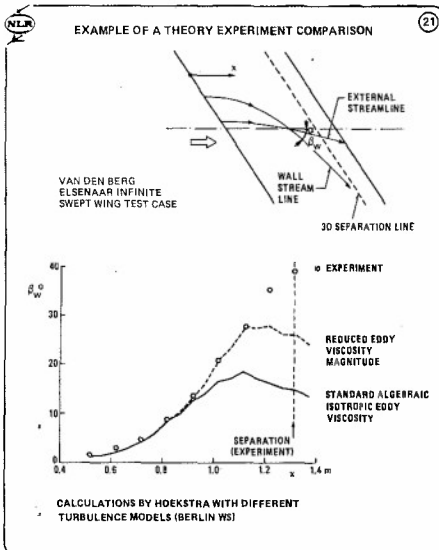
The empirical assumptions in calculation methods depend on the type of method. Integral methods generally assume a profile family for the stream-and cross-wise velocity, a skin-friction law and at least one further empirical relation, for instance about the turbulence entrainment rate. In field methods the empiricism is contained in the turbulence model. Mathematically simple turbulence models may be used, relating algebraically Reynolds stress and mean velocity gradient, as well as more sophisticated models, in which the Reynolds stresses are related to the mean flow by partially empirical differential equations based on the Reynolds stress transport equations.

There is no real prospect for a truly universal boundary layer velocity profile family with a limited number of parameters, for a universal simple skin-friction law, etc. One of the conclusions of the 1980-81 Stanford Conference has been that there is a yet also no universal turbulence model available and it seems that there is no soon prospect for such a universal model. This conclusion has important consequences for theory experiment comparisons. As emphasized already earlier in this paper, the restricted validity of the empiricism implies that checks of the empirical assumptions are only useful in flows approximately similar to the flows in which the empiricism is expected to hold. This normally means checks in the class of flows, to which the calculation method is expected to be applied.



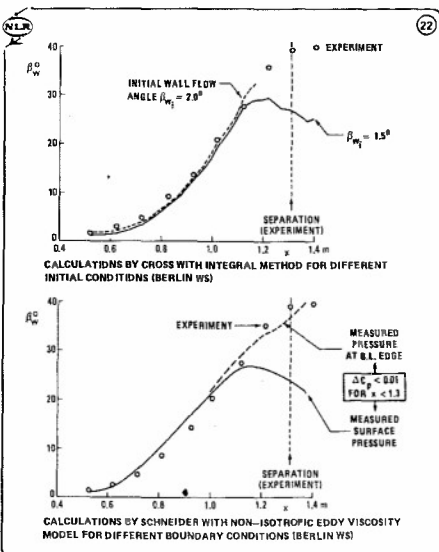
When comparing calculation results with experimental data, both measurement errors and numerical errors should be considered. Generally attention is focussed particularly on the error in the experimental comparison data and the error in the calculation results for the given boundary conditions. However, the boundary conditions are based normally on measurements and, therefore, are also subject to a possible error. To investigate the effect of such measurement errors, additional calculations must be carried out for different boundary conditions. Calculations may be performed, for instance, for different initial flow conditions within the experimental error band, and for different surface pressure distributions, with an increased or decreased pressure gradient, so far the error band of the measured pressures allows.

To draw a balance conclusion from a theory experiment comparison, generally it is recommendable to add an investigation of the role of the empirical assumptions on the calculated flow development. If the role would be small, obtained agreement between calculations and measurements may not mean much. As an example strongly pressure-driven flows may be considered, in which the Reynolds stresses have little effect on the mean flow development. Agreement between calculated and measured mean flow quantities then tells little about the accuracy of the assumed Reynolds stresses in the calculations. This can only be judged when direct comparisons with measured Reynolds stresses can be made.



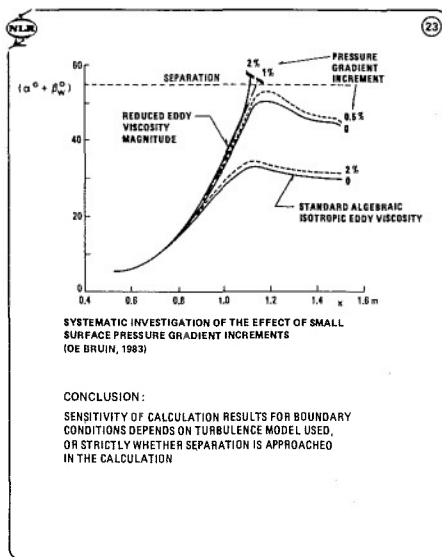
As an example the results of an extensive comparison between three-dimensional turbulent boundary layer calculations and experiment will be discussed. The case considered is an infinite swept wing flow, where the boundary layer is very nearly two-dimensional at the initial station and where three-dimensional separation takes place near the end of the measurement region. Many calculation methods have been applied to this case, so that suitable calculation results to illustrate the theory experiment comparison could be drawn from various sources. The comparisons will be focussed here on measured and calculated wall flow angles. The experimental accuracy estimate for the wall flow angle is $\pm 1^\circ$, while the numerical error in the calculation results depends on the method used, but is expected to be certainly not larger.

The first graph shows the results of a study by Hoekstra of the effect of a variation in the empirical assumptions. Calculations with a conventional algebraic isotropic eddy viscosity turbulence model are seen to underestimate substantially the wall flow angle increment in the downstream part and clearly fail to predict separation. With the eddy viscosity somewhat reduced (following Nituch, Sjolander, Head 1978), but still isotropic, agreement with experiment appears to exist to much further downstream. The results demonstrate that the empirical assumptions about the Reynolds shear stresses have an important influence on the flow development.

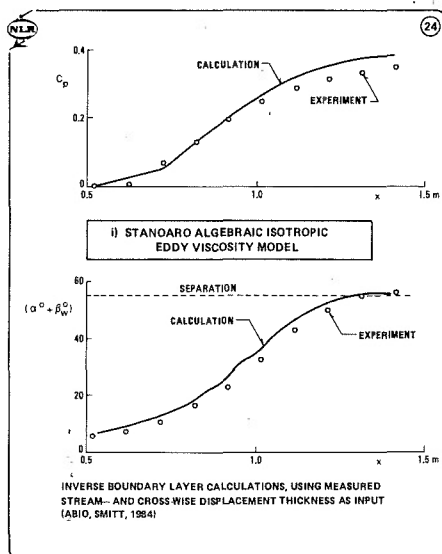


The next two graphs show the effect of variations in the boundary conditions. These graphs and the preceding one have been taken from the Berlin Workshop (Van den Berg et al 1986). The upper graph contains calculations by Cross with his integral method for different initial conditions. The measured initial wall flow angle is 1.5° and calculations have been carried out for this angle and a slightly larger initial wall flow angle. The effect on the calculation results is seen to be small up to a streamwise distance $x \approx 1.1$ m, but further downstream the two sets of calculation results start to deviate disproportionately.

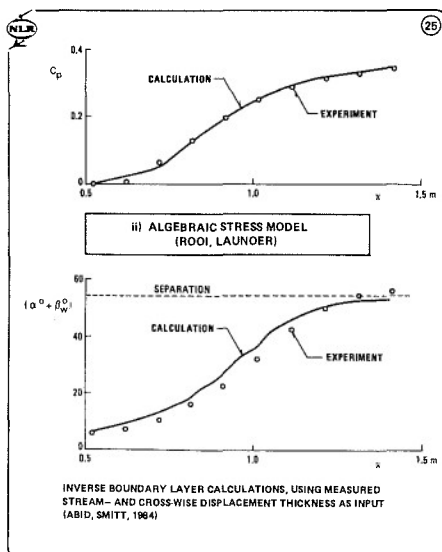
The lower graph shows the results of calculations by Schneider with a non-isotropic eddy viscosity model for different pressure distributions. The eddy viscosity non-isotropy applied is as proposed by Rotta (1977). With the normal boundary condition, i.e. the measured surface pressure distribution, the calculated wall flow angle increment is seen to fall below measurements already at $x \approx 1.1$ m. When the measured pressure at the boundary layer edge is used, agreement with experiment is maintained essentially further downstream, although the difference in pressure is small ($\Delta C_p < 0.01$ upstream of separation). The results demonstrate the sensitivity of the calculation results for the boundary conditions in the downstream part of the measurement region, near separation.



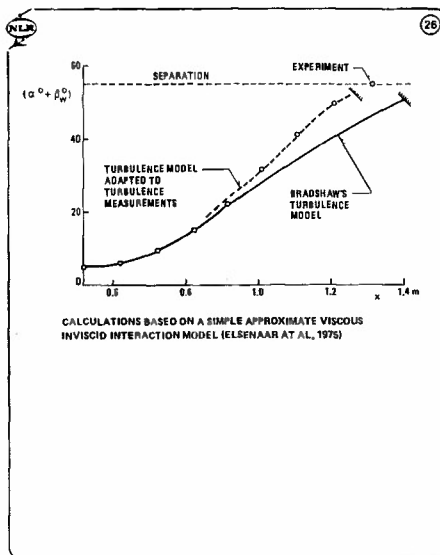
It is well known that boundary layer calculations carried out as done here, constitute an ill-posed mathematical problem at separation. If the singularity at separation is no part of the computational region, i.e. if the calculations are stopped before separation is reached, no problem exists in principle, but in practice the calculations may become very sensitive to the boundary conditions already upstream of separation. To assess the sensitivity of the calculations for the boundary conditions, a systematic investigation was performed by De Bruin (1983). The pressure gradient was increased over the whole measurement range by a small amount. Calculations were carried out with a standard type isotropic eddy viscosity model and with the same model with a reduced eddy viscosity in the boundary layer outer region. The results are depicted in a plot showing the angle $(\alpha + \beta_w)$ instead of β_w as in the preceding graphs. It is evident that with the reduced eddy viscosity the calculations come close to separation, and that the results near separation are very sensitive to small pressure gradient changes. It appears also, however, that the calculations with the standard eddy viscosity model are not unduly sensitive to pressure gradient changes. The sensitivity of the calculations to the boundary conditions seems to depend on the turbulence model used. The important point is, of course, whether separation is approached in the calculation or not.



The calculation problems near separation can be resolved by carrying out the calculations in a different way, for instance by inverse calculations prescribing the distribution of measured boundary layer properties over the surface instead of the pressure distribution. Such inverse calculations have been performed by various workers, but here the results of Abid and Smitt (1984) will be considered. They used the measured stream- and crosswise boundary layer displacement thickness as an input for the calculations. In the graphs shown here the angle $(\alpha + \beta_w)$ computed with a standard algebraic eddy viscosity model has been plotted as well as the calculated surface pressure distribution, which is part of the output in inverse calculations. The calculated wall flow angles are somewhat high, but on the whole agreement with experiment is reasonable. Actually this should not be surprising, however, as the stream- and crosswise displacement thickness agree from the outset, which means that the general level of the cross flow in the boundary layer is necessarily the same in calculations and experiment, so that large differences in the skewing angle in the boundary layer are not likely. Comparison of the calculated and measured pressures shows larger differences. The computed surface pressure gradient is essentially too large. On this ground one should conclude that agreement between calculations and measurements is not good here.



Abid and Smitt subsequently carried out inverse boundary layer calculations in the same way as described before, using different turbulence models. One of the models applied is an algebraic stress model, which is a simplification of the full solution of the six transport equations for the Reynolds stress components (Lauder 1971, Rodi, 1972). The results obtained with this turbulence model are depicted in the graph shown here. The agreement between calculations and measurements for the wall flow angle is reasonable, but not very good and certainly not better than obtained earlier with a simple standard algebraic eddy viscosity model. The real improvement becomes evident when considering the surface pressures. Agreement between calculated and measured pressures is seen to be very good indeed with the algebraic stress model. Detail comparisons between calculated and measured Reynolds stresses (not shown here) also exhibit fairly good agreement. The agreement can never be perfect, however, as the algebraic stress model leads to an isotropic eddy viscosity, while the measurement results indicate a distinct eddy viscosity non-isotropy. Though a completely satisfactory agreement also does not exist here, the improvement achieved with this turbulence model is evident, especially in the comparison of calculated and measured pressures.



An other possibility to circumvent the calculation problems near separation is by viscous inviscid interaction calculations. Such calculations were carried out for this case some time ago by Elsenaar et al (1975), using a simple approximate interaction model. As discussed earlier in the review of experiments, the test set-up considered here consists of a flat plate with a swept wing-like body suspended above the plate. This means that the flow can be regarded as a duct flow with an inviscid core and a boundary layer on the flat plate and the body. Assuming that both boundary layers are approximately of the same thickness and that the core flow is quasi-one-dimensional, a simple interactive flow calculation is possible with the pressure a function of the duct height minus the displacement thickness of the boundary layers. The results of these calculations are presented here. Calculations have been performed with two turbulence models: the original model of Bradshaw (1967) and an adapted version reproducing the measured Reynolds stresses. The interesting feature of calculation results obtained in this way is that they give a better evaluation of the consequences of wrong turbulence modelling in practical viscous-inviscid calculations. As shown here, in such calculations separation is still predicted even with a less accurate turbulence model, but it is predicted too far downstream.

POSSIBLE COMPARISON PROCEDURES

- DIRECT CALCULATIONS
INPUT: MEASURED SURFACE PRESSURE (AND FLOW ANGLE AT B.L. EDGE)
NO SENSIBLE COMPARISONS POSSIBLE IF CALCULATIONS APPROACH SEPARATION
- INVERSE CALCULATIONS
INPUT: MEASURED B.L. PROPERTIES
AS B.L. DATA ARE PARTLY GIVEN, COMPARISONS SHOULD FOCUS ON SURFACE PRESSURE (GRADIENT)
- INTERACTIVE CALCULATIONS
INPUT: MEASURED BOUNDARY CONDITIONS IN INVISCID FLOW WELL OUTSIDE B.L.
PREFERABLE PROCEDURE FOR THEORY EXPERIMENT COMPARISONS, WHICH INCLUDE A SEPARATION REGION

The various possibilities to compare boundary layer calculations with experiment will be recapitulated here. In the first place direct calculations may be carried out with the measured surface pressure distribution as an input. For calculations carried out in this way, no sensible comparisons with experiment are possible if the calculations approach separation.

The second possibility is to perform inverse calculations using measured boundary layer properties as an input. For three-dimensional boundary layer calculations two properties are generally provided. As this means that the boundary layer development is for a significant part given in the calculations, the comparison with experiment should focus on calculated and measured surface pressures, or actually pressure gradients, since these are the driving forces for the flow.

Finally theory experiment comparisons can be made by viscous inviscid interaction calculations. Then part of the inviscid flow should belong to the region to be computed, so that measured boundary conditions should be available well outside the viscous flow in the inviscid flow region. Though few experiments exist, which provide such boundary conditions, interactive calculations seem in principle the preferable procedure for comparisons with experiments, which include a separation region.

PRESENT STATUS AND PROSPECTS

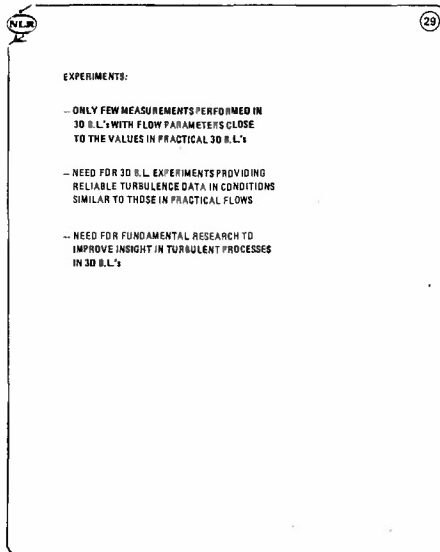
THEORY EXPERIMENT COMPARISONS PERFORMED SHOW:

- DIRECTION OF SHEAR STRESS ($\partial v / \partial y$, $\partial w / \partial y$) AND VELOCITY GRADIENT ($\partial u / \partial y$, $\partial u / \partial z$) DO NOT COINCIDE IN 3D B.L.'s
- MAGNITUDE OF SHEAR STRESS ($\partial v / \partial y$, $\partial w / \partial y$) IS SMALLER IN 3D B.L.'s THAN IN EQUIVALENT 2D B.L.'s
- IN GENERAL TURBULENCE ACTIVITY SEEMS TO DECREASE AS THE MEAN FLOW BECOMES THREE-DIMENSIONAL

PRESENT STATUS AND PROSPECTS

As turbulence is essentially three-dimensional, it was generally expected originally that turbulence models for two-dimensional flows could be applied without change to three-dimensional boundary layers. More and more experimental evidence has become available, however, which shows that this is not true. While a straightforward extension of most turbulence models to three dimensions leads to an isotropic eddy viscosity, i.e. a shear stress in the direction of the velocity gradient, measurements consistently show that these directions do not coincide. Moreover measurements indicate that the Reynolds shear stresses are substantially smaller than in two-dimensional boundary layers in equivalent conditions. Turbulence activity in general appears to have decreased in three-dimensional boundary layers. A recent survey of these experimental findings is contained in Bradshaw (1986).

The fact that the three-dimensionality of the flow affects so strongly the turbulence properties can only be explained when realizing the important role of the large eddies in turbulent flows. The structure of the large eddies will be distorted when the mean velocity profile in the boundary layer is skewed and so their development may be obstructed, leading to a decreased turbulence level in three-dimensional boundary layers.



As a consequence of the important role of the large eddies, whose properties are not easily generalized, universality of empirical assumptions about turbulence is difficult to achieve and in any case has not yet been achieved. This means that checking empirical assumptions is at present only useful in the flow conditions, where the empiricism is expected to hold. Unfortunately many of the experiments performed do not simulate practical flow conditions. Generally the boundary layer is thick in the experiments relative to the length of the measurement region, which often leads to pressure forces, which are comparatively large, and a tendency of turbulence history effects to dominate the turbulence development.

In view of the above, it is clear that there is a need for three-dimensional turbulent boundary layer experiments providing reliable data in flow conditions, which better resemble those in practical flows. In addition fundamental experiments should be carried out to shed more light on the turbulent processes in three-dimensional boundary layers. Initiative has been taken to perform more extensive collaborative experiments in this field (Humphreys, 1983). Since some time numerical simulations of turbulence by solving the Navier-Stokes equations have come within reach and these may provide a new means to augment knowledge about turbulence, also in three-dimensional boundary layers, as detail information can be made available not easily obtained from measurements.

REFERENCES

- Abid, R., Schmitt, R., 1984 - "Critical examination of turbulence models for a separated three-dimensional turbulent boundary layer". Recherche Aérospatiale no. 1984-6.
- Ausherman, D.W., Yanta, W.J., 1983 - "Measurement of the three-dimensional boundary layers on conical bodies at Mach 3 and Mach 5". AIAA Paper 83-1675.
- Berg, B. van den, 1982 - "Some notes on three-dimensional turbulent boundary layer data and turbulence modelling". Proc. IUTAM Symp. on "Three-dimensional turbulent boundary layers", Berlin, eds.: H.H. Fernholz, E. Krause.
- Berg, B. van den, Elsenaar, A., 1972 - "Measurements in a three-dimensional turbulent boundary layer under infinite swept wing conditions". NLR TR 72092 U.
- Berg, B. van den, Humphreys, D.A., Krause, E., Lindhout, J.P.F., 1986 - "Comparison of three-dimensional turbulent boundary layer calculations with experiment. The Eurovisc 1982 Berlin Workshop". Notes on Numerical Fluid Mechanics, Vieweg Verlag.
- Bertelrud, A., 1984 - "Pressure distribution on a swept wing aircraft in flight". AGARD AR-138 Addendum.
- Bradshaw, P., 1986 - "Physics and modelling of three-dimensional boundary layers". AGARD Special Course on "Computation of three-dimensional boundary layers including separation", VKI, Belgium.
- Bradshaw, P., Ferriss, D.H., Atwell, N.P., 1967 - "Calculation of boundary layer development using the turbulent energy equation". J. Fluid Mech. 28, 593.
- Bradshaw, P., Pontikos, N.S., 1985 - "Measurements in the turbulent boundary layer on an "infinite" swept wing". J. Fluid Mech. 159, 105.
- Bradshaw, P., Terrell, M.G., 1969 - "The response of a turbulent boundary layer on an "infinite" swept wing to the sudden removal of pressure gradient". NPL Aero Rep. 1305.
- Bruin, A.C. de, 1983 - "Sensitivity of computational results to modification in the pressure gradient for the Van den Berg Elsenaar three-dimensional boundary layer experiment". NLR Memo AI-83-007 U.
- Chou, J.H., Childs, M.E., 1985 - "An experimental study of three-dimensional shock wave/turbulent boundary layer interactions in a supersonic flow". AIAA Paper 85-1566.
- Cook, P.H., McDonald, M.A., Firmin, M.C.P., 1979 - "Wind tunnel measurements of the mean flow in the turbulent boundary layer and wake in the region of the trailing edge of a swept wing at subsonic speeds". RAE TR 79062.
- Cousteix, J., Pailhas, G., 1980 - "Measurements of mean velocity and Reynolds stress tensor within a wake of a swept wing". Rapport Techn. OA 41/2259 AYD.
- Cousteix, J., Pailhas, G., 1983 - "Three-dimensional wake of a swept wing". Proc. IUTAM Symp. on "Structure of complex turbulent shear flow", Marseille, eds.: R. Dumas, L. Fulachier.
- Dechow, R., Felsch, K.O., 1977 - "Measurements of the mean velocity and of the Reynolds stress tensor in a three-dimensional turbulent boundary layer induced by a cylinder standing on a flat wall". Symp. on "Turbulent shear flows", University Park.

- Demetriades, A., McCullough, G., 1985 - "Mean-flow measurements in a supersonic three-dimensional turbulent boundary layer". J. Fluid Mech. 156, 401.
- Doilling, D.S., McClure, W.B., 1985 - "Flowfield scaling in sharp fin-induced shock wave/turbulent boundary-layer interaction". AIAA J. 33, 201.
- East, L.F., 1973 - "Measurements of the three-dimensional incompressible turbulent boundary layer induced on the surface of a slender delta wing by the leading edge vortex". RAE TR 73141.
- East, L.F. 1976 - "Computation of three-dimensional turbulent boundary layers". FFA TN AE-1211.
- Elsenaar, A. Berg, B. van den, Lindhout, J.P.F., 1975 - "Three-dimensional separation of an incompressible turbulent boundary layer on an infinite swept wing". AGARD Conf. Proc. No. 168.
- Fernholz, H.H., Vagt, J.D., 1981 - "Turbulence measurements in an adverse-pressure-gradient three-dimensional turbulent boundary layer along a circular cylinder". J. Fluid Mech. 111, 233.
- Fulachier, L., Arzoumanian, E., Dumas, R., 1982 - "Effect on a developed turbulent boundary layer of a sudden local wall motion". Proc. IUTAM Symp. on "Three-dimensional turbulent boundary layers", Berlin, eds.: H.H. Fernholz, E. Krause.
- Grande, G. de, Hirsch, C., 1978 - "Three-dimensional incompressible turbulent boundary layers". Free Univ. Brussels, Internal Rep. VUB-STR-8.
- Hebbar, S.K., Driver, D.M., 1985 - "An experimental investigation of a swirling, axisymmetric, turbulent boundary layer with pressure gradient". AIAA Paper 85-1668.
- Higuchi, H., 1980 - "Relaxation of a subsonic swirling, turbulent boundary layer flow: An experimental documentation of the mean flow field survey". Dyn. Techn. Rep. DTN-8007-4.
- Humphreys, D.A., 1979 - "Comparison of boundary layer calculations for a wing: The May 1978 Stockholm Workshop test case". FFA TN AE-1522.
- Humphreys, D.A., 1983 - "Report of the first meeting of EUROEXPT - joint European three-dimensional turbulent boundary layer experiment". FFAP-65.
- Humphreys, D.A., Berg, B. van den, 1980 - "Evaluation of flow 0250: the three-dimensional turbulent boundary layer". Proc. 1980-81 AFSOR-HTM Stanford Conf. on "Complex turbulent flows: Comparison of theory and experiment", eds.: S.J. Kline, B.J. Cantwell, G.M. Lilley.
- Johnston, J.P., 1976 - "Experimental studies in three-dimensional turbulent boundary layers". Stanford Univ. Thermosc. Div. Rep. MD-34.
- Krogstad, P.A., 1979 - "Investigation of a three-dimensional turbulent boundary layer driven by simple two-dimensional potential flow". Norwegian Inst. Techn., Dissertation.
- Kussoy, M.I., Viegas, J.R., Horstman, C.C., 1980 - "An experimental and numerical investigation of a 3D shock separated turbulent boundary layer". AIAA Paper 80-0002.
- Larsson, L., 1981 - "SSPA-ITTC Workshop on ship boundary layers 1980". Swedish Maritime Res. Centre Publ. No. 90.
- Launder, B.E., 1971 - "An improved algebraic stress model of turbulence". Imperial Coll. Rep. TM/TN/A8.
- Lindhout, J.P.F., Berg, B. van den, Elsenaar, A., 1980 - "Comparison of boundary layer calculations for the root section of a wing: The September 1979 Amsterdam Workshop test case". NLR MP 80028 U.
- Lohmann, R.P., 1976 - "The response of a developed turbulent boundary layer to local transverse surface motion". J. Fluids Eng. 98, 354.
- McAllister, J.E., Pierce, F.J., Tennant, M.H., 1982 - "Direct force wall shear measurements in a pressure-driven three-dimensional turbulent boundary layer". J. Fluids Eng. 104, 150.
- Meier, H.U., Kreplin, H.P., Vollmers, H., 1983 - "Development of boundary layers and separation patterns on a body of revolution at incidence". Symp. on "Numerical and physical aspects of aerodynamic flows", Long Beach, ed.: T. Cebeci.
- Michel, R., Arnal, D., Coustols, E., Juillen, J.C., 1984 - "Experimental and theoretical studies of boundary layer transition on a swept infinite wing". Proc. IUTAM Symp. on "Laminar-turbulent transition", Novosibirsk, ed.: V.V. Kozlov.
- Müller, U., Krause, E., 1979 - "Measurements of mean velocities and Reynolds stresses in an incompressible three-dimensional turbulent boundary layer". Symp. on "Turbulent shear flows", London.
- Nituch, M.J., Sjolander, S., Head, M.R., 1978 - "An improved version of the Cebeci-Smith eddy-viscosity model". Aeronaut. Quart. 29, 207.
- Oskam, B., Vas, I.E., Bogdonoff, S.M., 1976 - "Mach 3 oblique shock wave/turbulent boundary layer interaction in three dimensions", AIAA Paper 76-336.
- Patel, V.C., 1982 - "Some aspects of thick three-dimensional boundary layers". IOWA Inst. Hydr. Res. Rep. 256.

- Peake, D.J., 1976 - "Three-dimensional swept shock/turbulent boundary-layer separations with control by air injection". Nat Res. Council Canada Rep. LR-592.
- Pierce, F.J., Harsh, M.D., Menna, J.D., 1985 - "The mean flow structure around and within a turbulent junction or horseshoe vortex". Virg. Polytechnic Inst. Rep. VPI-E-85-19.
- Poll, D.I.A., 1979 - "Transition in the infinite swept wing attachment line boundary layer". "Aeronaut. Quart. 30, 607.
- Ramaprian, B.R., Patel, V.C., Choi, D.H., 1981 - "Mean-flow measurements in the three-dimensional boundary layer over a body of revolution at incidence". J. Fluid Mech. 103, 479.
- Rodi, W., 1972 - "The prediction of free boundary layers by use of two equation model of turbulence". University of London, Ph. D. Thesis.
- Rotta, J.C., 1977 - "A family of turbulence models for three-dimensional thin shear layers". Symp. on "Turbulent shear flows", University Park.
- Seetharam, H.C., Pfeiffer, N.J., Ohmura, M., McLean, J.D., 1982 - "Experimental and theoretical studies of three-dimensional turbulent boundary layers on an empennage of a typical transport airplane". ICAS Paper 82-6.4.3.
- Schmitt, R.L., Chanetz, B.P., 1985 - "Experimental investigation of three-dimensional separation on an ellipsoid-cylinder body at incidence". AIAA Paper 85-1686.
- Spaid, F.W., 1984 - "Transonic airfoil and wing flowfield measurements". AIAA Paper 84-0100.
- Spaid, F.W., Roos, F.W., 1983 - "An experimental study of the turbulent boundary layer on a transport wing in transonic flow". AIAA Paper 83-1687.

THREE-DIMENSIONAL BOUNDARY LAYERS :

LAMINAR-TURBULENT TRANSITION

Daniel ARNAL

Office National d'Etudes et de Recherches Aéronautiques (ONERA)
 Centre d'Etudes et de Recherches de Toulouse
 2 avenue Edouard Belin
 31055 TOULOUSE Cédex - FRANCE

SUMMARY

The first part of this paper is devoted to a brief survey of transition problems in two-dimensional flows. The main elements of laminar instability theory are presented and used for elaborating some practical transition criteria. In three-dimensional situations, the problem is much more complex, because transition may occur through streamwise instability, cross-flow instability or leading edge contamination. It is assumed that the streamwise instability can be studied by using two-dimensional results. On the contrary, the cross-flow instability and the leading edge contamination constitute typical features of three-dimensional flows, as it is illustrated by experimental results. The extension of linear stability theory to these last problems is discussed, and transition criteria are developed. Moreover an "intermittency method" allows the transition region to be calculated. These techniques are applied to swept wings and bodies at incidence.

MAIN NOTATIONS

X, Z, y	general coordinate system
x, z, y	streamline coordinate system
u, w, v	velocity components in (x, z, y)
U, W, V	velocity components in (X, Z, y)
$\tilde{u}', \tilde{w}', \tilde{v}', \tilde{p}'$	complex velocity and pressure fluctuations
u', w', v', p'	physical disturbances (real parts of $\tilde{u}', \tilde{w}', \tilde{v}', \tilde{p}'$)
$\overline{u'v'}, \overline{v'w'}$	Reynolds shear stresses
c	chord normal to the leading edge
f^*	frequency
$F = \frac{2\pi f^* c}{u_e}$	dimensionless frequency
h_1, h_2	metric coefficients in the X and Z directions
\vec{k}	wave number vector
Tu	free-stream turbulence level
α_n	normal angle of attack
β_h	Hartree's parameter
γ	intermittency factor
δ	boundary layer thickness
$\varepsilon = \frac{\pi}{2} - \psi$	
θ_0	angle between the X axis and the external streamline
λ^*	wavelength
$\Lambda_2 = \frac{\theta^2}{v} \frac{du_e}{dx}$	Pohlhausen parameter
ν	kinematic viscosity
ξ	circumferential angle
φ	angle of sweep
ψ	angle between the external streamline and \vec{k}

Two-dimensional boundary layer parameters

Cf skin friction coefficient

$$\delta_1 = \int_0^{\delta} \left(1 - \frac{u}{u_e}\right) dy$$

$$\theta = \int_0^{\delta} \frac{u}{u_e} \left(1 - \frac{u}{u_e}\right) dy$$

H = δ_1/θ shape factor

$$Rx = \frac{u_e x}{\nu}$$

$$R\theta = \frac{u_e \theta}{\nu}$$

$$R\delta_1 = \frac{u_e \delta_1}{\nu}$$

Reynolds numbers

Three-dimensionnal boundary layer parameters

$$\delta_1 = \int_0^{\delta} \left(1 - \frac{u}{u_e}\right) dy$$

$$\theta_{11} = \int_0^{\delta} \frac{u}{u_e} \left(1 - \frac{u}{u_e}\right) dy$$

$$\delta_2 = \int_0^{\delta} -\frac{w}{u_e} dy$$

H = δ_1/θ_{11} streamwise shape factor

$$R\theta_{11} = \frac{u_e \theta_{11}}{\nu}$$

$$R\delta_2 = \frac{u_e \delta_2}{\nu} = \frac{1}{\nu} \int_0^{\delta} -w dy$$

Reynolds numbers

Subscripts

cr	critical
e	free-stream
E	end of transition
i	imaginary part
l	laminar
r	real part
t	turbulent
T	transition onset
∞	upstream

1 - INTRODUCTION

Since the classical experiments performed by Osborne Reynolds (1883), the instability of laminar flows and the transition to turbulence have maintained a constant interest in fluid mechanics problems. This interest results in the fact that transition controls important hydrodynamic quantities such as drag or heat transfer. The present paper is devoted to a general survey of transition calculation methods, in three-dimensional, incompressible flows. Most of these methods do not claim to represent the intricate physics of the transition process : they only constitute short term answers to practical problems.

Before to examine the difficulties associated with three-dimensional configurations, it is necessary to do a short review of the most important results obtained in two-dimensional flows ; this necessity arises from the fact that the properties of two-dimensional boundary layer profiles are similar to those of streamwise profiles in three-dimensional flows. As it can be expected, new problems will appear in the latter case due to the presence of cross-flow profiles.

2 - TRANSITION IN TWO-DIMENSIONAL FLOWS

2.1 General considerations

An overall picture of the boundary layer development on a given body is shown on figure 1. From the leading edge to a certain distance x_T , the flow remains laminar ; in the zero pressure gradient case, for instance, the shape factor is constant and equal to the Blasius value 2.591. At x_T , turbulence structures appear and transition occurs. From x_T to x_E , there is a noticeable change in the boundary layer properties : the process of transition involves a large increase in the momentum thickness θ and a large decrease in the shape factor H . As a result, the displacement thickness $\delta_1 = H\theta$ exhibits a more complex evolution. The skin friction coefficient C_f increases from a laminar value to a turbulent one, the latter being in some cases an order of magnitude greater than the former.

It is obvious that the location and the extent of the transition depend on a large range of parameters, such as free-stream turbulence, pressure gradient, noise level, vibrations, roughness, suction or blowing, wall curvature... In this paper, only the first two parameters will be considered ; an overall description of the effects of the other factors can be found in /1/.

2.1.1 Influence of free-stream turbulence

The effect of free-stream turbulence on transition location is shown on figure 2, where the transition Reynolds number R_{x_T} is plotted as a function of the external turbulence level Tu . These experimental results were obtained for a constant external velocity ; the high values of Tu , such as those used by Hall and Hislop, are achieved by installing grids just upstream of the test section.

At first sight, the experimental data seem to collapse onto a single curve : transition moves rapidly upstream when Tu increases. This effect appears to be very strong : the value for R_{x_T} corresponding to $Tu = 0,3 \cdot 10^{-2}$ is about three times greater than that corresponding to $Tu = 1,5 \cdot 10^{-2}$. On the other side, it is obvious that R_{x_T} depends not only on the root-mean-square value of the free-stream turbulence, but also on its spectrum. This is illustrated on figure 3, which presents an enlargement of the previous graph, for the lower values of Tu , say $Tu < 0,3 \cdot 10^{-2}$. As Tu becomes very small, the data of Schubauer-Skramstad /2/ and those of Wells /3/ exhibit the same trend, in the sense that R_{x_T} reaches a constant value. But this value is about $2,8 \cdot 10^6$ in /2/ and about $5 \cdot 10^6$ in /3/. In fact, sound component controls transition when Tu is very low, and the effect of "true" free-stream turbulence can be only observed at values of Tu greater than $0,2 \cdot 10^{-2}$.

2.1.2 Effect of streamwise pressure gradients

a) - Positive pressure gradients

The influence of a positive pressure gradient is illustrated in figures 4 et 5, where are presented typical experimental results obtained at ONERA/CERT/4/5/. Figure 4 shows the evolution of the shape factor as a function of R_x , for six external velocity distributions ; the case A corresponds to a nearly constant velocity distribution ; from case B to case F, the pressure gradient becomes stronger and stronger, but transition always occurs before laminar separation as indicated by laminar calculations. In the following lines, we will define the transition onset as the location where the shape factor exhibits a sudden negative slope. The free-stream turbulence level Tu is nearly constant from one configuration to another and is equal to about $0,2 \cdot 10^{-2}$. Another presentation of the results is given in figure 5, where the momentum thickness Reynolds number taken at the transition onset is plotted as a function of the shape factor at the same location. It can be seen that the transition Reynolds number decreases rapidly when the pressure gradient intensity increases.

When the pressure gradient is very strong, the laminar boundary layer often separates and transition may occur in this separated layer : it is the problem of separation bubbles occurring, for example, near the leading edge of an airfoil at incidence, downstream of the suction peak. In this case, there is an interaction between viscous and inviscid flows, so that the external velocity distribution depends strongly on the chord Reynolds number.

b) - Negative pressure gradients

Detailed transition experiments in negative pressure gradients are not numerous. As the flow acceleration acts to stabilize the laminar boundary layer (see paragraph 2.2.3), the lengths required for such studies would be too important in laboratory conditions, except if the free-stream turbulence level is high. In such cases, the external turbulence tends to counteract the favourable effect of the negative pressure gradient. This interplay can be encountered in many practical situations such as turbomachinery and was investigated, for instance, by Turner /6/ and by Blair and Werle /7/.

2.2 Laminar instability

This theory constitutes the first attempt to describe the initial stages leading to transition in a laminar boundary layer ; it postulates the existence of small, regular oscillations travelling in the laminar boundary layer, eventually growing and inducing turbulence. This idea was expressed many decades ago by Rayleigh (1887) and Prandtl (1921). Some years later, Tollmien and Schlichting worked out a complete theory of boundary layer instability, so that the waves are often named : "Tollmien-Schlichting waves". The celebrated experiments of Schubauer and Skramstad /2/ (1948) confirmed most of the numerical results, so that the stability theory is of first importance for studying transition problems.

2.2.1 Orr-Sommerfeld equation

A complete account of the stability theory can be found in /8/. Some important results will be recalled in this chapter.

Let us consider two dimensional disturbances, the components of which are assumed to be of the form :

$$\begin{pmatrix} \tilde{u}' \\ \tilde{v}' \end{pmatrix} = \begin{pmatrix} f(y) \\ \phi(y) \end{pmatrix} \exp \left[i (\alpha x - \omega t) \right] \quad (1)$$

Pressure fluctuations are also introduced :

$$\tilde{p}' = \pi(y) e^{i(\alpha x - \omega t)} \quad (2)$$

f , ϕ and π are complex amplitude functions, α and ω can be either real or complex, so that, in the general case, \tilde{u}' , \tilde{v}' and \tilde{p}' are complex quantities. The physical disturbances u' , v' and p' are the real parts of \tilde{u}' , \tilde{v}' and \tilde{p}' .

It is often assumed that the mean flow is parallel : $v = 0$ and u depends only on y . This means that the boundary layer does not grow in the streamwise direction. The introduction of relations (1) and (2) into the continuity and momentum equations leads to the Orr-Sommerfeld equation, after linearization and elimination of pressure :

$$\phi^{IV} - 2\alpha^2 \phi'' + \alpha^4 \phi - iR \left[(\alpha u - \omega) (\phi'' - \alpha^2 \phi) - \alpha \frac{d^2 u}{dy^2} \phi \right] = 0 \quad (3)$$

with boundary conditions :

$$\phi(0) = \phi'(0) = 0 \quad \text{at all the wall}$$

$$\phi(y) \text{ and } \phi'(y) \rightarrow 0 \quad \text{when } y \rightarrow \infty \quad (4)$$

All quantities were made dimensionless with a reference velocity V and a reference length L , usually linked with the boundary layer thickness (displacement thickness, momentum thickness, laminar length scale x/\sqrt{Rx} , for instance). The Reynolds number R is equal to VL/ν . The primes denote differentiations with respect to the y direction.

The mathematical nature of the two principal parameters α and ω leads to two theories : the spatial theory and the temporal theory.

. In the spatial theory, ω is a real quantity, which represents the circular frequency of the wave, and α is complex : $\alpha = \alpha_r + i\alpha_i$. Any fluctuation \tilde{q}' (\tilde{q}' represents \tilde{u}' , \tilde{v}' or \tilde{p}') takes the form :

$$\tilde{q}' = q(y) e^{-\alpha_i x} e^{i(\alpha_r x - \omega t)} \quad (5)$$

The amplification factor α_i determines the degree of amplification ($\alpha_i < 0$) or damping ($\alpha_i > 0$), and α_r denotes the wave number of the perturbation.

. In the temporal theory, α is real and ω is complex :

$$\tilde{q}' = q(y) e^{\omega_i t} e^{i(\alpha x - \omega_r t)} \quad (6)$$

It is possible to convert a temporal to a spatial amplification rate by using the relation derived by Gaster /9/ :

$$-\alpha_i = \frac{\omega_i}{\partial \omega_r / \partial \alpha} \quad (7)$$

where $Vg = \partial \omega_r / \partial \alpha$ is called the "group velocity".

2.2.2 Stability diagram - Local and total amplification rates

Due to the homogeneous boundary conditions, the problem is an eigenvalue one : when the mean velocity $u(y)$ is specified, a non zero solution of (3) is obtained for particular combinations of R , α and ω .

The Orr-Sommerfeld equation was solved by many authors. Some results of such computations for the Blasius flow are represented on figure 6, where $L = \delta_1$ and $V = u_e$, so that $\omega = 2\pi f^* \delta_1 / u_e$ (f^* is the physical frequency). The figure shows some curves of constant amplification rate α_i in the $(\omega, R\delta_1)$ plane ; curves of constant wave number α_r are not represented for clarity. In this diagram, curves of constant frequency $F = 2\pi f^* \nu / u_e^2 = \omega / R$ appear as straight lines through the origin. The locus $\alpha_i = 0$, called the neutral curve, separates the region of stable disturbances from that of unstable disturbances. In particular, there is a value of the Reynolds number below which all disturbances decay : it is the critical Reynolds number, $R\delta_{1,cr}$, which is slightly greater than 500.

Figure 6 indicates that a single frequency wave travelling in the laminar boundary layer is at first damped, then amplified, and again damped as it leaves the unstable region. An important parameter is the total amplification rate defined as :

$$\frac{A}{A_0} = \exp \left(\int_{x_0}^x -\alpha_i dx \right) \quad (8)$$

A is the wave amplitude and the index 0 refers to the streamwise position where the wave enters the unstable region. Figure 7 shows total amplification curves corresponding to various frequencies, obtained for the Blasius profile. The dashed line represents the envelope of these curves, which will be called n :

$$n = \max_F \left\{ \ln \left(\frac{A}{A_0} \right) \right\} \quad \text{at a given } x \text{ or } R\delta_1 \quad (9)$$

It is obvious that $n = 0$ for $R\delta_1 = R\delta_{1cr}$

2.2.3 Effect of pressure gradient

The same type of calculation can be performed for the self similar velocity profiles of the Falkner-Skan family. Let us recall that these profiles correspond to external velocity distributions of the form :

$$u_e = kx^m$$

For each value of m , the mean velocity profile $\frac{u}{u_e} \left(\frac{y}{x} \sqrt{Rx} \right)$ and the following boundary layer parameters remain unchanged in the streamwise direction :

$$\beta_h = \frac{2m}{m+1} \quad (\text{Hartree parameter})$$

$$\Lambda_2 = \frac{\theta^2}{\nu} \frac{du_e}{dx} \quad (\text{Pohlhausen parameter})$$

$$H = \delta_1/\theta \quad (\text{shape factor})$$

$$\frac{Cf}{2} R\theta, \quad R\delta_1/\sqrt{Rx} \dots$$

The main result of the stability calculations is that basic velocity profiles with an inflexion point (decelerating flows, $\Lambda_2 < 0$, $H > 2.591$) are more unstable than those developing in negative pressure gradients (accelerating flows, $\Lambda_2 > 0$, $H < 2.591$). This is illustrated on figure 8, where four similarity profiles are plotted. The dashed curve is the Blasius profile ($\beta_h = \Lambda_2 = 0$). The profile with $\beta_h = 1$ represents the two-dimensional stagnation point profile, and the other two curves correspond to positive pressure gradients ; for these profiles, the inflexion point is indicated by a cross ; the value $\beta_h = -0.1988$ characterizes the separation profile.

The destabilizing effect of positive gradients can be seen on figure 8b, which shows the neutral curves associated with the preceding profiles. When the shape factor increases, the critical Reynolds number decreases, the amplification factors become larger and larger, and the range of unstable wave numbers increases rapidly. In addition, important theoretical results were obtained by Lord Rayleigh (1880) and Tollmien (1935) by considering equation (3) in the limit of infinite Reynolds number :

$$(\alpha u - \omega) (\phi'' - \alpha^2 \phi) - \alpha \frac{d^2 u}{dy^2} \phi = 0$$

A study of this inviscid equation leads to the following conclusions :

- mean velocity profiles without inflexion point (flat plate and accelerating flows) have a neutral curve which tends to be closed at large Reynolds number. This is the case for profiles corresponding to $\beta_h = 0$ and 1 in figure 8b, their behaviour is dominated by a viscous instability.

- on the contrary, for mean velocity profiles having an inflexion point (decelerating flows), there is always a range of unstable frequencies as the Reynolds number goes to infinity. This is clearly visible on figure 8b for $\beta_h = -0.10$: for large values of $R\delta_1$, the upper branch of the neutral curve tends towards an asymptote (for the separation profile, this asymptote is out of the range of wave numbers represented on the figure). It is so-called inflexional instability, which plays a dominant role in three-dimensional flows.

For several values of H , the envelope curves defined by (9) are plotted on figure 9. The pressure gradient effects can be clearly pointed out : as the shape factor increases, the critical Reynolds number decreases and the slope $dn/dR\delta_1$ increases. This leads to the intuitive conclusion that transition will occur at lower Reynolds numbers in positive pressure gradients than in negative ones : this result is consistent with the experimental trends (paragraph 2.1.2).

Up to now, we considered only two-dimensional waves (i.e. waves, the crest of which travel normally to the main flow). A more general expression can describe the oblique, three-dimensional waves :

$$(\tilde{u}', \tilde{v}', \tilde{w}', \tilde{p}') = (f(y), \phi(y), h(y), \pi(y)) \exp \left[i (\alpha x + \beta z - \omega t) \right] \quad (10)$$

In fact, it can be demonstrated that, using the temporal theory, instability appears first for a two-dimensional disturbance : it is the celebrated Squire's theorem. For this reason, oblique waves are usually neglected in two-dimensional problems. However, when the mean flow is three-dimensional, the oblique waves must be taken into account.

2.2.4 Stability and transition

Since the experiments of Schubauer-Skramstad, much work has been done in order to check the stability theory results, either in natural or in artificial conditions. The experiments have revealed that the Tollmien-Schlichting waves constitute effectively the first stage in the transition process, for low free-stream turbulence levels. In a general manner, the measured frequencies, amplification rates, amplitude profiles were found in good agreement with numerical results. When transition is approached, non linear mechanisms take place, and the linearized equations are no longer valid; however, the non linear phase occurs over a relatively short distance, so that the linear stability controls most of the transition process.

The problem is that the theory is unable to predict the transition onset, and the link between stability and transition can only be done through experimental results. In this respect, Smith and Gamberoni /10/ and Van Ingen /11/ developed independently the well known "eⁿ method". In the general case where the flow is not of a constant β_H -type, these authors calculated at first the laminar boundary layer development; the second step was to use the stability charts established by Pretsch for self-similar velocity profiles; the envelope curve was obtained by computing the growth of waves of different frequencies. Smith and Gamberoni compared stability calculations with measured transition points, and transition was found to occur when $n \approx 9$. This means that transition occurs when the most unstable frequency is amplified by a factor e⁹. The same result was obtained by Van Ingen, but with the exponential factor equal to 7 or 8.

The success of the e⁹ method is certainly due to the fact that the experimental data were obtained in wind tunnels where the free-stream turbulence level was similar and rather low, let say $Tu \approx 0.1 \cdot 10^{-2}$. For higher values of Tu , the transition Reynolds number decreases rapidly, and the e⁹ method no longer applies. Mack /12/ suggests an empirical relation between Tu and the value of n at the transition location:

$$n_T = -8.43 - 2.4 \ln Tu \quad (11)$$

This relation has been established to fit the experimental results collected by Dryden for the flat plate case /13/. Its application to adverse pressure gradients has given fairly good results /14/. However, two remarks are to be made:

- . For $Tu < 10^{-3}$, sound disturbances may become the factor controlling transition rather than turbulence, and application of (11) may give poor results.

- . For high values of Tu ($Tu > 2$ or $3 \cdot 10^{-2}$), transition often occurs without appearance of Tollmien-Schlichting waves, at Reynolds numbers lower than the critical Reynolds number. The linear processes are completely "bypassed" and the eⁿ method has no significance.

2.3 Transition criteria

The word criterion can be interpreted as a more or less empirical correlation between boundary layer parameters at the transition onset. Transition criteria are often used for practical applications, because they are easily introduced in engineering prediction methods such as integral methods. Although the fundamental mechanisms of the transition process do not appear as clearly as in the stability calculations, they provide a fairly acceptable compromise between accuracy and simplicity.

For two-dimensional flows over airfoils, Michel /15/, 1951, correlated the values of two Reynolds numbers at transition, $R\theta$ and R_x .

Granville /16/, 1953, developed a correlation which takes into account two important parameters, namely the stability properties and the flow history:

- . the stability of the boundary layer is characterized by the difference in momentum thickness Reynolds number from the neutral stability point to the transition location.

- . as the amplification of disturbances depends on the cumulative effect of pressure gradient, an averaged Pohlhausen parameter is introduced:

$$\bar{\Lambda}_{2T} = \frac{1}{x_T - x_{cr}} \int_{x_{cr}}^{x_T} \frac{\theta^2}{v} \frac{du_e}{dx} dx \quad (12)$$

These criteria were established by using experimental data obtained in low turbulence wind tunnels or in flight tests; they take into account the pressure gradient effects, for low values of Tu . More recently, the influence of free-stream turbulence was introduced in practical criteria, see review in /1/.

For example, Arnal, Habiballah and Delcourt /17/, 1979, extended Granville's correlation on theoretical basis. For this, the envelope curves computed for the Falkner-Skan profiles (figure 9) were used, as well as Mack's relation (11). At first, the criterion was established for similarity flows ($\Lambda_2 = \text{constant}$); for applications in more general conditions, Λ_2 is replaced by the averaged Pohlhausen parameters $\bar{\Lambda}_2$. Curves corresponding to various values of Tu are plotted on figure 10. It can be observed that the proposed criterion coincides practically with the Granville's one for $Tu = 0.05 \cdot 10^{-2}$ to $0.1 \cdot 10^{-2}$. An analytical expression is:

$$R\theta_T - R\theta_{cr} = -206 \exp(25.7 \bar{\Lambda}_{2T}) \left[\ln(16.8 Tu) - 2.77 \bar{\Lambda}_{2T} \right] \quad (13)$$

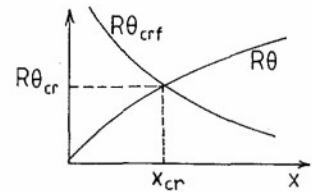
In order to apply relation (13), it is necessary to calculate $R\theta_{cr}$.

For self-similar velocity profiles, the critical Reynolds number depends on a single similarity parameter, for example :

$$R\theta_{cr} = R\theta_{cr}(H) \quad (14)$$

An analytical representation of (14) can be found in Cousteix /18/.

For any non similar flow, $R\theta_{cr}$ is computed as follows. The streamwise evolution of the thickness-momentum Reynolds number $R\theta$ is plotted for the considered case and is compared, at each abscissa, with the fictitious critical Reynolds number $R\theta_{crf}$ associated with the local boundary layer profile ; a simple solution is to use relation (14) in which the subscript cr is replaced by crf. If $R\theta < R\theta_{crf}$, the flow is locally stable. If $R\theta > R\theta_{crf}$, the flow is locally unstable. The true critical abscissa is located at the point where $R\theta = R\theta_{crf}$.



2.4 Intermittency methods

Let us assume that the transition onset is known. A second objective is to compute the transition region itself, the extent of which may be as important as the laminar region which precedes it. An important parameter characterizing the transitional boundary layer is the intermittency factor γ , which represents the fraction of the total time that the flow is turbulent. Most of the numerical models are based on the so-called "intermittency method", in which laminar and turbulent quantities are weighted by γ .

The streamwise evolution of the intermittency factor was studied by various authors /19/ /20/ /21/. The experiments performed at ONERA/CERT with zero and positive pressure gradients have shown that the momentum thickness θ_E at the end of the transition region was about twice the momentum thickness θ_T at the transition onset. Therefore, relations of the form :

$$\gamma = f\left(\frac{\theta}{\theta_T}\right) \text{ or } \gamma = f\left(\frac{R\theta}{R\theta_T}\right)$$

can be adopted.

a) - Integral method

In the code developed at ONERA/CERT, the boundary layer development is computed by using the integrated momentum equation and an auxiliary equation, such as the entrainment equation. At a given point in the transition region, the laminar relationships give fictitious laminar parameters, such as the shape factor H_1 and the skin friction coefficient Cf_1 . In the same way, H_t and Cf_t are deduced from turbulent relationships. The corresponding parameters in the transition region are expressed as :

$$H = \gamma H_t + (1 - \gamma) H_1 \quad (15)$$

$$Cf = \gamma Cf_t + (1 - \gamma) Cf_1$$

$$\text{with } \gamma = 1 - \exp(4.5 \left(\frac{\theta}{\theta_T} - 1\right)) \quad (16)$$

b) - Local equations

Intermittency methods have been applied to local equations by many authors. In the most simple models, the turbulent shear stress is expressed as :

$$-\overline{u'v'} = \gamma \nu_t \frac{\partial u}{\partial y} \quad (17)$$

where ν_t is computed by using a classical turbulence model. Cebeci /22/ employed a mixing length scheme, the intermittency factor being expressed by a relation proposed by Chen and Thyson /21/. A mixing length scheme was also used by Arnal et al /23/, who kept the assumption that γ depends on θ/θ_T ; however, it was found necessary to introduce an analytical expression somewhat different from (16) in order to obtain a good agreement with experiments, see Coustols /59/.

2.5 Example of application

Figure 11 presents an example of application of the techniques described in paragraph 2.3 and 2.4. In the considered case, transition occurs in a positive pressure gradient (case D of the experimental results reported in figure 4), with a relatively low free-stream turbulence level. The transition onset is determined by relation (13), and the evolution from the laminar to the turbulent state is computed by the intermittency method. Both calculations are in good agreement with experiments. Other applications can be found in /1/ and /14/.

3 - EXPERIMENTAL EVIDENCE OF THREE- DIMENSIONAL TRANSITION PROBLEMS

During flight tests on swept wing aircraft conducted at the RAE between 1951 and 1952, Gray (see Poll /24/) found that under certain conditions, transition moved towards the leading edge in a way which could not be explained through a two-dimensional analysis. This sudden movement occurred beyond a certain speed, which appeared to be a function of the leading edge radius and the leading edge sweep. In addition, sublimation patterns indicated the existence of streaks almost aligned with the external streamlines and regularly spaced in the spanwise direction.

Once recognized, the destabilizing effect of sweep back received rapid attention. By May 1952, two

wind tunnel experiments (Anscombe and Illingworth, Gregory and Walker, see Gregory et al /25/) were performed; they confirmed Gray's findings. Allen and Burrows (1956, /26/) and Burrows (1956, /27/) conducted measurements in flight on the boundary layer formed on untapered swept wings. Some years later, Boltz, Kenyon and Allen (1960, /28/) carried out extensive investigations into the dependence of transition position upon Reynolds number, sweep angle and angle of attack in the Ames 12' Pressure Tunnel. Measurements have been done in France by Schmitt and Manie /29/ and Arnal, Coustols and Juillen /23/, /30/ on an ONERA D profile. Poll /24/, /31/ performed careful experiments on a swept cylinder and gave detailed information about the flow developing close to the attachment line. Recently, a somewhat different approach was adopted by Saric and Yeates /32/ and by Bippes and Nitschke (DFVLR Göttingen, work en progress): a swept-wing flow is created on a flat plate, the leading edge of which is swept; an appropriate wall bump is used to obtain a specified pressure distribution. This method allows to avoid body curvature problems.

In all cases, transition was found to take place in regions of strong negative pressure gradients, for sufficiently large values of the Reynolds number. Such a situation is inconceivable in two-dimensional flow, where the accelerated regions stabilize the laminar boundary layer (paragraph 2.2.3); the three-dimensional nature of the flow must be put forward in order to explain this motion. In addition, wall visualizations techniques (sublimation, china-clay evaporation, oil-flow...) clearly indicate the presence of streaks upstream transition onset. Figure 12 shows an example of sublimation result, obtained on an ONERA D airfoil /23/ for $\Phi = 40^\circ$, $\alpha_n = -8^\circ$, $Q_\infty = 81\text{m/s}$ (Φ , α_n and Q_∞ are the angle of sweep, the angle of attack and the wind tunnel speed, respectively). Black regions, characterized by high values of the skin friction coefficient, are visible near the leading edge (laminar boundary layer at low Reynolds number) and beyond 25 or 30 % of chord (transitional and turbulent boundary layer). Between these regions, stream-wise striations can be observed; due to their presence, the transition front exhibits a "sawtooth" pattern in the spanwise direction.

The flow on a flat disk rotating in still fluid with a fixed angular velocity represents another example of three-dimensional flow. It is particularly convenient for stability analysis, because the steady laminar flow is described by an exact solution of the Navier-Stokes equations. Experimental observations were reported by Gregory et al /25/, Kobayashi et al /33/ and others. As in the wing experiments, stationary disturbances were found to exist in the laminar flow: they appear in the form of spirals, the axes of which are fixed relative to the surface of the disk. A china-clay photograph obtained by Gregory et al /25/ is presented in figure 13: it shows laminar flow near the centre, and about 30 spiral vortices which cause transition to turbulent flow near the rim.

The mechanism of boundary layer transition on other spinning axisymmetric bodies was studied by many authors. Spiral vortices were observed by Kobayashi and Kohama /34/ on a rotating cone, and by Kohama and Kobayashi /35/ on a spinning sphere. Smoke visualizations were performed by Kegelmann et al /36/ on an axisymmetric model consisting of an ogive nose, a cylindrical midsection and a conical boattail.

In addition to the swept wings and rotating bodies problems, there have been several investigations into more complex geometries. Eichelbrenner and Michel /37/ made transition measurements on an ellipsoid with a slenderness ratio of 6 : 1 at various incidences.

At zero incidence, the transition location was consistent with two-dimensional results; however, as the incidence was increased, the orientation of the transition front was modified by three-dimensional effects. More recently, experiments on a prolate spheroid at incidence were performed by Meier et al /38/; typical results will be presented later on.

In parallel with the experimental work, theoretical studies were devoted to the understanding of the physical phenomena. The investigations conducted by Stuart /25/ and others showed that the linear stability theory was able to explain some of the experimental features. For this reason, it seems useful to give the main elements of the stability theory in three-dimensional flows.

4 - LINEAR STABILITY THEORY IN THREE-DIMENSIONAL FLOWS

4.1 Stability equations

Let us define a set of orthogonal curvilinear coordinates X, Z, y . The X and Z coordinates lie in the plane of the surface, y being normal to it. Elements of length in this system are $h_1 dX, h_2 dZ, dy$. The mean velocity components in the X and Z directions are U and W ; by using the parallel flow assumption, the mean velocity v normal to the surface is set equal to zero, and U and W depend on y only. The velocity and pressure fluctuations are denoted by u', w', v', p' .

The continuity and linearized disturbance equations are :

$$\frac{1}{h_1} \frac{\partial u'}{\partial X} + \frac{1}{h_2} \frac{\partial w'}{\partial Z} + \frac{\partial v'}{\partial y} + u' m_{21} + w' m_{12} + v' (m_{13} + m_{23}) = 0 \quad (18)$$

$$\frac{\partial u'}{\partial t} + \frac{U}{h_1} \frac{\partial u'}{\partial X} + \frac{W}{h_2} \frac{\partial u'}{\partial Z} + v' \frac{dU}{dy} - 2 W w' m_{21} + m_{12} (W u' + U w') + m_{13} U v' = - \frac{1}{h_1} \frac{\partial p'}{\partial X} + D_x \quad (19)$$

$$\frac{\partial w'}{\partial t} + \frac{U}{h_1} \frac{\partial w'}{\partial X} + \frac{W}{h_2} \frac{\partial w'}{\partial Z} + v' \frac{dW}{dy} + m_{21} (U w' + W u') - 2 m_{12} U u' + m_{23} v' W = - \frac{1}{h_2} \frac{\partial p'}{\partial Z} + D_z \quad (20)$$

$$\frac{\partial v'}{\partial t} + \frac{U}{h_1} \frac{\partial v'}{\partial X} + \frac{W}{h_2} \frac{\partial v'}{\partial Z} - 2 m_{13} u' U - 2 m_{23} w' W = - \frac{\partial p'}{\partial y} + D_y \quad (21)$$

All the variables have been non-dimensionalized with a reference velocity V and a reference length L , so that the diffusion terms D_x , D_z and D_y are proportional to $\frac{1}{R}$, where the Reynolds number R is equal to $\frac{VL}{\nu}$. The pressure is made dimensionless by ρV^2 .

The "in plane" curvature coefficients are given by :

$$m_{12} = \frac{L}{h_1 h_2} \frac{\partial h_1}{\partial Z}, \quad m_{21} = \frac{L}{h_1 h_2} \frac{\partial h_2}{\partial X} \quad (22)$$

The surface curvature coefficients are given by :

$$m_{13} = \frac{L}{h_1} \frac{\partial h_1}{\partial y}, \quad m_{23} = \frac{L}{h_2} \frac{\partial h_2}{\partial y} \quad (23)$$

The velocity and pressure fluctuations are assumed to be of the form :

$$(u', w', v', p') = \text{Re} \left\{ (f, h, \phi, \pi) \exp \left[i(\alpha X + \beta Z - \omega t) \right] \right\} \quad (24)$$

f, h, ϕ and π are complex amplitude functions. As in two-dimensional flow, α, β and ω can be either real or complex :

. In the spatial theory, ω is real, α and β are complex. It is possible to define a wavenumber vector $\vec{k} = (\alpha_r, \beta_r)$ and a amplification vector $\vec{A} = (-\alpha_i, -\beta_i)$.

. In the temporal theory, α and β are real, ω is complex. ω_i represents the temporal amplification rate, whilst α and β are the components of the wavenumber vector \vec{k} .

Introducing (24) in (18) - (21) leads to the following set of equations :

$$i \left\{ \alpha_0 f + \beta_0 h \right\} + \phi' + m_{21} f + m_{12} h + \phi(m_{13} + m_{23}) = 0 \quad (25)$$

$$i \left\{ \alpha_0 U + \beta_0 W - \omega \right\} f + \frac{dU}{dy} \phi - 2m_{21} Wh + m_{12} (Wf + Uh) + m_{13} U\phi = -i\alpha_0 \pi + \frac{1}{R} \left\{ f'' - (\alpha^2_0 + \beta^2_0) f \right\} \quad (26)$$

$$i \left\{ \alpha_0 U + \beta_0 W - \omega \right\} h + \frac{dW}{dy} \phi - 2m_{12} Uf + m_{21} (Uh + Wf) + m_{23} W\phi = -i\beta_0 \pi + \frac{1}{R} \left\{ h'' - (\alpha^2_0 + \beta^2_0) h \right\} \quad (27)$$

$$i \left\{ \alpha_0 U + \beta_0 W - \omega \right\} \phi - 2m_{13} Uf - 2m_{23} Wh = -\pi' + \frac{1}{R} \left\{ \phi'' - (\alpha^2_0 + \beta^2_0) \phi \right\} \quad (28)$$

$$\text{with } \alpha_0 = \frac{\alpha}{h_1} \quad \text{and } \beta_0 = \frac{\beta}{h_2} \quad (29)$$

It can be observed that the curvature effects have been neglected in the diffusion terms. This set of equations was used by Malik and Poll /39/. The equations governing the stability of waves whose wavenumber is tangent to X ($\beta = 0$) have been derived by Stuart /25/.

4.2 Reduction to a two-dimensional problem

In most of the stability analysis in three-dimensional flows, the curvature terms are neglected. This means that m_{12}, m_{21}, m_{13} , and m_{23} are set equal to zero, h_1 and h_2 being equal to 1. In these conditions, it is possible to eliminate f, h and π in (25) - (28) and to obtain an equation for the amplitude function ϕ :

$$\phi^{IV} - 2(\alpha^2 + \beta^2)\phi'' + (\alpha^2 + \beta^2)^2\phi = iR \left\{ (\alpha U + \beta W - \omega) (\phi'' - (\alpha^2 + \beta^2)\phi) - \left(\alpha \frac{d^2 U}{dy^2} + \beta \frac{d^2 W}{dy^2} \right) \phi \right\} \quad (30)$$

This equation can be considered as an extension of the Orr-Sommerfeld equation.

Studying (30) in the framework of the temporal theory, Stuart /25/ has shown that the problem of three-dimensional stability reduces to a two-dimensional problem. To establish this important result, it is sufficient to introduce the following quantities :

$$\alpha^2 \psi = \alpha^2 + \beta^2 \quad \text{and} \quad \tan \psi = \beta/\alpha \quad (31)$$

where ψ represents the angle formed by the direction of the wavenumber vector \vec{k} and the X -direction.

Equation (30) then becomes :

$$\phi^{IV} - 2\alpha^2 \psi \phi'' + \alpha^4 \psi \phi = iR \left\{ (\alpha \psi U \psi - \omega) (\phi'' - \alpha^2 \psi \phi) - \alpha \psi \frac{d^2 U \psi}{dy^2} \phi \right\} \quad (32)$$

$U\psi = U \cos \psi + W \sin \psi$ represents the projection of the velocity in the ψ -direction. We have, therefore, a two-dimensional equation (Orr-Sommerfeld equation) in the direction of the wave number vector.

In spatial theory, the complex nature of α and β makes such a manipulation impossible, except if the amplification and the wave number vectors have the same direction.

5 - CROSS-FLOW INSTABILITY

Stuart's result has a very important implication : relation (32) shows that, for studying the stability of a temporal wave in a three-dimensional flow, we have to solve a two-dimensional stability problem in each wave direction ψ . At each ψ , one can obtain a stability diagram relative to the mean velocity profile

projected in this direction. The implications of this property will be discussed below for the infinite swept wing and rotating disk flows.

5.1 Infinite swept wing

Let us consider at first the flow near the leading edge of a swept body with constant cross-section and "infinite" span, see figure 14. φ is the sweep angle. The freestream velocity Q_∞ gives a component normal to the leading edge U_∞ and component parallel to the leading edge W_∞ . Two coordinate systems are defined: one, (X, Z, y) is linked to the wing, and the other (x, z, y) is linked to the external streamline. U and W designate the projections of the mean velocity along X and Z .

The infinite span assumption is expressed by an invariance of pressure and velocities according to the Z direction, so that the boundary layer equations take the simple form:

$$\frac{\partial U}{\partial X} + \frac{\partial V}{\partial y} = 0 \quad (33)$$

$$U \frac{\partial U}{\partial X} + V \frac{\partial V}{\partial y} = U_e \frac{dU_e}{dX} + \nu \frac{\partial^2 U}{\partial y^2} \quad (34)$$

$$U \frac{\partial W}{\partial X} + V \frac{\partial W}{\partial y} = \nu \frac{\partial^2 W}{\partial y^2} \quad (35)$$

It can be observed that the first two equations are decoupled from the third and are the same as in two-dimensional flows. At the boundary layer edge, U and W attain values U_e and W_e : U_e depends on the chordwise position, but W_e is constant and equal to W_∞ (equation (35)).

The projections of the mean velocity along x and z are denoted by u and w , which are called respectively the streamwise profile and the cross-flow profile. If θ_0 is the angle between the external streamline (x axis) and the direction normal to the leading edge (X axis), u and w can be expressed as:

$$u = U \cos \theta_0 + W \sin \theta_0 \quad (36)$$

$$w = -U \sin \theta_0 + W \cos \theta_0$$

$$\text{with } \theta_0 = \tan^{-1} \frac{W_e}{U_e} \quad (37)$$

5.1.1 Leading edge region

Close to the leading edge, U_e and W_e are given by:

$$U_e = kX, \quad W_e = W_\infty \quad (38)$$

For $X = 0$, $U_e = 0$, $\theta_0 = \frac{\pi}{2}$ (the x axis coincides with the Z axis), $U(y) = 0$, so that, according to equations (36):

$$u = W \quad \text{and} \quad w = 0 \quad (39)$$

The line $X = 0$ is a particular streamline, along which there is no cross-flow, figure 34. It is called the attachment line and will be considered further, paragraph 8.

For $X > 0$, typical u and w profiles are sketched on figure 15. In the external flow, u is equal to the total velocity $u = (U_e^2 + W_e^2)^{1/2}$, whereas w tends to zero. The laminar similarity solutions indicate that the maximum value $|w_{\max}|$ of the cross-flow profile is proportional to X .

The stability problem will be studied in the (x, z, y) axis system. In this case, the angle ψ defined in (31) represents the angle between the external streamline and any given wave vector direction. As it is usual, we define ϵ as:

$$\epsilon = \frac{\pi}{2} - \psi \quad (40)$$

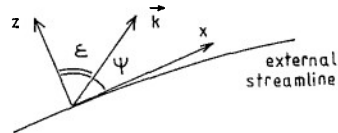
We have now to characterize the stability (or instability) of the velocity profiles projected in all directions from $\epsilon = 0$

(cross-flow profile) to $\epsilon = 180^\circ$. These profiles will be denoted by U_ϵ and are of course combinations of the cross-flow and streamwise profiles:

$$U_\epsilon = u \sin \epsilon + w \cos \epsilon \quad (41)$$

Figure 16 shows typical projected profiles for values of ϵ ranging from $\epsilon = 0$ (cross-flow profile) to $\epsilon = 90^\circ$ (streamwise profile). Crosses indicate the location of the inflexion points; the streamwise profile looks like a classical two-dimensional boundary layer profile in negative pressure gradient and for this reason its first derivative is monotonic; on the other hand, the cross-flow profile exhibits necessarily an inflexion point, and there is a range of low values of ϵ for which an inflexion point is also present. In particular, one can find a value of ϵ , denoted as ϵ_I , for which the inflexion point is located at the height where the mean velocity is equal to zero: this profile is called the critical profile.

Figure 17 presents schematic stability diagrams for $\epsilon = 0$, ϵ_I and 90° . The Reynolds number R is defined with the same reference variables for the three diagrams, for example $R = \left(\frac{U_e X}{\nu} \right)^{1/2}$.



The streamwise profile is very stable : the critical Reynolds number is high and, as R tends to infinity, there is no unstable frequencies (viscous instability). On the contrary, due to the presence of inflexion points, the other two profiles are highly unstable : the critical Reynolds number is low, the amplification factors are large and there is always a wide range of unstable waves at infinite Reynolds number (inflexional instability, see paragraph 2.2.3). The critical profile is even more unstable than the cross-flow one and can amplify zero frequency waves, which correspond to stationary waves ; this last property is also true for a narrow range of ϵ around ϵ_I , say $\epsilon \sim 2$ to 6 degrees. For the other values of ϵ , the stationary waves are damped.

The theoretical results can explain some of the experimental features described in paragraph 3. If the chord Reynolds number of a swept wing is large enough, cross-flow, or, more exactly, quasi-cross-flow instability is able to induce transition near the leading edge, in a region of strong negative pressure gradient. On the other hand, we expect that the streaks revealed by wall visualizations are the signature of zero-frequency waves amplified by the profiles in the neighbourhood of the critical profile. These points will be developed further in some length.

5.1.2 Downstream development

Consider now the downstream development of a laminar boundary layer on a typical airfoil where the external velocity reaches a maximum. As the equation of the external streamline is given by :

$$\frac{dz}{W_\infty} = \frac{dx}{U_e} \quad , \quad (42)$$

this external streamline will change its curvature at the abscissa x_M where U_e is maximum (figure 18). From the attachment line to x_M the cross flow is directed towards the concave part of the external streamline ; however, as x_M is approached, the pressure gradient intensity decreases, leading to a decrease in the cross-flow amplitude. The longitudinal pressure gradient then changes sign, and, somewhat downstream, the velocity w close to the wall reverses (S-shaped profiles). If the positive pressure gradient is sufficiently intense, the cross-flow profile can be completely reversed. In the same region, an inflexion point appears on the streamwise profile and, in most of the cases, this inflexional, streamwise instability leads to transition before the cross-flow instability begins to be significant again.

5.1.3 Falkner-Skan-Cooke profiles

This qualitative description explains the passage from the streamwise to the cross-flow instability. In order to study in a systematic manner the effects of three dimensionality on boundary layer stability, it is possible to use the so-called "Falkner-Skan-Cooke" similarity profiles. The inviscid velocities normal and parallel to the leading edge are given by :

$$U_e = kx^m \quad , \quad W_e = W_\infty \quad , \quad \text{where } k, m \text{ and } W_\infty \text{ are constants.} \quad (43)$$

By using the similarity variables :

$$\eta = \left(\frac{m+1}{2} \frac{U_e}{\nu x} \right)^{1/2} y \quad , \quad \frac{U}{U_e} = \bar{F}(\eta) \quad , \quad \frac{W}{W_e} = \bar{G}(\eta) \quad (44)$$

the boundary layer equations reduce to the ordinary differential equations :

$$\bar{F}''' + \bar{F} \bar{F}'' + \beta_h (1 - \bar{F}'^2) = 0 \quad (45)$$

$$\bar{G}'' + \bar{F} \bar{G}' = 0 \quad (46)$$

where $\beta_h = \frac{2m}{m+1}$. The leading edge flow corresponds to $\beta_h = 1$, $m = 1$.

The angle between the external streamline and the normal to the leading edge is $\theta_0 = \tan^{-1} \left(\frac{W_e}{U_e} \right)$, so that the streamwise and cross-flow profiles, made dimensionless with u_e , are expressed by :

$$\frac{u}{u_e} = \bar{F}' \cos^2 \theta_0 + \bar{G} \sin^2 \theta_0 \quad (47)$$

$$\frac{w}{u_e} = (\bar{G} - \bar{F}') \cos \theta_0 \sin \theta_0$$

It is now possible to construct streamwise and cross-flow profiles depending on two parameters : a pressure gradient parameter β_h , which is the same as in two-dimensional similarity solutions, and a "cross-flow" parameter θ_0 . Let us observe that the cross-flow velocity is maximum for $\theta_0 = 45^\circ$.

Figure 19 shows examples of cross-flow velocity profiles for $\theta_0 = 45^\circ$ and some values of β_h (Mack, /8/). It is clear from equations (45) - (46), that for $\beta_h = 0$, $\bar{F}' = \bar{G}$, so that $\frac{u}{u_e}$ is the Blasius

profile and $w = 0$. For $\beta_h < 0$, the whole cross-flow profile changes sign. This means that the Falkner-Skan-Cooke solutions cannot represent S-shaped profiles.

The stability of the Falkner-Skan-Cooke profiles was studied by Mack /8/ and Bieler /40/. An interesting result is given in figure 20 : it presents the critical Reynolds number of the zero-frequency disturbances as a function of β_h , for $\theta_0 = 45^\circ$; the critical Reynolds number of the two-dimensional Falkner-Skan

profiles is also shown ($\theta_0 = 0^\circ$). The Reynolds number is defined as :

$$R = \left(\frac{u_e X}{\nu} \right)^{1/2} \frac{1}{\cos \theta_0} = \left(\frac{u_e x}{\nu} \right)^{1/2} \quad (48)$$

For sufficiently strong negative pressure gradients ($\beta_h > 0.07$), the steady quasi cross-flow disturbances become unstable at Reynolds numbers well below the critical Reynolds number of the two-dimensional profiles. In adverse pressure gradients, the contrary is true.

Figure 21 shows the portion of the ψ -F plane for which there is instability, for two cases (from Mack, /8/) :

Figure	β_h	θ_0	R	H	$(w/u_e)_{\max}$
20 a	1	45°	400	2.301	- 0.1191
20 b	- 0.10	45°	555	2.698	0.0349

Let us recall that ψ is the angle between the external streamline and the wavenumber vector, and F is a dimensionless frequency ($F = 2\pi f^* \nu / u_e^2$). The dotted lines represent the loci of the maximum amplification rates, the maximum maximum being denoted by the letter M.

In the strong negative pressure gradient (figure 21a, $\beta_h = 1$), the instability is cross-flow dominated. The stationary waves are unstable in directions close to the cross-flow direction, but they are not the most unstable ones.

In a positive pressure gradient (figure 21b, $\beta_h = -0.1$), unstable stationary waves are still observed, and a wide range of unstable travelling waves extend around the streamwise direction. This is a typical example of boundary layer with both cross-flow and streamwise instabilities.

5.2 Rotating disk

The exact solution of the Navier-Stokes equations for a rotating disk was first given by von Karman (1921) and later improved by Cochran (1934). Let us consider a flat disk which rotates about an axis perpendicular to its plane, with a constant angular velocity ω , in a fluid at rest. The situation is depicted in figure 22 taken from Schlichting /41/. It is natural to use a coordinate system (r, θ, y) , where r is the radius, θ the azimuth angle and y is normal to the disk. If the corresponding velocity components are denoted as u_r, u_θ, u_y , von Karman's solution is obtained by setting :

$$u_r = r\omega \bar{F}(\zeta), \quad u_\theta = r\omega \bar{G}(\zeta), \quad u_y = \sqrt{\nu\omega} \bar{H}(\zeta) \quad (49)$$

where $\zeta = y\sqrt{\omega}$ is a dimensionless distance from the wall. The functions $\bar{F}, \bar{G}, \bar{H}$ are tabulated in /41/. The velocity field is sketched in figure 22. It is clear that the centrifugal forces give rise to a radial velocity which is directed outwards. Equations (49) show that, at a given height above the wall, the axial velocity u_y is constant, whereas the radial and circumferential velocities are proportional to r .

In the coordinate system rotating with the disk, the azimuthal and radial velocity profiles, made dimensionless with $r\omega$, are given by :

$$\frac{u}{r\omega} = 1 - \bar{G} \quad \text{and} \quad \frac{w}{r\omega} = \bar{F} \quad (50)$$

These profiles are plotted in figure 23. They look like the streamwise and cross-flow profiles encountered near the leading edge of a swept wing. The streamwise (azimuthal) profile has no inflexion point, so that it cannot explain the breakdown into turbulence which occurs some distance from the disk axis ; this breakdown is caused by the highly unstable nature of the profiles close to the cross-flow (radial) direction.

Stuart /25/ analyzed the linear, inviscid stability of rotating disk flow. He noted that the critical profile ($u'' = 0$ at ζ where $u = 0$) was located at an angle $\varepsilon = 13.2^\circ$ from the radial direction, ε being measured in the positive θ direction. This corresponds approximately to the direction perpendicular to the stationary vortices observed in the experiments of Gregory and Walker /25/, see figure 13. Brown /42/ extended Stuart's work to the viscous case. He demonstrated that, for $\varepsilon = 11.5^\circ$, stationary disturbances are unstable, and that these disturbances consist of a system of vortices all rotating in the same sense. The theoretical number of vortices was in fairly good agreement with experiments. However, Brown found a critical Reynolds number much less than the observed value. In fact, as he used the Orr-Sommerfeld equation, Coriolis force and streamline curvature were neglected. As it will be shown later, these parameters are of first importance in the rotating disk problem.

6 - STATIONARY AND TRAVELLING WAVES ON A SWEEPED BODY

6.1 Stationary waves

Both experiments and calculations have shown that zero frequency, stationary waves can be highly amplified in three-dimensional flows. We describe below some additional experimental results obtained on swept bodies and compare them with stability computations.

Stationary waves have been studied at ONERA/CERT on an ONERA D profile /23/ /30/. The angle of sweep φ and the normal angle of attack are equal to 40° and -8° respectively. The distribution of the external velocity normal to the leading edge is plotted in figure 24 ; it can be seen that the flow is accelerated over the entire profile.

For $Q_\infty = 81$ m/s, figure 25 shows the variation of the mean streamwise velocity measured in the Z direction parallel to the leading edge, at a fixed altitude $y = 0.09$ mm, for various abscissas. The test

conditions are the same as in figure 12. In laminar flow, the mean velocity exhibits a quite regular wavy evolution in the spanwise direction ; the spanwise wavelength corresponds to the spacing of the streaks revealed by the wall visualization shown in figure 12. In the transition region, the evolution becomes completely chaotic. However, when the turbulent regime is entered, the velocity variations are damped. It appears essentially that the laminar boundary layer is not uniform in the direction parallel to the leading edge. This leads to a wavy evolution of the skin friction coefficient, which produces alternate light and dark bands (streaks) when sublimation techniques are applied.

In order to make more accurate measurements, the wind tunnel speed Q_∞ was reduced to 48 m/s ; the wavelength of the streaks then increases, as well as the laminar boundary layer thickness, and transition moves back to $X_T/c = 0.85$ (instead of $X_T/c = 0.30$ with $Q_\infty = 81$ m/s). Detailed results can be found in /23/, /30/. Figure 26 shows the streamwise evolution of the wavelength λ^* measured in the direction parallel to the leading edge. λ^* increases with x , but the ratio λ^*/δ remains practically constant and close to 4. In fact, the increase in λ^* results from a decrease in the number of streaks : sublimations indicate that certain streaks broaden and coalesce, while other vanish. Stability computations can explain this behaviour : the temporal amplification factor ω_i^* of the stationary waves is plotted in figure 27 as a function of ϵ , at the station $X/c = 0.69$. The curve is parametrized by the wavelength λ^* . It is clear that the stationary waves are unstable through a narrow range of ϵ ($1.4^\circ < \epsilon < 3^\circ$, approximately) but that the range of their wavelengths is quite large. Similar computations were carried out at other streamwise locations, and the total amplification rate was computed for some selected wavelengths : the values of the locally most amplified wavelengths agree well with experimental data (figure 26).

Poll /24/, /31/ measured the characteristics of the streaks appearing on a swept cylinder. He found that their direction was close, but not perfectly aligned, with the critical profile direction. Stability calculations performed by Malik and Poll /39/ are in reasonable agreement with experiments : for the wavelength of the stationary disturbances, the discrepancy is less than 10 %, and for the wavenumber orientation, the difference is of order 2° . A similar agreement was obtained by Bieler /40/ who compared his numerical results with the experimental data of Bippes and Nitschke /43/.

Saric and Yeates /32/ made measurements on a flat plate having a swept leading edge ; the streamwise pressure gradient was induced by an appropriate wall bump. With $\phi = 25^\circ$ and $Q_\infty = 10$ to 14 m/s, wall visualizations show that the spacing of the streaks is approximately 1 cm ; linear stability theory indicates that the most unstable stationary wave has a wavelength of about 1 cm. However, hot-wire measurements indicate a dominating 0.5 cm structure away from the wall ; linear theory cannot explain this observation and it is necessary to use secondary instability theory for explaining this superharmonic pattern /44/.

6.2 Travelling waves

Stationary waves constitute the most clearly visible manifestation of quasi cross-flow instability, but linear theory predicts that travelling waves can also be highly amplified. This is illustrated on figure 28, which presents numerical results obtained for the experimental conditions of figure 26. The temporal amplification rate is plotted as function of ϵ for various frequencies : there is a large range of unstable frequencies, the most unstable of which corresponds to $f^* = 400$ Hz (and not to $f^* = 0$ Hz). Are all these frequencies present in the experiments ?

Profiles of the r m s velocity fluctuations measured at $X/c = 0.40$ and 0.60 are represented on figure 29 in the (y, Z) plane. As it can be expected, their spanwise evolution is not uniform. During a wavelength two maxima are observed near the wall ; they are located in the regions where $|\partial u / \partial Z|$ is large. At $X/c = 0.60$, the fluctuation amplitude reaches 20 % of the potential velocity, a value which is about twice that which is measured in a classical turbulent boundary layer ! So large values have already been reported by Poll /31/ in his experiments on a swept cylinder. Typical hot wire signals are also shown in figure 30. At $X/c = 0.40$, the signal is quite regular, with a dominant frequency of about 70 Hz while the other theoretically unstable waves are not detected. It is not easy to explain the origin of this preferred frequency (secondary, resonant instability ?). At $X/c = 0.60$, the fluctuations are less regular, and small amplitude, high frequency oscillations are superimposed on the large amplitude, low frequency oscillations. Poll /31/ found the same kind of hot wire signals, but at very different dimensionless frequency (influence of the local pressure gradients ?).

If it is assumed that large amplitude travelling waves appear only as a secondary instability of the primary, stationary waves, then one would like to know why the other linearly unstable mode are not excited. As pointed out by Malik (private communication), a possible reason may be that disturbance sources (such as wall roughness) favor the stationary mode.

7 - APPLICATION OF THE e^n METHOD IN THREE-DIMENSIONAL FLOWS

In two-dimensional flows, the use of linear stability theory associated with an e^n breakdown criterion, gives fairly good results ; the n factor can be related to the free-stream disturbances environment and takes a value of about 9-10 when the external turbulence level is low. Whatever theory one considers for solving the eigenvalue problem, four parameters are involved ; either $(R, \omega_r, \omega_i, \alpha)$ in the temporal theory or $(R, \omega, \alpha_r, \alpha_i)$ in the spatial theory.

7.1 Calculation of the n factor

The extension of the e^n method to three-dimensional flows is not straightforward : we now have either five real parameters in temporal theory $(R, \omega_r, \omega_i, \alpha, \beta)$ or six in spatial theory $(R, \omega, \alpha_r, \alpha_i, \beta_r, \beta_i)$. Only two of them must be determined as eigenvalues, while the others are given.

The increase in the number of parameters explains why three-dimensional problems are generally treated with respect to the temporal theory. The total amplification rate $\ln \frac{A}{A_0}$ for a given frequency ω_r is computed by using a generalized Gaster's transformation :

$$\ln \frac{A}{A_0} = \int_{s_0}^s \frac{\omega_i}{|\text{Re}(\vec{V}_g)|} ds \quad (51)$$

where $\vec{V}_g = (\partial\omega/\partial\alpha, \partial\omega/\partial\beta, 0)$ is the group velocity vector and s is the arclength along the group velocity direction, which is most of the time close to the external streamline direction. The n factor is then defined as in two-dimensional flow, relation (9).

In fact, when R and ω_r are fixed, the value of ω_i is not unique, because $\omega_i = \omega_i(\psi)$, where ψ is the wave number direction. The so called envelope method seeks the direction ψ for which ω_i is maximum; this maximum value is then integrated according to relation (51). This technique is the most widely used in three-dimensional stability computations. In order to reduce computer time requirements, Srokowski and Orszag /45/ simplify the problem by studying only the stationary waves.

Another solution is to use the fixed wavelength and frequency method: for given frequency and wavelength λ^* , the value of ω_i is integrated along the abscissa. The envelope curve is then obtained once considered several wavelengths and frequencies. Srokowski-Orszag /45/ and Dagenhart /46/ employed this technique for the zero-frequency waves, as well as Hefner-Bushnell /47/ for non zero-frequency waves.

In spatial theory, the problem is even more complicated, because of the appearance of an additional parameter: the amplification rate is not a scalar anymore, but a vector $A = (-\alpha_i, -\beta_i, 0)$. A simple solution is to assume $\beta_i = 0$, Mack /48/. Alternatively, it is possible to use wave packet theory to remove the arbitrariness in the definition of the total amplification rate; Nayfeh /49/ has derived the propagation condition that $d\alpha$ must be real. This approach was used by Cebeci and Stewartson /50/ for computing the stability properties of the laminar flow on a rotating disk.

Malik and Orszag /51/ compared the results given by the envelope method and a (modified) wave packet method. They demonstrated that "for a given case, the ultimate values of n are only very weakly dependent upon the approach adopted". Although the wave packet theory is physically more relevant, it is more expensive to use than the envelope method. On the other side, the fixed wavelength/ frequency approach leads to n factors somewhat lower than those deduced from the envelope method /47/.

7.2 Calibration of the e^n rule

Another problem is to see if experimental transitions occur at nearly constant n for several flow conditions. Figure 31 shows numerical results obtained by Hefner and Bushnell /47/ who used the SALLY code of Srokowski and Orszag /45/. The integrated cross-flow instability amplification ratios deduced from the envelope method are presented for the experimental conditions of Burrows and Allen /26/, /27/, and the symbols denote the (estimated) transition points. Although the n_T factors vary from 7.6 to 11, their values are not far from those currently computed in two-dimensional flows. An interesting result is that the most amplified cross-flow instabilities occur at relatively high frequencies; the stationary waves are unstable, but are not the most unstable ones. A similar result was obtained by Coustols (unpublished) for the experimental conditions of figures 25 to 28: at the transition location, n is equal to 7.4 for 500 Hz and to 4.4 for the stationary disturbances.

The COSAL code developed by Malik was tested by Malik and Poll /39/ for predicting transition on the windward face of a long yawed cylinder, for which experimental data were available (Poll /24/). The envelope method is also used, and the curvature terms are introduced in the stability equations (this is not the case in the SALLY code, which solves the Orr-Sommerfeld equation according to Stuart's theorem which neglects curvature terms). The integrated amplification rates of the most unstable frequencies are plotted in figure 32 for two experimental cases. It can be seen that for the computations including curvature effects, the n factors at transition are 11 or 12. However, when the curvature terms are omitted, the values of n_T are found to be 17 or 18. This shows that the body curvature and streamline curvature terms produce strong damping effects. On the other side, we observe that the cross-flow instability is dominated by non-zero frequency waves.

The stabilizing influence of streamline curvature was also demonstrated for the rotating disk flow by Malik, Wilkinson and Orszag /52/. In this case, the most unstable waves are stationary. Figure 33 shows the integrated growth factors deduced from the Orr-Sommerfeld equation by Cebeci-Stewartson (wave packet method, /50/) and by Malik et al (envelope method). Both calculations give n_T factors greater than 20. But, when the effects of Coriolis force and streamline curvature are taken into account, the value of n at transition is reduced to 11, and the amplification curve agrees well with experimental data. In particular, the critical Reynolds number is about 50 % greater than that found by Brown and Cebeci-Stewartson.

These examples indicate that the Orr-Sommerfeld equation cannot provide accurate estimates of the disturbances growth if the curvature effects and/or the Coriolis force are of importance. However, in the scope of airfoil applications, these terms can be neglected provided transition occurs not too close to the leading edge. It is encouraging to observe that the total amplification rates do not depend strongly on the integration procedure, and that the use of appropriate equations leads to n_T factors lying in the range 7-11, as in two-dimensional flows.

8 - ATTACHMENT LINE PROBLEMS

8.1 Laminar boundary layer characteristics

It has been said (paragraph 5.1.1) that the attachment line is a particular streamline, which divides the flow into one branch following the upper surface of the body and another branch following the lower surface, see figure 34. Let us consider the simplest case of a swept cylinder of constant radius r .

In the streamline coordinate system (x, z, y) , x coincides with the attachment line, and the potential velocity reduces to $u_e = Q_\infty \sin \varphi$. The boundary layer profile is obtained by setting $m = \beta_h = 1$ and $\theta_0 = \frac{\pi}{2}$ in the Falkner-Skan-Cooke solutions, relations (43) to (47) :

$$\frac{u}{u_e} = \bar{G}(\eta), \quad \frac{w}{u_e} = 0, \quad \frac{v}{u_e} = - (kv)^{1/2} \bar{F}(\eta) \quad (52)$$

with $\eta = y \left(\frac{k}{v}\right)^{1/2}$, $k = \left(\frac{du_e}{dx}\right)_{x=0}$

In other words, the mean velocity profile is two-dimensional. But, in contrast with true two-dimensional situations its thickness is constant in the x direction, although the velocity v normal to the wall is not equal to zero.

By integration of the $\bar{G}(\eta)$ profile, one can find :

$$\delta_1 = 1.026 (v/k)^{1/2} \quad \theta_{11} = 0.404 (v/k)^{1/2} \quad H = \delta_1/\theta_{11} = 2.54$$

$$R\theta_{11} = 0.404 Q_\infty \sin \varphi / (vk)^{1/2} \quad (53)$$

As it can be seen on figure 35, the attachment line velocity profile ($H = 2.54$) looks like the Blasius profile ($H = 2.59$).

For a circular cylinder of radius r , k and $R\theta_{11}$ can be expressed as :

$$k = 2 \frac{Q_\infty \cos \varphi}{r}, \quad \text{and } R\theta_{11} = 0.404 \left(\frac{Q_\infty r}{v} \frac{\sin^2 \varphi}{2} \right) \quad (54)$$

The characteristic Reynolds number $\bar{R} = R\theta/0.404$ was also used by many authors.

The preceding results are valid for an attachment line of infinite extent. In practical situation, however, the attachment line has an origin (say, $x = 0$), but, for the sake of simplicity, we will assume that the similarity solution described above applies as soon as $x > 0$.

8.2 "Free" transition

The neutral curves of the attachment line profile and of the Blasius profile are compared on figure 36 ; the former is somewhat more stable than the latter : its critical $R\theta_{11}$ is 260, instead of 201.

If there is no source of large disturbances at $x = 0$, we can guess that transition will be the result of the amplification of internalized small fluctuations which are present, for instance, in the free-stream. Pfenninger and Bacon /53/ made hot-wire measurements along the attachment line of a 45° swept wing. They observed the occurrence of regular, quasi sinusoidal oscillations in the form of modulated wave packets ; as these wave packets are convected along the leading edge, their amplitude increase and turbulent spots (break-down) eventually appear. Similar observations were reported by Poll/24/. In most of the cases, the waves are detected for configurations such that $R\theta_{11}$ is greater than 230, a value which is close to the critical $R\theta_{11}$ of the attachment line profile.

The theoretical calculation of the total amplification rate A/A_0 of a given frequency is very simple : for fixed values of Q_∞ , φ and r , $R\theta_{11}$ is constant in the spanwise direction, so that A/A_0 is expressed as :

$$A/A_0 = \exp \left\{ -\alpha_1 x \right\} \quad (55)$$

This means that, if we plot $\ln \frac{A}{A_0}$ as a function of x , we obtain straight lines parametrized with ω , and the n curve is reduced to the line corresponding to the most unstable frequency (the frequency for which $-\alpha_1$ is maximum). By applying the e^n rule, the transition location x_T is :

$$x_T = n / (-\alpha_1)_{MAX} \quad (56)$$

Figure 37 (Poll /24/) presents the results of such computations for $n_T = 6, 10, 14$, together with experimental data. For $R\theta_{11} < 230$, transition never takes place on the attachment line. For higher values, transition is observed and moves towards the attachment line origin as $R\theta_{11}$ is increased : in this case, a part of the leading edge is laminar, another part is transitional, and a third part is turbulent ! Theoretical results with $n_T \approx 6$ reflects fairly well this evolution.

8.3 Leading edge contamination

If the wing is in contact with a solid wall (fuselage, wind tunnel wall...), it has been observed that turbulence appears on the attachment line for $R\theta_{11} > 100$. Clearly, this observation cannot be explained in terms of linear stability theory. In fact, the leading edge is contaminated by the large turbulent structures coming from the wall at which the model is fixed, without resorting to linear processes (bypass).

In order to examine this behaviour, Poll /24/ investigated the response of the attachment line boundary layer to the presence of wires the axes of which were normal to the leading edge direction. If the wire diameter, d , is made dimensionless with the length scale $\bar{\eta} = (v/k)^{1/2}$, four $d/\bar{\eta}$ ranges are to be distinguished, as it is illustrated in figure 38 :



. For $0 < d/\bar{\eta} < 0.7$, the wire does not play any role, and transition is triggered by 'free' mechanisms

as describe above.

. For $0.7 < d/\bar{\eta} < 1.5$, the wire begins to control transition ; the location of the first turbulent spots moves closer to the wire when $R\theta_{11}$ is increased.

. For $1.5 < d/\bar{\eta} < 1.9$, the flow is either fully laminar or fully intermittent behind the wire, depending on the value of $R\theta_{11}$.

. For $d/\bar{\eta} > 1.9$, turbulent bursts always appear immediately behind the wire. But, if $R\theta_{11}$ is lower than 100, they decay more or less rapidly and vanish as they are convected along the attachment line. If $R\theta_{11}$ is greater than 100, the turbulent bursts are self-sustaining : they grow, overlap and turbulent contamination process takes place. It is clear that there is a strong similarity with the leading edge contamination induced at the wing-fuselage junction.

9 - TRANSITION CRITERIA

The use of linear stability theory for predicting the transition onset leads to satisfactory results, but involves time consuming and expensive calculations. For this reason, the development of simple criteria presents an unquestionable practical interest.

Generally speaking, the use of such criteria is based on the following rule : it is assumed that the turbulence will appear either by streamwise instability or by cross-flow instability, or else by leading edge contamination. Criteria are applied for each one of these mechanisms, and it is assumed that the boundary layer will cease to be laminar as soon as one of them is satisfied.

9.1 Leading edge contamination

Let us recall that the dominant parameter is the Reynolds number $R\theta_{11}$:

$$R\theta_{11} = 0.404 \frac{Q \cos \varphi}{\sqrt{v_k}} \quad , \quad \text{with } k = \left(\frac{dU_e}{dX} \right)_{X=0} \quad (57)$$

From experimental results, it appears that a complete leading edge contamination occurs when $R\theta_{11}$ is greater than 100 (paragraph 8.3).

9.2 Streamwise criterion

As the properties of the streamwise profiles are close to those of two-dimensional profiles, it is often assumed that two-dimensional criteria remain valid in three dimensional flows, provided they are applied along an external streamline. For example, the criterion described in paragraph 2.3 will take the following form :

$$R\theta_{11} - R\theta_{11cr} = f(\bar{\Lambda}_{2T}, Tu) \quad (58)$$

$$\text{with } \bar{\Lambda}_{2T} = \frac{1}{s_T - s_{cr}} \int_{s_{cr}}^{s_T} \frac{\theta_{21}}{v} \frac{du_e}{ds} ds$$

where s designates the curvilinear abscissa measured along the external streamline.

9.3 Cross-flow criteria

The first attempt to explain the destabilizing effect of sweepback on laminar boundary layer is due to Owen and Randall (1952, 1953, /54/, /55/), with an independant contribution by Squire (1952, /56/). Owen and Randall related the cross-flow instability mechanism to a Reynolds number χ defined as :

$$\chi = \frac{|w \max| \delta}{v} \quad (59)$$

and propose a critical value $\chi = 175$ at the transition location. Later studies showed that this value was too low, because the experiments from which the criterion was derived were biased by leading edge contamination problems.

In 1973, Beasley /57/ developed a criterion which involved the cross-flow Reynolds number $R\delta_2$. Calculating the value of this parameter at the transition onset for a certain number of experiments, Beasley proposed : $(R\delta_2)_T = 150$. However, it is clear that the use of a single value of any cross-flow parameter cannot give good results in all situations. For this reason, two more elaborate criteria, labelled C1 and C2, have been developed at ONERA/CERT /58/ /59/.

9.3.1 C1 Criterion

By computing the laminar boundary layer development for a rather great number of experimental cases, it was found that the cross-flow transitions did not take place for a unique value of $R\delta_2$. Various attempts to correlate $R\delta_{2T}$ with characteristics of the cross-flow profile have not allowed to put together the experimental data. Better results have been obtained by associating the transition Reynolds number with a parameter linked with the streamwise velocity profile. Figure 39 shows a correlation between $R\delta_{2T}$ and the streamwise shape factor, H , at the transition location. A mean curve can be represented by :

$$R\delta_{2T} = \frac{300}{\pi} \tan^{-1} \left(\frac{0.106}{(H_T - 2.3)^{2.05}} \right) \quad (60)$$

The application of this formula is limited to shape factors less than 2.7. For greater values, the transition phenomena are dominated by the streamwise instability. It can be observed that relation (60) does not take into account the free-stream turbulence level Tu .

Let us notice that Poll /31/ gave a similar correlation, by using χ instead of $R\delta_2$.

9.3.2 C2 Criterion

The cross-flow correlation presented above is fully empirical. As it was done for the streamwise criterion, we have tried to use the results of laminar instability theory to develop a more rigorous method for predicting cross-flow transitions.

This method is based on Stuart's theorem, already discussed in paragraph 4.2 : to study the stability of perturbations in a given direction which makes an angle ϵ with the cross-flow direction, it is sufficient to consider the mean velocity profile $U\epsilon$ projected in that direction. For purposes of more convenient analysis, $U\epsilon$ is normalized with $U\epsilon_e = u_e \sin \epsilon$ ($\epsilon \neq 0$ and 180°) :

$$\frac{U\epsilon}{U\epsilon_e} = \frac{u}{u_e} + \frac{w}{u_e} \cot \epsilon \quad (61)$$

By varying ϵ from 0° to 90° , one moves continuously from the cross-flow profile to the streamwise profile.

We then define for these profiles a displacement thickness $\delta_1\epsilon$ and the corresponding Reynolds number $R\delta_1\epsilon$:

$$\delta_1\epsilon = \int_0^\delta \left(1 - \frac{U\epsilon}{U\epsilon_e}\right) dy \quad (62)$$

$$R\delta_1\epsilon = \frac{U\epsilon_e \delta_1\epsilon}{\nu} = \sin \epsilon R\delta_1 + \cos \epsilon R\delta_2$$

The next step is to describe the stability, or instability, of the $U\epsilon$ profiles. In this regard, the critical Reynolds number $R\delta_1\epsilon_{cr}$ is an essential parameter. Stability calculations have therefore been carried out for a great number of typical $U\epsilon$ profiles computed in the conditions of Boltz, Kenyon and Allen experiments /28/. The reader will find a tabulation of the results in /59/.

For a given experimental case, with given chord Reynolds number and abscissa, a function $g(\epsilon)$ is defined as :

$$g(\epsilon) = R\delta_1\epsilon_{cr} / R\delta_1\epsilon \quad (63)$$

If $g(\epsilon)$ is greater than 1, the profile $U\epsilon/U\epsilon_e$ under consideration will be stable. If $g(\epsilon)$ is less than 1, it will be unstable. Let us observe that $R\delta_1\epsilon$ varies as the square root of R_c , whereas $R\delta_1\epsilon_{cr}$ remains invariant. In other words, if $g_1(\epsilon)$ and $g_2(\epsilon)$ correspond to R_{c1} and R_{c2} , we will have :

$$\frac{g_1}{g_2} = \left(\frac{R_{c2}}{R_{c1}}\right)^{1/2} \quad (64)$$

When the chord Reynolds number increases, g decreases and the range of unstable directions widens.

Figure 40 shows the change in g in three abscissas relative to the configuration $\varphi = 20^\circ$, $\alpha = 0^\circ$ of the Boltz, Kenyon and Allen experiments, for $R_c = 4.33 \cdot 10^6$. The chord Reynolds number R_c is defined as :

$$R_c = \frac{Q_\infty c}{\nu \cos \varphi} \quad (65)$$

where c is the chord normal to the leading edge.

At the first abscissa, close to the attachment line, the curve $g(\epsilon)$ is minimal for ϵ close to 2 degrees, but the streamwise flow remains very stable. At the last abscissa, $X/C = 0.48$, the curve $g(\epsilon)$ has two minimums, close to the cross-flow and streamwise directions, the second being an absolute minimum : streamwise instability is preponderant here. Let us note that at the intermediate position, $X/C = 0.35$, the two types of instability already coexist, with comparable levels. These curves show the passage from quasi-cross-flow instability to streamwise instability.

The computation of the critical Reynolds number $R\delta_1\epsilon_{cr}$ takes long, and therefore costly, calculations. As a consequence, $R\delta_1\epsilon_{cr}$ has been represented as a function of the height of the inflexion point and of the first derivative of $U\epsilon$ taken at the inflexion point (figure 41). If $U\epsilon$ does not exhibit some inflexion point, the critical Reynolds number is simply a function of some integral parameter, such as the shape factor.

At a given abscissa, a laminar boundary layer calculation supplies the streamwise and cross-flow profiles, as well as the Reynolds numbers $R\delta_1$ and $R\delta_2$. For each ϵ , $R\delta_1\epsilon$ is obtained from relation (62) and $R\delta_1\epsilon_{cr}$ is deduced from the previously described representations. This provides the plotting of the curve $g(\epsilon)$ and the determination of the direction ϵ_{min} for which $g(\epsilon)$ is minimum in the neighbourhood of the cross-flow direction. Such a calculation was carried out for available experiments on "infinite" swept wings.

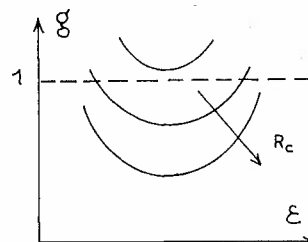


Figure 42 brings together the values of $R\delta_1 \varepsilon$ for $\varepsilon = \varepsilon_{\min}$, at the experimental transition points. As in the case of the Cl criterion, it was decided to plot this quantity as a function of the streamwise shape factor H. It is observed that the points collapse on different curves, a fact which seems to show the influence of the free-stream turbulence level Tu . Although such a representation is both "daring" and difficult, this set of curves $R\delta_1 \varepsilon_T(\varepsilon = \varepsilon_{\min}) = f(H, Tu)$ will be considered as a cross-flow criterion.

9.4 Examples of applications

9.4.1 Application to swept wings

At first the aforementioned criteria were applied to different experiments which were used to develop them. For each case, the movement of transition is represented as a function of the chord Reynolds number Rc , defined in relation (65).

Figure 43 gives a comparison of the calculations with two experiments carried out by Boltz, Kenyon and Allen /28/. The two cross-flow criteria give results that are very closed. The case $\varphi = 20^\circ$, $\alpha = 0^\circ$ clearly shows the passage from streamwise instability (in positive pressure gradient) to cross-flow instability (in negative pressure gradient). The value of Rc for which leading edge contamination occurs lies beyond the range of experimental Reynolds numbers. For $\varphi = 50^\circ$, $\alpha = 0^\circ$, there is practically no streamwise transition.

Detailed comparisons with other available data on "infinite" swept wings are given in Coustols /59/.

In figure 44, experimental and theoretical transition locations are compared in the case of a tapered wing. The measurements were performed by Schmitt /60/ on the M6 wing; the angle of sweep is 30° at the leading edge and $15,8^\circ$ at the trailing edge. Two calculations are presented for $Q_\infty = 90$ m/s, $\alpha = -5^\circ$ and -15° : the first one uses the integral method developed by Cousteix and Aupoix /62/, in which the Cl criterion is introduced. For $\alpha = -5^\circ$, streamwise and cross-flow instabilities are of equal importance, and the theoretical transitions lines are very sensitive to the numerical methods used. For $\alpha = -15^\circ$, cross-flow instability dominates, and both methods give similar results.

9.4.2 Attachment line in "free" conditions

It is a typical case where transition is entirely governed by the streamwise instability, see paragraph 8.2, but the streamwise criterion is unable to predict it; in fact, with $Tu \approx 0.1 \cdot 10^{-2}$ and $\Lambda_2 = 0$, relation (58) leads to $R\theta_T \approx 1100$. In addition, the criterion indicates that all the attachment line becomes at once turbulent from $x = 0$. All these results are in variance with available experiments, figure 36.

The shortcoming of the criterion (and of all criteria which involve boundary layer parameters) can be explained as follows: the perturbations leading to transition propagate and are amplified along the flow direction, that is to say along a physical distance. Presently, the criterion involves $R\theta$, a Reynolds number based on a characteristic boundary layer thickness; in two dimensional flow, it gives good results, because an implicit relation exists between $R\theta$ and the streamwise distance. This relation remains more or less verified along the external streamlines of a swept wing, but fails dramatically in more complex three-dimensional configurations, where the streamlines are far from being parallel. In fact, it is necessary to come back to the initial concept of waves propagation in the physical space.

9.4.3 Prolate spheroid

Experiments were carried out by Meier, Kreplin and Vollmers /38/ on a prolate spheroid at zero and non zero angles of incidence. Figure 45 shows the external streamlines pattern for $\alpha = 10^\circ$, as computed by Gleyzes and Cousteix /63/ from the measured wall pressure distributions.

Measured and computed transition lines are compared in figure 46. ξ is the circumferential angle; $\xi = 0$ and 180° correspond to the lower and upper symmetry lines, respectively (Gleyzes, Cousteix, Aupoix /65/, Jelliti /61/). A reasonable agreement is observed for $45^\circ < \xi < 180^\circ$: both local and integral methods indicate that transition is cross-flow dominated around $\xi = 90^\circ$, while streamwise instability is preponderant towards the upper symmetry line. However, there is a strong discrepancy for $0 < \xi < 45^\circ$: the experiments detected transition in this region, but the criteria were unable to predict it. In fact, the problem is similar to that previously discussed: if we except the region close to the stagnation point, the lower symmetry line looks like the attachment line of a cylinder with an angle of sweep $\varphi = \frac{\pi}{2} - \alpha$.

The laminar boundary layer calculations confirmed this point of view by showing that the characteristic thicknesses were nearly constant along the line $\xi = 0^\circ$, with a shape factor close to 2.5. The only way to improve the agreement with experiments is to solve the stability equations and to compute the n factor by integrating the local amplification rates along the external streamlines. When this is done, transition is found to occur in the region where criteria cannot detect it. (Jelliti, /61/). Cebeci /64/ used also the linear stability theory and predicted some points of the transition line with a very good accuracy.

Meier et al gave estimates of the transition region extent by measuring the evolution of the wall shear stress vector. These results were used for checking the intermittency method initially developed in two-dimensional flow (paragraph 2.4). The extension of this method to three-dimensional flows is described in /23/: when the local boundary layer equations are solved, the Reynolds shear stresses $-u'v'$ and $-v'w'$ are multiplied by the same intermittency function; when the global boundary layer equations are solved, three-dimensional integral parameters are weighted by γ , in addition to the parameters already used in two-dimensional flows. A comparison between numerical results and experimental data indicate that the both methods give a correct estimate of the transition length, as it is illustrated in figure 47. In these calculations, the transition onset is located at the experimental transition point. It is also clear that the skin friction coefficient is well predicted in the turbulent zone.

10 - DISCUSSION AND CONCLUSIONS

An important problem, which has not been discussed so far, is that of the interaction of cross-flow vortices and Tollmien-Schlichting waves, when streamwise and crossflow instabilities are simultaneously present. Let us recall that the fundamental assumption introduced into the practical calculation methods (e^n method or criteria) is that both kinds of instability are taken separately. However, Mueller et al /66/ presented a nice smoke visualization on a spinning body, where Tollmien-Schlichting waves were superimposed on cross-flow vortices; they concluded: "the nonlinear superposition of the two instability modes raises interesting questions for the experts on nonlinear theory and for the computer predictors of transition".

On the theoretical point of view, the approach commonly used is to consider Tollmien-Schlichting wave growth as a secondary instability in the presence of finite amplitude cross-flow vortices. The basic flow is the three-dimensional boundary layer profile with a superimposed primary disturbance of known amplitude. Two oblique, traveling waves are superimposed onto this basic flow. The problem is to find resonance conditions, that is to say relations between waves numbers and frequencies which give rise to strong interactions between primary and secondary disturbances. Reed /67/ used this technique for studying the effects of stationary disturbances induced by the crossflow instability: in this case, the primary instability is made of vortices rotating in the same sense. Reed showed that the interaction leads to magnified growth of the Tollmien-Schlichting waves beyond that predicted by linear theory.

In a further study, Reed /44/ was able to explain the seeming inconsistency detected in the experiments of Saric and Yeates /32/: the streaks made visible at the wall by sublimation techniques were spaced by 1 cm, whereas hot-wire measurements indicated a wavelength of 0.5 cm. A theoretical analysis revealed a strong interaction of the cross-flow/cross-flow type; this interaction occurs with stationary disturbances of half the primary wavelength. The secondary vortices are easily detected by hot-wire measurements, but as they are less intense near the wall as the primary ones, sublimation techniques cannot detect them.

It is obvious that such complex phenomena are difficult to include in practical calculation methods. When the e^n method is used, it is implicitly assumed that transition is driven by linear mechanisms. This seems inconsistent with experimental data (paragraph 6): fluctuations reaching 20 per cent of the external velocity cannot be considered as small perturbations. On the other side, smoke visualizations performed by Kegelman et al /36/ on an axisymmetric body with spin suggest the presence of helicoidal disturbances traveling along the cross-flow vortices just prior to the onset of turbulence (figure 48). It is tempting to relate this helical instability with secondary instability mechanisms as described above. In addition, as it is the case in two-dimensional flows, we can expect that different kinds of breakdown to turbulence still exist in three-dimensional situations.

In spite of the great number of experimental features which are not taken into account in the e^n method, it is surprising to see that this technique gives fairly good results (provided the curvature effects are properly introduced into the stability model). If one wants to use simpler methods, transition criteria such as those described in paragraph 9 provide us with useful informations. Another feature must be pointed out: when transition is dominated by cross-flow instability, the transition line is not rectilinear, but presents a sawtooth shape, which makes the definition of the transition point an intricate matter: in our experiments, uncertainties of 10 or 20 per cent of chord were currently observed, and the inaccuracies of the theoretical methods are not much more important than those of the experimental data.

Another source of discrepancies between calculations and experiments lies in the influence of free-stream turbulence level. In two-dimensional flows, a large amount of measurements made it possible to introduce the effect of Tu into the theoretical models. In three-dimensional flows, the problem is not so well documented, and one would like to have a larger number of systematic experiments (scanning in Tu) to confirm, for example, our C2 cross-flow criterion.

As far as the transition region is concerned, we believe that simple methods, such as the intermittency method, are able to give right predictions in very different situations. The inaccuracies of these techniques are certainly small as compared with large errors which can arise in the prediction of the transition onset.

REFERENCES

- /1/ ARNAL D. "Description and prediction of transition in two-dimensional, incompressible flow"
Special course on Stability and transition of laminar flow,
AGARD Report N° 709 (1984)
- /2/ SCHUBAUER G.B. "Laminar boundary layer oscillations and transition on a flat plate"
SKRAMSTAD H.K. Report 909 NACA (1948)
- /3/ WELLS C.S. "Effects of free-stream turbulence on boundary layer transition"
AIAA Journal, Vol 5, N° 1 (1967) 172-174
- /4/ ARNAL D. "Analyse expérimentale de la transition de la couche limite, avec gradient de pression
JUILLEN J.C. nul et positif"
MICHEL R. T.P. ONERA N° 1979 - 8 (1979)
- /5/ JUILLEN J.C. "Profils de vitesse moyenne et de turbulence mesurés dans une couche limite de tran-
ARNAL D. sition, en gradient de pression nul et positif"
Rapport Technique OA N° 17/5018 AND (ONERA, 1981)
- /6/ TURNER A.B. "Local heat transfert measurements on a gas turbine blade"
J. of Mechanical Engineering Science, Vol. 13, N° 1 (1971)
- /7/ BLAIR M.F. "Combined influence of free-stream turbulence and favourable pressure gradients on
WERLE M.J. boundary layer transition and heat transfer"
UTRC Report R 81 - 914388-17 (1981)
- /8/ MACK L.M. "Boundary layer stability theory"
Special course on stability and transition of laminar flow,
AGARD Report N° 709 (1984)
- /9/ GASTER M. "A note on the relation between temporally increasing and spatially increasing
disturbances in hydrodynamic stability"
J. Fluid Mech. Vol. 14 (1962) 222-224
- /10/ SMITH A.M.O. "Transition, pressure gradient and stability theory"
GAMBERONI N. Douglas Aircraft Co. Rept. ES 26 388, EL SEGUNDO, CALIF. (1956)
- /11/ VAN INGEN J.L. "A suggested semi-empirical method for the calculation of the boundary layer transi-
tion region"
Univ. of Technology, Dept. of Aero. Eng., Rept UTH - 74, DELFT (1956)
- /12/ MACK L.M. "Transition and laminar instability"
Jet Propulsion Laboratory Publication 77-15, PASADENA, CALIF. (1977)
- /13/ DRYDEN H.L. "Transition from laminar to turbulent flow"
Turbulent Flows and Heat Transfer, High Speed Aerodynamics and Jet Propulsion,
C.C. Lin Editor (1959)
- /14/ HABIBALLAH M. "Analyse de l'instabilité des couches limites laminaires et prévision de la tran-
sition du régime laminaire au régime turbulent"
Doctoral thesis, ENSAE (Toulouse, 1981)
- /15/ MICHEL R. "Détermination du point de transition et calcul de la traînée des profils d'ailes en
incompressible"
La Recherche Aéronautique N° 24 (1951)
- /16/ GRANVILLE P.S. "The calculation of the viscous drag of bodies of revolution"
David Taylor Model Basin Report 849 (1953)
- /17/ ARNAL D. "Synthèse sur les méthodes de calcul de la transition développées au DERAT"
HABIBALLAH M. Rapport Technique OA N° 11/5018 AYD (1980)
DELCOURT V.
- /18/ COUSTEIX J. "Three-dimensional boundary layers - Introduction to calculation methods"
VKI - AGARD Lecture Series on "Computation of three-dimensional boundary layers
including separation", Brussels, April 1986.

- /19/ SCHUBAUER G.B. "Contribution on the mechanics of boundary layer transition"
KLEBANOFF P.S. Rept. 1289, NACA (1956)
- /20/ DHAWAN S. "Some properties of boundary layer flow during the transition from laminar to turbulent motion"
NARASIMHA R. J. Fluid Mech., Vol. 3, Part 4 (1958)
- /21/ CHEN K.K. "Extension of Emmon's spot theory to flows on blunt bodies"
THYSON N.A. AIAA Journal, Vol. 9, N°5 (1971) 821-825
- /22/ CEBECI T. "Wall curvature and transition effects in turbulent boundary layers"
AIAA Journal, Vol. 9, N°9 (1971) 1868-1870
- /23/ ARNAL D. "Experimental and theoretical study of transition phenomena on an infinite swept wing."
COUSTOLS E. La Recherche Aéronautique N°1984-4 (1984)
JUILLEN J.C.
- /24/ POLL D.I.A. "Some aspects of the flow near a swept attachment line with particular reference to boundary layer transition"
Cranfield Institute of Technology, Co A Report N°7805 (1978)
- /25/ GREGORY N. "On the stability of three dimensional boundary layer with application to the flow due to a rotating disc"
STUART J.T. Philosophical Transactions of the Royal Society of London,
WALKER W.S. Series A, Vol. 248 (1955) 155-199
- /26/ ALLEN L.D. "Flight experiments on the boundary layer characteristics of a swept back wing"
BURROWS F.M. Cranfield, Co A Report N° 104 (July, 1956)
- /27/ BURROWS F.M. "A theoretical and experimental study of the boundary layer flow on a 45° swept back wing"
Cranfield, Co A Report N°109 (October 1956)
- /28/ BOLTZ F.W. "Effects of sweep angle on the boundary layer stability characteristics of an untapered wing at low speeds"
KENYON G.C. NASA TN D-338 (1960)
ALLEN C.Q.
- /29/ SCHMITT V. "Ecoulements subsoniques et transsoniques sur une aile à flèche variable"
MANIE F. La Recherche Aéronautique N° 1979-4 (1979), English translation ESA, TT-612
- /30/ MICHEL R. "Experimental and theoretical studies of boundary layer transition on a swept infinite wing"
ARNAL D. 2nd Symposium IUTAM on laminar-turbulent transition - Novosibirsk, USSR, 1984,
COUSTOLS E. Springer-Verlag
JUILLEN J.C.
- /31/ POLL D.I.A. "Some observations of the transition process on the windward face of a long yawed cylinder"
J. Fluid Mech., Vol. 150 (1985) 329-356
- /32/ SARIC W.S. "Generation of cross-flow vortices in a three-dimensional flat-plate flow"
YEATES L.G. 2nd Symposium IUTAM on laminar-turbulent transition
Novosibirsk, USSR, 1984, Springer-Verlag
- /33/ KOBAYASHI R. "Spiral vortices in boundary layer transition regime on a rotating disk"
KOHAMA Y. Acta Mechanica 35 (1980) 71-82
TAKAMADATE Ch.
- /34/ KOBAYASHI R. "Spiral vortices in boundary layer transition on a rotating cone"
KOHAMA Y. 2nd Symposium IUTAM on laminar-turbulent transition
Novosibirsk, USSR, 1984, Springer-Verlag
- /35/ KOHAMA Y. "Boundary layer transition and the behaviour of spiral vortices on rotating spheres"
KOBAYASHI R. J. Fluid Mech., Vol. 137 (1983) 153-164
- /36/ KEGELMAN J.T. "The boundary layer on an axisymmetric body with and without spin"
NELSON R.C. AIAA Journal, Vol. 21, N°11 (1983) 1485-1491
MUELLER T.J.
- /37/ EICHELBRENNER E. "Observations sur la transition laminaire-turbulent en trois dimensions"
MICHEL R. La Recherche Aéronautique, N° 65 (1958) 3-10
- /38/ MEIER H.U. "Development of boundary layer and separation patterns on a body of revolution at incidence"
KREPLIN H.P. 2nd Symposium on Numerical and Physical Aspects of Aerodynamic Flows, LONG BEACH,
VOLLMEERS H. CALIF. (1983)

- /39/ MALIK M.R. "Effect of curvature on three-dimensional boundary layer stability"
POLL D.I.A. AIAA Journal, Vol. 23, N° 9 (1985) 1362-1369
- /40/ BIELER H. Results presented at the Eurovisc Working Party on Transition, DFVLR Göttingen, Germany (1985)
- /41/ SCHLICHTING H. "Boundary layer theory"
6 th ed. Mc Graw-Hill, New-York (1968)
- /42/ BROWN W.B. "Exact numerical solution of the stability equations of the laminar boundary layer"
International Congress of Applied Mechanics, Stresa, Italy (1960)
- /43/ NITSCHKE P. Results presented at the Eurovisc Working Party on Transition, DFVLR Göttingen, Germany (1985)
- /44/ REED H. "Disturbance-wave interactions in flows with cross-flow"
AIAA Paper N° 85-0494 (1985)
- /45/ SROKOWSKI A. "Mass flow requirements for LFC wing design"
ORSZAG S.A. AIAA Paper N° 77-1222 (1977)
- /46/ DAGENHART J.R. "Amplified cross-flow disturbances in the laminar boundary layer on swept wings with suction"
NASA Technical Paper 1902 (1981)
- /47/ HEFNER J.N. "Status of linear boundary layer stability theory and the e^n method, with emphasis on swept-wing applications"
BUSHNELL D.M. NASA Technical Paper 1645 (1980)
- /48/ MACK L.M. "On the stabilization of three-dimensional boundary layers by suction and cooling"
First IUTAM Symposium on laminar-turbulent transition
Stuttgart, Germany, 1979, Springer-Verlag
- /49/ NAYFEH A.H. "Stability of three-dimensional boundary layers"
AIAA Paper N° 79-0262 (1979)
- /50/ CEBECI T. "On stability and transition in three-dimensional flows"
STEWARTSON K. AIAA Journal Vol. 18, N°4 (1980) 398-405
- /51/ MALIK M.R. "Comparison of methods for prediction of transition by stability analysis"
ORSZAG S.A. AIAA Paper N° 80-1375 (1980)
also AIAA Journal Vol. 18, N° 12 (1980) 1485-1489
- /52/ MALIK M.R. "Instability and transition in rotating disk flow"
WILKINSON S.P. AIAA Journal, Vol. 19, N° 9 (1981) 1131-1138
ORSZAG S.A.
- /53/ PFENNINGER W. "Amplified laminar boundary layer oscillations and transition at the front attachment line of a 45° swept flat-nosed wing with and without boundary layer suction"
BACON J.W. Viscous Drag Reduction, C.S. Wells editor, Plenum Press (1969)
- /54/ OWEN P.R. "Boundary layer transition on a sweptback wing"
RANDALL D.G. R.A.E. TM 277 (1952)
- /55/ OWEN P.R. "Boundary layer transition on a sweptback wing : a further investigation"
RANDALL D.G. R.A.E. TM 330 (1953)
- /56/ SQUIRE H.B. Letter to Dr Douglas (1952)
- /57/ BEASLEY J.A. "Calculation of the laminar boundary layer and the prediction of transition on a sheared wing"
ARC R and M 3787 (October 1973)
- /58/ ARNAL D. "Laminar instability theory and transition criteria in two and three-dimensional flow"
HABIBALLAH M. La Recherche Aéronautique N° 1984-2 (1984)
COUSTOLS E.
- /59/ COUSTOLS E. "Stabilité et transition en écoulement tridimensionnel : cas des ailes en flèche"
Doctoral thesis, ENSAE (Toulouse, 1983)
- /60/ SCHMITT V. "Etude de la couche limite tridimensionnelle sur une aile en flèche"
COUSTEIX J. Rapport Technique N° 14/1713 AN, ONERA (1975)
- /61/ JELLITI M. Thesis en preparation
- /62/ AUPOIX B. "Etude et développement d'une méthode intégrale de calcul de la couche limite tridimensionnelle (laminaire-turbulente) adaptée aux compresseurs"
COUSTEIX J. Rapport Technique N° 8/3327 EY, ONERA (1980)
- /63/ GLEYZES C. "Calcul des lignes de courant à partir des pressions pariétales sur un corps fuselé"
COUSTEIX J. La Recherche Aéronautique N° 1984-3 (1984)

- /64/ CEBECI T. "Problems and opportunities with three-dimensional boundary layers" in "Three-dimensional boundary layers", AGARD Report N° 719 (1984)
- /65/ GLEYZES C. "Couches limites tridimensionnelles sur des corps de type fuselage" Rapport Technique OA N° 4/5025 AYD, ONERA (1985)
COUSTEIX J.
AUPOIX B.
- /66/ MUELLER T.J. "Smoke visualization of boundary layer transition on a spinning axisymmetric body"
NELSON R.C. AIAA Journal, Vol. 19, N° 12 (1981) 1607-1608
KEGELMAN J.T.
MORKOVIN M.V.
- /67/ REED H. "An analysis of wave interactions in swept-wing flows"
2nd Symposium IUTAM on laminar-turbulent transition
Novosibirsk, USSR, 1984, Springer-Verlag

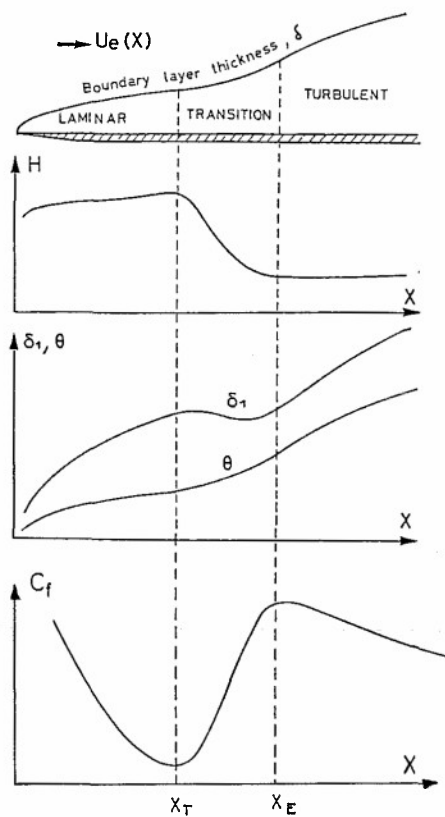


Fig. 1 - Boundary layer development.

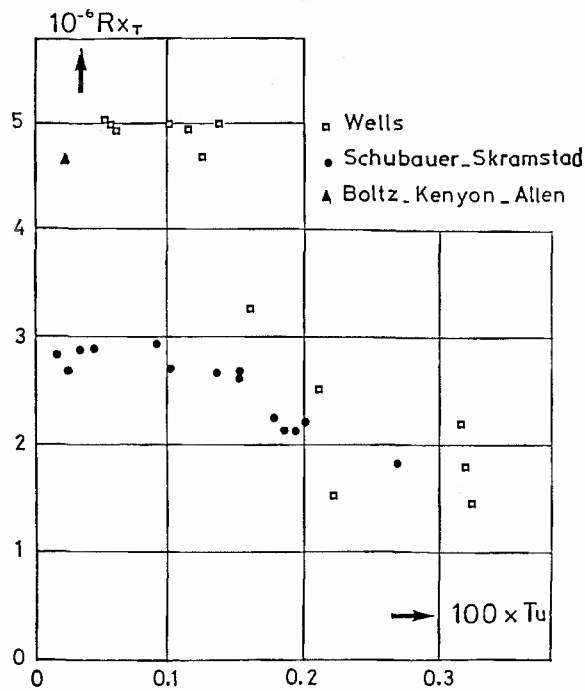
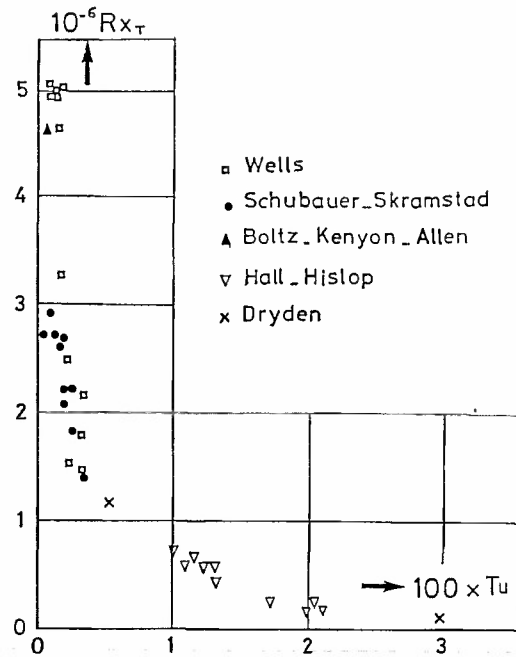
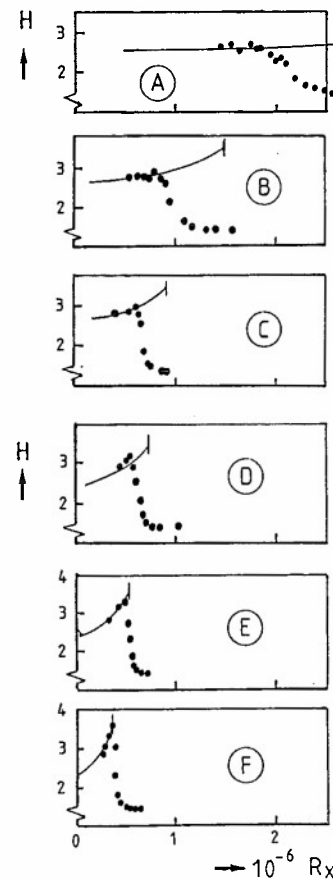


Fig. 3 - Effect of free-stream turbulence on transition Reynolds number for low turbulence intensities.

Fig. 2 - Effect of free-stream turbulence on transition Reynolds number : $0 < Tu < 3 \cdot 10^{-2}$.Fig. 4 - Effect of positive pressure gradients.
● experiments /4/ /5/.
— laminar calculation, with theoretical separation point.

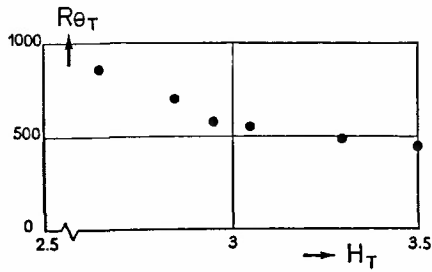


Fig. 5 - Momentum-thickness Reynolds number and shape factor at transition onset /4/ /5/.

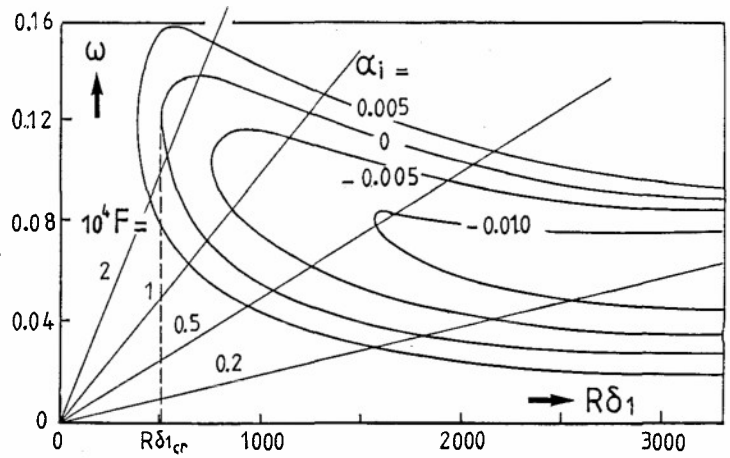


Fig. 6 - Stability diagram for the Blasius flow.

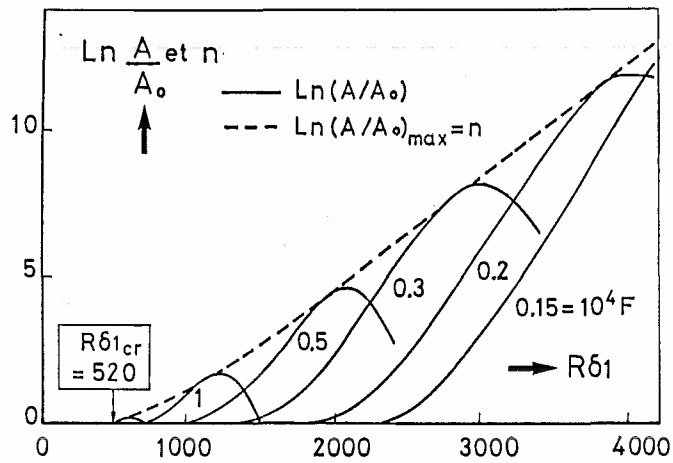


Fig. 7 - Total amplification rates for the Blasius flow.

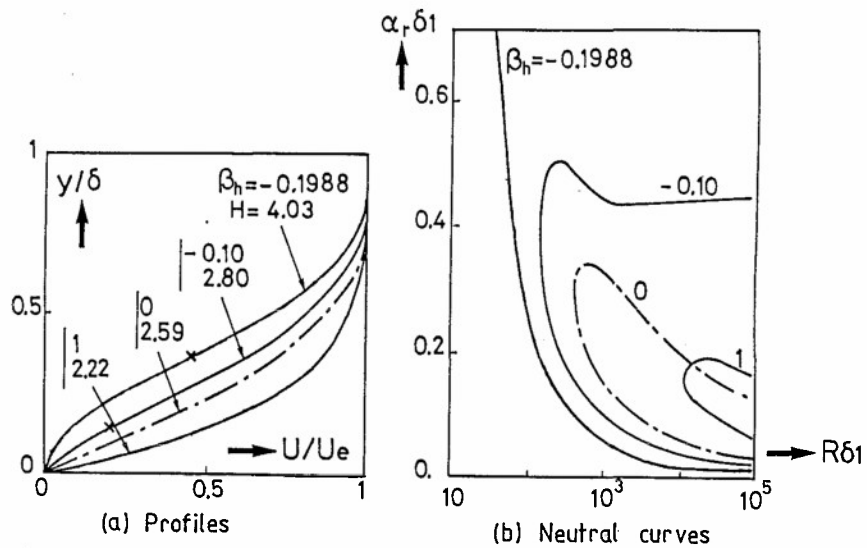


Fig. 8 - Mean velocity profiles (Falkner-Skan) and neutral curves.

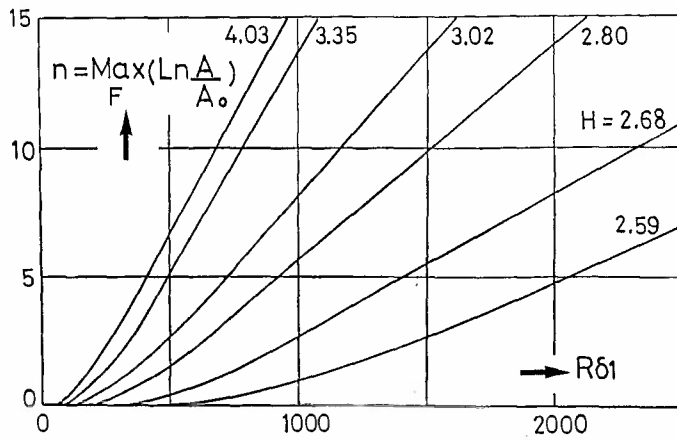


Fig. 9 - Envelope curves for the Falkner-Skan similarity profiles.

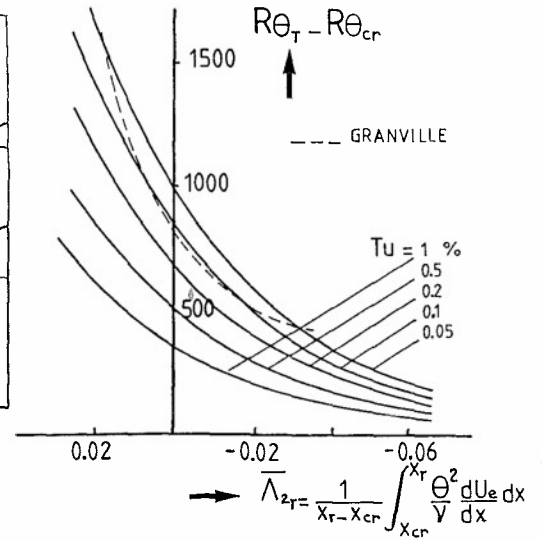


Fig. 10 - Two-dimensional transition criterion /17/.

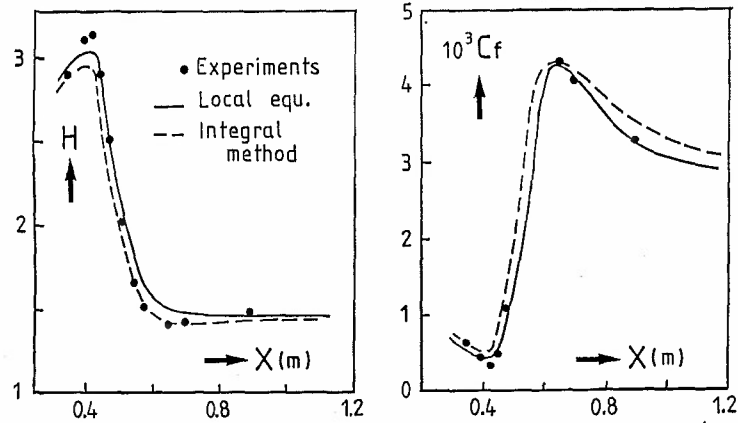


Fig. 11 - Boundary layer transition in a mild positive pressure gradient : comparison between experiments /4/ /5/ and calculations /1/ /14/.

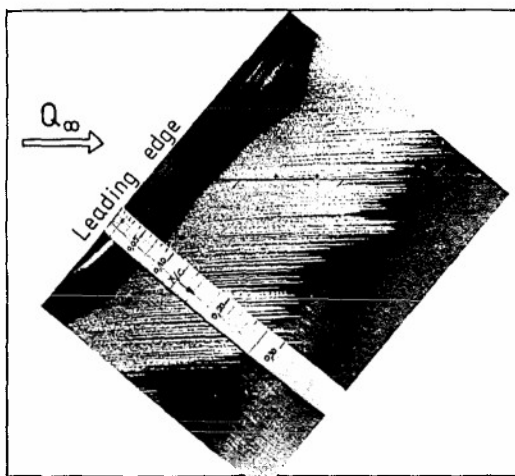


Fig. 12 - Example of wall visualization (sublimation) on a swept wing /23/.
 $\varphi = 40^\circ$, $\alpha_n = -8^\circ$, $Q_\infty = 81$ m/s.
 Chord $C = 0.35$ m.

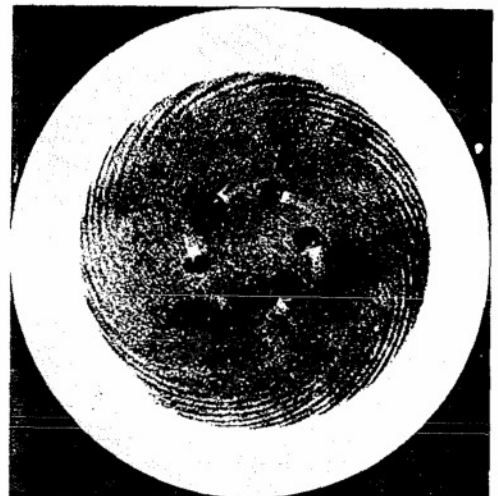


Fig. 13 - Example of wall visualization (china-clay) on a rotating disk /25/.

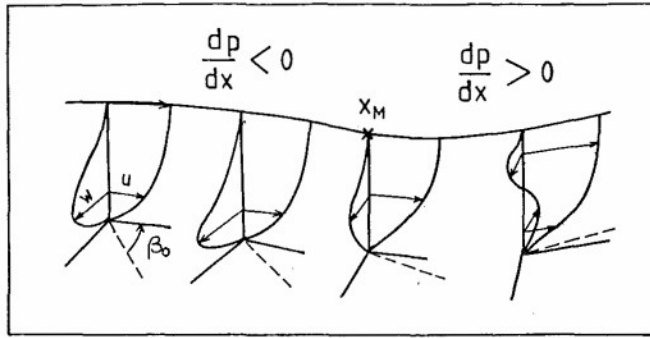


Fig. 18 - Laminar boundary layer development on a swept wing.
 x_M : inflexion point of the external streamline.
 β_0 is the angle between wall and external streamlines.

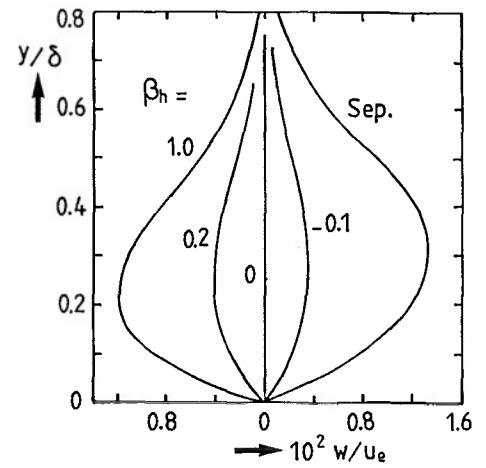


Fig. 19 - Falkner-Skan-Cooke cross-flow profiles, for $\theta_0 = 45^\circ$. From Mack /8/.

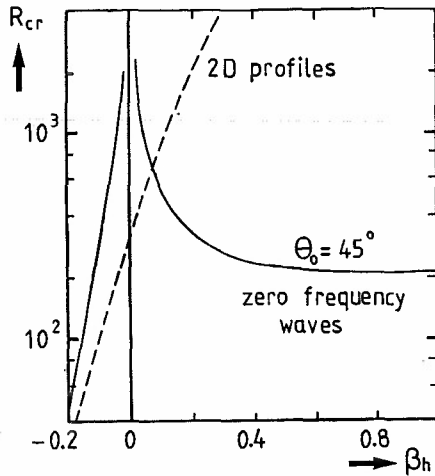


Fig. 20 - Critical Reynolds numbers for the two-dimensional profiles and for the zero-frequency waves. From Mack /8/.

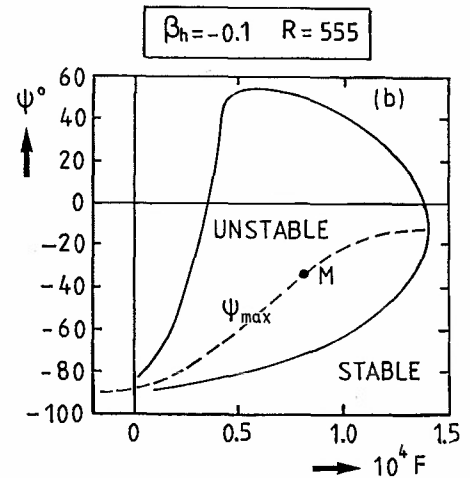
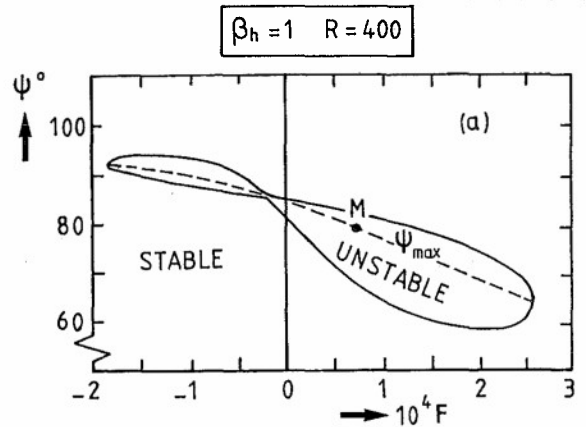


Fig. 21 - Stability and instability in the (ψ, F) plane, for two Falkner-Skan-Cooke profiles, in negative (a) and positive (b) pressure gradient, at a given Reynolds number. From Mack /8/.

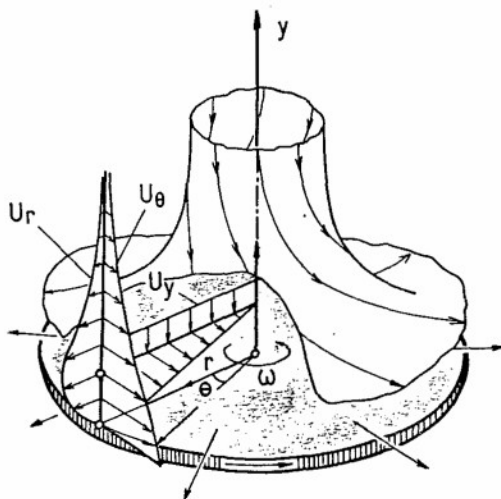


Fig. 22 - Rotating disk flow, from Schlichting /41/.

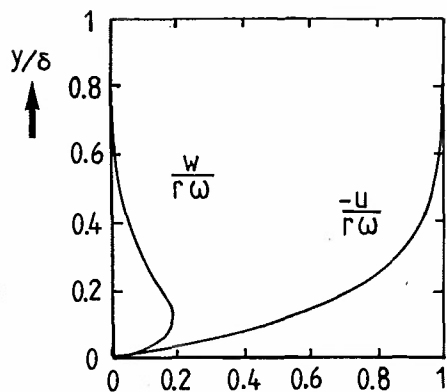


Fig. 23 - Azimuthal and radial profiles on a rotating disk.

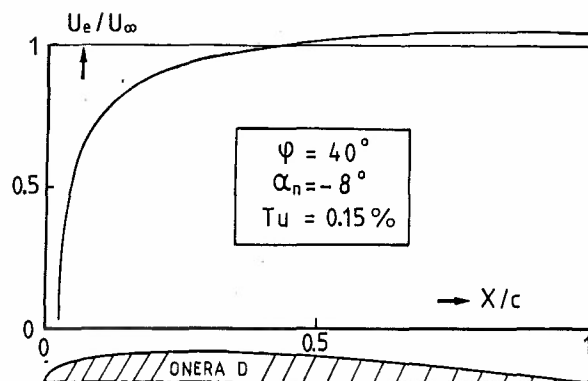


Fig. 24 - Swept wing flow : external velocity normal to the leading edge.

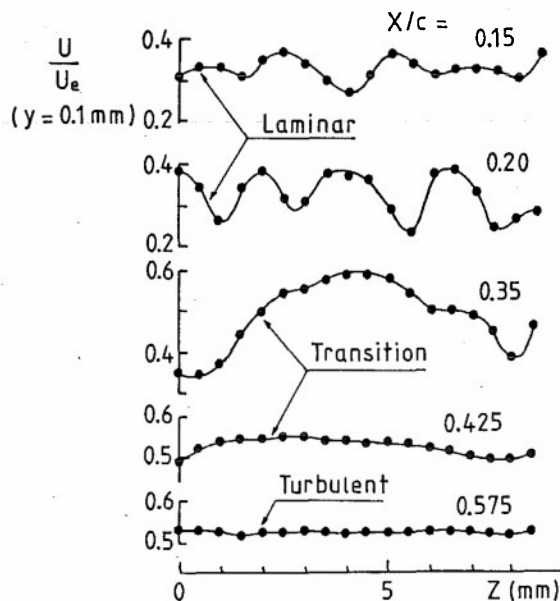


Fig. 25 - Mean streamwise velocity in the direction parallel to the leading edge. Same conditions as in figure 12.

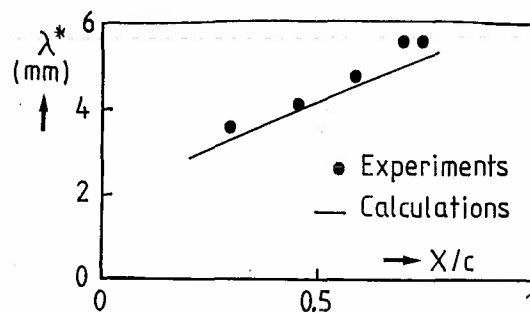


Fig. 26 - Experimental and theoretical evolution of the streaks wavelength. $\varphi = 40^\circ$, $\alpha_n = -8^\circ$, $Q_\infty = 48$ m/s.

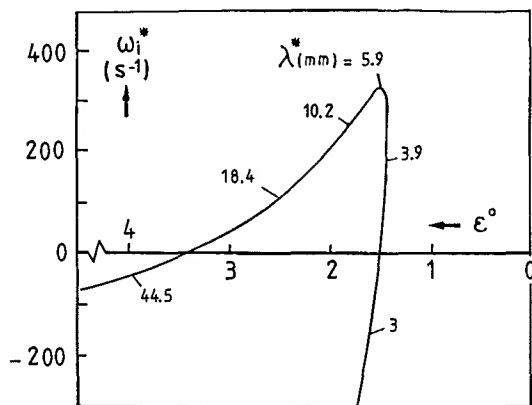


Fig. 27 - Temporal amplification rate of the stationary waves at $X/C = 0.69$. $\epsilon = 0^\circ$ is the cross-flow direction. Same conditions as in figure 26.

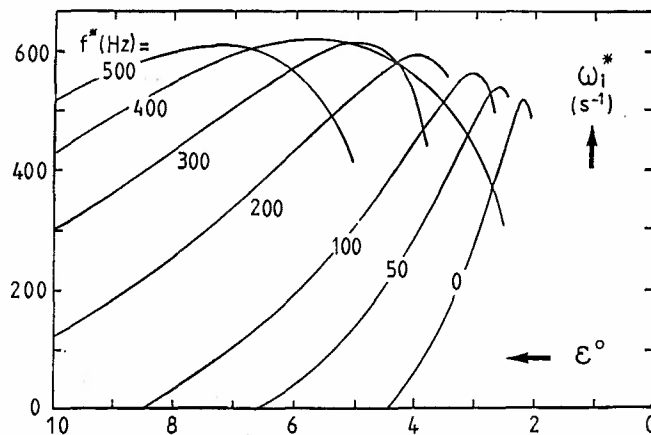


Fig. 28 - Temporal amplification rate of various frequencies at $X/C = 0.40$. Same conditions as in figure 26.

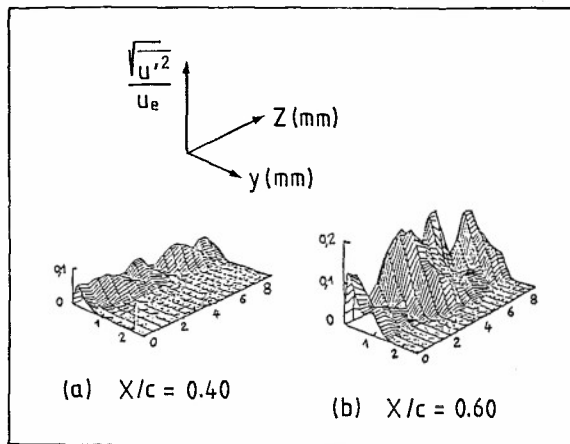


Fig. 29 - Fluctuations intensity distributions in the laminar boundary layer. Same conditions as in figure 26.

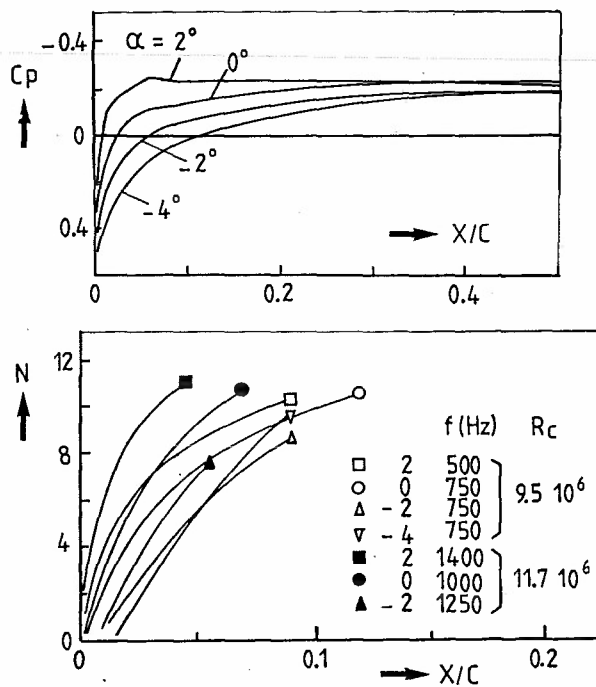


Fig. 31 - Total amplification rates computed by Hefner and Bushnell /47/ for various pressure distributions on a swept wing /26/ /27/. Symbols denote experimental transition points.

- Experiments (Malik et al. /52/)
- Calculations:
 - (a) Malik et al. /52/
 - (b) Cebeci - Stewartson /50/
 - (c) Malik et al. /52/, complete stability equations

Fig. 33 - Total amplification rates for stationary waves on a rotating disk.

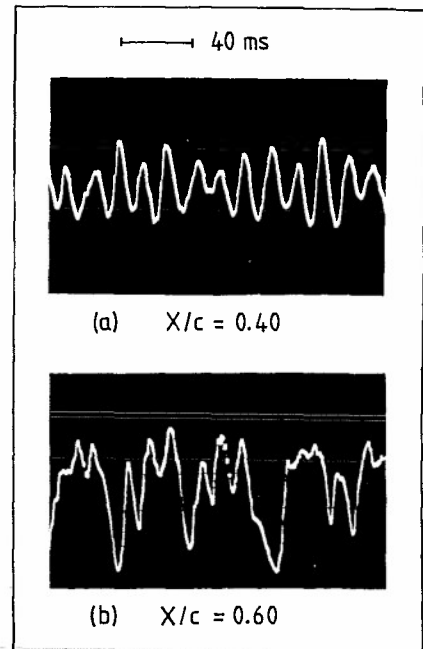


Fig. 30 - Typical hot-wire records. Same conditions as in figure 26.

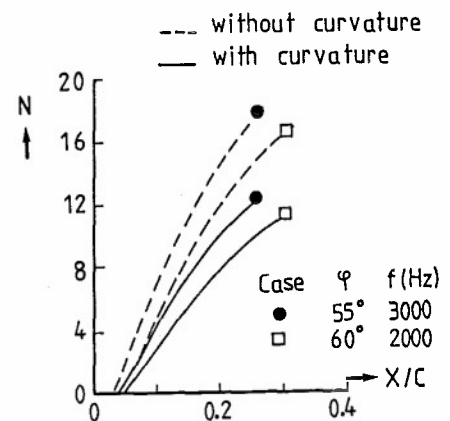
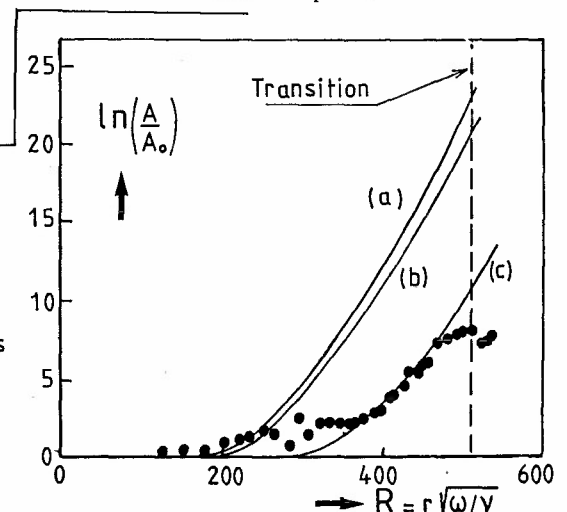


Fig. 32 - Total amplification rates computed by Malik and Poll /39/. Symbols denote experimental transition points.



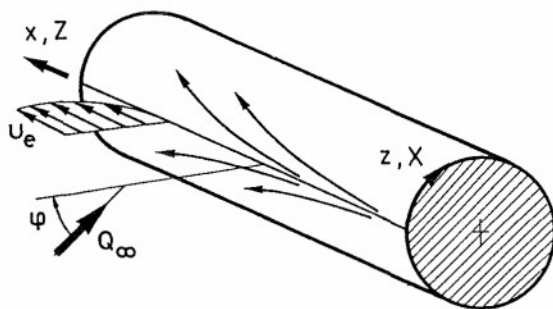


Fig. 34 - Attachment line flow.

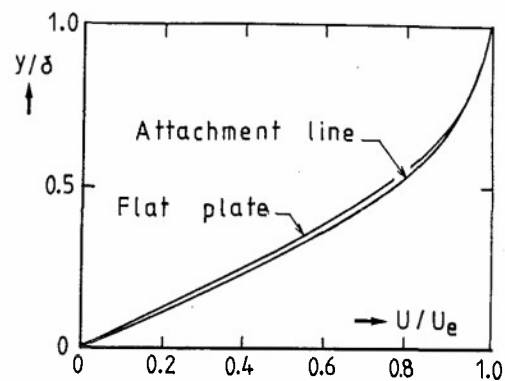


Fig. 35 - Attachment line and flat plate mean velocity profiles.

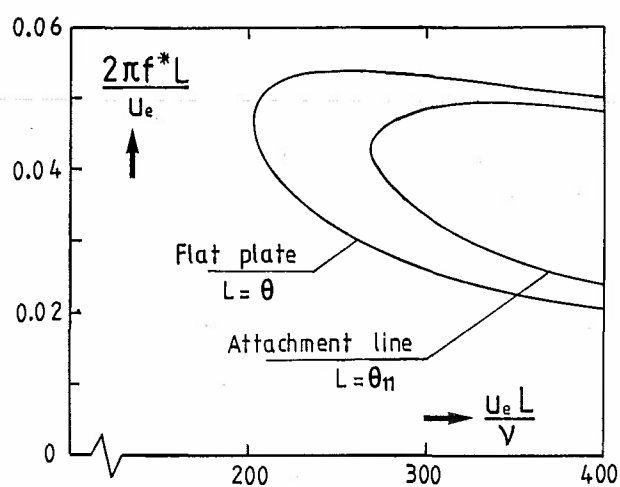


Fig. 36 - Neutral curves for the attachment line and flat plate mean velocity profiles.

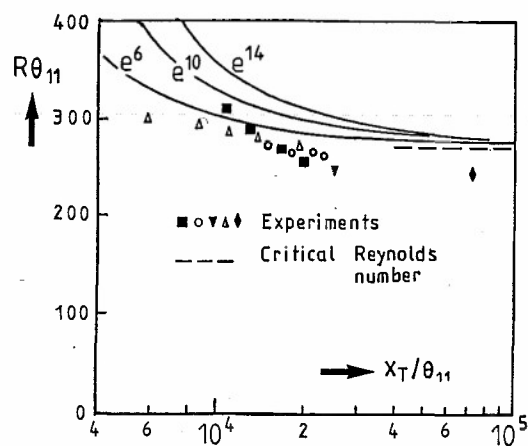


Fig. 37 - "Free" transition Reynolds number along the attachment line. From Poll /24/.

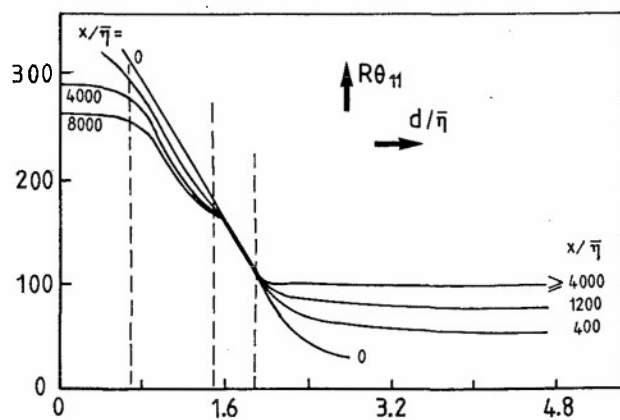
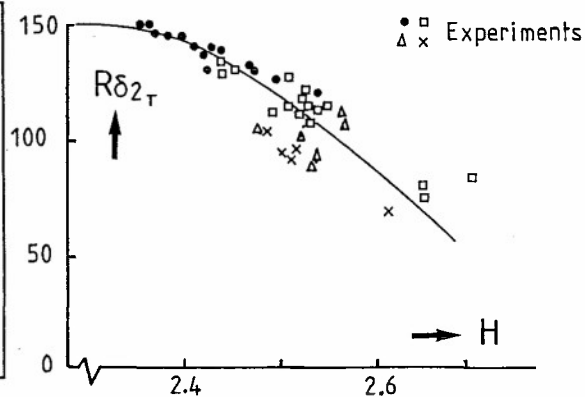
Fig. 38 - Variation of $R\theta_{11}$ with $d/\bar{\eta}$ and $x/\bar{\eta}$ for the appearance of first turbulent burst in the presence of trip wires. From Poll /24/.

Fig. 39 - Cross-flow transition criterion Cl.

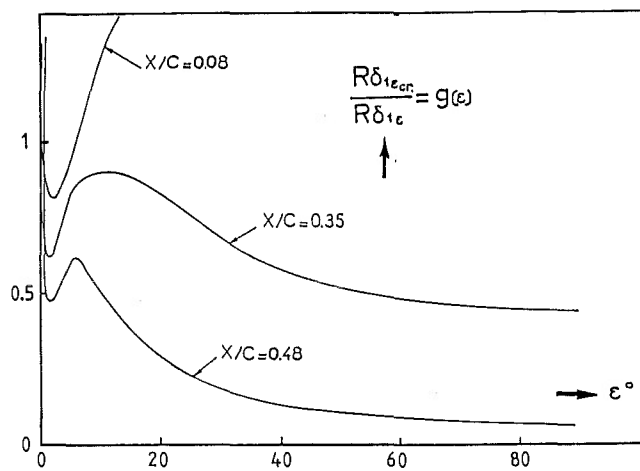


Fig. 40 - Evolution of g as a function of ϵ , at three abscissas.

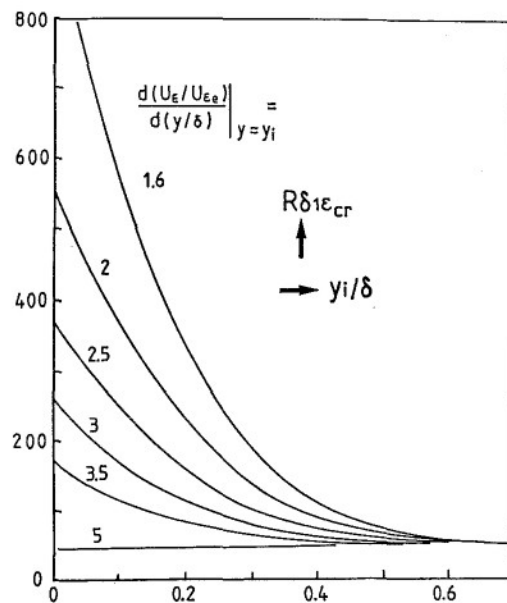


Fig. 41 - Critical Reynolds number for inflexional mean velocity profiles.

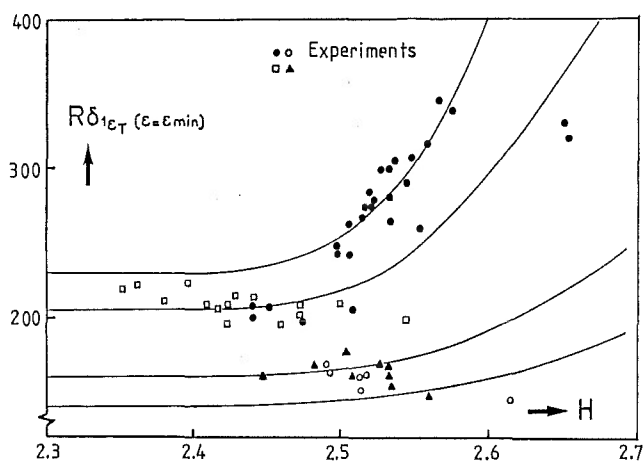


Fig. 42 - Cross-flow transition criterion C2.

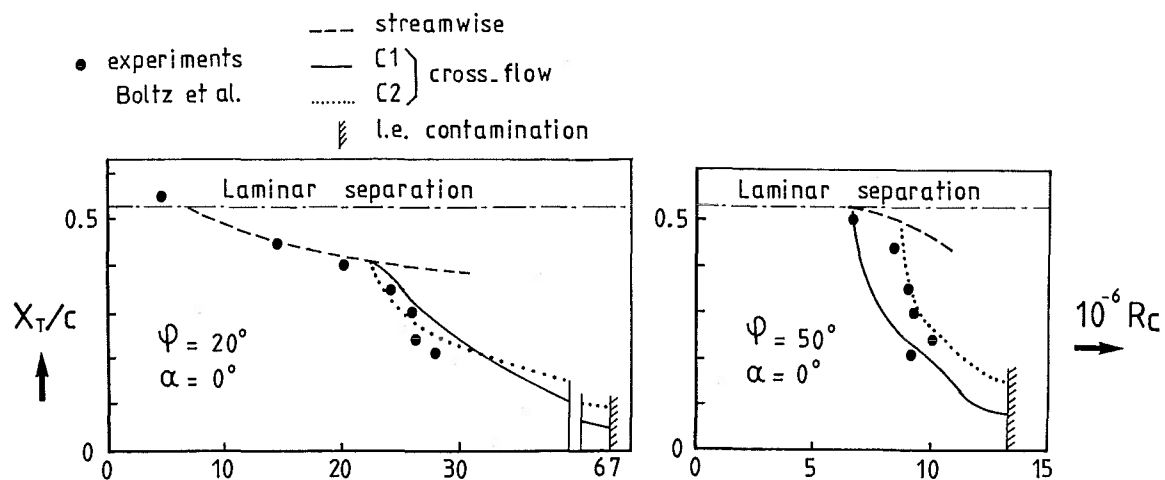


Fig. 43 - Application of transition criteria for an "infinite" swept wing case.

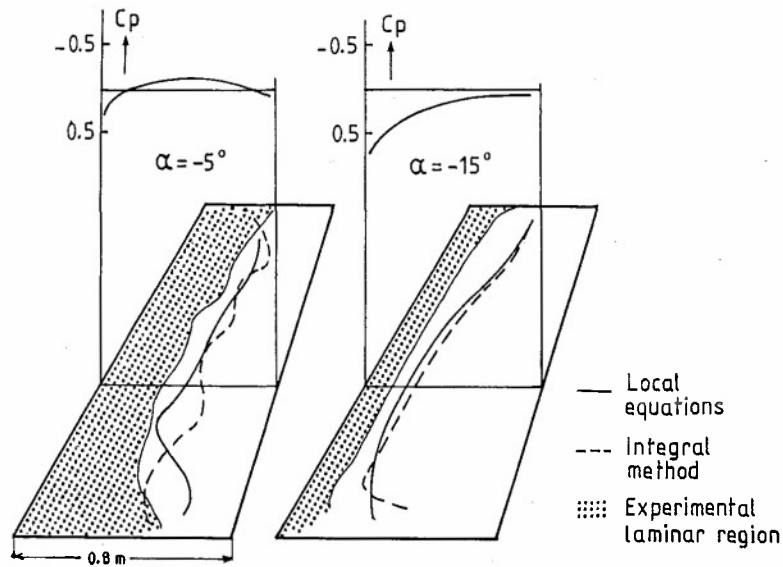


Fig. 44 - Comparison between experimental /60/ and theoretical transition lines on a tapered wing, $Q_\infty = 90 \text{ ms}^{-1}$.

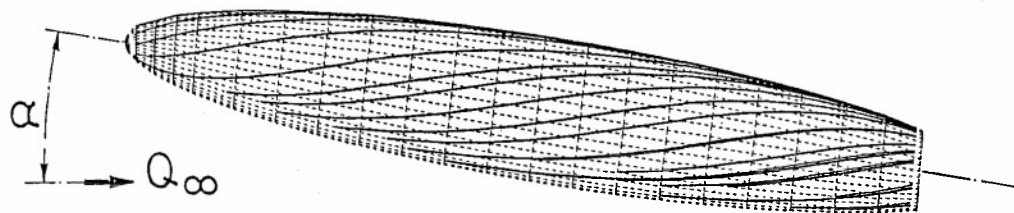


Fig. 45 - Theoretical external streamlines /63/ on a prolate spheroid. Experimental conditions of Meier et al /38/, $\alpha = 10^\circ$, model length = 2.4 m, slenderness ratio 6:1.

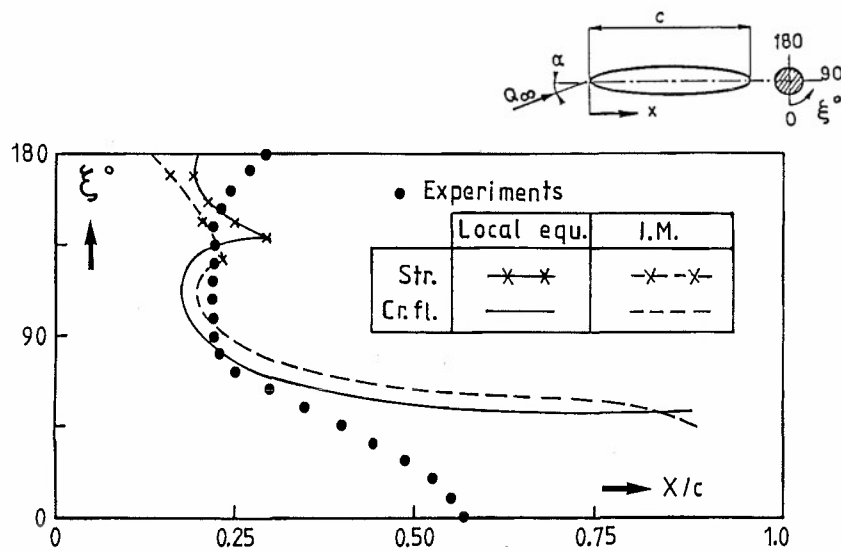


Fig. 46 - Comparison between measured /38/ and computed transition lines on a prolate spheroid, $\alpha = 10^\circ$, $Q_\infty = 10 \text{ ms}^{-1}$. I.M. : Integral method /65/, and local equations /61/.

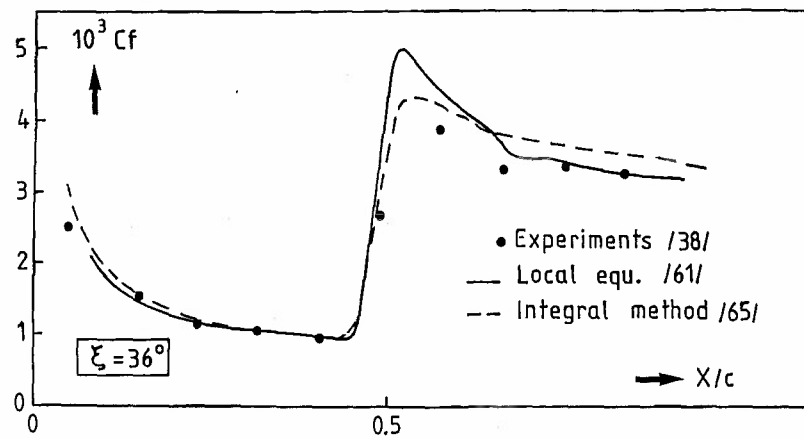


Fig. 47 - Comparison between theoretical and experimental skin friction coefficient on a prolate spheroid.

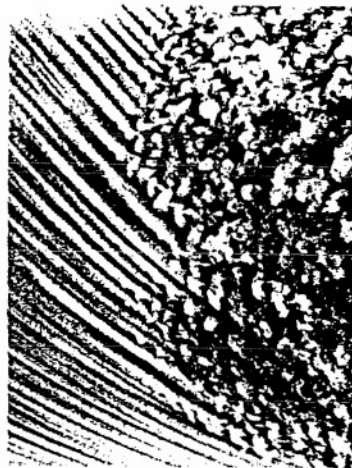


Fig. 48 - Smoke visualization on a spinning axisymmetric body. From Kegelmann et al /36/.

EVALUATION OF RESULTS OF BOUNDARY-LAYER CALCULATIONS WITH REGARD TO DESIGN AERODYNAMICS

E.H. Hirschel
Messerschmitt-Bölkow-Blohm GmbH, LKE122
Postfach 801160
8000 München 80, FRG

SUMMARY

The tools for the preprocessing of geometrical and inviscid flow data for boundary-layer computations, and for the postprocessing of the computed data are discussed. After a presentation of some important basic properties of three-dimensional boundary layers, the definition of coordinates, the computation of the metric properties, and transformation laws are given. Then the relations for the boundary-layer parameters, which are used in engineering work, like the wall-shear stress, friction forces, skin-friction lines, displacement properties etc., are presented. They are complemented with applications from design aerodynamics. The question what can be seen from boundary-layer results with regard to separation is then addressed. Basic topographical considerations are made, and basic topological rules are demonstrated. Finally practical separation indicators which can be applied to boundary-layer results are listed. Applications from design aerodynamics close the paper.

Contents

	Page
1. Introduction	2
2. Some Basic Properties of Three-Dimensional Boundary Layers	2
3. Boundary-Layer Parameters	4
3.1 Coordinates, Metric Properties, Transformations	4
3.2 Wall-Shear Stress and Friction Forces	8
3.3 Streamlines and Skin-Friction Lines	8
3.4 Heat Flux	9
3.5 Displacement Thickness and Equivalent Source Strength	9
4. Boundary-Layer Separation	10
4.1 Basic Considerations	10
4.2 Basic Global Topology Rules	12
4.3 Local Topography of Separation Lines, $ \tau $ -Minimum Line	12
4.4 Separation Indicators and their Application	13
5. Conclusions	14
6. References	15
7. List of Symbols	17
8. Figures	18

1. INTRODUCTION

Boundary-layer computation methods are widely used today in industrial design aerodynamics. Of course, the concept of boundary-layer theory has its limitations. It is applicable only where the boundary layer is attached. Separation including flow-off separation at the rear end of a body cannot be described, and the total drag of a body cannot be found in the frame of pure boundary-layer theory.

In the present paper an attempt is made to show the possible applications three-dimensional boundary-layer theory can find in design aerodynamics. The range of applications presented includes flow past wings, fuselages, car bodies etc. at all Mach-Numbers, except for hypersonic cases. In hypersonic cases frequently viscous-shock layer methods are used, which, however, are kind of higher-order boundary-layer methods.

Very important points in the application of boundary-layer theory are the preprocessing of the geometrical data and the outer boundary values (inviscid flowfield), and the postprocessing of the results of the boundary-layer computation. In this paper the tools for the pre- and postprocessing are developed and demonstrated with applications.

For the formulation of these tools contravariant vector components are used. Although applied rather seldom in fluid mechanics they offer a very easy and elegant way of handling all kind of mathematical operation and data in curvilinear and non-orthogonal coordinates. However, in the frame of this paper only the application is shown, no derivations and proofs are given. The reader is referred for instance to [1,2,3].

Contravariant velocity components allow also a more compact formulation of the boundary-layer equations [3]. Because these components arise in the transformation from the Cartesian reference coordinate system in a natural way (Chapter 3.1), the equations can be used without changes. On the other hand, the conversion from physical to contravariant components and back is very simple and cheap. Therefore the advantages of using contravariant vector components in pre- and postprocessing can and should be exploited, even if the boundary-layer equations are used and solved in the classical formulation.

Separation of three-dimensional boundary layers is treated in this paper in the sense that the solutions of these equations are investigated with regard to indications of separation. No methods for the computation of separated flow are discussed in this paper. For a view on viscous-inviscid interaction methods, inverse methods, and the solution of the Navier-Stokes equations in the frame of engineering applications see for instance [4].

The present author develops in this respect the concept of zonal solutions for viscous flow problems [5], where the Euler and the boundary-layer equations are coupled with local solutions of the Navier-Stokes equations. This leads directly to an extension of first-order boundary-layer theory to second-order theory because in many applications the boundary layers become very thick compared to the smallest local radius of curvature of the configuration under investigation. This concerns many experiments used for verification, but also real scale applications, for instance fuselage base flow and the like. In [6] to this end a higher-order boundary-layer code has been developed on the basis of the concepts given in [3].

The present paper starts with a review of basic properties of three-dimensional boundary layers (Chapter 2). Some of the peculiarities in the development of these flows are explained. The characteristic properties which govern the formulation of the computation method, the orientation of the coordinate system, and the position of the initial data are discussed.

In Chapter 3 coordinates and their metric properties are developed. The transformation laws allowing the handling of vector quantities are given. Then the boundary-layer parameters which are of interest for the engineer are discussed. Relations for the calculation of friction forces, streamlines, skin-friction lines, displacement properties etc. are derived, applications are given.

Chapter 4 finally is devoted to the problem of separation, its detection and to a certain degree, its control. Basic topological rules and observations from applications are presented. Separation indicators are formulated. Again applications are given in order to show where and how the results can be used in engineering work.

In general no details are given about the computation methods used. Neither is the turbulence modelling discussed, nor the, in many cases much more important problem of stability and transition laminar-turbulent addressed. The reader is referred instead to the literature.

2. SOME BASIC PROPERTIES OF THREE-DIMENSIONAL BOUNDARY LAYERS

In two-dimensional boundary layers any stream surface remains in its original form as it moves along. In three-dimensional boundary layers any stream surface gets skewed. This can be explained as a local centrifugal effect. In order to study this, the flow is considered in an orthogonal coordinate system, where the t -direction lies along the inviscid external streamline, and the n -direction normal to it. Fig. 2.1a.

The inviscid external streamline is curved parallel to the t , n -plane. A centrifugal

force balance can be formulated as first approximation, Fig. 2.1b:

$$(2.1) \quad \frac{\rho_e |\underline{v}_e|^2}{r_e} = \frac{\partial p_e}{\partial n}.$$

Because the pressure is constant in direction normal to the wall

$$(2.2) \quad \frac{\partial p}{\partial z} = 0,$$

the pressure gradient $\partial p / \partial n$ acts throughout the boundary layer.

For every boundary-layer streamline a relation like (2.1) holds:

$$(2.3) \quad \frac{\rho |\underline{v}|^2}{r} = \frac{\partial p}{\partial n} \approx \frac{\partial p_e}{\partial n}.$$

Because in the boundary layer $|\underline{v}| < |\underline{v}_e|$, $\rho = 0(\rho_e)$, the curvature radius of every streamline is smaller than that of the external streamline:

$$(2.4) \quad r = r_e \frac{\rho |\underline{v}|^2}{\rho_e |\underline{v}_e|^2} < r_e.$$

Of course, this relation does not hold in the very vicinity of the wall, because there viscous forces cannot be neglected. The radius of curvature of the skin-friction line usually is finite.

From this result the following conclusions can be drawn:

- any boundary-layer streamline including the skin-friction line is curved in the same sense but stronger than the inviscid external streamline,
- the skin-friction lines for instance from an oilflow picture don't have the same direction as the external streamline if the boundary layer is three-dimensional,
- any deceleration in main-flow direction, Fig. 2.1a, (point of inflexion appears in the main-flow profile) leads to a strong deflection in cross-flow direction (three-dimensional separation, wing trailing-edge flow).

The picture changes somewhat, if the external streamline exhibits a point of inflexion, Fig. 2.2. Such a feature is always present on the suction side of swept wings. Immediately behind the point of inflexion the cross-flow profile begins to swing to the other side and complicated s-shape profiles can appear. After a short transition zone all streamlines are curved again in the same manner, but opposite to the original one.

This behaviour of a three-dimensional boundary layer is important because all streamlines including the skin-friction line are characteristics. In order to show this, the boundary-layer equations for incompressible flow in Cartesian coordinates, Fig. 2.3a, are considered:

$$(2.5a) \quad \frac{\partial u}{\partial x} + \frac{\partial v}{\partial y} + \frac{\partial w}{\partial z} = 0,$$

$$(2.5b) \quad u \frac{\partial u}{\partial x} + v \frac{\partial u}{\partial y} + w \frac{\partial u}{\partial z} = -\frac{1}{\rho} \frac{\partial p}{\partial x} + \nu \frac{\partial^2 u}{\partial z^2},$$

$$(2.5c) \quad u \frac{\partial v}{\partial x} + v \frac{\partial v}{\partial y} + w \frac{\partial v}{\partial z} = -\frac{1}{\rho} \frac{\partial p}{\partial y} + \nu \frac{\partial^2 v}{\partial z^2}.$$

Following [8] characteristic manifolds $\varphi(x, y, z)$ are introduced, for instance like

$$(2.6) \quad \frac{\partial \varphi}{\partial x} = \frac{\partial \varphi}{\partial x} \frac{d}{d\varphi} = \varphi_x \frac{d}{d\varphi}.$$

This leads after some manipulation to the characteristic form

$$(2.7) \quad C = \begin{vmatrix} \varphi_x & \varphi_y & \varphi_z \\ \Delta - \nu \varphi_z^2 & 0 & 0 \\ 0 & \Delta - \nu \varphi_z^2 & 0 \end{vmatrix} = \varphi_z (\Delta - \nu \varphi_z^2)^2 = 0,$$

with the abbreviation

$$(2.8) \quad \Delta = u\varphi_x + v\varphi_y + w\varphi_z.$$

Note that the pressure gradients do not enter the problem because the pressure field is imposed on the boundary layer. Note further that the consideration of only the highest derivatives in eqs. (2.5) is not sufficient, because it is a system of partial differential equations.

In order to prove that (2.8) represents the streamlines as characteristic manifolds the total differential of φ

$$(2.9) \quad d\varphi = \varphi_x dx + \varphi_y dy + \varphi_z dz = 0$$

is combined with the definition of three-dimensional streamlines:

$$(2.10) \quad \frac{dx}{u} = \frac{dy}{v} = \frac{dz}{w}$$

to yield

$$(2.11) \quad d\varphi = u\varphi_x + v\varphi_y + w\varphi_z = \Delta = 0.$$

Thus it is shown that streamlines are characteristics, and that moreover a fivefold characteristic in z-direction exists, which is in accordance with the five boundary conditions in z-direction necessary to solve eqs. (2.5), Fig. 2.3a.

The following conclusions can be drawn:

- the system of equations (2.5) is parabolic, this holds also for compressible flow in non-orthogonal curvilinear coordinates,
- where the boundary-layer flow enters the computation domain, initial data must be prescribed, no data are necessary where the flow leaves the computation domain (no elliptic properties!),
- a solution procedure for the boundary-layer equations must follow the flow in the sense, that the analytical domain of dependence (the streamline fan) of the flow (for instance at P(x,y) in Fig. 2.3b) is enclosed by the numerical domain of dependence (for instance the quadratic difference molecule in Fig. 2.3b). This is the Courant-Friedrichs-Lewy condition (see for instance [9]),
- the boundary-layer coordinate system must be oriented accordingly,
- negative cross-flow, a concept found in older literature is too limited, what counts, is that the CFL-condition is fulfilled.

3. BOUNDARY-LAYER PARAMETERS

3.1 Coordinates, Metric Properties, Transformations

In order to develop the tools necessary for the pre- and postprocessing a description of the most important geometrical properties of boundary-layer coordinates is given. For details see [3].

In Fig. 3.1a and b a change of notation is indicated. Boundary-layer coordinates are a special case of locally monoclinic surface-oriented coordinates. Consider the surface element in Fig. 3.1c, which is embedded in a Cartesian reference coordinate system, the $x^{i'}$ -system ($i' = 1, 2, 3$). The boundary-layer coordinates (x^j -system ($j = 1, 2, 3$)) are defined on the surface. The lines $x^2 = \text{const.}$ (x^1 -coordinates) and $x^1 = \text{const.}$ (x^2 -coordinates) lie on the surface. The x^3 -coordinate is rectilinear and normal to both, and therefore locally normal to the surface. Both x^1 and x^2 , or x^α , $\alpha = 1, 2$ - called Gaussian parameters - have no length properties in general. Both parameters are not necessarily counted along the coordinate lines.

The coordinate base indicated in Fig. 3.1c is called covariant base. The covariant base vectors belonging to the x^α -coordinates are defined by (the Einstein summation convention is used):

$$(3.1) \quad \underline{a}_\alpha = \beta_{\alpha}^{i'} \underline{e}_{i'} = \beta_{\alpha}^{1'} \underline{e}_{1'} + \beta_{\alpha}^{2'} \underline{e}_{2'} + \beta_{\alpha}^{3'} \underline{e}_{3'},$$

where

$$(3.2) \quad \beta_{\alpha}^{i'} = \frac{\partial x^{i'}}{\partial x^{\alpha}} \quad (i' = 1, 2, 3; \quad \alpha = 1, 2)$$

are the derivatives of the contour functions

$$(3.3) \quad x^{i'} = x^{i'}(x^{\alpha}),$$

which define the x^α -coordinates on the configuration under consideration.

The third base vector \underline{a}_3 is a unit vector which points in x^3 -direction:

$$(3.4) \quad \underline{a}_3 = \frac{\underline{a}_1 \times \underline{a}_2}{|\underline{a}_1 \times \underline{a}_2|} = \beta_3^{i'} \underline{e}_{i'}.$$

The components are

$$(3.5) \quad \beta_3^{1'} = \frac{\Delta^{1'}}{\Delta},$$

with

$$(3.6) \quad \begin{aligned} \Delta^{1'} &= \beta_1^{2'} \beta_2^{3'} - \beta_1^{3'} \beta_2^{2'}, \\ \Delta^{2'} &= \beta_2^{1'} \beta_1^{3'} - \beta_2^{3'} \beta_1^{1'}, \\ \Delta^{3'} &= \beta_1^{1'} \beta_2^{2'} - \beta_2^{1'} \beta_1^{2'}. \end{aligned}$$

Once the components of the covariant base vectors are known, every geometrical aspect of the problem can be described. The difficulty lies in the definition of the contour functions.

To demonstrate the necessary steps for the definition of the contour functions, a percent-line coordinate system on a wing, Fig. 3.2 is considered.

Choosing the halfspan as normalizing length, $L_{x2} = s$, Fig. 3.2a, rather than the length of the individual $x^1 = \text{const.}$ -lines yields

$$(3.7) \quad x^{2'} = x^2 L_{x2} = x^2 s ,$$

so that the root lies at $x^2 = 0$, and the tip of the wing at $x^2 = 1$, Fig. 3.2b.

If the wing is defined as usual by airfoil sections $x^2 = \text{const.}$, the normalizing length $L_{x1}(x^2)$ on the upper and the lower side simply are the respective arc lengths from the leading edge to the trailing edge, as indicated for the upper side of the wing in Fig. 3.2a. If the airfoil sections are given pointwise, the normalizing length, for instance for the upper side of the wing, can be computed with

$$(3.8) \quad L_{x1}^u(x^2) = \sum_{i=2}^{i_{\max}} [(x^{1'}(i) - x^{1'}(i-1))^2 + (x^{3'}(i) - x^{3'}(i-1))^2]^{1/2} ,$$

where $i=1$ denotes the point in the leading edge, and i_{\max} the point in the trailing edge on the upper side of the wing.

By normalizing then the lengths from the leading edge to the individual points i with L_{x1}^u one finds the x^1 -parameter for each point i , with $x^1 = 0$ in the leading edge, and $x^1 = 1$ in the trailing edge, Fig. 3.2.

The coordinates $x^{1'}$ and $x^{3'}$ for each point can then be presented as function of x^1 by means for instance of a spline function (a smoothing spline like [10] is recommended):

$$(3.9) \quad x^2 = \text{const.} : x^{1'} = x^{1'}(x^1), \quad x^{3'} = x^{3'}(x^1) .$$

Once the functions (3.9) are given as spline functions, the necessary discretization either with $\Delta x^1 = \text{const.}$, or with varying Δx^1 can be made, however, for each cross section $x^2 = \text{const.}$ in the same manner.

Then spline functions are produced for the $x^1 = \text{const.}$ lines:

$$(3.10) \quad x^1 = \text{const.} : x^{1'} = x^{1'}(x^2), \quad x^{3'} = x^{3'}(x^2) ,$$

in order to find the necessary discretization in x^2 -direction, again either with $\Delta x^2 = \text{const.}$ or with varying Δx^2 . This is necessary, if the number of cross sections which define the wing is different from the number of stations x^2 to be used in the boundary-layer calculation.

The whole procedure can be simplified by using a surface spline (bi-cubic spline), but experience shows that a smoother representation of the geometry results with the present parametric approach.

From relation (3.7) one gets two components of the covariant base vectors a_α :

$$(3.11) \quad \beta_1^{2'} = 0, \quad \beta_2^{2'} = s .$$

The other components $\beta_1^{1'}, \beta_2^{1'}, \beta_1^{3'}, \beta_2^{3'}$ result directly from the spline representations (3.9) and (3.10).

The components of the - symmetric - covariant metric tensor of the surface coordinates

$$(3.12) \quad (a_{\alpha\beta}) = \begin{pmatrix} a_{11} & a_{12} \\ a_{21} & a_{22} \end{pmatrix}$$

are defined as follows:

$$(3.13a) \quad a_{11} = (\beta_1^{1'})^2 + (\beta_1^{2'})^2 + (\beta_1^{3'})^2 ,$$

$$(3.13b) \quad a_{12} = a_{21} = \beta_1^{1'} \beta_2^{1'} + \beta_1^{2'} \beta_2^{2'} + \beta_1^{3'} \beta_2^{3'} ,$$

$$(3.13c) \quad a_{22} = (\beta_2^{1'})^2 + (\beta_2^{2'})^2 + (\beta_2^{3'})^2 .$$

Note that the metric terms used in many boundary-layer computation methods are related to the above by

$$(3.14) \quad \begin{pmatrix} h_1 & g \\ g & h_2 \end{pmatrix} = \begin{pmatrix} \sqrt{a_{11}} & a_{12} \\ a_{12} & \sqrt{a_{22}} \end{pmatrix} .$$

The length element ds , the surface element dA and the volume element dV are defined by (note that x^3 has a length dimension [3]):

$$(3.15) \quad (ds)^2 = a_{11}(dx^1)^2 + 2a_{12}dx^1dx^2 + a_{22}(dx^2)^2 + (dx^3)^2;$$

$$(3.16) \quad dA = \sqrt{a} dx^1 dx^2,$$

with a the determinant of the metric tensor:

$$(3.17) \quad a = a_{11}a_{22} - (a_{12})^2;$$

$$(3.18) \quad dV = \sqrt{a} dx^1 dx^2 dx^3.$$

The angle ϑ between the coordinate lines $x^1 = \text{const.}$ and $x^2 = \text{const.}$, Figs. 3.1, 3.2 is found from the scalar product $\underline{a}_1 \cdot \underline{a}_2 = |\underline{a}_1| |\underline{a}_2| \cos \vartheta$:

$$(3.19) \quad \cos \vartheta = \frac{a_{12}}{\sqrt{a_{11}} \sqrt{a_{22}}}.$$

Orthogonal coordinates with $a_{12} = 0$ yield $\vartheta = \frac{\pi}{2}$ as expected.

In Fig. 3.3 the metric properties of a forward swept wing are given [11]. Because in this example the wing has no thickness, L_{x^1} is always the chord length and the metric is the same on the upper and the lower side.

The coordinates for a fuselage can be constructed in an analogous way. If the stagnation point lies close to the nose point (slender fuselage, small angle of attack) cross-section coordinates can be employed, Fig. 3.4.

In this case the x^1 -parameter is counted along the axis:

$$(3.20) \quad x^1 = x^1 L_{x^1} = x^1 L.$$

Because a fuselage usually is defined by cross sections, the normalizing lengths $L_{x^2}(x^1)$ are the circumferential lengths, and the spline representations first of

$$(3.21) \quad x^1 = \text{const.}: x^{2'} = x^{2'}(x^2), \quad x^{3'} = x^{3'}(x^2)$$

and then

$$(3.22) \quad x^2 = \text{const.}: x^{2'} = x^{2'}(x^1), \quad x^{3'} = x^{3'}(x^1)$$

are constructed.

Fig. 3.5 shows the metric properties of the right half of a helicopter fuselage. The coordinate system covers only the bulk fuselage up to $x^1 = 0.61$ [11].

Because the inviscid flow usually is given with Cartesian components a transformation into the surface boundary-layer coordinates is necessary. As will be shown in Chapter 3.2 on the other hand the skin-friction components have to be transformed back into the Cartesian system in order to get the friction-drag coefficient.

In the following the transformation laws are given starting with the fundamental transformation from the boundary-layer coordinates into the Cartesian coordinates. A vector \underline{F} is defined in the covariant base \underline{a}_i by

$$(3.23) \quad \underline{F} = F^i \underline{a}_i = F^1 \underline{a}_1 + F^2 \underline{a}_2 + F^3 \underline{a}_3.$$

Note that in the frame of first order boundary-layer theory only tangential components of the external flow and the wall-shear stress are considered, hence only two components are shown in Fig. 3.6a.

The components F^i are contravariant components which belong to the covariant base. They are related to the physical components F^{*i} by

$$(3.24) \quad F^i = \frac{F^{*i}}{\sqrt{a_{ii}}}, \quad (i=1,2,3),$$

because the base vectors are no unit vectors (the brackets around ii mean that no summation has to be made).

The fundamental transformation is from the $x^{i'}$ -system into the Cartesian ref. system:

$$(3.25) \quad F^{i'} = \beta_j^{i'} F^j = \beta_1^{i'} F^1 + \beta_2^{i'} F^2 + \beta_3^{i'} F^3, \quad (i' = 1,2,3).$$

The inverse transformation from the $x^{i'}$ -system into the x^i -system reads

$$(3.26) \quad F^k = \beta_{\ell'}^k F^{\ell'}, \quad (k, \ell' = 1,2,3).$$

The inverse transformation matrix $\{\beta_{\ell'}^k\}$, also called the Jacobian, is given in terms

of the components $\beta_j^{i'}$ of the base vectors:

$$(3.27) \quad \{\beta_{k'}^{i'}\} = \begin{pmatrix} \beta_1^{1'} & \beta_2^{1'} & \beta_3^{1'} \\ \beta_1^{2'} & \beta_2^{2'} & \beta_3^{2'} \\ \beta_1^{3'} & \beta_2^{3'} & \beta_3^{3'} \end{pmatrix} = \frac{1}{\sqrt{a}} \begin{pmatrix} (\beta_2^{2'} \beta_3^{3'} - \beta_2^{3'} \beta_3^{2'}) (\beta_2^{3'} \beta_3^{1'} - \beta_2^{1'} \beta_3^{3'}) (\beta_2^{1'} \beta_3^{2'} - \beta_2^{2'} \beta_3^{1'}) \\ (\beta_1^{3'} \beta_3^{2'} - \beta_1^{2'} \beta_3^{3'}) (\beta_1^{1'} \beta_3^{3'} - \beta_1^{3'} \beta_3^{1'}) (\beta_1^{2'} \beta_3^{1'} - \beta_1^{1'} \beta_3^{2'}) \\ (\beta_1^{2'} \beta_3^{3'} - \beta_1^{3'} \beta_3^{2'}) (\beta_1^{3'} \beta_2^{1'} - \beta_1^{1'} \beta_2^{3'}) (\beta_1^{1'} \beta_2^{2'} - \beta_1^{2'} \beta_2^{1'}) \end{pmatrix},$$

where \sqrt{a} again is the square root of the determinant of the covariant metric tensor, eq. (3.17).

The two-dimensional form, for instance for $x^{1'}$, $x^{3'}$ -coordinates, is

$$(3.28) \quad \{\beta_{\delta'}^{i'}\} = \frac{1}{\sqrt{a}} \begin{pmatrix} \beta_3^{2'} & -\beta_3^{1'} \\ -\beta_1^{2'} & \beta_1^{1'} \end{pmatrix}.$$

As example the transformation of the external inviscid flow from the Cartesian into the surface coordinates is considered:

$$(3.29) \quad v_e^i = \beta_j^i v_e^{j'}.$$

Of course v_e^3 should be zero, but it should be computed in order to check the accuracy of both the inviscid flow data, and the whole geometrical representation. The physical components v_e^{α} , when needed, are

$$(3.30) \quad v_e^{\star\alpha} = v_e^{\alpha} \sqrt{a_{\alpha\alpha}}.$$

The amount of the velocity is

$$(3.31) \quad |\underline{v}_e| = [(\sqrt{a_{11}} v_e^1)^2 + 2 a_{12} v_e^1 v_e^2 + (\sqrt{a_{22}} v_e^2)^2]^{1/2},$$

or with physical components

$$(3.32) \quad |\underline{v}_e| = [(v_e^{\star 1})^2 + 2 v_e^{\star 1} v_e^{\star 2} \cos \vartheta + (v_e^{\star 2})^2]^{1/2}.$$

The angle ψ_e (for the definition of ψ see Fig. 3.6b) reads

$$(3.33) \quad \tan \psi_e = \frac{\sqrt{a} v_e^2}{a_{11} v_e^1 + a_{12} v_e^2},$$

or

$$(3.34) \quad \tan \psi_e = \frac{\sin \vartheta v_e^{\star 2}}{v_e^{\star 1} + \cos \vartheta v_e^{\star 2}}.$$

On the other hand the components v_e^{α} or $v_e^{\star\alpha}$ are found with

$$(3.35) \quad \begin{pmatrix} v_e^1 \\ v_e^2 \end{pmatrix} = \begin{pmatrix} \frac{v_e^{\star 1}}{\sqrt{a_{11}}} \\ \frac{v_e^{\star 2}}{\sqrt{a_{22}}} \end{pmatrix} = \begin{pmatrix} \frac{\sin(\vartheta - \psi_e)}{\sqrt{a_{11}} \sin \vartheta} & 0 \\ \frac{\sin \psi_e}{\sqrt{a_{22}} \sin \vartheta} & 0 \end{pmatrix} \begin{pmatrix} |\underline{v}_e| \\ 0 \end{pmatrix}.$$

In closing this sub-chapter the problem of placing the initial data for the boundary-layer computation is addressed. It is closely related to the problem of coordinate definition.

In general the rule holds that initial data placed into a region of strongly accelerated external flow very fast loose their influence on the solution in favour of the local external conditions. The contrary is true if these data are placed into or close to a portion of decelerated flow. In such cases the results of computations with approximate initial data must be considered with care [12].

Consider now the flow past a wing, Fig. 3.7a to c. At the attachment line, which in general does not lie on the leading edge at $x^1 = 0$, the flow is directed towards the wing tip and not in chord direction. In many applications it is sufficient to start shortly above or below the leading edge where the flow has changed sufficiently into chord direction. Approximate initial conditions, locally from an infinite swept-wing solution (to be found for instance in [13]), serve well in such cases.

However, if one is interested in the exact flow at the leading edge, for instance in

order to study hydrodynamic stability (necessary for laminar wing design), a special solution must be employed. In [14] as well as in [15], although with different approaches, the solution is marched from the root towards the tip in a small stripe, Fig. 3.7b. The width Δx_{LE}^1 must at least encompass the attachment line to such an extent, that all the important features are captured. Note that the relative pressure maximum in chord direction lies at a distance Δx_p^1 to the attachment line [3]. Only for an infinite swept wing this distance is zero.

The computation in chord direction on the upper and the lower side of the wing proceeds as indicated in Fig. 3.7b. In Fig. 3.7c the starting lines (inflow boundaries) near the leading edge as used with the technique [14] are shown [16]. At the wing tip an inflow boundary on the upper side of the wing can only be defined with a locally infinite swept wing approximation [3].

In Fig. 3.7d finally the hybrid coordinates for a car body at yaw are given [17]. The $x^2 = \text{const.}$ -lines are inviscid external streamlines, while the $x^1 = \text{const.}$ -lines are constructed by partitioning each external streamline in the same manner. In the forward stagnation point a quasi one-dimensional solution [3] can be used to find the starting data for the boundary-layer computation. In this way the whole nose region can be covered with the boundary-layer solution, which is of interest in many other cases, too.

3.2 Wall-Shear Stress and Friction Forces

The wall-shear stresses in general boundary-layer coordinates read

$$(3.36) \quad \tau_W^{\alpha 3} = \mu \frac{\partial v^{\alpha}}{\partial x^3}, \quad (\alpha = 1, 2),$$

and with contravariant components

$$(3.37) \quad \tau_W^{\alpha 3} = \mu \frac{\partial v^{\alpha}}{\partial x^3},$$

where

$$(3.38) \quad \tau_W^{\alpha 3} = \frac{\tau_W^{\alpha 3}}{\sqrt{a(\alpha\alpha)}}.$$

Magnitude $|\tau_W|$ and angle ψ_W between the $x^2 = \text{const.}$ -coordinate line and τ_W can be computed like the velocity data, eqs. (3.31 to 3.35).

The computed wall shear-stress distribution often is presented in iso-line plots. Another possibility is to show it in carpet diagrammes (see for instance Fig. 4.10a).

In the following only the computation of the friction forces acting on a general configuration is considered [18]. The friction forces on a surface element are with eq. (3.16):

$$(3.39) \quad dR^{\alpha} = \tau_W^{\alpha 3} dA = \tau_W^{\alpha 3} \sqrt{a} dx^1 dx^2, \quad (\alpha = 1, 2).$$

The Cartesian components follow with eq. (3.25)

$$(3.40) \quad dR^{i'} = \beta_{\alpha}^{i'} dR^{\alpha} = \beta_1^{i'} dR^1 + \beta_2^{i'} dR^2 \quad (i' = 1, 2, 3).$$

In Fig. 3.8 a surface element is given. By applying the above relations in finite form to the surface element by choosing for instance

$$(3.41a) \quad \Delta x_{i,j}^1 = 0.5 (\Delta x_{i-1,j}^1 + \Delta x_{i+1,j}^1),$$

$$(3.41b) \quad \Delta x_{i,j}^2 = 0.5 (\Delta x_{i,j-1}^2 + \Delta x_{i,j+1}^2),$$

and summarizing over the whole parameter plane the friction forces are found.

As an example results for a fighter nose at $M_{\infty} = 2$, $Re_{L=1m} = 2.7 \cdot 10^7$ are given [19]. The inviscid flow was computed with the Euler code [20]. The turbulent boundary-layer computation up to the position of the inlet, Fig. 3.9a, was made with the integral method [21]. The boundary-layer computation domain in axis direction extends over approximately 6m ($0 \leq x^1 \leq 1$).

In Fig. 3.9b the cumulated friction forces $R^{1'}$ and $R^{3'}$ are given for the whole configuration. $R^{2'}$ is given for one half, only, because it is compensated by the force on the other half. Note that the friction force $R^{3'}$ first is directed upward and then downward. This reflects the direction of the skin-friction lines, Fig. 3.9a, which will be discussed in the next sub-chapter, and in Chapter 3.5.

3.3 Streamlines and Skin-Friction Lines

One of the advantages of the use of contravariant vector components is that streamlines in non-orthogonal curvilinear coordinates are defined like in Cartesian coordinates [3]:

$$(3.41) \quad \frac{dx^1}{v^1} = \frac{dx^2}{v^2} = \frac{dx^3}{v^3}.$$

The construction of the streamlines for boundary-layer problems is made in the parameter plane, for instance with an iterative shooting technique [22]. Starting from P_m a point $P_{m+1}^{v^1}$ is found on the next crossing point with either a $x^2 = \text{const.}$ or a $x^1 = \text{const.}$ -coord.-line, Fig. 3.10. The angle ψ_m is then corrected: $\psi_{m+1}^{v^1} = 1/2(\psi_m + \psi_{m+1}^v)$, until it does not change any more. The last point $P_{m+1}^{v^1}$ is then the new streamline point. All interpolations are made linearly. Once the x^a -coordinates of the streamline are known, a back transformation into the physical space can be made with the contour-function relation (3.7), (3.9), and (3.10) for a wing, or (3.20) to (3.22) for a body.

In Fig. 3.11 inviscid external streamlines with

$$(3.42) \quad \frac{dx^1}{v_e^1} = \frac{dx^2}{v_e^2},$$

and the skin-friction lines with

$$(3.43) \quad \frac{dx^1}{\tau_w^{13}} = \frac{dx^2}{\tau_w^{23}}$$

are shown for a helicopter fuselage [19]. Instead of the contravariant components τ_w^{a3} also contravariant components c_x^a of the skin-friction coefficient can be used, provided they are computed with the same reference data.

The inviscid flowfield past the helicopter fuselage was computed with a panel method, and the boundary layer with the integral method [21]. Because a laminar separation bubble occurs at the nose (see the oil flow picture [23], Fig. 3.11c), the boundary layer was computed completely turbulent. The agreement between computed and visualized skin-friction lines (oil flow picture, Fig. 3.11c) is very good, except for the vicinity of the primary separation line. Although neither local nor global interaction (see Chapter 4.1) was taken into account, they lie quite close to each other, the computed separation line a little bit downstream of the other.

The computed external streamlines and skin-friction lines on the fighter nose, Fig. 3.9a, appear to be plausible. Here only the direction of the external flowfield was measured in three stations. The agreement with the computed directions is good.

In general it is strongly recommended to compute and plot at least the skin-friction lines. They give compared to a vector plot much more information. This will become more evident in Chapter 4.

3.4 Heat Flux

The heat flux q_w per unit surface at the wall is defined as in Cartesian coordinates:

$$(3.44) \quad q_w = -k \frac{\partial T}{\partial x^3}.$$

Like for the other parameters iso-plots can be drawn, which is not demonstrated here.

The heat flux through a surface element is simply

$$(3.45) \quad dQ_w = q_w dA = q_w \sqrt{a} dx^1 dx^2.$$

3.5 Displacement Thickness and Equivalent Source Strength

The true three-dimensional displacement thickness δ_1 of a computed or measured boundary layer can only be found by solving a linear partial differential equation of first order. This holds even for some quasi two-dimensional cases like for instance the plane-of-symmetry flow [3].

In [3] the original formulation of [24] for orthogonal coordinates was extended to non-orthogonal curvilinear boundary-layer coordinates and contravariant velocity components:

$$(3.46) \quad [\sqrt{a} \rho_e v_e^1 (\delta_1 - \delta_{1x1})]_{,1} + [\sqrt{a} \rho_e v_e^2 (\delta_1 - \delta_{1x2})]_{,2} = (\sqrt{a} \rho_e v_0^3)_w.$$

Here $[\]_{,\alpha}$ stands for $\partial[\]/\partial x^\alpha$. On the right-hand side a source term for possible wall suction or blowing is included. The quantities $\delta_{1x\alpha}$ denote the familiar two-dimensional definitions:

$$(3.47a) \quad \delta_{1x1} = \int_0^\delta \left(1 - \frac{\rho v^1}{\rho_e v_e^1}\right) dx^3,$$

$$(3.47b) \quad \delta_{1x2} = \int_0^\delta \left(1 - \frac{\rho v^2}{\rho_e v_e^2}\right) dx^3.$$

If from an integral-method solution the quantities (in external streamline coordinates, see Chapter 2)

$$(3.48a) \quad \delta_{1t} = \int_0^\delta \left(1 - \frac{\rho v_t}{\rho_e v_e}\right) dx^3,$$

$$(3.48b) \quad \delta_{1n} = - \int_0^\delta \frac{\rho v_n}{\rho_e v_e} dx^3$$

are given, eq. (3.46) changes to

$$(3.49) \quad [\sqrt{a} \rho_e v_e^1 \delta_{1,1}]_1 + [\sqrt{a} \rho_e v_e^2 \delta_{1,2}]_2 - \left[\frac{\sqrt{a}}{\sqrt{a_{11}}} \rho_e v_e \Delta_{1x1} \right]_1 - \left[\frac{\sqrt{a}}{\sqrt{a_{22}}} \rho_e v_e \Delta_{1x2} \right]_2 = (\sqrt{a} \rho_0 v_0^3)_w$$

with

$$(3.50a) \quad \Delta_{1x1} = \int_0^\delta \frac{\rho_e v_e^{*1} - \rho v^{*1}}{\rho_e v_e} dx^3 = \frac{\sin(\vartheta - \psi_e)}{\sin \vartheta} \delta_{1t} - \frac{\cos(\vartheta - \psi_e)}{\sin \vartheta} \delta_{1n},$$

$$(3.50b) \quad \Delta_{1x2} = \int_0^\delta \frac{\rho_e v_e^{*2} - \rho v^{*2}}{\rho_e v_e} dx^3 = \frac{\sin \psi_e}{\sin \vartheta} \delta_{1t} + \frac{\cos \psi_e}{\sin \vartheta} \delta_{1n}.$$

Other formulations are possible, too.

The external inviscid streamlines are the characteristics of eq. (3.46) and (3.49). These equations therefore can be solved in the boundary-layer coordinate system.

In Fig. 3.12 as example the computed boundary-layer thickness δ and the displacement thickness δ_1 are given at three stations of the supersonic fighter nose, Fig. 3.9. The distributions reflect the flow pattern seen in Fig. 3.9a. In Fig. 3.12b the thinning of the boundary layer over the canopy is evident, as well as the accumulation of boundary-layer material at the lower part of the fuselage, Fig. 3.12c, due to the downward flow direction at $x^1 > 0.5$, Fig. 3.9a. Separation is not imminent. It is interesting to note that the ratio boundary-layer thickness to displacement thickness is more or less of the order of that of the 1/7-power turbulent boundary layer. The computed boundary-layer thickness in cut D, Fig. 3.12c, compares well with experimental data.

Finally the relation for the equivalent inviscid source distribution $(\sqrt{a} \rho_0 v_0^3)_{inv}$ is given for general boundary-layer coordinates [3]:

$$(3.51) \quad (\sqrt{a} \rho_0 v_0^3)_{inv} = [\sqrt{a} \rho_e v_e^1 \delta_{1,1}]_1 + [\sqrt{a} \rho_e v_e^2 \delta_{1,2}]_2 + (\sqrt{a} \rho_0 v_0^3)_w,$$

and for integral-method results and external streamline coordinates:

$$(3.52) \quad (\sqrt{a} \rho_0 v_0^3)_{inv} = \left[\frac{\sqrt{a}}{\sqrt{a_{11}}} \rho_e v_e \Delta_{1x1} \right]_1 + \left[\frac{\sqrt{a}}{\sqrt{a_{22}}} \rho_e v_e \Delta_{1x2} \right]_2 + (\sqrt{a} \rho_0 v_0^3)_w.$$

These relations are solved locally. They are used regularly (transpiration concept), where weak interactions are to be described (see for instance [5]).

4. BOUNDARY-LAYER SEPARATION

4.1 Basic Considerations

As was already mentioned it is not possible to describe the phenomenon of separation in terms of pure boundary-layer theory. However, many conclusions can be drawn from a solution of the boundary-layer equations with regard to the location and to the configuration of the separation region.

Compared to two-dimensional separation the situation is very complicated in three-dimensional flows. Two-dimensional separation should be considered as a very special case of separation, even if only steady flow is considered, as is done here. In Fig. 4.1 some prototypes of separating flow are given. In the two-dimensional case, Fig. 4.1a, the wall-shear stress vanishes, which usually is taken as criterion for separation. The angle λ , under which the separation streamline leaves the surface was found in [25] to be

$$(4.1) \quad \tan \lambda = \frac{3 d\tau_w/dx}{dp/dx}.$$

In three-dimensional flows only a few points exist on a surface where the wall-shear stress actually is zero. In these singular points the skin-friction lines can form nodal points, saddle points etc., Fig. 4.1b. The reader is referred with regard to these topological properties, and to separation and vortex-flow topology in general to for instance [25-33]. Apart from the singular points vortex-sheet separation lines appear, Fig. 4.1c, whose structure, however, is closely connected to the structure of the flow at the

singular points.

The classical - two-dimensional - definition of separation must be extended, because in any case the formation of vortex sheets, which may roll up to vortices, Fig. 4.2, and of vortex filaments, which begin at focal points Fig. 4.1b, is coupled with the whole flowfield structure. In [7] the following definition is tried:

"Separation is present, if locally the boundary-layer assumptions break down, if vorticity is transported away from the body surface by convection, and subsequently vortex sheets and vortices are formed".

This definition encompasses two basic forms of separation [7]. The first one can be called flow-off separation. It appears at acute corners, where the boundary layers simply flow off the surface, like at wing-trailing edges, Fig. 4.2a, 4.2b, or at highly swept sharp wing leading edges, Fig. 4.2b. The second one can be called squeeze-off separation, which is the separation form usually considered, and which appears at round flanks, like round wing tips, Fig. 4.2a, or highly swept round wing leading edges, Fig. 4.2b, or at fuselages, Fig. 4.2c.

Squeeze-off separation in its simplest form appears on an ellipsoid at angle of attack, where a vortex-sheet separation line forms in a situation which is termed open separation in [26]. It can be explained by the curvature behaviour of the boundary layer discussed in Chapter 2, Fig. 2.1. In Fig. 4.3a it is sketched how the two boundary-layer streams from above and from below move against each other, starting at $x^1 \approx 0.4$. Note the curvature properties of the skin-friction lines. Note further that this picture appears already on the base of an inviscid flowfield calculation without taking into account the lee-side vortices which are fed by the open separation lines. Despite this the results of the laminar boundary-layer solution are in rather good agreement with the experimental results [34] for this flow situation.

In Fig. 4.3b the development of the energy-loss thickness δ_3 and the displacement thickness δ_1 reflects the convergence of the two boundary-layer streams against each other. Boundary-layer material is accumulated at the body flank and the final squeeze-off separation is clearly indicated.

This consideration can be applied, however, somewhat idealizing, to the flow situation on a rounded wing tip, Fig. 4.4. The boundary-layer flow moves from the lower side of the wing around the tip to the upper side. Because of the curvature properties a convergence of two boundary-layer streams like in Fig. 4.3a occurs. A tip vortex results therefore, which lies on the upper side (suction side) of the wing. If the wing tip is sharp, a flow-off separation will occur, Fig. 4.2a.

By means of boundary-layer considerations [7], flow-off separation at the trailing edge of a lifting wing can be analyzed, Fig. 4.5. The boundary layers on the upper and the lower side of the wing are sheared against each other, Fig. 4.5a. Downstream of the trailing edge they form a vortex layer (wake), which is represented by the discontinuity surface in potential theory models of lifting wings.

Departing from the bi-sector of the upper and the lower inviscid flow direction of the wake, a kinematically inactive wake part ($v^1(x^3)$ -profile in Fig. 4.5c) can be identified, together with an active part ($v^2(x^3)$ -profile). The inactive part carries the friction drag and the friction induced pressure drag like for a two-dimensional airfoil. The active part carries the induced drag. At the trailing edge locally the shear of the upper and the lower inviscid flows against each other, Fig. 4.5b, must be compatible with the spanwise derivative of the circulation $d\Gamma/dy$ [7,16]:

$$(4.2) \quad -2|v_{e\ell}| \sin \psi_{e\ell} = \frac{d\Gamma}{dy}.$$

Note that many first-order panel methods yield wrong velocity fields on the upper and the lower side of the wing in this respect [7,16]. Even if the overall forces and moments are predicted correctly, the velocity fields can only be used for boundary-layer studies if the condition (4.2) is fulfilled. In Fig. 3.7c the shear of the upper and lower inviscid flows against each other, which increases in spanwise direction, according to the increasing $d\Gamma/dy$, is clearly discernable.

In connection with the observation made with the boundary-layer development on the ellipsoid, Fig. 4.3, finally the locality principle [7,16] is mentioned. Many experimental and numerical results of flowfield investigations suggest that a change in body shape or in the flow configuration, for instance by separation, is felt only locally and downstream of that location. This is the reason why in general a boundary-layer computation yields good results compared to experimental results, although usually only inviscid solutions without modelling of the separation phenomena are applied.

The fact that also the location of primary separation lines usually can be predicted to a good degree of accuracy is connected with this principle. The global interaction due to the separating boundary layer obviously is weak in most cases. The local interaction, however, because of the elliptic properties of the flow near a separation line or point, finally makes it impossible to predict exactly the location of separation.

The locality principle must be used with care. Of course, the flow is changed upstream too, because of the elliptic property of subsonic flowfields. These changes are

small as was seen. They can be significant if for instance the wake of the body carries kinematically active vorticity. Then a global interaction can occur which may not be significant for the boundary-layer development, but for the global forces on the body. An example for this is the induced drag of wings.

4.2 Basic Global Topology Rules

The number of singular points obeys topological rules. Here only two of these rules will be demonstrated in order to show how such rules can be used. The reader is referred to [27] for a thorough discussion of this topic.

Two classes of singular points exist, Fig. 4.1b: a) nodal points N, which include focal points F, b) saddle points S. Half-nodes and half-saddles are denoted N' , and S' , respectively.

The first of the two rules concerns the connection of streamlines and skin-friction lines in a two-dimensional plane cutting a three-dimensional body [27]:

$$(4.3) \quad \left(\epsilon_N + \frac{1}{2} \epsilon_{N'} \right) - \left(\epsilon_S + \frac{1}{2} \epsilon_{S'} \right) = -1.$$

Two applications are shown in Fig. 4.6.

The body with the longitudinal cut, Fig. 4.6a, exhibits the familiar attachment point in the nose, which is a half-saddle. The separation region contains two recirculation areas in the cutting plane, which are counted as focal points, Fig. 4.1b. Three more half-saddles lie on the body surface and a free saddle point closes the recirculation areas. Note that this is a real stagnation point, which lies away from the body surface. It is seen that the near wake has an orderly structure, which, however, may not exist as steady structure at every Reynolds number. The fluid in the recirculation area is locked if the flow is steady.

Fig. 4.6b shows a different situation with real focal points, which represent the longitudinal vortices on the lee-side of the wing. These vortices in turn induce secondary suction peaks on the upper surface of the wing, and finally - secondary - vortex-sheet separation which leads to secondary vortices. Even higher order vortices may appear. It is seen that three attachment lines with half saddles are necessary on the upper wing surface in order to complete the picture. In the lower part it is indicated that a laminar boundary layer separates at a higher velocity level (note that the local interaction due to the separation process is not indicated in the pressure distribution) than a turbulent one. This leads to stronger vortices in the laminar case compared to the turbulent case, because of the higher vorticity content [7].

The second rule concerns the connection of skin-friction lines on a three-dimensional body [27]:

$$(4.4) \quad \epsilon_N - \epsilon_S = 2.$$

This rule will be demonstrated in Chapter 4.4, Fig. 4.12.

The topological structure, i.e. the topography of skin-friction lines and streamlines, can be very complicated. In Fig. 4.7 [30] the vicinity of the nose of a blunt body is shown with possible topographies, indicating that vortex filaments and vortex sheets leave the surface (vortex filaments may attach, too, case 15), and arrange themselves above the body surface. It is very important to note that the same skin-friction line topography on the surface does not necessarily mean the same vortex topography above the surface, cases 2 and 3, cases 10 and 11. Therefore the interpretation of computed skin-friction patterns or of oil-flow patterns on a body surface must be made with great care.

Many of the patterns shown in Fig. 4.7 have been verified in experiment [35]. They are partly very sensitive to changes in angle of attack, Reynolds number and Mach number. It appears, however, that with increasing Reynolds number a decrease of complexity occurs [36].

4.3 Local Topography of Separation Lines, $|\underline{\tau}|$ -Minimum Line

In [37,3] the flow in the vicinity of vortex-sheet separation lines was studied by means of local series expansions (see also [25,28]). One of the results was that very close to a separation line a $|\underline{\tau}|$ -minimum line exists, Fig. 4.8. Consider a point P_0 on the separation line, Fig. 4.8a. Locally a coordinate system is oriented such that x^1 is normal to the separation line, and x^2 tangential to it. Schematically the wall-shear stresses have a distribution like shown in Fig. 4.8b, with $\tau^{13} = 0$ at $P_0(x^1=0)$, and τ^{23} finite. A minimum of $|\underline{\tau}|$ occurs at

$$(4.5) \quad \Delta x_m^1 = \frac{-\tau^{23} \tau_{,1}^{23}}{(\tau_{,1}^{13})^2 + (\tau_{,1}^{23})^2} \Big|_{P_0}.$$

For details see [37,3]. In two-dimensional flows and in plane-of-symmetry flows $\Delta x_m^1 = 0$, because there $\tau^{23} = 0$, $\tau_{,1}^{13} \neq 0$. In general three-dimensional cases, including the

infinite swept wing case Δx_m^1 is finite. This means that the $|\tau|$ -minimum line, which can be observed in any experiment too, lies close, but not on the separation line. In three-dimensional boundary-layer calculations the occurrence of the $|\tau|$ -minimum line can be used as an indicator of a separation line. If locally eq.(4.5) is evaluated, especially if other indicators of separation are present (see next sub-chapter), and

$$(4.6) \quad \Delta x_m^1 \ll 1$$

holds, a separation line is imminent. In Fig. 4.8c the situation on a swept wing is sketched, where iteratively the location of the separation line was approximated [37].

Usually the $|\tau|$ -minimum line appears already much upstream of an open separation line. If the separation line is curved, also a points-of-inflection line occurs [37, 3].

With the series expansion technique also the local topography of an attachment line can be studied [3]. As was already mentioned in Chapter 3.1, the pressure-maximum line lies close but not on the attachment line, Fig. 3.7b. Other details of the attachment line - inviscid streamline and skin-friction line patterns - can be deduced, too [3].

4.4 Separation Indicators and their Application

The fact that on a three-dimensional separation line the wall-shear stress does not vanish, Fig. 4.8, makes it difficult in principle to decide, if the computation process breaks down, whether separation is found by the computation or not. The computation process can break down if the CFL-condition, Chapter 2, is violated. This indeed occurs usually in the vicinity of separation. It can, however, also occur, if the coordinate system, at least locally, is wrongly oriented.

Although the matter of three-dimensional separation in boundary-layer computations was studied by several authors (see for instance [38-41]), no simple single criterion exists. For practical purposes the following indicators serve well to detect separation in computed boundary-layer data:

1. local convergence of skin-friction lines (Fig. 4.3a),
2. bulging of the boundary-layer thickness (δ), and the displacement-thickness (δ_1) contours (Fig. 4.3b),
3. occurrence of a $|\tau|$ -minimum line (Fig. 4.3a, Fig. 4.8c).

Other indicators of more limited value are

4. wall-shear stress approaches zero, $|\tau_w| \rightarrow 0$ (Fig. 4.10a),
5. sudden rise of streamwise form parameter $H_{tt} = \delta_{1t} / \delta_{2tt}$ (Fig. 4.10b),
6. sudden rise of equivalent inviscid source strength.

In the following these indicators are applied to the results of boundary-layer computations for a car body, and for an airplane fuselage.

In [42] (see also [12]) the flow past a research car body [43] was studied, Fig. 4.9. The length of the body is $L = 4.328\text{m}$. The Reynolds number was $Re_{ref} = 9.74 \cdot 10^6$, and the free-stream Mach number $M_{ref} = 0.1$. The inviscid flowfield was computed with a panel method at zero yaw, but in the presence of the ground. The turbulent boundary layer was computed with the integral method [21].

Because this car body has a good aerodynamic shape ($C_D = 0.16$), the separation zone is small, Fig. 4.9b. Wall shear-stress distribution, Fig. 4.10a, and streamwise form parameter, Fig. 4.10b, show apart from two peculiar regions (K_3) nothing which points to separation.

In Fig. 4.11a strong variations especially of the displacement thickness δ_1 are seen. From the considerations in Chapter 4.1 it is known that a positive bulging (location c in Fig. 4.11a) points to squeeze-off separation, if it is accompanied by a convergence of skin-friction lines (indicators 1 and 2). This is the case here: the convergence of skin-friction lines at this location can be seen clearly in Fig. 4.12a. Consequently a negative bulging, and especially a negative δ_1 (locations a, b, and d in Fig. 4.11a) points to a divergence of skin-friction lines, Fig. 4.12a. This feature is indicated in Fig. 4.3b for the flow past the ellipsoid, too. In Fig. 4.11b it is shown that the bulging is a property of the real displacement thickness δ_1 only, and not of its components δ_{1x} , eq.(3.47). Therefore in order to work with the separation indicator 2 eq.(3.46) has to be solved.

The point $c_f \rightarrow 0$ in Fig. 4.10a is accompanied by a convergence of skin-friction lines, too, Fig. 4.12a, point K_3 . This feature is reflected in Fig. 4.10b, but not in the thickness distributions, Fig. 4.11. It can be concluded that this is a singular point, a nodal point, especially because it lies in the - upper - line of symmetry.

Finally on the base of the computed results and with the help of the second topological rule eq.(4.4) the possible surface separation topography shown in Fig. 4.12 emerges. At the left and right flanks a short vortex-sheet separation line each is present. In the back a pair of vortex filaments leaves the surface. Five nodal points, two focal points, and five saddle points are distributed over the body surface. The nodal points K_1

and K_2 and also the saddle point S_1 are evident from the computation, as well as the two vortex-sheet separation lines. The other points are constructed. Experimental results seem to confirm this pattern [12], which is also discussed in [31].

The boundary-layer computations for the airplane fuselage [44] were made in order to study means of passive boundary-layer control by geometry shaping. The computations were made for a freestream Mach number $M_{ref} = 0.8$, and a Reynolds number with respect to the fuselage length of $Re = 7 \cdot 10^8$. The angle of attack was $\alpha = 0^\circ$. The inviscid flowfields were found with panel computations, the turbulent boundary layers were computed with the integral method [21].

In Fig. 4.13 the panel model is shown. The original configuration (M0) has circular cross-sections all over. The modifications M1 and M2 were found by a smooth blending of the cross-sections, starting at $x^1_B = 0.6$ from the circular section, to a rounded triangle (M1), and a rounded circle/rectangle (M2) at $x^1 = 1$, respectively [44]. The center of gravity of the modified cross-sections M1 and M2 lies always deeper than that of the original cross-sections M0. The side-view contour and the largest width of the fuselage are the same for all three configurations.

In Fig. 4.14 the development of the inviscid flow and the boundary layer is shown. A strong downwash and indications for a massive separation at $x^1 = 0.9$ are evident for the original fuselage, Fig. 4.14a. The down-shift of the center of gravity of the cross-sections reduces the downwash: the inviscid flow does not converge towards the lower symmetry line at $x^1 = 0.9$, and the skin-friction lines don't get swept away from it, Figs. 4.14b and c, as for M0, Fig. 4.14a.

The distributions of the boundary-layer thickness δ and the displacement thickness δ_1 at $x^1 = 0.76$, Fig. 4.15 are only a little bit different for the three configurations. At $x^1 = 0.89$, however, it is seen that for M0 massive separation is present, whereas for M1 and M2 a vortex-sheet separation is indicated, Fig. 4.16, see also Figs. 4.14b and c.

Taking together all clues, the computational results indicate a strong thickening of the boundary layer below the upswept fuselage end and a massive separation for the original configuration M0, Fig. 4.17a. The modifications bring about a somewhat lesser thickening, and especially a change of the structure of the separation region, as indicated in Fig. 4.17b. This structure certainly is favourable and possibly will lead to a smaller total drag of the configuration.

The results are subject to the following criticisms: a) The boundary-layer thickness is of the order of the fuselage radius around the lower symmetry line at $x^1 = 0.9$. First-order boundary-layer theory certainly is inadequate here. The displacement of the external inviscid flow must be taken into account. b) Neither the global nor the local interaction was taken into account. The locality principle says that the global interaction might play no large role, however, in order to make a statement about the drag changes, the complete interaction must be taken into account.

The fact that neither the influence of the wing nor that of the tail unit was taken into account, makes it clear that the basic reason for the adverse boundary-layer behaviour beneath an upswept fuselage end is the upsweep itself. Wing and tail unit, however, may modify to a certain extent the picture.

5. CONCLUSIONS

It was shown how results from boundary-layer computations can be post-processed, and how they can be used in design aerodynamics. With the techniques available practically every geometric configuration can be handled as long as only the boundary-layer concept is valid.

In design aerodynamics boundary-layer studies are used for many purposes. Typical applications are: airfoil and wing design, fuselage design, boundary-layer control by cooling, heating, suction, blowing, boundary-layer stability and transition, separation detection and control. New technologies like the laminar wing or hypersonic transport systems demand the application of boundary-layer theory.

The problem of turbulence modeling seems not to be very critical, at least as long as the boundary layers are pressure-field driven. Eddy viscosity models and the assumption of turbulent isotropy usually are sufficient. The situation is different with regard to hydrodynamic stability and transition laminar-turbulent. Empirical criteria exist only for two-dimensional and for swept-wing cases at low Mach numbers. The reason for this unsatisfactory situation is that transition in three-dimensional boundary layers can occur by several highly complex mechanisms, which are not yet well explored.

Integral methods and finite-difference methods seem to give results of comparable quality. Boundary-layer control as cooling, heating, suction, and blowing usually is handled with finite-difference methods because of their higher flexibility. For most of the problems of design aerodynamics first-order boundary-layer theory suffices. If the Reynolds numbers are low and for instance at the end of fuselages, where a reverse Mangler-effect occurs, second or higher-order boundary-layer theory should be employed.

Separation locations, at least the primary separation line, can be found in many cases with sufficient accuracy, even if no global interaction is taken into account. In

some cases even the separation topography can be deduced to a certain extent. There is, of course, always the desire to treat separation in more detail, and also to compute drag and lift of a configuration without the classical modeling approaches. In such cases the local and the global interactions must be taken into account.

The ultimate approach to this end is the uniform solution of the Navier-Stokes equations, which, however, completely leads away from boundary-layer theory. For several reasons, one of them the high costs of such solutions, other approaches are in use or in development, like inverse methods, interaction schemes etc.. An approach, where boundary-layer theory will play a large role in future, too, is the concept of zonal solutions, where the Navier-Stokes equations will be solved only where the boundary-layer concept breaks down. Finally, boundary-layer theory will increasingly be used for unsteady problems of all kind.

6. REFERENCES

- [1] W.Flügge: "Tensor Analysis and Continuum Mechanics", Springer, New York, 1972.
- [2] R.Aris: "Vectors, Tensors, and the Basic Equations of Fluid Mechanics", Prentice Hall, Englewood Cliffs, 1962.
- [3] E.H.Hirschel, W.Kordulla: "Shear Flow in Surface-Oriented Coordinates", Vol. 4 of Notes on Numerical Fluid Mechanics, Vieweg, Braunschweig-Wiesbaden, 1981.
- [4] T.Cebeci: "Problems and Opportunities with Three-Dimensional Boundary Layers", in: AGARD-R-719, 1985, pp. 6-1 to 6-35.
- [5] E.H.Hirschel, M.A.Schmatz: "Zonal Solutions for Viscous Flow Problems", in: Finite Approximations in Fluid Mechanics (E.H.Hirschel, ed.), Vol. 14 of Notes on Numerical Fluid Mechanics, Vieweg, Braunschweig-Wiesbaden, 1986, pp. 99-112.
- [6] F.Monnoyer: "Second-Order Three-Dimensional Boundary Layers", in: Proc. 6th GAMM-Conference on Numerical Methods in Fluid Mechanics (D.Rues, W.Kordulla, eds.), Vol. 13 of Notes on Numerical Fluid Mechanics, Vieweg, Braunschweig-Wiesbaden, 1986, pp. 263-270.
- [7] E.H.Hirschel: "On the Creation of Vorticity and Entropy in the Solution of the Euler Equations for Lifting Wings", MBB-LKE122-AERO-MT-716, 1985.
- [8] R.Courant, D.Hilbert: "Methods of Mathematical Physics", Vol. II, Interscience, New York, 1962.
- [9] E.Krause, E.H.Hirschel, Th.Bothmann: "Die numerische Integration der Bewegungsgleichungen dreidimensionaler, laminar, kompressibler Grenzschichten", in: DGLR-Fachbuchreihe, Band 3, Braunschweig, 1969, pp. 3-1 to 3-49.
- [10] C.Reinsch: "Smoothing by Spline Functions", Num. Math., Vol. 10, 1967, pp. 177-183.
- [11] E.H.Hirschel: "Boundary-Layer Coordinates on General Wings and Bodies", ZFW, Vol. 6, No. 3, 1982, pp. 194-202.
- [12] E.H.Hirschel, N.Bretthauer, H.Röhe: "Theoretical and Experimental Boundary-Layer Studies of Car Bodies", Int. J. of Vehicle Design, Vol. 5, No. 5, 1984, pp. 567-584.
- [13] H.Schlichting: "Boundary-Layer Theory", McGraw-Hill, New York, 1979.
- [14] D.Schwamborn: "Boundary Layer on Finite Wings and Related Bodies with Consideration of the Attachment Line Region", in: Proc. 4th GAMM-Conference on Numerical Methods in Fluid Mechanics (H.Viviani, ed.), Vol. 5 of Notes on Numerical Fluid Mechanics, Vieweg, Braunschweig-Wiesbaden, 1982, pp. 291-300.
- [15] J.P.F.Lindhout, A.C. de Bruin, J.H.M.Godden: "A Method for Three-Dimensional Boundary-Layer Calculations on Arbitrary Bodies: Some Results on Aircraft Wings and Engine Cowls", in: Three-Dimensional Boundary Layers (H.H.Fernholz, E.Krause, eds.), Springer, Berlin-Heidelberg, 1982, pp. 298-308.
- [16] E.H.Hirschel, L.Fornasier: "Flowfield and Vorticity Distribution near Wing-Trailing Edges", AIAA-Paper No. 84-0421, 1984.
- [17] N.Grün, personal communication, BMW, München, 1986.
- [18] E.H.Hirschel: "Three-Dimensional Boundary-Layer Calculations in Design Aerodynamics", in: Three-Dimensional Boundary Layers (H.H.Fernholz, E.Krause, eds.), Springer, Berlin-Heidelberg, 1982, pp. 353-365.
- [19] E.H.Hirschel: "Computations of Three-Dimensional Boundary Layers on Fuselages", J. of Aircraft, Vol. 21, No. 1, 1984, pp. 23-29.

- [20] C.Weiland: "Calculation of Three-Dimensional Stationary Supersonic Flowfields by Applying the "Progonka" Process to a Conservative Formulation of the Governing Equations", J. of Comp. Physics, Vol. 29, No. 2, 1978, pp. 173-198.
- [21] J.Cousteix: "Theoretical Analysis and Prediction Methods for a Three-Dimensional Turbulent Boundary Layer", ESA TT-238, 1976.
- [22] S.Rezanka: "Ein Verfahren zur Berechnung von äußeren Stromlinien und Grenz-Wand-stromlinien für Grenzschichtberechnungen an räumlichen Konfigurationen", MBB-UFE 122-AERO-MT-625, 1983.
- [23] G.Polz, J.Quentin, J.Amtsberg, A.Kühn: "Windkanaluntersuchungen zur optimalen Gestaltung von Transporthubschrauberzellen hinsichtlich Leistungsbedarf und Stabilitätsverhalten", MBB-UD-299/80, 1981.
- [24] F.K.Moore: "Displacement Effect of a Three-Dimensional Boundary Layer", NACA Rep. 1124, 1953.
- [25] K.Oswatitsch: "Die Ablösebedingungen von Grenzschichten", in: Boundary Layer Research (H.Görtler, ed.), Springer, Berlin-Göttingen-Heidelberg, 1958, pp. 357-367, also as NASA TTF-15200 "The Separation Conditions of Boundary Layers".
- [26] K.C.Wang: "Separation Patterns of Boundary Layer over an Inclined Body of Revolution", AIAA J., Vol. 10, 1972, pp. 1044-1050.
- [27] D.J.Peake, M.Tobak: "Three-Dimensional Interaction and Vortical Flows with Emphasis on High Speeds", AGARDograph No. 252, 1980.
- [28] U.Dallmann: "Topological Structures of Three-Dimensional Flow Separations", DFVLR IB 221-82 A 07, 1982.
- [29] U.Dallmann: "Topological Structures of Three-Dimensional Vortex Flow Separation", AIAA-Paper 83-1735, 1983.
- [30] U.Dallmann: "Three-Dimensional Vortex Separation Phenomena - A Challenge to Numerical Methods", in: Proc. 5th GAMM-Conference on Numerical Methods in Fluid Mechanics (M.Pandolfi, R.Piva, eds.), Vol. 7 of Notes on Numerical Fluid Mechanics, Vieweg, Braunschweig-Wiesbaden, 1984, pp. 40-48.
- [31] H.Hornung, A.E.Perry: "Some Aspects of Three-Dimensional Separation - Part I: Streamsurface Bifurcations", ZFW, Vol. 8, No. 2, 1984, pp. 77-87.
- [32] A.E.Perry, H.Hornung: "Some Aspects of Three-Dimensional Separation - Part II: Vortex Skeletons", ZFW, Vol. 8, No. 3, 1984, pp. 155-160.
- [33] U.Dallmann: "Structural Stability of Three-Dimensional Vortex Flows", in: Proc. Nonlinear Dynamics of Transcritical Flows (H.L.Jordan, H.Oertel, K.Robert, eds.), Lecture Notes in Engineering, Vol. 13, Springer, Berlin-Heidelberg, 1985, pp. 81-102.
- [34] H.U.Meier, H.-P.Kreplin: "Experimental Investigation of the Boundary-Layer Transition and Separation on a Body of Revolution", ZFW, Vol. 4, 1980, pp. 65-71.
- [35] H.Bippes, M.Turk: "Oil-Flow Patterns of Separated Flow on a Hemisphere Cylinder at Incidence", DFVLR IB 222-83 A 07, 1983.
- [36] H.Bippes: "Experimente zu dreidimensional abgelösten Strömungen", DGLR-Paper 84-129, 1984.
- [37] E.H.Hirschel, W.Kordulla: "Local Properties of Three-Dimensional Separation Lines", ZFW, Vol. 4, 1980, pp. 295-307.
- [38] K.C.Wang: "Boundary Layer over a Blunt Body at High Incidence with an Open-Type Separation", Proc. Royal Society, London A340, 1974, pp. 33-55.
- [39] T.Cebeci, A.A.Khattab, K.Stewartson: "Three-Dimensional Laminar Boundary Layers and the Ok of Accessibility", J. Fluid Mechanics, Vol. 107, 1981, pp. 57-87.
- [40] J.Cousteix, R.Houdeville: "Singularities in Three-Dimensional Turbulent Boundary Layers. Calculations and Separation Phenomena", AIAA J., Vol. 19, No. 8, 1981, pp. 976-985.
- [41] K.C.Wang: "New Developments in Open Separation", in: Three-Dimensional Boundary Layers (H.H.Fernholz, E.Krause, eds.), Springer, Berlin-Heidelberg, 1982, pp. 94-105.
- [42] E.H.Hirschel, N.Bretthauer: "Grenzschichtberechnungen am SCHLOER-Kraftfahrzeug", MBB-UFE122-AERO-MT-577, 1982.
- [43] M.Hansen, K.Schloer: "Der AVA-Versuchswagen", AVA-Bericht 43 W 26, 1943.
- [44] E.H.Hirschel: "Theoretical Study of Boundary-Layer Control", AGARD CP 365, 1984, pp. 13-1 to 13-11.

7. SYMBOLS7.1 Latin Letters

a	$= a_{11}a_{22}-(a_{12})^2$, determinant of covariant surface metric tensor
\underline{a}_α	covariant base vector of surface-tangential coordinate
\underline{a}_3	covariant base vector of surface-normal coordinate
$a_{\alpha\beta}$	component of covariant surface metric tensor
CFL	Courant-Friedrichs-Lewy condition
c_D	drag coefficient
c_f	$= \underline{\tau}_w /(0.5\rho_e(v_e)^2)$, wall-shear-stress coefficient
ds, dA, dV	length, surface, and volume element
\underline{e}_i	unit vector of Cartesian reference coordinate system
F	focus point
\underline{F}	vector
F_i, F^{*i}	contravariant, and physical component of vector
H_{tt}	$= \delta_{1t}/\delta_{1tt}$, formparameter of streamwise (t) boundary-layer profile
k	heat-conductivity coefficient
L	length
L_{x^α}	normalizing length of x^α -coordinate
M	Mach number
N, N'	nodal point, and half-nodal point
n	surface-tangential coordinate normal to external inviscid streamline (cross-flow direction)
P	point
p	(static) pressure
Q_w	heat flux
q_w	heat flux per unit surface area
Re	Reynoldsnnumber
$R^{i'}$	$= R^{*i'}$, Cartesian shear-force comp.
R^α	contravariant shear-force component in surface-tangential coordinate
r	radius
S, S'	saddle point, and half-saddle point
T	(static) temperature
t	surface-tangential coordinate in direction of external inviscid streamline (streamwise direction)
u, v, w	Cartesian velocity components
\underline{v}	velocity vector
v	$= \underline{v} $, amount of velocity, speed
$v^{j'}$	$= v^{*j'}$, Cartesian components of velocity
$v^\alpha, v^{*\alpha}$	contravariant, and physical component of velocity in surface-tangential coordinate
v^3	$= v^{*3}$, velocity component in surface-normal coordinate
v_t, v_n	streamwise, and crossflow velocity component

x, y, z	Cartesian coordinates
$x^{j'}$	Cartesian reference coordinate
x^α	surface-tangential coordinate, Gaussian surface parameter
x^3	surface normal locally monoclinic coordinate
y	spanwise coordinate on wings
z	surface-normal coordinate

7.2 Greek Letters

α	angle of attack
$\beta_{\alpha}^{i'}$	$= \partial x^{i'}/\partial x^\alpha$, coordinate of surface-tangential base vector
$\beta_3^{i'}$	$= \partial x^{i'}/\partial x^3$, coordinate of surface-normal base vector
β_{ℓ}^k	inverse of $\beta_j^{i'}$
Γ	circulation
Δ_{1x^α}	integral thickness
δ	boundary-layer thickness
δ_1	displacement thickness
δ_2	momentum-loss thickness
δ_3	energy-loss thickness
δ_{1x^α}	integral thickness
ϑ	angle between $x^2=\text{const.}$, and $x^1=\text{const.}$ -coordinate line
λ, λ_1	separation angle
μ	viscosity coefficient
ν	$= \mu/\rho$, cinematic viscosity coefficient
ξ, η	wing coordinates
ρ	density
$\underline{\tau}$	(wall) shear-stress vector
τ	$= \underline{\tau} $, amount of (wall) shear stress
$\tau^{\alpha 3}, \tau^{* \alpha 3}$	contravariant, and physical component of (wall) shear-stress vector
φ	characteristic manifold
$\varphi_x, \varphi_y, \varphi_z$	derivatives of φ in x, y, z -direction
ψ	angle between $x^2=\text{const.}$ -coordinate line (x^1 -coordinate) and velocity or shear-stress vector

7.3 Indices7.3.1 Upper and Lower Indices

i, j, k, \dots	$= 1, 2, 3$; denotes general tensor quantities, parameters, etc.
$\alpha, \beta, \gamma, \dots$	$= 1, 2$; denotes surface-tangential tensor quantities, parameters, etc.
3	denotes surface-normal tensor quantities, parameters, etc.

7.3.2 Upper Indices

$'$	quantity in Cartesian reference coordinate system
$*$	physical quantity

7.3.3 Lower Indices

e	external inviscid flow
inv	inviscid flow

l lower side of wing
 m refers to $|\tau|$ -minimum line
 n cross-flow direction
 ref reference quantity
 t streamwise direction
 u upper side of wing
 $w, wall$ wall or surface
 $(aa), (ii)$ no summation
 $(i), (a)$ no summation

7.3.4 Other Symbols

∞ freestream condition
 $\underline{}$ underbar, vector quantity
 $|_P$ quantity at point P
 ∂_i partial derivative: $v_{ij}^i = \partial v^i / \partial x^j$
 $q(x^i)$ $i = 1, 2, 3$: $q = q(x^1, x^2, x^3)$

The Einstein summation convention is used throughout, e.g.:

$$\beta_{ij}^j, v^{i'} = \beta_{ij}^j, v^{i'} + \beta_{2j}^j, v^{2'} + \beta_{3j}^j, v^{3'}.$$

8. FIGURES

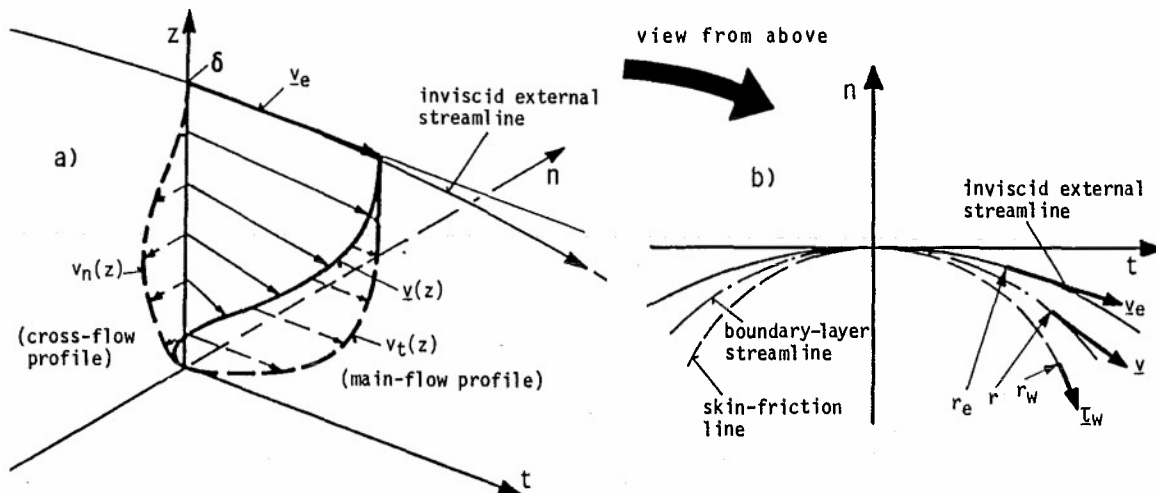


Fig. 2.1 Schematic of three-dimensional boundary layer [7],
 a) flow in external streamline coordinates,
 b) local centrifugal consideration (for convenience in Cartesian coordinates).

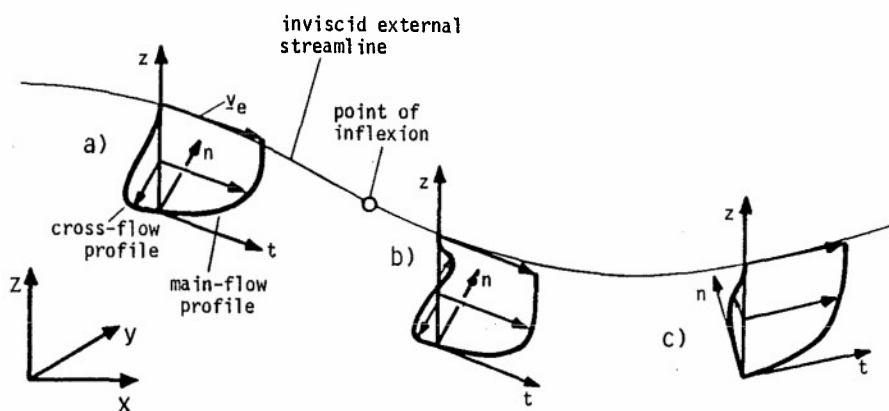


Fig. 2.2 Streamline curvature of a three-dimensional boundary layer (schematically) [7],
 a) negative for all streamlines,
 b) positive in upper part, negative in lower part,
 c) positive for all streamlines.

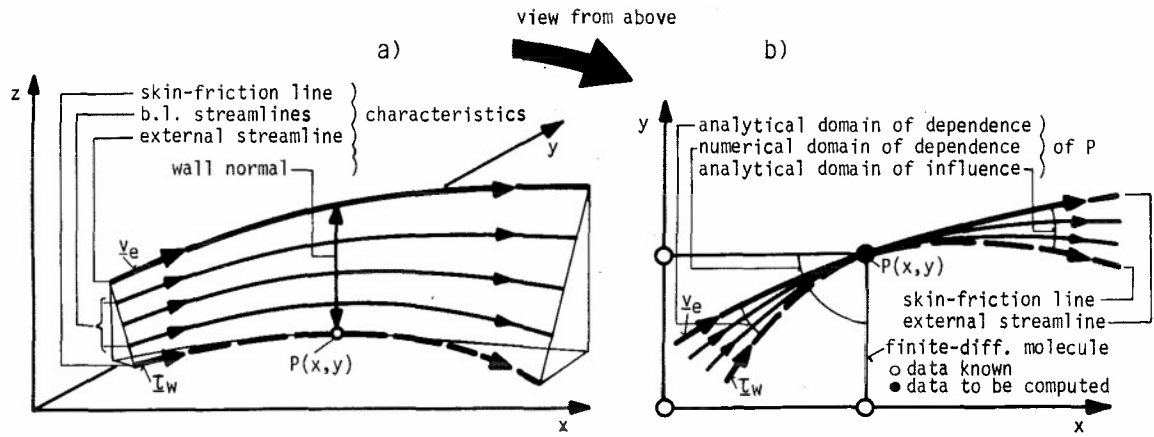


Fig. 2.3 Three-dimensional boundary layer,
a) characteristics (skewed stream surface),
b) analytical and numerical domain of dependence of flow at $P(x,y)$.

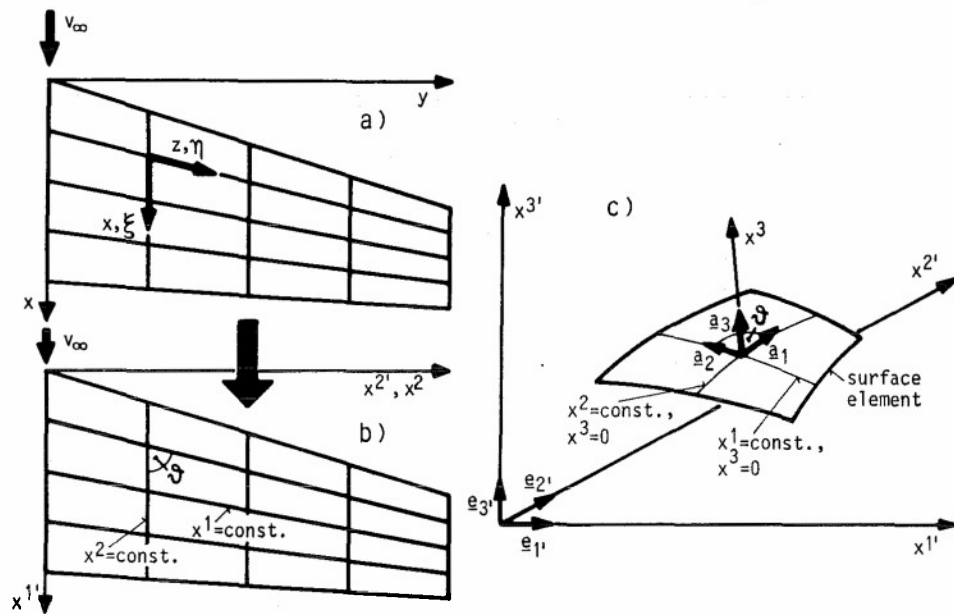


Fig. 3.1 Boundary-layer coordinates,
a) classical nomenclatures,
b) present nomenclature,
c) surface element.

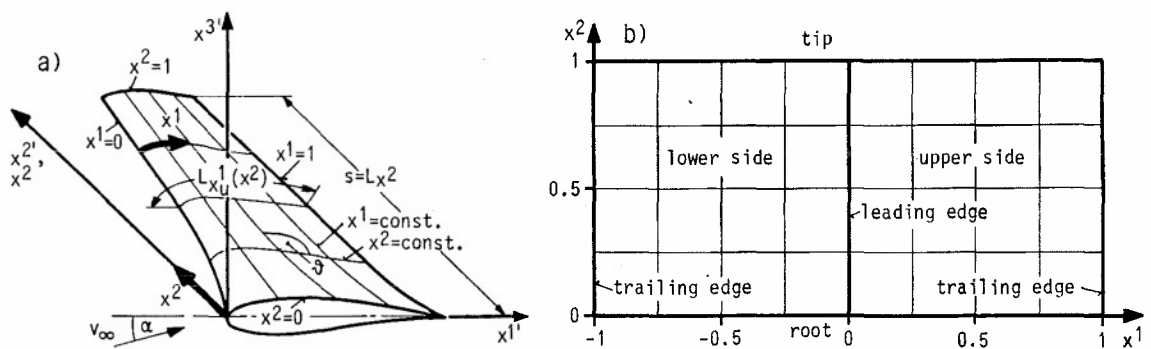


Fig. 3.2 Wing percent-line coordinate system,
a) surface coordinates,
b) parameter plane x^α .

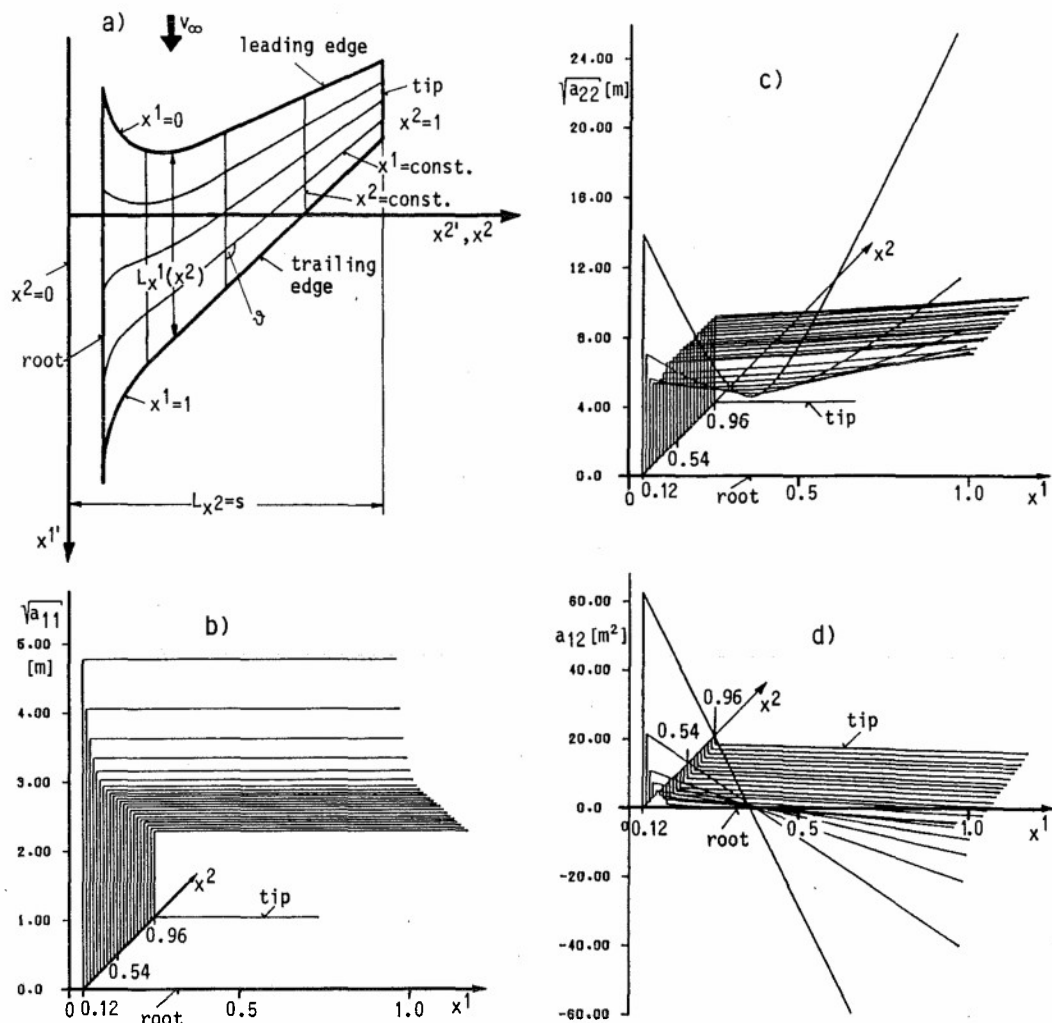


Fig. 3.3 Metric properties of wing coordinates [11],
a) planform,
b) to d) components of metric tensor.

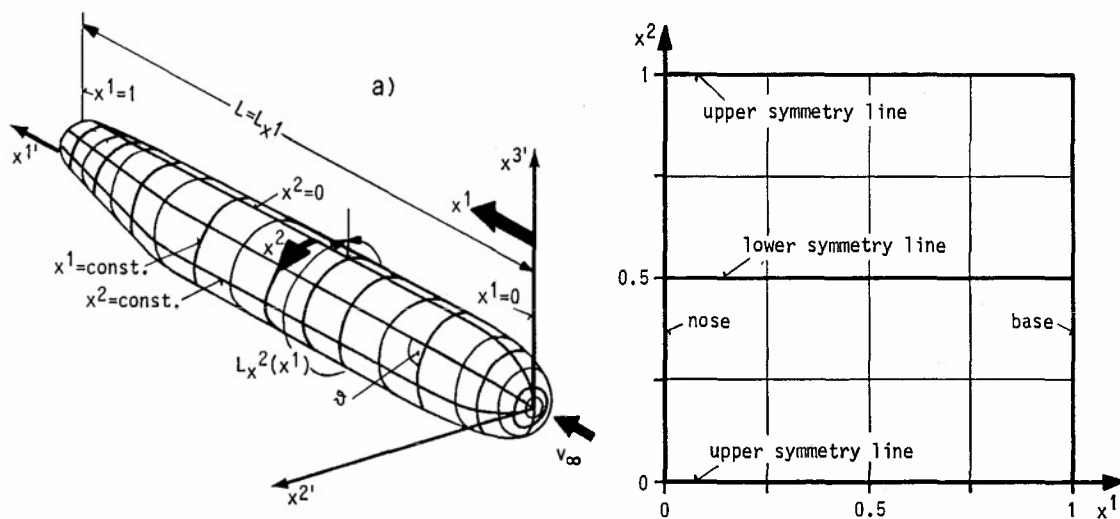


Fig. 3.4 Fuselage cross-section coordinate system,
a) surface coordinates,
b) parameter plane x^α .

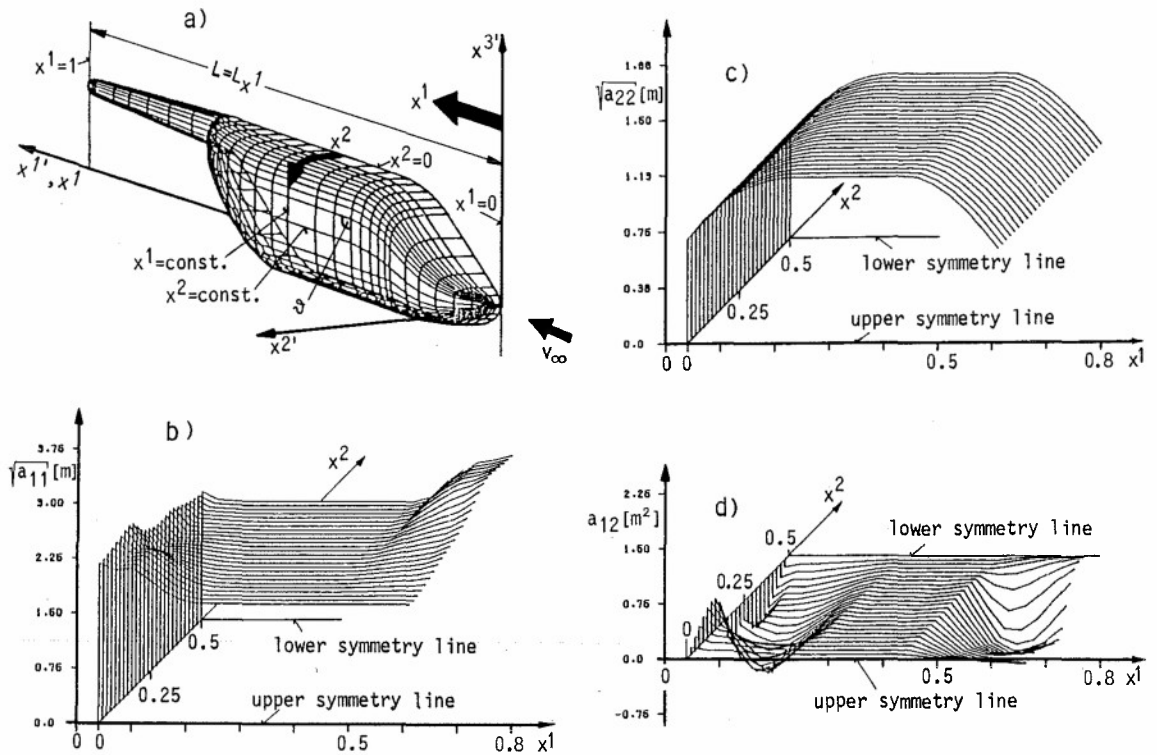


Fig.3.5 Metric properties of fuselage coordinates (right half) [11],
a) configuration,
b) to d) components of metric tensor.

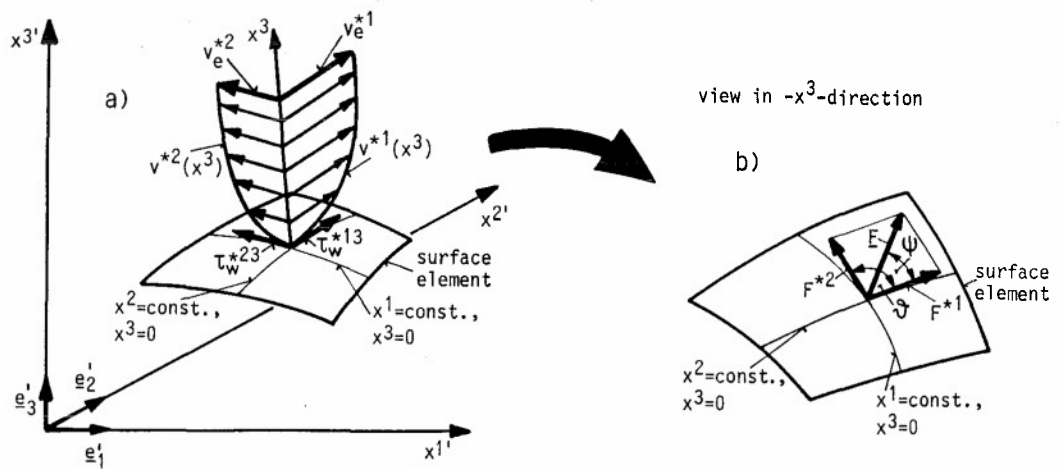


Fig.3.6 a) Vector components to be transformed,
b) general components and angle ψ

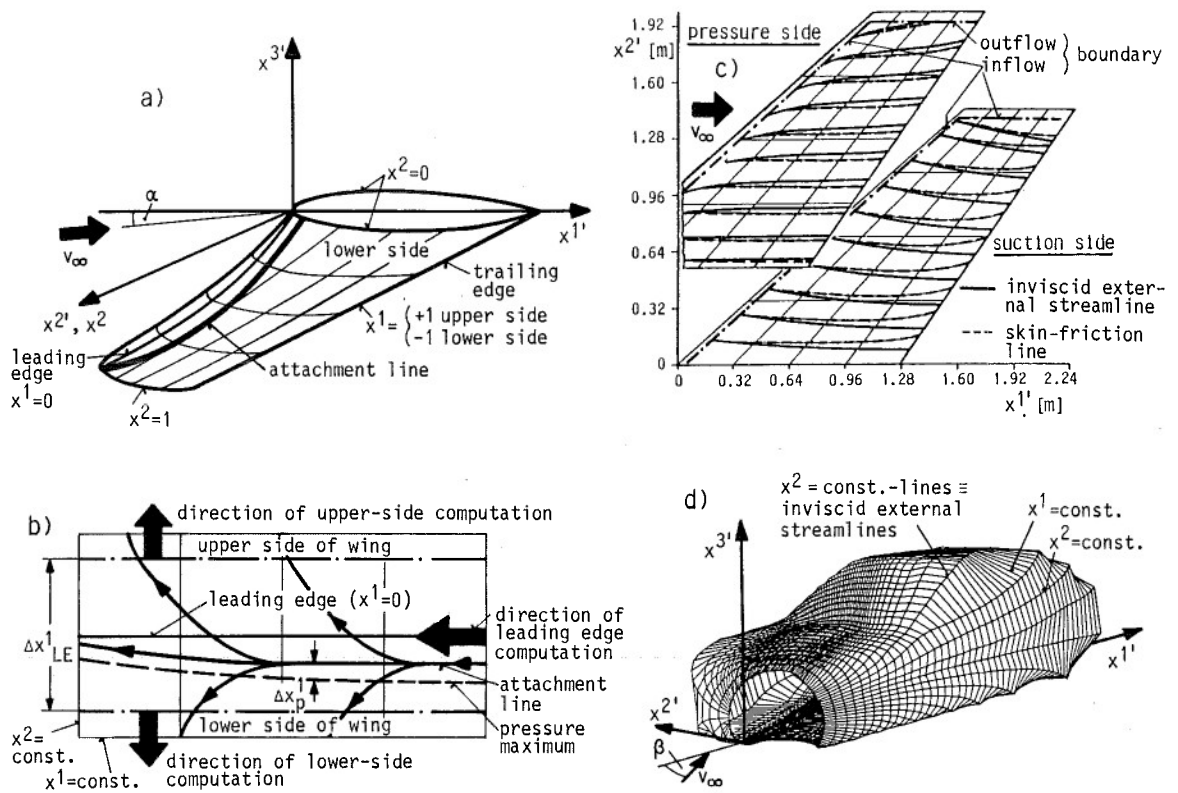


Fig. 3.7 Placement of initial data,
 a) attachment line on a swept wing at angle of attack (schematically),
 b) computational approach at the leading edge [14],
 c) inflow and outflow boundaries on a wing [16],
 (Kolbe wing, $M_\infty = 0.25$, $Re = 18 \cdot 10^6$, $\alpha = 8.2^\circ$)
 d) hybrid coordinates for car body with freestream at yaw angle β [17].

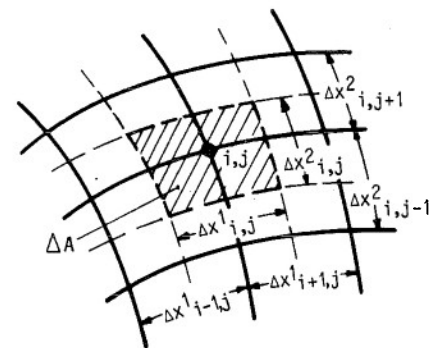
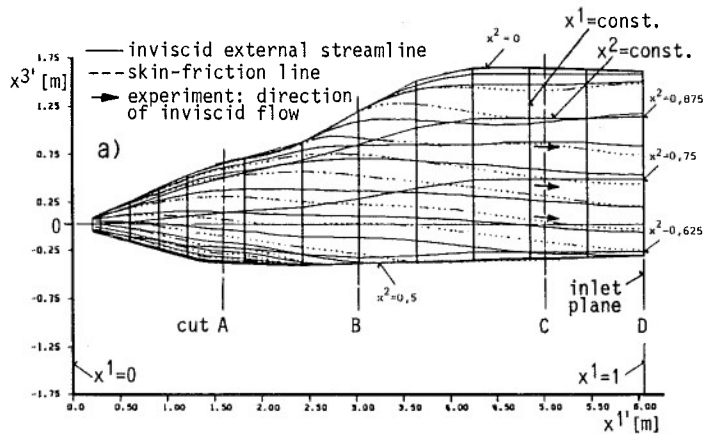


Fig. 3.8 Surface element for the computation of friction forces.

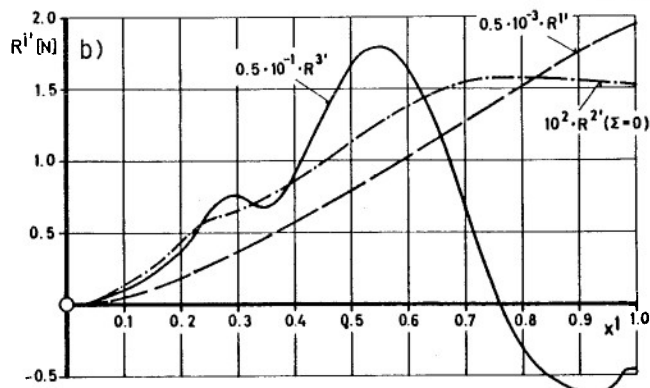


Fig. 3.9 Boundary-layer computation for a super-sonic fighter nose [19] ($M_\infty = 2$, $Re_{L=1m} = 2.7 \cdot 10^7$)
 a) side view with inviscid streamlines, and skin-friction lines,
 b) cumulated friction forces.

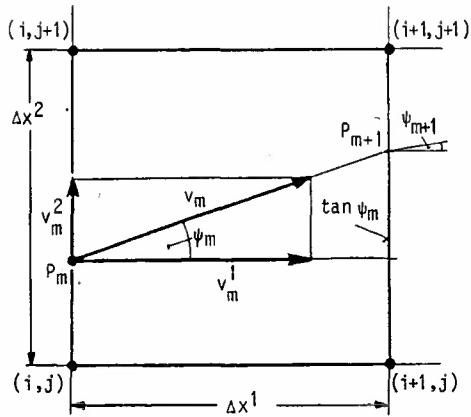


Fig. 3.10 Schematic of iterative shooting technique [22]

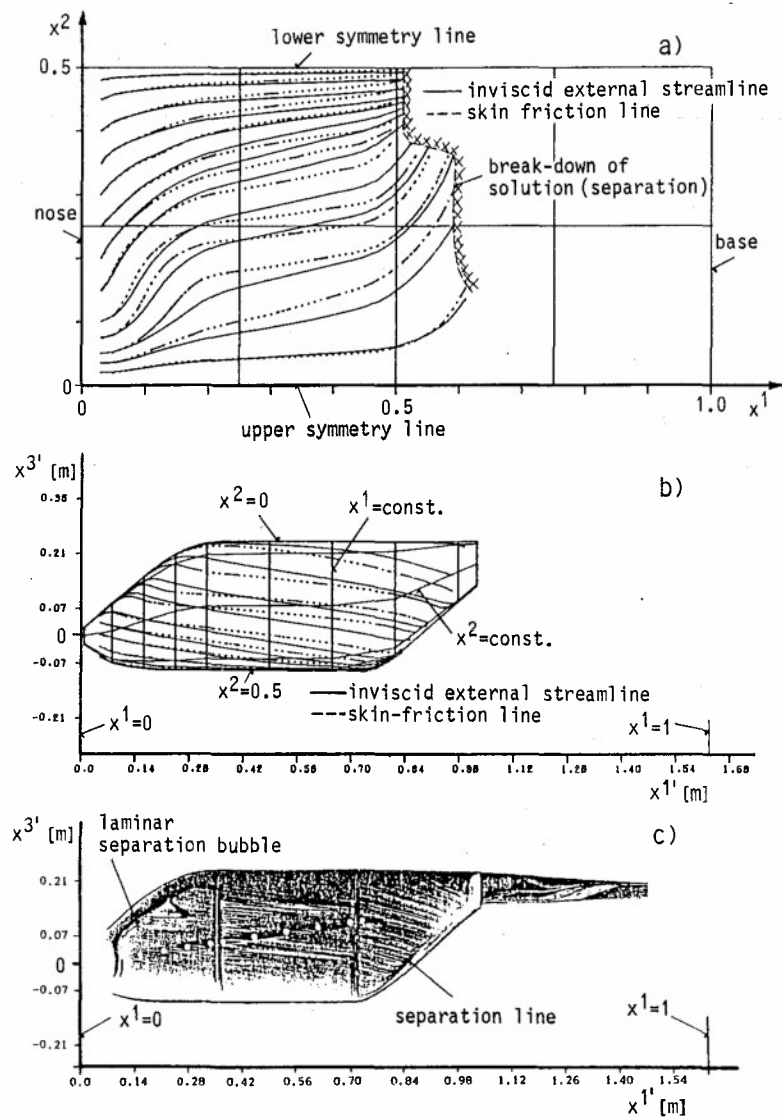


Fig. 3.11

Boundary-layer computation for a helicopter fuselage [19]
 $(M_\infty = 0.184, Re = 6.6 \cdot 10^6 (L_{ref} = 1.63m), \alpha = -5^\circ)$,
 a) external streamlines and skin-friction lines in the x^a -plane,
 b) side view of true configuration,
 c) oil-flow picture [23].

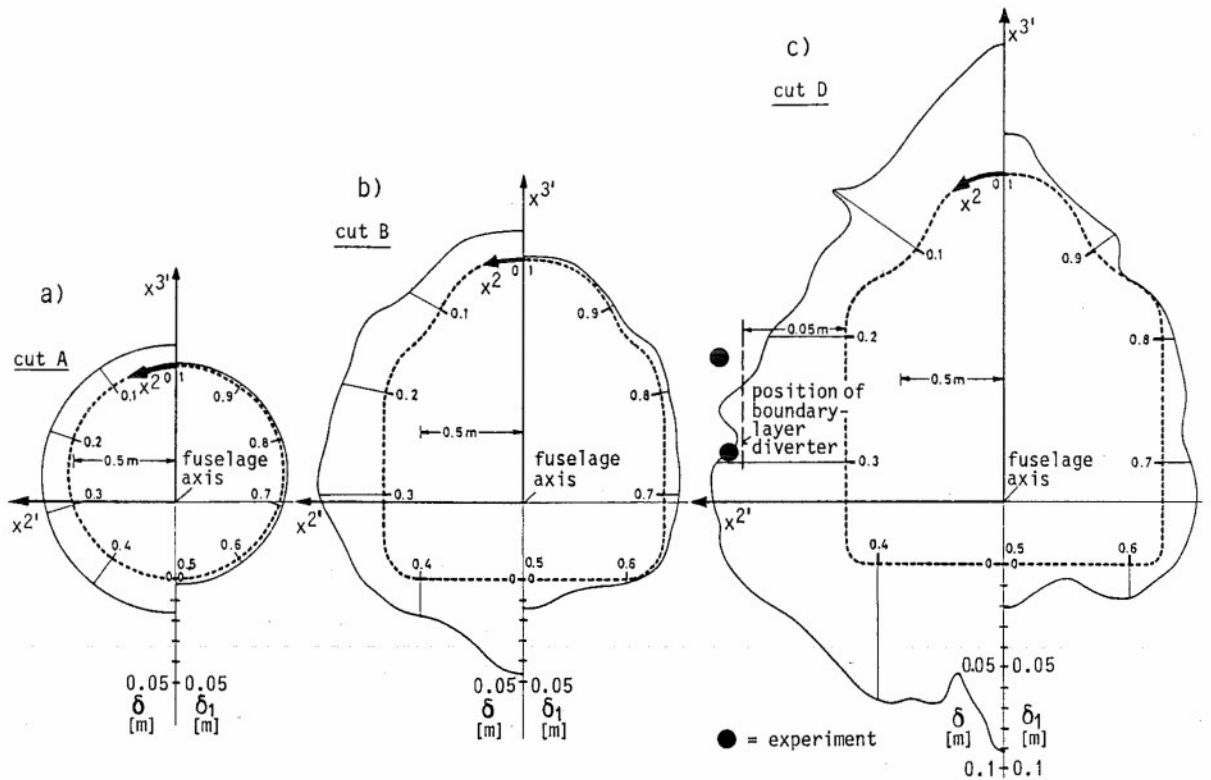


Fig. 3.12 Boundary-layer computation for a supersonic fighter nose [19]
 $(M_\infty = 2, Re_L = 1m = 2.7 \cdot 10^7)$,
 a) to c) cross-sections A, B and D as indicated in Fig. 3.9a,
 left side: boundary-layer thickness δ ,
 right side: displacement thickness δ_1 .

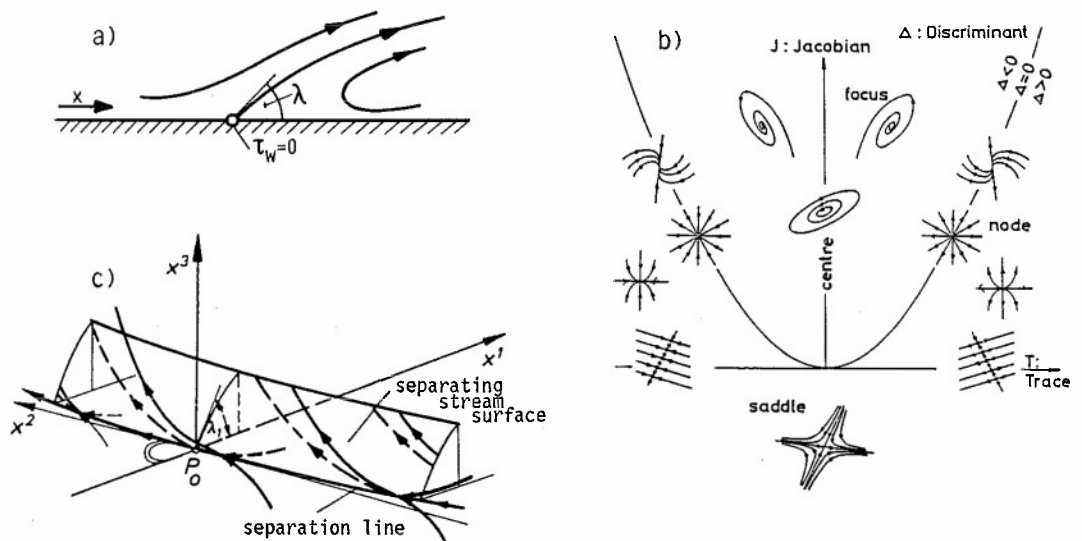


Fig. 4.1 Separation patterns,
 a) two-dimensional flow,
 b) singular points of three-dimensional separation [28],
 c) vortex-sheet separation line [3].

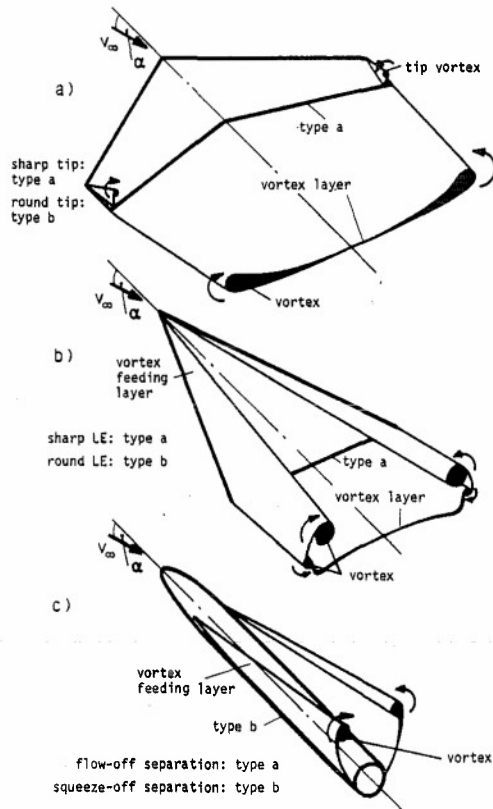


Fig. 4.2
Schematic of vortex layers and vortices [7] at
a) wing with small leading-edge sweep,
b) wing with large leading-edge sweep,
c) fuselage

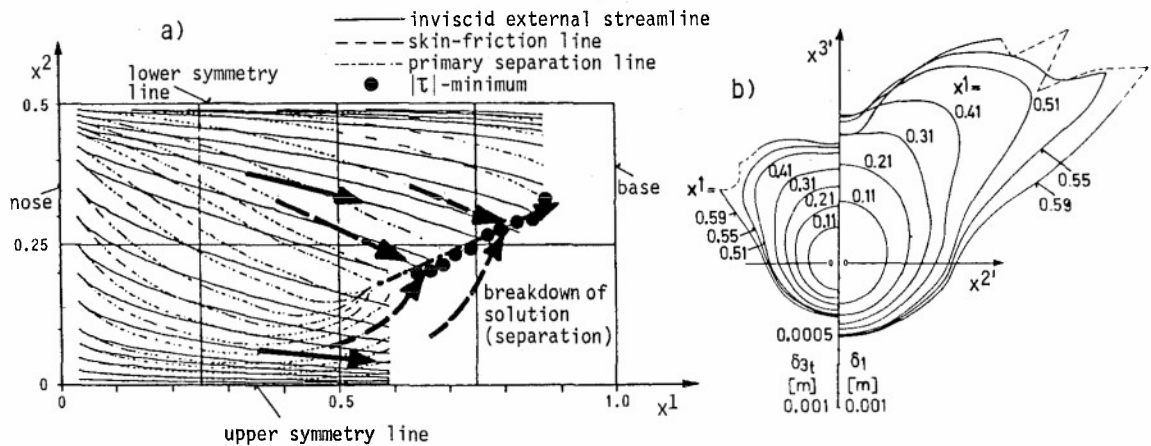
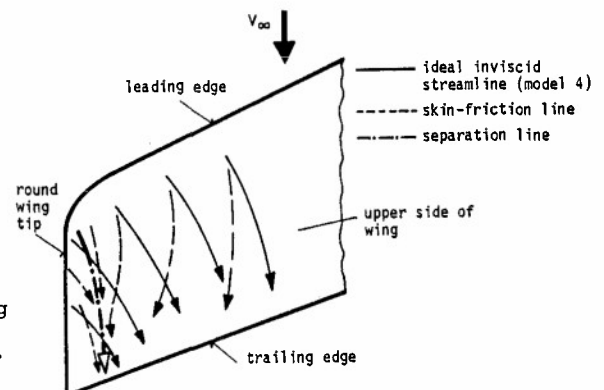


Fig. 4.3
Schematic of squeeze-off separation [7],
a) inviscid streamlines, skin-friction lines, primary separation line, $|\tau|$ -minimum line in the x^1 plane of a 1:6 ellipsoid at $\alpha=5^\circ$ angle of attack, laminar flow [7, 18] (right half of ellipsoid),
b) energy-loss thickness δ_{3t} , and displacement thickness δ_1 at stations $x^1 = \text{const. of solution a)}$ [18].

Fig. 4.4
Schematic of squeeze-off separation on a round wing tip (idealized), which leads to a tip vortex [7].



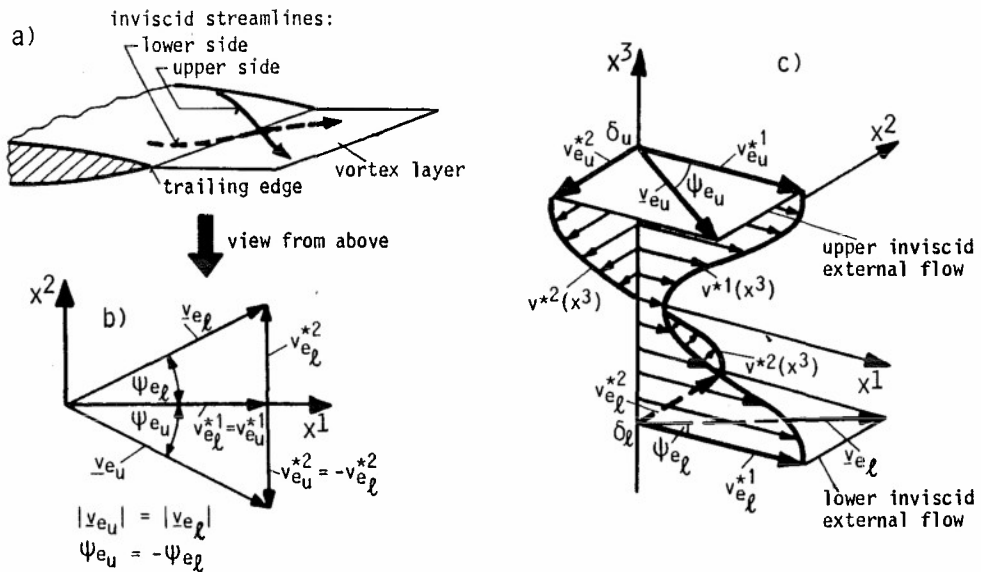


Fig. 4.5 Schematic of the three-dimensional wake of a lifting wing in steady sub-critical flow [7],
a) trailing edge detail,
b) inviscid flow just downstream of the trailing edge (view from above),
c) idealized wake structure downstream of a trailing edge.

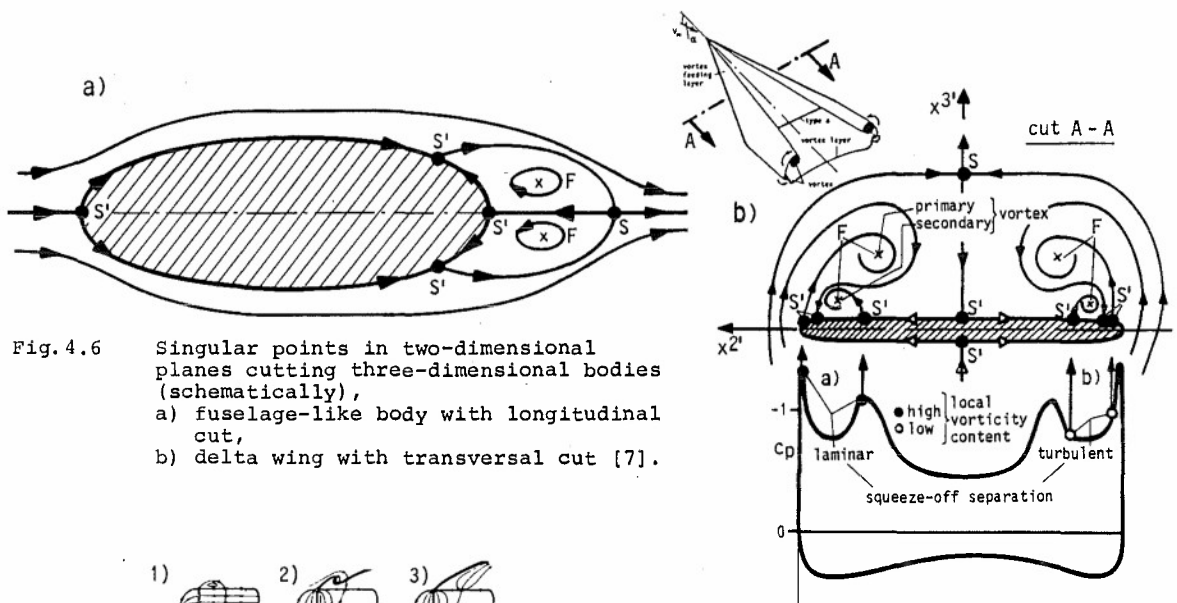


Fig. 4.6 Singular points in two-dimensional planes cutting three-dimensional bodies (schematically),
a) fuselage-like body with longitudinal cut,
b) delta wing with transversal cut [7].

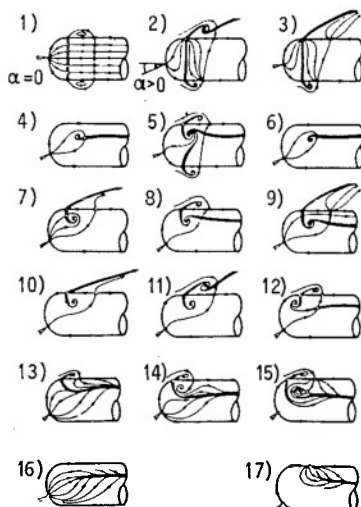


Fig. 4.7 The most important topographical structures of skin-friction lines and streamlines (symmetry plane) on a blunt body [30], case 1: $\alpha=0^\circ$.

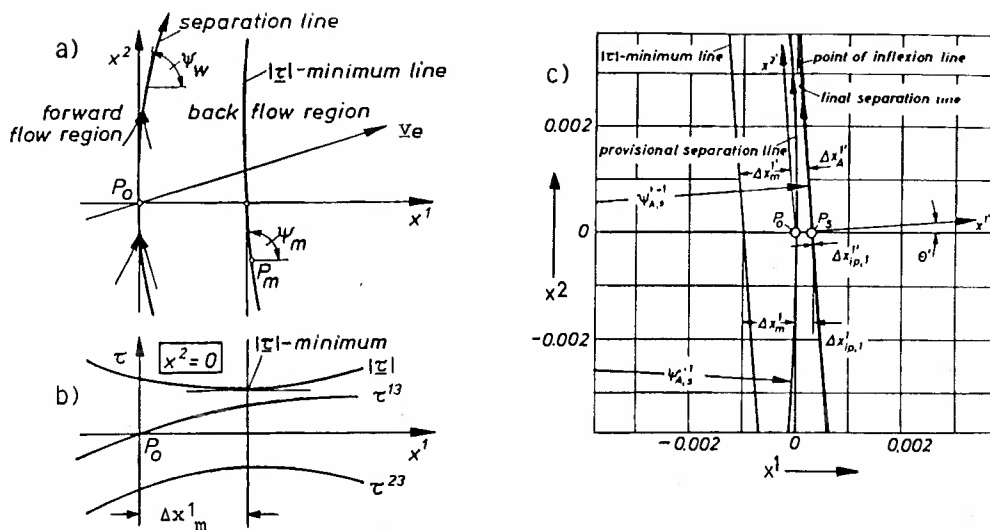


Fig. 4.8 Local topography of vortex-sheet separation lines [3],
 a) separation line and $|z|$ -minimum line,
 b) distributions of wall-shear stress,
 c) application on a swept wing [37].

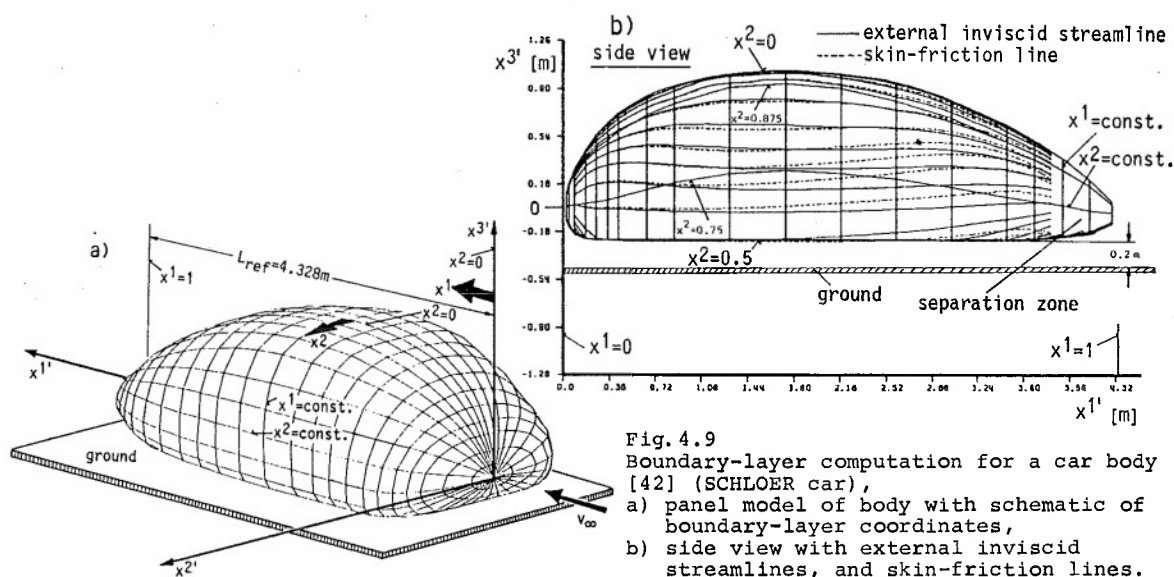


Fig. 4.9 Boundary-layer computation for a car body [42] (SCHLOER car),
 a) panel model of body with schematic of boundary-layer coordinates,
 b) side view with external inviscid streamlines, and skin-friction lines.

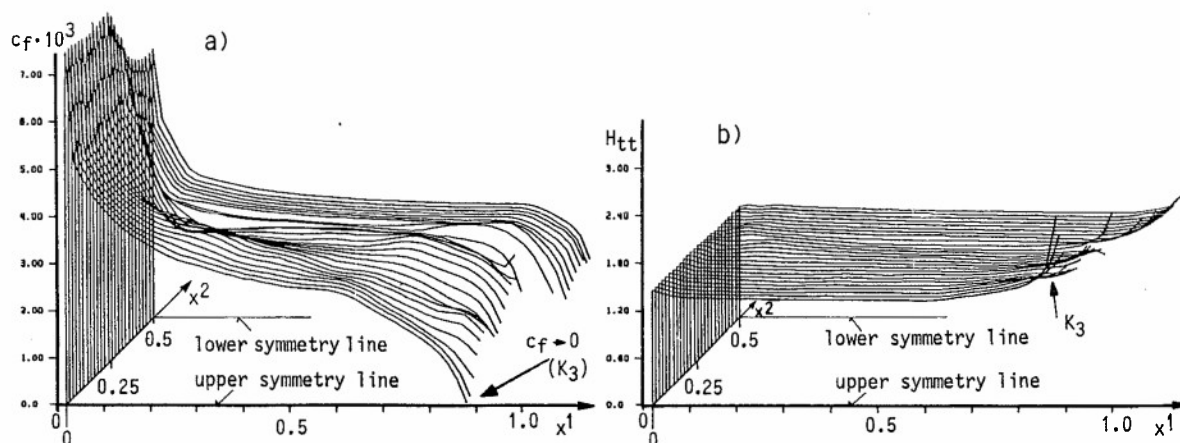


Fig. 4.10 Results of boundary-layer computation [42],
 a) amount of wall-shear stress coefficient $c_f(x_1, x_2)$ (right half of car),
 b) streamwise form parameter $H_{tt}(x_1, x_2)$ (right half of car).

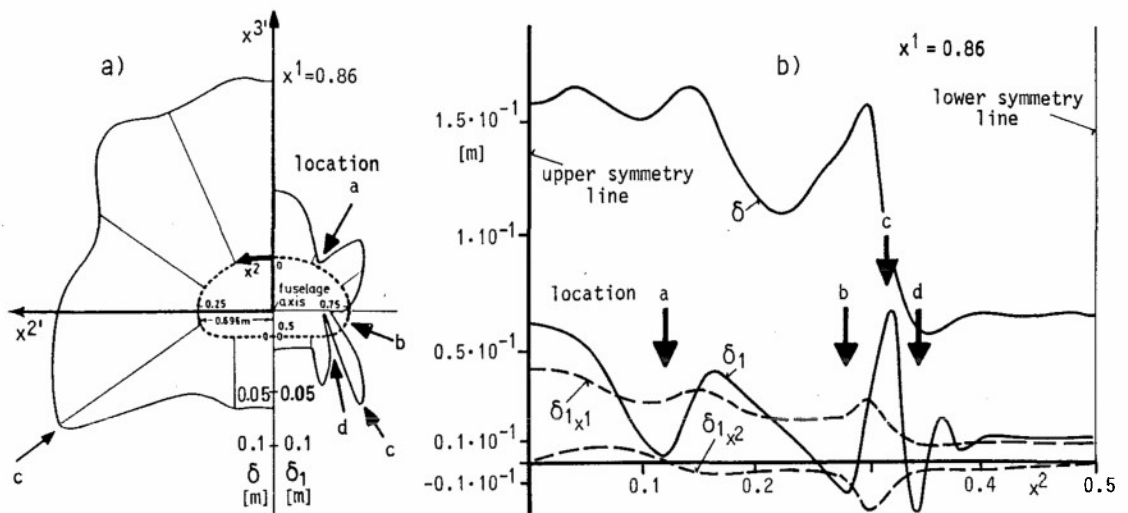


Fig. 4.11 Results of boundary-layer computation [42],
 a) distribution of boundary-layer thickness δ , and displacement thickness δ_1 at $x^1 = 0.86$,
 b) δ and δ_1 and the components δ_{1x^1} , δ_{1x^2} at $x^1 = 0.86$ (right half of car).

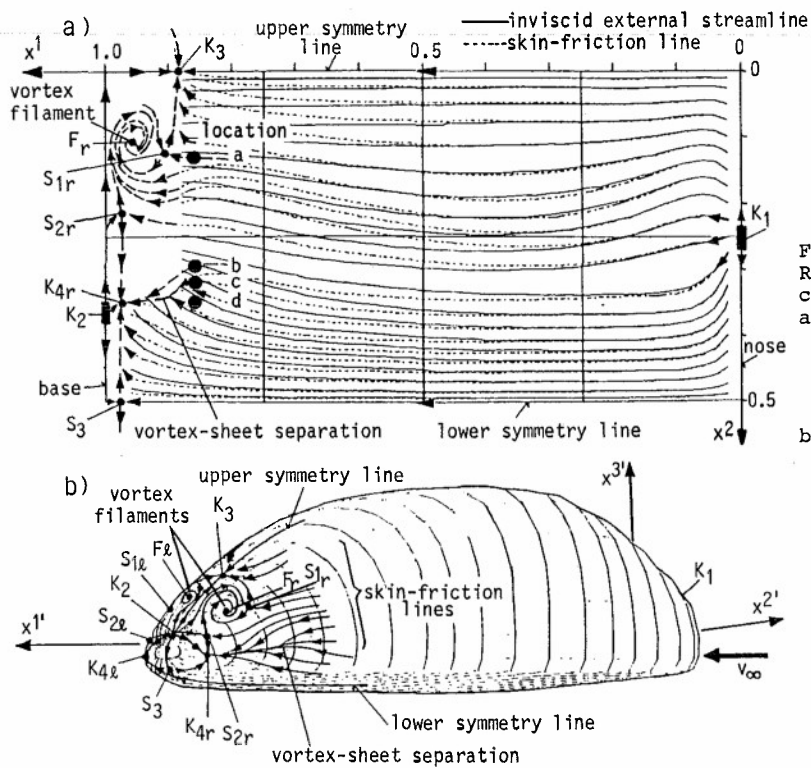


Fig. 4.12 Results of boundary-layer computation [42],
 a) inviscid streamlines, skin-friction lines, and possible separation topography in the x^1 - x^2 plane (right half of car),
 b) possible separation topography on real configuration.

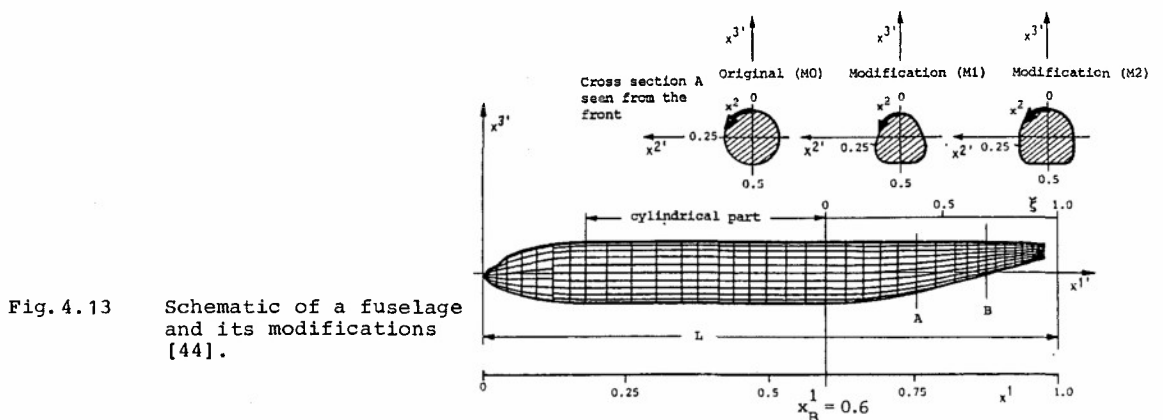


Fig. 4.13 Schematic of a fuselage and its modifications [44].

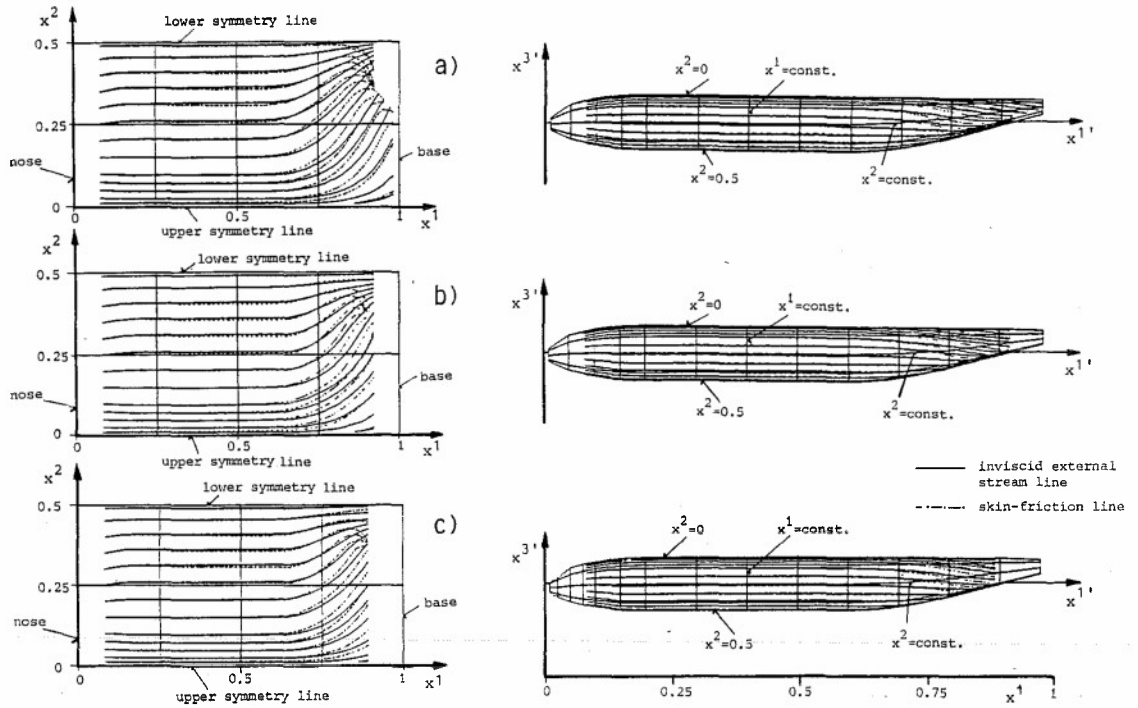


Fig. 4.14 External inviscid streamlines, and skin-friction lines [44] in the x^a -plane (right half of fuselages), and in the side view of the fuselages, a) original fuselage M0, b) modification M1, c) modification M2.

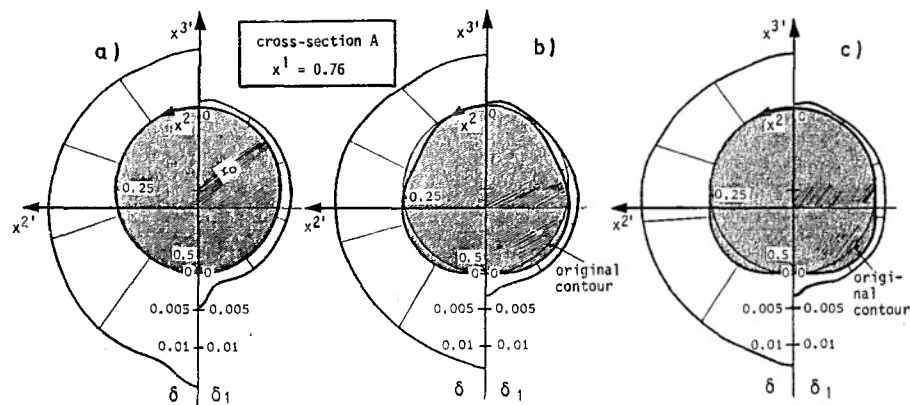


Fig. 4.15 Distribution of boundary-layer thickness δ , and displacement thickness δ_1 at $x^1 = 0.76$ [44], a) original fuselage M0, b) modification M1, c) modification M2.

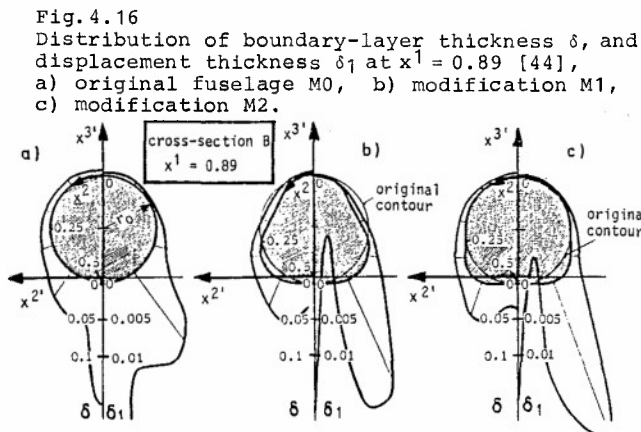


Fig. 4.16 Distribution of boundary-layer thickness δ , and displacement thickness δ_1 at $x^1 = 0.89$ [44], a) original fuselage M0, b) modification M1, c) modification M2.

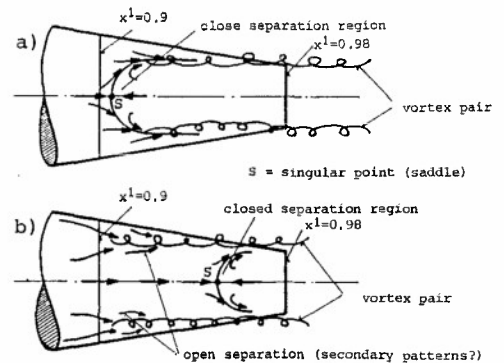


Fig. 4.17 Schematic of possible separation pattern [44] (fuselage end seen from below), a) original fuselage M0, ...

AN APPROACH TO PRACTICAL AERODYNAMIC CALCULATIONS*

by

Tuncer Cebeci
Douglas Aircraft Company
3855 Lakewood Boulevard
Long Beach, California 90846

SUMMARY

The emphasis of these lectures is on the numerical solution of three-dimensional boundary-layer equations using forms of Keller's Box scheme and interaction with solutions of inviscid-flow equations. Calculations are described for the flow over a circular cylinder started impulsively from rest and a prolate spheroid at angle of attack and were obtained with prescribed free-stream velocity distribution; the results emphasize the need for the Characteristic Box finite-difference scheme, which automatically satisfies the numerical stability criterion, in regions of flow where the w -velocity component is negative. Corresponding calculations, this time with a novel interactive method, are reported for the flow over the leading edge of a thin ellipse, over an oscillating airfoil and around wings; the results confirm that the interactive procedure provides accurate solutions, without numerical problems, in regions of flow separation.

1.0 INTRODUCTION

The design and development of aircraft configurations relies heavily on expensive and time-consuming experimental programs involving the evaluation of a large number of possible components, with a range of flow velocities and orientations and of power installation effects. The present goal is to develop reliable, accurate and efficient methods for computing aerodynamic flows over a wide variety of complex aircraft configurations and thereby help to improve aircraft performance with designs of greater simplicity and increased reliability.

It is generally accepted that all significant aspects of a fluid flow can be adequately described by an appropriate solution of the Navier-Stokes equations. Since their solution for flows over complex configurations is rather difficult and expensive, emphasis has been placed on particular forms such as those appropriate to regions of inviscid flow and boundary layers. In recent years, with the availability of supercomputers and advances in numerical methods, attention has also been paid to the Reynolds-averaged Navier-Stokes equations and various further-reduced forms including their so-called parabolized forms and the thin-layer Navier-Stokes equations. Significant advances have been made in this area by, for example, Shang and Scherr [1], who made the first attempt to numerically simulate the flowfield around a complete aircraft by solving the Navier-Stokes equations. To demonstrate the feasibility of their approach they chose the hypersonic research aircraft X24C-10D, for which a detailed experimental database exists. Using a mesh system around $1/2 \times 10^6$ nodes, they performed impressive calculations at an angle of attack of six degrees with a nominal Mach number of 5.95, and indicated the areas where future research should concentrate to make this approach more efficient and practical.

Even though the intermediate forms of the Navier-Stokes equations in the form of inviscid-flow and boundary-layer equations have been popular for many years, completely satisfactory solutions have not been obtained for general flows due to the lack of a proper coupling procedure between inviscid and viscous flows. The main obstacle to this approach has been associated with flow separation. When the boundary-layer equations are solved for a prescribed pressure distribution, the solution breaks down at the point of vanishing wall shear. However, the solution does not break down if the external flow velocity is computed as part of the solution by, for example, prescribing a displacement thickness: this is known as the inverse approach and allows the solution of the boundary-layer equations with separation.

Very recently, my colleagues and I have made progress towards the general goal by the development of novel techniques for the solution of inviscid- and viscous-flow equations and for the coupling of the solutions. The interactive boundary-layer approach is very general and allows any inviscid flow method to be coupled with the boundary-layer equations. For example, in its application to two-dimensional subsonic flows over airfoils, it employs Halsey's inviscid procedure [2] based on the conformal mapping and Fourier analysis techniques and computes the flow over the airfoil and its wake. Successive viscous sweeps are performed, after each of which the external inviscid solution is recomputed, until a converged solution is obtained. The boundary-layer method involves an inverse finite-difference scheme developed by Cebeci [3], uses an algebraic eddy-viscosity formulation due to Cebeci and Smith [4] and is able to compute flows with large regions of separation without numerical difficulties. In regions of reverse flow, it uses the FLARE approximation [5] in which the streamwise convective term is set equal to zero in the recirculating region.

The boundary-layer calculation is initiated on each surface of the airfoil by a direct solution in which the boundary condition at the outer edge follows from matching the viscous velocity with the latest computed inviscid surface-velocity distribution. As the calculation proceeds downstream, the boundary-layer algorithm is switched into an inverse mode in which the viscous-edge velocity is computed as part of the solution and

*This work was performed under Contract F49620-84-C-0007 for the Air Force Office of Scientific Research.

is accomplished by applying an interaction procedure suggested by Veldman [6] and further developed by Cebeci et al. [7-10]. An overrelaxation scheme is employed and has been shown to improve considerably the rate of convergence when combined with the interactive viscous calculation. When calculations are required for a range of angles of attack, the solution for each successive angle employs the previous solution as an initial approximation and the converged solution for each angle requires less than 10 iterations.

The method for calculating the wake region has some novel features which allow results to be obtained at high angles of attack with which a sudden jump can occur at the trailing edge by the removal of the no-slip boundary condition on the airfoil surface. A small step, with the size related to chord Reynolds number, is employed in the immediate vicinity of the trailing edge to avoid this jump. For wake calculations involving reverse-flow regions, an additional iterative scheme, based on the homotopy continuation method, is employed with the FLARE approximation. Studies by Cebeci et al. have shown that the boundary-layer calculations would break down without this added feature, when a significant trailing-edge separation region is present. To avoid this, the trailing-edge velocity profile is modified to correspond to an attached flow profile which allows boundary-layer calculations to be performed at the next downstream station; the upstream profiles are gradually modified and the downstream profile is recomputed until a solution is obtained for the original separated velocity profile. This computational scheme is employed at each wake station for which there is flow reversal.

In the past year, this interactive boundary-layer method has been further developed to represent two-dimensional steady and two-dimensional time-dependent flows. It has also been extended to three-dimensional flows by using a strip-theory as well as a quasi-three-dimensional approximation to the boundary-layer equations. Currently, the interactive boundary-layer method is being extended to full three-dimensional flows.

The substance of these lectures is provided in the following four sections which deal, in turn, with equations, coordinate systems and initial conditions, numerical solution procedures and results obtained by the application of the calculation method. The emphasis of the following section is on three-dimensional boundary-layer equations and their solutions, and reference is made to the inviscid-flow equations where appropriate. The correct choice of a coordinate system is essential to the subject and, together with the provision of initial conditions, is addressed in connection with wings. The turbulence model, appropriate transformations and further comments on interaction are included. Section 3 deals with numerical methods for the solution of boundary-layer equations and considers separately flows without and with reversal, and with separation. The applications of Sections 4 and 5 have been selected to demonstrate problems and solutions associated with a hierarchy of problems which include some of direct relevance to airplane configurations.

Some of the material of these sections is taken from referenced publications to which the reader is directed for further information.

2.0 CONSERVATION EQUATIONS

2.1 Boundary-Layer Equations

Consider a flow over a three-dimensional body which is defined in the Cartesian coordinate system $\bar{x}, \bar{y}, \bar{z}$ by

$$F(\bar{x}, \bar{y}, \bar{z}) = 0 \quad (2.1)$$

A convenient coordinate system for three-dimensional boundary-layer equations for laminar and turbulent flows is nonorthogonal and curvilinear as shown in Fig. 2.1. Here x and z denote the coordinate system on the surface of the body, θ represents the angle between

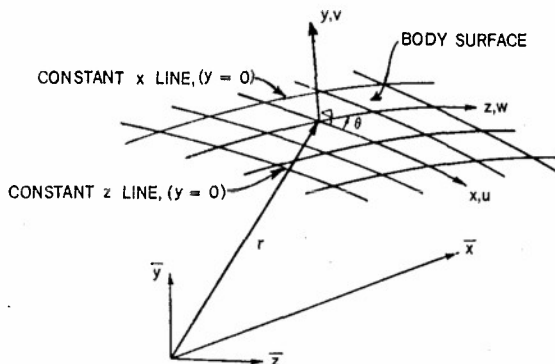


Figure 2.1. Notation for nonorthogonal curvilinear coordinate system on the body surface. Note that x and z are not orthogonal to each other but y is to x and z .

the coordinate lines x and z , and y is the actual distance measured normal to the surface. First-order boundary-layer theory assumes that the pressure is constant across the shear layer and stress gradients in directions parallel to the surface are negligible compared with those normal to the surface. The resulting equations have been given, for example, by Bradshaw et al. [11] and can be written in the following form for an incompressible flow.

Continuity Equation

$$\frac{\partial}{\partial x} (u h_2 \sin \theta) + \frac{\partial}{\partial z} (w h_1 \sin \theta) + \frac{\partial}{\partial y} (v h_1 h_2 \sin \theta) = 0 \quad (2.2)$$

x-Momentum Equation

$$\begin{aligned} \frac{u}{h_1} \frac{\partial u}{\partial x} + \frac{w}{h_2} \frac{\partial u}{\partial z} + v \frac{\partial u}{\partial y} - \cot \theta K_1 u^2 + \csc \theta K_2 w^2 + K_{12} u w \\ = - \frac{\csc^2 \theta}{\rho h_1} \frac{\partial p}{\partial x} + \frac{\cot \theta \csc \theta}{\rho h_2} \frac{\partial p}{\partial z} + \frac{\partial}{\partial y} (v \frac{\partial u}{\partial y} - u^T v^T) \end{aligned} \quad (2.3)$$

z-Momentum Equation

$$\begin{aligned} \frac{u}{h_1} \frac{\partial w}{\partial x} + \frac{w}{h_2} \frac{\partial w}{\partial z} + v \frac{\partial w}{\partial y} + \csc \theta K_1 u^2 - \cot \theta K_2 w^2 + K_{21} u w \\ = \frac{\cot \theta \csc \theta}{\rho h_1} \frac{\partial p}{\partial x} - \frac{\csc^2 \theta}{\rho h_2} \frac{\partial p}{\partial z} + \frac{\partial}{\partial y} (v \frac{\partial w}{\partial y} - w^T v^T) \end{aligned} \quad (2.4)$$

$$y = 0: \quad u, v, w = 0 \quad (2.5a)$$

$$y = \delta: \quad u = u_e(x, z), \quad w = w_e(x, z) \quad (2.5b)$$

Here h_1 and h_2 denote the surface metric coefficients and θ denotes the angle between the coordinate lines x and z and, as a result of first-order boundary-layer theory, the metric coefficients are functions of the surface coordinates x and z only. They can be obtained from the relations between $\bar{x}, \bar{y}, \bar{z}$ and x, y, z and are given by

$$h_1^2 = \left(\frac{\partial \bar{x}}{\partial x} \right)^2 + \left(\frac{\partial \bar{y}}{\partial x} \right)^2 + \left(\frac{\partial \bar{z}}{\partial x} \right)^2 \quad (2.6a)$$

$$h_2^2 = \left(\frac{\partial \bar{x}}{\partial z} \right)^2 + \left(\frac{\partial \bar{y}}{\partial z} \right)^2 + \left(\frac{\partial \bar{z}}{\partial z} \right)^2 \quad (2.6b)$$

$$\cos \theta = \frac{(\partial \bar{x} / \partial x)(\partial \bar{x} / \partial z) + (\partial \bar{y} / \partial x)(\partial \bar{y} / \partial z) + (\partial \bar{z} / \partial x)(\partial \bar{z} / \partial z)}{h_1 h_2} \quad (2.7)$$

The parameters K_1 and K_2 are known as the geodesic curvatures of the curves $z = \text{constant}$ and $x = \text{constant}$, respectively, and are given by

$$K_1 = \frac{1}{h_1 h_2 \sin \theta} \left[\frac{\partial}{\partial x} (h_2 \cos \theta) - \frac{\partial h_1}{\partial z} \right] \quad (2.8a)$$

$$K_2 = \frac{1}{h_1 h_2 \sin \theta} \left[\frac{\partial}{\partial z} (h_1 \cos \theta) - \frac{\partial h_2}{\partial x} \right] \quad (2.8b)$$

The parameters K_{12} and K_{21} are defined by

$$K_{12} = \frac{1}{\sin \theta} \left[-K_1 - \frac{1}{h_1} \frac{\partial \theta}{\partial x} + \cos \theta \left(K_2 + \frac{1}{h_2} \frac{\partial \theta}{\partial z} \right) \right] \quad (2.9a)$$

$$K_{21} = \frac{1}{\sin \theta} \left[-K_2 - \frac{1}{h_2} \frac{\partial \theta}{\partial z} + \cos \theta \left(K_1 + \frac{1}{h_1} \frac{\partial \theta}{\partial x} \right) \right] \quad (2.9b)$$

and the magnitude of the velocity vector u_t in the boundary layer is given by

$$u_t = (u^2 + w^2 + 2uw \cos \theta)^{1/2} \quad (2.10)$$

2.2 Coordinate System

The determination of a coordinate system depends on the choice of the (x, z) net on the body surface. This choice is not completely arbitrary and should take advantage of flow symmetry conditions which are needed to generate the initial conditions for the boundary-layer calculations. Two distinct coordinate systems form the basis for most three-dimensional boundary-layer calculations on general shapes. The streamline coordinate system is formed by the inviscid streamlines and their orthogonal trajectories on the surface. As shown in Fig. 2.2, the projection of the freestream velocity vector on

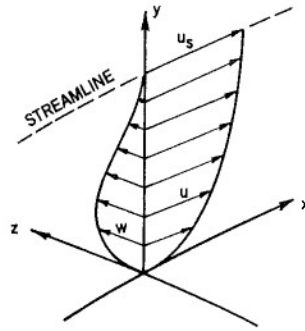


Figure 2.2. Streamline coordinate system.

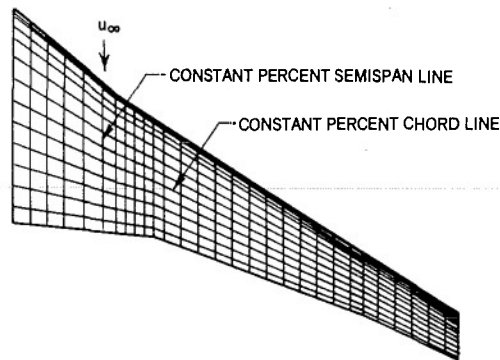


Figure 2.3. Nonorthogonal coordinate system on a wing.

the surface is aligned with the surface coordinate x and the velocity component along the z -axis, is zero at the edge of the boundary layer, and is referred to as the crossflow velocity. A second coordinate system is the so-called body-oriented coordinate system, which can be either orthogonal or nonorthogonal, although the latter is more natural for complex geometries like wings and ship hulls. Figure 2.3 shows a nonorthogonal coordinate system on a typical transport wing.

Each coordinate system has advantages and disadvantages. The body-oriented system has the advantage that it is independent of the angle of attack and easy to calculate even if the body is not defined analytically. In addition, second order boundary-layer effects such as transverse or longitudinal curvature, can be included easily in the equations with an orthogonal system but singularities in the geometric parameters h_1 , h_2 , K_1 and K_2 may be introduced and can require elaborate transformations [12] to remove them.

The main advantage of the streamline coordinate system is that it can be constructed for most flow conditions once the stagnation point has been calculated, and the geometric parameters do not have the singularities of a body-oriented coordinate system. Its main disadvantage is that it depends on the angle of incidence although this can be unimportant when the inviscid flowfield is determined analytically. More will be said about the computation of flows of this type in the lectures of Dr. Govindan.

2.3 Initial Conditions

The three-dimensional boundary-layer equations require initial conditions in the (x,y) -plane at some $z = z^*$ and initial conditions in the (z,y) -plane at $x = x^*$. In some problems these conditions can be established with ease and in others they require additional effort. As an example, consider Fig. 2.4 in which the initial conditions in the (z,y) plane correspond to line AB and can be obtained from the solutions of the so-called attachment-line equations for which $u_e = 0$. For most wing calculations, however, this does not correspond to a line of constant x and approximations are required with u_e small but greater than zero.

The initial conditions in the (x,y) -plane that form the wing-fuselage junction are more difficult to compute since, as discussed in [13], the viscous flow along the line AC is not of the boundary-layer type and belongs to a class known as the boundary-region type. Approximations must be made to specify initial conditions on that line.

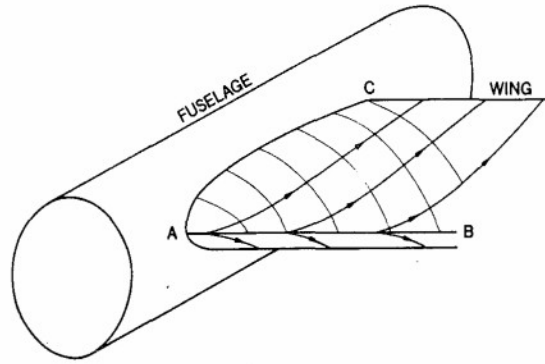


Figure 2.4. Fuselage-wing configuration.

2.4 Turbulence Model

The boundary-layer equations discussed in Section 2.1 contain Reynolds stress terms which have to be expressed in terms of known or obtainable quantities in order to reduce the number of unknowns to the number of equations. This so-called closure problem can be solved in several ways and the most common is to define an eddy viscosity, ν_t , in the same form as the laminar viscosity.

The specification of ν_t may be made in terms of algebraic equations or as a combination of algebraic and differential equations and this has given rise to terminology involving the number of differential equations as discussed, for example, in [4,11,14]. The zero-equation approach is preferred here and relates two Reynolds shear stress terms to the gradient of the mean velocity profiles by

$$-\overline{u'v'} = \nu_t \frac{\partial u}{\partial y}, \quad -\overline{w'v'} = \nu_t \frac{\partial w}{\partial y} \quad (2.11)$$

with two separate expressions to represent the eddy viscosity across the shear layer. In the so-called inner region of the boundary layer, ν_t is defined by

$$(\nu_t)_i = L^2 \left[\left(\frac{\partial u}{\partial y} \right)^2 + \left(\frac{\partial w}{\partial y} \right)^2 \right]^{1/2} \quad (2.12)$$

where

$$L = 0.4y[1 - \exp(-y/A)], \quad A = 26 \frac{\nu}{u_\tau}, \quad u_\tau = \left(\frac{\tau_{tw}}{\rho} \right)^{1/2},$$

$$\tau_{tw} = \mu \left[\left(\frac{\partial u}{\partial y} \right)_w^2 + \left(\frac{\partial w}{\partial y} \right)_w^2 + 2 \left(\frac{\partial u}{\partial y} \right)_w \left(\frac{\partial w}{\partial y} \right)_w \cos \theta \right]^{1/2} \quad (2.13)$$

In the outer region ν_t is defined by

$$(\nu_t)_o = 0.0168 \left| \int_0^\infty (u_{te} - u_t) dy \right| \quad (2.14)$$

The extensive boundary-layer calculations of Cebeci and Smith [4], Cebeci and Meier [15], Chang et al. [16] and Cebeci et al. [17] suggest that the Cebeci-Smith algebraic specification of eddy viscosity is adequate for two-dimensional boundary-layer flows and the more recent results of Cebeci and Chang [18] lead to a similar conclusion although the experimental data upon which the conclusion is drawn for three-dimensional flows is sparse. The conclusion is supported by the calculation costs quoted by Cebeci [19] which show that, in a two-dimensional calculations, the zero-equation approach is three times cheaper than with two-equation models and ten times cheaper than with Reynolds-stress models.

2.5 Transformed Equations

The boundary-layer equations can be solved in physical or transformed coordinates and each has its advantages. In three-dimensional flows, computer storage and time are particularly important and transformed coordinates are essential as well as convenient because they allow large steps to be taken in the streamwise and circumferential directions. In addition, they reduce the growth in boundary-layer thickness with increasing x and/or z and can be used to generate the initial conditions [20] in some problems.

There are several transformations that can be used and it is convenient to express the independent variables of Eqs. (2.2) to (2.4) by

$$x = x, \quad z = z, \quad d\eta = \left(\frac{u_0}{\sqrt{s_1}}\right)^{1/2} dy \quad (2.15)$$

Here u_0 is a reference velocity and s_1 denotes the arc length in the longitudinal direction measured from the initial line $x = x^*$. The dependent variables are transformed by using a two-component velocity potential such that

$$uh_2 = \frac{\partial \psi}{\partial y}, \quad wh_1 = \frac{\partial \phi}{\partial y}, \quad vh_1h_2 = -\left(\frac{\partial \psi}{\partial x} + \frac{\partial \phi}{\partial z}\right) \quad (2.16)$$

In addition, dimensionless ψ and ϕ are defined by

$$\psi = (\nu u_0 s_1)^{1/2} h_2 f(x, z, \eta), \quad \phi = (\nu u_0 s_1)^{1/2} h_1 g(x, z, \eta) \quad (2.17)$$

With the transformations defined by Eqs. (2.15) to (2.17) and with the definition of eddy viscosity, Eq. (2.11), the three-dimensional boundary-layer equations of Section 2.1 and their boundary conditions in a body-oriented coordinate system, can be written in the following general form:

$$(bf'')' + f''\theta + m_2(f')^2 + m_3f'g' + m_5(g')^2 + m_6 = m_7f' \frac{\partial f'}{\partial x} + m_8g' \frac{\partial f'}{\partial z} \quad (2.18)$$

$$(bg'')' + g''\theta + m_{10}(g')^2 + m_{11}f'g' + m_{13}(f')^2 + m_{14} = m_7f' \frac{\partial g'}{\partial x} + m_8g' \frac{\partial g'}{\partial z} \quad (2.19)$$

$$\theta' = m_1f' + m_4g' + m_7 \frac{\partial f'}{\partial x} + m_8 \frac{\partial g'}{\partial z} \quad (2.20)$$

$$\eta = 0, \quad f' = g' = \theta = 0; \quad \eta = \eta_e, \quad f' = \frac{u_e}{u_0} = \bar{u}_e, \quad g' = \frac{w_e}{u_0} = \bar{w}_e \quad (2.21)$$

Here the primes denote differentiation with respect to η and f' and g' denote dimensionless velocities, u/u_0 and w/u_0 , respectively. The parameters m_1 to m_{14} and b are given by:

$$m_1 = \frac{\sqrt{s_1}}{h_1 h_2 \sin \theta} \frac{\partial}{\partial x} (\sqrt{s_1} h_2 \sin \theta), \quad m_2 = s_1 K_1 \cot \theta, \quad m_3 = -s_1 K_{12}$$

$$m_4 = \frac{\sqrt{s_1}}{h_1 h_2 \sin \theta} \frac{\partial}{\partial z} (\sqrt{s_1} h_1 \sin \theta), \quad m_5 = -s_1 K_2 \csc \theta$$

$$m_6 = \frac{s_1}{h_1} \bar{u}_e \frac{\partial \bar{u}_e}{\partial x} + \frac{s_1}{h_2} \bar{w}_e \frac{\partial \bar{u}_e}{\partial z} + s_1 K_2 \bar{w}_e^2 \csc \theta + s_1 K_{12} \bar{u}_e \bar{w}_e - s_1 K_1 \bar{u}_e^2 \cot \theta$$

$$m_7 = \frac{s_1}{h_1}, \quad m_8 = \frac{s_1}{h_2}, \quad m_{10} = s_1 K_2 \cot \theta, \quad m_{11} = -s_1 K_{21}, \quad m_{13} = -s_1 K_1 \csc \theta$$

$$m_{14} = \frac{s_1}{h_1} \bar{u}_e \frac{\partial \bar{w}_e}{\partial x} + \frac{s_1}{h_2} \bar{w}_e \frac{\partial \bar{w}_e}{\partial z} + s_1 K_1 \bar{u}_e^2 \csc \theta + s_1 K_{21} \bar{u}_e \bar{w}_e - s_1 K_2 \bar{w}_e^2 \cot \theta$$

$$b = (1 + v_t^+), \quad v_t^+ = \frac{v}{v}$$

2.6 Interaction Problem

It is well known that the boundary-layer equations for two- or three-dimensional flows are singular at separation when solved for a prescribed external velocity distribution and not singular when the external velocity is computed as part of the solution by, for example, prescribing a displacement thickness. The inverse approach to the latter case, allows the boundary-layer equations to be solved in the presence of separation.

For flows with separation, a special procedure is used to overcome the stability problem associated with the negative u -velocity and is referred to as FLARE after the originators, Reyhner and Flugge-Lotz [5]. This procedure neglects the longitudinal convection terms $u(\partial u/\partial x)$, $u(\partial w/\partial x)$ in the momentum equations (2.2) and (2.3) and is satisfactory provided the region of separated flow is small. As the size of the recirculation region increases, the FLARE approximation becomes less accurate and several procedures have been suggested to allow the reinstatement of the neglected term. One successful scheme which was devised and stated for two-dimensional flows is referred to as DUIT [11,21] (Downstream, Upstream Iteration) and requires several sweeps through the

recirculation region. Thus, FLARE can be used to compute an approximate solution within the recirculation region and the $u(\partial u/\partial x)$ term is progressively introduced in successive sweeps until it is fully represented. An alternative approach is to make use of unsteady boundary-layer equations in which solutions are obtained by the Mechul function method as a function of time and to introduce the longitudinal convective term as time progresses. This time-dependent approach was investigated by Cebeci [22] and found to be satisfactory.

In an interactive boundary-layer scheme, a link between a displacement thickness and external flow is provided, and two types of procedures have been developed for this purpose for two-dimensional flows. In the first [23-27], the solutions of the boundary-layer equations are computed initially for a prescribed external velocity to obtain an estimate of the displacement thickness $\delta^*(x)$ distribution, and then in an inverse mode for a specified displacement-thickness distribution $\delta^*(x)$. If this initial calculation encounters separation, $\delta^*(x)$ is extrapolated to the trailing edge. The subsequent boundary-layer calculations are then performed in an inverse mode to compute the blowing velocity needed in the inviscid flow method. In general, this procedure leads to two external velocity distributions, $u_{ev}(x)$ derived from the inverse boundary-layer solution and $u_{ei}(x)$ derived from the updated approximation to the inviscid velocity past the body with viscous effects. A relaxation formula in the form

$$\delta^{*v+1}(x) = \delta^{*v}(x) [1 + \omega (\frac{u_{ev}(x)}{u_{ei}(x)} - 1)], \quad v = 0, 1, 2, \dots \quad (2.23)$$

where ω denotes a relaxation parameter, is then introduced to define an updated displacement thickness distribution and to obtain new solutions of the boundary-layer equations so that the interactive procedure between inviscid and viscous flow solutions can be carried out until convergence.

The second approach [6], which is recommended on the grounds of generality and physical basis, treats the external velocity $u_e(x)$ and the displacement thickness $\delta^*(x)$ as unknown quantities. The boundary-layer equations are solved simultaneously in an inverse mode and with successive sweeps over the body surface. For each sweep, the external boundary condition is written as the sum of the inviscid velocity $u_g^0(x)$ over the body, and a perturbation velocity $\delta u_e(x)$, that is,

$$y = \delta, \quad u_e(x) = u_e^0(x) + \delta u_e(x) \quad (2.24)$$

with $\delta u_e(x)$ computed from the Hilbert integral given by

$$\delta u_e(x) = \frac{1}{\pi} \int_{x_a}^{x_b} \frac{d}{d\sigma} (u_e \delta^*) \frac{d\sigma}{x - \sigma} \quad (2.25)$$

and the interaction region confined between x_a and x_b .

This second approach has been extended recently to three-dimensional incompressible flows with small spanwise pressure gradients [28]. In this case the flow variations with respect to z are neglected and the equations are reduced to a form which provides a better approximation to Eqs. (2.2) to (2.4) than those based on the strip theory or infinite swept-wing approximations. The resulting equations are referred to as quasi-three-dimensional boundary-layer equations and are written as

$$\frac{\partial}{\partial x} (u h_2 \sin \theta) + \frac{\partial}{\partial y} (v h_1 h_2 \sin \theta) = 0 \quad (2.26)$$

$$\frac{u}{h_1} \frac{\partial u}{\partial x} + v \frac{\partial u}{\partial y} - K_1 u^2 \cot \theta + K_2 w^2 \csc \theta + K_{12} u w = - \frac{\csc^2 \theta}{h_1 \rho} \frac{\partial p}{\partial x} + \frac{\partial}{\partial y} (v \frac{\partial u}{\partial y} - \overline{u'v'}) \quad (2.27)$$

$$\frac{u}{h_1} \frac{\partial w}{\partial x} + v \frac{\partial w}{\partial y} + K_1 u^2 \csc \theta - K_2 w^2 \cot \theta + K_{21} u w = \frac{\csc \theta \cot \theta}{h_1 \rho} \frac{\partial p}{\partial x} + \frac{\partial}{\partial y} (v \frac{\partial w}{\partial y} - \overline{u'w'}) \quad (2.28)$$

The relationship between displacement thickness and external velocity needed in the interactive calculations was obtained by generalizing the formulation used for two-dimensional flows. The irrotationality condition, which for an orthogonal system is

$$\frac{\partial}{\partial x} [h_2 (w_e^0 + \delta w_e)] = \frac{\partial}{\partial z} h_1 (u_e^0 + \delta u_e) \quad (2.29)$$

was used to provide a relationship between the two velocity components u_e and w_e and shows that the choice of computing the perturbation velocities due to viscous effects is not arbitrary. The assumption that δu_e is a function of x alone requires that

$$\frac{\partial}{\partial x} (\delta w_e) = 0$$

and that

$$w_e = w_e^0 \quad (2.30)$$

In this way the edge boundary conditions for a quasi-three-dimensional boundary-layer flow with interaction are given by Eqs. (2.24) and (2.27).

2.7 Closure

The equations and procedures described in Sections 2.1 through 2.5 are general and can be applied to the flow over aircraft components, including wings, fuselages and empennages. The concept of the interactive procedure of Section 2.6 is also general but its application has so far been restricted to two-dimensional and quasi-three-dimensional flows such as those associated with airfoils, and with wings at small angles of attack, as will be discussed in Section 5.0. It is clearly desirable that the formulation of interactive procedures should be extended to include full three-dimensional flows. At the same time, improved numerical procedures are required to solve the three-dimensional boundary-layer equations, as discussed in the next section.

3.0 NUMERICAL METHODS

3.1 Features of the Boundary-Layer Equations

Before we describe the numerical methods which can be used to solve the three-dimensional equations described in the previous section, it is helpful to review briefly the general principles which must be satisfied if accurate solutions are to be obtained. These follow from the realization that the momentum equations are diffusive in the direction normal to the body and wave-like in planes parallel to the body, the direction of propagation being along the local stream direction. Since this direction varies across the boundary layer, it is possible to identify zones of influence and dependence for any point and to obtain solutions to the three-dimensional boundary-layer equations such that they obey these zones. To explain this further, it is useful to consider the grid of Fig. 3.1, in which the solutions are known at the points indicated by x and are required at P . The wall and external streamlines have been drawn on the assumption that both u and w velocity components are positive. The domain of dependence of point P is denoted by the shaded area and its region of influence corresponds to the hatched area where the solution is altered when a change occurs in the solution at the point P . The information to point P comes from the domain of dependence. When the u velocity is positive across the layer but the w velocity component is negative near the wall, the wall streamlines cause the domains of dependence and region of influence to change, as shown in Fig. 3.2. The wall streamlines, which were beneath the external streamlines move above the external streamlines. The angle between these two streamlines widens further when both velocity components of the wall streamlines become negative (Fig. 3.3) and information comes from

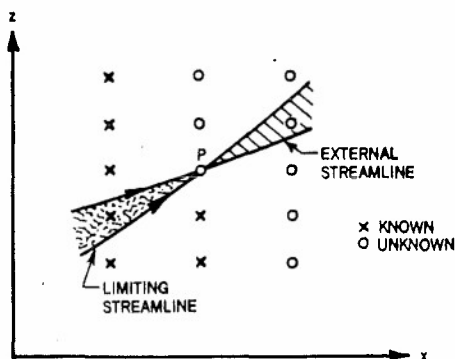


Figure 3.1. Domains of dependence (shaded area) and regions of influence (hatched area) of point P when both u and w in the boundary layer are positive.

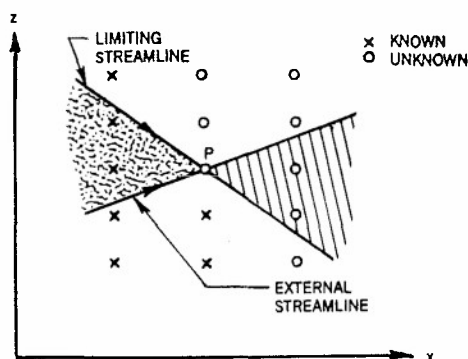


Figure 3.2. Domains of dependence (shaded area) and regions of influence (hatched area) of point P when u is positive across the layer and w is negative near the wall.

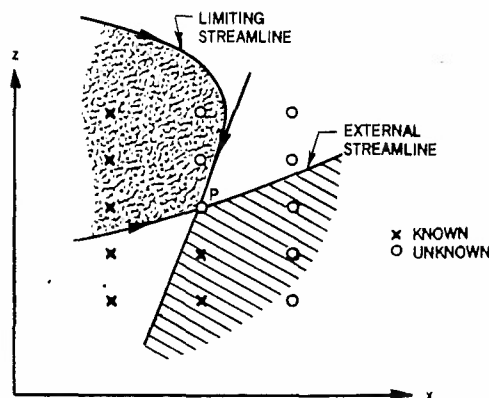


Figure 3.3. Domains of dependence (shaded area) and region of influence (hatched area) of point P when both u and w are negative.

a region, which is not relevant to P so that the extent of possible calculations is restricted.

3.2 Flows Without Reversal

There are several numerical methods that can be used to solve the three-dimensional boundary-layer equations discussed in the previous section including the popular finite-difference methods of Crank-Nicolson [29] and Keller [30] which have been used extensively for the solution of two-dimensional equations. Their solution for three-dimensional flows with either method is somewhat routine, as described in several references, see for example, Blottner [31] and Bradshaw et al. [11] when velocity components u and w are both positive. When the circumferential velocity component contains regions of flow reversal, however, the solution of three-dimensional boundary-layer equations is not so straightforward and requires special procedures to avoid the numerical instabilities which can result from reversal in w . This can be best achieved by the Characteristic scheme developed by Cebeci and Stewartson [32] which is based on the solution of governing equations along local streamlines, employs Keller's method, and is described in Section 3.3 together with the zig-zag scheme.

One of the basic ideas of Keller's method is that Eqs. (2.18) and (2.19) are expressed in the form of a first-order system before the finite-difference approximations to them are written. The resulting difference approximations are lengthy, and to illustrate the procedure, we shall consider the following reduced forms of Eqs. (2.18) and (2.20),

$$f'' + f''\theta = f' \frac{\partial f'}{\partial x} + g' \frac{\partial f'}{\partial z} \quad (3.1)$$

$$\theta' - mf' = \frac{\partial f'}{\partial x} + \frac{\partial g'}{\partial z} \quad (3.2)$$

and discuss their solution subject to the boundary conditions given by Eq. (2.21).

To express Eqs. (3.1) and (3.2) in the form of a first-order system, we represent the derivatives of f and g with respect to η by new functions, e and s , and define n by

$$e' = n \quad (3.4a)$$

and write Eqs. (3.1) and (3.2) as

$$n' + n\theta = e \frac{\partial e}{\partial x} + s \frac{\partial e}{\partial z} \quad (3.4b)$$

$$\theta' - me = \frac{\partial e}{\partial x} + \frac{\partial s}{\partial z} \quad (3.4c)$$

Depending on the signs of the velocity components u and w , or e and s in terms of new variables, the solution of the above system can be obtained by Keller's method by using different variants of this method. When both u and w are positive, we can use the Standard Box scheme, and when u is positive but w is not, we can use either the Zig-Zag or Characteristic Box schemes as we shall discuss in some detail in Section 3.3. When u is negative, then we need to reformulate the problem so that the above system is solved in an inverse mode as we shall discuss in Section 3.4.

The solution of the system given by Eqs. (3.4) by the Standard Box, Zig-Zag Box or Characteristic Box methods depends on the difference equations for Eq. (3.4b); the remaining equations are unchanged. In the following paragraphs we first consider Eqs. (3.4a and c) and show how the difference equations are written.

Consider the net cube shown in Fig. 3.4 and denote the net points by

$$\begin{aligned} x_0 &= 0, & x_i &= x_{i-1} + k_i & i &= 1, 2, \dots, I \\ z_0 &= 0, & z_k &= z_{k-1} + r_k & k &= 1, 2, \dots, K \\ \eta_0 &= 0, & \eta_j &= \eta_{j-1} + h_j & j &= 1, 2, \dots, J \end{aligned} \quad (3.5)$$

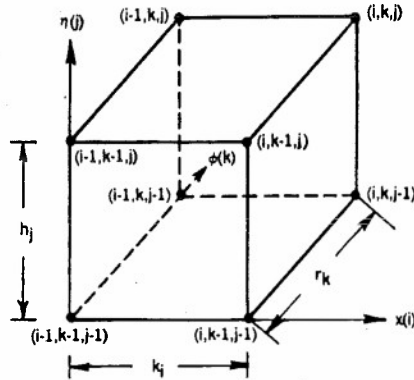


Figure 3.4. Notation for the net cube.

The difference approximations that are to represent Eq. (3.4a) are obtained by averaging about the midpoint $(x_i, z_k, \eta_{j-1/2})$,

$$h_j^{-1} (e_j^{i,k} - e_{j-1}^{i,k}) = n_{j-1/2}^{i,k} \quad (3.6)$$

where, for example,

$$n_{j-1/2}^{i,k} = 1/2 (n_j^{i,k} + n_{j-1}^{i,k}) \quad (3.7)$$

The difference approximations to Eq. (3.4c) are obtained by centering all quantities except θ at the center of the cube $(x_{i-1/2}, z_{k-1/2}, \eta_{j-1/2})$ by taking the values of each parameter, say q , at the four corners of the Box, that is,

$$q_{j-1/2}^{i-1/2,k} = \frac{1}{2} (q_j^{i-1/2,k} + q_{j-1}^{i-1/2,k}) = \frac{1}{4} (q_j^{i,k} + q_j^{i-1,k} + q_{j-1}^{i,k} + q_{j-1}^{i-1,k}) \quad (3.8a)$$

and θ is centered by writing it as

$$\theta_{j-1/2}^{i-1/2,k-1/2} = \frac{1}{2} (\theta_j^{i-1/2,k-1/2} + \theta_{j-1}^{i-1/2,k-1/2}) \quad (3.8b)$$

The unknown parameters of Eqs. (3.8) correspond to $q_j^{i,k}$ and $\theta_j^{i-1/2,k-1/2}$ so that, when a solution of the system given by Eqs. (3.4) is obtained, e and s are computed at (i,k,j) and θ at $(i-1/2,k-1/2,j)$. This modified centering procedure is necessary to avoid oscillations due to the use of the continuity equation in the form given by Eq. (2.20) rather than the use of the stream function [33].

In terms of this notation, the finite-difference approximations to Eq. (3.4c) can be written in the following form:

$$h_j^{-1} (\theta_j - \theta_{j-1}) - \bar{m}(\bar{e})_{j-1/2} = k_i^{-1} (\bar{e}_i - \bar{e}_{i-1}) + r_k^{-1} (\bar{s}_k - \bar{s}_{k-1}) \quad (3.9)$$

where, for example,

$$\begin{aligned} \theta_j &= \theta_j^{i-1/2,k-1/2}, & \bar{e}_j &= \frac{1}{2} (e_j^{i-1/2,k} + e_j^{i-1/2,k-1}) \\ \bar{e}_i &= \frac{1}{2} (e_j^{i,k-1/2} + e_{j-1}^{i,k-1/2}), & \bar{s}_k &= \frac{1}{2} (s_j^{i-1/2,k} + s_{j-1}^{i-1/2,k}) \end{aligned} \quad (3.10)$$

$$\bar{m} = (m)^{i-1/2,k-1/2}$$

With the Standard Box scheme, the difference equations corresponding to Eq. (3.4b) are formulated in the same way as has been described above. With the Zig-Zag or Characteristic Box schemes, however, an alternative procedure is followed and is described in the next section.

It should be noted that the computational problems associated with time-dependent boundary layers are similar to those for three-dimensional steady boundary layers. To illustrate this point further, let us consider a two-dimensional flow for which the continuity and momentum equations can be written in the following form, as discussed in [33],

$$(bf'')' + \frac{\partial u_e}{\partial \tau} + u_e \frac{\partial u_e}{\partial x} = \frac{\partial f'}{\partial \tau} + f' \frac{\partial f'}{\partial x} - f'' \frac{\partial f}{\partial x}$$

or as the reduced equation

$$f''' + f''\theta = \frac{\partial f'}{\partial \tau} + f' \frac{\partial f'}{\partial x} \quad (3.11)$$

which is similar to Eq. (3.1). As a result, its solution for positive u can be obtained easily by the Standard Box scheme described here and in detail in [13]. When there is backflow in the u -velocity profile, which is a situation roughly analogous to a three-dimensional reverse crossflow problem, Eq. (3.11) can also be solved with either the Zig-Zag or Characteristic Box schemes described below.

3.3 Flows with Reversal

When there is flow reversal, it is necessary to modify the Standard Box scheme of the previous section in order to avoid the numerical instabilities resulting from integration opposed to the flow direction. A convenient procedure is to include the Zig-Zag formulation of Krause et al. [34] which, in common with the often used Crank-Nicolson method, is easy to employ, particularly since the orientation of the numerical mesh is chosen a priori. This advantage has a corresponding and potentially dangerous drawback in the presence of large reverse flows, either steady or unsteady, since the mesh ratio must be related to the velocity field according to the Courant, Friedrichs, Lewy (CFL) condition [35] if stability is to be achieved. For a fixed grid chosen a priori, this condition may be violated as the flow velocities are determined in ever-increasing computational domains. Thus, a natural boundary limiting the domain in which stable computations can be made must also be determined a priori.

One way to avoid the above limitation is to allow the grid to be determined along with the flow calculations. This requirement can be accomplished by using the Characteristic scheme so that the grid spacings and orientation can be adjusted depending upon the magnitude and direction of the velocity field in order to satisfy a condition like the CFL condition. The scheme is, in a sense, intelligent in that it maximizes the domain in which the computations can be carried out for both steady and unsteady flows. For completeness we shall first describe the Zig-Zag Box scheme and then proceed with the Characteristic Box scheme.

To solve Eqs. (3.1) and (3.2) by the Zig-Zag scheme, we follow the procedure of the previous section and express them as a first-order system. In this case, however, it is more convenient to write Eq. (3.1) as

$$f''' + mff'' = f' \frac{\partial f'}{\partial x} - f'' \frac{\partial f}{\partial x} + g' \frac{\partial f'}{\partial x} - f'' \frac{\partial g}{\partial z}$$

without the definition of θ and consider it as

$$f''' + mff'' = f' \frac{\partial f'}{\partial x} + g' \frac{\partial f'}{\partial z} \quad (3.12)$$

which is applicable to steady (3-D) flows, and to unsteady (2-D) flows provided we set $g' = 1$ and associate the z -coordinate with τ . As a first-order system, Eq. (3.12) can be written as

$$f' = e \quad (3.13a)$$

$$e' = n \quad (3.13b)$$

$$n' + mfn = e \frac{\partial e}{\partial x} + s \frac{\partial e}{\partial z} \quad (3.13c)$$

The main difference between the Standard and Zig-Zag Box schemes depends on the difference equations for Eq. (3.13c); the remaining two equations, Eqs. (3.13a,b), remain unchanged.

To write the difference equations for Eq. (3.13c) centered at P (see Fig. 3.5), we use quantities centered at P , Q and R , where

$$P \equiv (x_i, z_{k-1/2}, h_{j-1/2}), \quad Q \equiv (x_{i-1/2}, z_k, h_{j-1/2}), \quad R \equiv (x_{i+1/2}, z_{k-1}, h_{j-1/2}) \quad (3.14)$$

Equation (3.13c) is then written as

$$n'(P) + [mfn](P) = \lambda_1 e(Q) \left[\frac{\partial e}{\partial x}(Q) \right] + \lambda_2 e(R) \left[\frac{\partial e}{\partial x}(R) \right] + s(P) \left[\frac{\partial e}{\partial z}(P) \right] \quad (3.15)$$

where

$$\lambda_1 = \frac{x_{i+1} - x_i}{x_{i+1} - x_{i-1}}, \quad \lambda_2 = \frac{x_i - x_{i-1}}{x_{i+1} - x_{i-1}} \quad (3.16)$$

The Characteristic Box scheme is based on the solution of the governing equations along the local streamlines. In this case, we prefer the form of the equations given by Eqs. (3.4) and by denoting the streamline direction with ψ and the angle that it makes with the x -axis (3-D steady) or τ -axis (2-D unsteady) by α , write Eq. (3.4b) as

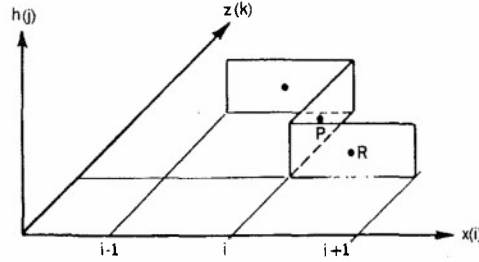


Fig. 3.5. Finite-difference molecule for the Zig-Zag Box.

$$n' + n\theta = \lambda \frac{\partial e}{\partial \psi} \quad (3.17)$$

where

$$\lambda = \sqrt{e^2 + s^2}, \quad \alpha = \tan^{-1} \left(\frac{s}{e} \right) \quad (3.18)$$

With the notation shown in Fig. 3.6, the difference approximations to Eq. (3.17) at point B are

$$\begin{aligned} & \frac{h_j^{-1}}{2} [n_j^{i,k} - n_{j-1}^{i,k}] + \frac{h_j^{-1}}{2} [n_j^{i-1,k} - n_{j-1}^{i-1,k}] + \frac{1}{2} [n_{j-1/2}^{i,k} + n_{j-1/2}^{i-1,k}] \theta_{j-1/2}^B \\ & = \frac{1}{2} (\lambda_{j-1/2}^{i,k} + \lambda_{j-1/2}^{i-1,k}) \frac{(e_{j-1/2}^{i,k} - e_{j-1/2}^{i-1,k})}{\Delta \psi_{j-1/2}} \end{aligned} \quad (3.19)$$

where the relation between θ_j^B and $\theta_{j-1/2}^{i-1/2,k-1/2}$ is

$$\theta_j^B = \frac{\theta_{j-1/2}^{i-1/2,k-1/2} - \theta_j^{i-1/2,k-3/2}}{z_{k-1/2} - z_{k-3/2}} (z_B - z_{k-1/2}) + \theta_j^{i-1/2,k-1/2} \quad (3.20)$$

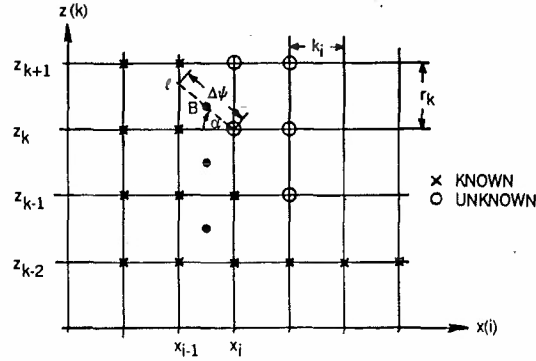


Figure 3.6. Notation for the Characteristic scheme.

The boundary conditions for the velocity field follow from Eqs. (2.21) and can be written as

$$e_0 = s_0 = \theta_0 = 0; \quad e_j = \bar{u}_e, \quad s_j = \bar{w}_e \quad (3.21)$$

The algebraic system given by Eqs. (3.6), (3.9) and two equations that result from Eqs. (2.18) and (2.19), similar in principle to Eq. (3.17), together with the boundary conditions given by Eq. (3.21) is nonlinear. Linearization is achieved with Newton's method and the equations are then solved by the block-elimination method described, for example, in [11].

3.4 Flows With Separation

For flows with separation, it is necessary to use an inverse method and compute the external velocity as part of the solution. To discuss this point further, let us consider a two-dimensional incompressible laminar flow. It can be shown that, with the transformation

$$\eta = \sqrt{u_0} \sqrt{v x} y, \quad \psi = \sqrt{u_0} \sqrt{v x} f(x, \eta) \quad (3.22)$$

the continuity and momentum equations and their boundary conditions can be written as [10]

$$f''' + \frac{1}{2} f f'' + x u_e \frac{du_e}{dx} = x (f' \frac{\partial f'}{\partial x} - f'' \frac{\partial f}{\partial x}) \quad (3.23)$$

$$\eta = 0, \quad f = f' = 0 \quad (3.24a)$$

$$\eta = \eta_e, \quad f' = u_e \quad (3.24b)$$

There are several procedures which can be used to solve the above equations in inverse form. In the Mechul function approach used by Cebeci and associates, Eqs. (3.23) and (3.24) are expressed as a first-order system in a form similar to that given by Eqs. (3.13). Since u_e is unknown and is independent of η , a fourth equation is obtained by differentiating $u_e(x)$ with respect to η , that is,

$$u_e' = 0 \quad (3.25)$$

and adding a fourth boundary condition given by Eqs. (2.24) and (2.25).

Straightforward application of the Box scheme to the four first-order equations leads to the algebraic finite-difference expressions. The solution of Eq. (2.25) is less straightforward and is discussed in [10]. It requires that a discrete approximation be introduced to Eqs. (2.24), (2.25) so that the resulting expression can be written as

$$u_e - c_{ij} \sqrt{\frac{vx}{u_0}} (\eta_e u_e - f_e) = g_i \quad (3.26)$$

where c_{ij} is a matrix of interaction coefficients defining the relationship between the displacement thickness and the external velocity. The parameter g_i represents terms whose values are assumed to be known and given by

$$g_i = u_e^K + \sum_{j=1}^{i-1} c_{ij} (D_j - D_j^K) - c_{i1} D_1^K \quad (3.27)$$

where

$$D = \sqrt{vx/u_0} (\eta_e u_e - f_e) \quad (3.28)$$

The solutions of the three-dimensional boundary-layer equations by an inverse method with the Mechul function formulation follows a procedure similar to that discussed for two-dimensional flows although there is much less experience of its use. It requires that the two external velocities are treated as unknowns and, since they are independent of η ,

$$u_e' = 0 \quad (3.29a)$$

$$w_e' = 0 \quad (3.29b)$$

represent the two additional equations needed in the solution of three-dimensional flow equations. These equations and two additional boundary conditions obtained from relationships between the displacement thicknesses and external velocities constitute a solvable set. The finite-difference approximations again make use of the Standard Box or Characteristic Box scheme depending on the complexity of the problem.

3.5 Closure

The previous sections identified the role of three variations of Keller's Box scheme which have been used in the solution of two- and three-dimensional boundary-layer equations. The Standard Box is used in regions of flow where the u and w velocity components are positive and the Characteristic Box where the u component is positive and the w component negative. The Zig-Zag Box offers few advantages and, since it does not automatically satisfy the required stability criterion, should not be used.

4.0 APPLICATIONS: STANDARD PROBLEM

In this section we shall discuss applications of the numerical procedures described in the previous section to problems in which we seek solutions of the boundary-layer equations for a prescribed pressure distribution. We shall refer to this as the standard problem and postpone the discussion of the application of the numerical procedures used in the interaction problem to Section 5.0. In Section 4.1 we will consider a two-dimensional unsteady flow and discuss the calculation of boundary layers with considerable backflow. We shall examine both Zig-Zag and Characteristic schemes in regions of backflow and the importance of step lengths in the x - and t -directions. The calculation of three-dimensional steady boundary layers will be covered in Section 4.2 and results will be presented for a laminar flow over a model problem corresponding to a prolate spheroid.

4.1 Unsteady Boundary Layers

The laminar flow around a circular cylinder started impulsively from rest is an excellent model problem with which to study the importance of the accuracy of the numerical solutions in the presence of large backflow and to clarify the problem of singularity associated with separation in unsteady flows. For this flow, the external velocity is given by $u_e = \sin x$. Its steady-state solution has a singularity at $x = x_s = 1.82 = 104^\circ$ and for $x_s < x < \pi$ it does not exist. A number of numerical studies have been conducted for this flow, as discussed in [33], and conflicting results obtained regarding separation in an evolving boundary layer in essence due to the inaccuracy of numerical procedures used by different authors. Except for those of van Dommelen and Shen [36,37], calculations either broke down at a specific time at a certain x -station from the stagnation point or they could not be extended to times much greater than 2. While all previous studies on this problem were conducted by using an Eulerian coordinate system, that of van Dommelen and Shen made use of a Lagrangian coordinate method and showed that, for $t > 2$, a hump developed in the displacement thickness $\delta^*(x,t)$ in the neighborhood of $x = 2$, i.e. a little way into the reversed flow region. This evolved into a very sharp singularity at $t = 3.004$, $x = 1.937$. My calculations utilized the Zig-Zag Box scheme of Section 3.3 and confirmed the results of van Dommelen and Shen up to $t = 2.75$, but they had to be terminated at larger times due to the numerical problems encountered in regions of flow reversal.

The need to satisfy the CFL condition in regions of flow reversal was not considered until recently [38]; calculations were made using the Characteristic scheme of Section 3.3, which allows the orientation of the finite-difference mesh to vary across the shear layer and includes the procedure for the automatic selection of time steps so as to maintain the angle (see Fig. 3.6)

$$\alpha < \tan^{-1} \frac{r_i}{k_n} \quad (4.1)$$

The resulting values of k_n for the predetermined values of steps in the x -direction are shown in Table 1 and become extremely small at $\tau = 3.0$. The total number of increments used in calculations were 101, 161 and 435 in x , y and τ , respectively, and the calculations could have been extended beyond $\tau = 3$ but at considerable expense, as witnessed by the small and decreasing values of k_n . The values of k_n and r_i are shown in Table 1.

Table 1. The distribution of step sizes in τ and ξ .

τ	k_n	ξ	r_i
0 \rightarrow 1	0.05	0 \rightarrow 0.54	0.02
1 \rightarrow 1.5	0.02	0.54 \rightarrow 0.57	0.01
1.5 \rightarrow 2.3	0.01	0.57 \rightarrow 0.58	0.0025
2.3 \rightarrow 2.73	0.005	0.58 \rightarrow 0.60	0.0020
2.73 \rightarrow 3.024	0.002	0.60 \rightarrow 0.612	0.0015
3.024 \rightarrow 3.1	0.001	0.612 \rightarrow 0.64	0.0020
		0.64 \rightarrow 0.67	0.0025
		0.67 \rightarrow 0.72	0.01
		0.72 \rightarrow 1.0	0.02

The above increments were subsequently used in conjunction with the Zig-Zag scheme, which had previously failed to permit calculations for times greater than $\tau > 2.75$. The results were found to be identical to those presented here. The alternative approach of using the Zig-Zag scheme and the relationship given by Eq. (4.1) was not, however, successful. This confirms that the selection of k_n must depend upon the direction of the local streamlines.

Figures 4.1, 4.2 and 4.3 display the variations of dimensionless displacement thickness, Δ^* , local skin-friction coefficient c_f^* and dimensionless displacement velocity $\bar{v}_w [\equiv v_w/u_0 = d/ds (u_e \delta^*)]$. It is of particular note that the displacement thickness is close to monotonic with the small maximum and minimum for $\tau = 3.1$ at which the calculations were terminated. The Zig-Zag Box results are also shown in the figure and reveal the maxima which stemmed from the use of a numerical scheme which did not meet the requirements imposed by the CFL condition.

The distributions of local skin-friction coefficients of Fig. 4.2 show trends which are similar to those of the previous results but with differences in magnitude consistent with those of Fig. 4.1. It should be noted that the results of Figs. 4.1 and 4.2 are identical with those obtained with the Zig-Zag scheme up to the value of θ at which the displacement thickness gradient reaches its maximum and for values of τ less than

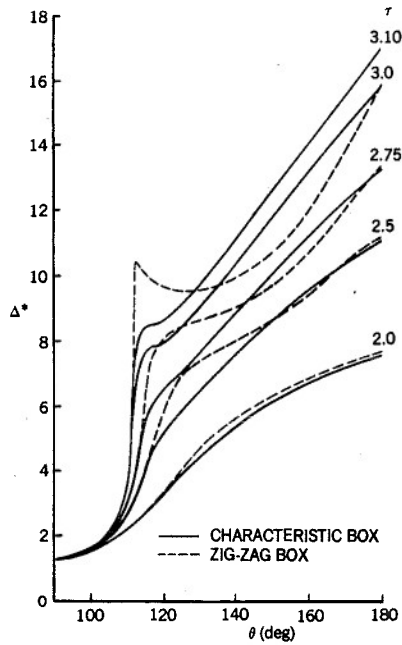


Fig. 4.1 Variation of displacement thickness for the impulsively started circular cylinder.

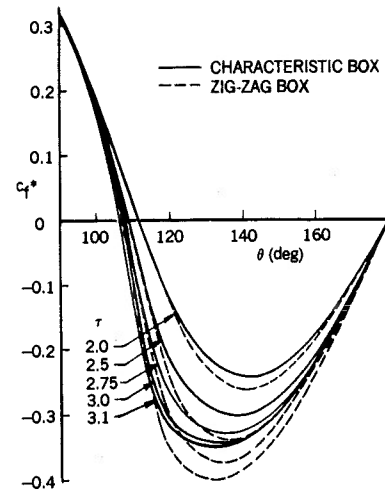


Fig. 4.2 Variation of local skin friction coefficient for the impulsively started circular cylinder.

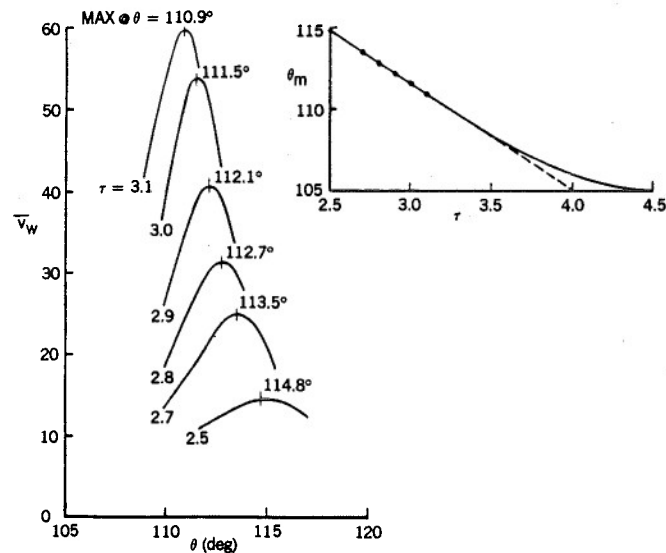


Figure 4.3. Variation of displacement velocity for the impulsively started circular cylinder. The insert shows the variation of the location of maximum displacement velocity θ_m with solid circles indicating the computed values, the dashed lines indicate the linear extrapolation of θ_m and the solid line a conjectured variation of θ_m to steady state, Cebeci [38].

around 2.75. The differences for large values of θ and τ are associated with the numerical procedure and, in particular, with its ability to satisfy the CFL condition as discussed previously.

The dimensionless displacement velocity, \bar{v}_w , is shown in Fig. 4.3 together with the locus of points corresponding to its maxima which increases with time and decreasing angle. At $\tau = 3.0$, the calculated value of θ is 111.5 and corresponds very closely to that determined by van Dommelen and Shen who terminated their calculations at this time. As the peak in the displacement velocity moves upstream with increasing time, the location at which the skin-friction coefficient becomes zero also moves upstream but at a slower rate and towards its steady-state value of 105° [4]. Figure 4.3 also shows that it is desirable to perform calculations at higher values of τ so as to confirm the

conjecture that the only singularity is associated with the steady-state solution. To make a conclusive judgment, calculations should be performed up to $\tau = 4.1$ but, as Table 1 suggests, the required time steps are likely to be very small. The time required to obtain results in the range $\tau = 3.024$ to 3.1, which corresponds to 75 time-steps, was 7 hours on a CYBER 175. The computer time likely to be required to reach $\tau = 4.1$ is clearly excessive.

It is clear that the characteristic box scheme has successfully permitted the calculation of the flow properties for the unsteady flow associated with a cylinder impulsively started from rest. The large reverse flow regions found with this model problem occur in the more practical application of oscillating airfoils as we shall see in Section 5.0. In particular, the use of the Characteristic Box scheme together with Eq. (4.1) leads to solutions which approach and pass the region of the singularity without numerical difficulty whereas the Zig-Zag scheme leads to solutions which oscillate and break down in the same manner experienced with the cylinder.

4.2 Three-Dimensional Boundary Layers

The CFL condition must also be satisfied in the calculation of steady three-dimensional flows with cross-flow reversal as discussed in Section 3.1. The need to satisfy this condition and the consequences of not doing so will now be demonstrated for a prolate spheroid which is a convenient shape for which to perform boundary-layer calculations since analytical expressions are available for inviscid pressure distribution and computer calculations are not required to determine the inviscid flow. Furthermore, the flow properties become complex as the angle of incidence is increased beyond fully-attached flow and the numerical calculations for this body serve as an excellent test case to develop and evaluate numerical methods for three-dimensional flows and investigate the properties and the behavior of the solutions in regions of negative cross-flow and in regions near separation.

The equation of a prolate spheroid can be written as (see Fig. 4.4),

$$\left(\frac{\bar{x}}{a}\right)^2 + \left(\frac{r_0}{b}\right)^2 = 1 \quad (4.2)$$

and the geometric parameters and the inviscid velocity distribution can be obtained from analytical expressions as described, for example, in [12,39]. The initial conditions in the (x,y) plane consist of the attachment-line equations, which can be easily solved away from the nose, but troubles arise in the nose region due to singularities in the geometrical parameters. They can be removed by suitable transformations and the calculations, which originate at S_0 , can be performed on both windward and leeward lines of symmetry as well as in the circumferential direction where now $z = \phi$. Thus, with initial conditions in the (y,ϕ) plane, say at $x = x_0$, and with initial conditions in the (x,y) plane at $\phi = 0$ and $\phi = \pi$, the boundary-layer equations can be solved by the numerical procedures of Section 3 for the prescribed inviscid velocity distribution and with specified thickness ratio $t(=b/a)$ and angle of incidence α .

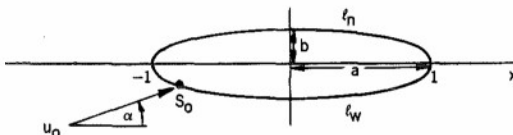


Figure 4.4 Notation for prolate spheroid at incidence: l_w and l_n denote windward and leeward sides.

Wang [40], Patel and Baek [41] and Cebeci et al. [39] have reported calculations for this flow and in the last case the Box method was used. At a specified x -station, the calculations were started on the windward line of symmetry and marched in the circumferential direction with equal $\Delta\phi$ increments of 2.5° . When the calculations broke down at some ϕ -location, the procedure was repeated, this time starting on the leeward line of symmetry and marching towards the windward line of symmetry. The grid in both directions was assigned a priori and two separate numerical methods corresponding to the Zig-Zag and Characteristic Box schemes were used. With the former scheme, there is no implicit procedure with which to determine whether or not the CFL criterion is satisfied. The Characteristic Box scheme does allow the CFL criterion to be assigned, as was discussed in the previous section, but the calculations of [39] did not make use of this possibility.

Figure 4.5 shows the separation lines and the line on which the circumferential skin-friction coefficient $c_{f\phi}$ is zero for $t = 1/4$ and $\alpha = 6^\circ$, as computed by Cebeci et al. [39]. In the region upstream of the zero- $c_{f\phi}$ -line (Region A) all u and w velocities are positive, in the region between the zero- $c_{f\phi}$ -line and the two separation lines (Region B) u is positive but w is negative near the surface. Downstream of the separation lines (Region C) both u and w are negative near the surface and positive away from the surface. The boundary-layer calculations in regions A and B can be performed for a prescribed pressure distribution because the flow is not separated. The calculations can be performed with initial conditions started on either line of symmetry. They can also be performed by first computing the region $0 \leq \phi \leq \phi_0$ with initial conditions started on

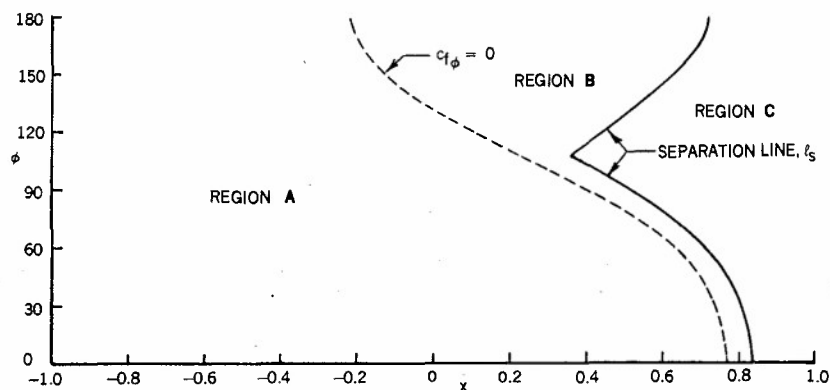


Figure 4.5. Separation lines and the zero $c_{f\phi}$ -line for laminar flow on a prolate spheroid at $\alpha = 6^\circ$ [39].

the windward line of symmetry and the remaining region $\phi_0 \leq \phi \leq \pi$ with initial conditions started on the leeward line of symmetry. Each procedure has its own advantages but if the numerical method is accurate, the results will not depend on a preferred direction of marching.

The numerical solution of the boundary-layer equations for Region A is straightforward and can be obtained easily with the Standard Box scheme of Section 3.2 with initial conditions computed on the windward line of symmetry. In Region B, a method that accounts for negative cross-flow velocity is needed and the Characteristic Box scheme of Section 3.3 can be used for this purpose. However, the calculations in this case must be performed with care since the accuracy of the solutions depends on the choice of the net in the circumferential and streamwise directions. To discuss this further, we shall consider a portion of Region B denoted by $x_A \leq x \leq x_B$ and present recent results obtained by Cebeci and Su [42] who used uniform step lengths of 2.5° in the circumferential direction as in [39] and nonuniform step lengths in the streamwise direction (see Table 2) to investigate the role of the CFL criterion on the computed results.

Table 2. Step Lengths in the Streamwise Direction for the Region $x_A \leq x \leq x_B$

x	GRID Δx					
	I	II	III	IV	V	VI
0.1500 - 0.2500	0.02500					
0.2500 - 0.2700	0.02000					
>0.2700	0.01000					
0.1500 - 0.2750		0.01250				
>0.2750		0.00500				
0.1600 - 0.2700			0.00500			
>0.2700			0.00250			
0.1600 - 0.2000				0.00500		
0.2000 - 0.2700				0.00250		
>0.2700				0.00125		
0.1600 - 0.2000					0.00250	
0.2000 - 0.2700					0.00125	
>0.2700					0.00050	
0.1600 - 0.2000						0.00250
0.2000 - 0.2700						0.00125
0.2700 - 0.2820						0.00050
>0.2820						0.00025
x > 0.2820	I	II	III	IV	V	VI
$\Delta x =$	0.01000	0.00500	0.00250	0.00125	0.00050	0.00025

With initial conditions given at $x = x_A$, the calculations were started at the next specified x -location on the line of symmetry and were continued towards the leeward line of symmetry with the Standard Box scheme in regions where w is positive and the Characteristic Box scheme where w is negative. The results obtained with Grid I are shown in Figures 4.6 and 4.7. Figure 4.6a shows the variation of the streamwise wall shear-stress parameter f_w'' with ϕ for several values of x , and for values of $x = 0.200$ and 0.2225 the solutions are smooth and free of oscillations. A slight oscillation occurs around $\phi = 125^\circ$ for $x = 0.250$ and increases substantially, covering a range of ϕ from 120° to 135° , at $x = 0.270$, after which the solutions are smooth and free of wiggles. The situation worsens for subsequent values of $x < 0.310$, but solutions do not break down in spite of the oscillations covering a larger region until they become smooth around $\phi = 135^\circ$. At $x = 0.310$, the wall shear becomes negative and causes the calculations to terminate. With solutions available for $x < 0.310$, the calculations at $x = 0.310$ are started on the leeward line of symmetry and are continued towards the windward line of symmetry. Again solutions exhibit oscillations in the same neighborhood as those which have originated from the windward line of symmetry (see Fig. 4.6b) but they do not break down until $x = 0.350$.

The cause of the oscillations was investigated by computing the maximum value of the CFL parameter $\beta (= \delta\phi_1/\Delta\phi)$, see Fig. 4.7) at each ϕ -station at a given x -location. Figure 4.7 shows the results for several values of x . We note from the results in Fig. 4.7a that β increases with increasing value of x , and attains a maximum value at $x = 0.27$ which is about 40% bigger than its maximum value at $x = 0.20$. It also exhibits oscillations at the same value of x as f_w'' . We also observe from the results in Fig. 4.7b that, the value of the CFL parameter β increases further with increasing x and oscillations worsen so that the accuracy of the solutions for values of x greater than 0.27 become increasingly suspect.

To obtain stable solutions free of oscillations, additional studies were conducted with grids other than I. Since the solutions obtained with Grid I were acceptable up to $x = 0.270$, the subsequent calculations, with the grids of Table 2, began at this value. Figure 4.8 shows the variation of the CFL parameter β for six grids in which the

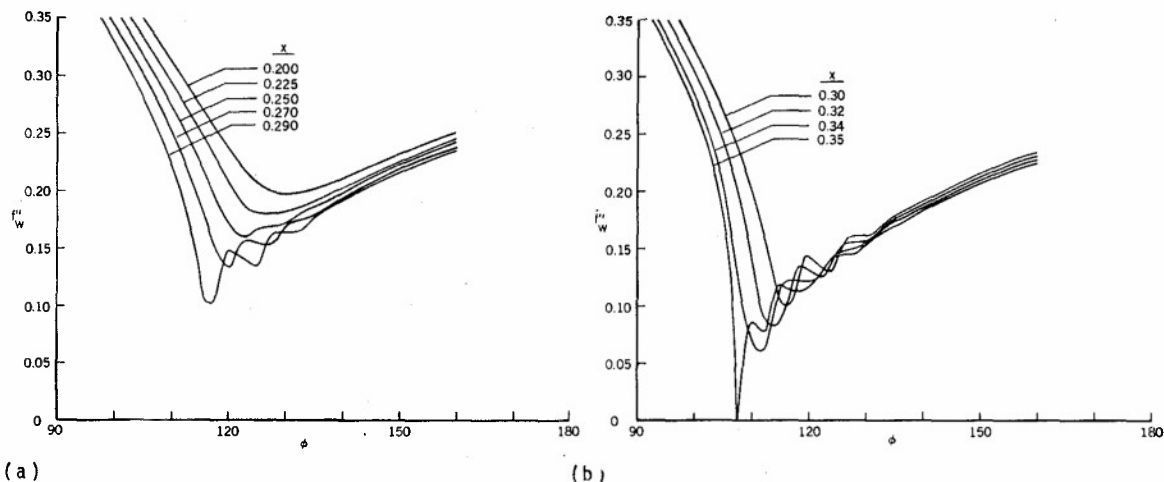


Figure 4.6. Variation of streamwise wall shear parameter f_w'' with ϕ .

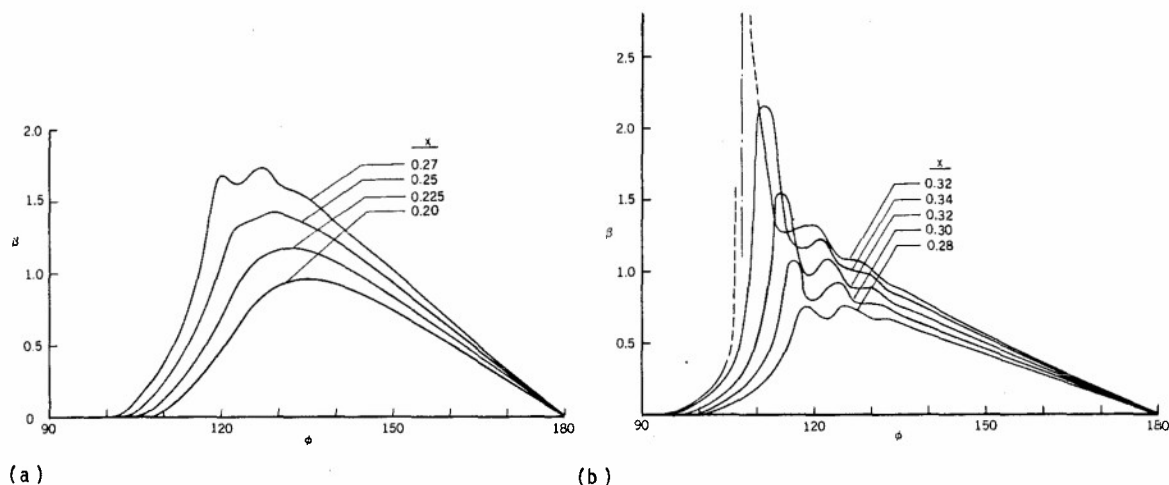


Figure 4.7. Variation of CFL parameter β with ϕ .

Δx -spacing diminishes from I to VI. We note from the results that, as expected, decreasing Δx -spacing decreases the maximum value of β . Figure 4.9 shows the effect of Δx -spacing on the computed values of f_w'' at $x = 0.30$ and we note from Fig. 4.8 that β exceeds unity at this x -station with Grid I and the solutions of Fig. 4.9a oscillate as a result. With Grid III, however, the value of β decreases to 0.27 and the solutions improve considerably (Fig. 4.9a) although there are still some wiggles. When the grid is refined further by using Grid VI, the value of β at $x = 0.30$ drops from 0.27 to 0.028 and the wiggles disappear, as shown in Fig. 4.9b.

Figures 4.10 and 4.11 show the variation of f_w'' with ϕ for conditions approaching flow separation. Figure 4.10 shows that the solutions computed with Grids V and VI are the same at $x = 0.315$ and that they contain no oscillations although a rapid decrease occurs in f_w'' around $\phi = 112.5^\circ$ and is followed by a sharp increase and decrease and another continuous increase. The results in Figure 4.11 exhibit a similar behavior with Grid VI; again there are no oscillations in the solutions but the dip in f_w'' moves towards the windward line of symmetry with increasing x with f_w'' and finally becomes negative at $x = 0.32375$.

The use of different grids allows us to determine whether or not the CFL criterion is satisfied, and if there is a preferred direction of marching from one line of symmetry to another. One would expect that the solutions obtained by marching from either line of symmetry must be identical if the solutions were accurate, but this was not the case when Grid I was used and the reason for it was the CFL criterion. Additional calculations with the grids of Table 2 confirm this conclusion and clearly show that if the grid is chosen so that the CFL criterion is satisfied, they break down at the same location regardless of which line of symmetry the solutions originate. As shown in Figure 4.8 and in Table 3 with Grid II, for example, solutions originating from the windward line of symmetry break down at $x = 0.315$ but those from the leeward line of symmetry at $x = 0.325$. The latter result is not reliable even though the maximum value of β at $x = 0.325$ is around 0.6 because the solutions at previous x -stations have not satisfied the CFL condition and allowed β to exceed unity. With Grid IV, windward-originated solutions break down at $x = 0.3225$ but leeward solutions at $x = 0.325$. Closer examination of

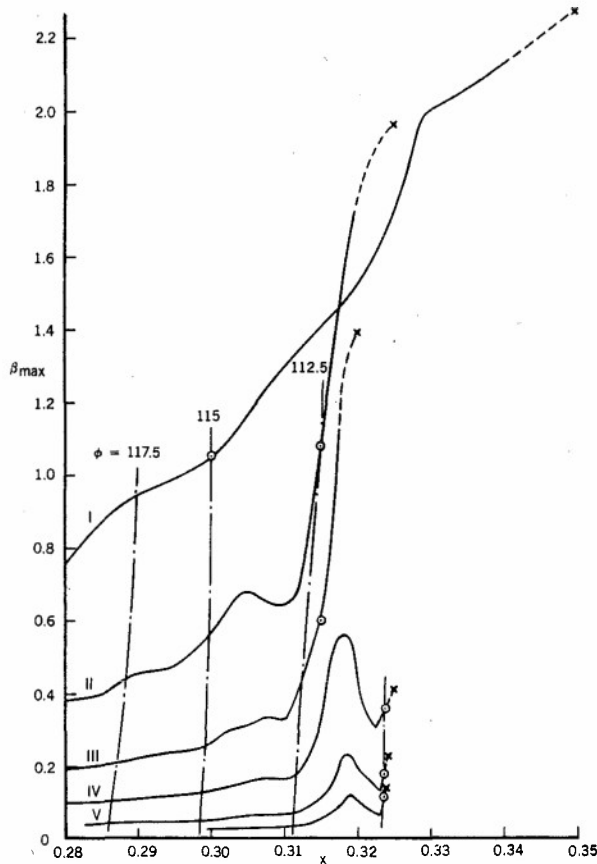


Figure 4.8. Effect of grid on the variation of the CFL parameter β with x .

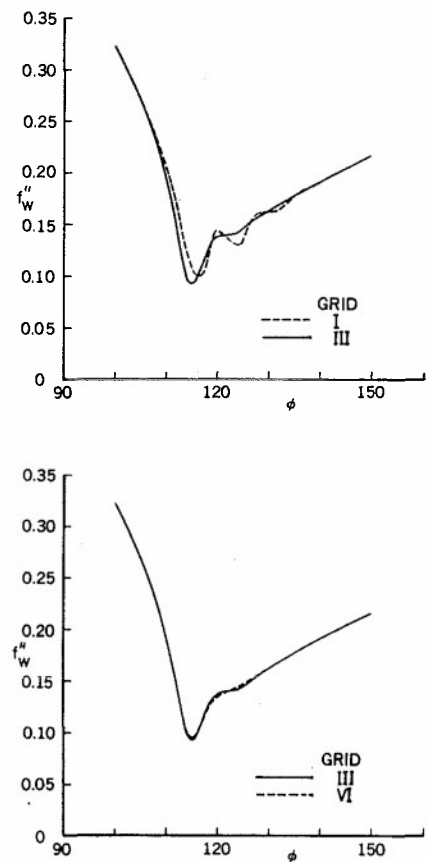


Figure 4.9. Effect of grid on the variation of the streamwise wall shear parameter f_w'' with ϕ at $x = 0.30$.

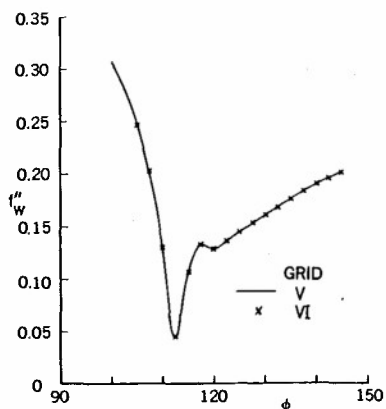


Figure 4.10. Variation of f''_w with ϕ for two grids V and VI at $x = 0.315$.

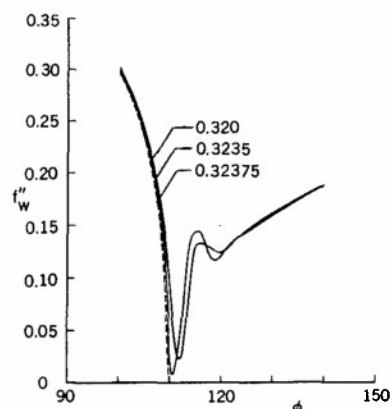


Figure 4.11. Variation of f''_w with ϕ for grid VI at various values of x .

Table 3. Effect of Grid on the Marching Direction. Calculation Breakdown Point at o - from Windward Side, * - from Leeward Side.

Grid		x	ϕ
I	o	0.30	115°
	*	0.35	107.5°
II	o	0.315	112.5°
	*	0.325	110°
III	o	0.315	112.5°
	*	0.32	112.5°
IV	o	0.32375	110°
	*	0.325	110°
V	o	0.3235	110°
	*	0.3240	110°
VI	o	0.3235	110°
	*	0.32375	110°

β for this grid (see Fig. 4.8) shows that the solutions obtained for previous values of x are more accurate than those which used Grids I and II. The solutions become even more accurate and lead to almost the same break-down location if a more refined grid, like VI, is used, for now the two x -values are 0.3235 and 0.32375 at $\phi = 110^\circ$.

5.0 APPLICATIONS: INTERACTION PROBLEM

In this section we shall discuss applications of the numerical procedures described in Section 3.0, and especially in Section 3.4, to the interaction problem discussed in Section 2.6. Since the development and application of calculation methods for three-dimensional flows tends to originate from that for two-dimensional flows, but with considerable delay, we shall begin by considering the application of the interactive approach to two-dimensional flows and particularly, in Section 5.1, to the problems of laminar, leading-edge separation [7]. The geometry corresponds to a thin ellipse with its axis located at the center of the coordinate system (\bar{y}, \bar{z})

$$\left(\frac{\bar{y}}{b}\right)^2 + \left(\frac{\bar{z}}{c}\right)^2 = 1 \quad (5.1)$$

at an angle of attack α and in a uniform stream of speed u_∞ . Attention is directed to its nose region and the ellipse is approximated locally by a "nose-fitting" parabola so that its external velocity distribution u_e can be represented by

$$\bar{u}_e = \frac{u_e}{u_\infty(1+t)} = \frac{\xi + \xi_0}{\sqrt{1 + \xi^2}} \quad (5.2)$$

Here t denotes the thickness ratio c/b , ξ_0 corresponds to a reduced angle of attack, α/t , and the parameter ξ is the reduced polar coordinate ϕ/t and is related to the \bar{y} and \bar{z} -coordinates of the ellipse by $\bar{y} + b = 1/2 bt^2 \xi^2$, $\bar{z} = bt^2 \xi$, and to the surface distance x by

$$x = bt^2 \int_0^{\xi} (1 + \xi^2) d\xi \quad (5.3)$$

Section 5.1 also considers the calculation of flow over airfoils for a wide range of angles of attack including stall and presents comparisons with experiment, and with solutions obtained by a thin Navier-Stokes method.

In Section 5.2 we shall extend the two-dimensional steady flow calculations to unsteady flows but restrict our attention to the leading edges of thin oscillating airfoils with external velocity distribution given by

$$\bar{u}_e = \frac{u_e}{u_\infty} \frac{1}{(1 + t)} = \frac{\xi + \xi_0 (1 + A \sin \omega t)}{(1 + \xi^2)^{1/2}} \quad (5.4)$$

where A denotes a parameter that needs to be specified.

The calculation of three-dimensional steady flows is discussed in Section 5.3 and results are first presented for wings for which the interactive-viscous calculations are performed with a strip-theory approximation to the boundary-layer equations. Next, laminar flow results are presented for another model problem chosen to facilitate examination of leading-edge separation on thin wings and were obtained with the numerical procedure described briefly in Section 3.4 by solving quasi-three-dimensional boundary-layer equations. This time the model problem corresponds to a triaxial ellipsoid given by

$$\left(\frac{\bar{x}}{a}\right)^2 + \left(\frac{\bar{y}}{b}\right)^2 + \left(\frac{\bar{z}}{c}\right)^2 = 1$$

where \bar{x} , \bar{y} , \bar{z} denote the Cartesian coordinates and a , b , c represent the lengths of the principal axis. With the proper choice of the axis ratios $a:b:c$, and the onset flow directions, this problem represents an extension of the two-dimensional model problem discussed in Section 5.1. The relationship of the ellipsoid to the wing becomes clearer by observing that the longest dimension of the ellipsoid (\bar{x}) is in the swept spanwise direction and the \bar{y} -axis is in the chordwise direction normal to the sweep line (see Fig. 5.1). The maximum thickness of the sections normal to the sweep line, as before, is given by $t = c/b$ and the wing planform area is πab . The aspect ratio of the wing, with λ denoting the sweep angle, is given by $(4/\pi)(a/b) \cos^2 \lambda$.

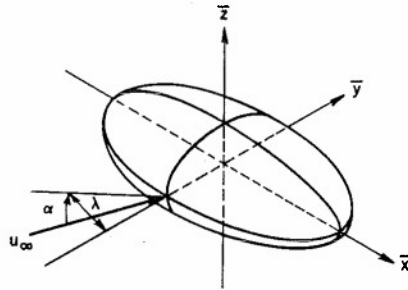


Figure 5.1. Orientation of the ellipsoid.

As in the case of a thin ellipse at incidence α , we can derive expressions for the external velocity components for the nose region [28] and apply the "nose-fitting" parabolas normal to the \bar{x} -axis. With the assumption that $t \ll 1$, this leads to the expressions:

$$u_e = \frac{H[BH - A\lambda(\bar{x}/a)](\xi + \xi_0)(1 + \xi^2)^{1/2}}{H^2(1 + \xi^2) + (\bar{x}/a)^2 \lambda^2} \quad (5.5a)$$

$$w_e = \frac{[AH(1 + \xi^2) + \bar{x}/a \lambda(B - C\xi)][H^2 + (\bar{x}/a)^2 \lambda^2]^{1/2}}{H^2(1 + \xi^2) + (\bar{x}/a)^2 \lambda^2} \quad (5.5b)$$

Here $H = [1 - (\bar{x}/a)^2]^{1/2}$, λ denotes the principal axis ratio, b/a , the parameters A , B and C denote the maximum velocities over the ellipsoid induced by the freestream velocity u_∞ in the x , y and z directions, respectively, and are given in [28]. As before, ξ_0 corresponds to a reduced angle of attack and is given by

$$\xi_0 = - \frac{C[H^2 + (\bar{x}/a)^2 \lambda^2]}{H[A\lambda(\bar{x}/a) - BH]} \quad (5.6)$$

We note that for an ellipse defined by Eq. (5.1), the external velocity u_e given by Eq. (5.5a) is identical to that of Eq. (5.2) since, by letting $a \rightarrow \infty$ and keeping b fixed, $\lambda \rightarrow 0$, $V_2 = 1 + t$. For small angles of attack $\cos \alpha = 1$, $B = u_\infty \cos \lambda$, and B can be thought of as an equivalent freestream velocity.

5.1 Two-Dimensional Flows

To compute the flow over an airfoil with the interactive method discussed in Sections 2.6 and 3.4, it is necessary at first to solve the inviscid flow equations for the airfoil shape and angle of attack. With the resulting pressure distribution and specified freestream conditions, the laminar boundary-layer equations are solved next from the stagnation point along both surfaces for a short distance. The standard boundary-layer approach is replaced by the inverse approach and is used to calculate laminar as well as turbulent flows with separation, with transition location either specified or computed by an empirical formula.

For the simple leading-edge separation problem, the calculations of Cebeci et al. [7] were performed with the external velocity distribution given by Eq. (5.2) and successive sweeps on the airfoil. The results showed that the laminar boundary layer near the leading edge is well behaved and unseparated if $\xi_0 < \xi_s = 1.16$, although there was significant adverse pressure gradient. At higher values of ξ_0 , however, separation occurred with an associated singularity and required the use of an interactive theory to link the viscous and inviscid flows. With this interaction, solutions were obtained for separation bubbles but reattachment occurred in a very limited range of the reduced angle of attack. For $\xi_0 > 1.218$, the calculation broke down shortly after flow reversal occurred in the boundary layer and the subsequent studies of Stewartson, Smith and Kaups [43] seemed to imply that a dramatic switch to another separated form of motion can occur. Their results suggest that separated and reattached-flow solutions are not always unique and a similar phenomenon may also be present in two-dimensional calculations at least in the sense that a small change in the calculation may cause the reattachment location to move in space or in time by a disproportionately large amount. These conjectures may also have a physical counterpart in that separation bubbles can be unstable with a tendency to form an open region of separation.

In Fig. 5.2, we show calculated distributions of the reduced skin friction at different values of ξ_0 for $t = 0.1$ and $R (= 2u_\infty b/\nu) = 10^6$ and in Fig. 5.3 we demonstrate the failure of the iteration sequence at a slightly larger value of $\xi_0 = 1.218$. It is interesting to note that these observations provide support to the notion of a critical value of ξ_0 beyond which attached flow is impossible [44] but it should be remembered that transition occurs in flows which have separated and causes reattachment, as was studied by Cebeci and Schimke [8] for the experimental data of Gault [45] on an NACA 663-018 airfoil. The data include pressure distributions and velocity profiles in the separated-flow region which covers about 10% chord and extends from $s/c = 0.62$ to 0.725 for $\alpha = 0^\circ$ and from $s/c = 0.61$ to 0.715 for $\alpha = 2^\circ$ at $R_L = 2 \times 10^6$. Note that we now use s to denote surface distances in order to distinguish it from the chordwise distance x used for airfoils.

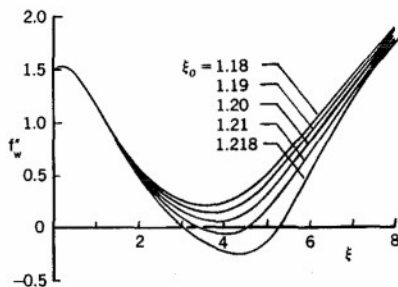


Figure 5.2. Variation of f''_w with ξ for various values of ξ_0 .

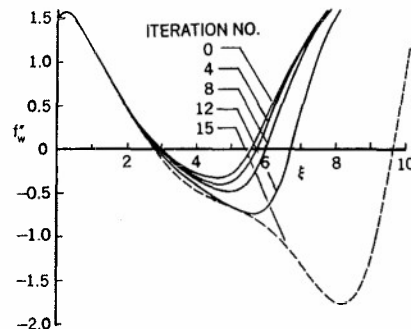


Figure 5.3. Variation of f''_w with number of iterations for ξ_0 slightly greater than 1.218.

The calculations of Cebeci and Schimke were first made by computing the pressure distribution from Halsey's conformal mapping method [2]. Since the location of transition was not known prior to the boundary-layer calculations, solutions were first obtained for the specified inviscid pressure distribution by the standard method and by computing transition from the empirical formula given in [13],

$$R_\theta = 1.174 \left(1 + \frac{22,400}{R_x} \right) R_x^{0.46} \quad (5.7)$$

Subsequent iterations were performed by the standard method from the stagnation point up to $s/c = 0.30$, at which point the inverse boundary-layer calculations were started and continued to the trailing edge. If a region of separated flow was found to exist, then the new location of transition was determined from the formula given by Crimi and Reeves [46]

$$\frac{y_{u=0}}{\delta^*} = \frac{10^6}{(u_e \delta^*/\nu)_s^2} \quad (5.8)$$

where $y_{u=0}$ denotes the distance from the wall where $u = 0$ and subscript s denotes separation. This process was repeated until the solutions converged.

Figures 5.4 and 5.5 show the calculated and experimental results for $\alpha = 0^\circ$. Figure 5.4 shows the computed wall-shear parameter f_w for several sweeps on the airfoil, and Figure 5.5 allows comparison of calculated and experimental velocity profiles at different streamwise locations. From Figure 5.4 we see that the inverse calculations do not reveal a separated region in sweep 1 with transition corresponding to laminar separation. In the second sweep, however, the calculations show a small separated region with the transition location still at $s/c = 0.66$, indicating that Eq. (5.8) did not indicate transition during that sweep. The third set of calculations (not shown on the figure) indicated a larger region of separated flow with the transition location computed by Eq. (5.8) to be at $s/c = 0.69$. Table 4 presents the location of transition as a function of

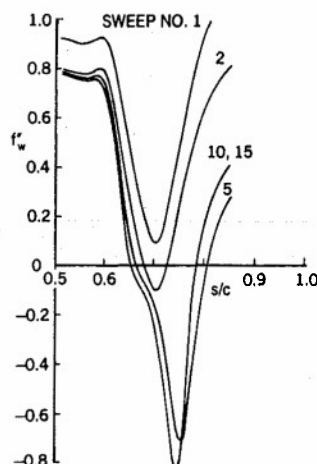


Figure 5.4. Variation of wall-shear parameter f_w'' with number of sweeps for $\alpha = 0$, $R_c = 2 \times 10^6$.

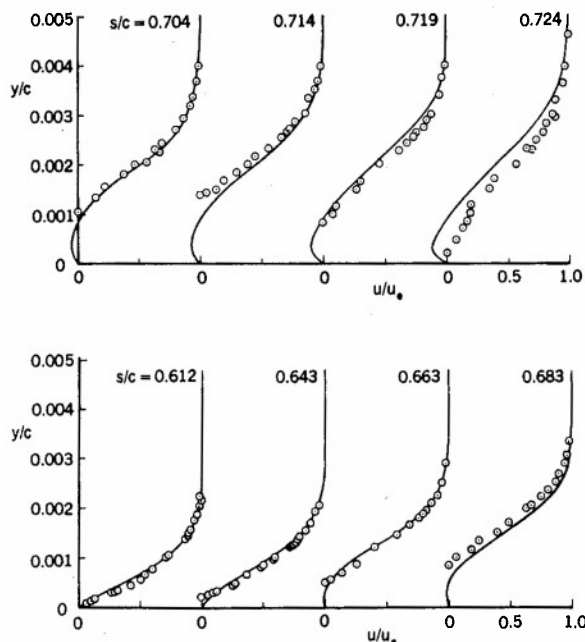


Figure 5.5. Comparison of calculated (solid line) and experimental (symbols) velocity profiles for $\alpha = 0$, $R_c = 2 \times 10^6$ after 15 sweeps.

Table 4. Variation of Transition Location for Different Sweeps
for $\alpha = 0^\circ$

Sweep	$(s/c)_{tr}$
1	0.66 (laminar separation)
2	0.66
3	0.69
4	0.68
5	0.68
6-15	0.67

sweep number and confirms that the transition location remains unchanged at $s/c = 0.67$ after sweep 6. Figure 5.4 also shows that the overall solution converges after about ten sweeps. According to the results of Figure 5.5, the agreement between computed and measured velocity profiles is good, apart from the last streamwise station $s/c = 0.724$ at which there are differences in the reattachment location.

The calculations of Cebeci and Schimke for this angle of attack and for $\alpha = 2^\circ$ indicate that the converged solutions are very sensitive to the transition location in the boundary-layer calculations. If the transition location is specified a short distance upstream of the laminar separation point, the size of the separation bubble is reduced or eliminated entirely. However, if the transition location is specified a short distance downstream of this point, as in the model problem discussed above, the separated region grows with each sweep and the solutions eventually break down.

The method discussed in this section has also been used to calculate the lift and drag characteristics of several airfoils for a wide range of angles of attack including stall [10]. The calculations include both wall boundary layer and wake flows and are presented in the following paragraphs in a sequence which corresponds to the complexity of the flow. Thus, the first results are presented for a symmetrical airfoil, NACA 0012, at angles of attack up to and including stall. The second airfoil, NACA 4412, has camber and the measurements again correspond to angles of attack up to and including stall. Finally, results are presented for an aft-loaded airfoil, GA(W)-2, which is 13%-thick. These airfoils have been investigated for angles of attack up to 16° and, since the chord Reynolds numbers imply that transition can play an important role and it was treated here in the manner described previously.

Figures 5.6 and 5.7 allow a comparison between the computed and experimental [47] lift and drag curves for the NACA 0012 airfoil. As can be seen from Fig. 5.6, the calculated results are in very good agreement with measurements up to $\alpha = 15^\circ$ and suggest that stall occurs for α beyond 19° , whereas the experiments indicate stall for $\alpha > 16^\circ$. As shown in the figure, a very small adjustment to the location of transition results in calculations of stall angle in accord with measurements. To further elaborate on this point and to show the role of transition, Table 5 presents calculated results for three angles of attack. Those in Table 5a were obtained for $\alpha = 6^\circ$ with the transition location computed from the empirical formula given by Eq. (5.8). As can be seen from

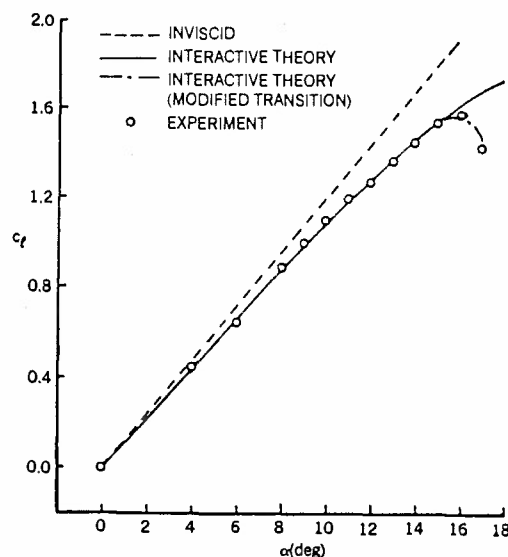


Figure 5.6. Variation of c_d with α - NACA 0012 airfoil, $R_c = 6.0 \times 10^6$.

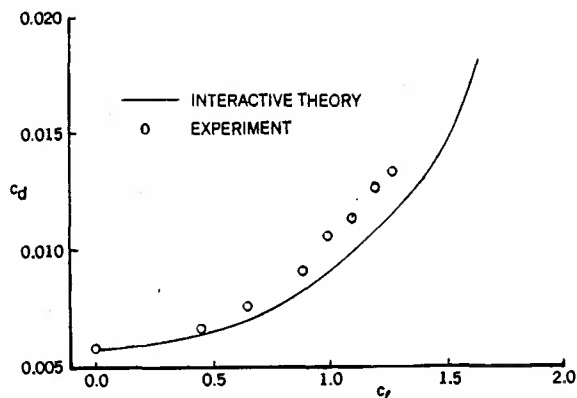


Figure 5.7. Variation of c_d with c_l - NACA 0012 airfoil, $R_c = 6.0 \times 10^6$.

Table 5. Effect of Transition on the Flow Properties of an NACA 0012 Airfoil for $R_c = 6 \times 10^6$.

(a) $\alpha = 6^\circ$. Experimental value of $c_l = 0.65$. Transition computed from Eq. (5.8).

$(x/c)_{tr}$	c_l	$(\frac{\delta^*}{c})_{t.e.}$
0.031 (fixed)	0.625	0.0091
0.052 (computed)	0.628	0.0089
0.070 (fixed)	0.633	0.0084
0.078 (fixed)	-	-

(b) $\alpha = 12^\circ$. Experimental value of $c_l = 1.29$. Transition location corresponds to laminar separation. (Negative values of x/c indicate points on the lower surface.)

$(x/c)_{tr}$	c_l	$(\frac{\delta^*}{c})_{t.e.}$	$(\Delta x/c)_{sep}$
-0.0030 (fixed)	1.270	0.0195	0.965 \sim TE
0.0025 (fixed)	1.283	0.0172	0.986 \sim TE
0.0083 (computed)	1.286	0.0167	0.986 \sim TE
0.0170 (fixed)	-	-	-

(c) $\alpha = 17^\circ$. Experimental Value of $c_l = 1.42$. Computed transition location corresponds to laminar separation.

$(x/c)_{tr}$	c_l	$(\frac{\delta^*}{c})_{t.e.}$	$(\Delta x/c)_{sep}$
-0.0173 (fixed)	1.502	0.0768	0.56 \sim TE
-0.00925 (fixed)	1.514	0.0737	0.60 \sim TE
-0.00250 (fixed)	1.573	0.0615	0.66 \sim TE
0.000493 (computed)	1.669	0.0453	0.77 \sim TE

the values of c_l and displacement thickness at the trailing edge, movement of the transition location by 2% of chord has a negligible effect. Location of transition at $x/c = 0.078$, however, leads to a breakdown in the solutions for reasons consistent with those found by Cebeci and Schimke and discussed earlier. In an adverse pressure gradient, as in this case, it appears that transition must occur upstream of some limiting location for solutions to exist.

The same phenomenon is evident in Table 5b, which corresponds to $\alpha = 12^\circ$ and a much higher lift coefficient. In this case, transition was assigned to the location corresponding to laminar separation since Eq. (5.7) was inappropriate and a small adjustment to the location of transition has a small effect on lift, although movement of transition to $x/c = 0.0170$ causes the solutions to break down. The results of Table 5c for $\alpha = 17^\circ$ indicate that the lift coefficient is strongly dependent on the location of transition and that the extent of the region of trailing-edge separation is large and becomes larger as the transition location is moved upstream. Consistent with this result, the displacement thickness at the trailing edge increases and the lift coefficient decreases as the transition location moves upstream.

Figure 5.7 shows calculated and measured variations of total drag coefficient versus lift coefficient with discrepancies which increase with angle of attack and are undoubtedly due in part to measurement accuracy. In addition, the accuracy of the calculations in the wake region requires further examination of numerical uncertainties and of those due to the neglect of normal pressure gradient.

In the experiments of Wadcock [48] and Coles and Wadcock [49], a flying hot-wire arrangement was used to measure the velocity characteristics of the flow around an NACA 4412 airfoil at angles of attack up to that corresponding to maximum lift. Figures 5.8 to 5.10 show the experimental and computed lift and drag curves and the pressure distribution respectively, with calculated transition locations corresponding to the procedure described earlier and to that obtained by the tripping arrangement of the experiment. The measured and calculated values of c_L are in close agreement up to $\alpha = 12^\circ$, with those calculated according to experimentally determined transition location in slightly better agreement. The drag curves of Fig. 5.9, agree fairly well at low values of c_L and poorly at higher values. It should be noted, however, that the two sets of experimental data differ by amounts larger than could be expected from their Reynolds numbers. The results in Fig. 5.10 confirm the close agreement between the measured and calculated distributions of pressure coefficient. It is clear that the inclusion of viscous effects influences the pressure distribution considerably in the leading and trailing edge regions.

Figures 5.11-5.13 compare computed results for the 13% thick GA(W)-2 airfoil with the experimental data of [50]. The pressure distribution, shown in Fig. 5.11 for $\alpha = 12^\circ$ agrees well with the experimental data suggesting that the present interactive theory provides a good prediction of the viscous effect. The lift curve slope of Fig. 5.12 shows that the present method gives good agreement up to an angle of attack of approximately 16° , which is better than the 10° obtained by Melnik and Brook [51] with the GRUMFOIL program. The variation of drag with lift, presented in Fig. 5.13, shows that the present method predicts the drag very well over the whole range considered.

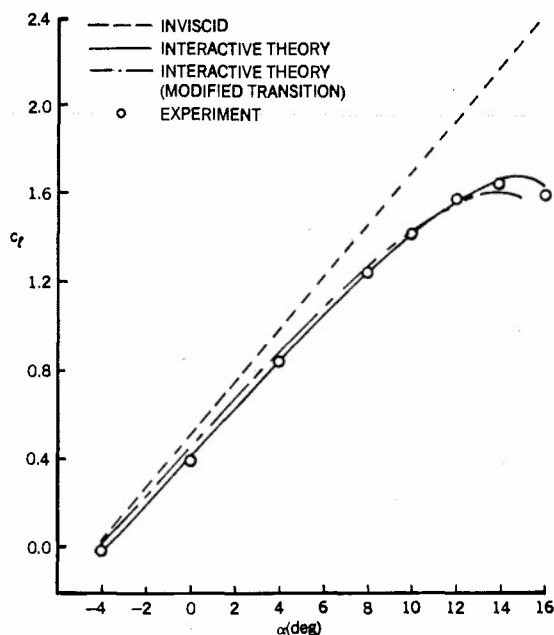


Figure 5.8. Variation of c_L with α - NACA 4412 airfoil, $R_C = 1.523 \times 10^6$. (Modified transition corresponds to experimental location.)

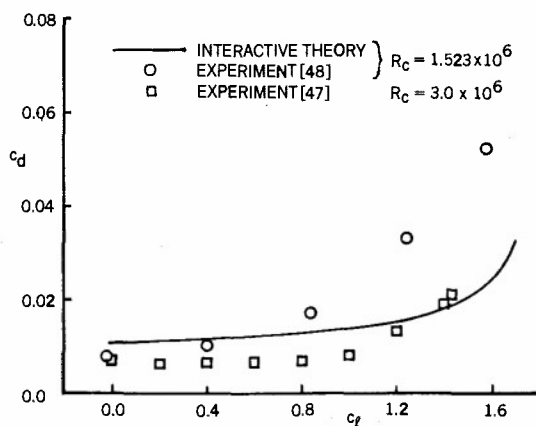


Figure 5.9. Variation of c_d with c_L - NACA 4412 airfoil, $R_C = 1.523 \times 10^6$.

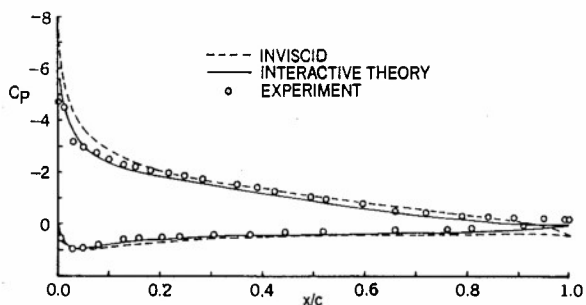


Figure 5.10. Variation of C_p with x/c - NACA 4412 airfoil, $\alpha = 12^\circ$.

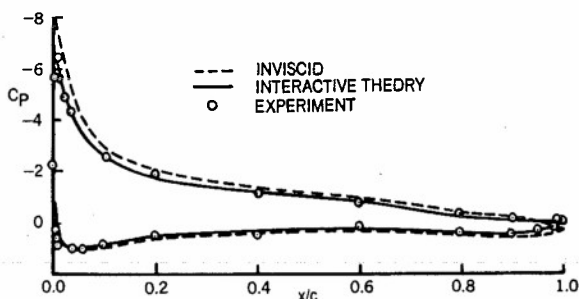


Figure 5.11. Variation of C_p with x/c - GA(W)-2 airfoil, $\alpha = 12^\circ$, $R_c = 4.3 \times 10^6$.

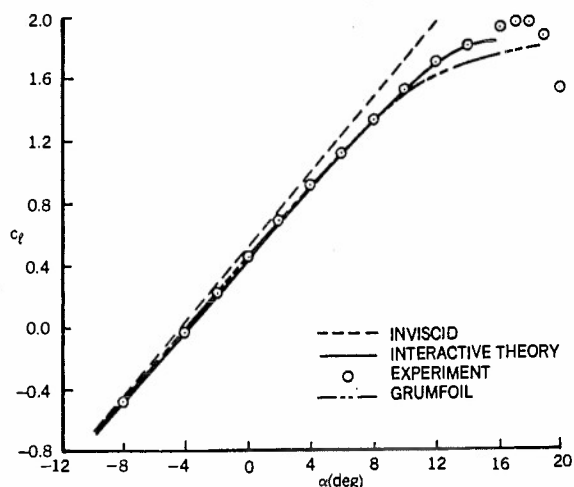


Figure 5.12. Variation of c_l with α - GA(W)-2 airfoil, $R_c = 4.3 \times 10^6$.

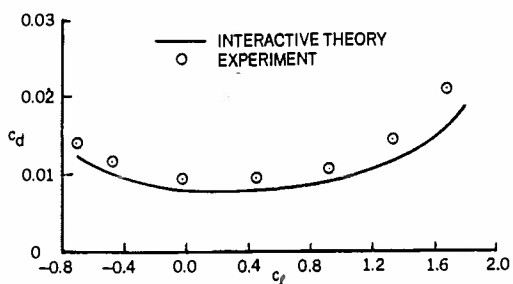


Figure 5.13. Variation of c_d with c_l - GA(W)-2 airfoil, $R_c = 4.3 \times 10^6$.

In calculating the results of Figs. 5.6 to 5.13, the FLARE approximation was found to be satisfactory only when the separation region was small. As the extent of the separation region increased, an additional iterative scheme based on the homotopy continuation method was introduced at the start of the wake calculation. Under this scheme an initial velocity profile at the trailing edge was defined by

$$u = u_{\text{ref}} + n(u - u_{\text{ref}}), \quad n = 0, 0.50, 1.0 \quad (5.9)$$

and the boundary-layer solution was computed at the first point in the wake with $n = 0$. Here u_{ref} corresponds to a nonseparating velocity profile constructed from the separated velocity profile at the trailing edge. This procedure was repeated with $n = 0.50$ and 1.0 until the solutions converged and, since it was applied to each wake profile with separation; it was necessary for angles of attack greater than around 15° . Attempts to avoid the problem by approaching from lower angles of attack with smaller increments of angle were unsuccessful.

In the course of the development of interactive methods, it is common to perform calculations for the flow over an airfoil and to omit consideration of the wake. Figure 5.14 shows that this practice has consequences which also increase with angle of attack and, for the NACA 0012 airfoil of the figure, are important for angles greater than around 10 degrees.

The predictions of the above interactive procedure were compared with those of the thin Navier-Stokes (TNS) solutions in [52]. The NACA 0012 airfoil was considered for this purpose and the calculations were performed at $R_c = 2.88 \times 10^6$ with Reynolds stresses modeled by the algebraic eddy-viscosity formulation of Cebeci and Smith [4]. Both calculations used the same transition location. The TNS calculations made use of a C-type grid topology with 257×57 node points, and with 36 points in the wake region of the airfoil along the freestream direction. Except near the leading edge and the trailing edge of the airfoil, the first grid-point off the airfoil surface was at a distance of $0.00001L$, where L is the chord length, and corresponded to y^+ in the range of 0.15 to 3.5, depending on chordwise location and angle of attack. The first grid-point upstream of the leading edge and downstream of the trailing edges was at a distance of $0.001L$ and the outer boundary was located 10 chord lengths from the airfoil.

The interactive boundary-layer (IBL) calculations were performed with approximately 80 and 60 x -stations on the upper and lower surfaces, respectively. The number of y -stations varied from 37 to 50 for small angles of attack, and was equal to 70 for large angles of attack. There were 30 x -stations in the wake, which extended to three chord lengths downstream of the trailing edge.

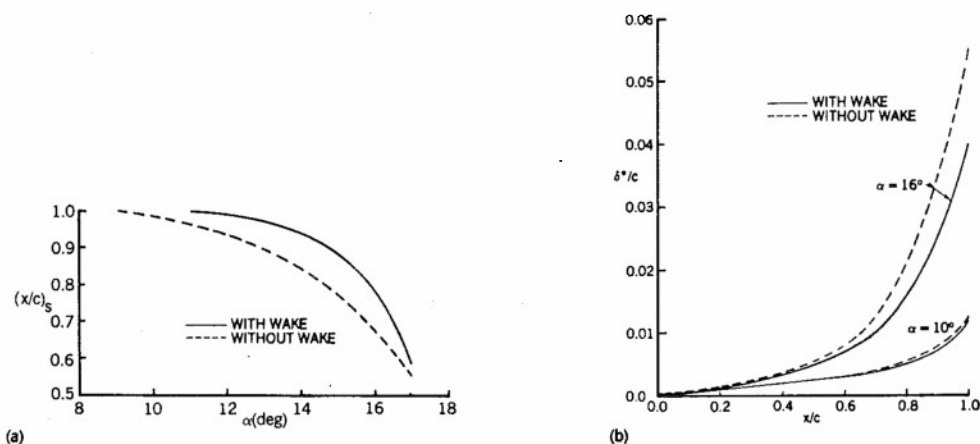


Figure 5.14. Effect of wake on the (a) separation region, and (b) displacement thickness - NACA 0012 airfoil, $R_c = 6 \times 10^6$.

The calculated and measured values of lift coefficient, c_l , shown on Figure 5.15 as a function of angle of attack, are in close agreement up to 12° and the expected fall off in c_l occurs in the IBL solutions but not in the TNS solutions. With very small changes in transition location, as was discussed previously, the IBL-computed lift coefficient changes significantly and the TNS solution is less sensitive. There are several possible reasons for the differences but is evident that better modeling of the wake is required to compute the expected fall off in c_l with the TNS method.

Distributions of pressure coefficient are shown on Figs. 5.16-5.18. Figures 5.16 and 5.17 present the TNS and IBL results, respectively, with the experimental data of [53] for angles of attack of 0 to 16° and Fig. 5.18 compares the results of the two procedures for angles of attack 10° and 12° . The calculated results of the two procedures agree very well with each other as well and with the experimental data except at 14° and 16° where the TNS results show some irregularities near the suction peak due to an improper transition location [54].

The drag results of Table 6 and Figure 5.19 require more detailed discussion. The IBL approach has used the velocity defect in the wake to compute the drag coefficient, c_d , whereas the TNS procedure has integrated forces around the airfoil surface. The pressure drag ranges from about 13 to 86% of the total drag, for angles of attack from 0 to 16° . It is likely that the pressure drag integrated using surface pressure distribution is determined with acceptable accuracy, especially in view of the quality of the calculations suggested by the comparisons between computed and experimental pressure

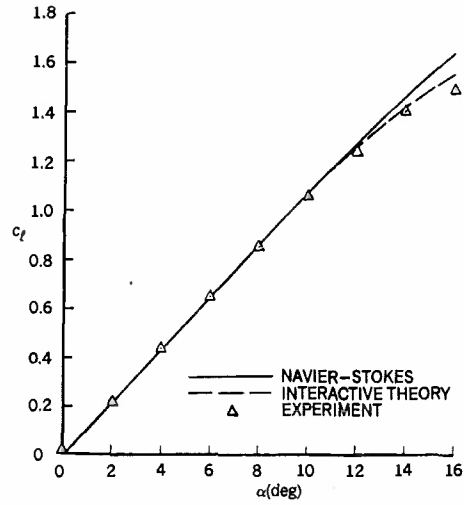


Figure 5.15. Comparison of IBL and TNS results for the NACA 0012 airfoil.

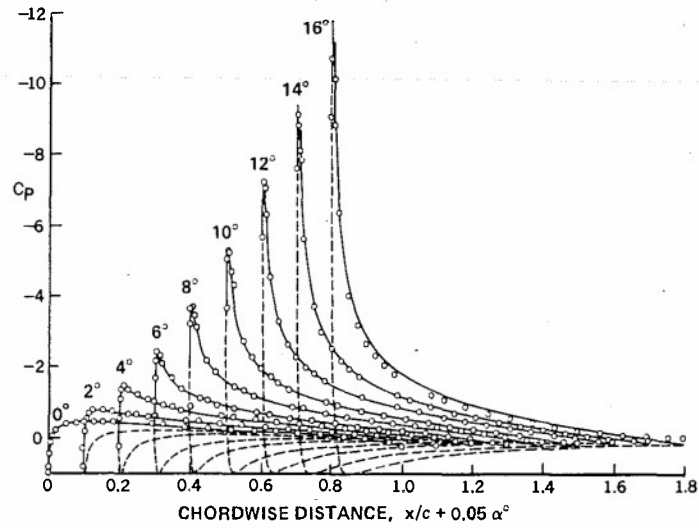


Figure 5.16. Comparison of pressure distribution for the NACA 0012 airfoil - TNS results (solid and dashed) and experimental (symbols) data.

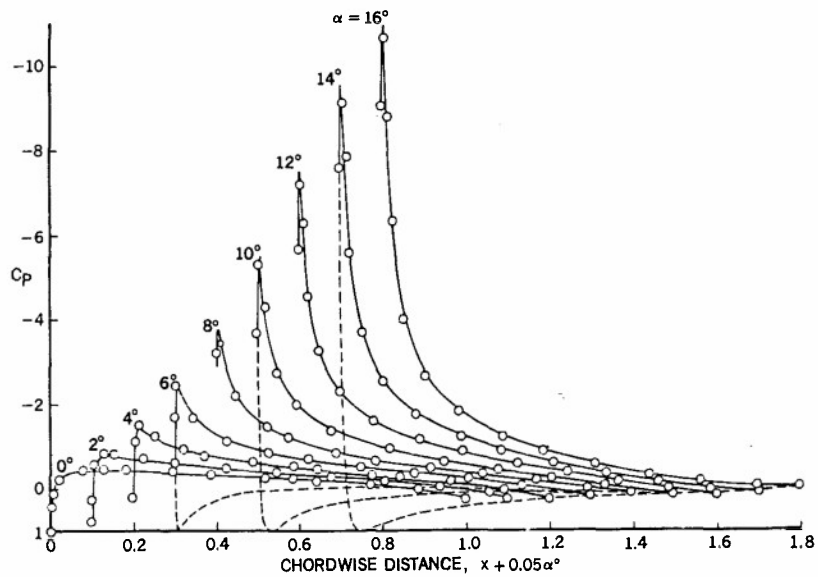


Figure 5.17. Comparison of pressure distributions for the NACA 0012 airfoil - IBL results (solid and dashed) and experimental (symbols) data.

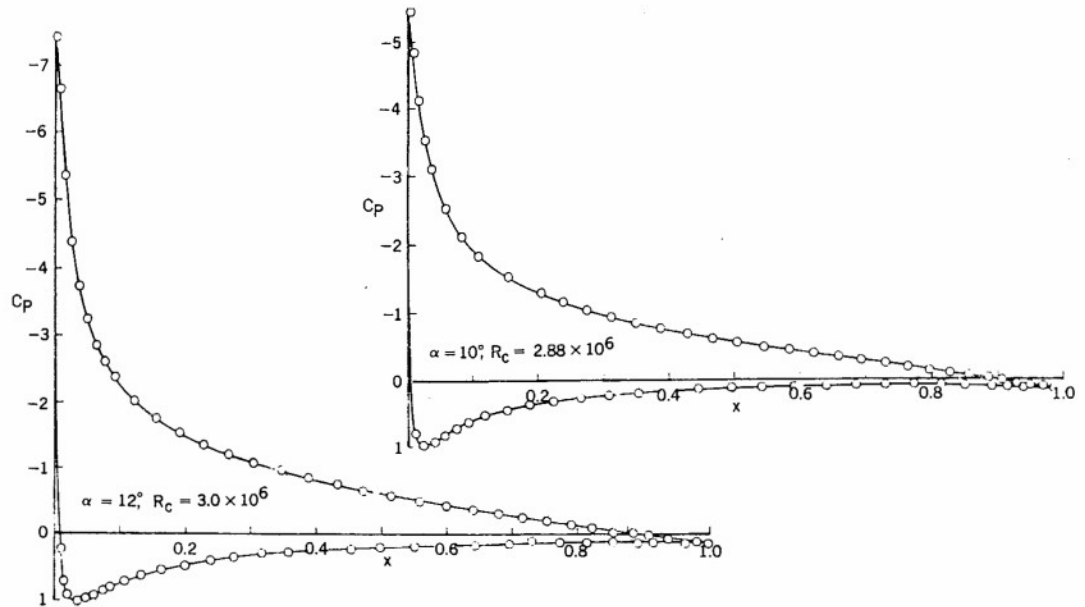


Figure 5.18. Comparison of pressure distributions for the NACA 0012 airfoil - TNS (solid) and IBL (symbols) results.

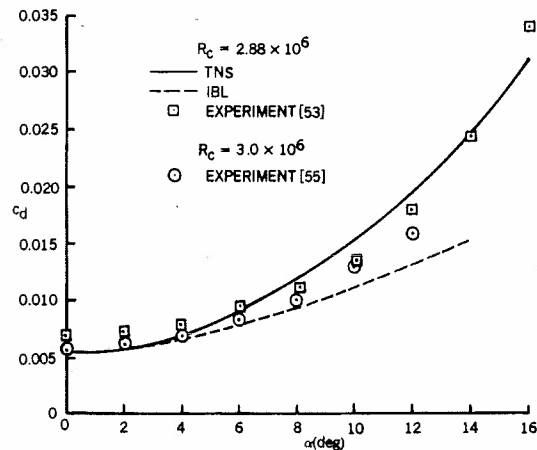


Figure 5.19. Drag characteristic of the NACA 0012 airfoil at $R_c = 2.88 \times 10^6$.

Table 6. Lift and Drag Coefficients for the NACA 0012 Airfoil at $R_c = 2.889 \times 10^6$

α deg	C_L			C_D		
	EXP.	IBL	TNS	EXP.	IBL	TNS
0	0.025	0.0	0.0	0.0069	0.00596	0.00568
2	0.220	0.209	0.213	0.0073	0.00611	0.00572
4	0.440	0.421	0.430	0.0080	0.00633	0.00750
6	0.650	0.639	0.641	0.0094	0.00689	0.00921
8	0.850	0.873	0.857	0.0112	0.00899	0.01207
10	1.055	1.077	1.065	0.0134	0.01070	0.01547
12	1.240	1.256	1.265	0.0180	0.01294	0.01962
14	1.400	1.422	1.457	0.0244	0.01662	0.02469
16	1.490	1.545	1.640	0.0338	0.02315	0.03121

coefficients discussed earlier. At angles of attack from zero to 2° , and transition specified at the experimental location, the total drag computed by the IBL method is within six counts (ten thousandths) of that computed by the TNS method and both methods agree well with the experimental values. At higher angles of attack, before the appearance of the transitional bubble, the computed results of the IBL method are lower than those determined by experiments and the TNS method. At still higher angles of attack, in the presence of this bubble and, with turbulent flow separation, still lower pressure coefficients exist along the aft region of the upper surface and are underpredicted by the IBL method. This difference is probably due to the wake-curvature and the cross-stream pressure gradient effects which are not represented by this approach. The cross-stream pressure gradient increases the momentum thickness of the wake and consequently the total drag. This conjecture is consistent with the findings of [16], which examined the use of the Cebeci-Smith eddy viscosity formulation for wake flows.

Further examination of the calculated values of c_d showed that they are different from those reported by Loftin and Smith [55] for $R_c = 3 \times 10^6$ and almost the same value as those in [53] (Fig. 5.19). Since the NPL data are 25 years newer than those of [55], they are probably more accurate. The TNS procedure appears to do a better job of predicting drag than the IBL procedure, which underpredicts it at high angles of attack. However, it is evident that the uncertainties associated with the calculation procedures and with measurement of c_d require further examination.

5.2 Two-Dimensional Unsteady Flows

We now present results for a model oscillating airfoil whose external velocity distribution is given by Eq. (5.4). One part of the calculations was carried out for the standard problem by choosing $\xi_0 = 1$, $A = -1/2$ and $\omega = 0.1$ [56]. With these choices, the maximum value of α_{eff} , defined by

$$\alpha_{eff} = \xi_0(1 + A \sin \omega t) \quad (5.10)$$

is sufficient to provoke separation with a strong singularity if the boundary layer were steady. Numerical calculations were made initially with the Zig-Zag box scheme and the results of Fig. 5.20 show that the boundary layer eventually separates, the flow remaining smooth. Immediately downstream of separation, however, it is evident that a singularity appears to develop in the neighborhood of $\xi = 2.12$ and $\omega t = 308.75^\circ$ and that it is not possible to continue the calculation beyond this time with the standard formulation and the Zig-Zag scheme.

Figure 5.20a shows that the variation of the displacement thickness

$$\delta^* = \frac{\delta^*}{a} \left(\frac{1 + \tau}{\tau} \right) \frac{1}{\epsilon \pi} \quad (5.11)$$

is generally smooth except in the neighborhood of $\xi = 2.12$ and for $\omega t = 308.75^\circ$. The first sign of irregularity is the steepening of the slope of δ^* when $\omega t = 300^\circ$ and the local maximum of δ^* at $\xi = 2.12$ when $\omega t = 308.75^\circ$. When the same results are plotted for a displacement velocity ($\bar{u}_e \delta^*$), (Fig. 5.20b), we observe that the steepening of the displacement velocity near $\xi = 2.12$ is dramatic. For example the peak is at $\xi = 2.125$ for $\omega t = 300^\circ$; at $\xi = 2.105$ for $\omega t = 305^\circ$; at $\xi = 2.09$ for $\omega t = 307.5^\circ$; and finally at

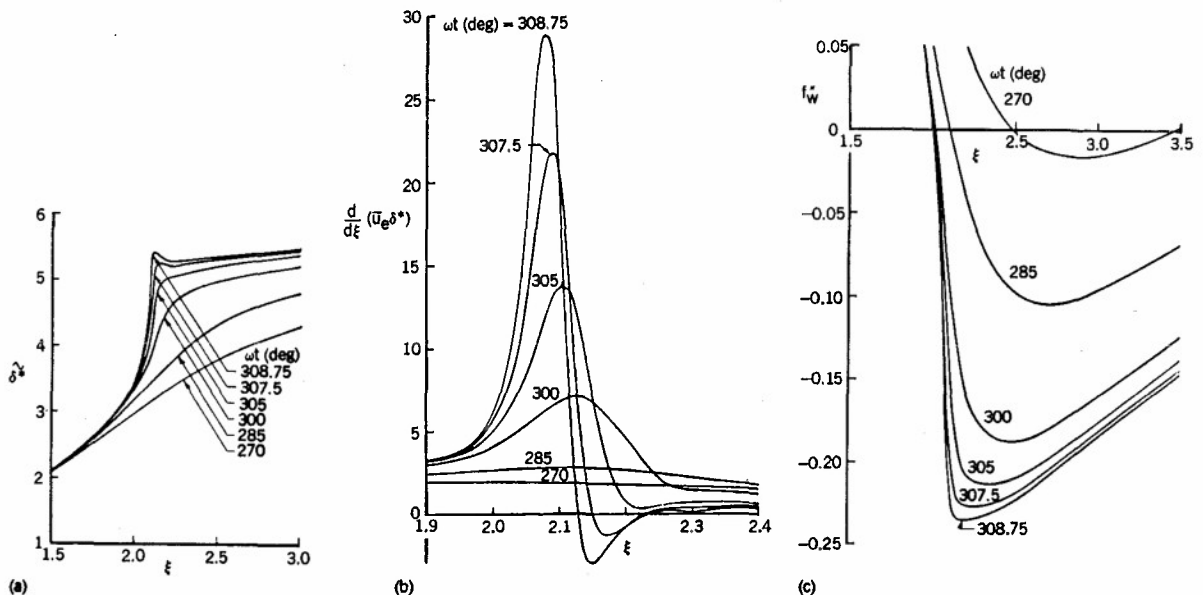


Figure 5.20. Computed results for the oscillating airfoil, $A = -1/2$, $\bar{\omega} = 0.1$ using the Zig-Zag scheme. (a) Displacement thickness δ^* . (b) Displacement velocity, $d/d\xi(\bar{u}_e \delta^*)$. (c) Wall shear parameter f_w .

$\xi = 2.08$ for $\omega t = 308.75^\circ$. It should be noted that the maximum value of displacement velocity moves towards the separation point with increasing ωt as we observed previously with the circular cylinder.

As shown in Fig. 5.20c, the wall shear parameter f_w'' shows no signs of irregularity for $\omega t \leq 308.75^\circ$ but a deep minimum in f_w'' occurs near $\xi = 2.15$, i.e. near the peak of δ^* .

These results suggest that the solutions have a singularity in the neighborhood of $\xi = 2.12$ and $\omega t = 308.75^\circ$ and that, as in steady flows, it is necessary to use an interactive theory to remove it. The procedure of Section 2.6 was used to investigate this possibility further for a specific value of Re ($\approx 10^5$). The standard method was used to compute the unsteady boundary layers up to $\xi = 0.5$ for all time and with these initial conditions and for each value of ωt , the inverse method was used to calculate the unsteady flow from $\xi = 0.5$ to $\xi = 5.5$. As before, up to three sweeps in the ξ -direction were made to achieve a converged solution where flow reversal was encountered, as happens for values of $\omega t > 270^\circ$ and $\xi > 2$.

Figure 5.21a shows the variation of displacement thickness δ^* and Fig. 5.21b the wall shear parameter f_w'' as a function of nondimensional distance ξ and time, and it is evident that the solutions are well behaved for values of $\xi < 2.5$. As expected, the displacement thickness increases with ξ for all values of time and reaches a maximum around $\omega t = 300^\circ$ as a consequence of the change in the angle of attack. In the same range of ξ , the wall shear decreases for all values of ωt and reaches a minimum corresponding to the maximum in displacement thickness.

For values of $\xi > 2.5$, the solutions remain well behaved until around $\omega t = 290^\circ$. The general trends are in accord with expectations and there is negligible difference between the results obtained with the standard and interactive methods for values of ωt up to the maximum for which the standard method allowed solutions. Although the calculations were carried out for one complete cycle, the solutions had wiggles for $\omega t > 295^\circ$ and several attempts to eliminate them by using different step sizes in time and space as well as Reynolds number were not successful. Indeed, in some cases the solutions broke down before the calculations completed one cycle.

Calculations were performed for the model oscillating airfoil with the Characteristic Box, as had previously been found necessary with the circular cylinder [38]. At first, calculations were made for the standard problem with the same net spacing used in the Zig-Zag scheme and the solutions broke down at $\xi = 2.12$ and $\omega t = 305^\circ$ when the CFL condition given by Eq. (4.1) was not satisfied. As in the case of the circular cylinder problem, the original ξ -distribution was maintained and the value of k_n was reduced until the CFL condition was met and the resulting calculations were performed smoothly and without numerical problems for one complete cycle. More important, however, the solutions did not break down at $\omega t = 308.75^\circ$ when the same calculations were repeated with the Zig-Zag scheme, and we were able to obtain them for one cycle. These results were also identical to those obtained with the characteristic box scheme indicating that with the "proper" net the predictions of both schemes are the same.

Figures 5.22 and 5.23 show the variation of displacement thickness δ^* and wall shear parameter f_w'' , respectively. As expected, the new results are the same up to the location of flow reversal as those in Figs. 5.20a and 5.20c, but substantially different in the region of flow reversal.

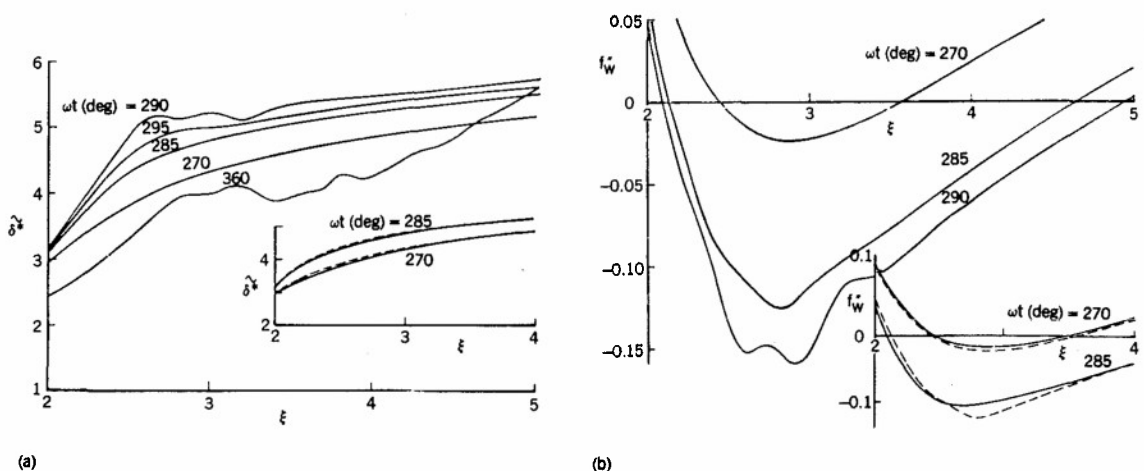


Figure 5.21. Effect of interaction on the variation of (a) displacement thickness δ^* , (b) wall shear parameter f_w'' for an oscillating airfoil with $c = 4.5 \times 10^{-3}$. Solid lines in the insert represent the results obtained by the Standard method and dashed lines those by the inverse method. Calculations made use of the Zig-Zag Box scheme.

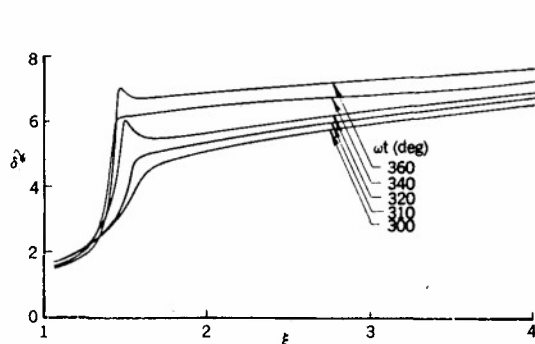


Figure 5.22. Computed displacement thickness δ^* for the oscillating airfoil, $A = -1/2$, $\omega = 0.1$ using the Characteristic Box scheme.

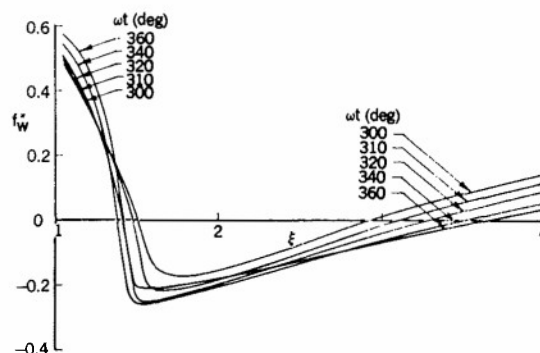


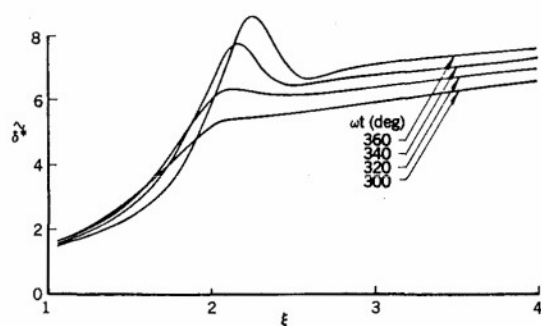
Figure 5.23. Computed wall shear parameter f_w for the oscillating airfoil, $A = -1/2$, $\omega = 0.1$ using the Characteristic Box scheme.

Calculations were also conducted using the unsteady interactive method for the net determined in the standard problem by the characteristic scheme. The results obtained with the Zig-Zag scheme are shown in Figs. 5.24 and 5.25 for Reynolds numbers, R_L , of 10^5 and 10^4 . The results obtained by the interactive method are nearly the same as those obtained by the standard method prior to flow reversal and are substantially different when flow reversal is present by an amount which increases as the Reynolds number decreases. We also note that the wiggles observed in the calculations with the "wrong" net are absent, and that the rate of convergence is the same as in the standard problem.

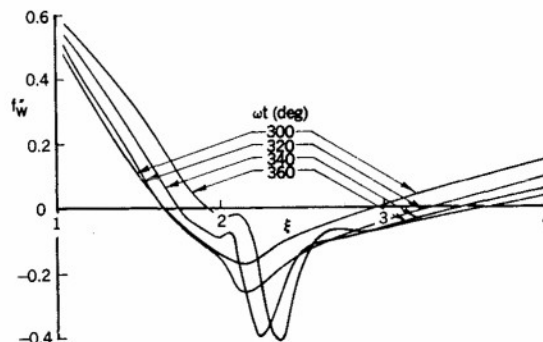
5.3 Three-Dimensional Flows

Except for the studies of Yoshihara and his associates [57-59] and Cebeci and his associates [28,60,61], most interactive studies for three-dimensional flows have been conducted by direct boundary-layer methods. For a given pressure distribution, boundary-layer solutions are obtained up to the separation line, determined either by a sudden increase in shape factor (integral method) or by the vanishing of the wall shear stress in the streamwise direction (differential method). These signals for separation do not correspond to a true definition of flow separation but are chosen because of the limitations of the direct boundary-layer method and of the numerical procedure. Ad hoc assumptions are made in the separated region so that the displacement thickness distribution computed by the boundary-layer method can be added to the basic wing shape in the surface normal direction. This technique was chosen by Yoshihara and Wai [59], Street [62] and by Chow et al. [63] for transonic flow in preference to using surface transpiration boundary conditions because it was easier to incorporate in their transonic codes. All studies show the expected strong influence of viscosity on the location of the shock wave and on the pressure distribution; the interaction schemes, however, break down in regions of flow separation and the effect of assumed displacement thickness distribution on the results is not clear.

The application of interactive methods to three-dimensional flows with separation has not received the considerable attention assigned to two-dimensional flows. Recently Cebeci and his associates explored the merits of their interactive scheme applied in a strip theory sense to wings at subsonic [60,64] and transonic [61] flow conditions. Figures 5.26 and 5.27 show the results for subsonic flows. As can be seen from Figure 5.26, the computed results agree well with experiment as long as flow on the wing is not



(a)



(b)

Figure 5.24. Interactive solutions of (a) displacement thickness δ^* , and (b) wall shear parameter f_w , for the oscillating airfoil, $A = -1/2$, $\omega = 0.1$ obtained with the Characteristic Box scheme for $R_L = 10^5$.

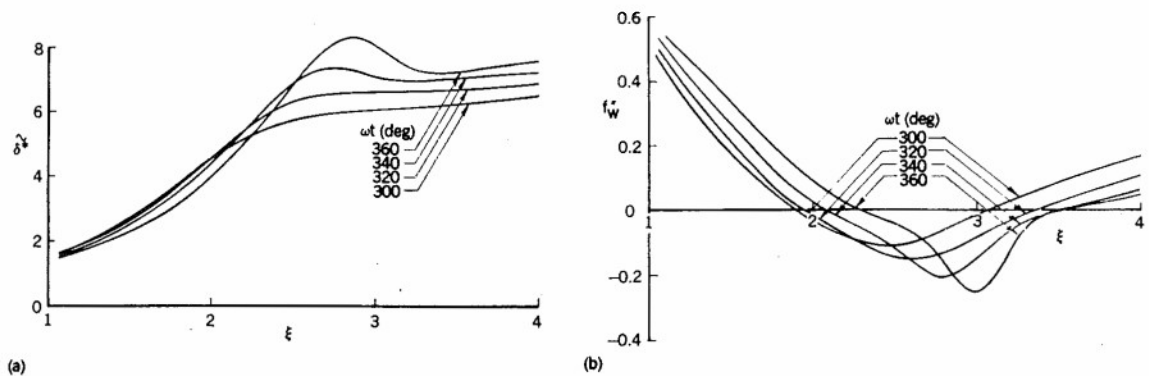


Figure 5.25. Interactive solutions of (a) displacement thickness δ^* and (b) wall shear parameter f_w'' , for the oscillating airfoil, $A = -1/2$, $\omega = 0.1$ obtained with the characteristic box scheme for $Re_L = 10^4$.

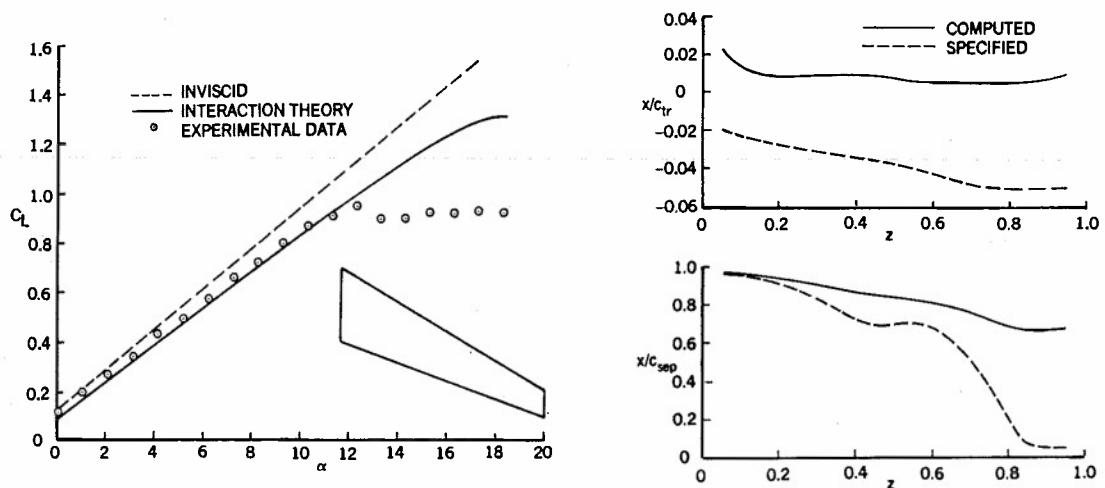


Figure 5.26. Calculated and experimental lift coefficient for a tapered wing.

Figure 5.27. Effect of transition location on the separation pattern of a tapered wing at $\alpha = 17.5^\circ$.

"too" three dimensional, which is the case at small and moderate angles of attack when the flow separation is small. At higher angles of attack, and starting around $\alpha \sim 12^\circ$, however, the computed results begin to deviate from the experimental results and the discrepancy may be attributed to several causes.

The first is the use of the strip theory approximation to account for viscous effects: at the higher angle of attack, the flow becomes increasingly three-dimensional and the viscous effects computed by a two-dimensional procedure are insufficiently representative. The second reason is the use of a two-dimensional method to compute transition: the results of Figure 5.27 show that the computed transition location for $\alpha = 17.5^\circ$, is close to 1% chord but its location at 5% chord causes significant changes in the flow separation pattern, especially near the tip, and decreases the total lift by 5%.

The third, and perhaps the most important reason, is the wake effect. The calculations for Figures 5.26 and 5.28 extended only to the trailing edge and, although this may be acceptable at small angles of attack, it is not acceptable at higher angles of attack.

Recently the interactive approach described in Section 5.1 for two-dimensional flows has been extended to three-dimensional flows [28] by a quasi-three-dimensional flow approximation which is a significant improvement over the strip-theory approximation discussed above. We shall now present results obtained with this procedure to study the separation and reattachment on the leading edge of a model problem corresponding to a thin wing discussed earlier. The results are presented here for two sweep angles with a range of angles of attack and the corresponding flows include some with separation.

Results obtained with the sweep angle of $\lambda = 20^\circ$ are shown in Fig. 5.28 for a range of reduced angles of attack from 1.306 to 1.319. As can be seen from Fig. 5.28a, the streamwise wall shear parameter f_w'' becomes negative with a value of $\xi_0 = 1.312$. The calculations proceed smoothly until $\xi_0 = 1.323$ is reached at which value they change substantially with the number of sweeps as shown in Fig. 5.28b. Up to this angle of attack, the region of separated flow is small and did not change much with each sweep although the rate of convergence of the solutions at a given ξ -location was

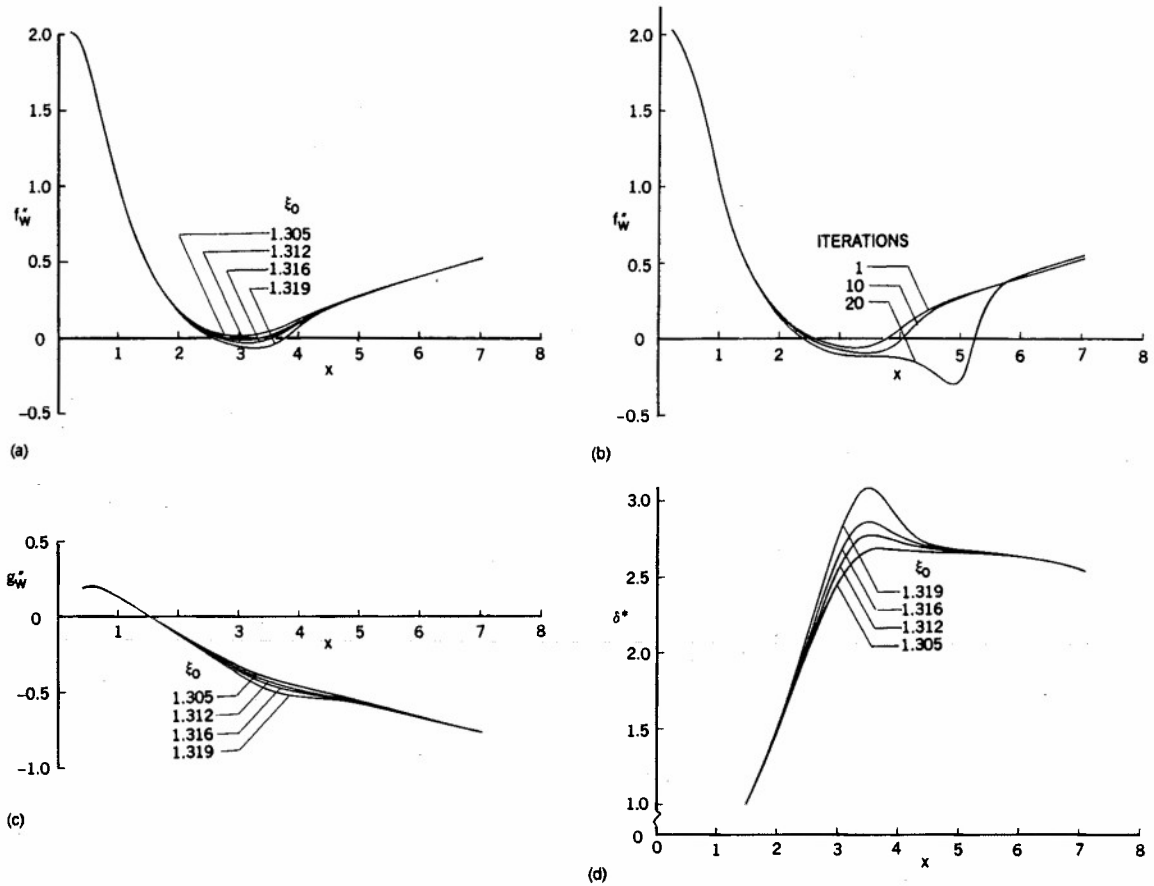


Figure 5.28. Results for $\lambda = 20$ for various reduced angles of attack, ξ_0 . (a) Variation of streamwise wall shear parameter f''_w with x . (b) Variation of streamwise wall shear parameter f''_w with x for several iterations at $\xi_0 = 1.323$. (c) Variation of spanwise wall shear parameter g''_w with x . (d) Variation of displacement thickness δ^* with x .

slow. Further work is in progress to accelerate the rate of convergence and to investigate the reasons for the sudden increase of the separation region of Fig. 5.28b.

The distributions of spanwise wall shear parameter g''_w are shown in Fig. 5.28c and, although they exhibit a sign change, they are well behaved in the range of angles of attack of Fig. 5.28a. Since the two momentum equations are coupled, the problems encountered for $\xi_0 = 1.323$ and shown in Fig. 5.28b for f''_w were also present in g''_w . The displacement thickness variations of Fig. 5.28d exhibit the features of flows with separation so, for example, the displacement thickness varies rapidly with angle of attack.

It is likely that the problem associated with high angle of attack is similar to that explored for two-dimensional flows discussed in Section 5.1. The influence of sweep angle is, however, important since the present critical angle of attack is much higher than that for two-dimensional flows. To explore this influence further, calculations were also performed for a sweep angle of $\lambda = 30^\circ$. The results shown in Figures 5.29 confirm the dependence of the critical angle of attack on sweep angle.

The above calculations for the model problem were performed for a given inviscid pressure distribution with successive boundary-layer sweeps on the body. As in the two-dimensional model problem discussed in Section 5.1, the blowing velocity can be computed from

$$v_n = \frac{1}{h_1 h_2 \sin \theta} \left[\frac{\partial}{\partial x} (u_e h_2 \sin \theta \delta_x^*) + \frac{\partial}{\partial z} (w_e h_1 \sin \theta \delta_z^*) \right] \quad (5.12)$$

where

$$\delta_x^* = \int_0^\infty \left(1 - \frac{u}{u_e} \right) dy, \quad \delta_z^* = \int_0^\infty \left(1 - \frac{w}{w_e} \right) dz \quad (5.13)$$

but was not fed back into the inviscid flow to obtain a modified inviscid pressure distribution. This possible improvement can readily be incorporated so that several cycles

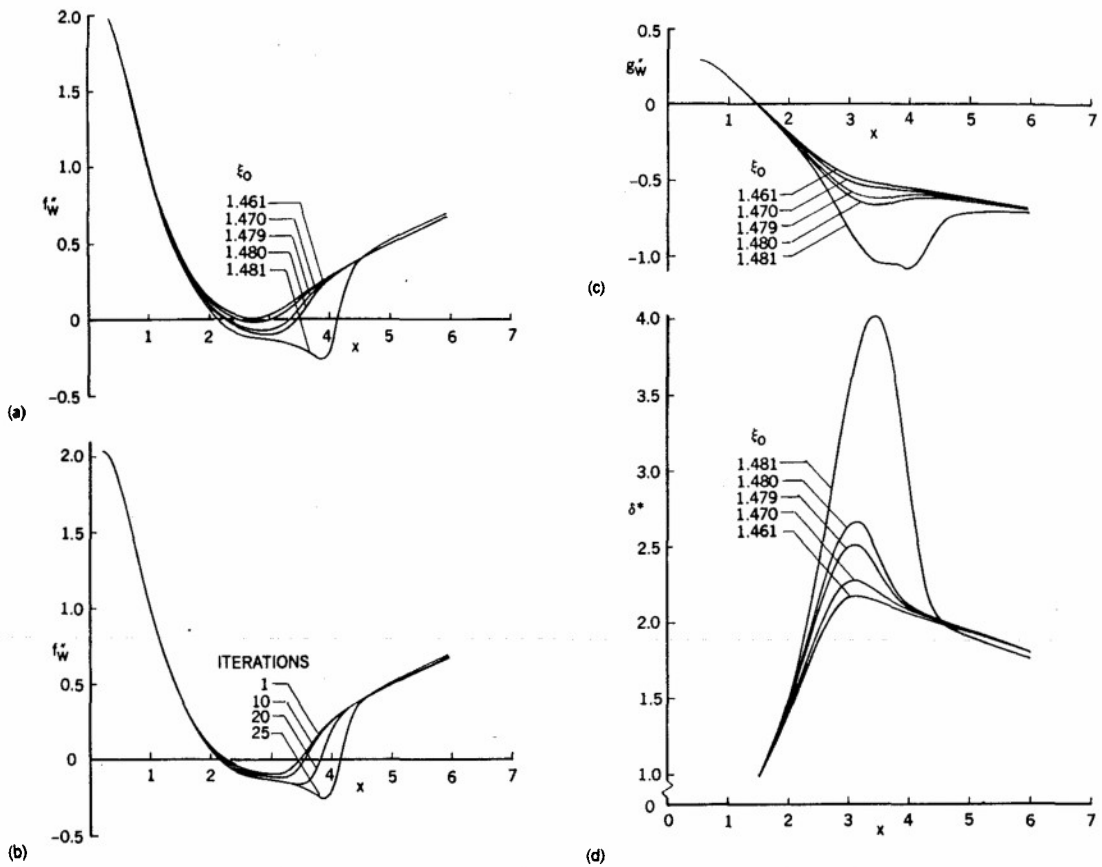


Figure 5.29. Results for $\lambda = 30$ for various reduced angles of attack, ξ_0 . (a) Variation of streamwise wall shear parameter f'_w with x . (b) Variation of streamwise wall shear parameter f'_w with x for several iterations at $\xi_0 = 1.481$. (c) Variation of spanwise wall shear parameter g'_w with x . (d) Variation of displacement thickness δ^* with x .

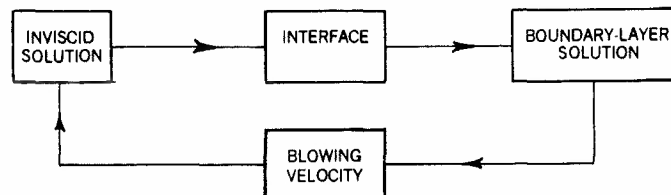


Figure 5.30. Interactive solution procedure.

between inviscid and viscous flow calculations can be performed to obtain a converged solution, as discussed in [65].

The use of a quasi- or full-three-dimensional interactive boundary-layer scheme involves considerable work and/or changes in the manner in which inviscid and viscous flow calculations are performed. Unlike two-dimensional flows, we now need to compute the geometric properties of the coordinate system, namely the metric coefficients and geodesic curvatures appearing in the boundary-layer equations. The use of this interactive procedure suggests the following sequence of events in the calculations, as shown in Figure 5.30.

The inviscid method first computes the external velocity distribution around the body without viscous effects and transfers it to the interface program which rearranges the data from the inviscid computation to the form needed for the viscous flow calculations and computes the geometric properties of the coordinate system. After the boundary-layer calculations, the blowing velocity can be fed into the inviscid method to start a new cycle.

This strategy of computing three-dimensional flow fields employing the quasi-three-dimensional interactive boundary-layer method and a subsonic surface panel method with interface program, is being investigated by the author and his associates. The results

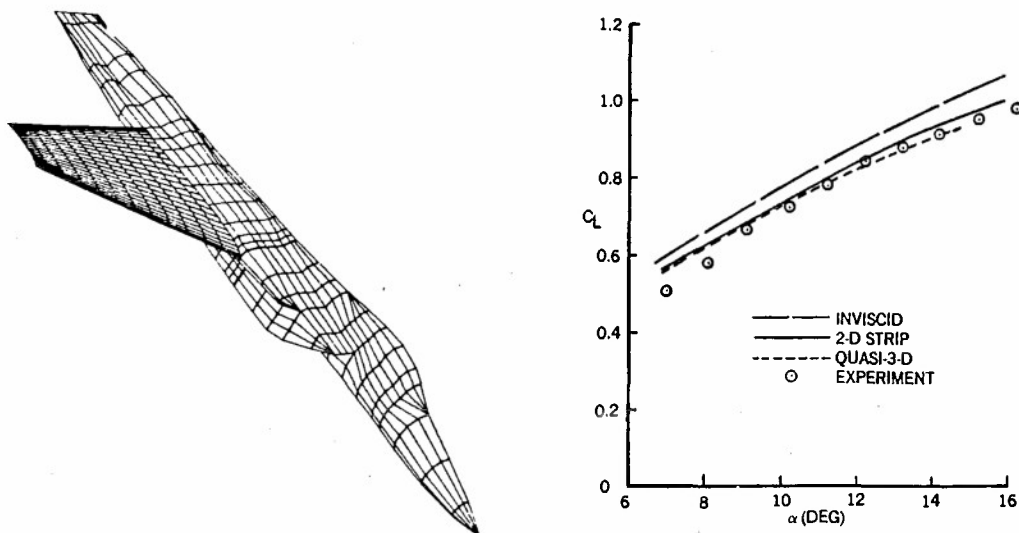


Figure 5.31. Computed results for the F-15 wing [65].

indicate that turbulent flows with considerable separation can be calculated for a wide range of angles of attack, as discussed in [65]. Figure 5.31 shows a sample of calculations performed for the F-15 wing with leading-edge separation and, as can be seen, the computed results with this procedure are slightly better than those obtained with the strip-theory procedure. Considering that inviscid calculations on the fuselage are not corrected for viscous effects, the agreement with experiment is satisfactory.

6.0 CONCLUDING REMARKS

It is evident that calculation procedures for two-dimensional flows can be used to provide accurate information of aerodynamic properties for angles of attack up to and including stall. Interaction between solutions of viscous- and inviscid-flow equations is necessary and the wake should form part of the solution domain for angles of attack greater than around 10 degrees. There is, however, an urgent need for a procedure to represent accurately the onset of transition, particularly for flows involving flow separation at high angles of attack.

The status of calculation procedures for three-dimensional flows is less satisfactory. It has been shown that the CFL stability criterion must be satisfied in the solution of boundary-layer equations and that interaction and consideration of the wake are again likely to be necessary as the angle of attack is increased. The formulation, testing and use of an appropriate interaction procedure is required and, although the work performed in relation to two-dimensional flows provides essential guidelines, much remains to be done. The problems associated with the specification of transition in two-dimensional flows are likely to be at least as severe in three-dimensional flows and effort is also required to improve the accuracy and efficiency of numerical methods for three-dimensional equations.

7.0 REFERENCES

1. Shang, J.S. and Scherr, S.J.: Navier-Stokes Solution of the Flowfield Around a Complete Aircraft. AIAA Paper No. 85-1509, AIAA 7th Computational Fluid Dynamics Conference, 1985.
2. Halsey, N.D.: Potential Flow Analysis of Multielement Airfoils Using Conformal Mapping. AIAA J., 17, 1281, 1979.
3. Cebeci, T.: Separated Flows and Their Representation by Boundary-Layer Equations. ONR-CR215-234-2, Mech. Eng. Rept. California State University, Long Beach, 1976.
4. Cebeci, T. and Smith, A.M.O.: Analysis of Turbulent Boundary Layers, Academic Press, New York, 1974.
5. Reyhner, T.A. and Flügge-Lotz, I.: The Interaction of a Shock Wave with a Laminar Boundary Layer. Int. J. Nonlinear Mech. 3, 173, 1968.
6. Veldman, A.E.P.: New Quasi-Simultaneous Method to Calculate Interacting Boundary Layers. AIAA J. 19, 769, 1981.
7. Cebeci, T., Stewartson, K. and Williams, P.G.: Separation and Reattachment Near the Leading Edge of a Thin Airfoil at Incidence. AGARD CP 291, Paper 20, 1981.

8. Cebeci, T. and Clark, R.W.: An Interactive Approach to Subsonic Flows with Separation. In Numerical and Physical Aspects of Aerodynamic Flows II, (ed. T. Cebeci), Springer-Verlag, NY, 193, 1984.
9. Cebeci, T. and Schimke, S.M.: The Calculation of Separation Bubbles on Interactive Turbulent Boundary Layers. J. Fluid Mech. 131, 305, 1983.
10. Cebeci, T., Clark, R.W., Chang, K.C., Halsey, N.D. and Lee, K.: Airfoils with Separation of the Resulting Wakes. J. Fluid Mech. 163, 323, 1986.
11. Bradshaw, P., Cebeci, T. and Whitelaw, J.H.: Engineering Calculation Methods for Turbulent Flow. Academic Press, London, 1981.
12. Cebeci, T., Khattab, A.A. and Stewartson, K.: On Nose Separation. J. Fluid Mech 97, 435, 1980.
13. Cebeci, T. and Bradshaw, P.: Momentum Transfer in Boundary Layers. McGraw-Hill/Hemisphere, 1977.
14. Marvin, J.G.: Turbulence Modeling for Computational Aerodynamics. AIAA J. 21, 941, 1983.
15. Cebeci, T. and Meier, H.U.: Modeling Requirements for the Calculation of the Turbulent Flow Around Airfoils, Wings and Bodies of Revolution. Turbulent Boundary Layers - Experiments, Theory and Modeling. AGARD CP 271, Paper 16, 1979.
16. Chang, K.C., Bui, M.N., Cebeci, T. and Whitelaw, J.H.: The Calculation of Turbulent Wakes. Mech. Eng. Rept. ME-84-3, California State University, 1984. Also AIAA J. 24, 200, 1986.
17. Cebeci, T., Chang, K.C., Li, C. and Whitelaw, J.H.: Turbulence Models for Wall Boundary Layers. Mech. Eng. Rept. ME-84-2, California State University, Long Beach. Also in AIAA J. 24, 359, 1986.
18. Cebeci, T. and Chang, K.C.: On the Turbulence Modeling Requirements of Three-Dimensional Flows. In Recent Contributions to Fluid Mechanics (ed. W. Haase), Springer-Verlag, NY, 1982.
19. Cebeci, T.: Problem and Opportunities with Three-Dimensional Boundary Layers. AGARD Round Table Discussion on Three-Dimensional Boundary Layers. Invited Paper, Brussels, 1984.
20. Cebeci, T., Kaups, K., Mosinskis, G.W. and Rehn, J.A.: Some Problems of the Calculation of Three-Dimensional Boundary-Layer Flows on General Configurations. NASA CR 2285, 1973.
21. Williams, P.G.: A Reverse Flow Computation in the Theory of Self-Induced Separation. Proc. 4th Int. Conf. Numer. Meth. Fluid Mech., Lecture Notes in Physics 35, 445, 1975.
23. LeBalleur, J.C.: Couplage visqueux-non visqueux: Methode Numerique et Applications Aux Ecoulements Bidimensionnels Transsoniques et Supersoniques. Le Recherche Aero-spatiale No. 1978-2, 65, 1978.
24. Carter, J.E.: A New Boundary-Layer Inviscid Interaction Technique for Separated Flow. AIAA Paper 75-1450, 1979.
25. Carter, J.C.: Viscous-Inviscid Interaction Analysis of Transonic Turbulent Separated Flow. AIAA Paper 81-1241, 1981.
26. Carter, J.C. and Vatsa, V.N.: Analysis of Airfoil Leading-Edge Separation Bubbles. NASA Contractor Report 165935, Contract NAS1-16585, 1982.
27. LeBalleur, J.C.: Numerical Viscid-Inviscid Interaction in Steady and Unsteady Flows. In Numerical and Physical Aspects of Aerodynamic Flows II (ed. T. Cebeci), Springer-Verlag, NY, 259, 1984.
29. Crank, J. and Nicolson, P.: A Practical Method of Numerical Evaluation of Solutions of Partial-Differential Equations of the Heat-Conduction Type. Proc. Cambridge Phil. Soc. 43, 50, 1947.
30. Keller, H.B.: Accurate Difference Methods for Two-Point Boundary-Value Problems, SIAM J. Numer. Anal. 11, 305, 1974.
31. Blottner, F.G.: Computational Techniques for Boundary Layers. AGARD LSP-73 on Computational Methods for Inviscid and Viscous Two- and Three-Dimensional Flow-fields, 1975.
32. Cebeci, T. and Stewartson, K.: Unpublished work, 1978.

34. Krause, E., Hirschel, E.H. and Bothmann, Th.: Die Numerische Integration der Bewegungsgleichungen Dreidimensionaler Laminarer, Kompressibler Grenzschichten. In OGLR - Fachbuchreihe, Band 3, 1 Braunschweig, 1969.
35. Isaacson, E. and Keller, H.B.: Analysis of Numerical Methods, John Wiley, New York, 1966.
36. van Oommelen, L.L. and Shen, S.F.: The Spontaneous Generation of the Singularity in a Separating Laminar Boundary Layer. J. Comp. Phys. **38**, 125, 1981.
37. van Oommelen, L.L. and Shen, S.F.: The Genesis of Separation. In Numerical and Physical Aspects of Aerodynamic Flows, (ed. T. Cebeci), Springer-Verlag, N.Y., 293, 1982.
38. Cebeci, T.: Unsteady Boundary Layers with an Intelligent Numerical Scheme. J. Fluid Mech. **163**, 129, 1986.
39. Cebeci, T., Khattab, A.A. and Stewartson, K.: Three-Dimensional Laminar Boundary Layers and the Ok of Accessibility. J. Fluid Mech. **107**, 57, 1981.
40. Wang, K.C.: Boundary Layer Over a Blunt Body at Low-Incidence with Circumferential Reversed Flow. J. Fluid Mech. **72**, 49, 1975.
41. Patel, V.C. and Baek, J.H.: Calculation of Three-Dimensional Boundary Layers on Bodies at Incidence. Iowa Inst. of Hydraulic Research Rept. No. 256, 1982.
42. Cebeci, T. and Su, W.: Accuracy Requirements in the Numerical Solution of Three-Dimensional Boundary-Layer Equations. Paper in preparation.
43. Stewartson, K., Smith, F.T. and Kaups, K.: Marginal Separation. Studies in App. Math. **67**, 45, 1982.
44. Stewartson, K.: Some Recent Studies in Triple-Deck Theory. In Numerical and Physical Aspects of Aerodynamic Flows (ed. T. Cebeci), Springer-Verlag, 129, 1982.
45. Gault, O.E.: An Experimental Investigation of Regions of Separated Laminar Flow. NACA TN 3505, 1955.
46. Crimi, P. and Reeves, B.L.: Analysis of Leading-Edge Separation Bubbles on Airfoils. AIAA J. **14**, 1548, 1976.
47. Abbott, J.H. and von Doenhoff, A.E.: Theory of Wing Sections. Dover Publications, 1959.
48. Wadcock, A.J.: Flying-Hot-Wire Study of Two-Dimensional Turbulent Separation on an NACA 4412 Airfoil at Maximum Lift. Ph.D. Thesis, California Institute of Technology, Pasadena, CA, 1978.
49. Coles, D. and Wadcock, A.J.: Flying-Hot-Wire Study of Flow Past an NACA 4412 Airfoil at Maximum Lift. AIAA J. **17**, 321, 1979.
50. McGhee, R.J., Beasley, W.D. and Somers, D.M.: Low-Speed Aerodynamic Characteristics of a 13-percent Thick Airfoil Section Designed for General Aviation Applications. NASA TMX 72697, 1977.
51. Melnik, R.E. and Brook, J.W.: The Computation of Viscous/Inviscid Interaction on Airfoils with Separated Flow. In Numerical and Physical Aspects of Aerodynamic Flows III (ed. T. Cebeci), Springer-Verlag, 1986.
52. Mehta, U., Chang, K. and Cebeci, T.: A Comparison of Interactive Boundary Layer and Thin-Layer Navier-Stokes Procedures. In Numerical and Physical Aspects of Aerodynamic Flows III (ed. T. Cebeci) Springer-Verlag, 1986.
53. Gregory, N. and O'Reilly, C.L.: Low-Speed Aerodynamic Characteristics of NACA 0012 Airfoil Section, Including the Effects of Upper-Surface Roughness Simulating Hoar Frost. NPL AERO Rept. 1308, 1970.
54. Mehta, U., Chang, K.C. and Cebeci, T.C.: Relative Advantages of Thin-Layer Navier-Stokes and Interactive Boundary-Layer Procedures. NASA TM-86778, 1985.
55. Loftin, Jr., L.K. and Smith, H.A.: Aerodynamic Characteristics of 15 NACA Airfoil Sections at Seven Reynolds Numbers from 0.7×10^6 to 9.0×10^6 . NACA TN 1945, 1949.
56. Cebeci, T., Khattab, A.A. and Schimke, S.M.: Can the Singularity be Removed in Time-Dependent Flows? In Workshop on Unsteady Separated Flow (M.S. Francis and M.W. Luttges, eds.), Colorado Springs, Colorado, 1984.
57. Wigton, L. and Yoshihara, H.: Viscous-Inviscid Interactions with a Three-Dimensional Inverse Boundary-Layer Code, 2nd Symp. on Numerical and Physical Aspects of Aerodynamic Flows, California State University, Long Beach, 1983.

58. Wai, J.C., Baillie, J.C. and Yoshihara, H.: Computation of Turbulent Separated Flows Over Wings. In Numerical and Physical Aspects of Aerodynamic Flows III (ed. T. Cebeci) Springer-Verlag, 1986.
59. Yoshihara, H. and Wai, J.: Transonic Turbulent Separation on Swept Wings - A Return to the Direct Formulation, AIAA Paper No. 84-0265, 1984.
60. Cebeci, T.: How the Calculation of Aerodynamic Properties of General Configurations Can Benefit from Supercomputers, Presented at the NCAR Supercomputer Workshop, Boulder, Colorado, 1983.
61. Cebeci, T., Chen, L.T. and Chang, K.C.: An Interactive Scheme for Three-Dimensional Transonic Flows. In Numerical and Physical Aspects of Aerodynamic Flows III (ed. T. Cebeci) Springer-Verlag, 1986.
62. Street, C.L.: Viscous-Inviscid Interaction for Transonic Wing-Body Configurations Including Wake Effects. AIAA J. 20, 915, 1982.
63. Chow, R.R., Melnik, R.E., Marconi, F. and Steinhoff, J.: Viscous Wing Theory Development, Vol. I - Analysis, Method and Results, NASA CR in preparation, 1985.
64. Cebeci, T.: Calculation of Boundary-Layer Flows with Separation. Proceedings of Osaka International Colloquium on Ship Viscous Flows, Osaka, Japan, 23-25 October 1985.
65. Cebeci, T., Chang, K.C., Clark, R.W., Mack, D.P. and Schimke, S.M.: Applications to Two- and Three-Dimensional Interactive Boundary-Layer Theory to Finite Wings with Flow Separation. MDC Rept. No. J3968, March 1986.

PROGRESS IN VISCOUS-INVISCID SOLVERS (VIS)

J.C. LE BALLEUR

ONERA - BP 72 - 92322 Chatillon Cedex (France)

I - SUMMARY :

The aim of these lectures was an introduction to the further extensions of boundary layer theory which rely on the development of full viscous-inviscid interaction solvers, in three-dimensional flows.

At the present time, however, the state of the art still does not allow to handle the full 3D-problem. It is more or less restricted, on one hand, to advances in uncoupled 3D-boundary layer problems [3,4], direct or inverse, and, on the other hand, to developments in full viscous-inviscid solvers for the 2D or quasi-3D infinite swept wings flows [1,2], the latter developments involving the coupling and the calculation of quasi-3D "closed" separations.

The present lectures were mainly devoted to the developments obtained by the author and his colleagues in these two areas. These developments were outlined after describing shortly the different strategies which can be used to split the Navier-Stokes problem into a viscous-inviscid interaction problem, in two or three dimension.

The detailed content of these lectures can be found in four written publications, available in references [1 to 4].

The progress in uncoupled 3D-boundary layer problems includes the modelling of the 3D turbulent mean velocity profiles in attached or separated layers, with possibly reverse flows in streamwise direction and very high shape parameters. This modelling provides also a generalised entrainment closure for 3D integral equations.

The progress includes also the space-marching integration-scheme used to solve the spatially-hyperbolic boundary layers equations on arbitrary grids at the surface of the bodies. Such arbitrary grids are specified in order to satisfy the constraints of the geometry and of the inviscid solver, but are not well behaved with respect to the local characteristic cones of dependance of the boundary layer problem. A Multi-Zonal and Multi-Marching "MZM" method has then been developed to perform the numerical integration, starting at the stagnation point, and giving access to both sides of the open-separation lines, for ellipsoids, fuselages or slender-bodies, at incidence and yaw conditions. In case of wings, the "MZM" method allows to compute without approximation the leading-edge 3D-boundary layer.

The progress in full Viscous-Inviscid Solvers (VIS) includes first the numerical algorithms for coupling in two dimensional flows [1,2]. Theoretical work has made it possible to control the numerical stability of the "Direct" and "Inverse" coupling methods, and to define the "Semi-Inverse" coupling method, for steady separated flows. These methods are explicit, overrelaxation like, free of any adjustable or empirical parameter, and have been extended to the infinite swept wings (quasi-3D) separated flows [2]. The theory is also shortly summarized [1] for the recent "Semi-Implicit" method, which is presently used for time-consistent solutions, and which is different from Veldman's "Quasi-Simultaneous" method.

The progress in full Viscous-Inviscid solvers includes on the other hand the capabilities which have been developed in the steady case, to compute separated flows over airfoils and spoilers,

REFERENCE to documents :

- [1] LE BALLEUR J.C. - Viscous-inviscid interaction solvers and computation of highly separated flows - Proceedings of ICASE workshop on Vortex Dominated Flows, Nasa-Langley, USA (July 9-10, 1985), SPRINGER VERLAG 1986, or ONERA-TP-n°1986-4.
- [2] LE BALLEUR J.C. - Numerical flow calculation and viscous-inviscid interaction techniques (*). Recent Advances in Numerical Method in Fluids, Third volume : Computational methods in viscous flows, Pineridge Press 1984, p.419-450, W. Habashi editor.
- [3] LE BALLEUR J.C., LAZAREFF M. - A "Multi-Zonal-Marching" integral method for 3D-boundary layer with viscous-inviscid interaction - Proceedings 9th ICNMFD, 1984, Saclay (France), Lecture Notes in Physics, SPRINGER VERLAG 1985, Soubbaramayer editor, or ONERA-TP-n°1984-67.
- [4] LAZAREFF M., LE BALLEUR J.C. - Computation of three-dimensional flows by viscous-inviscid interaction using the "MZM" method - Proceeding 58th AGARD-FDP meeting on Applications of Computational Fluid Dynamics in Aeronautics, Aix-en-Provence, France (April 7-10, 1986), to be published, or ONERA-TP-n°1986-29.

(*) Erratum in reference [2], page 431, formula (34). It must be read :

$$(34) \quad q_{i,1}^{n+1} - q_{i,1}^n = \omega_i^I [\tilde{q}_i - q_{i,1}^n]$$

COMPUTATION OF TIP AND CORNER REGION FLOWS

T.R. Govindam and H. McDonald

Scientific Research Associates, Inc.

P.O.B. 498, Glastonbury, Connecticut 06033

USA

Summary

The flow field in corner and tip regions of wings and propellers is complex, three-dimensional, and viscous with large secondary/transverse velocities. The large secondary velocities, usually associated with streamwise vorticity development in the flow, preclude the use of conventional boundary-layer solution techniques to compute such flow fields. On the other hand, solution techniques for the full Navier-Stokes equations that adequately resolve the length scales of tip and corner region flow fields would require formidable computer resources for use routinely. Sets of approximate three-dimensional viscous flow equations which are applicable to tip and corner region flow fields and which can be solved economically are sought. Clearly, economy of solution must result from approximations to the governing equations for such procedures to be attractive. A spatial marching computation procedure that solves approximate three-dimensional viscous flow equations economically is presented here and application of the procedure to compute tip and corner region flow fields discussed.

Spatial marching computation procedures for three-dimensional equations achieve economy of solution by solving the three-dimensional equations on transverse surfaces one at a time, from given initial conditions, along a chosen coordinate direction (marching direction). The equations being solved must be a well-posed initial value problem along the marching direction for the procedure to be applicable. The steady Navier-Stokes equations are elliptic-like and not amenable to a spatial marching procedure of the type described. Approximations need to be introduced in the Navier-Stokes equations to obtain a well-posed initial value problem along a chosen coordinate direction. The validity of the approximations determines the class of flow problems for which a spatial marching computation procedure is suitable. Conventional three-dimensional boundary layer approximations provide one such approximation set that are, however, not suitable for tip and corner region flow fields.

Many three-dimensional flows are characterized by a dominant flow direction (streamwise direction). Streamwise viscous diffusion is small for such flows compared to diffusion in transverse directions and can be neglected in the momentum equations. This approximation is, however, not sufficient to convert

the steady Navier-Stokes equations into a well-posed initial value problem in the streamwise direction. Additional physically realistic approximations need to be introduced to achieve this goal. Two approximations are presented here, each of which convert the steady Navier-Stokes equations (with streamwise diffusion neglected) into well-posed initial value problems, and are termed

- (a) the pressure approximation
- (b) the small scalar potential approximation.

In the pressure approximation the streamwise pressure gradient in the streamwise momentum equation is approximated and treated as known. Typically the streamwise pressure gradient is obtained from the inviscid potential flow for the geometry under consideration. No approximations are made for the transverse pressure gradients in the equations and this allows a new pressure field compatible with the computed viscous flow velocity field to be computed from the transverse momentum equations. The streamwise pressure gradient associated with the computed pressure field will, in general, be different from that assumed known in the streamwise momentum equation. The difference between the two streamwise pressure gradients represents the level of approximation made to the Navier-Stokes equations. Details of the pressure approximation, solution procedure, and computed results can be found in Reference [1].

The small scalar potential approximation can be considered to be a non-trivial extension of two-dimensional slender channel theory to three-dimensional flow with large secondary velocities. In this approximation convection effects of a defined scalar potential velocity are neglected in the transverse momentum equations. Simple order-of-magnitude estimates can be made to show that the neglected convection effects are small for many three-dimensional flow fields. No approximations are introduced in the equations for the pressure gradients or for the dominant component of the secondary velocity field. Details of the small scalar potential approximation, solution procedure, and computed results can be found in Reference [2].

The pressure approximation and the small scalar potential approximation each provide a set of approximate three-dimensional viscous flow equations that are amenable to solution by a spatial marching algorithm. Numerical procedures employed in the solution of the equations must exploit the approximations made to provide economy of solution (one to two orders of magnitude over an efficient Navier-Stokes algorithm). Further, the numerical procedures must be consistent, stable and accurate. The approximate flow equations are solved in terms of a set of new dependent variables; namely, the streamwise velocity, defined scalar and vector potentials, the streamwise vorticity, and the pressure. The scalar and vector potentials together define the transverse velocity field. The flow equations in terms of the new dependent variables are weakly coupled sub-systems of equations that can be solved sequentially on each transverse plane rather

than the strongly coupled system of equations in terms of primitive variables. This decoupling of the equations enhances economy of the solution algorithm. Efficient, stable and accurate numerical procedures are used to solve each sub-system of equations. Details of the solution algorithm for the pressure approximation can be found in Reference [1] and for the small scalar potential approximation in Reference [2].

Application of the spatial marching algorithm to compute tip vortex generation on propeller blades using the pressure approximation can be found in Reference [3]. Computation of the flow in the internal corner of a curved square duct using the small scalar potential approximation can be found in Reference [2]. These typical computations demonstrate the capability of the procedure to compute complex three-dimensional viscous flows economically and accurately.

Acknowledgement

Work presented in these lectures was sponsored by the NASA Lewis Research Center under contracts NAS3-21735 and NAS3-22014 and the Office of Naval Research under contract N00014-83-C-0768. The authors would also like to thank W.R. Briley and Ralph Levy for their contributions to this presentation.

References

1. Levy, R., Briley, W.R. and McDonald, H.: Viscous Primary/Secondary Flow Analysis for Use with Nonorthogonal Coordinate Systems, AIAA Paper 83-0556 presented at the AIAA 21st Aerospace Sciences Meeting, January 10-13, 1983.
2. Briley, W.R. and McDonald, H.: Three Dimensional Viscous Flows with Large Secondary Velocity, Journal of Fluid Mechanics, pp. 47-77, Vol. 144, 1984.
3. Govindan, T.R., Levy, R. and Shamroth, S.J.: Computation of the Tip Vortex Generation Process for Ship Propeller Blades, presented at the Fourth International Conference on Numerical Ship Hydrodynamics, September 24-27, 1985.

OUTLINE

- LECTURE I

CONCEPTS, REQUIREMENTS, AND GENERAL FEATURES
OF A SOLUTION ALGORITHM TO COMPUTE TIP AND
CORNER REGION FLOWS ECONOMICALLY

- LECTURE II

DETAILS OF FORMULATION, APPROXIMATIONS, AND
NUMERICAL PROCEDURES OF THE FORWARD MARCHING
COMPUTATION PROCEDURE FOR 3-D VISCOUS FLOWS

Scientific
Research
Associates

LECTURE I - OUTLINE

- CHARACTERISTICS OF TIP AND CORNER REGION FLOW AND THEIR COMPUTATION
- A CLASSIFICATION OF 3-D VISCOUS FLOW COMPUTATION SCHEMES
- BASIC CONCEPTS IN FORMULATING A FORWARD-MARCHING COMPUTATION PROCEDURE
- COORDINATE SYSTEM
- COMPUTATION OF TIP VORTEX GENERATION

Scientific
Research
Associates

'EXTEND' BOUNDARY LAYER ANALYSIS

- EXTEND BOUNDARY LAYER ANALYSIS ALL THE WAY TO FULL NAVIER-STOKES EQUATIONS. CURRENTLY TOO EXPENSIVE TO ROUTINELY SOLVE IN 3-D
- INTRODUCE SUITABLE PHYSICALLY REALISTIC APPROXIMATIONS TO NAVIER-STOKES EQUATIONS IN AN ATTEMPT TO FORMULATE AN ECONOMICAL SOLUTION PROCEDURE
- RETAIN DIFFUSION IN BOTH TRANSVERSE COORDINATES. HENCE, NO PREFERRED TRANSVERSE DIRECTION
- CAN NEGLECT STREAMWISE DIFFUSION
(NOTE: IDENTIFICATION OF A DIRECTION)
- MAKE NO ATTEMPT TO IDENTIFY 'BOUNDARY LAYER' AND 'FREE STREAM'
- INTRODUCE ANY ADDITIONAL SUITABLE PHYSICALLY REALISTIC APPROXIMATIONS TO ACHIEVE GOAL OF AN ECONOMICAL SOLUTION PROCEDURE

Scientific
Research
Associates

THREE-DIMENSIONAL VISCOUS FLOW PREDICTION SCHEMES

- A CLASSIFICATION -

- I. CONVENTIONAL THREE-DIMENSIONAL BOUNDARY LAYERS SUBJECTED TO IMPOSED PRESSURE GRADIENTS.
- II. FORWARD MARCHING OF FLOW EQUATIONS WHICH CONTAIN BOTH CROSS-SECTION STRESSES. STRESS IN MARCHING DIRECTION NEGLECTED. ADDITIONAL APPROXIMATIONS INTRODUCED TO ALLOW SOLUTION BY EFFICIENT MARCHING IN SPACE.
- III. ITERATED FORWARD MARCHING OF CATEGORY II SYSTEM OF EQUATIONS. GOAL IS TO REMOVE BY ITERATION ADDITIONAL APPROXIMATIONS INTRODUCED TO ALLOW SOLUTION BY EFFICIENT MARCHING IN SPACE.
- IV. SOLUTION OF FULL THREE-DIMENSIONAL NAVIER-STOKES EQUATIONS.

Scientific
Research
Associates

CATEGORY III

ITERATED FORWARD MARCHING

- BOTH CROSS-SECTION STRESSES RETAINED -
FORWARD-MARCHING DIRECTION STRESS NEGLECTED
GOAL IS TO REMOVE ADDED CATEGORY II APPROXIMATIONS

- ATTEMPT TO DERIVE BENEFIT FROM FORWARD-MARCHING AS IN CATEGORY II
- REVERSED VELOCITIES IN MARCHING DIRECTION NOT RIGOROUSLY PERMITTED.
- NUMBER OF GLOBAL ITERATIONS SIGNIFICANTLY LARGE.
- CENTRAL MEMORY REQUIREMENTS LESS THAN WITH FULL NAVIER-STOKES TECHNIQUES ALTHOUGH OVERALL COMPUTER RESOURCE REQUIREMENTS MAY BE COMPARABLE.

Scientific
Research
Associates

CATEGORY IV

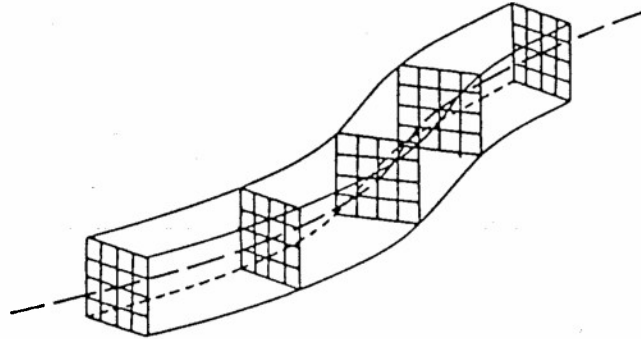
SOLVES THE FULL NAVIER-STOKES EQUATIONS

- NO FLOW APPROXIMATIONS REQUIRED OTHER THAN TURBULENCE MODEL.
- COMPUTATIONALLY EXPENSIVE. TO REDUCE NUMERICAL ERRORS TO TOLERABLE LEVEL MAY NOT BE FEASIBLE. RUN TIMES ONE ORDER OR GREATER THAN ONE PASS SPATIAL MARCHING SCHEMES.
- SOME FLUID PROBLEMS INHERENTLY ELLIPTIC.

Scientific
Research
Associates

ORTHOGONAL REFERENCE-LINE COORDINATES

- SIMPLIFY THE FORM OF THE APPROXIMATED GOVERNING EQUATIONS
- NOT BODY FITTED

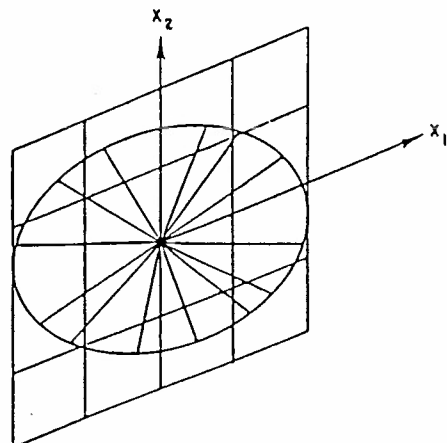
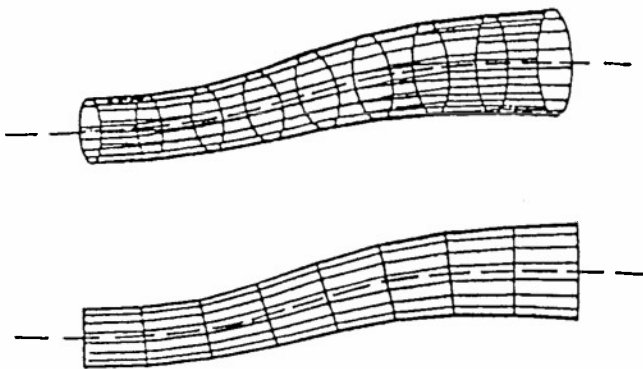


Scientific
Research
Associates

BODY FITTED COORDINATES ARE USED TO SOLVE THE GOVERNING EQUATIONS

- NONORTHOGONAL

$$\frac{\partial}{\partial x_1} = \frac{\partial y_1}{\partial x_1} \frac{\partial}{\partial y_1}$$



Scientific
Research
Associates

APPROXIMATIONS

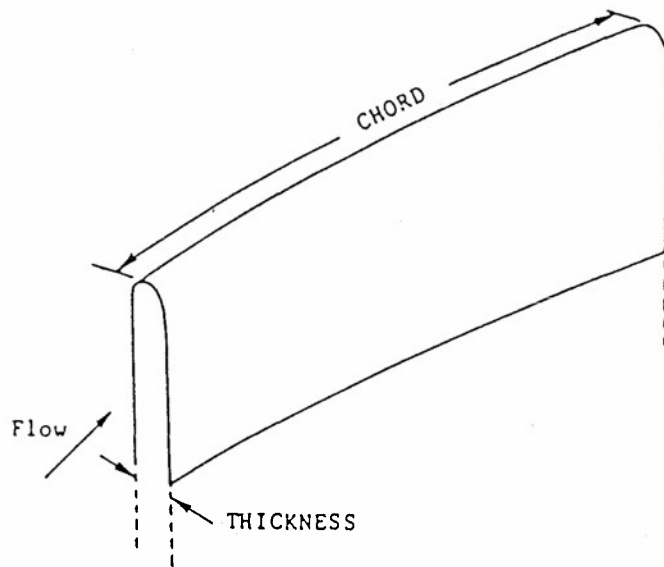
- STREAMWISE DIFFUSION NEGLECTED
- STREAMWISE PRESSURE GRADIENT TREATED
AS KNOWN SOURCE TERM
(NO APPROXIMATION ON THE TRANSVERSE
PRESSURE GRADIENTS)

Scientific
Research
Associates

PRESENT ANALYSIS

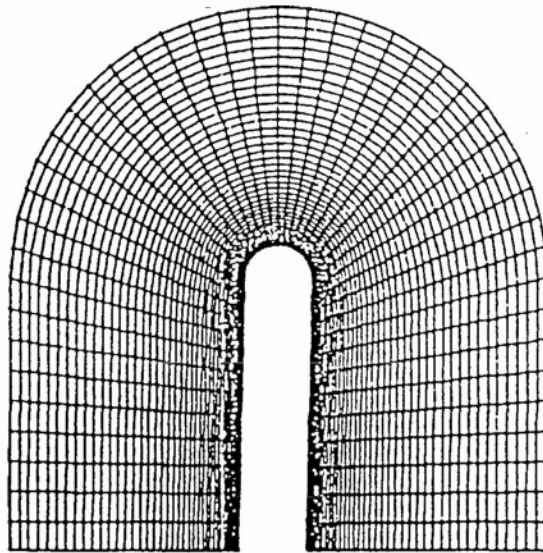
- STREAMWISE MOMENTUM EQUATION
- SCALAR POTENTIAL EQUATION
- COUPLED VECTOR POTENTIAL AND
VORTICITY EQUATIONS
- ASSOCIATED PRESSURE EQUATION

Scientific
Research
Associates



Perspective view of the straight blade.

Scientific
Research
Associates



Computation grid for the straight blade

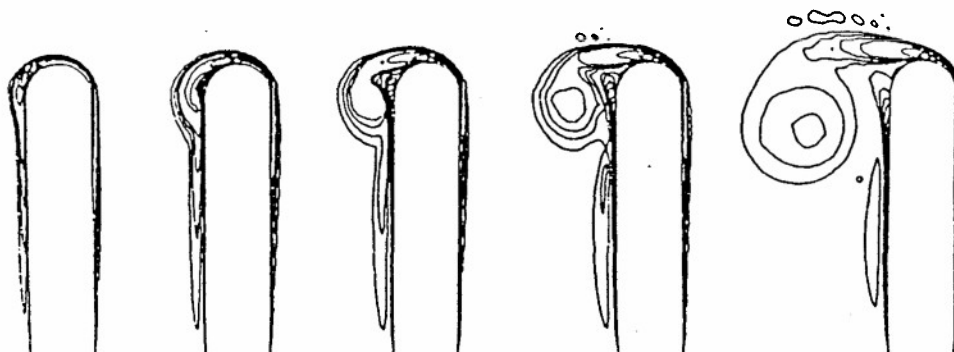
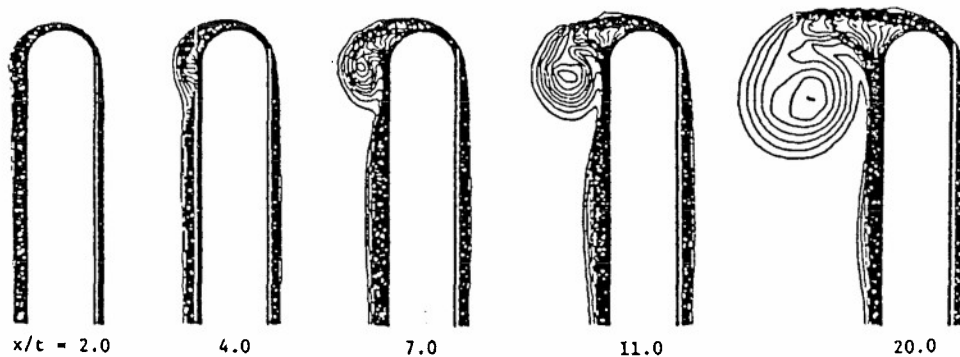
Scientific
Research
Associates

CASE II - TIP VORTEX FLOW FOR A ROTATING STRAIGHT BLADE

BLADE THICKNESS	=	1.0
BLADE CHORD	=	20.0
REYNOLDS NUMBER	=	1000.0
INITIAL θ	=	0.20
INCIDENCE ANGLE	=	6°
ADVANCE RATIO	=	1.0
GRID	=	60 x 47 x 40

Scientific
Research
Associates

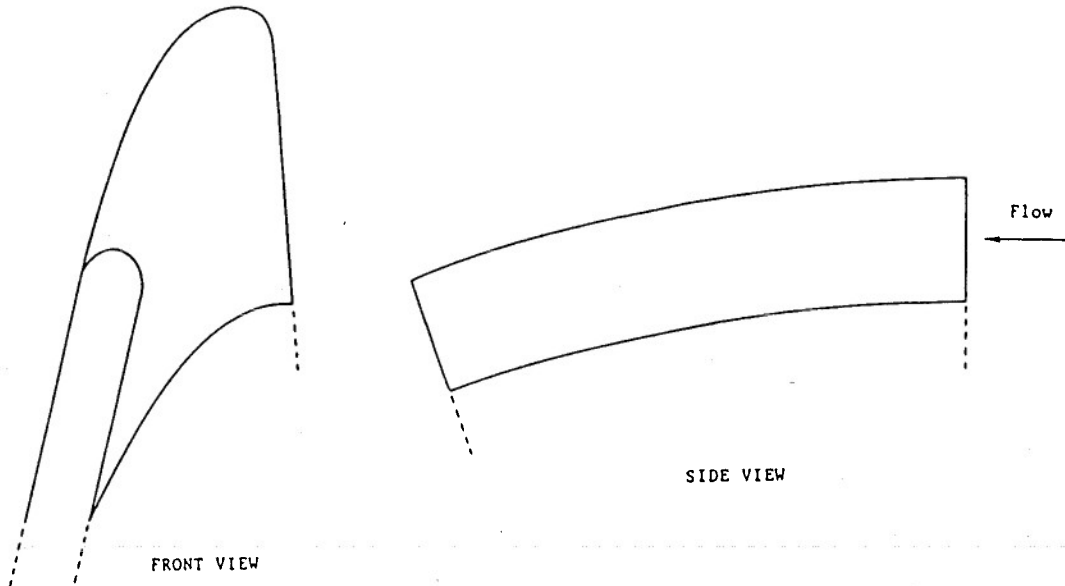
Streamwise Velocity



Scientific
Research
Associates

Streamwise Vorticity

Straight blade - rotation



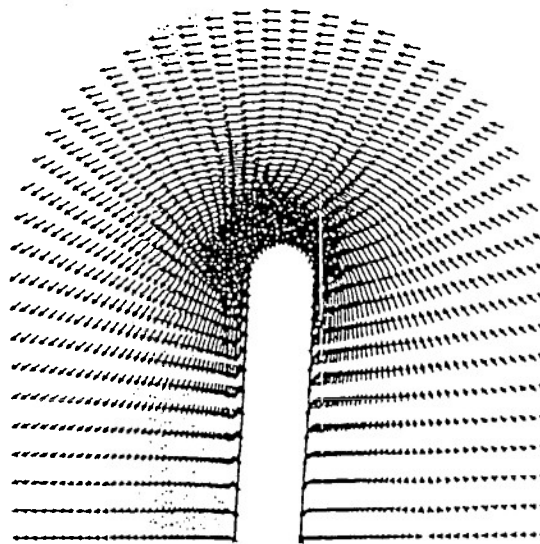
Perspective views of the twisted blade.

Scientific
Research
Associates

Streamwise
Velocity



Streamwise
Vorticity

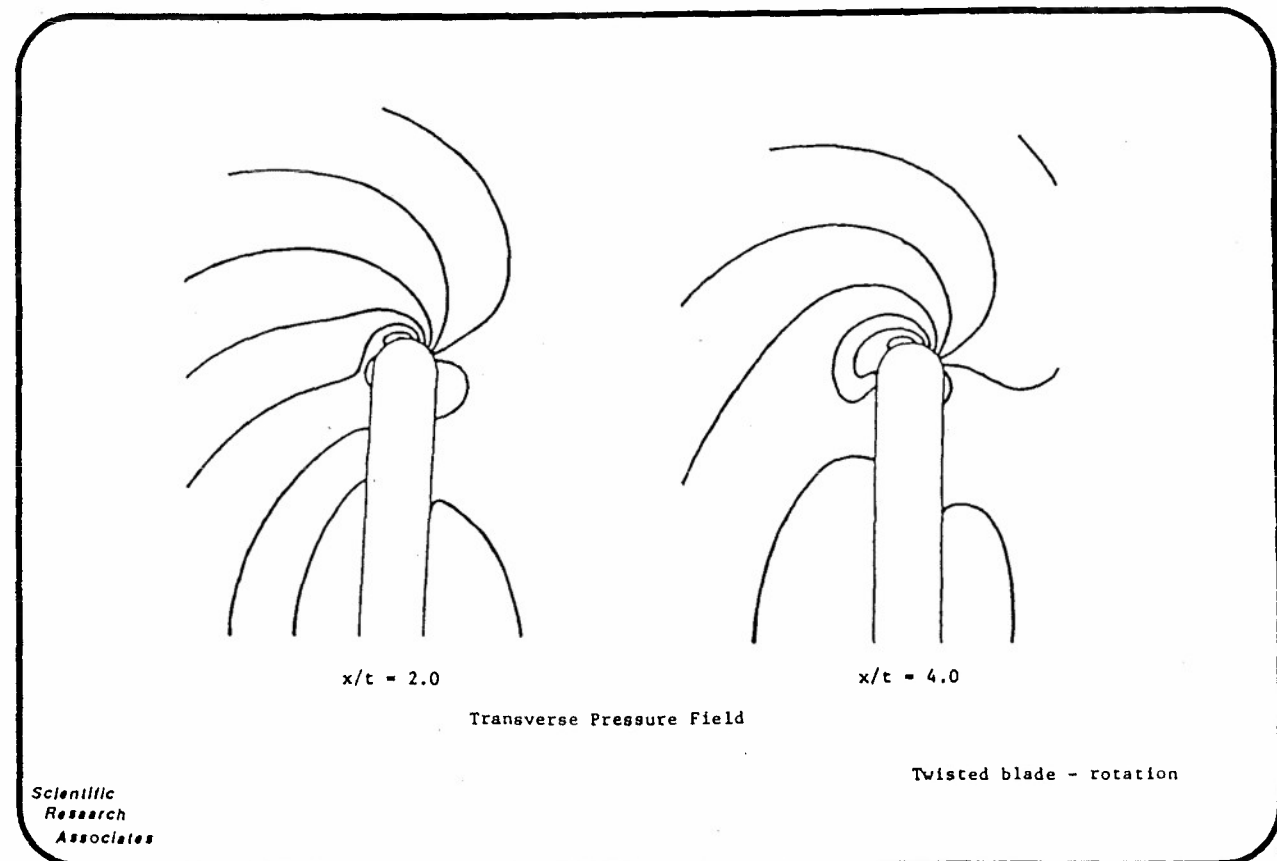
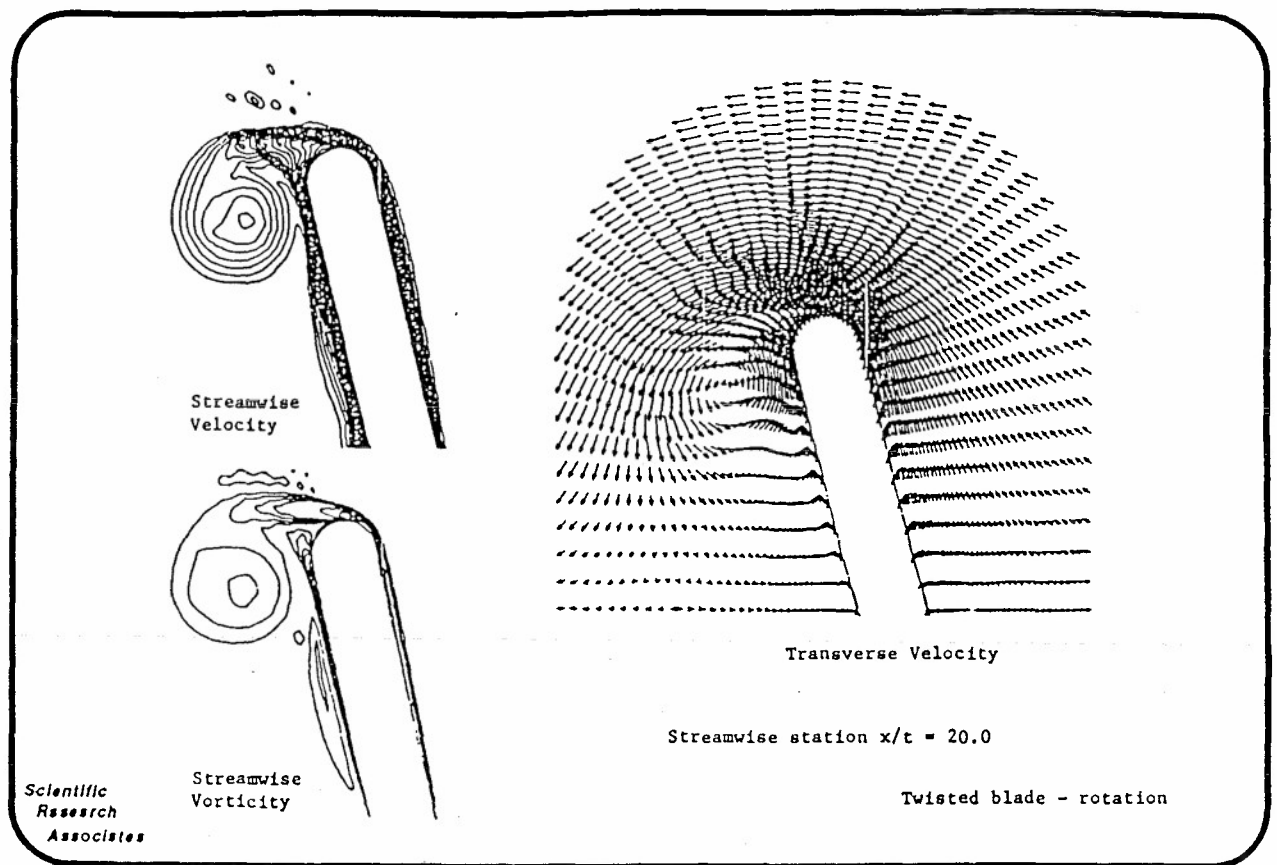


Transverse Velocity

Streamwise station $x/t = 2.0$

Twisted blade - rotation

Scientific
Research
Associates



LECTURE II - OUTLINE

- CRITERIA FOR WELL-POSED INITIAL VALUE PROBLEMS
- THE "PARABOLIZED" NAVIER-STOKES EQUATIONS
- SMALL SCALAR POTENTIAL APPROXIMATION
- SOLUTION ALGORITHM
- NUMERICAL PROCEDURES FOR SOLUTION OF GOVERNING EQUATIONS
- BOUNDARY CONDITIONS
- COMPUTATION OF FLOW IN A CURVED SQUARE DUCT (INTERNAL CORNER FLOW)

Scientific
Research
Associates

SUITABILITY FOR FORWARD MARCHING

(COURANT AND HILBERT 1966, GARABEDIAN 1964)

- WRITE SYSTEM OF M GOVERNING PDE'S AS

$$A_1 \frac{\partial \phi}{\partial x} + A_2 \frac{\partial \phi}{\partial y} + A_3 \frac{\partial \phi}{\partial z} = B$$

ϕ IS A COLUMN VECTOR OF M DEPENDENT VARIABLES

MTH ORDER CHARACTERISTIC EQUATION GIVEN BY

$$|A_1 \lambda_x + A_2 \lambda_y + A_3 \lambda_z| = 0$$

- SYSTEM TERMED "ELLIPTIC" IF FOR ARBITRARY REAL λ_y, λ_z
 λ_x HAS IMAGINARY ROOTS
- SYSTEM TERMED "NONELLIPTIC" IF FOR ARBITRARY REAL λ_y, λ_z
 λ_x HAS ONLY REAL ROOTS
- ONLY "NONELLIPTIC" SYSTEMS CANDIDATES FOR FORWARD MARCHING

Scientific
Research
Associates

SMALL SCALAR POTENTIAL APPROXIMATION

- CAN BE INTERPRETED AS (NON-TRIVIAL) EXTENSION OF 2-D SLENDER CHANNEL THEORY TO 3-D FLOWS WITH LARGE SECONDARY VELOCITIES.
- APPROXIMATIONS BASED ON SCALAR POTENTIAL VELOCITIES ALLOW FORMULATION OF A WELL-POSED INITIAL VALUE PROBLEM.
- NO APPROXIMATION MADE FOR THE STREAMWISE PRESSURE GRADIENT AS IN THE PRESSURE APPROXIMATION. PRESSURE TREATED AS A DEPENDENT VARIABLE TO BE SOLVED FOR IN THE EQUATION SET.

Scientific
Research
Associates

ORDER-OF-MAGNITUDE ANALYSIS (CARTESIAN CONTEXT)

- PRIMARY FLOW DIRECTION AND VELOCITY - X,U
- NEGLECT AXIAL DIFFUSION
- VECTOR DECOMPOSITION OF SECONDARY VELOCITY

$$V = V_{\phi} + V_{\psi} = \frac{\partial \phi}{\partial y} + \frac{\partial \psi}{\partial z}$$

$$W = W_{\psi} + W_{\phi} = \frac{\partial \phi}{\partial z} - \frac{\partial \psi}{\partial y}$$

- EXAMINE 3-D BOUNDARY LAYER SCALING
- $\phi = O(\delta^2)$ AND $\psi = O(\delta)$ IS ONLY SCALING CONSISTENT WITH EITHER Y OR Z AS NORMAL COORDINATE
- THUS $V_{\phi}, W_{\phi} = O(\delta)$ AND $V_{\psi}, W_{\psi} = O(1)$
- ASSUMPTION: $|\vec{V}_{\phi}| \ll |\vec{V}_{\psi}|$

Scientific
Research
Associates

APPROXIMATIONS - SUMMARY

- NEGLECT STREAMWISE DIFFUSION
- PRESSURE APPROXIMATION
TREAT STREAMWISE PRESSURE GRADIENT AS KNOWN SOURCE TERM
NO APPROXIMATION ON TRANSVERSE PRESSURE GRADIENTS
- OR
- SMALL SCALAR POTENTIAL APPROXIMATION
NEGLECT CONVECTION OF SCALAR POTENTIAL VELOCITY
IN TRANSVERSE MOMENTUM EQUATIONS
- NO APPROXIMATIONS ON PRESSURE
- BOTH APPROXIMATIONS PROVIDE WELL-POSED INITIAL VALUE PROBLEMS
SUITABLE FOR SOLUTION BY A SPATIAL MARCHING ALGORITHM

Scientific
Research
Associates

IMPLEMENTATION

- EQUATIONS IN REFERENCE LINE ORTHOGONAL SYSTEM
- VELOCITY DECOMPOSITION

$$\bar{U} = u_p \hat{i}_n + \nabla_s \phi + \frac{p_o}{\rho} \nabla \times \hat{i}_n \psi$$

$$\nabla_s \phi \equiv (0, v_\phi, w_\phi)$$

$$\frac{p_o}{\rho} \nabla \times \hat{i}_n \psi \equiv (0, v_\psi, w_\psi)$$

- CHANGE OF DEPENDENT VARIABLES

$$v_\phi, w_\phi, v_\psi, w_\psi \rightarrow \phi, \psi, \Omega$$

- CHOICE OF DEPENDENT VARIABLES FOR EFFICIENT
SOLUTION ALGORITHM

Scientific
Research
Associates

GOVERNING EQUATIONS AND ORDER OF SOLUTION

- | | | | |
|----------------------------|-----------------------------|---|----------------------|
| • SECONDARY VORTICITY | $u \Omega_x = \dots$ | } | ITERATIVE BLOCK ADI |
| • VECTOR SURFACE POTENTIAL | $\nabla_s^2 \Psi = -\Omega$ | | |
| • PRESSURE EQUATION | $\nabla_s^2 P = \dots$ | | SCALAR ITERATIVE ADI |
| • ENERGY | $u E_x = \dots$ | | SCALAR ADI |
| • X MOMENTUM | $uu_x + P_x = \dots$ | | SCALAR ADI |
| INTEGRAL MASS FLUX | $\int u dA = \dot{m}$ | } | SECANT
ITERATION |
| • STATE EQUATION | (ALGEBRAIC) | | |
| • CONTINUITY | $\nabla_s^2 \phi = -u_x$ | | SCALAR ITERATIVE ADI |
| • TURBULENCE EQUATION(S) | | | SCALAR ADI, OR LBI |

Scientific
Research
Associates

SECANT METHOD FOR GLOBAL MASS FLUX ITERATION

- MASS FLUX ERROR E IS ZERO WHEN MEAN PRESSURE p_m^{n+1} IS "CORRECT"
- LET P_i DENOTE A "GUESS" FOR p_m^{n+1}
- GIVEN P_i , SOLUTION OF X MOMENTUM GIVES NONZERO $E_i(P_i)$
- THE GOAL IS TO FIND P_{i+1} WHICH GIVES $E_{i+1} = 0$

- EXPAND IN TAYLOR SERIES ABOUT P_i

$$E_{i+1} = E_i + \left(\frac{\partial E}{\partial P} \right)_i (P_{i+1} - P_i) + 0(P_{i+1} - P_i)^2$$

- SET $E_{i+1} = 0$ AND SOLVE FOR P_{i+1} (NEWTON-RAPHSON)

$$P_{i+1} = P_i - E_i \left(\frac{\partial E}{\partial P} \right)_i^{-1}$$

- SECANT METHOD OBTAINED BY SETTING

$$\left(\frac{\partial E}{\partial P} \right)_i = \frac{E_i - E_{i-1}}{P_i - P_{i-1}}$$

- SINCE $E(P)$ IS ESSENTIALLY LINEAR AT LOW MACH NUMBER, CONVERGENCE OCCURS ON THIRD ITERATION

Scientific
Research
Associates

SIMPLIFICATION AND ANALYSIS

- SUBTRACT 1ST STEP FROM 2ND STEP (REPLACES 2ND STEP)
 $(\phi^{**} - \phi^*) / \Delta t = D_y (\phi^{**} - \phi^n)$
- REWRITE 1ST STEP AS:
 $(1 - \beta \Delta t D_x) (\phi^* - \phi^n) = \Delta t D \phi^n$
- REWRITE 2ND STEP AS:
 $(1 - \beta \Delta t D_y) (\phi^{**} - \phi^n) = \phi^* - \phi^n$
- COMBINE TO ELIMINATE $(\phi^* - \phi^n)$:
 $(1 - \beta \Delta t D_x) (1 - \beta \Delta t D_y) (\phi^{**} - \phi^n) = \Delta t D \phi^n$
- REWRITE ORIGINAL UNSPLIT EQUATION:
 $(1 - \beta \Delta t D) (\phi^{n+1} - \phi^n) = \Delta t D \phi^n$
- EXPAND FACTORS IN ADI SCHEME:
 $(1 - \beta \Delta t D) (\phi^{**} - \phi^n) = \Delta t D \phi^n - (\beta \Delta t^2) D_x D_y (\phi^{**} - \phi^n)$
- SPLITTING ERROR IS $O(\Delta t^2)$ AND DOES NOT INCREASE ORDER OF TIME TRUNCATION ERROR. DISAPPEARS WHEN $\phi^{**} = \phi^n$
- STEADY SOLUTION HAS $\phi^{n+1} = \phi^{**} = \phi^* = \phi^n$

} THIS FORM OF THE
ALGORITHM IS
ACTUALLY SOLVED

Scientific
Research
Associates

LINEARIZED BLOCK IMPLICIT (LBI) SCHEMES

- SYSTEMATIC SOLUTION PROCEDURE FOR SYSTEMS OF
- COUPLED NONLINEAR PDE'S
 EFFICIENT STABLE NONITERATIVE SOLUTION
 OF "NONELLIPTIC" SYSTEMS
 EFFICIENT RAPIDLY-CONVERGING ITERATION
 FOR "ELLIPTIC" SYSTEMS
- OUTLINE OF LBI SCHEME:
 IMPLICIT TIME-DEPENDENT FORMULATION
 LOCAL TIME LINEARIZATION
 BLOCK FORMULATION
 CONSISTENT SPLITTING
 BLOCK ADI

Scientific
Research
Associates

- SPLITTING OF THE L OPERATOR:

$$L = L_x + L_y + L_{xy}$$

- NEGLECTING L_{xy} DOES NOT AFFECT STABILITY OR CONSISTENCY

- UNSPLIT LBI SCHEME BECOMES:

$$[A - \beta \Delta t (L_x + L_y)](\Phi^{n+1} - \Phi^n) = \Delta t (D^n + S^n)$$

- SPLIT LBI SCHEME (DOUGLAS-GUNN SPLITTING)

$$(A - \beta \Delta t L_x)(\Phi^* - \Phi^n) = \Delta t (D^n + S^n)$$

$$(A - \beta \Delta t L_y)(\Phi^{**} - \Phi^n) = A(\Phi^* - \Phi^n)$$

} EACH STEP IS
(m x m) BLOCK
TRIDIAGONAL

- COMBINED FORM (APPROXIMATE FACTORIZATION) OF LBI SCHEME

$$(A - \beta \Delta t L_x) A^{-1} (A - \beta \Delta t L_y)(\Phi^{**} - \Phi^n) = \Delta t (D^n + S^n)$$

- SPLITTING (FACTORIZATION) ERROR IS

$$(\beta \Delta t)^2 L_x A^{-1} L_y (\Phi^{**} - \Phi^n)$$

- IF A^{-1} IS SINGULAR, METHOD CANNOT BE APPLIED TO COMPLETE SYSTEM
ADD TIME DERIVATIVES AND ITERATE
PARTITION, DECOUPLE, SOLVE SEQUENTIALLY

Scientific
Research
Associates

BOUNDARY CONDITIONS

- NO SLIP CONDITIONS

- a) SET STREAMWISE VELOCITY TO ZERO

} STREAMWISE
MOMENTUM
EQUATION

- b) SET NORMAL GRADIENT OF ϕ TO ZERO
 \Rightarrow NORMAL ϕ -VELOCITY ZERO
TANGENTIAL ϕ -VELOCITY IN GENERAL NON-ZERO

} SCALAR
POTENTIAL
EQUATION

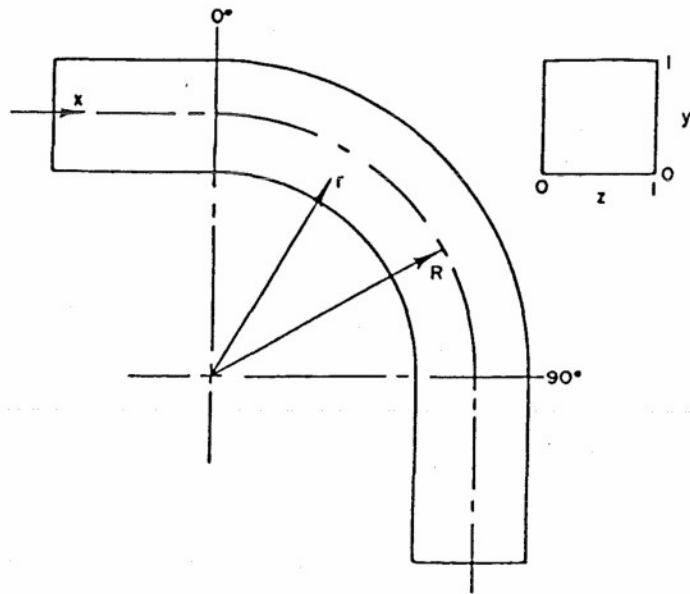
- c) SET ψ CONSTANT (ZERO)

} VECTOR
POTENTIAL
VORTICITY
EQUATIONS

- d) COMPUTE WALL VORTICITY SUCH THAT COMPOSITE
TRANSVERSE VELOCITY IS ZERO

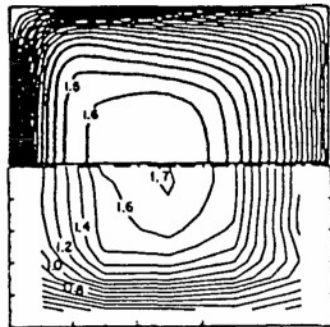
Scientific
Research
Associates

90 DEGREE BEND GEOMETRY

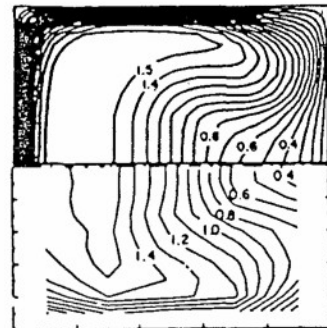


Scientific
Research
Associates

90 DEGREE BEND STREAMWISE VELOCITY

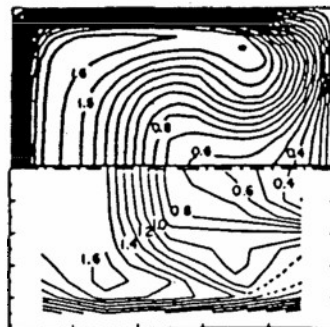


(a). 30°

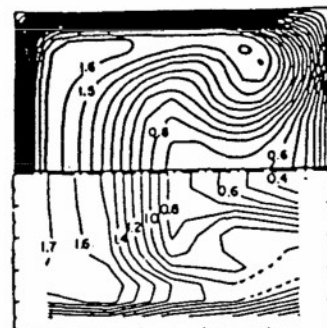


(b). 60°

PREDICTED



(c). 77.5°



(d). 90°

MEASURED

Scientific
Research
Associates

REPORT DOCUMENTATION PAGE

1. Recipient's Reference	2. Originator's Reference	3. Further Reference	4. Security Classification of Document						
	AGARD-R-741	ISBN 92-835-0407-0	UNCLASSIFIED						
5. Originator	Advisory Group for Aerospace Research and Development North Atlantic Treaty Organization 7 rue Ancelle, 92200 Neuilly sur Seine, France								
6. Title	COMPUTATION OF THREE-DIMENSIONAL BOUNDARY LAYERS INCLUDING SEPARATION								
7. Presented at									
8. Author(s)/Editor(s)	Various		9. Date February 1987						
10. Author's/Editor's Address	Various		11. Pages 218						
12. Distribution Statement	This document is distributed in accordance with AGARD policies and regulations, which are outlined on the Outside Back Covers of all AGARD publications.								
13. Keywords/Descriptors									
<table border="0"> <tr> <td>Aerodynamic characteristics</td> <td>Boundary layer transition</td> </tr> <tr> <td>Boundary layer flow</td> <td>Turbulent flow</td> </tr> <tr> <td>Boundary layer separation</td> <td>Mathematical models</td> </tr> </table>				Aerodynamic characteristics	Boundary layer transition	Boundary layer flow	Turbulent flow	Boundary layer separation	Mathematical models
Aerodynamic characteristics	Boundary layer transition								
Boundary layer flow	Turbulent flow								
Boundary layer separation	Mathematical models								
14. Abstract									
<p>The Special Course on Computation of Three-Dimensional Boundary Layers Including Separation was sponsored by the AGARD Fluid Dynamics Panel and the von Kármán Institute and presented at the von Kármán Institute, Rhode-Saint-Genèse, Belgium, on 14—18 April 1986.</p> <p>The Course presented a comprehensive review of experimental aspects of three-dimensional boundary layers with emphasis on the use of fundamental experiments to improve models for turbulence and transition. A review of various calculation methods was given, including the calculation of transition and calculations which aid in aerodynamic design. Numerical differential methods were discussed and viscous-inviscid interactive schemes and procedures were reviewed. Calculations of corner and tip region flows was covered in detail.</p>									

<p>AGARD Report No.741 Advisory Group for Aerospace Research and Development, NATO COMPUTATION OF THREE-DIMENSIONAL BOUNDARY LAYERS INCLUDING SEPARATION Published February 1987 218 pages</p> <p>The Special Course on Computation of Three-Dimensional Boundary Layers Including Separation was sponsored by the AGARD Fluid Dynamics Panel and the von Kármán Institute and presented at the von Kármán Institute, Rhode-Saint-Genèse, Belgium, on 14—18 April 1986.</p> <p>The Course presented a comprehensive review of</p> <p>P.T.O</p>	<p>AGARD-R-741</p> <p>Aerodynamic characteristics Boundary layer flow Boundary layer separation Boundary layer transition Turbulent flow Mathematical models</p>	<p>AGARD Report No.741 Advisory Group for Aerospace Research and Development, NATO COMPUTATION OF THREE-DIMENSIONAL BOUNDARY LAYERS INCLUDING SEPARATION Published February 1987 218 pages</p> <p>The Special Course on Computation of Three-Dimensional Boundary Layers Including Separation was sponsored by the AGARD Fluid Dynamics Panel and the von Kármán Institute and presented at the von Kármán Institute, Rhode-Saint-Genèse, Belgium, on 14—18 April 1986.</p> <p>The Course presented a comprehensive review of</p> <p>P.T.O</p>	<p>AGARD-R-741</p> <p>Aerodynamic characteristics Boundary layer flow Boundary layer separation Boundary layer transition Turbulent flow Mathematical models</p>
<p>AGARD Report No.741 Advisory Group for Aerospace Research and Development, NATO COMPUTATION OF THREE-DIMENSIONAL BOUNDARY LAYERS INCLUDING SEPARATION Published February 1987 218 pages</p> <p>The Special Course on Computation of Three-Dimensional Boundary Layers Including Separation was sponsored by the AGARD Fluid Dynamics Panel and the von Kármán Institute and presented at the von Kármán Institute, Rhode-Saint-Genèse, Belgium, on 14—18 April 1986.</p> <p>The Course presented a comprehensive review of</p> <p>P.T.O</p>	<p>AGARD-R-741</p> <p>Aerodynamic characteristics Boundary layer flow Boundary layer separation Boundary layer transition Turbulent flow Mathematical models</p>	<p>AGARD Report No.741 Advisory Group for Aerospace Research and Development, NATO COMPUTATION OF THREE-DIMENSIONAL BOUNDARY LAYERS INCLUDING SEPARATION Published February 1987 218 pages</p> <p>The Special Course on Computation of Three-Dimensional Boundary Layers Including Separation was sponsored by the AGARD Fluid Dynamics Panel and the von Kármán Institute and presented at the von Kármán Institute, Rhode-Saint-Genèse, Belgium, on 14—18 April 1986.</p> <p>The Course presented a comprehensive review of</p> <p>P.T.O</p>	<p>AGARD-R-741</p> <p>Aerodynamic characteristics Boundary layer flow Boundary layer separation Boundary layer transition Turbulent flow Mathematical models</p>

experimental aspects of three-dimensional boundary layers with emphasis on the use of fundamental experiments to improve models for turbulence and transition. A review of various calculation methods was given, including the calculation of transition and calculations which aid in aerodynamic design. Numerical differential methods were discussed and viscous-inviscid interactive schemes and procedures were reviewed. Calculations of corner and tip region flows was covered in detail.

ISBN 92-835-0407-0

experimental aspects of three-dimensional boundary layers with emphasis on the use of fundamental experiments to improve models for turbulence and transition. A review of various calculation methods was given, including the calculation of transition and calculations which aid in aerodynamic design. Numerical differential methods were discussed and viscous-inviscid interactive schemes and procedures were reviewed. Calculations of corner and tip region flows was covered in detail.

ISBN 92-835-0407-0

experimental aspects of three-dimensional boundary layers with emphasis on the use of fundamental experiments to improve models for turbulence and transition. A review of various calculation methods was given, including the calculation of transition and calculations which aid in aerodynamic design. Numerical differential methods were discussed and viscous-inviscid interactive schemes and procedures were reviewed. Calculations of corner and tip region flows was covered in detail.

ISBN 92-835-0407-0

experimental aspects of three-dimensional boundary layers with emphasis on the use of fundamental experiments to improve models for turbulence and transition. A review of various calculation methods was given, including the calculation of transition and calculations which aid in aerodynamic design. Numerical differential methods were discussed and viscous-inviscid interactive schemes and procedures were reviewed. Calculations of corner and tip region flows was covered in detail.

ISBN 92-835-0407-0

AGARD

NATO  OTAN

7 rue Ancelle • 92200 NEUILLY-SUR-SEINE
FRANCE

Telephone (1)47.38.57.00 • Telex 610 176

**DISTRIBUTION OF UNCLASSIFIED
AGARD PUBLICATIONS**

AGARD does NOT hold stocks of AGARD publications at the above address for general distribution. Initial distribution of AGARD publications is made to AGARD Member Nations through the following National Distribution Centres. Further copies are sometimes available from these Centres, but if not may be purchased in Microfiche or Photocopy form from the Purchase Agencies listed below.

NATIONAL DISTRIBUTION CENTRES

BELGIUM

Coordonnateur AGARD — VSL
Etat-Major de la Force Aérienne
Quartier Reine Elisabeth
Rue d'Evere, 1140 Bruxelles

ITALY

Aeronautica Militare
Ufficio del Delegato Nazionale all'AGARD
3 Piazzale Adenauer
00144 Roma/EUR

CANADA

Defence Scientific I
Dept of National D
Ottawa, Ontario K1



National Aeronautics and
Space Administration

Washington, D.C.
20546

**SPECIAL FOURTH CLASS MAIL
BOOK**

Postage and Fees Paid
National Aeronautics and
Space Administration
NASA-451

Official Business
Penalty for Private Use \$300



DENMARK

Danish Defence Res
Ved Idraetsparken
2100 Copenhagen C

FRANCE

O.N.E.R.A. (Directi
29 Avenue de la Di
92320 Châtillon

5 1 4B,4, 870325 A05101DU
DEPT OF THE AIR FORCE
ARNOLD ENG DEVELOPMENT CTR (AFSC)/DOT/
ATTN: DR MARION L LASTER
DIR OF TECHNOLOGY
ARNOLD AF STA TN 37389

GERMANY

Fachinformationsze
Physik, Mathematik
Kernforschungszent
D-7514 Eggenstein

GREECE

Hellenic Air Force
Research and Develo
Holargos, Athens

ICELAND

Director of Aviation
c/o Flugrad
Reykjavik

ANKARA

UNITED KINGDOM

Defence Research Information Centre
Kentigern House
65 Brown Street
Glasgow G2 8EX

UNITED STATES

National Aeronautics and Space Administration (NASA)
Langley Research Center
M/S 180
Hampton, Virginia 23665

THE UNITED STATES NATIONAL DISTRIBUTION CENTRE (NASA) DOES NOT HOLD STOCKS OF AGARD PUBLICATIONS, AND APPLICATIONS FOR COPIES SHOULD BE MADE DIRECT TO THE NATIONAL TECHNICAL INFORMATION SERVICE (NTIS) AT THE ADDRESS BELOW.

PURCHASE AGENCIES

National Technical
Information Service (NTIS)
5285 Port Royal Road
Springfield
Virginia 22161, USA

ESA/Information Retrieval Service
European Space Agency
10, rue Mario Nikis
75015 Paris, France

The British Library
Document Supply Division
Boston Spa, Wetherby
West Yorkshire LS23 7BQ
England

Requests for microfiche or photocopies of AGARD documents should include the AGARD serial number, title, author or editor, and publication date. Requests to NTIS should include the NASA accession report number. Full bibliographical references and abstracts of AGARD publications are given in the following journals:

Scientific and Technical Aerospace Reports (STAR)
published by NASA Scientific and Technical
Information Branch
NASA Headquarters (NIT-40)
Washington D.C. 20546, USA

Government Reports Announcements (GRA)
published by the National Technical
Information Services, Springfield
Virginia 22161, USA



Printed by Specialised Printing Services Limited
40 Chigwell Lane, Loughton, Essex IG10 3TZ